GIS-based Analysis of Geo-Potentials for a Tropical Metropolitan Area: the Northern Periphery of Belo Horizonte (Minas Gerais, Brazil)

PhD-Thesis

Genehmigte Dissertation am
Fachbereich Material- und Geowissenschaften
der Technischen Universität Darmstadt
zur Erlangung des akademischen Grades
Doktor der Naturwissenschaften (Dr. rer. nat.)

TECHNISCHE UNIVERSITÄT DARMSTADT

Vorgelegt von
Diplom Geoökologin Monika Hofmann
geboren am 01.11.1977 in Aschaffenburg

Erstreferent: Prof. Dr. Andreas Hoppe
Korreferent: Prof. Dr. Joachim Karfunkel

Tag der Einreichung: 14.10.2013
Tag der Disputation: 15.11.2013

Darmstadt 2014

D17

Abstract

For a sustainable, resource-protecting and participatory land use planning, an easily understandable visualization of geo-scientific factors is important, since only then these data can be accessed by a large group of decision makers and stake holders.

The present study aims at supplying this information for the northern periphery of Belo Horizonte, which is under strong pressure of urbanization.

In a base step, available geo-scientific data for the study area around the city of Lagoa Santa were collected and checked for consistency. Excursions and field studies supplemented the analysis of literature data.

Based on this information, the geological map was updated and the weathering depth and thickness of geological strata estimated. Using a descriptive concept of geology-soil-landscape interrelation, maps of hydrological soil properties were derived. During this process, a detailed analysis of relief structures played an important part.

From these geological and pedological base data, several maps of easily interpretable parameters were derived that are relevant for land use planning. Among these are maps showing the intrinsic vulnerability of the aquifer, the distribution of mass resources for construction, areas of high agricultural value and hazard maps with a focus on erosion and pollution of surface water.

In total, nearly 90 maps of geo-scientific parameters were derived, among which about one third are aggregated thematic maps that can be directly included into the land use decision process. The rest of the maps display base data regarding relief, geology, hydrology and soil science.

The data base of the project and the workflow for the regionalization of the geo-scientific parameters are transparently documented and stored in a Geo-Information-System (GIS). This allows for inclusion of new data into the algorithms and an easy update of the generated thematic maps.

Extended Abstract

Geo-potentials, which are **resources and hazards** controlled by the geological underground, are important factors for a sustainable urban development. The display of geo-potentials in thematic maps allows their integration in decision making and thus facilitates a sustainable, resource-protecting and participatory land use planning. The present project supplies an atlas of such maps for a study area of 400 km² in the northern periphery of Belo Horizonte, which is the fast growing capital of the state Minas Gerais in SE Brazil with over five Million inhabitants in its metropolitan region. The geological underground of the study area is composed of a more or less flat lying sequence of Late Proterozoic limestone – marl-alternations covered in places by tropical weathering products of various thicknesses.

The following geo-potentials play an important role in the area:

In an intensely karstified zone, a potent aquifer is highly vulnerable to pollution. Its protection competes with the exploitation of karst outcrops in profitable limestone quarries and with agriculture on fertile soils near doline bottoms. In alluvial plains of the Riberão da Mata, a small tributary of the Rio das Velhas, exploitation of sand resources interferes with other land use projects. Hills composed of deeply weathered pelite or basement rocks are often cut by deep gullies and in the whole study area, increased sealing quickly changes the catchment hydrology. Since the urban area is only partly connected to sanitation systems, pollution of surface and subsurface water is also an important issue.

To integrate these geo-potentials into land use decision making, over 90 **thematic maps** have been created **inside a flexible GIS** (Geo-Information-System). Data scarcity, especially regarding high resolution pedologic and geological information, lead to the following **methodology**:

After a consistency check between the topographic map (1:25.000) and the geological map (1:50.000), both were combined to regionalize soil information that is relevant for catchment hydrology and for groundwater protection. As a regionalization method, an expert-knowledge based “Semantic Import Model” was chosen. This method transfers knowledge gained from field and literature studies into a rule based reasoning algorithm that automatically generates maps of the desired output parameters. The topographic input parameters include slope, topographic position, elevation above and distance to surface water, basin delineation, specific catchment area, wetness index and stream power index. From the geological map, the interpolated thickness of the lithological strata and their typical properties were included in the regionalization process. Among the derived pedological parameters are the depth of highly permeable red topsoil layer, hydrological soil class, degree of lateral flow, hydromorphic soils, effective field capacity, base saturation, soil erodibility, risk of near surface epikarst and weathering depth.

During the regionalization process, the output maps were recursively checked by a plausibility analysis using intrinsic knowledge from field experience and information provided by Google Earth.

Out of these intermediate parameters, the following maps of geo-potentials were created:

Groundwater vulnerability was estimated based on of the protection by overlying strata combined with the risk of bypassing these layers by lateral flow into ponors.

The protection map uses a point score system that evaluates the protective function of each stratum. The second map focuses on the degree of lateral flow in catchments of sinking streams and uses values ranging from 0 to 1. For the final map of intrinsic groundwater vulnerability, both maps are multiplied. It is important to note that every sealed area with uncontrolled runoff close to an entrance point into the karst aquifer will automatically pose a high risk for its pollution. Thus, integration of current and high resolution land use data will probably increase the vulnerability in the karst area considerably due to better identification of areas with high surface runoff.

Limestone resources and their accessibility were estimated by a weighted overlay of the thickness of overburden and the thickness of limestone resources. For definite project decisions, this map needs to be combined with other parameters, especially from the ecological and archeological perspective.

Sand resources in the area are restricted to Quaternary sediments especially in the alluvial plains of the Riberão da Mata, where their extraction in open pit mines consumes large areas. In a case study covering 6,6 km² in the central part of the alluvial plain, about 2,5 km² had been altered by sand extraction in the last 40 years. Additionally, the quantity of available sand resources was estimated based on sedimentary structures and a GIS-based volume calculation of the Quaternary sediments.

Agricultural value is primarily related to the chemical soil properties, which are the most important parameters in deeply weathered tropical soils. This variable was estimated based on combinations of topographical and hydrological conditions and favorable lithology. The resulting map shows soils with highest natural fertility in the karst area, especially near doline bottoms. Including a restriction to flat areas to avoid severe erosion problems, lowlands on carbonates were identified as the most favorable locations for agriculture.

Gully erosion hazard was estimated based on findings from regional geomorphological studies. If surface erosion cuts the protecting soil cover and colluvium, erosion quickly progresses into the erodible saprolite, especially if a zone of subsurface flow or even a regional aquifer is reached. Thus, for the prediction of gully erosion hazard, the problem was divided into two sub-processes: The first one focuses on processes that remove the protecting topsoil cover, especially on concentrated surface flow and small landslides that may act as trigger.

The second process focuses on gully propagation, for which the most important parameters include concentration of subsurface flow, depth of saprolite, location inside a headwater hollow and the existence of a temporary aquifer.

For both processes, the effect of concentrated surface and subsurface flow was derived using a modified topographic threshold method based on drainage area and slope. The modification consisted of calculating a weighted drainage area that includes the relative amount of surface or subsurface flow in each raster cell.

For the final map on gully erosion hazard, both maps were combined, with the risk of gully propagation receiving a higher importance than the risk of gully initiation. The protecting function of land use was added to this map only at the latest step since the available land use database was of a comparatively low resolution.

The risk of **surface water contamination** by rain-wash was calculated independently of polluting sources since this information was not available. Instead, only the hydrological closeness to water courses including the degree of lateral flow was used for the regionalization rule. Thus, if a polluting source is identified, this map yields the information how quickly it will reach the next water course.

While the maps of geo-potentials are designed to be understandable for all stakeholders, their creation process is documented in GIS tools and thus accessible and modifiable for experts. This provides the **possibility for updates and integration of new data,** so that the maps can always reflect the current state of knowledge. For actual land use planning issues, the GIS can be used to compare the geo-scientific information in a Spatial Decision Support System (SDSS) with maps of infrastructure, social factors, current land use and biotic habitats to detect areas of potential conflicts and help to solve them in an objective way.

For **future investigations**, a field validation of the regionalization rules and the integration of recent and high resolution land use data is suggested. The later would especially improve the maps on groundwater vulnerability and gully erosion hazard.

Zusammenfassung

Für eine nachhaltige, ressourcenschonende und partizipatorische Landnutzungsplanung ist die allgemeinverständliche Aufbereitung geowissenschaftlicher Faktoren wichtig, denn nur dann sind diese Informationen einem breiten Kreis an Entscheidungsträgern und Interessengruppen zugänglich. Die vorliegende Studie möchte dabei helfen, dies für die unter starkem Siedlungsdruck stehende nördliche Peripherie der Brasilianischen Metropole Belo Horizonte zu realisieren.

Für das Projektgebiet um die Stadt Lagoa Santa wurden zunächst die verfügbaren geowissenschaftlichen Daten zusammengetragen und auf ihre Konsistenz überprüft. Exkursionen und Studien im Gelände ergänzten die Literaturanalyse.

Aus den vorhandenen Informationen wurde die geologische Karte überarbeitet und die Mächtigkeit der Verwitterungsdecke und der Gesteinsschichten geschätzt. Mit Hilfe eines beschreibenden Geologie-Boden-Landschafts-Konzepts wurden Karten hydrologischer Bodenparameter erstellt. Dabei spielte die detaillierte Analyse des Reliefs eine wichtige Rolle.

Aus den geologischen und bodenkundlichen Grunddaten wurden anschließend mehrere allgemeinverständliche Karten planungsrelevanter Parameter abgeleitet. Dazu gehören Karten zur intrinsischen Vulnerabilität des Grundwassers, der Verteilung der Ressourcen für Baustoffe und für landwirtschaftliche Nutzung sowie Risikokarten bezüglich linearer Erosion und Verschmutzung des Oberflächenwassers.

Insgesamt wurden so knapp 90 Karten zu auf einander aufbauenden geowissenschaftlichen Parametern erstellt. Von diesen Karten sind etwa ein Drittel stärker aggregierte Daten, die direkt in den Entscheidungsprozess zu Landnutzungsfragen einbezogen werden können während der Rest aus Basisdaten zu Relief, Geologie, Hydrologie und Bodenkunde besteht.

Die Daten des Projekts sowie die Programme zur Regionalisierung der geowissenschaftlichen Parameter wurden transparent dokumentiert und mit Hilfe eines Geo-Informations-System (GIS) gespeichert. Dadurch bleibt die Möglichkeit bestehen, bei Vorliegen neuer Informationen diese in dem Algorithmus einzuarbeiten und die erstellten thematischen Karten ohne großen Aufwand zu aktualisieren.

Erweiterte Zusammenfassung

Geo-Potentiale, also durch geologische Gegebenheiten bedingte **Ressourcen und Risiken**, sind wichtige Faktoren für eine nachhaltige Stadtentwicklung. Ihre Darstellung in thematischen Karten ermöglicht es, Geo-Potentiale bei Entscheidungen zu berücksichtigen und unterstützt auf diese Weise eine nachhaltige, ressourcenschonende und partizipatorische Landnutzungsplanung.
Das vorliegende Projekt bietet einen Atlas dieser Karten für ein 400 km² umfassendes Gebiet in der nördlichen Peripherie von Belo Horizonte, der schnell wachsenden Hauptstadt des Staates Minas Gerais in SO-Brasilien mit derzeit über fünf Millionen Einwohnern im Ballungszentrum. Der geologische Untergrund des Projektgebiets besteht aus einer Abfolge von mehr oder weniger flach liegenden Spätproterozoischen Kalk-Mergel Schichten, die von einer tropischen Verwitterungsdecke von unterschiedlicher Mächtigkeit bedeckt sind. In diesem Gebiet spielen die folgenden Geo-Potentiale eine wichtige Rolle:
In einem stark verkarsteten Bereich gibt es einen ergiebigen aber sehr verschmutzungsempfindlichen Aquifer. Der Schutz dieses Grundwasserkörpers konkurriert mit der Nutzung der Karst-Aufschlüsse in profitablen Kalksteinbrüchen und mit der Landwirtschaft auf den fruchtbaren Böden der Dolinen. In den Schwemmebenen des Riberão da Mata, einem kleinen Nebenfluss des Rio das Velhas, beeinflusst der Abbau von Sandressourcen die weitere Nutzung des Standorts. Hügelige Bereiche aus tiefgründig verwittertem Pelit- und Grundgebirgsgestein sind oft von tiefen Gullies durchschnitten und im ganzen Projektgebiet führt eine fortschreitende Versiegelung zu einer Veränderung des Abflussverhaltens. Da die urbanisierten Gebiete nur teilweise an ein Abwassersystem angeschlossen sind, ist auch die daraus resultierende Verschmutzung von Oberflächen- und Grundwasser ein wichtiges Thema. Insgesamt wurden in der Arbeit über 90 **thematische Karten** mit Hilfe eines **flexiblen GIS** (Geo-Information-System) generiert.
Die besonders hinsichtlich detaillierter bodenkundlicher und geologischer Information knappe Datengrundlage führte zu folgender **Methode**:
Nach einem Konsistenzabgleich zwischen topographischer Karte (1 : 25 000) und geologischer Karte (1 : 50 000) wurden aus beiden bodenhydrologische Informationen abgeleitet, die wichtig für das Abflussverhalten und den Grundwasserschutz sind. Als Regionalisierungsmethode wurde ein Experten-basiertes „Semantic Import Model“ verwendet. Diese Methode transferiert das Wissen aus Gelände- und Literaturstudien in einen regelbasierten Algorithmus, mithilfe dessen automatisch Karten der gewünschten Parameter erzeugt werden. Die topographischen Eingangsparameter sind Hangneigung, Hangposition, Höhe über und Entfernung zu Oberflächengewässern, Abgrenzungen lokaler Einzugsgebiete, spezifisches Einzugsgebiet für jede Zelle, Wetness-Index und Stream-Power-Index. Von der geologischen Karte wurden die interpolierte Mächtigkeit der Schichten sowie deren typische Eigenschaften einbezogen. Die abgeleiteten Bodenparameter umfassen die Tiefe des hochpermeablen roten Oberbodens,

hydrologische Bodenklasse, Anteil der lateralen Wasserbewegung, hydromorphe Böden, effektive Feldkapazität, Basensättigung, Erodibilität, Risiko von oberflächennahem Epikarst und Verwitterungstiefe. Während des Regionalisierungsprozesses wurden die erstellten Karten immer wieder hinsichtlich ihrer Plausibilität im Vergleich zu Geländeerfahrungen und zu Satellitenbildern von Google Earth überprüft.

Aus diesen intermediären Parametern wurden anschließend thematische Karten von Geo-Potentialen erstellt:

Die **Grundwasservulnerabilität** wurde aus der Schutzfunktion der Deckschichten und dem Risiko einer Kontamination durch Oberflächenabfluss in Ponore abgeleitet. Während die erste Karte ein Punktesystem benutzt, das die Schutzwirkung jeder einzelnen Schicht bewertet, berücksichtigt die zweite Karte den Anteil an lateraler Wasserbewegung im Karst-Oberflächen-einzugsgebiet und nimmt Werte zwischen 0 und 1 an. Für die endgültige Karte der intrinsischen Grundwasservulnerabilität wurden beide Karten miteinander multipliziert. Bei der abschließenden Beurteilung muss berücksichtigt werden, dass jede versiegelte Fläche mit unkontrolliertem Abfluss in hydrologischer Nähe zu einem Ponor automatisch eine Fläche mit hohem Gefährdungspotential darstellt. Aus diesem Grund würde die Einbeziehung aktueller und hoch auflösender Landnutzungsdaten eine höhere Vulnerabilität im Karstgebiet ausweisen, da in diesem Fall Gebiete mit hohem Oberflächenabfluss besser identifiziert werden können.

Kalkstein Ressourcen und ihre Verfügbarkeit wurden durch eine gewichtete Verschneidung der Überdeckung und der Mächtigkeit der Kalksteinschichten bewertet. Für konkrete Projektentscheidungen muss diese Karte noch mit anderen Parametern kombiniert werden, besonders aus ökologischer und archäologischer Perspektive.

Sand Ressourcen sind im Arbeitsgebiet auf Quartäre Ablagerungssysteme beschränkt, besonders entlang des Riberão da Mata, wo der Sandabbau große Flächen beansprucht. In einer Studie über 6,6 km² im breitesten Abschnitt der Schwemmebene des Riberão da Mata wurde in den letzten 40 Jahren etwa 2,5 km² durch Sandabbau verändert. Auch das Volumen noch verfügbarer Sandressourcen wurde geschätzt, basierend auf den Sedimentstrukturen und einer GIS-basierten Volumenberechnung der Quartären Sedimente.

Die **landwirtschaftliche Nutzbarkeit** hängt in dem tiefgründig verwitterten tropischen Gebiet in erster Linie von den chemischen Bodeneigenschaften ab. Diese wurden aus Überlegungen zu topographischen und hydrologischen Bedingungen sowie zu günstigem Ausgangsgestein abgeleitet. Die resultierende Karte zeigt die höchste natürliche Bodenfruchtbarkeit im Karstgebiet, besonders am Grund von Dolinen. Berücksichtigt man noch eine Einschränkung auf flache Gebiete zur Vermeidung von starker Erosion, so sind die flachen Niederungen im Karstgebiet die Flächen mit der höchsten landwirtschaftlichen Eignung.

Die Schätzung des Risikos von tiefer **Gully Erosion** basiert auf Ergebnissen von regionalen geomorphologischen Studien. Sobald die Oberflächenerosion die schützende Bodenschicht

durchschneidet, schreitet sie im leicht erodierbaren Saprolit schnell in die Tiefe voran, besonders wenn eine Zone von hohem Zwischenschichtabfluss oder ein regionaler Aquifer erreicht wird. Aus diesem Grund wurde die Bewertung des Gully Erosionsrisikos in zwei Schritte unterteilt:
Der erste Schritt beschreibt Prozesse, die dazu führen dass die schützende Oberbodenschicht abgetragen wird. Dazu zählen konzentrierter Oberflächenabfluss und lokale Hangrutschungen, die als Trigger für die Gully-Entstehung dienen können.
Der zweite Schritt beschreibt Prozesse, die zur weiteren Eintiefung eines Gullies führen. Die wichtigsten Parameter hierfür sind konzentrierter Zwischenschichtabfluss, Mächtigkeit des Saprolits, Lage in einem „headwater hollow“ und die Existenz eines temporären Aquifers.
Bei beiden Prozessen wurde der Effekt von konzentriertem Oberflächen- und Zwischenschichtabfluss durch eine Variante der „topographic threshold“-Methode modelliert, die Einzugsgebiet und Hangneigung zu einem Schwellenwert kombiniert. Dabei wurde das Einzugsgebiet hinsichtlich des Anteils an Oberflächen bzw. Zwischenschichtabfluss gewichtet.
Für die abschließende Bewertung des Gully-Erosionsrisikos wurden beide Karten kombiniert, wobei dem Risiko der Gully-Eintiefung ein höheres Gewicht zugewiesen wurde als dem Risiko der Gully Initialisierung. Die schützende Funktion der Landnutzung wurde nur in einem letzten Schritt hinzugefügt, da hierfür die Datenbasis eine zu schlechte Auflösung hatte.
Das Risiko einer **Kontamination von Oberflächengewässern** durch Oberflächenabfluss wurde unabhängig von einer Verschmutzungsquelle berechnet, da hierzu keine Informationen verfügbar waren. Stattdessen wurde nur die hydrologische Nähe zu Oberflächengewässern zusammen mit dem Anteil an lateraler Bodenwasserbewegung als Eingangsparameter verwendet. Sobald also eine Verschmutzungsquelle identifiziert ist, zeigt diese Karte, wie schnell das nächste Oberflächengewässer erreicht wird.
Während diese Geo-Potentialkarten für alle Interessengruppen verständlich dargestellt sind, ist ihr Entstehungsprozess in GIS-Werkzeugen dokumentiert und dadurch zugänglich und modifizierbar. Dies schafft die **Möglichkeit für Updates und die Integration neuer Daten**, so dass die Karten immer den aktuellen Wissensstand reflektieren können.
Für konkrete Landnutzungsprojekte kann die GIS-Umgebung auch für eine Verschneidung der geowissenschaftlichen Informationenmit Karten der Infrastruktur, sozialen Faktoren, aktueller Landnutzung und biotischen Faktoren genutzt werden. So können mit Hilfe eines Spatial Decision Support System (SDSS) potentielle Konflikte erkannt und sachlich diskutiert werden.
Eine sinnvolle Erweiterung sind z**ukünftige Studien** zur geländebasierten Validierung und zur Integration von aktuellen, hochauflösenden Landnutzungsdaten. Letzteres würde besonders bei den Karten zur Grundwasservulnerabililtät und zur Prognose des Risikos der Gully-Erosion zu höherer Genauigkeit führen.

Acknowledgements

In the first place I would like to thank my supervisor Prof. Dr. Andreas Hoppe, who initiated and facilitated the project and contributed many helpful suggestions. I am especially grateful that he never lost his faith in the project even during difficult periods.
Equal thanks I owe to Prof. Dr. Joachim Karfunkel, without his strong support I would have been lost in Brazil. Many thanks also to Fatima Karfunkel who was always very welcoming and to Pepi Karfunkel who allowed me to borrow her car for field excursions. Also thanks to the Geologists Allan Büchi and Ricardo Pagung, who accompanied me during field trips and helped in many ways. I would like to thank Wagner, Tatiane, Leticia and Glaucia who welcomed me as a friend in Brazil. I also want to thank Prof. Dr. Heinz Charles Kohler, who helped to initiate the project and introduced me to the geomorphology of the study area.
I am very grateful to the DAAD for the financial support of two trips to Brazil.

Many thanks also to the staff working in the CPRM in Belo Horizonte for the support, interesting discussions and supply of digital data, especially to the geologists Carlos Alberto Heineck, Manoel Pedro Tuller, Maria Antonieta Mourão, Julio Murilo and the geographer Rosângela Gonçalves Bastos Souza.
I would also like to thank the staff at the Prefeitura do Lagoa Santa who provided me in a very uncomplicated way with digital topographic data.

My thanks go also to Dr. Paulo Fernando Pereira Pessoa who showed me interesting aspects of the study area and sent me his PhD thesis. Also many thanks to the geologist Mylena Luiza Cunha Berbert Born who allowed me to accompany her into a cave near Lagoa Santa during her research project, which was a very interesting experience.

I would also like to thank the working group at the TU-Darmstadt, namely geographer Ulrike Simons, Dr. Stefan Lang, Dr. Christian Lerch, Dr. Rouwen Lehné, geographer Constanze Bückner, Dr. Dirk Arndt and geologist Ina Lewin for their interesting discussions and cooperation. Many thanks to Dr.Jens Hornung who helped with the sedimentological interpretation of the alluvial profiles.

And, last but not least, I wish to thank my family who always supported me.
Many thanks to De-In, Emil and Lilo for their patience and especially to my mother in law who looked after the children so many hours while I was sitting at the computer. Without her, this project would not have been possible.

Index

List of figures

List of outcrop photographs

List of tables

List of equations

List of acronyms

AHP = Analytical Hierarchy Process

APA = Area de Proteção Ambiental (Environmental Protection Area)

CEMIG = Compahia Energética de Minas Gerais

CETEC = Fundação Centro Tecnológico de Minas Gerais

COPASA = Companhia de Saneamento de Minas Gerais

CPRM = Serviço Geológico do Brasil, Geological Service of Brazil

DEM = Digital Elevation Model

GIS = Geo-Information System

eCEC = effective Cation Exchange Capacity

eFC = effective Field Capacity

IBAMA = Instituto Brasileiro do Meio Ambiente e dos Recursos Naturais Renováveis (Brazilian Institute of Environment and Renewable Natural Resources)

IGA = Instituto de Geociêncials Aplicadas (Institute of Applied Geosciences)

MaP = Macropores,

MeP = Mesopores

MiP = Micropores

PLAMBEL = Planejamento da Região Metropolitana de Belo Horizonte

PROMETHEE = Preference Ranking Organisation MeTHod for Enrichment Evaluations

WdC = Water dispersible Clay

RMBH = Região Metropolitana de Belo Horizonte

SDSS = Spatial Decision Support System

SIM = Semantic Import Model

SRTM = Shuttle Radar Topographic Mission

TPI = Topographic Position Index

LTPI = Local TPI

MTPI = Medium TPI

RTPI = Regional TPI

RMBH = Região Metropolitana de Belo Horizonte

UFMG = Universidade Federal de Minas Gerais

1 Introduction

1.1 Motivation

1.1.1 Cities and their environment

Cities are no isolated structures but embedded within their natural landscape. From there, they draw their raw materials for existing and growing and into this landscape they dispose of their waste in all its forms. Thus, it is not astonishing that the geological environment and relief of a region has an influence on the character and the development of a city, restricting its growth in one area and favoring it towards another. A good example showing the interrelation of landscape and city is the study of Bückner and Hoppe (2012), which compares two cities – Mainz and Wiesbaden – that are similar only at a first glance but differ on their natural local conditions and also on their intrinsic development, also termed "Eigenlogik" (Berking and Löw 2008, Hoppe 2011).

Of course, with technological advances since the middle of last century, the influence of natural local conditions on urban life is less grave than in former times, where most resources (food, water, raw materials) were needed to be available close to the city and where relief shaped the layout of the city instead of the opposite.

In the age of globalization, technology transfer is very quick and cities become more and more similar all around the world. Besides the loss of local culture and "urbanality" (i.e. city personality, Hoppe (2011)), this global assimilation of city construction bears also risks, especially if the applied technologies are not adapted to local conditions: a drainage system that works well in a temperate region might not be a good solution for a tropical area and housing constructions that are well designed for stable regions may collapse under a medium strong earthquake that happens regularly in another part of the world.

It is important to bear in mind that also today, the influence of geo-potentials (i.e. resources and hazards that are related to local place) on urban development is still there: If mass resources that are needed in large quantities for building the city are sealed and made unavailable, this will result in higher transport costs, often accompanied by a higher impact on the environment. If the groundwater is polluted, other sources for fresh water have to be found, usually at higher costs. If the natural vulnerability to erosion or land sliding is not respected during planning, damage to infrastructure and also threats to people's life can be the result. Industries handling dangerous substances need safe building ground and a buffer distance to ecologically sensitive areas or important natural resources.

Although technological solutions can reduce adverse effects due to unfavorable natural settings (i.e. earth-quake safe buildings, dams in floodplains, geo-engineering for slope stabilization etc.),

this is only possible at elevated costs and resource consumption and needs strict regulations and controls to avoid severe risks.

1.1.2 The concept of sustainability and "good life"

Discussing the human changes of the environment, the concept of sustainability is a central term for evaluating any action. In 1987, the Brundtland report (United Nations 1987) defined a sustainable development as a "development that meets the needs of the present without compromising the ability of future generations to meet their own needs".
This definition has been widely used since and was the basis for several international conferences, with the most well known in Rio de Janeiro (1992) and the most recent again in Rio de Janeiro in 2012. In this last conference, a "Peoples Summit for Social and Environmental Justice" alongside the official United Nations Conference "Rio + 20" drew attention to a new concept: the South-American ideal of "Buen vivir" or "Sumac kawsay" (Fatheuer 2011, Cúpula dos povos 2012), which evades the notion of a linear development towards "having more" but focuses on the attainment of a state of equilibrium that allows a "good life for all", encompassing humans and their environment. The right for a "good life" has even been added into the constitution of Ecuador, which, similarly to the kingdom of Bhutan, seeks to replace the "western" aim of economic growth and accumulation of wealth by a new concept that reflects better the viewpoint of the local people.
Realizing that humans move the same amount of material each year that is moved by geogenic processes such as natural erosion, fluvial transport and subduction of the earth's crust (Wellmer and Becker-Platen 1999, Hoppe 2011), the dimension of human influence on the environment becomes apparent. Also the consumption of raw material has risen so strongly that since the Second World War, more resources have been consumed than in the whole time before (Wellmer and Becker-Platen 1999).
With respect to the human impact on environment and the aim of sustainability and "good life", the wise incorporation of the local geo-scientific parameters into land use planning at an early stage is desirable if not mandatory. Nevertheless, this is only possible, if most environmental factors are known and published in a way that is understandable for all stakeholders.

1.1.3 Thematic maps of geo-potentials for urban planning

Even in "old" industrialized countries such as Germany, where the density of geo-scientific base data is very high, these data are often not incorporated into land use decisions by urban planners. This is often due to the difficult interpretability of geo-scientific maps:
Units displayed in standard geological maps are identified by their age, which needs much expertise to translate into properties that are relevant for land use decisions. Also the information

regarding the three-dimensional architecture of the underground that is indicated in geological maps can be retrieved rarely by non-geoscientists. Also soil maps are very difficult to interpret since their units are defined by a detailed classification system that is based on a lot of background information.
Seeing this, geological surveys in Germany started at the end of last century to supply decision makers with a catalog of thematic maps that are relevant for land use decisions. A good example is the geo-scientific atlas published by Hoppe and Mittelbach (1999) that contains maps of agricultural potential, groundwater vulnerability or availability of resources.
These thematic maps of geo-hazard and geo-resources are also often summarized as geo-potentials (Lerch 2005). If the thematic maps are generated from a data base inside a Geo-Information System (GIS), it has the additional benefit of allowing experts to check on the quality of the base data and interpolation algorithms. With the development of computer based geological analysis tools, also the three-dimensional subsurface architecture can be included into the analysis of geo-potentials. Good examples of informative maps and partly also three-dimensional databases of geo-potentials can be found in Lerch (2005), Lerch and Hoppe (2007), Lamelas et al. (2007), Hoppe et al. (2008), (Lamelas et al. 2008a, 2009), Thapa and Hoppe (2010), Arndt et al. (2011), Bär et al. (2011).

1.1.4 Spatial decision processes

In the stronger growing demand for stakeholder participation in land use decisions, an adequate supply of unbiased, easily understandable display of geo-potentials is essential. In the projects mentioned above, the mean of information transport is in the form of maps, which are direct visual representations of knowledge that is otherwise difficult to transfer and compare due to many technical terms used in other means of communication (Hoppe 2011).
In a multi-stakeholder environment such as urban planning, so called GIS-integrated Spatial Decision Support Systems (SDSS) can superpose the available thematic maps and visualize the spatial output of different priorities of each stakeholder group. Hoppe et al. (2006), Marinoni and Hoppe (2006) and Lamelas et al. (2008b), (2010, 2012) give examples of this process for densely populated areas in Spain and Germany. Using a SDSS, land use decision making can be more participatory while in the same time including all available geo-scientific information.

1.2 The situation in South America

While the cities in central Europe are more or less static or even declining in their population, the cities in newly industrialized countries are growing rapidly. Especially South America has already reached a state of urbanization greater than Europe (Figure 1-1) and its urban population is still growing at an annual rate of 1.6 % (United Nations 2011).

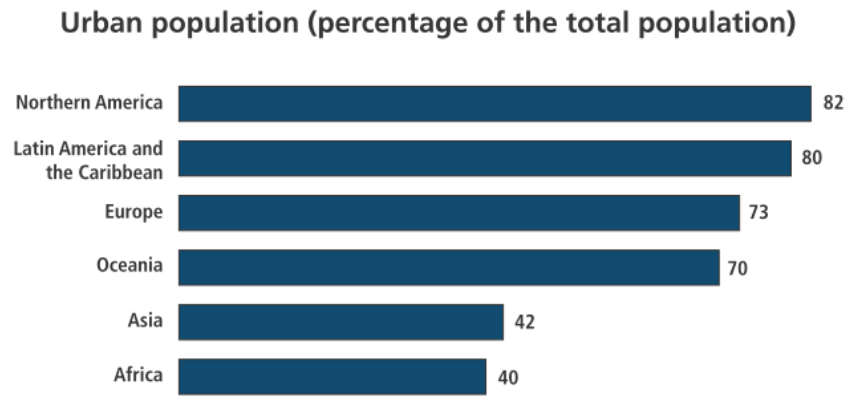

Figure 1-1 Urban population 2010 (United Nations 2011).

With this dynamic urban growth, unplanned settlements are a common feature of South-America's cities. In Brazil, about 29% of the urban population lives in such areas (United Nations 2011).

Since the end of last century, the highest growth rate is found not any more in the largest mega cities with more than 10 Million inhabitants - where life quality has often deteriorated due to uncontrolled growth - but in medium cities between 1 and 5 Million inhabitants (United Nations 2002). Also there, the strongest growth is in the urban periphery instead of in the already highly densified and expensive city centers.

Thus, especially in the urban peripheries, land use conflicts are a typical issue since room for settlement, infrastructure or waste deposits compete with the use of resources (e.g. sand, drinking water) and agriculture.

In the northern periphery of Belo Horizonte (Figure 1-2), dynamic urbanization confronts urban planners with the difficult task of making rapid land use decisions in a multi-stakeholder environment that should also be viable in long term perspective.

The awareness of the importance of geo-data for land use planning is high in Brazil. Although the density of the geo-scientific base data is lower, its interpretation for land use planning is a common procedure. For the study area in the northern periphery of the city of Belo Horizonte, already two compendia of geo-scientific thematic maps were available at the beginning of the current project (CPRM and CETEC 1994, CPRM and IBAMA 1998), also including detailed zonation rules for land use restriction.

Figure 1-2 Location of Belo Horizonte in South-America.

Modified open source image from:
http://www.mygeo.info/landkarten/brasilien/brasilien_topographie_staedte.jpg

1.3 Aim and structure of the study

The aim of the current study is to generate thematic maps of geo-resources and geo-hazards that can be the basis for sustainable urban planning, especially as input for a SDSS. Taking into account the existing compendia of thematic maps, the translation and interpretation of already available geo-scientific data could not be the only focus. Instead, a complete workflow from the analysis and enlargement of the geo-scientific data base until the regionalization of new geo-scientific parameters was designed for the project.

The structure of the study is summarized as follows:

- Chapter 2 gives an overview of the study area and its geo-potentials, including also two case studies, one on the exploitation of sand resources and the other one on gully erosion.
- Chapter 3 describes the applied methodology for deriving geo-scientific thematic maps.
- Since the methodology is based on a good understanding of the geological setting and landscape evolution, chapter 4 to chapter 6 give a literature review on these topics, supplemented by own ideas and modifications of the available maps.
- In chapter 7 to 9, the soils of the study area and their typical distribution in the landscape are discussed and visualized through catenas.
- This information is then used in chapter 10 to regionalize intermediate geo-scientific parameters, most of them focusing on hydrological soil properties.
- Chapter 11 to 14 are used to derive thematic maps of geo-potentials such as groundwater vulnerability, resource availability and erosion hazard that are also understandable by non-experts.
- The last chapters contain a summary of the results, error analysis and a discussion on the interpretation and quality of the results.
- In the first part of the annex, the interrelation of all parameters is described in a workflow scheme to help assess the individual sensitivity of each parameter. This is supplemented by an input-/ output parameter table of all tools stored in the ArcGIS-toolbox.
- In the second part of the annex, the created thematic maps are displayed in an overview version. Higher resolution maps can be created using the supplied GIS-base data.
- All data and the ArcGIS-Toolbox are available in the enclosed DVD. A summary of the digital data is given in Annex III.

2 Overview of the study area and its geo-potentials

The study area is located about 35 km north of the city Belo Horizonte and comprises 409 km² (Figure 2-1). In the center of the study area, the city of Lagoa Santa is built around the homonymous lake. While archeological record of human settlement in the region dates back to at least 12 000 YBP, European settlers arrived in the 17th century and the city of Lagoa Santa was founded in the 18th century.

2.1 Urban dynamic in the metropolitan area of Belo Horizonte (RMBH)

In 1897, Belo Horizonte was founded and systematically constructed in order to exploit the rich deposits of the Precambrian banded iron formation in the Serra do Curral (Figure 2-2) , which is the northern border of the "Quadrilátero Ferrífero", a rectangular geological structure that is famous for its resources in iron ore and gold.

Today, the metropolitan area of Belo Horizonte is the third largest agglomeration in Brazil with a population of 5.4 million (IBGE 2010) and strongly growing, similar to many megacities in Latin America.

To the south, the city climbs the steep hills of the Serra do Curral and urban growth is restricted in this direction by accentuated relief, mining areas and also by an environmental protection area. Thus, the present and future tendency of urban development is towards the north, where soft hills, are not impeding settlement (Figure 2-2). Towards the W and E, other large cities (Contagem, Betim) hamper the growth.

Since 2005, the government of Minas Gerais has been actively promoting the urbanization of the northern periphery of Belo Horizonte with large investments in the infrastructure. The old state road MG-010 has been upgraded into the highway "Linha Verde", which connects the International Airport Tancredo Neves to the city (Figure 2-1). Since 2006, most flights have been transferred from the airport Pampulha near the center of the city to this larger airport 40 km north of Belo Horizonte. Within the framework of the project "Aeroporto Industrial", industrial settlement around the new Airport is attracted with tax reductions. All these factors accelerate the urban growth along "Linha Verde" and the municipalities Vespasiano and Lagoa Santa connected by it.

While the population of the inner city of Belo Horizonte stagnated in the last years, the population growth of Lagoa Santa, an urban center of about 50 000 inhabitants, accelerated in the last years to an average of 5% per year between 2007 and 2010 (Figure 2-3).

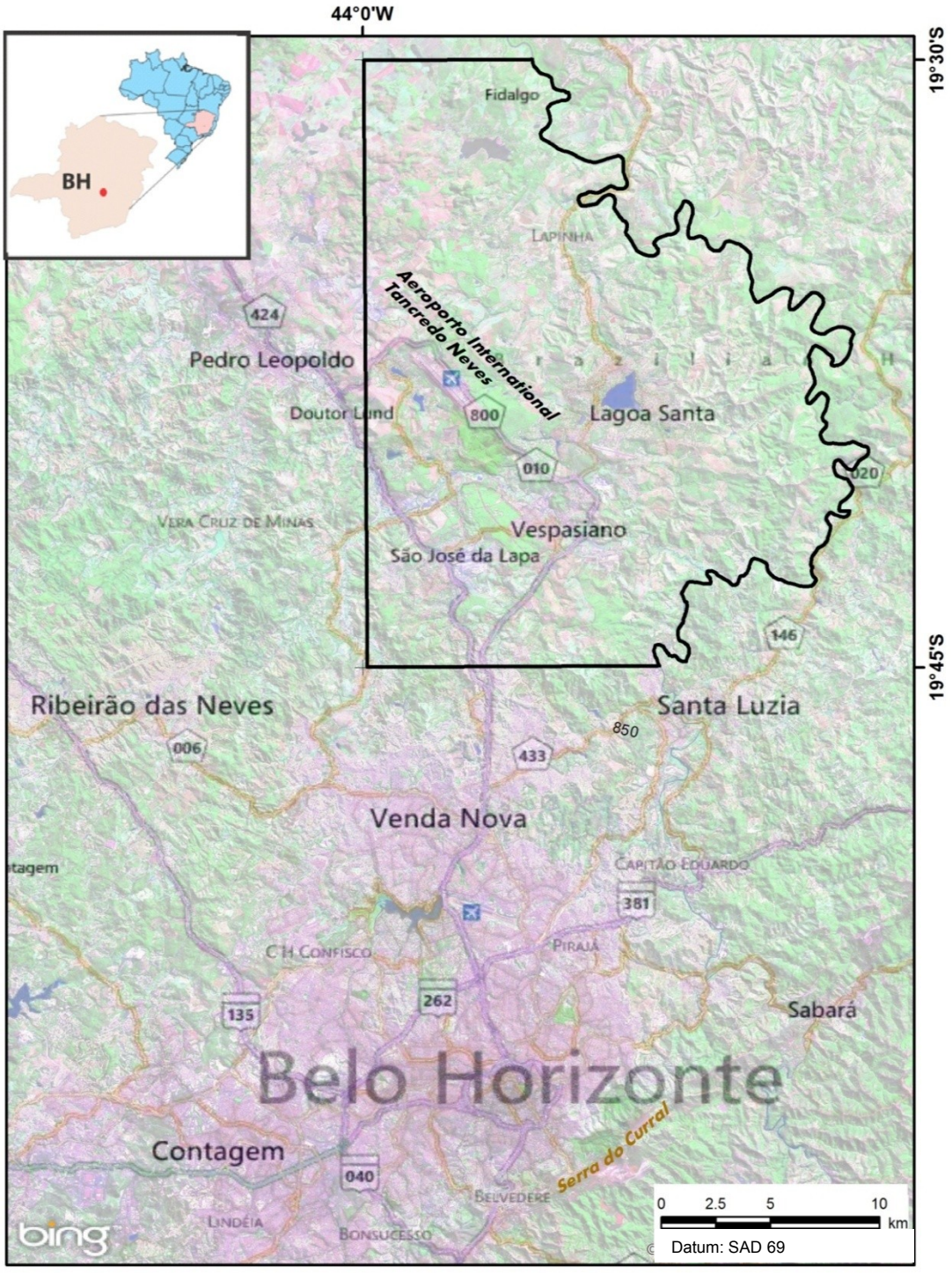

Figure 2-1 Location of the study area.

The study area is indicated by the black outline and comprises the municipal area of Lagoa Santa and parts of the municipal areas of Vespasiano, São José da Lapa, Confins, Pedro Leopoldo and Matozinhos. Data source: Bing maps (http://www.bing.com/maps 16.10.2012) and Landsat ETM+ image from 03.August 2002.

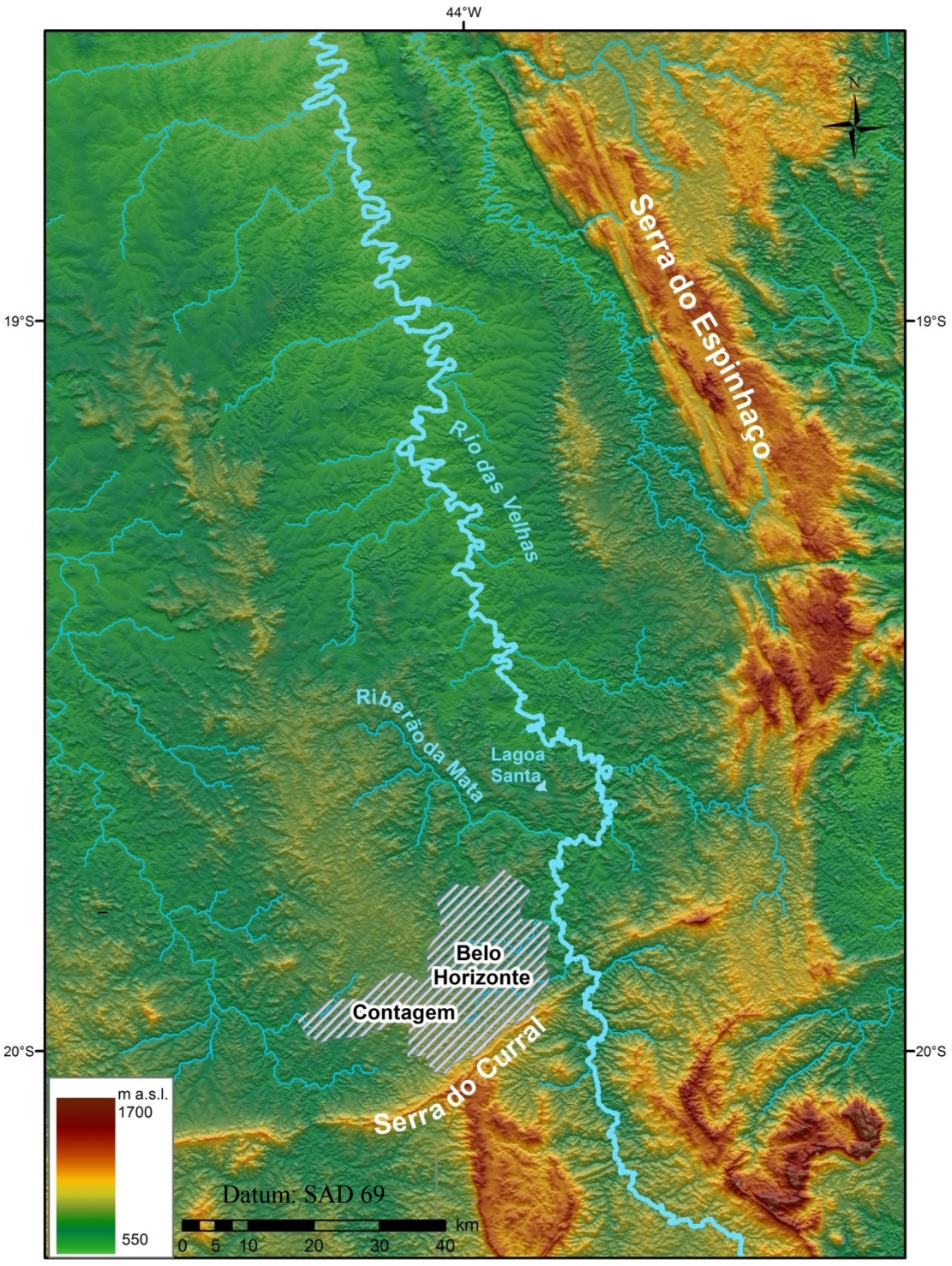

Figure 2-2 Topography and hydrology around Belo Horizonte.

Data Source: SRTM elevation data.

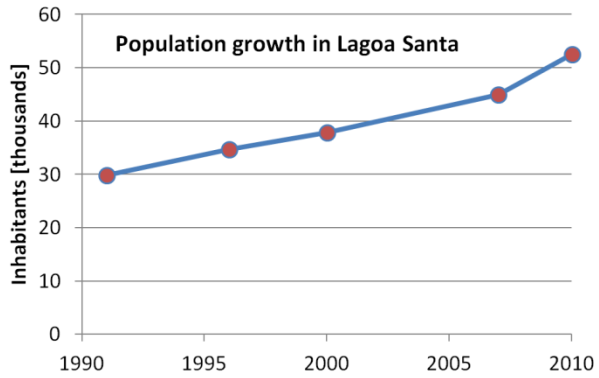

Lagoa Santa

Year	Population	Average annual rate of change
1991	29.824	
1996	34.639	3%
2000	37.872	2%
2007	44.922	2%
2010	52.52	5%

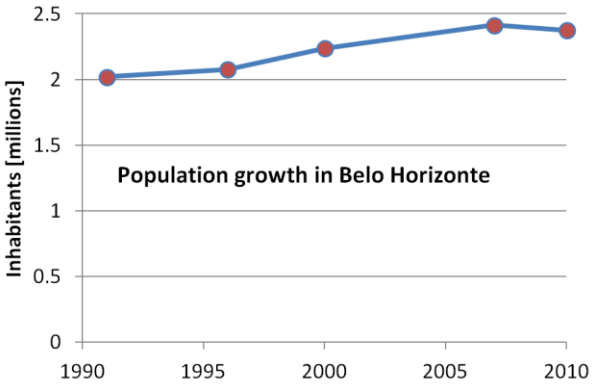

Belo Horizonte

Year	Population	Average annual rate of change
1991	2.020161	
1996	2.077136	1%
2000	2.238526	2%
2007	2.412937	1%
2010	2.375151	-1%

Figure 2-3 Population growth in Lagoa Santa and Belo Horizonte 1991 - 2010.

Source: IBGE (2010).

2.2 Geo-potentials of the study area

2.2.1 Topography and climate

The study area lies in the Brazilian cerrado region at 20° latitude south with an elevation between 650 and 920 m a.s.l. (Figure 2-2). The area drains towards the north into the Rio das Velhas, which is part of the large basin of the Rio São Francisco that reaches the Atlantic between the states Alagoas and Sergipe in north-eastern Brazil. To the east, the mountain range Serra do Espinhaço delimits the basin (Figure 2-2).

The climate of the study area is tropical on high altitudes with humid warm summers and dry cool winters, falling into a classification Aw after Köppen-Geiger (Peel et al. 2007). The mean temperature varies around 20°C and the annual precipitation of 1300 mm falls mainly during the summer raining season between October and March. The dry season lasts from April until October with the water deficiency reaching a maximum in September (Figure 2-4). Compared to its surroundings, the region around the city Lagoa Santa receives slightly less rainfall (Figure 2-5). This seasonality is also reflected in the mean monthly discharge of the drainage network as shown in Figure 2-6.

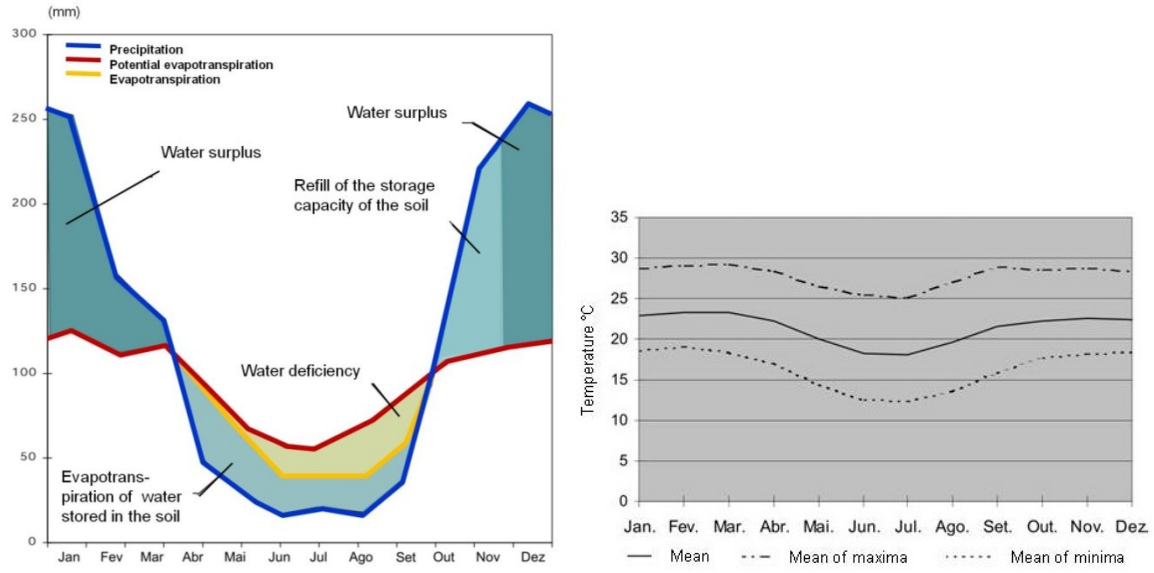

Figure 2-4 Climate diagram for the study area.

Left: Water balance for the region around Lagoa Santa based on the method of Thornthwaite and Mather (1955). Right: mean monthly temperature values between 1961 and 1990 for the climate station in Lagoa Santa. Source for both images: Patrus (1998).

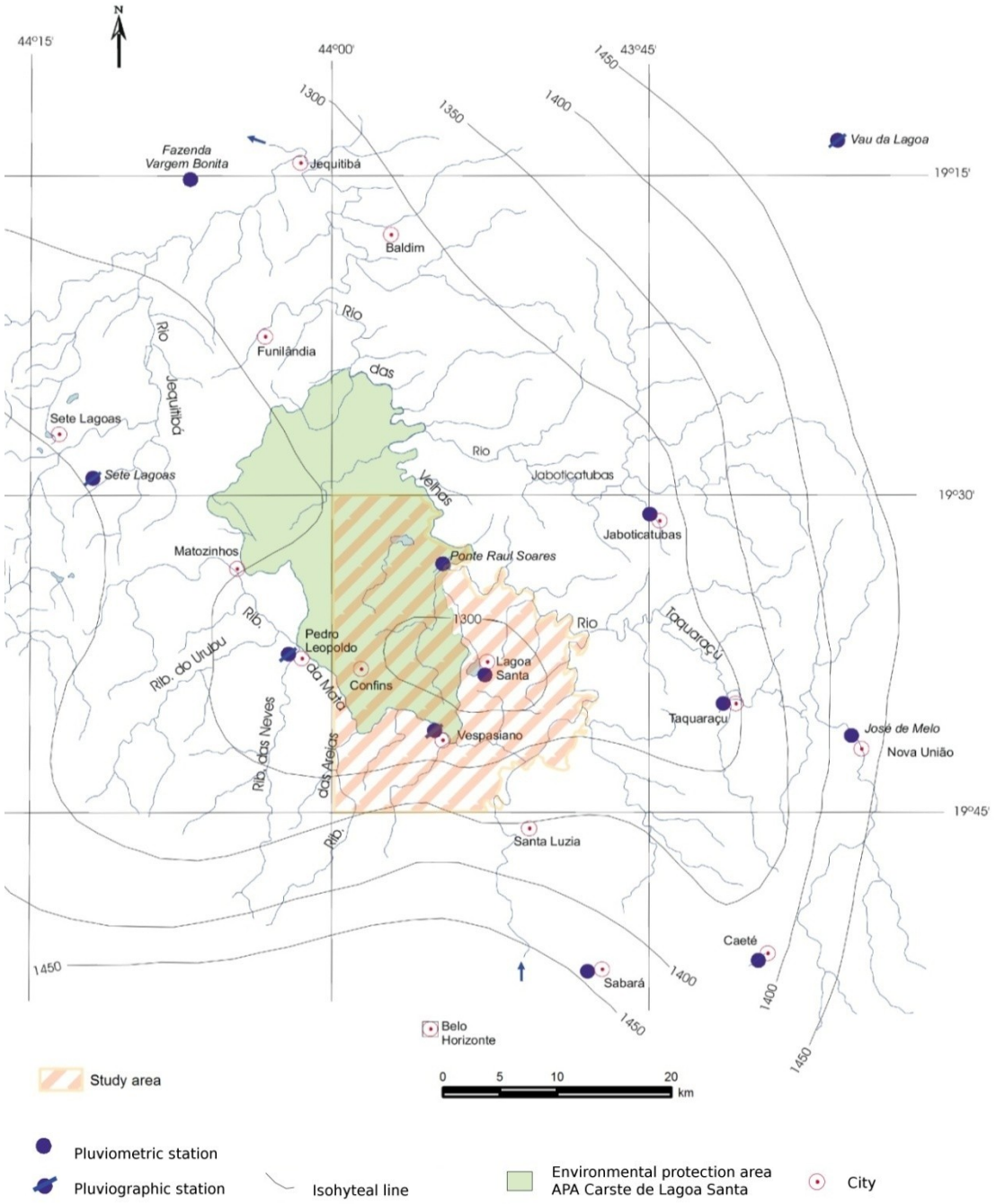

Figure 2-5 Mean annual precipitation [mm].

Isohyetal lines for the region around Lagoa Santa (center of the image) based on the period from 1961 – 1990. Map detail extracted from Patrus (1998).

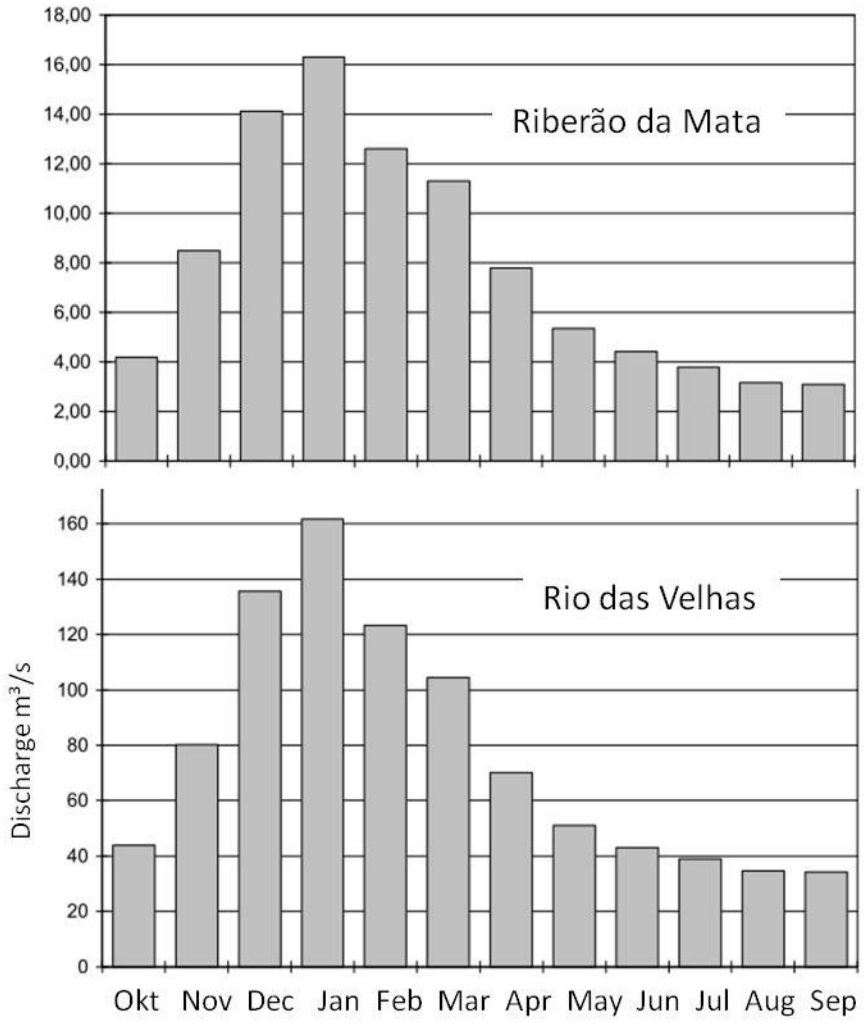

Figure 2-6 Mean monthly discharge.

Mean discharge during the hydrological year from October to September of the Rio das Velhas at the "Ponto Raul Soares" (location see Figure 2-5) and of the Riberao da Mata near Vespasiano during the period 1940 – 1992. Source: Patrus (1998).

2.2.2 Geology and local relief

Belo Horizonte is located at the southern tip of the Sao Francisco Craton (Figure 2-7), an Archean stable structure that is surrounded by Neo-Proterozoic orogens. The city itself is mostly built on Archean crystalline basement, limited in the south by the Archean volcano-sedimentary series (Dorr 1969) that make up the mountain range of the Serra do Curral (Figure 2-8). In the north, where the current study area is located, the crystalline basement is overlain by Late Proterozoic carbonates and meta-pelites of the Bambuí Group (Schöll 1972).

Especially the meta-pelites of the Bambuí Group and the crystalline basement are deeply weathered and thick saprolites cover the hard rocks. The relief is accentuated, with old plateau surfaces interchanging with concave slopes on meta-pelites east of Lagoa Santa. Where pure limestone is close to the surface, a distinct karst relief developed, especially in the north-western part of the study area (Environmental protection area APA Carste de Lagoa Santa). In the central part, the limestone is covered by meta-pelites and while underground dissolution processes also influenced the relief in this area, the karst features are plugged by the overlying meta-pelites.

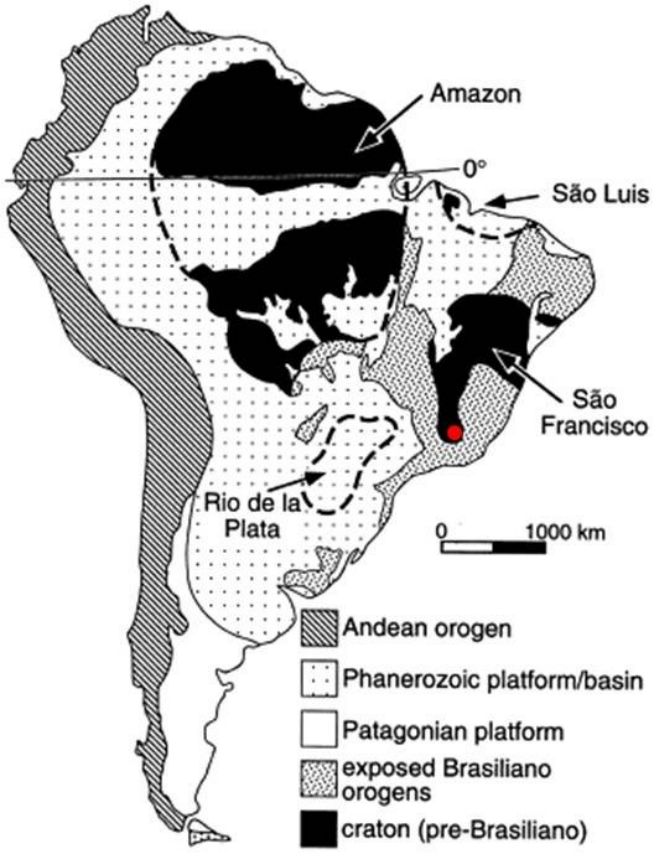

Figure 2-7 Location of Belo Horizonte (red dot) at the southern tip of the São Francisco craton.

Map from Alkmim and Marshak (1998).

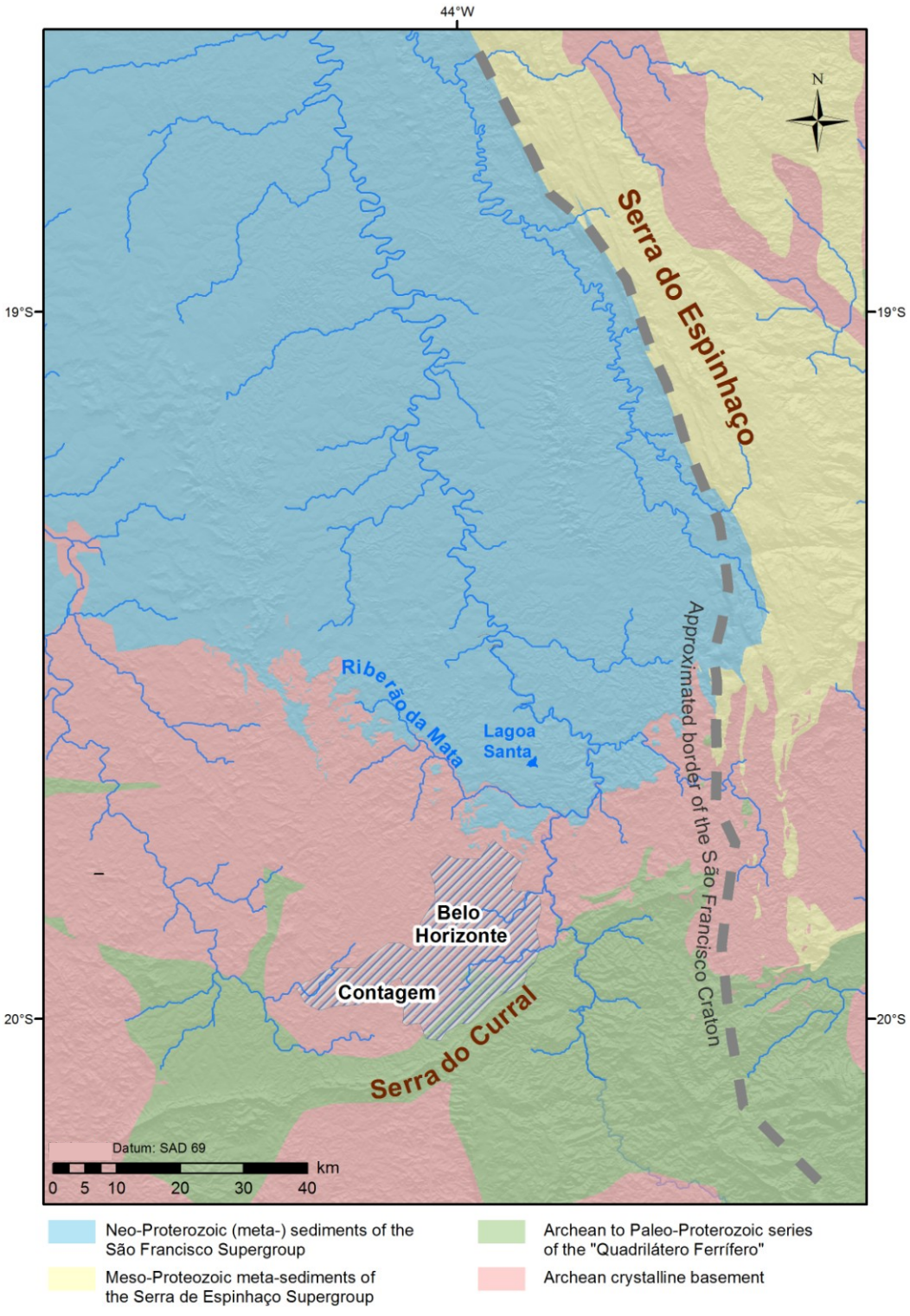

Figure 2-8 Belo Horizonte – geological overview.

For sources see Figure 4-4 (p.56).

2.2.3 Drinking water

In 2006, the water supply in the study area was mainly from wells in the karst area that yielded about 280 l/s drinking water, supplying 97% of the inhabitants of the city of Lagoa Santa (Lagoa Santa - revista virtual da cidade 2006). These wells are highly productive, yielding often more than 100 m³/s (Pessoa and Mourão 1998). Nevertheless, common complaints about drinking water quality and supply continuity lead to an initiative started in 2007 to connect the drinking water supply of Lagoa Santa to the supply system Bacia do Paraopeba. This supply network draws drinking water from surface water reservoirs south-west of Belo Horizonte (Varzéa das Flores, Serra Azul, Rio Manso, Figure 2-9) and is responsible for 50% of the drinking water supply of the metropolitan area of Belo Horizonte (Copasa 2009).
Nevertheless, many local settlements will still depend on drinking water from karst wells and a protection of the karst aquifer is needed. The velocity of subsurface water flow is very high in the region (about 80 m/h, Pessoa (2005)) which is typical for karst areas. An estimation of a 50 day timeline zone around wells as is common for granular aquifers e.g. in Germany (DVGW 2006) would result in a circular protection zone with a radius of nearly 100 km. Thus, a method that generates an intrinsic vulnerability map with the total aquifer surface as target and focusing on typical karst entrance points is chosen in this study for indicating the risk for groundwater contamination (chapter 13).

2.2.4 Erosion hazard

Due to the tropical climate, the underground is deeply weathered and outside the open karst area, deeply weathered saprolites cover the landscape, resulting in high vulnerable for deep gully erosion, especially on meta-pelites and crystalline basement.
In intensively used agricultural areas of the karst region, relatively small linear erosion features can be noted. Although the pelite hills around Lagoa Santa are used only extensively due to their low fertility, they are cut by very deep permanent gullies. The largest gullies are connected to anthropogenic features such as mud-roads or sealed areas that are not connected to the city drainage network. In the eastern part of the city of Lagoa Santa, several gullies cut through the urban settlement as shown in detail in section 2.4 (p. 29 ff). In chapter 14 (p. 267 ff.), gully erosion hazard has been regionalized based on the available topographic, geologic and pedological data.

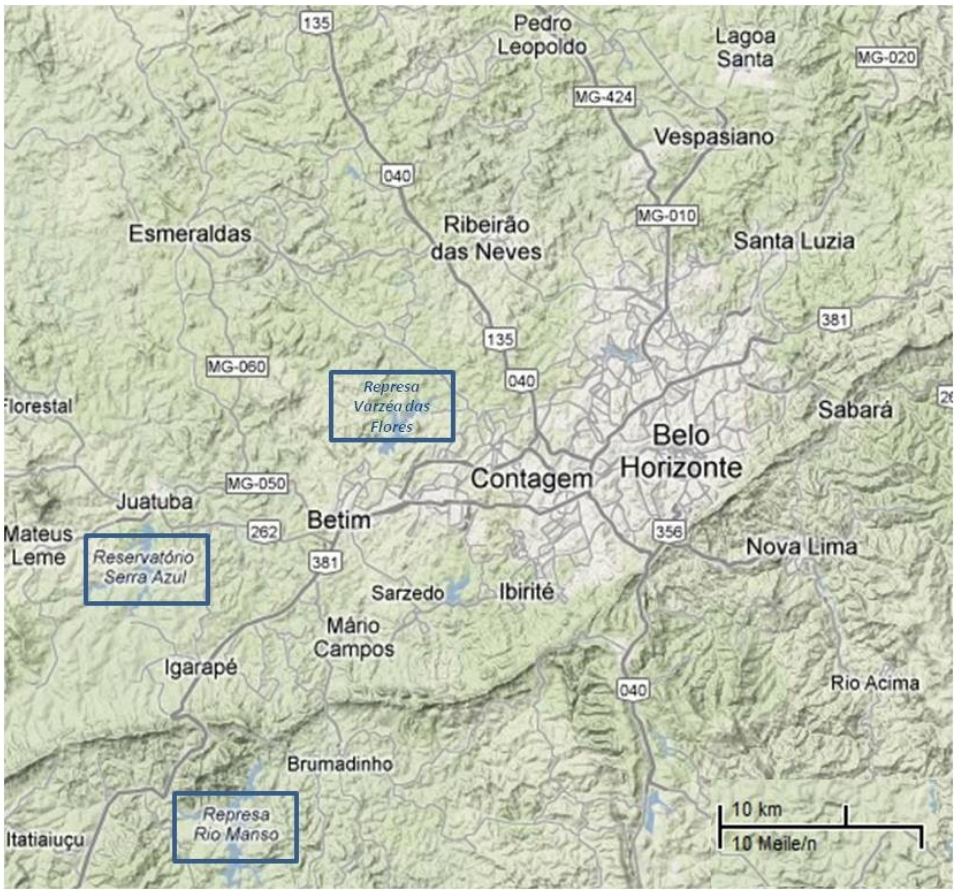

Figure 2-9 Main drinking water reservoirs for the RMBH.

Image from Google Maps.

2.2.5 Soils and agricultural value

The agricultural value of the soils in the study area is generally low due to chemical disadvantages that are typical for most tropical soils on old stable land surfaces. The soils are depleted of most weatherable minerals and only stable minerals such as iron and aluminum oxides and two layer clay minerals (kaolinite) remain. Thus, the soils are lacking the major nutrients (potassium, nitrogen, phosphorous) and also most micro-nutrients. Since basic cations are leached, the soils are very acidic and free aluminum in the soil solution can lead to aluminum toxicity. Direct application of fertilizer is often not very successful since the low cation exchange capacity of the soils hinders effective storage of the applied nutrients and phosphorous is bound in stable Al-complexes. Thus liming is often necessary before the application of fertilizer is sensible.
The physical properties of the soils are relatively good due to a strong and waterstable microstructure in the ferralitic topsoil. Nevertheless, the subsoil and exposed saprolite (especially on the pelite hills around Lagoa Santa) do not have this favorable property and are highly erodible. Still, water scarcity can be a problem in soils with strong micro- and macro-structure

(e.g. on Ferralsols on old plateau surfaces) due to a very high permeability and low effective field capacity. An exception to the overall chemical poverty in the region are soils on steep slopes on carbonates, in karst depressions or along rivers. Nevertheless, these soils with highest natural fertility are still difficult to put under intensive agricultural use, since steep slopes favor erosion and temporary waterlogging poses a problem in karst depressions and along rivers. Thus, most areas are extensively used for cattle grazing. Only smaller areas, especially in the karst area or along rivers, are intensively used for agriculture. In chapter 12.3 (p. 242 ff.), an attempt has been made to regionalize soil fertility and agricultural value for the study area.

2.2.6 Mass resources for construction

Gravel, sand, clay and limestone are the main mass resources needed for building the city. The demand for gravel in the area is mostly met by exploiting the older terraces of Rio das Velhas and its tributaries from the east (Heineck 1999), which drain quartzites of the Serra de Espinhaço and pelitic meta-sediments dissected by many quartz veins. Some of the terraces contain also small amounts of gold and have been washed by gold miners in the past. These deposits yield pure quartz for various purposes (Heineck 1999).

The gravel resources are located in higher positions and thus are not subject to inundations like the sand extraction in the alluvial plains. To meet the high demand of the growing city, gravel is also substituted in large amounts by crushed limestone from major quarries. This substitution is not economically possible for sand and thus sand resources in alluvial plains are valuable resources needed for the growth of the city. The extraction of sand is often associated with land use conflict since it consumes large areas in alluvial plains as demonstrated in the case study in section 2.3 (p. 20 ff.). For resource mapping, the quantity of extractable sand in the alluvial plain of the Riberão da Mata (Figure 2-8) and its affluents has been estimated in section 12.2 (p. 237 ff.).

Clay for making bricks and tiles is found in alluvial plains but often also as by-product in limestone and sand quarries or in eluviated gneiss saprolite. Regionally much more important is the demand for cement, which is met by large limestone quarries. An attempt to assess these resources has been made for the study area in section 12.1 (p. 237 ff) .

2.2.7 Flora, Fauna and natural heritage

The karst region north-west of Lagoa Santa is famous for its speleological discoveries ((Berbert-Born 2002) and high biodiversity and has been declared an environmental protection area in 1998. Since it also hosts important geo-resources (limestone for the cement industry, groundwater), and is under strong pressure of urbanization, zonation rules were established during the announcement of the environmental protection area to manage the balance between urbanization and resource

and environment protection (CPRM and IBAMA 1998). While the complete environmental zonation rules of the APA Carste de Lagoa Santa can be found in de Lima Cabral et al. (1998), two specific zonation maps from the environment protection area are included into the annex: Map 4 shows the proposed zonation to protect important habitats of the local fauna and flora and Map 5 the zonation for the protection of the archeological and speleological heritage.

2.3 Case study: Sand extraction and land use change

In a case study published by Büchi and Pagung (2008) and Hofmann et al. (2009), which was based on a cooperation between the UFMG and the TU-Darmstadt, the land use change following sand extraction was analyzed in a multi-temporal study of the central alluvial plain of the Riberão da Mata between its confluence with the Riberão das Areias and the city of Vespasiano (Figure 2-10). Although this river or creek is rather small with a mean discharge between 4 and 16 m³/s (compare p.13), it flows through an alluvial plain of a width of nearly 1 km in its central part.
In the area, sand deposits are restricted to alluvial plains where many land use conflicts and ecological problems arise. Sand is needed in large amounts as supplement for concrete and difficult to substitute. In Figure 2-10, radii of 15 km and 30 km around the urban growth centers Lagoa Santa and Vespasiano indicate the possible and feasible supply area for sand with respect to this consumption site. It has to be taken into account that in reality distances along roads are often twice as long compared to the linear distances. The Riberão da Mata system together with the rivers east of Rio das Velhas are the main source areas for sand extraction lying within this distance. The first one, being a small creek with an average discharge between 3 and 16 m³/s (compare Figure 2-6 on page 13) drains the gneiss and migmatite rocks of the Archean basement. The sand-loaded rivers east of the larger Rio das Velhas come also from the outliers of the Serra de Espinhaço, where quartzite rocks dominate. North-east of the Riberão da Mata, carbonaceous and pelitic rocks of the Late Proterozoic Bambuí-Group cover the basement delivering only clay and silt to the rivers.

2.3.1 Multi-temporal analysis

The development of sand and clay extraction sites in the central alluvial plain of the Riberão da Mata was analyzed during the past four decades by visual analysis of aerial photographs and satellite images. The study area was defined by the availability of multi-temporal aerial photographs in this area and by the fact that sand extraction played a decisive role in this part of the alluvial plain. The aim was to analyze the effect of sand extraction on land use change in a rural to urban transition area and to evaluate future strategies for sustainable urban growth, which take the needs and effects of sand extraction into account.
The study site comprises 6.6 km² in the alluvial plain of the Riberão da Mata after its confluence with the Riberão das Areias (red area in Figure 2-10). Here, the alluvial plain of is extremely broad (up to 1 km wide) and has been subject to sand, clay and to a minor extent also gravel extraction in the past decades due to its close location to the growing northern periphery of Belo Horizonte. To the West and East, the study site is delimited by two major roads: the state road BR 424 in the West and the state road MG 010 or “Linha Verde” in the East. To the North and South, the study site is defined by the topographic boundaries of the alluvial plain itself.

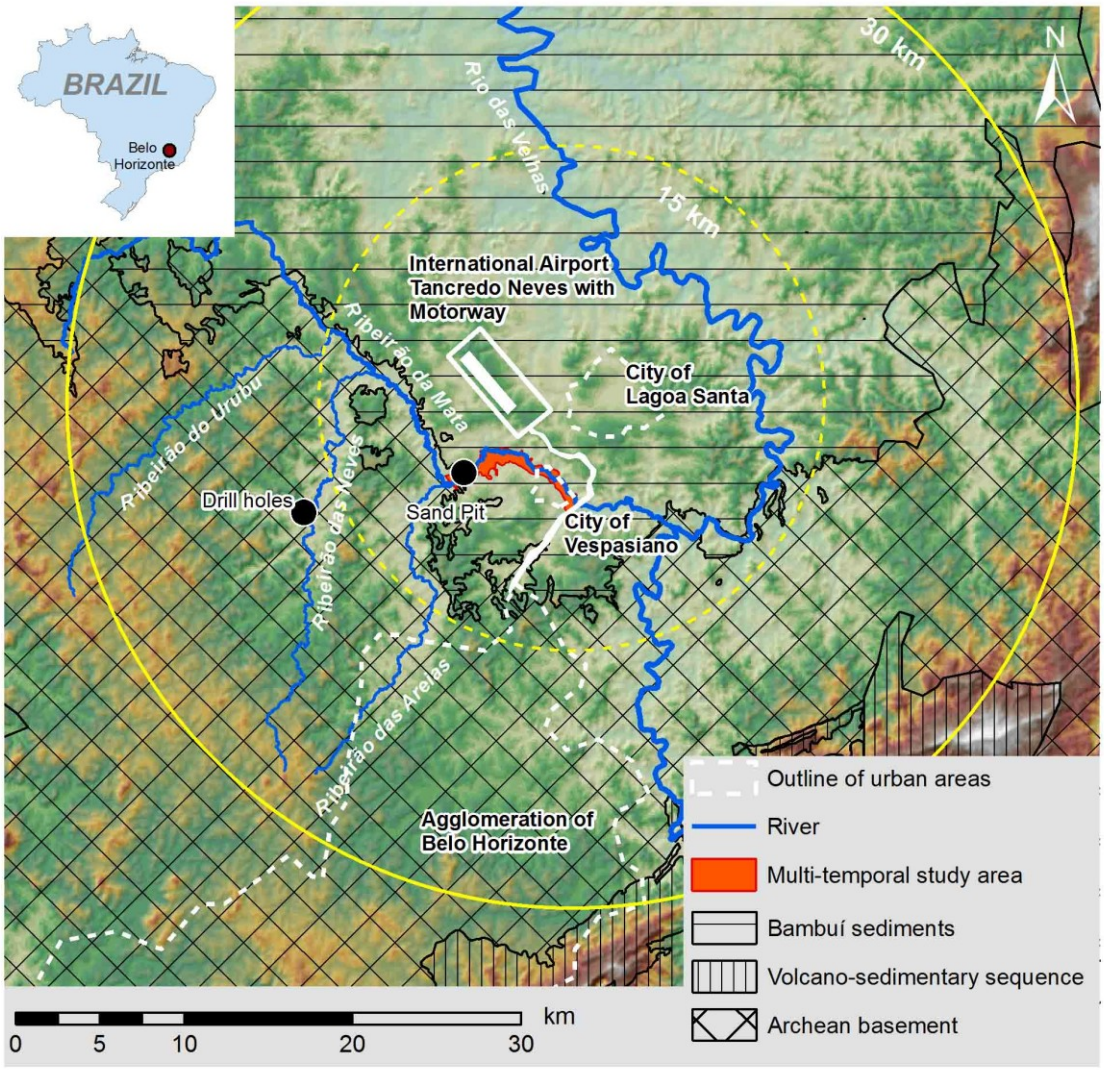

Figure 2-10 Topographic and geological overview of the study area.

The area around the International Airport Tancredo Neves and the city of Lagoa Santa is one of the future growth centers in the periphery of Belo Horizonte. Two circles with diameters of 15 km and 30 km represent distances to this center. The Riberão da Mata and its affluents are one of the main sources for sand in the area. The location of the sand pit studied in section 5.8 and the additional drill holes used for estimation of sand content in section 5.8.1 are indicated by black dots. Source: Hofmann et al. (2009).

The following pictures have been used for the multi-temporal analysis:

Aerial photographs:

- 1964 (1:60,000 from US Air Force);
- 1977 (1:8,000 from CEMIG/PLAMBEL);
- 1982 (1:30 000, from CEMIG/PLAMBEL);

Aerial ortho-photographs:

- 1990 (1:10 000, from CEMIG);

Satellite images:

- 2004 (Google Earth).

All images have been joined together as a mosaic and geo-referenced using the software ERDAS Imagine 9.0 from LEICA GEOSYSTEMS and the ortho-photographs from 1990 as reference. The geo-referenced mosaic was then imported into the GIS software ArcGIS 9.0 from ESRI and the land use classes were digitized from visual interpretation, based on the observations from previous field studies and stereoscopic analyses of the original aerial photographs. ArcGIS was also used for the calculation of the "area per land use" and for the intersection and statistical analyses of the vectorized data. Seven land use classes could be distinguished on all images:

- extraction areas (areas where sand and clay was actively extracted),
- urban areas (housing and industrial areas),
- roads (linear features, not necessarily asphalted),
- water (river and lakes),
- bare soil (areas without vegetation that could not be identified as active mining, roads or settlement),
- high vegetation (bushes and trees, also eucalyptus reforestation),
- low vegetation (mostly pasture, in some cases agricultural fields).

For the recent images, the land use classes could be verified also during field trips in the study area; for older images, comparison with areas of known land use type helped the interpretation. Only the ortho-photograph from 1990 could be geo-referenced using an existing grid on the image. All other images had to be geo-referenced using prominent features such as road intersections that could be found also on the ortho-photograph from 1990. Thus, the resolution of each image was important not only for identifying the land use features but also for geo-referencing. The image with the lowest resolution is the aerial photograph from 1964. This image has a scale of 1:60 000 and thus limits the accuracy of the analysis, which is estimated to be 0.01 km² (approx. 1.5 mm error on the photo from 1964).

2.3.2 Results

In 1964, 13% of the study area could be classified as extraction area, showing that the demand for sand was already high in the region during the 1960s. The extraction areas were distributed over the whole floodplain area, but they remained shallow since no lakes can be detected in later images. 61% of the area was covered with low vegetation, while high vegetation accounted for only 10%. In the eastern part, the outline and streets of the city Vespasiano (which had spread into the study area in 1981) can already be detected. Overall, the photo from 1964 shows a landscape that is dominated by pasture and sand extraction with the beginnings of urbanization (Figure 2-11).

By 1977, the sand extraction had intensified (22% of the area) and many new areas were exploited for sand (18% of the area), mainly along the river and intruding into the five meter protection zone that was established in 1965. Despite the law, the course of the river was altered and straightened (Figure 2-12).

Between 1964 and 1977, the highest increase (from 0,1% to 12%) of urban area can be found, accounting for the necessity of sand exploitation. Low vegetation diminished from 61% to 51% and high vegetation from 10% to 8%. The area covered by water was only 3% in 1977 compared to 6% in 1964. This reduction can be due to the straightening of the river and to possible instream mining in 1964. Another explanation could be that due to the small scale of the picture from 1964, it was hard to identify the exact course of the river and thus its width was overestimated (Figure 2-11, Figure 2-13).

In 1981, the sand extraction diminished slightly to 15% of the total area. Only few new extraction areas were opened (3% of the total area). Instead, those areas that had already been exploited in 1977 were now exploited more deeply (12% of the total area). Also the urbanization within the alluvial plain slowed down (13% of the total area). The area left open after sand extraction showed mostly low vegetation (67%), bare soil (10%) or water (11%; Figure 2-11, Figure 2-13). The increase in expanses of water shows that the extraction reached the groundwater level now in some places.

In 1990, most of the old extraction areas along the river were abandoned (only 4% of the total area was left) and few new extraction sites in the floodplain were created (2% of the total area). Both roads and urban areas together covered 25% of the area and reforestation (mostly eucalyptus) resulted in a doubling of the high vegetation percentage (14% compared to 7% in 1981). In the abandoned mining areas, lakes appeared due to deeper sand extraction, accounting for the increase of the area covered by water (5% compared to 4% in 1981; Figure 2-11, Figure 2-13).

In the last image from approximately 2004, the trend of 1990 had continued: sand extraction diminished (only 3% of the total area) and moved away from the river to the floodplain, where the

sand must be extracted below thick loamy alluvial sediments. The distant mining left lakes after the extraction had ceased. Roads and urban area increased to 29% and also the reforestation of the alluvial plain continued to increase (16%; Figure 2-11, Figure 2-13). In 2004, the area that had previously been subject to sand and clay extraction shows mainly low vegetation (53%), reforestation (11%), water (14%) and bare soil (9%). Only 12% are reused for roads or urban areas.

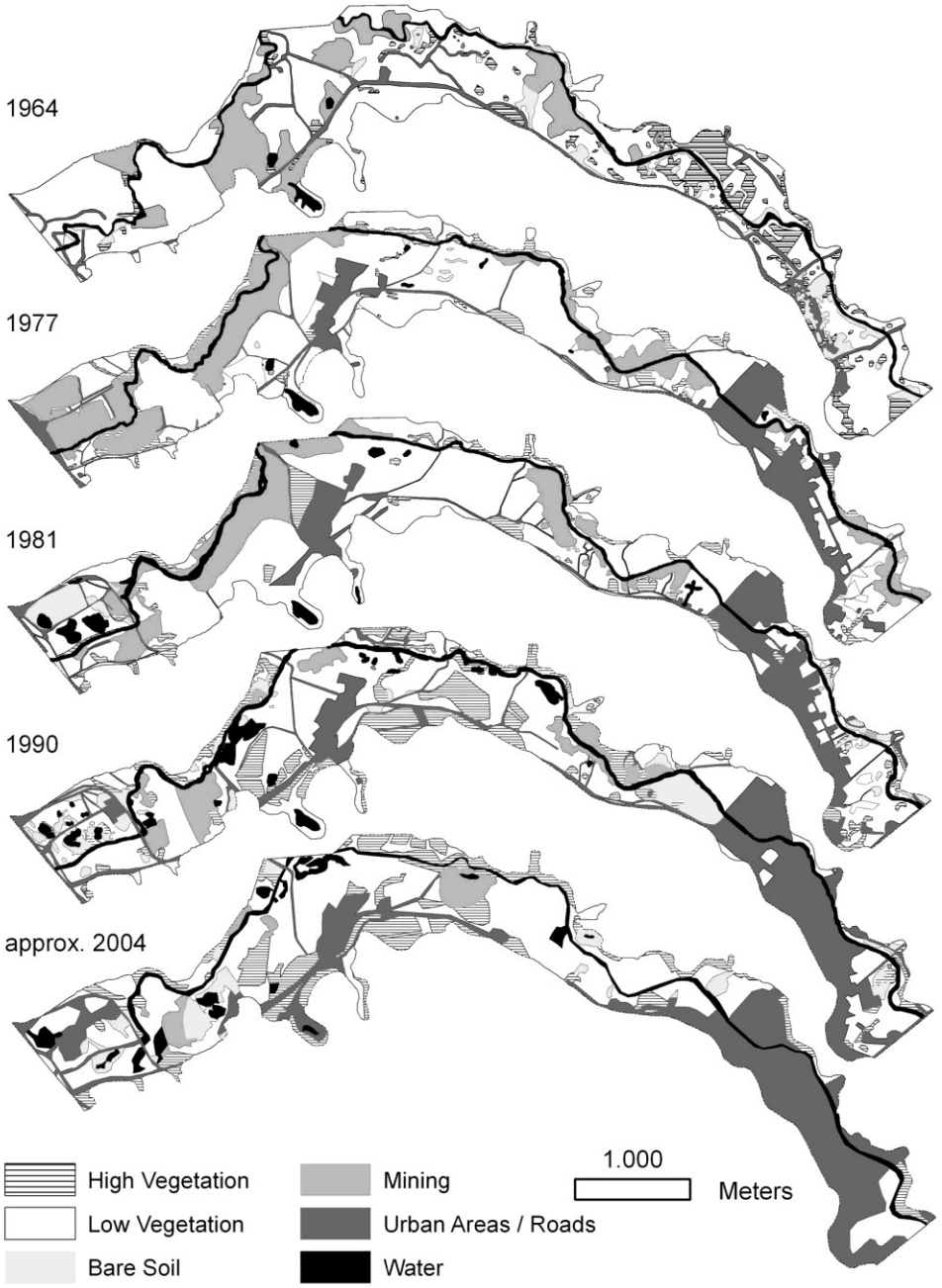

Figure 2-11 Land use change in the alluvial plain of Riberão da Mata 1964 - 2004.

Source: Hofmann et al. (2009)

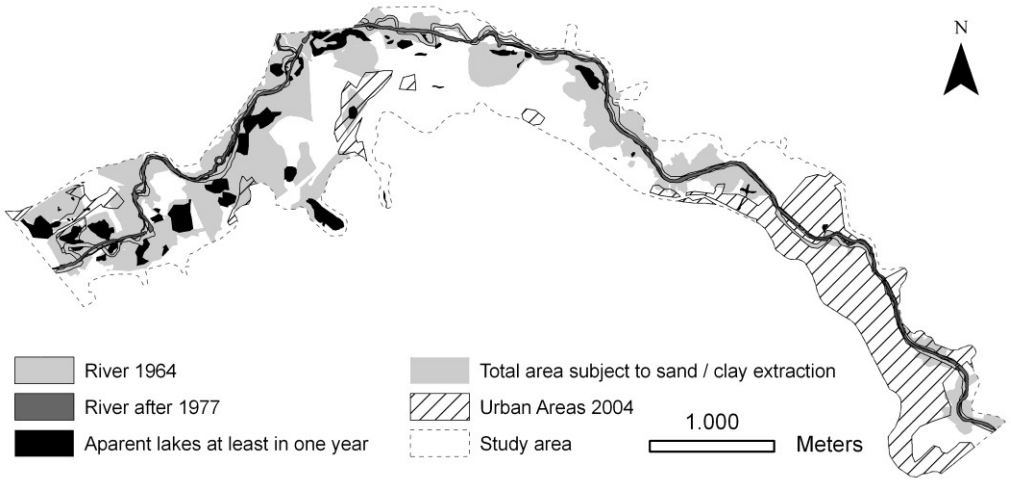

Figure 2-12 Straightening of the river course from 1964 to 1977.

Black areas indicate lakes and grey areas sand extraction pits that could be detected on any of the different images between 1964 and approximately 2004. Urbanization took place mainly in areas where sand had never been extracted. Source: Hofmann et al. (2009)

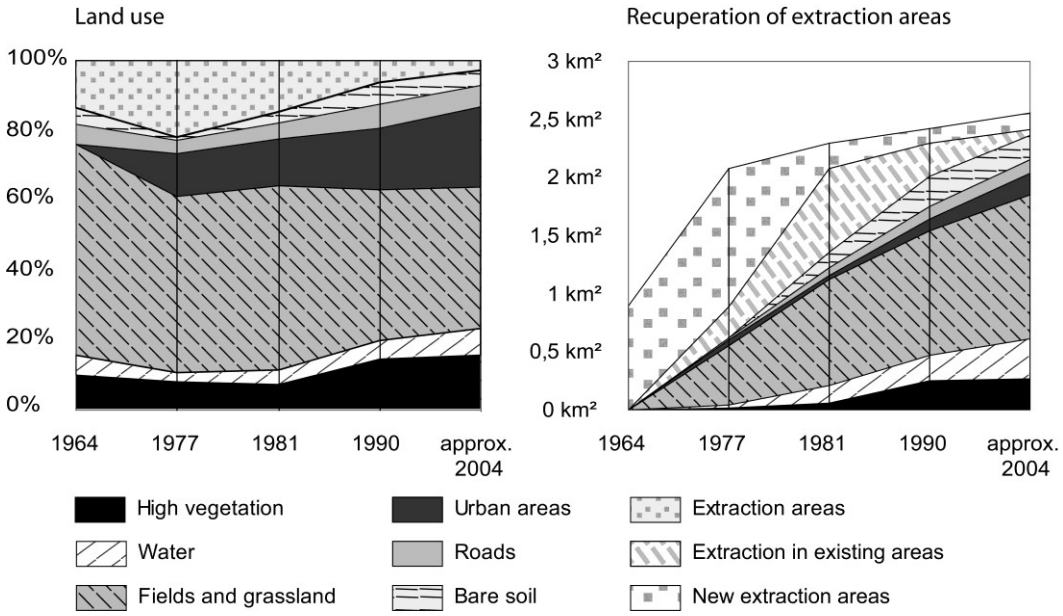

Figure 2-13 Land use change (left) and recuperation of abandoned mining areas (right).

The category "new extraction areas" is the area that was classified as active extraction area in places where no mining was detected before. Source: Hofmann et al. (2009)

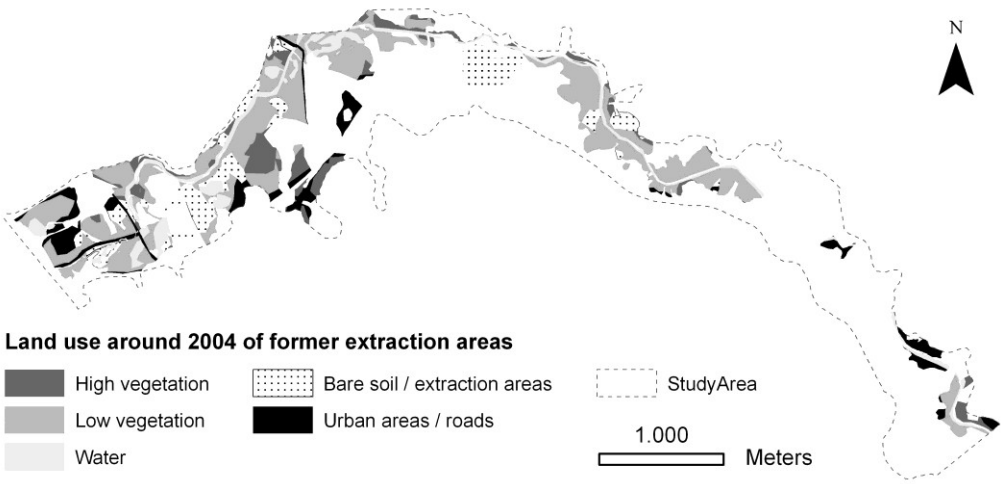

Figure 2-14 Land use of old mining areas around 2004.

White areas have not been classified as extraction areas on any image. Source: Hofmann et al. (2009)

Altogether, in the period between 1964 and approximately 2004, nearly 39 % of the total study area - and 50 % of the non-urban area in 2004 - have been altered by sand and clay extraction (Figure 2-12). During the first decades of the study period until the 1980s, this extraction seemed to be mainly small-scale (clandestine) exploiting above the water table close to the riverbed or even instream mining - thus destroying the natural course of the river and generating aggradation of the river downstream. By 1990, the sand extraction moved away from the river. As extraction of sand below the water level needs a higher investment in stationary equipment which is not possible for small-scale or clandestine companies, this either indicates that law enforcement became stricter with increasing urbanization or that the easily accessible resources close to the surface were already exploited.

2.3.3 Interpretation and discussion

Instream sediment mining is proven to have many negative effects on the river ecosystem due to siltation, erosion and increased turbidity (Padmalal et al. 2008). In 1965, federal forest law required the Riberão da Mata River to have a 5 meter buffer zone to conserve diversity of species and to protect the watercourse from erosion. In 1989, the federal legislation was tightened further, redefining the protection buffer zone to 30 - 50 m for rivers the size of Riberão da Mata. These laws prohibited also instream mining because the sand or gravel extracted from the active riverbed intruded into the protection zone. Nevertheless, many mining areas in or very close to the river course could be detected in the early images until 1981 and in some places until 1990. This leads to the assumption that instream mining has been a common practice in these areas for

decades. It can also be seen that the course of the river was straightened between 1964 and 1977, thus reducing freshwater habitat and accelerating the incisive activity of the river. It was not until 1990 that most sand pits could be found distant from the river. This observance also shows that the river ecosystem was worst affected during the beginning of the urbanization in the region when environment legislation was less strictly controlled.

Already the earliest image (1964) shows a large area altered by sand extraction, thus it is difficult to estimate the loss of riparian and alluvial habitats. However, since the landscape in 1964 was dominated by pasture with nearly no riparian forest, the damage done to natural riparian ecosystems does not seem to be too grave - they had probably already been destroyed before the mining started. The early shallow extraction sites in the alluvial plain were not recuperated actively but eventually turned into pasture when the uneven sand pits were covered by low vegetation again. The remnant relief can still be seen in the pastures today. In later years, the wet pit sand extraction distant from the river destroyed mainly pasture vegetation of the alluvial plain. In the abandoned extraction pits, new freshwater habitats appeared, which is a welcome side effect for biodiversity - especially since the ecosystem of Riberão da Mata suffers from severe pollution stress (Brandt Meio Ambiente 2002).

Due to reforestation in the last two decades, there is probably more forest in the area now than there had been before the sand extraction started. This reforestation trend may have resulted from federal legislation that requires mining companies to actively recover the area after the sand extraction. However, economic reasons may play a role, too, because many former extraction pits were not officially registered and the reforestation is mainly done by planting eucalyptus monoculture which is used as charcoal for cement production in the region. From the viewpoint of riparian habitat biodiversity it seems to be clear that a monoculture is not an adequate substitute for native riparian forest.

As enforcement of the Brazilian administration is stricter around urban areas, sand extraction sites close to cities tend to become either abandoned or registered (Valverde 2001) - as could also be observed in our study - while uncontrolled extraction moves on to more rural parts. There, it may cause destruction of still existent intact riparian forest and erosion and siltation of riverbeds, especially as small-scale, clandestine sand extraction often causes more damage than registered companies that are controlled by mining and environmental institutions (Brandt Meio Ambiente 2002). In addition, higher air pollution and CO_2 production due to larger transport distances are generated if the exploitation of sand resources moves away from the urban center of demand.

With more and more areas in the catchment sealed, flood hazards are an increasing problem in the floodplain of Riberão da Mata (Brandt Meio Ambiente 2002, Hundecha and Bárdossy 2004) which was exemplified in 1997 when a big flood event damaged many settlements and industrial areas along the Riberão da Mata (Brandt Meio Ambiente 2002). While incised and straightened riverbeds can aggravate flood events (e. g. after instream mining), abandoned extraction sites in

alluvial plains may mitigate extreme flood events by accommodating water in the lowered floodplain and lakes (Mathias Kondolf 1994, Rinaldi et al. 2005). In the area of the multi-temporal study, about 2.6 km² have been subject to sand extraction, which translates to around 7.7 million m³ of excavated material if the average extraction depth of the shallow clandestine pits above the water table is assumed to be 3 m. This space is now available as additional water retention capacity upstream of the city of Vespasiano.

Once lakes have been created, further use of the old extraction areas is not possible for urban settlement and industrial plants. Even for shallow extraction sites, the risk of flooding increases if the surface has been lowered some meters. The present study showed that urban settlement in former mining areas remained rare (Figure 2-12, Figure 2-13). This shows that sand extraction areas are lost for future settlement - which is an important aspect in an area, where alluvial plains are the only really flat areas. Settlements on the steep hills face severe gully erosion problems and a large part of the municipal areas are in a protected karstic zone with land use restrictions. Thus, suitable expansion areas are rare for the cities north of Belo Horizonte and the exclusion of alluvial plains from possible settlement areas aggravates this problem. On the other hand, the alluvial plain is a risk area due to possible inundations. Therefore, settlement in the floodplain should not be seen as a primary goal, especially not for industries handling dangerous substances.

After the sand is extracted, other land use possibilities are available. The study shows that while some previous sand extraction sites eventually turned to bare soil areas, most areas were on their way to being recovered into pasture, forests or wetlands. For areas within an urban environment, recuperation efforts could turn abandoned extraction areas into a recreation park. This effort may include the generation of habitats for the riparian fauna and flora that used to live along the river. Already today, abandoned mining pits are used for fishing and recreation and many birds come to the new wetlands. Of course, care has to be taken to avoid pollution of the lakes and to prevent shallow ponds devoid of fish which turn quickly into mosquito breeding grounds.

2.4 Case study: Gully erosion in the city of Lagoa Santa

In the slope around the lake Lagoa Santa, especially on the southern and eastern side, many deeply incised drainage ways or gullies dissect the city. Aerial photos from 1968 taken by the Força Aérea Brasileira, which is stationed in the small military airport in the hills south of Lagoa Santa (see also Figure 9-9 on page 164), document the construction period of new housing areas on these slopes and already show gully erosion features. Thus, strong gully erosion is previous or contemporary to the period around 1968 (Figure 2-15). For the city area of Lagoa Santa, 1 m equidistant contour lines were available for the estimation of the volume of eroded soil material from gullies. This was done during a scientific training project by Farida (2010) for 18 gullies using the following procedure:

2.4.1 Method for estimation of gully volumes

First, the outline of the gully was drawn based on change in curvature of the slope. Then, the contour lines inside the gully were eliminated and a DEM was derived from the remaining surrounding contour lines, thus interpolating a smooth surface across the gully. From this surface, the recent digital elevation model was subtracted within the boundary of the erosion feature and the difference interpreted as loss due to erosion.
The first difficulty during this procedure was to define the outline of the erosion feature. Most of them are old and without sharp edges – at least as documented in the available dataset of one meter equidistant contour lines. Thus, two different outlines were drawn, one including the surrounding area influenced by the gully and one delineating only the steepest inner part of it (Figure 2-17). From these two outlines, the maximal and minimal eroded volume was estimated and the mean of both volume calculations was used as best estimate of the real eroded volume.

2.4.2 Estimated eroded volume

The depth of the gullies calculated from the contour lines ranges from 1.5 m for the small ones up to more than six meters for the larger ones. Figure 2-16 indicates the maximum depth of the gullies. It can be seen that the deepest gullies are those that drain large open spaces such as the military airport at the southern slope (number 7 in Figure 2-18) or the gully in the south-east (number 5 in Figure 2-18) that drains large areas with bare soil documented in the aerial photo of 1964 (Figure 2-15). The mean values and the upper and lower estimates for the eroded soil volume of the analyzed gullies is shown in Figure 2-20.

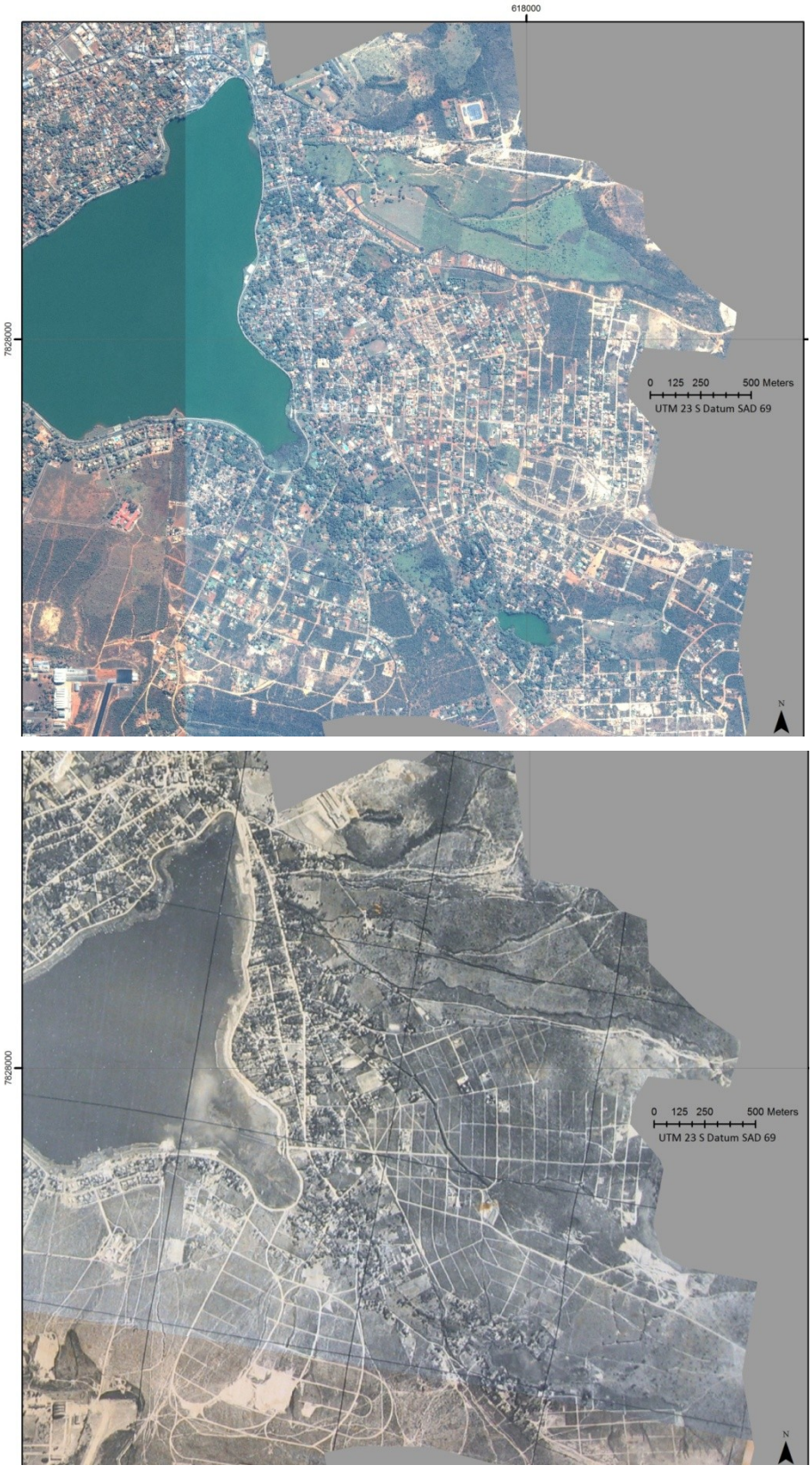

Figure 2-15 The eastern part of the city of Lagoa Santa today and in 1968. Upper image from Google Maps, lower image from the Força Aérea Brasileira.

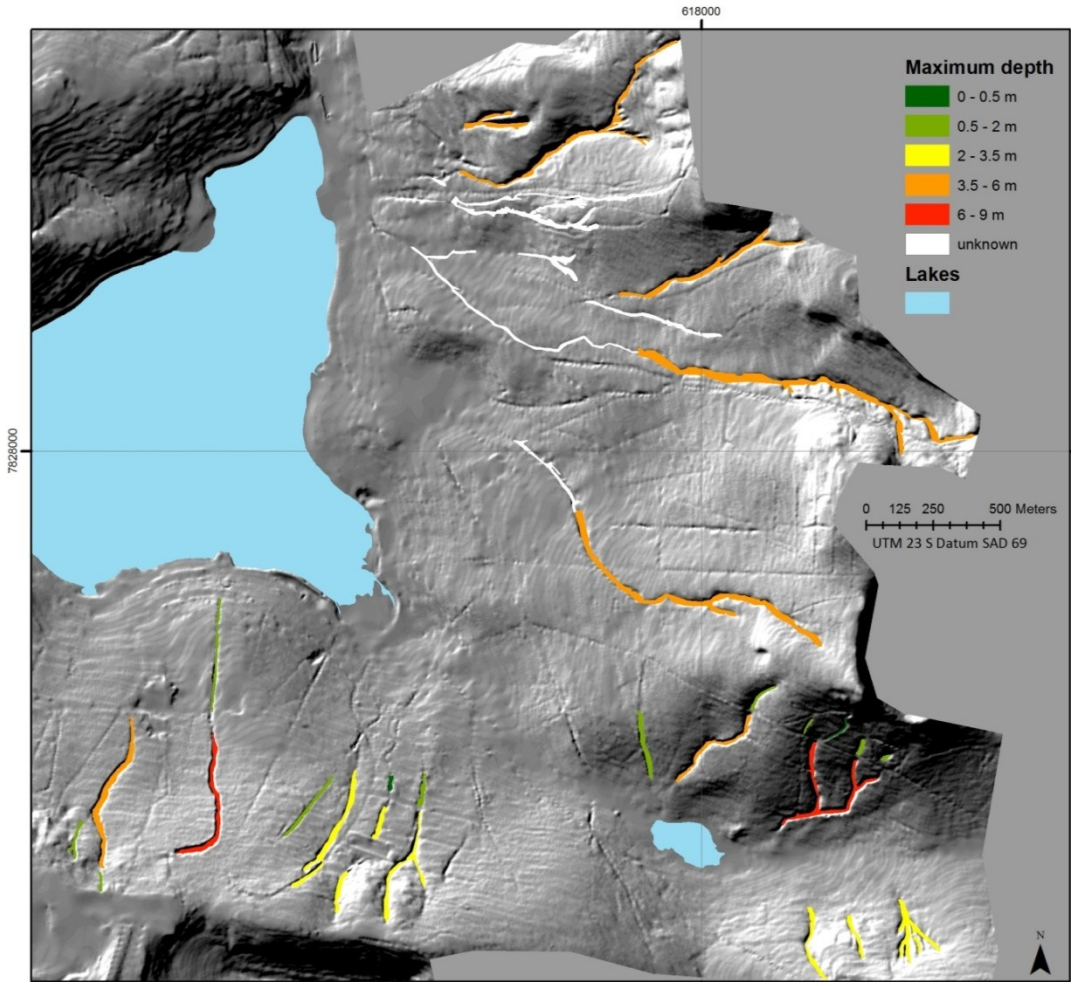

Figure 2-16 Shaded relief model based on one-meter equidistant contour lines.

From this information, the volume and depth of 18 gullies was estimated. The colors of the gullies indicate the maximum estimated incision depth of the gully. The terrace-like structure visible all over the elevation model is due to the interpolation algorithm (Hutchinson 1989) that results in slight flattening at each contour line. The large lake is the lake Lagoa Santa, the small one in the south-east is the lake Lagoa dos Preiras. Image source: Farida (2010).

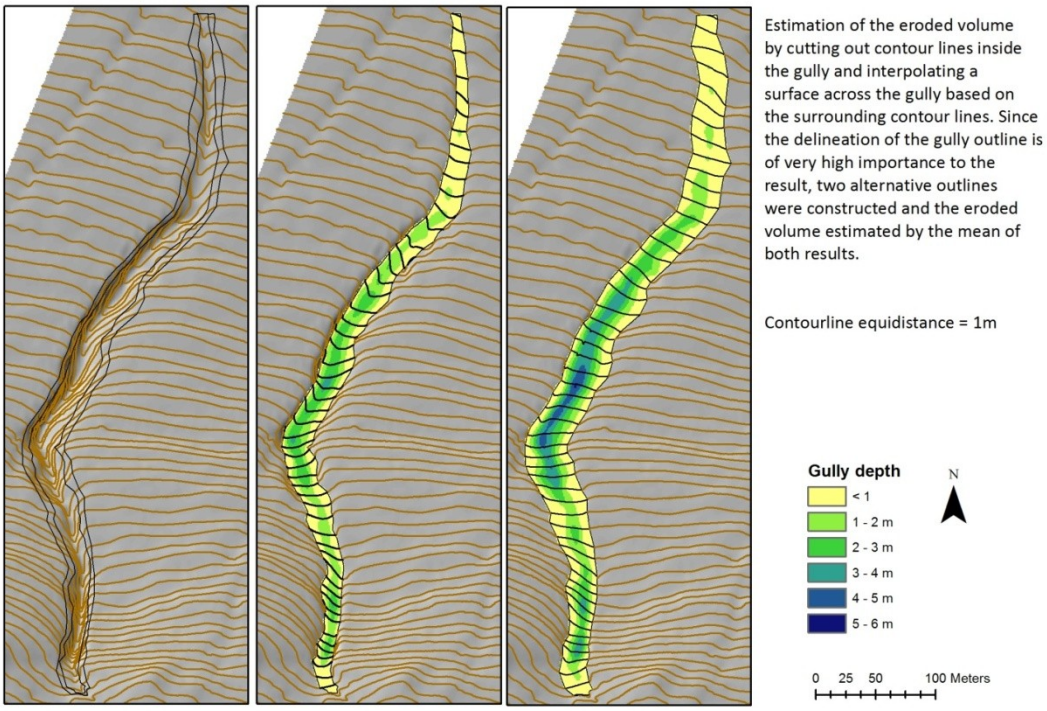

Figure 2-17 Example of gully depth estimations.

Left: original contour lines with two outline estimations. Middle: gully depth calculation based on the inner gully outline. Right: gully depth calculation based on the wider gully outline. The total eroded volume was estimated by the mean of both versions. Source: Farida (2010).

The thus derived total sediment volume disposed into lake Lagoa Santa was 182 ± 62 $\cdot 10^3 m^3$. Into the small lake south-east of the lake Lagoa Santa (Lagoa dos Preiras), 48 ± 17 $\cdot$ 10^3 m^3 were deposited (see lower part of Figure 2-18).

In reality, the eroded sediment volume from gullies that reached the lake Lagoa Santa is certainly higher since for many deep gullies the contour lines were missing (white areas in Figure 2-19).

From the sediment volume and the area of the lakes, the thickness of deposited sediment from gully erosion can be calculated:

The polygon area of the Lake Lagoa Santa shown in Figure 2-16 is 1.65 km^2 and the area of the lake Lagoa dos Preiras 0.05 km^2. Although Parizzi et al. (1998) give a different surface area for the lake Lagoa Santa (1.31 km^2), the surface area calculated above was used for the estimation of the sediment thickness.

Based on these data, gully erosion would have lead to an additional sediment layer of 11 cm in the lake Lagoa Santa and of 160 cm in the small lake in the south-east.

The age of the gullies is unknown. It is only clear from the aerial photo that they existed already before 1964, and while some may be connected to this phase of intensive construction, others may have been already induced by the land use change after European settlers arrived in the region. Assuming a gully age of 100 ± 50 years, the estimated sedimentation rate for Lagoa Santa Lake is at least 11 ± 5.5 cm/100 years. Using the same assumption of the gully age, the estimated sedimentation rate for the small lake Lagoa dos Preiras is 160 ± 80 cm/100 years.

2.4.3 Interpretation and discussion

Parizzi et al. (1998) note a mean sediment delivery rate into the Lagoa Santa Lake of 2.5 cm/100 years from drill hole data for the time between 1440 and 5020 YBP. This is about four times lower than the estimated sediment entry from recent gully erosion after human intervention. Although it is difficult to compare data from drill holes and from eroded material due to the process of compaction, the difference of the sedimentation rate is still remarkable, especially since not all existing gullies could be included into the calculation due to lacking contour lines. There is also large significant difference in sedimentation rate between Lagoa Santa lake and the small lake Lagoa dos Preiras. The estimated sedimentation rate into the small lake is about 14 times higher than the one into the Lagoa Santa Lake. For the calculation, the total amount of the sediment was transported into the small lake. However, in reality the eroded material probably did not completely reach the lake but some deposited in the alluvial plain. Thus, it might have been necessary to take the total area of the flat sedimentation plane around the small lake as deposition zone.

Nevertheless, this short estimation showed well the strong impact of gully erosion to increase in sedimentation rate in the region.

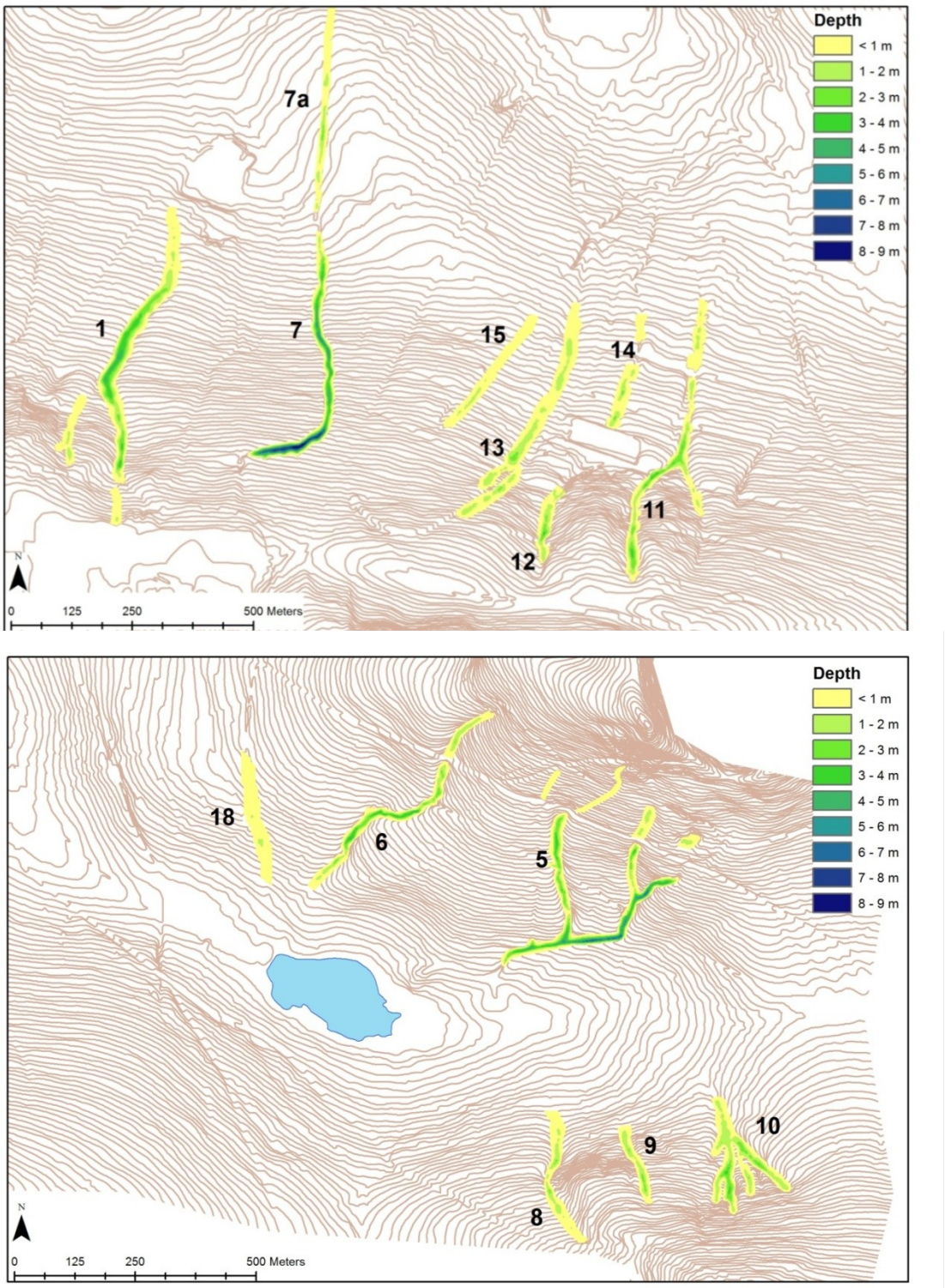

Figure 2-18: Depth of the gullies around Lagoa dos Preiras.

The calculation is based on the difference of interpolated surfaces using the wider gully outline (compare Figure 2-17). Source: Farida (2010).

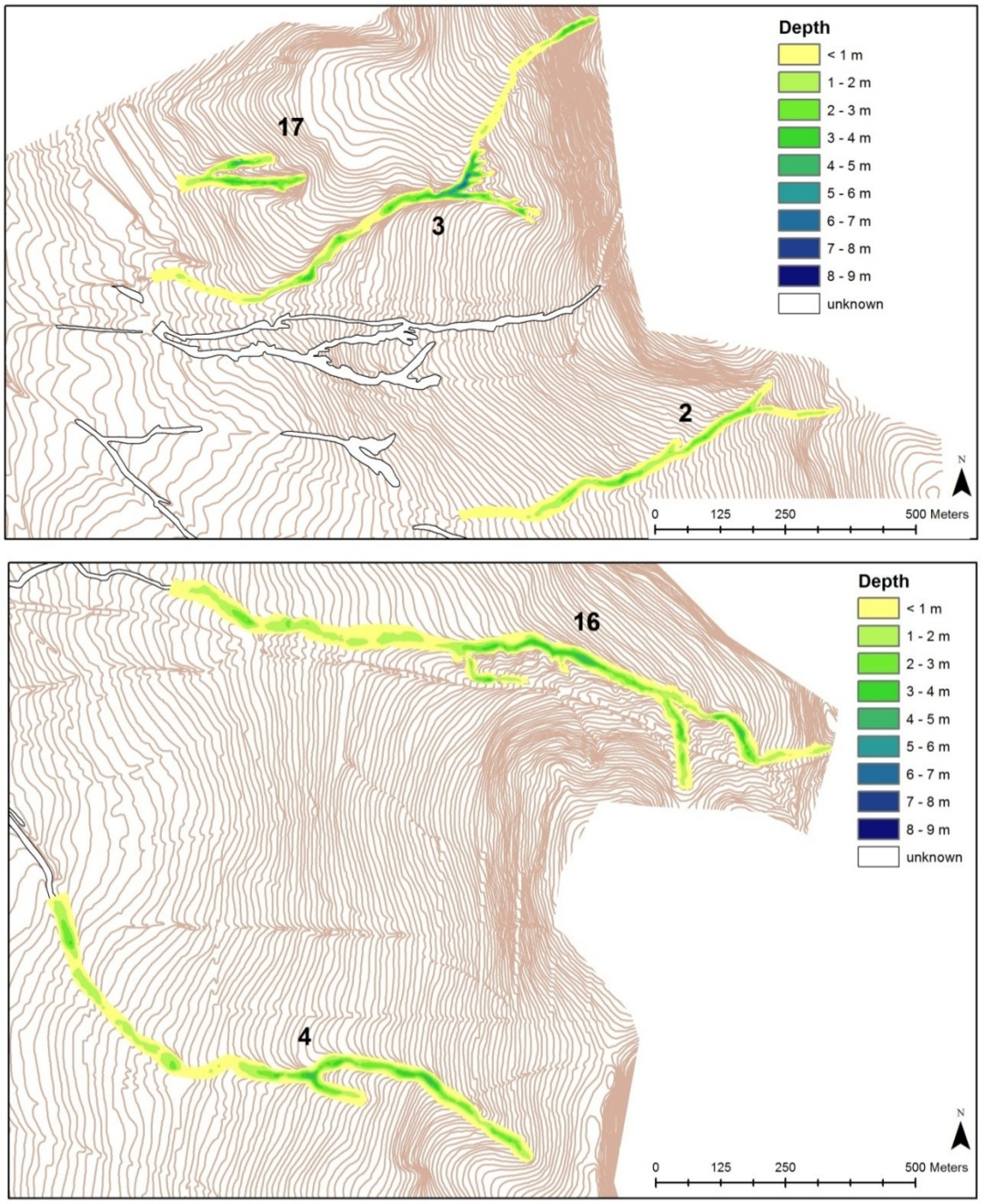

Figure 2-19: Depth of the gullies on the eastern flank of the Lake Lagoa Santa. The calculation is based on the difference of interpolated surfaces using the wider gully outline (compare Figure 2-17). Source: Farida (2010).

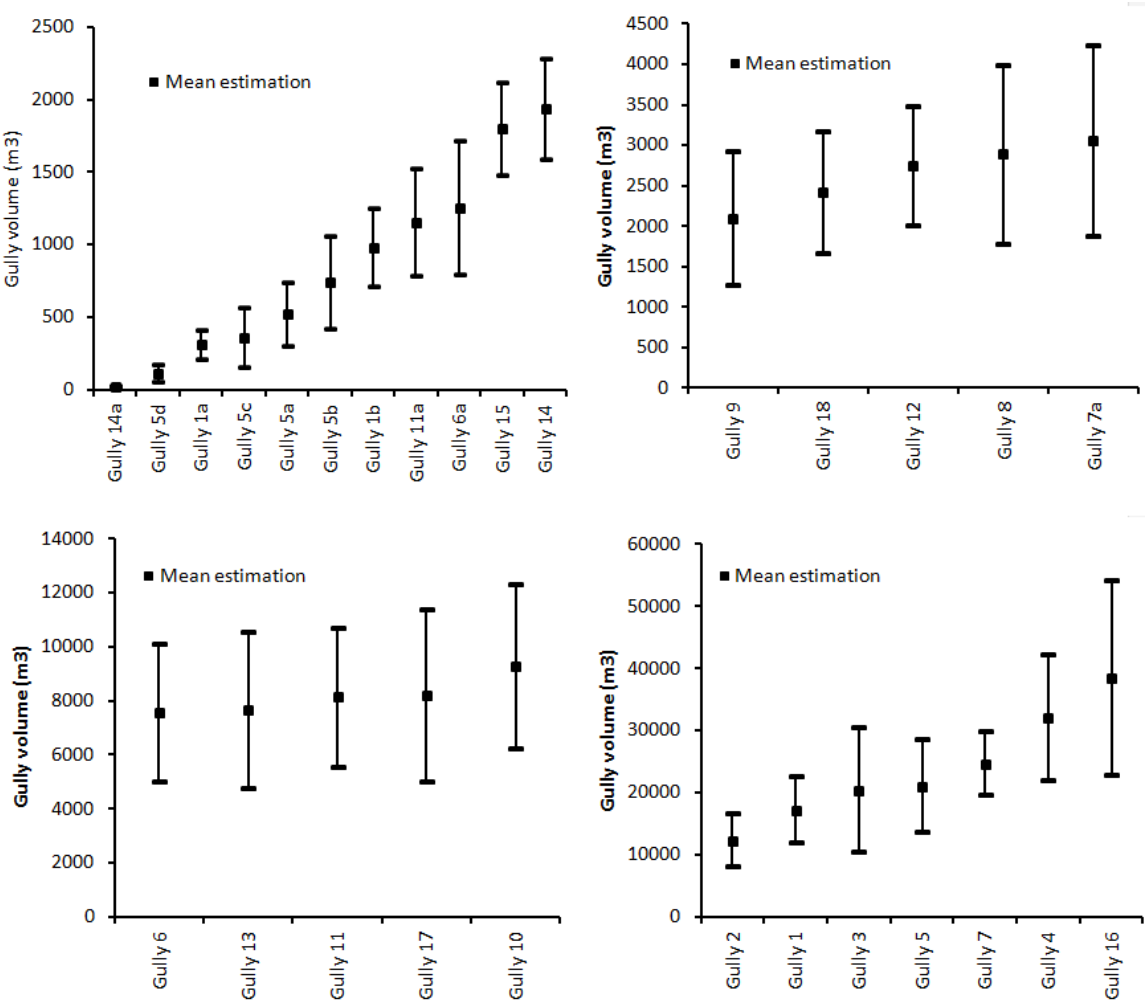

Figure 2-20 Results of the estimation of the gully volume.

The calculation is based on two different outlines of the gully and 1 m equidistant contour lines. The gully identification number is shown in Figure 2-18 and Figure 2-19. For gullies dissected by a road (e.g. gully 5), volume was calculated for each section separately. Source: Farida (2010).

3 Methodology for deriving maps of geo-potentials

For the further assessment of geo-potential in the study area and for the creation of thematic maps that can be integrated by land use planners into their decisions, the following workflow was designed (Figure 3-1):

The basis of the workflow is a general understanding of the geological architecture, the geomorphological evolution and the spatial distribution of hydrological soil properties.
Thus, in a first step, existent information on geology, geomorphology and soils has been collected for the study area (step 1 in Figure 3-1). In a second step, this information is checked for consistency (e.g. the geological map needs to be consistent with relief data) and updated using field observation and remote sensing data. In this part, also a conceptual model of landscape evolution and spatial distribution of hydrological soil units is developed. The thus gained understanding of soil-landscape interrelation is visualized through catenas, which are idealized landscape cross-sections equipped with prototype soil profiles at typical relief locations. For each prototype location along these representative catenas, typical hydrological soil properties as well as typical relief and bedrock parameters are described.

These spatial parameters (e.g. slope, topographic position, thickness of geological strata) are collected in a database in a GIS. Afterwards, hydrologically relevant soil properties such as depth of the upper soil layer or effective field capacity are inferred from environmental parameters. An overview of this critical regionalization process is given in section 3.3 while the methodology is described in detail in chapter 10. The thus created thematic maps of geological parameters and hydrological soil properties can be used as input for catchment scale models on groundwater vulnerability, erosion hazard and resource estimation (see also chapter 13 to 12). The resulting easily understandable maps can be incorporated into a Spatial Decision Support System (SDSS) at catchment scale involving multiple stakeholders. Examples for this procedure – which is not part of this project - are described in Hoppe et al. (2006), Marinoni and Hoppe (2006), Lamelas et al. (2010, 2012).

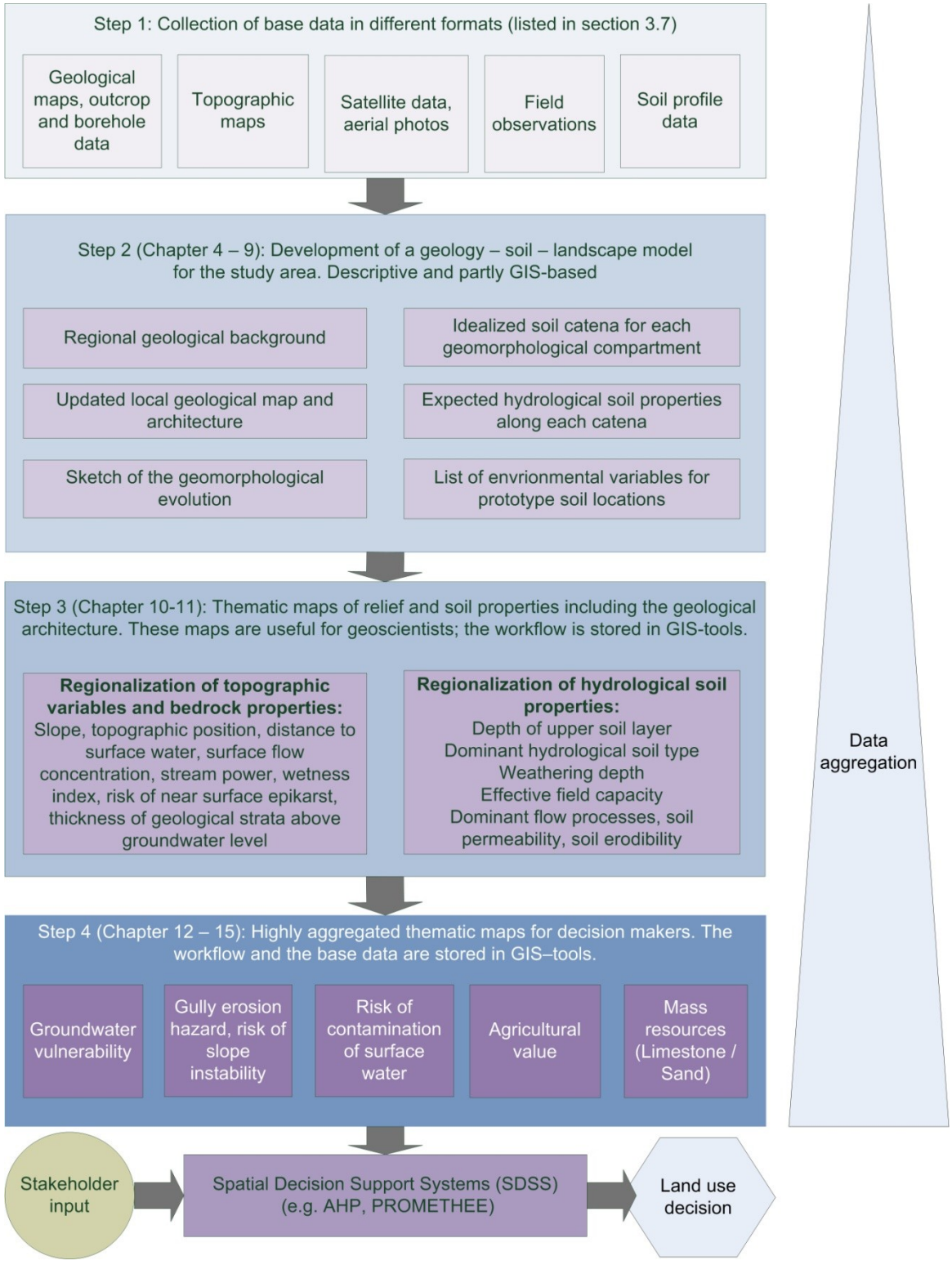

Figure 3-1 General workflow of the project.

Throughout the workflow shown in Figure 3-1, the rate of data aggregation and thus the directly accessible information content for non-experts is rising from the beginning of the workflow until the final thematic maps. Altogether, four levels of data and knowledge aggregation can be distinguished:

1. Primary input data available in different formats and qualities
2. Geology – soil – landscape model based on the primary input data. This model is mainly descriptive but involves also updated base information (e.g. an updated geological map).
3. Transfer of the descriptive geology – soil – landscape model into regionalization rules for the spatial prediction of parameters that are relevant for experts. This is done inside a Geo-Information-system.
4. Easily understandable and highly aggregated thematic maps for decision makers regarding geo-hazards and geo-resources.

The workflow of step 3 and 4 (Figure 3-1) is implemented and stored in transparent tools in the GIS environment. It can be modified during any aggregation level by experts to match advances in knowledge about the soil-landscape model or to incorporate new spatially available information.
The aim and output of the current project reaches only step 4 in Figure 3-1, yielding the final output thematic maps for groundwater vulnerability, gully erosion hazard, risk of contamination of surface water, risk of gully erosion and slope instability, agricultural value and mass resources. For a SDSS, separate tools are available (e.g. Marinoni (2004, 2005)) and require the input of stakeholders, which was not feasible within the current project.

3.1 Step 1: Collection of base data

Base data regarding topography, geology and geomorphology were collected from institutions and relevant publications. Many geological and pedological data were available from the Projeto VIDA, a regional project conducted by the geological survey (CPRM) in 1994 that aimed at a viable industrial development and protection of the environment in the northern periphery of the metropolitan area of Belo Horizonte. Also the large volume describing the physical environment of the protected area APA Carste de Lagoa Santa, which was published by the CPRM and the national environmental protection agency (IBAMA) in 1998, yielded a large data base. The CPRM also provided other geological maps and the field data source from the geological map created in the context of Projeto VIDA. Also different scientific works on the local geology were very useful for the project (Pessoa 2005, Büchi and Pagung 2008). The prefecture of Lagoa Santa provided digital data on elevation, hydrology and infrastructure that were highly valuable for the

derivation of relief parameters. Additionally, own field work resulted in a large data base and helped the interpretation of the literature data.
The available base data for the study area are listed in detail in chapter 3.7.

3.2 Step 2: Geology – soil – landscape model

In this second step, the available data were combined, checked for errors and mutually validated for integrity:

- The geological map was checked for plausibility compared with elevation data and updated using all available data (chapter 5).
- The sedimentological architecture of the alluvium of the Riberão da Mata was studied in an open pit mine (section 5.8).
- From literature and field data, the geomorphological evolution of the area was described, explaining the spatial distribution of distinct soil horizons in the landscape (section 6.4).
- From this understanding, six geomorphological compartments were distinguished and for each a catena constructed that shows the typical relief positions of idealized soil profiles (section 6.5).

3.3 Step 3: Regionalizing geo-scientific parameters for experts

In this step, continuous hydrological soil parameters were derived from interpolated base parameters on geology, relief and hydrology and the understanding of geology-soil-landscape interaction gained in step 2. Thus, several thematic maps of geo-scientific parameters that are useful for experts were created. The workflow includes:

- The digitally available contour lines were checked for errors and corrected.
- From the contour lines, a digital elevation model was interpolated and checked for hydrological plausibility. For the detailed workflow see section 10.4.1
- Thickness of different geological strata were interpolated using the DEM, the outlines of geological strata and data from drill-holes. See chapter 11 for details.
- Regionalization of hydrological soil parameters and other geo-scientific variables using a SIM method described in section 10.2.

3.4 Step 4: Highly aggregated thematic maps

Based on the expert thematic maps created in step 3, highly aggregated thematic maps are derived in step 4 that are understandable also for non-experts:

3.4.1 Agricultural value

Agricultural value in the tropics is often limited by adverse chemical properties of the soils. This can be estimated from the geo-scientific parameters that were regionalized in the previous chapters. Additionally, slope and risk of waterlogging are hindering factors that are included in a second step when estimating the total agricultural value. More details can be found in chapter 12.3.

3.4.2 Sand and limestone resources

The evaluation of availability of mass resources was restricted to carbonates (e.g. for cement production) and aggregates for construction, mainly sand. While the first is derived from geological and pedological variables such as thickness of geologic strata and weathering depth, the second is derived from volume estimation of the material stored in the larger alluvial plains. This is described in more detail in chapter 12. For sand resources, also a sedimentological study of structures in an open sand pit was useful.

3.4.3 Groundwater vulnerability

For the current project, the PI-method (Goldscheider et al. 2000) has been chosen to evaluate the intrinsic groundwater vulnerability, i.e. the groundwater vulnerability independent on the type of hazardous substances posing a risk for the pollution of the aquifer. This method is based on the general travel time vertically through all layers overlaying the groundwater surface. Thus, it is very similar to the method used by the German geological surveys (Hölting et al. 1995). The difference is that the PI-method also integrates the vulnerability of the aquifer by lateral surface flow into karst ponors. The method is described in detail in the introduction to chapter 13.

3.4.4 Gully erosion hazard and risk of contamination of surface water

To estimate the gully erosion hazard, general information to gully development in south-east Brazil were combined with theoretical considerations regarding topographic threshold conditions. Thus, general parameters such as dominant flow processes in the soil, erodibility and sensitive locations such as rims of plateau areas or headwater hollows are combined with a parameter based on slope and drainage area that indicates the eroding power of the water. The method and its results are described in detail in chapter 14. The risk of contamination of surface water is primarily based on the hydraulic closeness of a location to the next stream, lake or swallow hole. The applied scheme can be found in chapter 14.7.

3.5 Spatial Decision Support Systems for Land use Planning

Often, land use decisions imply consequences for several stakeholders, from local residents, urban planners, resource managers, industries, water suppliers, farmers or biologists. For every stakeholder group, the mapped parameters have different priorities: while for water suppliers, protection of the karst aquifer may have highest importance, this parameter is not so important for the stakeholder group of farmers or cement producing companies. If relevant parameters are available in a digital mapping system such as a GIS, Spatial Decision Support Systems (SDSS) can help to objectify the decision making process by visualizing the individual spatial preferences of each stakeholder group. In this chapter, two methods (AHP and PROMETHEE) are described in an exemplary way to illustrate the possibilities of SDSS.
Although this last step is not covered in the present thesis, two types of SDSS are shortly presented to give an idea what can be done with the thematic maps created during this project. A general overview of SDSS methods can be found in Malczewski (1999).

3.5.1 Multi-attribute techniques: AHP

One type of SDSS is summarized as multi-attribute-techniques, i.e. techniques that help combine many different attributes into one suitability map in a transparent, comprehensive process. The implementation of the Analytical Hierachy Process (AHP) from Saaty (1977) into a GIS (Marinoni 2004) is a good example for this method.
To aid in objective decision making, every stakeholder group can combine the available parameters in a weighted addition to generate maps showing the ideal place for a given project based on their interests (Figure 3-2). The preferences of each stakeholder group are incorporated via the choice of weights for the different parameters.
The comparison of different output maps can detect areas of conflict and areas of agreement between stakeholder groups and thus help to solve land use conflicts in a transparent process.
Since it is not easy for a more or less homogeneous stakeholder group to rank the parameters effectively so that represent their viewpoint, Saaty (1977) developed a scaling method that helps to generate consistent weights by pair-wise comparison of the importance of parameters.

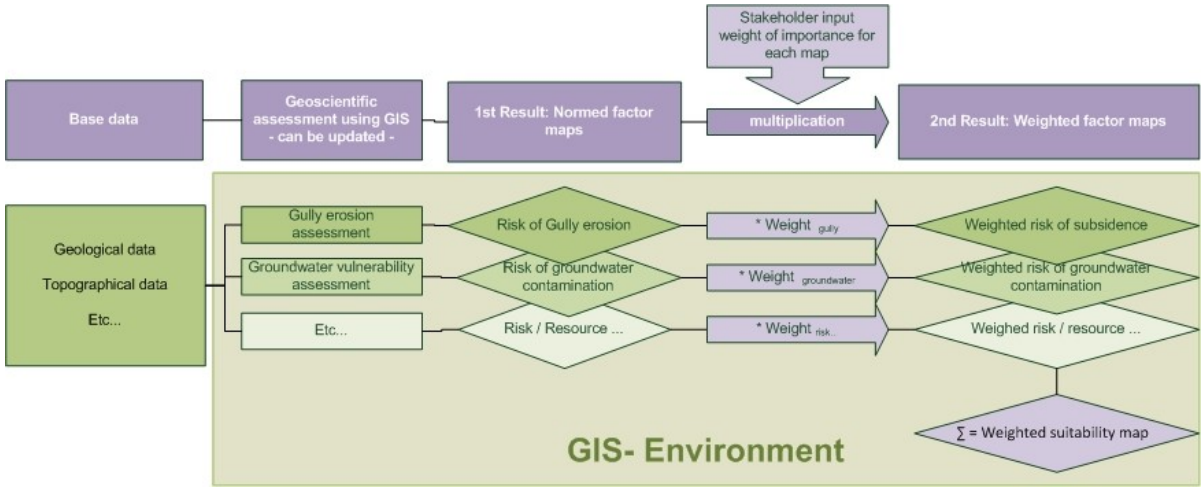

Figure 3-2 Principle of the weighted overlay for regionalized parameter raster data sets.

The weights W_1 – W_n can be generated using AHP and add up to 1.

Each two parameters are compared in a matrix operation regarding their importance according to the stakeholders view for the current project. The scale ranges from 1 = equal importance of both paramters until 9 = extreme importance of one parameter over another, the rest of the matrix is filled with the inverse values (Table 3-1). In this exemplary case, parameter P1 is slightly more important than parameter P2 but P3 is very much more important than P2 and considerably more important than P1.

Parameter	P1	P2	P3
P1	1	2	1/5
P2	1/2	1	1/8
P3	5	8	1

Table 3-1 Example of a preference matrix using the AHP from Saaty (1977).

By normal reasoning it is clear, that if P1 is more important than P2 and P2 more important than P3, P3 must also be more important than P1. Nevertheless, with many parameters and in large discussion groups, this general plausibility check might become difficult and therefore, Saaty (1977) provides also an index of matrix consistency that checks for errors in the overall consistency.

If this value is small enough, i.e. if the matrix is sufficiently consistent, the largest eigenvector of this matrix yields numerical values for each parameter that can be interpreted as relative weights of importance (Saaty 2003). In the final mapping process, these numbers can be used as weights before adding up the different parameter layers. A good implementation of this Analytical

Hierarchy Process into ArcGIS that transforms this relatively old multi-criteria analysis method into a powerful tool for spatial decision making can be found in Marinoni (2004).

Of course it is necessary before applying this method that all parameters are standardized to the same value range, which is the case for the optimality maps generated in this project.
Since the weighted addition is a function that can be easily applied for each raster cell in a large area, this method is suitable for the creation of "suitability maps" for large project areas. If different explicit location alternatives are to be compared, they can be characterized by different statistical attributes (mean, median, range, standard deviation) of the raster suitability values inside each location.

3.5.2 Outranking method: PROMETHEE

If no suitability maps covering entire areas are needed but rather a comparatively low number of location alternatives are to be compared, outranking methods such as PROMETHEE (Brans et al. 1986) might yield better results. Outranking methods do not require the input parameters to be standardized to a certain range and also do not work in an additive way such as the creation of the suitability map by the AHP implementation of Marinoni (2004). Instead, a dominance structure between the different location alternatives is constructed based on the direct pair-wise comparison of each location with regard to the given criteria values. If a location is "better" with regard to a certain criterion compared to another location, it receives the value 1, if it is "worse", it receives the value 0. If both locations are equal, both receive the value 0. After this has been done for all criteria in all locations, a "net flow" value is calculated that defines a ranking list of alternatives. Thus, instead of standardizing each criterion to a certain range for comparison, it is only necessary to decide if lower or higher values of a criterion are better and how large the difference has to be to interpret the values as "not equal".
Since it is not always clear which statistical value (e.g. mean, max, median etc.) of a criterion should be compared in the outranking method, Marinoni (2005) suggests repeated automatic runs of the GIS-implemented PROMETHEE method combined with an artificial enlargement of the sample size using a Monte Carlo simulation. This method combination results in a statistical distribution of ranking lists and leads thus to a more reliable result that is not influenced by outliers. An overview and a discussion of the PROMETHEE method can be found in Behzadian et al. (2010).

3.6 Implementation of the workflow in GIS

The calculation method for the regionalized variables is stored in transparent GIS-tools that were created using the model-builder window in ArcGIS. Thus, they can be analyzed and modified without knowing any programming language. An overview of the toolboxes created for this project is given in Figure 3-3:
After some basic functions stored in toolbox A, the toolbox B contains the tools for deriving most relief parameters. Toolbox C contains the tools for hydrological soil parameters and toolbox D the tools for the geological architecture and groundwater vulnerability. In the last toolbox E, the tools that predict erosion hazard and the agricultural value are stored.

The tools from toolbox B – E are numbered and meant to be executed consecutively since the outputs of the first tools are used as input for the following. For a better overview, the numbers of the tools whose output is needed as input are listed in brackets for each tool. For example, the tool 11 that calculates dominant flow processes needs the outputs from tool 5 (dominant topsoil) and 9 (subsoil permeability) as input. Additionally, small letters list basic input parameters needed for the tool:

t = basic topographic input data (contour lines)
h = basic hydrologic input data (rivers, lakes, locations of sinkholes, drainage basins)
g = basic geologic input data (geological map with different attributes)
gm = basic geomorphologic input data (karst features from Kohler et al. (1998)
hg = basic hydrogeologic input data (groundwater isolines)
b = borehole data (drill holes from Pessoa (2005))
v = vegetation or land use (classified Landsat 7 ETM+ data)

A graphic overview of the variable –dependence is given in the Annex on p. 327 in the form of a flow-chart. This diagram helps to understand the interrelation of different variables and detect errors or sensitive parameters.
In following pages (pp. 329 ff)., a list shows all parameters that are used as input for the GIS-tools. An idea of the importance and sensitivity of an output parameter can be gained by the frequency of its use as input for other tools, which is listed in the last column of these tables.

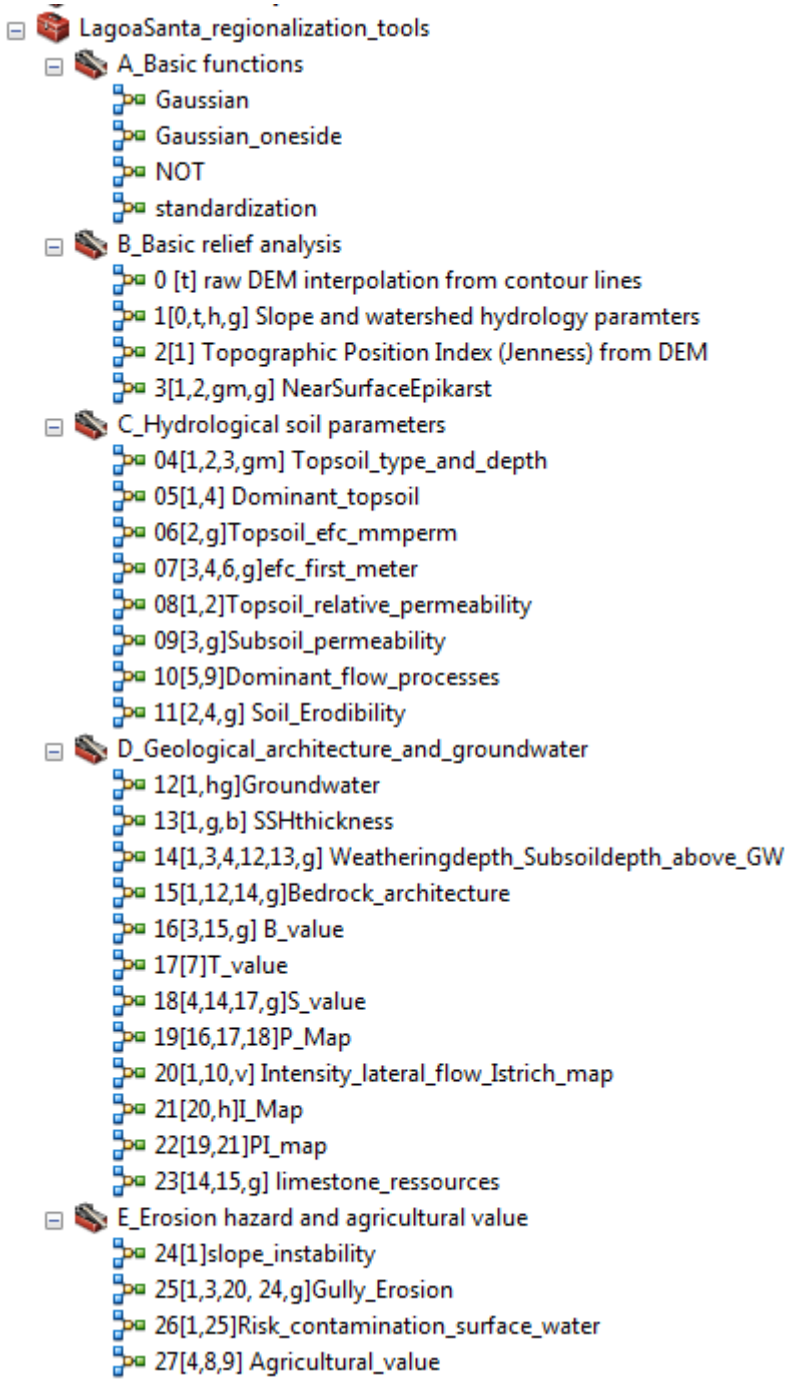

Figure 3-3 Overview of the toolbox for regionalizing geo-potentials.

3.7 List of data sources

For the outline of the different maps and projects see Figure 4-4

3.7.1 Elevation and surface hydrology data sources

Contour lines and drainage system were available digitally from 4 x 1 : 25 000 topographical maps around Lagoa Santa (extent of the map 1 : 50 000 of Lagoa Santa as indicated in Figure 4-4) . For the larger surrounding, remote sensing SRTM elevation data were available.

From the chapter on surface hydrology (Patrus 1998) of the APA Carste de Lagoa Santa protection zone, climatological data and surface water quality and quantity data were available.

From the geomorphological map (Kohler et al. 1998) of the APA Carste de Lagoa Santa protection zone, karst features such as dolines, uvalas, towers, walls or other karst outcrops were available in vector format.

3.7.2 Geological data sources

After early regional studies, Schöll (1972) was the first to map the Bambuí rocks in this area in detail.

Later, geological maps were developed for the metropolitan region of Belo Horizonte (RMBH) at a scale of 1 : 50 000 (IGA 1982).

In 1993, a new geological map 1 : 50 000 (Tuller et al. 1991) was published for the area west of the Rio das Velhas within the first edition of the Projeto VIDA. This map was published digitally in a second edition 2003 (Ribeiro et al. 2003). From this mapping, 170 outcrop descriptions were available from the CPRM.

In 1998, the intensely karstified area north-west of the city Lagoa Santa was analyzed in detail to define an environmental protection area (APA Carste de Lagoa Santa). The geological map for this project from Santos Viana et al. (1998) is based on the map from Projeto VIDA (Ribeiro et al. 2003, Tuller et al. 1991).

In 1999, the CPRM published a geological map 1 : 100 000 which summarizes, generalizes and updates the previous maps in the region (Brandalise and Heineck 1999).

In the southern part of the study area, a graduation thesis geological mapping was available (Büchi and Pagung 2008) in the central part of the study area.

23 outcrop points, 154 drill-hole data and ten geological cross-sections were available from a PhD thesis focusing on hydrogeology (Pessoa 2005).

The sedimentological Phd thesis of (Vieira 2007) published also in Vieira et al. (2007a), Vieira et al. (2007b) gave new insights into the sedimentological architecture of the Sete Lagoas Formation near the study area.

3.7.3 Soil data sources

From the Projeto VIDA, a soil map 1 : 50 000 was digitized and 27 soil profiles with analytical data were available (CPRM 1994b).

From the APA Carste de Lagoa Santa protection zone, also a soil map 1 : 50 000 (Shinzato and Lumbreras 1998) was available in vector format. In the same project, 15 soil profiles with analytical data, 15 descriptive soil profiles and 49 short descriptions from piston samplers were available.

The analytical data comprised the following parameters:

- Soil texture: Percentage of coarse sand, fine sand, silt, total clay and natural (=water dispersible) clay
- Density and total porosity
- pH (H_20), pH (KCl)
- Percent organic carbon (only APA Carste de Lagoa Santa), % organic material
- Plant available phosphorous
- Amount of basic cations, effective cation exchange capacity, base saturation, Al saturation
- Clay activity (only APA Carste de Lagoa Santa)
- For few exemplary profiles documented by Shinzato and Lumbreras 1998, also the total content of SiO2, Al_2O_3, Fe_2O_3, TiO_2 and P_2O_5 are given.
- Plant available water (only Projeto VIDA).
- Water content at 0.1 Atm (pF 2) and 15 Atm (pF 4.2)

Additionally, several soil catenas including description of the profiles were available for a study site inside the karst area (Piló 1998).

The chapter on geotechnical properties of the APA Carste de Lagoa Santa protection zone summarizes the physical properties of the soil-saprolite complex for each geological unit (de Lima Cabral 1998).

3.7.4 Hydrogeological data sources

From the APA Carste de Lagoa Santa protection zone in the chapter on hydrogeology (Pessoa and Mourão 1998), production data of wells and chemical analysis data of the groundwater were available.
In the same project, isolines of the gorundwater level with 20 m equidistance were indicated in a groundwater vulnerability map (Pessoa 1998).

In the central area around the Lapa Vermelha mining area,piezomentric drill-hole data from Pessoa (2005) were available for one day in the rainy season and one day in the dry season.

3.7.5 Remote sensing data sources

Satellite images were taken from freely available sources such as Landsat ETM+ Mapper, Google Earth and Bing maps.

3.7.6 Own data

General field observations

Own field work conducted between 2004 and 2006 resulted in

- 250 geological observations plus
- 204 observations regarding only soil color and erosion phenomena.

Since it was often difficult to find fresh outcrops in the highly weathered landscape, also outcrops of strongly altered saprolites had to be used for mapping. For the Serra de Santa Helena Formation, no fresh outcrop could be found.

The 250 geological data points were divided into three categories of data quality:

- 76 are based on fresh rock outcrops (category I),
- 68 are based on the interpretation of weathered saprolite or similar data (category II) and
- 40 are indirect hints for the geological underground such as karst features (dry valleys, dolines), typical vegetation, typical soil color or distant views to outcrops (category III).
- The remaining 66 data points are observations of the sediment structure in the Quaternary alluvial plains.

Geological measurements

- 84 measurements of S_0 and S_1 (bedding and first shear plane), which are nearly parallel in the region
- 219 measurements of joints (55 joints if parallel measurements at large outcrops are omitted)
- 5 measurements of fault planes at two locations.

Measurement of soil properties

Saturated hydraulic conductivity was measured for four different soil materials using a double ring infiltrometer: red topsoil, yellowish subsoil and saprolite of Serra de Santa Helena meta-pelites and crystalline basement. These measurements are not statistically significant since the thus measured saturated hydraulic conductivity is strongly influenced by local conditions (e.g. macropores) and needs several repetitions to be integrated in a sound regional estimation of soil properties. Nevertheless, it was used as a hint about the scale range of saturated hydraulic conductivity of characteristic soil horizons in the study area.

Mapping of geomorphological features

- Using views from Google Earth and relief structure, hummocky slopes and erosion scarps were identified that could indicate the location of paleo-gullies as described by Bacellar et al. (2005).
- The images supplied by Google Earth were also searched for visible erosion features which were maped.
- From relief structure, possible locations of old mass movements were inferred.
- These data were not retrieved systematically but only exemplary and give thus only a non-comprehensive overview.
- Dolines and ouvalas were inferred using based on the difference between filled and unfilled DEM. It was also noted if the depression was (probably) sealed or in direct contact with the groundwater.
- Regions that were remarkably covered by a surface stone layer during field excursions were noted. This feature is also non-comprehensive since the information was retrieved only along roads that were passed during the excursions.
- The result is shown in Map 7 in the annex.

4 Geology – overview

Belo Horizonte is located at the southern border of the São Francisco Craton (Almeida 1977), where the Archean gneiss-migmatite basement crops out. Inserted into this basement just south of the city is the Quadrilátero Ferrífero (Iron Quadrangle), a folded and faulted greenstone belt structure of Paleoproterozoic meta-volcano-sedimentary sequences known for their gold and iron resources (Dorr 1969, Hoppe et al. 1987).

4.1 Archean basement

The Archean basement at the southern tip of the São Francisco Craton is dominated by amphibolite facies tonalite-trondhjemite-gneiss and migmatite that are intruded by tonalitic to granitic plutons (Teixeira et al. 2000). In the region of the Quadrilátero Ferrífero, the gneissic terrains occur in domes surrounded by troughs containing the Rio das Velhas Archean greenstone belt and the Paleoproterozoic Minas Supergroup (Alkmim and Marshak 1998, Dorr 1969). The Rio das Velhas Supergroup consists in its basal Nova Lima Group of a meta-volcano-sedimentary sequence hosting the main gold deposits of the Quadrilátero Ferrífero (Baltazar and Zucchetti 2007). The Paleoproterozoic Minas Supergroup contains, next to quartzites and dolomites, a Lake-Superior-type banded iron formation that is exploited extensively for the metallurgical industry in Belo Horizonte.
Intruded into the Belo Horizonte dome are SW-NE-striking acid dykes containing intensely fractured milky and smoky quartz associated with feldspars and occasionally epidot (Ribeiro et al. 2003). Nearly orthogonal to them are two mafic dyke swarms cutting the Archean gneiss-migmatite complex and the Archean Rio das Velhas greenstone belt (Chaves 1996). The older swarm (ca. 2 Ga, K-Ar of Amphiboles), strikes 330-350° (main) and 50-70° (subordinate) is metamorphosed in high amphibolite facies. The younger dyke swarm strikes approximately 290-310° and still preserved its igneous structure. It cuts not only the Archean units but also the Paleoproterozoic Minas Supergroup of the Quadrilátero Ferrífero (Chaves 1996).

4.2 Macaúbas Group

In the eastern region of the São Francisco Craton, the Neoproteozoic Bambuí Group and Macaúbas Group are combined into the São Francisco Supergroup (Schmidt HL 1972, Schöll 1972). Relationships between the Macaúbas sediments - whose glaciogenic origin is well documented in outcrops at the Serra da Agua Fria (Karfunkel et al. 2002) - and the marine Bambuí sediments have been discussed by several authors: Schmidt HL (1972) described lateral interdigitations of Bambuí and Macaúbas sediments, combining both as contemporaneous facies

into the São Francisco Series. Schöll (1972) and later works (e.g. Karfunkel and Hoppe (1988), Martins-Neto et al. (2001)) assumed a primarily vertical and only rarely lateral interdigitation of both units, with the Macaúbas Group being the older one, deposited in a partly separated basin in the east (Figure 4-1).

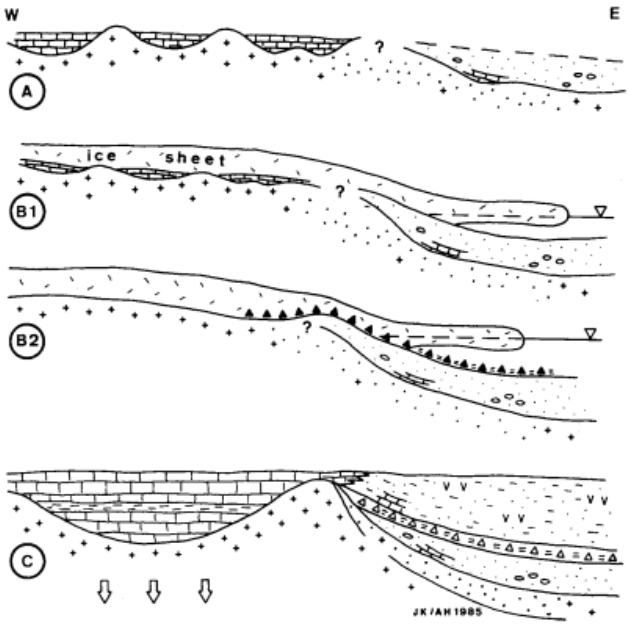

Figure 4-1 Schematic paleo-geographic evolution of the eastern part of the São Francisco Basin during the late Proterozoic (Macaúbas and early Bambuí Group).

Previously deposited carbonates (A) are eroded and transported from the cratonic center to the eastern margin by ice sheets (B). Afterwards, the central cratonic area subsides (C) and the Bambuí sediments are deposited while in the eastern part psammopelitic sediments cover the glacial deposits. (Karfunkel and Hoppe 1988).

4.3 Bambuí Group

The Neoproterozoic Bambuí – Group consists of generally flat lying carbonate and pelite rocks that are deformed near the cratonic border (Figure 4-2).

After the early works in the nineteenth century from v. Eschwege (1832), Derby (1880) and Rimann (1917), it was v. Freiberg (1932) who gave the first detailed description of the Bambuí Group. Branco and Costa (1961) established the first regional litho-stratigraphic division. Later, Barbosa (1965), Braun (1968), Schöll (1972) and Dardenne (1978) refined and modified it according to new observations. Of these authors, Schöll (1972) studied the base formations of the Bambuí Group occurring at the south-eastern border of the São Francisco Craton with highest detail. He rearranged the uppermost units and his classification has been - together with that of Campos and Dardenne (1997) - the basis for the stratigraphy used also by recent publications (Table 4-1).

Martins-Neto and Alkmim (2001) and Martins-Neto (2007) interpret the Bambuí first order sequence as classical foreland deposit. According to their interpretation, the cratonic portion of the São Francisco paleocontinent covered by the Bambuí Group acted as a flexural basin in

response to tectonic loads from the Brasília fold belt and later also from the Araçuaí fold belt. To detect the basis of the Bambuí, gravity anomaly maps were interpreted by Lesquer et al. (1981) and Ortu (1990) for the southern part of the São Francisco Craton (Figure 4-3). In the southern central part around the city of Sete Lagoas, a high paleo-relief structure (Alto de Sete Lagoas, (D'Arrigo 1995)) controlled the sedimentation of the Bambuí Group and was continuously reactivated as flexural highland during the folding of the Brasília and Araçuaí belts (Alkmim and Martins-Neto 2001).

In the study area, the following units of the Bambuí Group can be found: Carrancas Formation, Sete Lagoas Formation and Serra de Santa Helena Formation; all younger units are either eroded or have not been deposited.

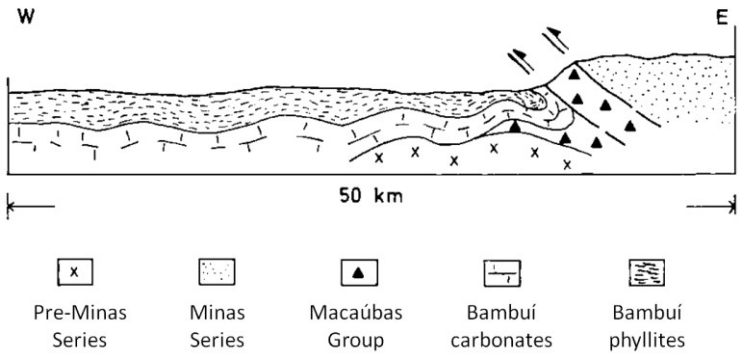

Figure 4-2 Tectonic overview at the SE-border of the São Francisco Basin (Schöll 1972).

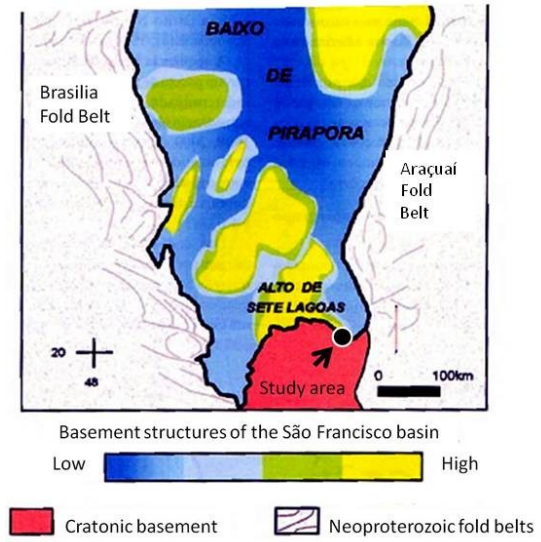

Figure 4-3 Basement structures of the southern São Francisco Craton.

Data derived from Bouguer gravity anomaly data. The blue to yellow colors indicate the elevation of the basement below the Neoproterozoic cover of the Bambuí group (or younger). Source: Alkmim and Martins-Neto (2001).

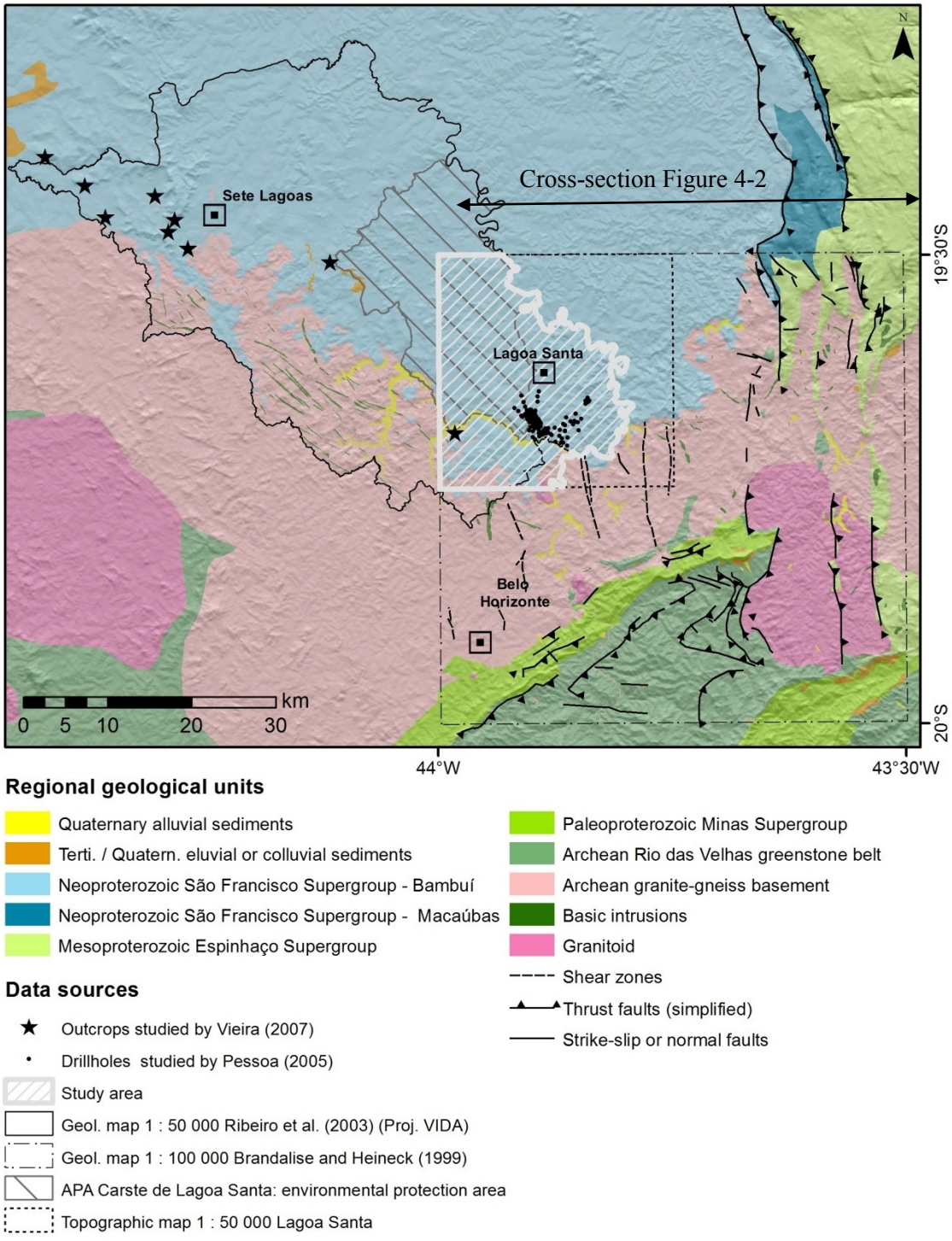

Figure 4-4 Location of the study area and geological data sources.

Geological units simplified from the geological map of Minas Gerais 1 : 1 000 000 (Heineck et al. 2003), with details in the focus area from the geological map of Projeto VIDA 1 : 50 000 (Ribeiro et al. 2003)and the geological map of Belo Horizonte 1 : 100 000 (Brandalise and Heineck 1999)

Lithology		Stratigraphy				
Modified from Schöll (1972) and Dardenne (1978)		Branco & Costa (1961)		Schöll (1972)		Dardenne (1978)
		Formation	Members	Formation	Members	Formation
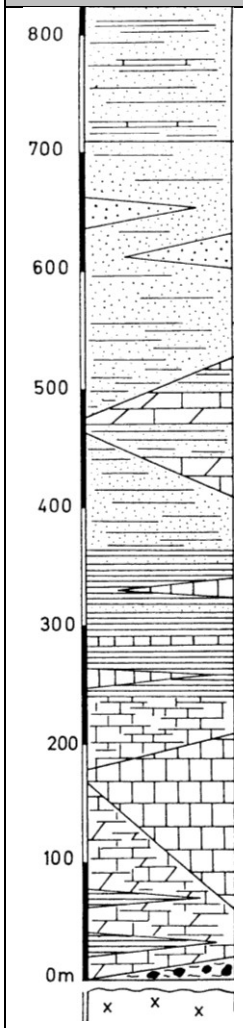	Green siltstones and shales containing carbonates	RIO PARAOPEBA	Serra da Saudade	RIO PARAOPEBA	Serra da Saudade	TRÊS MARIAS
	Grey-green siltstones, lenses of brown arcoses		Três Marias		Três Marias	SERRA DA SAUDADE
	Grey-brown siltstones and shales					
	Carbonates and dolomites with intraclasts, oolithes, grey-black siltstones and shales		Lagoa do Jacaré	LAGOA DO JACARÉ		LAOGA DO JACARÉ
	Siltstones and shales		Serra de Santa Helena	SERRA DE SANTA HELENA		SERRA DE SANTA HELENA
	Shales, meta-pelites, mudstones, meta- siltstones, carbonate lenses					
	Carbonates with quartz and chlorite, meta-pelites					
	Grey-black, finely laminated carbonates	SETE LAGOAS		SETE LAGOAS	Lagoa Santa	SETE LAGOAS
	Carbonates w. quartz and chlorite, meta-pelites				Pedro Leopoldo	
	Conglomerates, diamictites	CARRANCAS			Carrancas	JEQUITAÍ
	Archean Gneiss-Migmatite Basement					

Table 4-1 Lithology and stratigraphy from different authors.

4.3.1 Carrancas Formation

A discontinuous basal conglomerate unit can be observed below the Bambuí sediments in the platformal area of the São Francisco Craton (Carrancas unit, Branco and Costa (1961). This unit is not correlated to the basal glacial Macaúbas Formation at the cratonic border (Martins-Neto et al. 2001, Vieira et al. 2007a) but represents "subaquatic reworking levels and aquatic detritus flux formed in paleodepressions of the cratonic basement" (Kohler and Karfunkel 2002). The single outcrop (Outcrop C on page 68) of the Carrancas unit in the study area is a polymictic conglomerate in a carbonate matrix that is interbedded with pebbly sandstone lenses with incipient lamination (Vieira et al. 2007a). Only recently it has been correlated to a second outcrop about 40 km to the West (Uhlein et al. 2012).

4.3.2 Sete Lagoas Formation

(Schöll 1972, 1973) divided the Sete Lagoas Formation into two facies: the lower Pedro Leopoldo Facies consists of low grade metamorphic marls with carbonate content around 70% interfingering with carbonate free pelitic sediments. The non-carbonaceous materials consist of quartz and in fewer amounts of feldspar and clay minerals (muscovite-sericite, biotite, chlorite), the carbonates contain subordinately dolomite which could indicate sedimentation in the tidal range (Schöll 1973). Pessoa (2005) describes also marbles in drill-holes at the base of the Sete Lagoas Formation. The overlying Lagoa Santa Facies is characterized by very pure (95%) grey-black limestone showing typical millimeter-thick lamination that could indicate seasonal or climatic changes (Schöll 1973). Since the Pedro Leopoldo Facies occurs closer to the cratonic center, Schöll (1973) interpreted it as rim facies with the Lagoa Santa Facies being the corresponding still-water basin facies. Later, the Lagoa Santa Facies transgraded onto the Pedro Leopoldo Facies in the west, while from the east more clastic sediments were deposited (Serra de Santa Helena Formation). Although the Pedro Leopoldo Facies usually lies below the Lagoa Santa Facies, also lateral interfingering occurs and in some parts, the pure carbonates of the Lagoa Santa Facies are completely missing. Although many micro-facies are described from field outcrops in Ribeiro et al. (2003), the authors revert to the two original facies Lagoa Santa and Pedro Leopoldo from Schöll (1972, 1973) for the final map. Ribeiro et al. (2003) describe both facies primarily according to their grain size: the impure carbonates of the Pedro Leopoldo Facies show fine silt-like grain size and are classified as calcilutites whereas the coarse-grained pure carbonates of the Lagoa Santa Facies are classified as calcarenites. The coarse grain size of the Lagoa Santa Facies is due to a recrystallization process and varies with the organic content in the lamina that hindered the crystallization process (Schöll 1973). In the Pedro Leopoldo Facies,

recrystallization was hindered by non-carbonaceous impurities and thus grain size remained small.

Vieira (2007) studied twelve outcrops of the Bambuí group in detail (location see Figure 4-4) and describes nine facies associations (FA) :

- FA1 summarizes the Carrancas conglomerates and is interpreted as basement-incised channels.
- FA2 comprises the basal carbonate unit showing aragonite pseudomorph crystal fans which were also previously described by (Peryt et al. 1990) and are documented as an important geological and paleontological site (Hoppe et al. 2002). This facies association is interpreted as $CaCO_3$-oversaturated deep platform.
- FA3 consists of crystalline limestone that shows cross-stratification and (mega-) ripple marks and is interpreted as storm dominated middle ramp.
- FA4 is a crystalline limestone with asymmetric ripple marks and mud drapes, plane parallel lamination and channel geometries. It is interpreted as tide-dominated inner ramp.
- FA5 is a lime mudstone / pelite rhythmite tabular layers of facies association which is interpreted as mixed carbonate siliciclastic outer ramp.
- FA6 shows black crystalline limestone with planar lamination, wave truncated lamination and stromatolites; it is interpreted as wave-influenced stromatolitic inner ramp.
- FA7, also consisting of black crystalline limestone but with convolute and planar lamination is interpreted as steepened carbonate outer ramp. Facies associations
- FA8 and FA9 contain the basal part of the Serra de Santa Helena Formation. FA8 consists of siltites and marls typical for this Formation and interpreted as sediments deposited offshore a siliciclastic platform. FA9, a local arenite, is interpreted as delta sediment at the basin border.

Comparing the facies association of Vieira (2007) with those of Schöll (1972, 1973) and Ribeiro et al. (2003), FA5 seems characteristic for the Pedro Leopoldo Facies and FA3 + FA6 for the Lagoa Santa Facies. Also in the hydro-geological study from (Pessoa 2005), five different lithologies were distinguished for the Sete Lagoas carbonates instead of only two facies. Thus, the composition of the Sete Lagoas is in detail more complicated than a simple dichotomy into two distinct facies. Nevertheless, for the current map, the facies division from Schöll (1972, 1973) and Ribeiro et al. (2003) was adopted since the pure carbonates of the Lagoa Santa Facies are associated with the characteristic karst landscape in the western part of the study area, also known and protected as the Lagoa Santa karst area (APA Carste de Lagoa Santa). In the rest of the area, interdigitation of pure and impure limestones and meta-pelites are characteristic for the Sete Lagoas Formation. Nevertheless, also in the eastern part of the study area an attempt has been made to distinguish between these facies based on cross-sections and drill-hole data.

4.3.3 Serra de Santa Helena Formation

On top of the Sete Lagoas Formation, fine siliciclastic sediments of the Serra de Santa Helena Formation were deposited uniformly over large parts of the São Francisco Basin (Schöll 1973). Next to meta-pelites, this Formation contains also lenses of carbonates. It is interpreted as sediments of deeper water deposited during rapid marine transgression (Vieira 2007).

4.3.4 Geological structure of the Bambuí Group

While the crystalline basement suffered several cycles of deformation, the covering Bambuí meta-sediments show only the traces of the tectonic stress. Near the study area, the deformation of the Bambuí meta-sediments increases from west to east with the highest deformation close to the Serra do Espinhaço and the Araçuaí fold belt (Figure 4-2, p.55).

Schöll (1973) found the highest degree of metamorphism reaching lower green schist facies close to the southern border of the Serra do Espinhaço studying the crystallinity of illite minerals in the area north of Belo Horizonte. Since the zones of similar degree of metamorphism did not stretch parallel to this eastern fold belt, Schöll (1973) concluded that the metamorphism was not directly related to the folding of the Araçuaí Belt but due to local heat sources in the crystalline basement.

For the VIDA project, Ribeiro et al. (2003) describe three tectonic domains based on field analysis of tectonic deformation (micro-petrography) and structural geological maps (Figure 4-5). According to this map, the study area around the city of Lagoa Santa belongs completely to the highly deformed eastern domain.

For the same project, joint measurements and measurements of cumulative length of caves and their frequent directions were collected (Figure 4-6). For domain III, east-west-striking joints dominate, with an additional high frequency of joints in SW-NE direction for the pure carbonates of the Lagoa Santa Facies. Cave length and frequency have highest frequency in direction N-S and E-W (these measurements were not published separately for the different structural domains).

Alkmim and Martins-Neto (2001) suggest a thin-skinned tectonic movement including duplex structures for the Bambuí Group. This idea is also included in local studies on the geological architecture of the area (Ribeiro et al. 2003, Pessoa 2005) based on many field observations of low-angle deformation structures that are not found in the crystalline basement. This includes also thrust ramps, local folds and even duplicate layers of the Pedro Leopoldo Facies on top of the Lagoa Santa as summarized in the cross-section of Figure 4-7.

Pessoa (2005) developed this idea further and stacked five different lithologies distinguishable in drill-hole analysis into several duplex-layers. Three out of ten cross-sections from Pessoa (2005) were chosen to illustrate his interpretation of the internal structure of the Sete Lagoas carbonates (Figure 4-8). In these cross-sections, the Serra de Santa Helena meta-pelites are combined with the rest of the soil cover to a general overburden above the carbonates into a single unit.

Although the idea of thin-skinned tectonics for the region is sensible and in concordance with numerous field observations of low-angle movement, it is not clear how far the different strata have been transported and if there really exist large-scale tectonic duplex structures. Next to this tectonic explanation, the sedimentological arguments of Schöll (1972, 1973) and Vieira et al. (2007a), which assume not only a vertical but also a lateral transition between the different facies, can explain the regional pattern of the facies distribution. Probably both tectonic and

sedimentological processes together led to the spatial distribution of the different Sete Lagoas facies. Based on these considerations, the stratigraphic column from Ribeiro et al. (2003) and Pessoa (2005) was modified to incorporate a lateral facies transition between the Lagoa Santa and the Pedro Leopoldo Facies of the Sete Lagoas Formation, with the Lagoa Santa Facies inserted into the Pedro Leopoldo Facies and wedging out towards the east (Figure 4-10). Thus, without denying that there can exist tectonic duplex structures within the thin-skinned tectonic framework, it is important to bear in mind that probably already during sedimentation a lateral heterogeneity was installed.

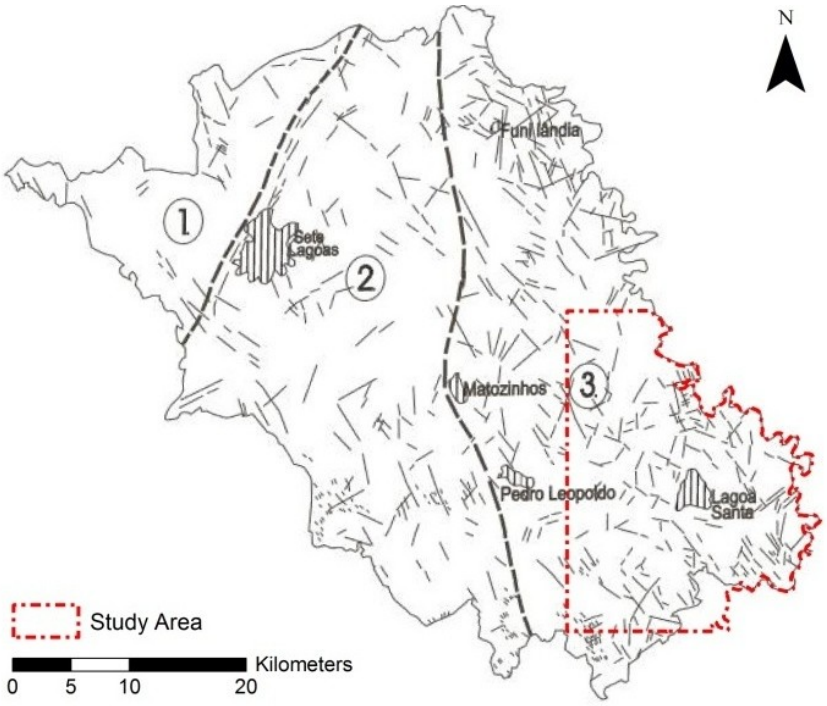

Figure 4-5 Tectonic domains at the south-eastern tip of the Bambuí basin. Domain 1 = not deformed, domain 2 = medium deformed and domain 3 = highly deformed. Lines indicate lineaments. Modified from Ribeiro et al. (2003).

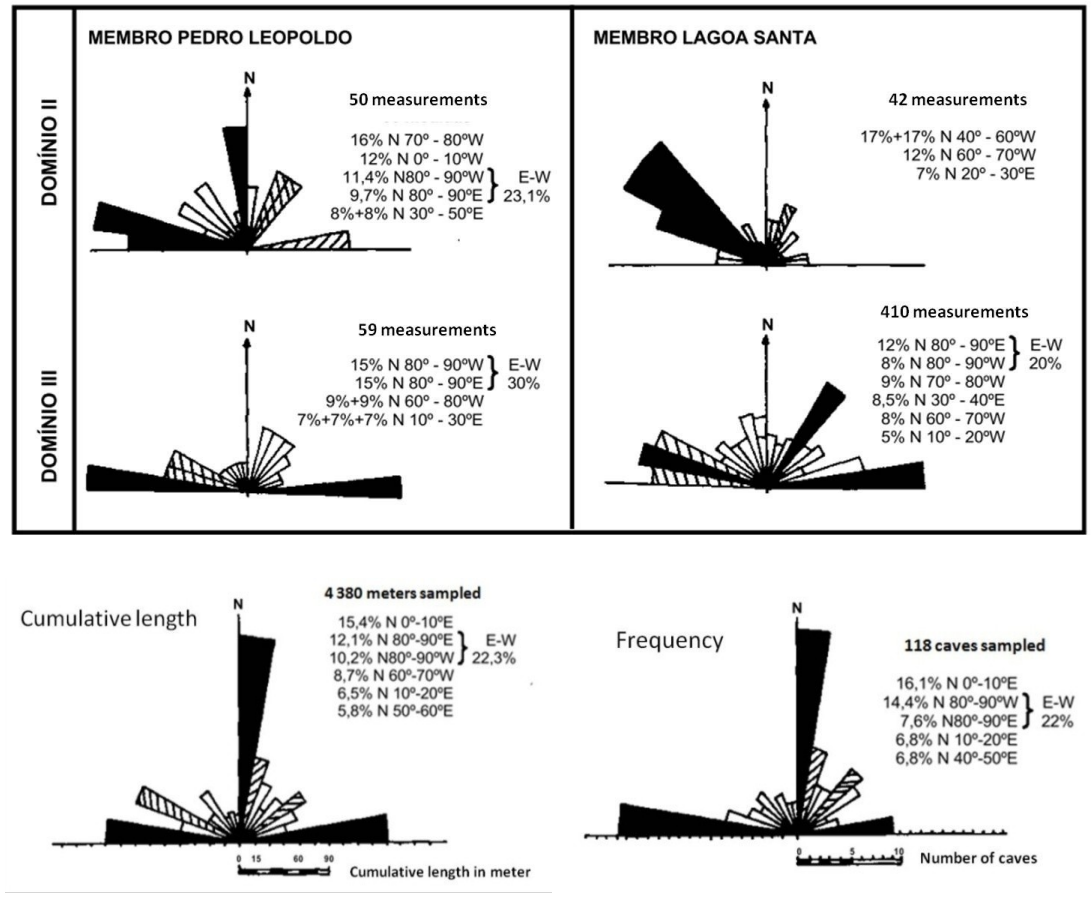

Figure 4-6 Rose diagrams showing joints and cave directions.

The information is given for the Sete Lagoas Formation in the structural domains 2 and 3 in Figure 4-5 (Horta et al. 1998). The measurements of cave length and directions are not divided into structural domains but summarized for the total area.

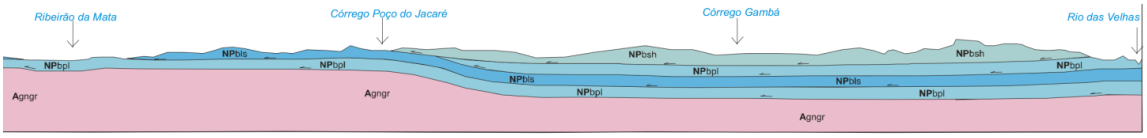

WSW Cross-section Projeto VIDA, length approx. 12.5 km ENE

Figure 4-7 Cross-section from Riberão da Mata until Rio Das Velhas (Projeto VIDA).

Original scale: 1 : 50 000, location see Figure 4-9. NPbsh: Serra de Santa Helena Formation; NPbls: Lagoa Santa Facies (Sete Lagoas Formation); NPbpl: Pedro Leopoldo Facies (Sete Lagoas Formation); Agngr: Archean Basement. Source: Ribeiro et al. (2003)

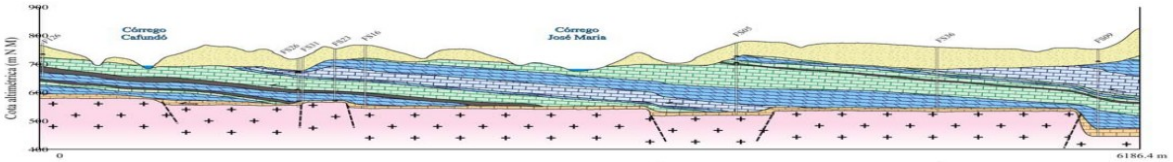

WSW Cross-section F, length approx. 6.2 km ENE

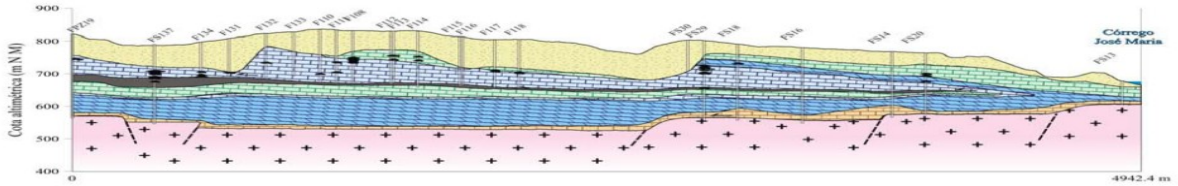

NW Cross-section C, length approx. 5 km SE

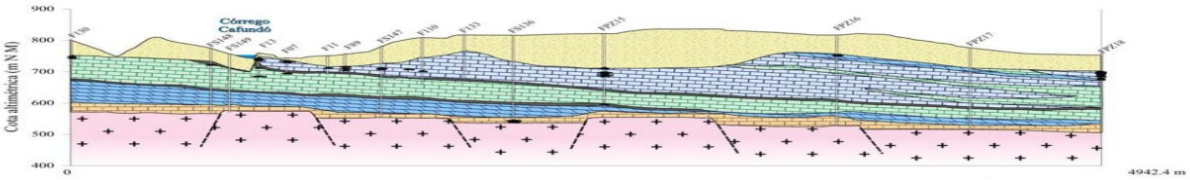

SSW Cross-section D, length approx. 4.8 km NNE

Soil cover over and meta-pelites | Calcitic limestone | Carbona-ceous schist | Carbona-ceous phyllite | Phyllitic carbonates | Marble | Basement complex

Figure 4-8 Cross-sections F, C and D from Pessoa (2005) without vertical exaggeration.

From west to east, low angle thin skinned tectonic movement is assumed together with facies interdigitation in north-south direction. Black areas indicated caves. The locations of the cross-sections are indicated in Figure 4-9.

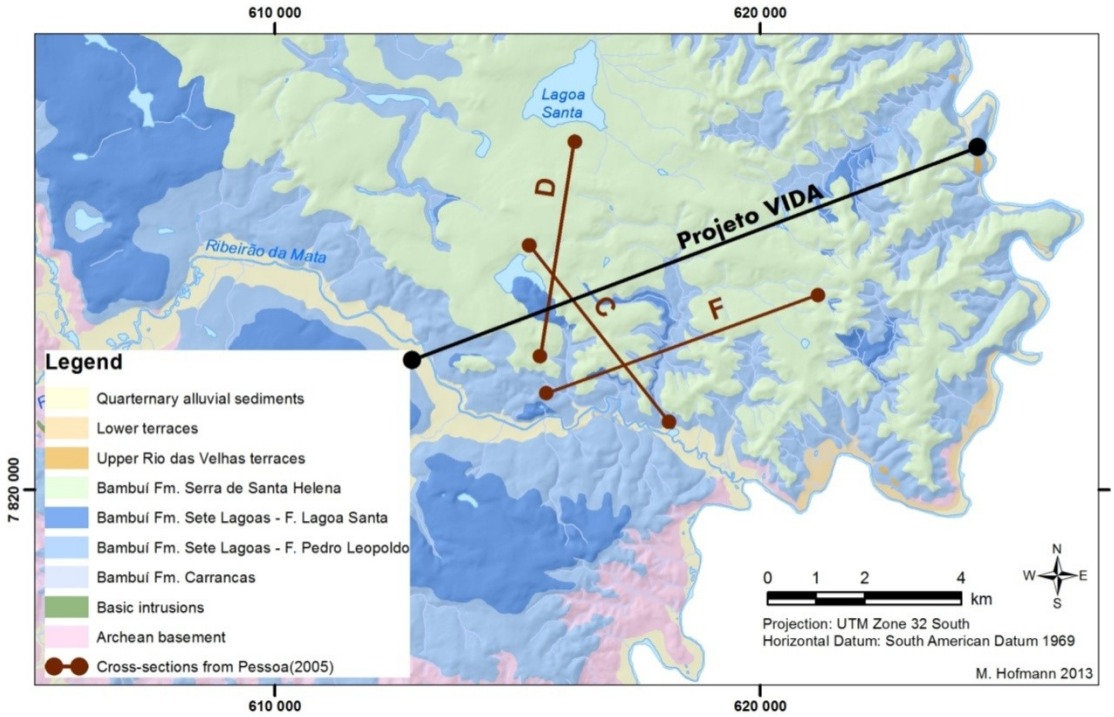

Figure 4-9 Locations of the cross-sections from Figure 4-7 and Figure 4-8.

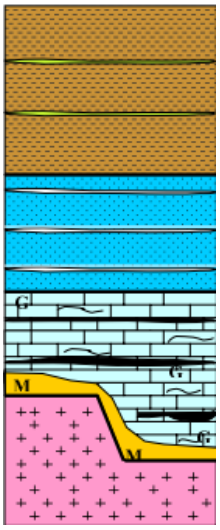

A)

Version published by (Pessoa 2005), based on (Ribeiro et al. 2003).

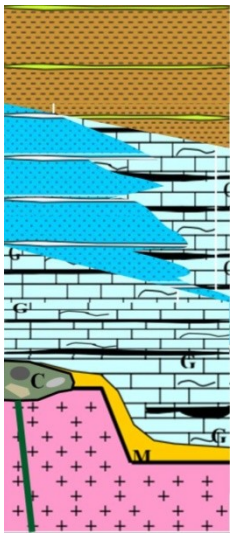

B)

Suggested modification including N-E wedging out of the Lagoa Santa Facies

Figure 4-10 Modification of the local stratigraphic column from Pessoa (2005).

The modification was done according to assumptions of lateral interdigitation of the Pedro Leopoldo and Lagoa Santa facies as described in Schöll (1973) and Vieira et al. (2007a). For a detailed legend see Figure 5-21 on p. 100.

5 Geology – own data

Since the spatial distribution of the geological units is essential for the mapping of geo-resources and geo-hazards, the available geological maps were updated with new field and satellite information and combined with local topography.
This process consisted of two steps: several field trips were made to the area to get familiar with the local stratigraphy and tectonic structures as well as collecting data. These field data were compared with data from literature, satellite images and relief structure in a GIS environment using the software ArcGIS from ESRI.

5.1 Field identification of lithological units

Own field work resulted in 250 geological data points plus 204 data points regarding only soil color and erosion phenomena. Since it was often difficult to find fresh outcrops in the highly weathered landscape, also outcrops of strongly altered saprolites and indirect hints such as soil color had to be used for mapping (compare also Karfunkel (2013)). For the Serra de Santa Helena Formation, no fresh outcrop could be found. The 250 geological data points were divided into three categories of data quality: 76 are based on fresh rock outcrops (category I), 68 are based on the interpretation of weathered saprolite or similar data (category II) and 40 are indirect hints for the geological underground such as karst features (dry valleys, dolines), typical vegetation or typical soil color (category III). The remaining 66 data points refer to the sedimentary structure in the Quaternary alluvial plains from an open pit mine. These field data together with field data from previous studies are drawn on the final geological map in the annex (Map 32).
While it was not difficult to distinguish the saprolite of the crystalline basement from that of the Bambuí group (Outcrop A), the differentiation between the saprolites of the Pedro Leopoldo facies (Sete Lagoas Formation) and the saprolite of the Serra de Santa Helena Formation was not always possible with security. The saprolite of the Pedro Leopoldo facies often showed darker colors and has a less silky shining texture than the silt-rich saprolites of the Serra de Santa Helena Formation.
The following pictures show the typical field aspects of the different geological strata and their saprolites in the study area. The location of each outcrop (except outcrop A) is indicated in Map 35 in the annex.

Outcrop A: Saprolite of Basement and Bambuí rocks

Bambuí saprolite is yellow to orange (above the concrete wall) compared to the pale pink color of the basement saprolite (below the wall). Location: -19.758793 / -43.947791

Outcrop B: Gneiss-migmatite basement.

Location: -19.735828 / -43.956947

Outcrop C: Unique Carrancas outcrop in the region.

Rounded and angular stones of various sizes are floating in a carbonaceous matrix. Location: -19.693065 / -43.980253

Outcrop D: Pedro Leopoldo Facies

Chlorite-rich, thin and tectonically deformed siliciclastic layers are intercalated with banks of purer limestone. Location: -19.69962534/ -43.89403763

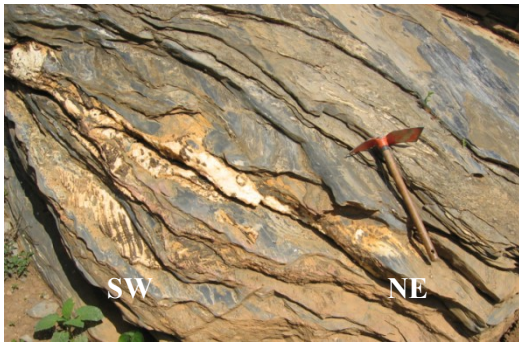

Outcrop E: Pedro Leopoldo Facies.

Typical are the frequent thin chlorite layers between the carbonates. Location: -19.61588426/ -43.85047948

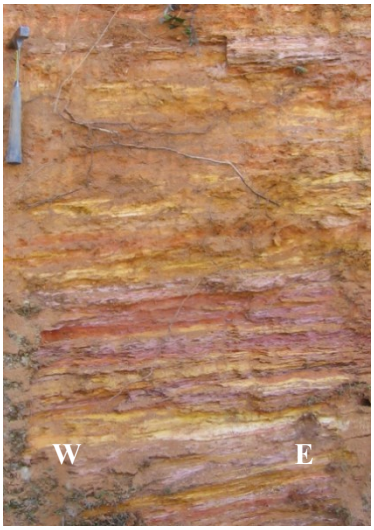

Outcrop F: Saprolite of the Pedro Leopoldo Facies

Differentiation between a saprolite of this unit and that of the Serra de Santa Helena meta-pelites is often difficult. Location:

-19.70209348 /

-43.87664049

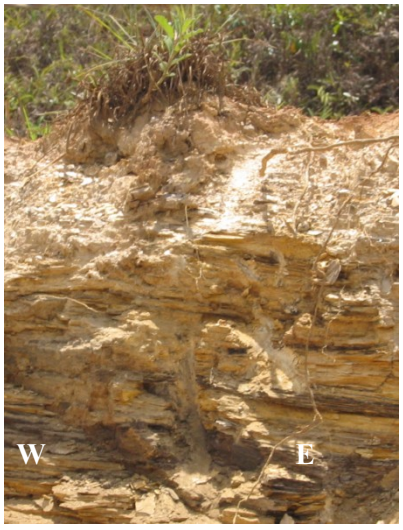

Outcrop G: Saprolite of the Serra de Santa Helena Formation above that of the Pedro Leopoldo Facies.

Silty shining layers near the top and dark (chlorite?) layers at the lower part of the profile. Location: -19.65190197 /

-43.84732202

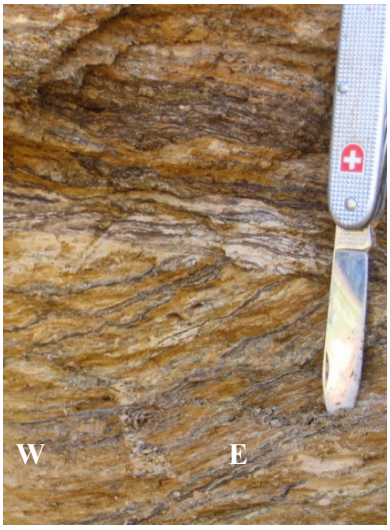

Outcrop H: Saprolite of the Pedro Leopoldo Facies.

The fine chlorite layers appear as fine black lines. The discordance between layers is probably a synsedimentary cross-bedding since no hints for tectonic movement could be detected at the profile.

Location: -19.69105326 / -43.91163653

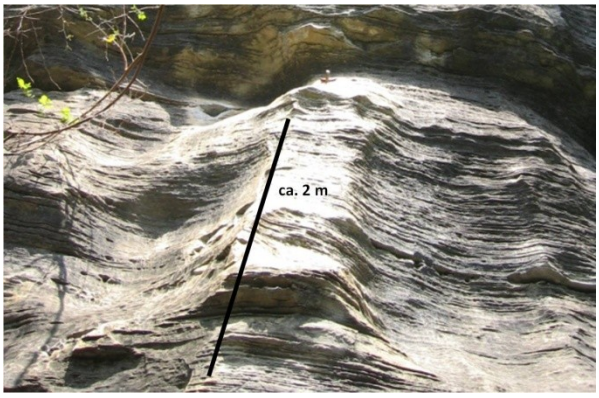

Outcrop I: Naturally eroded outcrop of the Lagoa Santa Facies.

The fine lamination of the black carbonates stands out due to preferential erosion. Location: -19.559629 / -43.959517

Outcrop J: Naturally eroded outcrop of the Lagoa Santa Facies near the Gruta da Lapinha.

Caves and other Karst features are typical for this facies.

Location: -19.559629 / -43.959517

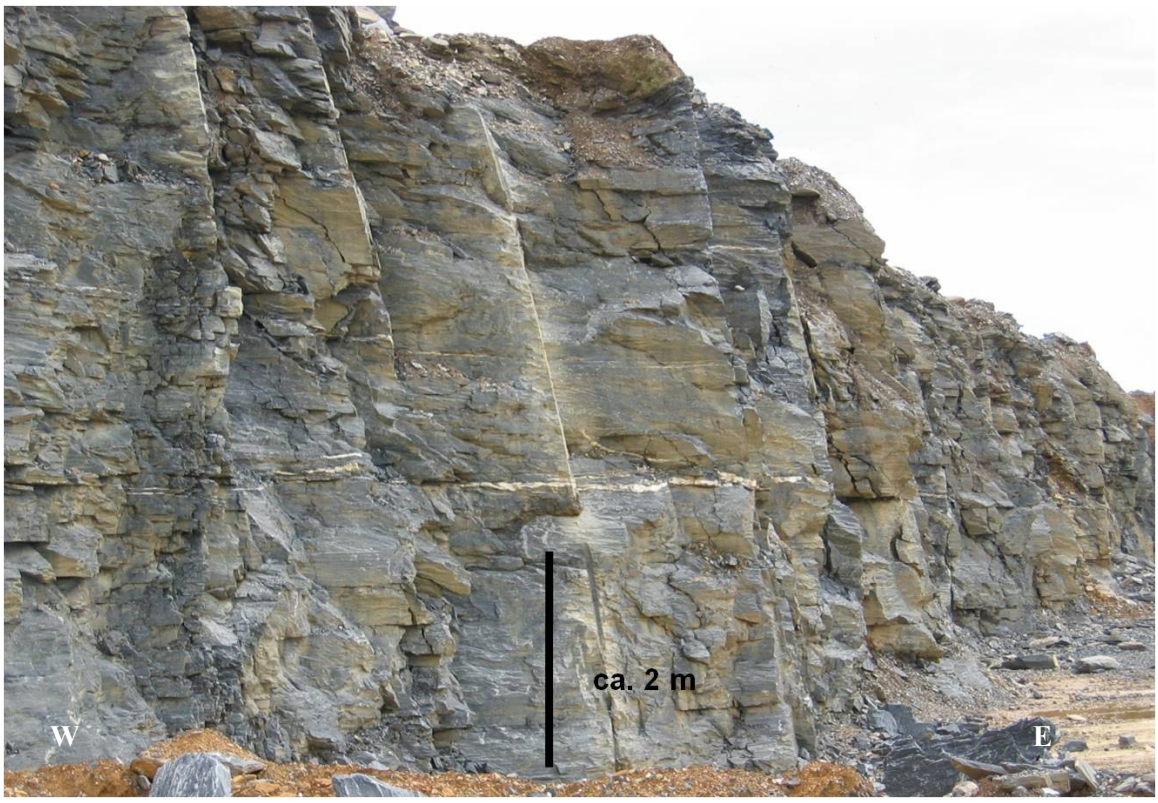

Outcrop K: Lagoa Santa facies at the Lapa Vermelha cement mine.

Sub-horizontal layers of calcite and quartz dissect the otherwise finely laminated black carbonates. Location: -19.678437 / -43.898915

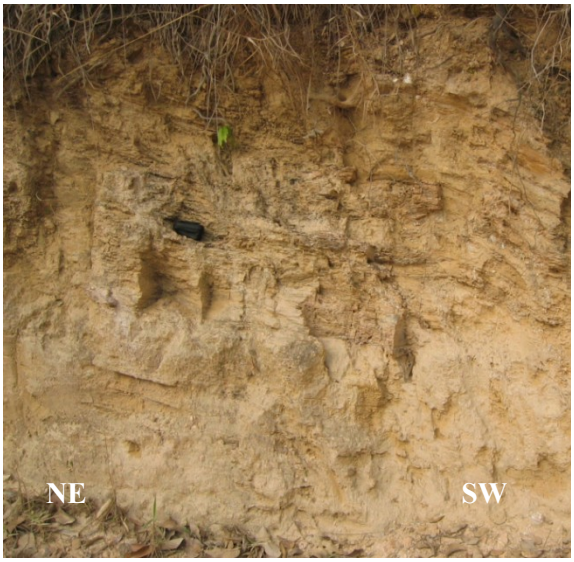

Outcrop L: Typical saprolite of the Serra de Santa Helena Formation.

The coloring of the layers is usually more uniform than that of the saprolite of the Pedro Leopoldo Facies of the Sete Lagoas Formation. The small black camera bag in the middle is about 10 cm. Location: -19.678888 / -43.838783

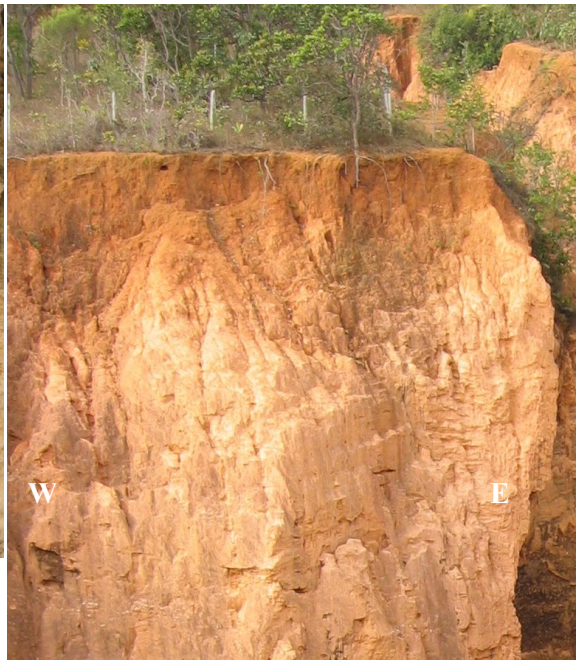

Outcrop M: Large gully incised into homogeneous saprolite of the Serra de Santa Helena Formation.

A pole of the fence on its boundary is about 1m. Location: -19.618240 / -43.886795

Outcrop N: Quartz veins cutting through Serra de Santa Helena meta-pelites.

The small black camera is about 10 cm. Location: -19.699508 / -43.825381

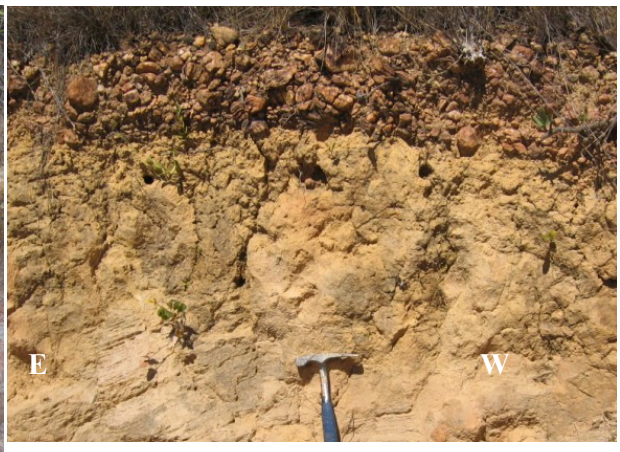

Outcrop O: Accumulation of angular quartz stones at the surface.

Preferential erosion sometimes leads to a decimeter thick stone layer in the Serra de Santa Helena Formation. Location: -19.640162 / -43.844107

5.2 Typical vegetation patterns

Already during field trips, correlation between lithology and vegetation could be noticed. According to personal communication from J. Karfunkel and P. Pessoa, limestone outcrops are often highlighted by decidous aroeira-preta trees (*Myracrodruon urundeuva Fr. Allem*.) within the semi-decidous forest or cerrado that characterizes the natural vegetation of the area (Figure 5-1). The aroeira trees have a slender V-shaped silhouette and can be detected easily from afar during the dry season. Besides using this information during field mapping, it was also useful for identification of probable limestone outcrops on satellite images distributed by GoogleEarth and Bing Maps (Figure 5-2).

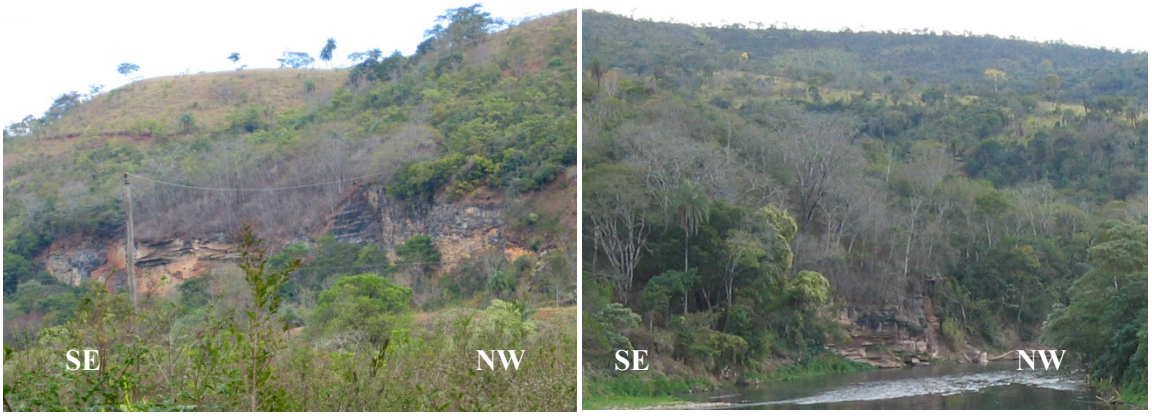

Figure 5-1 V-shaped deciduous aroeira-preta trees (*Myracrodruon urundeuva Fr. Allem.)* on limestone outcrops.

Left side: Outcrop Y (-19.706475 / -43.871304) as seen from the other side of the Riberão da Mata, right side: outcrop near the Rio das Velhas. (-19.658186 / -43.810406).

Figure 5-2 Patches of deciduous trees seen on satellite images distributed by Google Earth.

The meta-pelite hills of the Serra de Santa Helena Formation show typically sparse cerrado vegetation that is often used as extensive pasture. The poverty of the soil and sometimes thick surface layers of quartz stones (compare Outcrop O, p. 71) allow only for sparse vegetation with low trees. Higher trees are found only along drainage lines or gullies (Figure 5-3).

Figure 5-3 Typical vegetation on the eastern meta-pelite hills.

Scattered low cerrado trees and scarce grass cover. Only along deeply incised drainages, higher vegetation occurs. View from -19.670282 -43.842863 towards NW.

This vegetation pattern can be detected on satellite images from GoogleEarth or Bing Maps. Often, a distinct line can be drawn, separating sparse grass vegetation along hilltops from denser and higher vegetation in the valleys (Figure 5-4). While much of this vegetation pattern is controlled by topography (higher moisture content in the valleys, inaccessibility of steep slopes by cattle), it is also related to geology. Soil on limestone is generally less acid and more fertile with less risk of aluminum-toxicity (Shinzato and Lumbreras 1998), which is one of the main restrictions for vegetation growth in the region. Also the low permeability of the subsoil on pelitic meta-sediments favors surface runoff and thus results in stronger water stress during the dry season. Since the Serra de Santa Helena meta-pelites overly the Sete Lagoas carbonates, vegetation and morphological features identified on satellite images can help to delineate the border between the generally sparsely vegetated concave meta-pelite hilltops and the often greener and more convex limestone footslopes.

Figure 5-4 Manually outlined vegetation boundary using images from Google Earth. The white line separates the tops of the meta-pelite hills from their carbonate foothills. This boundary is not always easy to draw and interpret since also land use (e.g. cattle stocking rates, manual clearance or reforestation) and moisture concentration in valleys play an important role in vegetation control.

5.3 Consistency check between geology and relief

Using the generally simple vertical structure of the geological layers, a consistency checkup between relief and geology was done for the geological units outlined in previous maps. Although the strata have been tectonically deformed, most movements were more or less sub-horizontal and did not result in a major rearrangement. Thus, the surface contact line between the geological units should not deviate too much from the horizontal in general. Additionally, relief form was used to help distinguish meta-pelite sediments from carbonate sediments. While meta-pelite sediments are often characterized by concave sideslopes and cut by deep gullies, carbonate hills tend to be more convex with steep footwalls in the valleys. Since limestone is generally harder and more resistant to physical erosion, an analysis of knick-points along rivers can help to find the contact between both lithologies, i.e. knick-points are locations where a river profile steepens, deviating from the idealized concave equilibration profile of a mature river in a stable, lithologically homogeneous region. The reason for a knick-point can be an active fault, changing

lithologies, (sub-) horizontally bedded strata or lowering of the baselevel. In the study area, knick-points often indicate the contact between the soft, deeply weathered meta-pelites of the Serra de Santa Helena Formation and the more resistant limestone of the Sete Lagoas Formation. Figure 5-5 shows an idealized longitudinal profile of a river cutting through the Bambuí sediments in the area.

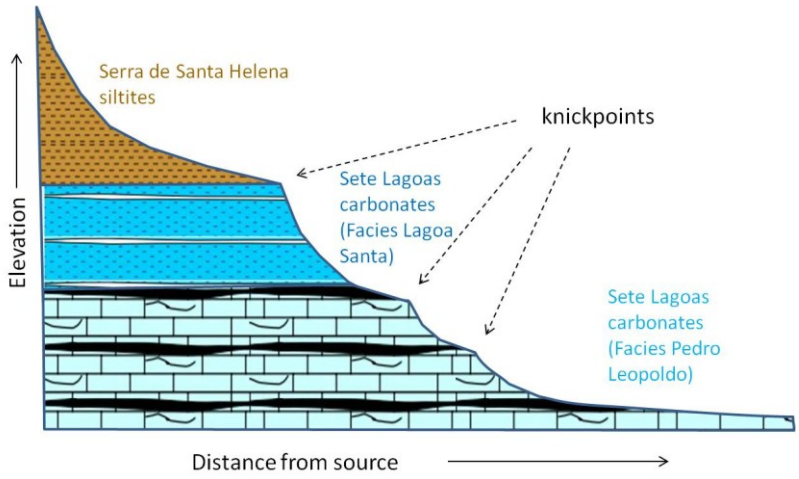

Figure 5-5 Exaggerated schematic longitudinal river profile with knick-points at lithological changes (not to scale).

Also inside the Sete Lagoas carbonates, knick-points are common due to intercalation of softer and harder strata. Thus, the top-most knick-point can be a hint for the contact between the Serra de Santa Helena meta-pelites and the Sete Lagoas carbonates. Nevertheless, also the Serra de Santa Helena meta-pelites can have knick-points induced by occasional intercalation of limestone. Also active gullies are characterized by knick-points due to their typically episodic growth (Morgan (2009), p.30). For the study area, contour lines from the topographic map 1 : 25 000 were evaluated manually to detect knick-points along thalwegs or rivers.

Figure 5-6 shows two examples of a modification of the 1 : 50 000 geological map from (Ribeiro et al. 2003) based on geomorphological reasoning. The contact lines of the geological units in the left images were assumed improbable given the geological architecture and substituted by a version that was more compatible with the relief. Doing this, also data from own and previous field observations as well as knick-points were taken into account. A difficult problem during this relief-based post-processing was how to identify and deal with local mass movements caused by intrastratal karstification. While in the western part of the study area, open karst structures dominate, the eastern part of the study area shows little direct signs of karstification because the carbonates of the Sete Lagoas Formation are covered by the meta-pelites of the Serra de Santa Helena Formation. Nevertheless, intrastratal carbonate dissolution occurs also here and if a deep cave collapses, all overlying layers are locally lowered.

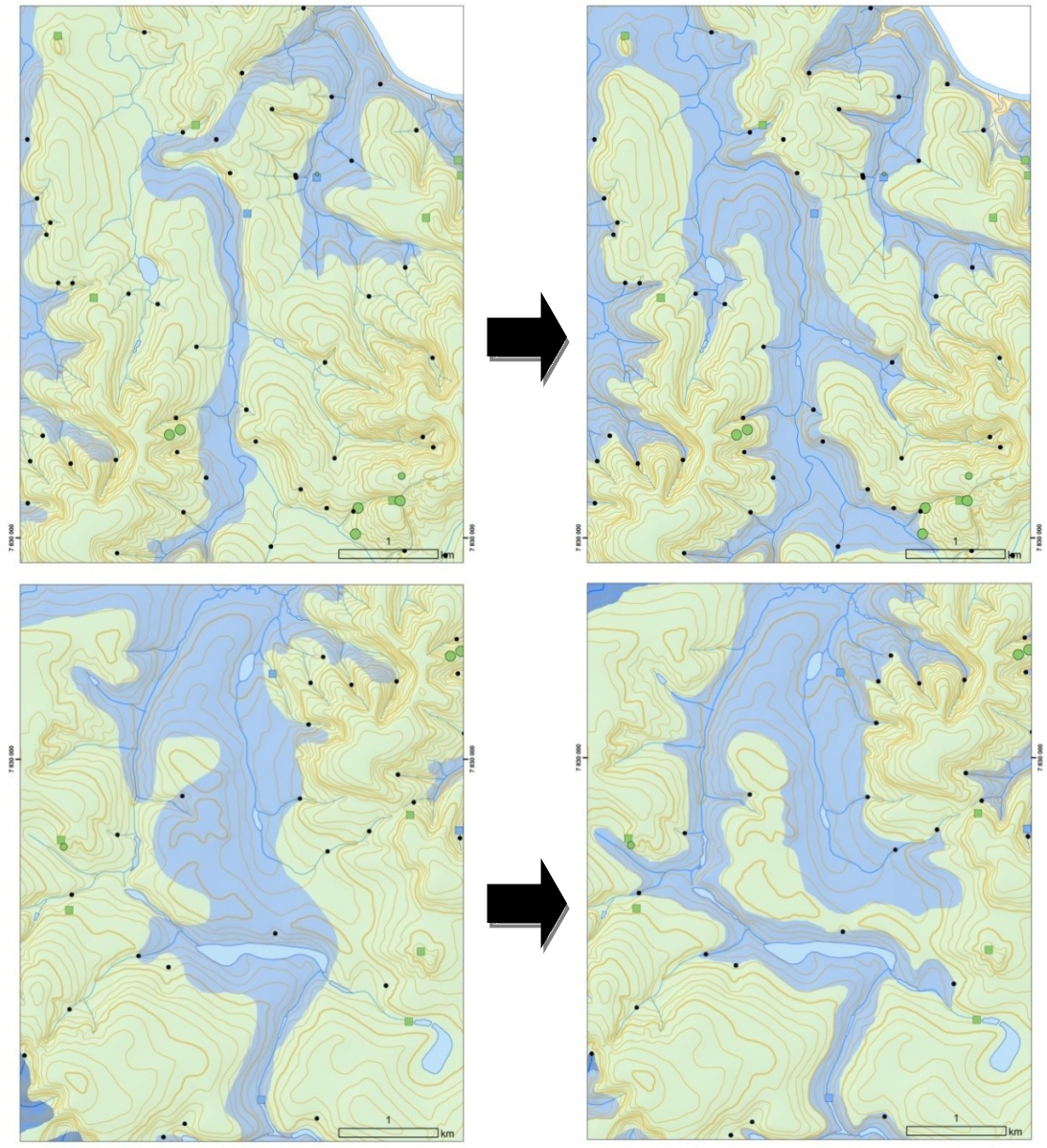

Figure 5-6 Examples of topographical and geological consistency check.

The situations on the left, taken from the existing 1 : 50 000 geological map (Ribeiro et al. 2003), were estimated improbable compared with the 10 m equidistance contour lines of the 1 : 25 000 topographical map. On the right, the adjusted version is shown. For this new version, also own field observations (colored circles), vegetation patterns, knick-points and probable mass movements were taken into account. Location: upper maps: 2 km west, lower maps: 1 km north of Lagoa Santa.

Intrastratal karstification has probably also caused the depression in which the lake Lagoa Santa exists today (Kohler 1989, Parizzi et al. 1998) and also the neighboring smaller lake Lagoa Olhos d'Agua, which is not directly connected to the karst groundwater level according to a study by Kohler (personal communication). Parizzi et al. (1998) and Salgado-Labouriau et al. (1998) point out that pollen records show an increase in humidity after a long dry period around 4600 BP, which was also the time when the Lagoa Santa depression was probably obstructed by a landslide that lead to the formation of the present lake (Parizzi et al. 1998).
The scar of this landslide is still visible and topography hints to several more ancient mass movements in the region. If mass movements interpreted from topography and satellite images seemed clear and large enough (see also Map 7, p. 344), the resulting dislocation of geological strata was taken into account while adjusting the geological map according to the topography.

5.4 Information from drill-holes

For a small area south-west of the lake Lagoa Santa, additional information from drill-holes was available, which made it possible to gain insight into the three-dimensional architecture of the geological strata and thus adapt the geological map. The information was drawn from the PhD thesis of Pessoa (2005), who evaluated 154 drill-holes in ten cross-sections for the region around the cement mine Lapa Vermelha. For the current study, these bore hole data were digitized using the coordinates given in the thesis. For five of them, information was missing and they had to be digitized from cross-sections. After removing duplicate bore-hole data (e.g. several drillings at the same location) and excluding those with implausible location / elevation combination, 139 data points remained. For 134, the following information was available:
Year of execution, ID-number, UTM-coordinates, elevation, depth of the drill-hole, thickness of firm rock, if they encountered basement rocks or not. The remaining five were taken from cross-sections only. From all drillholes, 59 reached the basement, 62 were equipped with a piezometers for groundwater monitoring, 97 were included into the ten cross-sections created by Pessoa (2005) , 12 had a chemical analysis of their mineralogy, 36 had a lithological description, 32 had an explicitly given elevation of the epikarst which was compared with groundwater level during dry and wet season and 9 had a chemical analysis of the groundwater.

The ten cross-sections and the lithological descriptions were used to enhance the detail of the spatial distribution of the two facies of the Sete Lagoas carbonates: Pessoa (2005) distinguished six different types of hard rock (see also Figure 4-8, p. 64) for the drill-holes and in the cross-sections. For the creation of the current map, the units “carbonaceous shist”, “carbonaceous phyllite”, “phyllitic carbonate” and “marble” were associated with the Pedro Leopoldo Facies, the unit classified as “calcitic limestone” was associated with the Lagoa Santa Facies and the unit

"basement" with the crystalline basement. The unit "soil cover" was partly associated with the overlying Serra de Santa Helena Formation. The distinction between soil cover and the Serra de Santa Helena Formation was difficult based on these data since the Serra de Santa Helena Formation is always deeply weathered and pelite saprolite was not differentiated from soil or saprolite of the Sete Lagoas Formation in the drill-hole data. Even from the 36 drill-holes with lithological description, the origin of the soil could only be estimated from soil texture (soil grain size distribution) since no observation of any primary structure was documented for the soft material overlying the carbonate bedrock. Absence of any primary structure in this material would imply that either pedoturbation took place until a depth of more than 40 m (sometimes up to 70 m) – which is rather improbable - or that mass movements, e.g. initiated by collapsing underground caves, mixed the saprolite cover so thoroughly that no primary structures can be observed anymore. Taking all these considerations into account, the data from the drill-holes and cross-sections were used – together with own field observations and remote sensing techniques – to modify the surface contact line between the geological units (Figure 5-7).

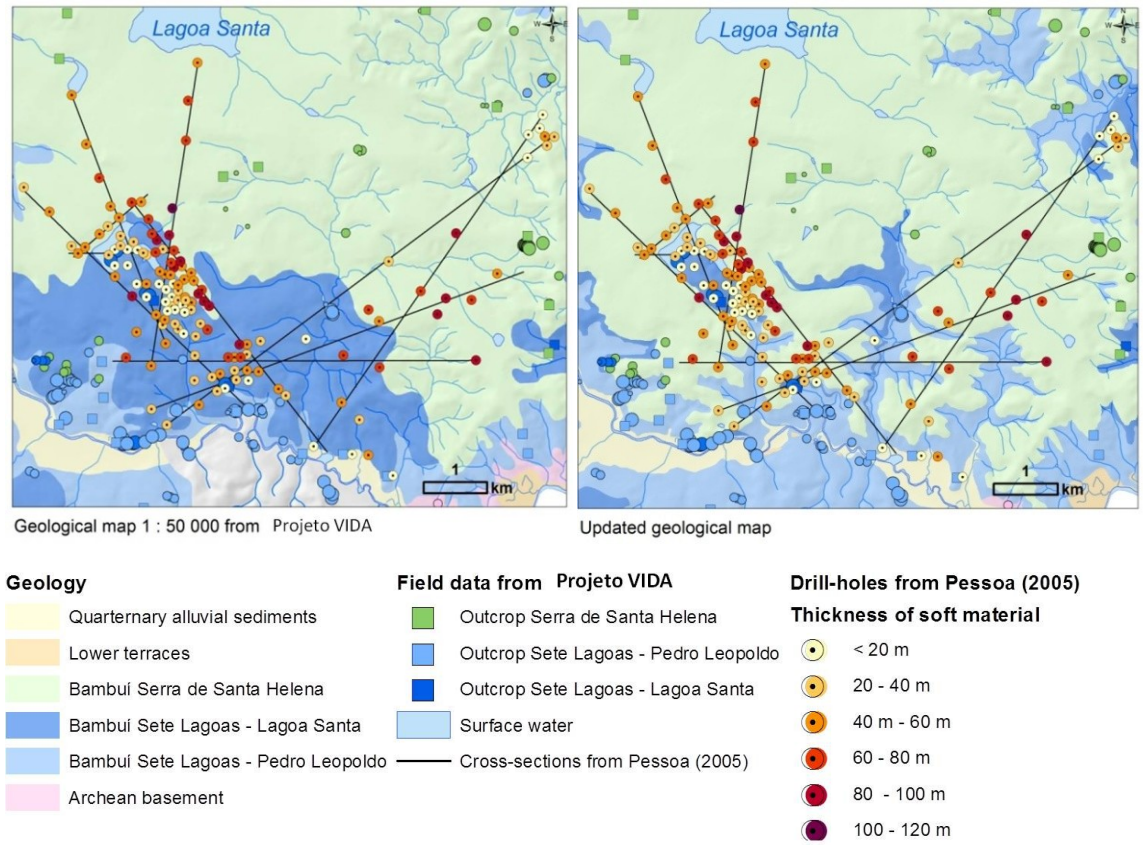

Figure 5-7 Examples of modifications of the geological map.

The changes are based on drill-holes from Pessoa (2005), own field data (green and blue circles, the larger the circle, the higher the data quality), field data from Projeto VIDA and remote sensing data.

5.5 Field data of geological structures

The metamorphism of the Bambuí sediments in the study area generally does not exceed lower green schist facies at surface outcrops (Schöll 1972, 1973). In drill-holes, (Pessoa 2005) also observed graphite layers in the Pedro Leopoldo Facies and marble at its contact to the basement. In outcrops, fine siliciclastic intercalations often show shining dark surfaces of movement (probably chlorite or sericite, Outcrop D and Outcrop E, p. 69). In the carbonates, recrystallization is common, with crystal size increasing with increasing pureness of the carbonates. This grain size difference resulted in the terms "calcilutites" for the impure Pedro Leopoldo Facies and "calcarenites" for the purer Lagoa Santa Facies of the Sete Lagoas Formation in previous works (Ribeiro et al. 2003).

The primary structure of the meta-sedimentary rocks, the bedding S_0, is recognizable through texture changes (Pedro Leopoldo Facies, Serra de Santa Helena Formation) or fine black lamination caused by changing organic content in the Lagoa Santa Facies (Outcrop K, p. 70, Outcrop T, p. 82). Parallel or at a very low angle to the bedding, a S_1 foliation exists (see e.g. Outcrop R, p. 81).

In the Bambuí carbonates, the pureness of the material controlled its behavior during deformation: in the Pedro Leopoldo Facies at the base of the Sete Lagoas Formation, west-verging folds indicate low-angle tectonic movement from East to West (Outcrop P, p. 80 and Outcrop S, p. 81). Layers of impure limestone reacted more ductile and formed smooth folds around the more competent and brittle pure limestone layers, which sometimes broke up into boudins of various sizes (Outcrop P, p. 80). Inside the competent parts of the boudins, cracks along Riedel-directions were secondarily filled with calcite crystals (lower part in the images from Outcrop P). The overlying Lagoa Santa Facies shows ductile deformation only along horizontal weakness zones of intercalated siliciclastic layers (Outcrop T, p.82). In the meta-pelites of the Serra de Santa Helena Formation, ductile deformation dominates (Outcrop U, p.82), but also ruptures along shear planes can be observed (Outcrop W, p.83).

At the south-eastern border of the study area, close to the mouth of the Riberão da Mata, a huge outcrop of apparently pure limestone exists, which does not show the typical black color and fine lamination of the Lagoa Santa Facies but is rather light in color (Outcrop Y, p.86). At its northern side, also siliciclastic intercalations are visible as fine green lamina (chlorite?) between the light, considerably recrystalized carbonates. In this part, also a low angle SSE-dipping thrust fault can be observed (Outcrop Z, p.89). The largest part of the outcrop of Outcrop Y does not show signs of ductile deformation, but regular joints dipping steeply SSE.

The following outcrop photos and stereonet plots give an illustration of the tectonic of the study area. All stereonet plots were done using the open-source software OpenStereo 0.1.2 devel (Grohmann and Campanha 2010).

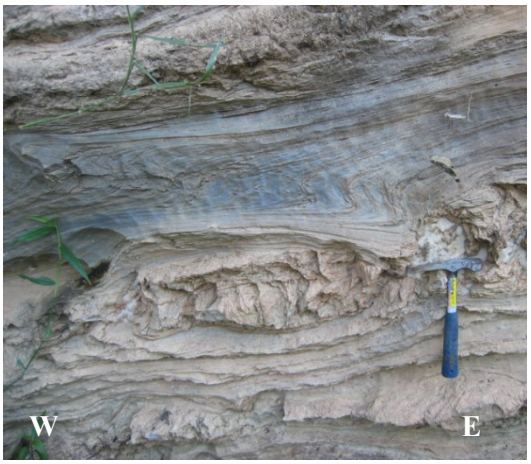

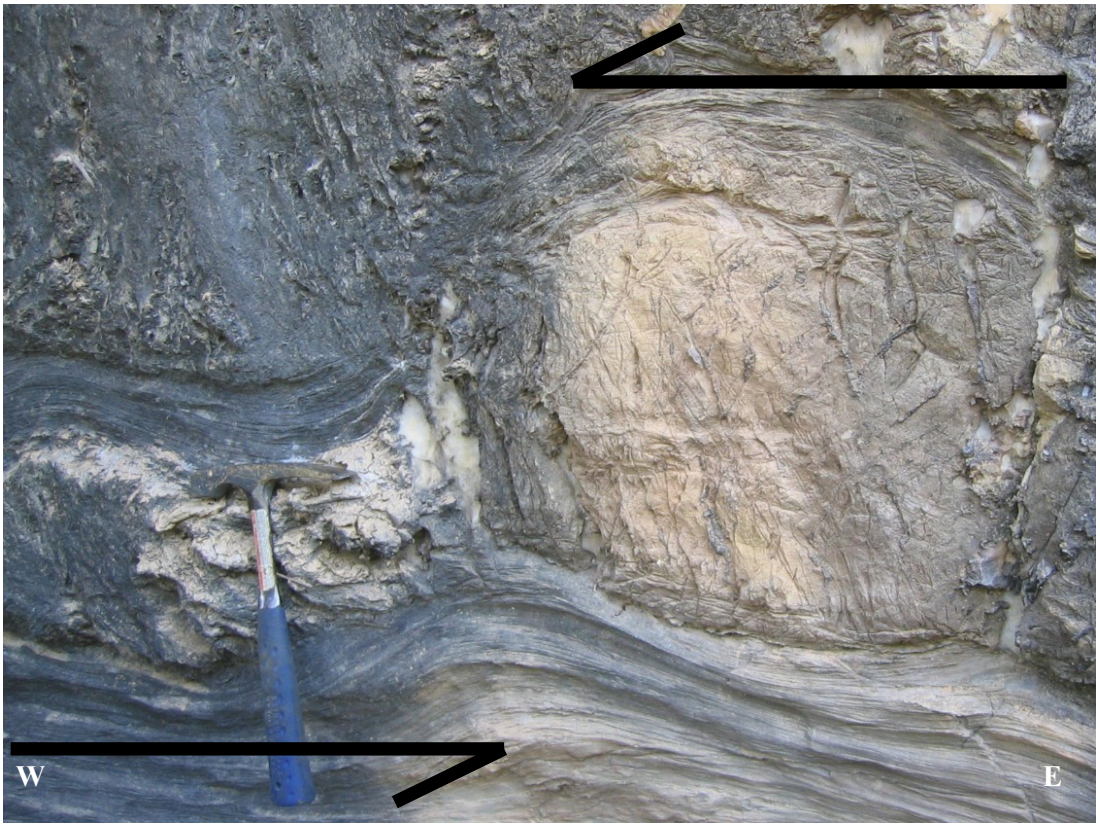

Outcrop P: Boudins and folds of various sizes at the base of the Sete Lagoas carbonates.

The direction of movement is East to West. Inside the boudins, cracks along Riedel-directions are filled with calcite crystals.

Location: -19.69993338 / -43.90307944

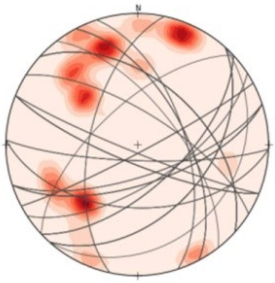

N = 65, cracks inside various boudins.

Equal area lower hemisphere stereonet.

Counting method: fisher distribution

Outcrop Q: Asymmetrical fold at the base of the Sete Lagoas Carbonates.

The axis of the fold is dipping NNW (245 / 10)

The width of the picture is about 20 cm. Location close to Outcrop P (p. 80).

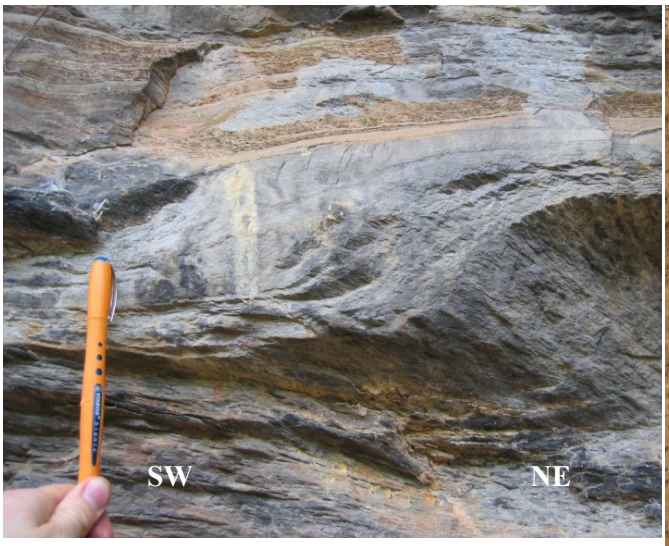

Outcrop R: Ductile deformation of impure Sete Lagoas carbonates.

Location: -19.66855589 / -43.82942305

Outcrop S: Saprolite of the Pedro Leopoldo Facies showing intense deformation.

The shovel is about 20cm. Location: -19.722103 / -43.933041

Outcrop T: Deformation along horizontal weakness zones in the pure carbonates of the Lagoa Santa Facies.

Location: -19.678437 / -43.898915

Outcrop U: West-verging fold in the saprolite of the Serra de Santa Helena Formation.

The camera bag is about ten centimeters in length.

Location. -19.685308 / -43.906568.

Figure 5-8 view to Outcrop D

The tectonically deformed layers of impure limestones crop out in the middle of the valley of the Riberão da Mata and dip to the East (90/14).

Location: -19.69962534/ -43.89403763

Outcrop V: steeply inclined layers at the bottom western part of the gully.

Location: -19.67164228/ -43.84280073

Outcrop W: thrust fault planes dipping east

Location: -19.67186750/ -43.84235758

see also Figure 5-9

Outcrop X: undisturbed horizontal layers at the gully head.

Location: -19.67205316/ -43.84230025

Photos at locations V, W and X were taken in a gully dissecting the western flank of a ridge in the south-eastern region of the study area (Figure 5-10, p. 84). Apparently, a thrust fault was revealed by the gully, the measurements are shown in the map of Figure 5-10.

Figure 5-9 Detail of the photo from Outcrop W.

Location: -19.67186750 / -43.84235758).

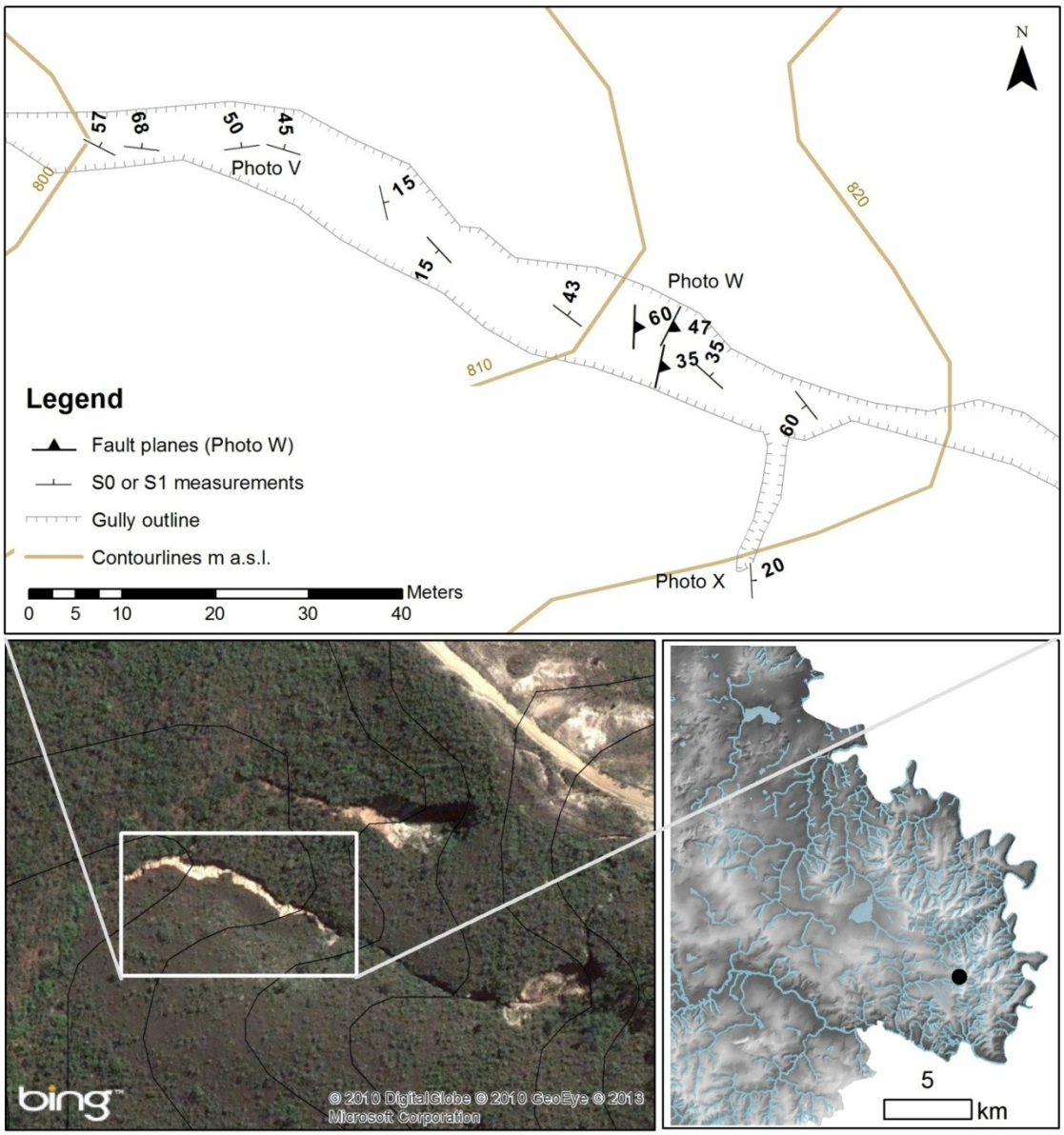

Figure 5-10 Detail map of the gully where the photos of Outcrop V, Outcrop W and Outcrop X were taken.

The locatiFigure 5-10on of the gully is indicated in the overview map at the bottom right, measurements taken in the gully are shown in Figure 5-11.

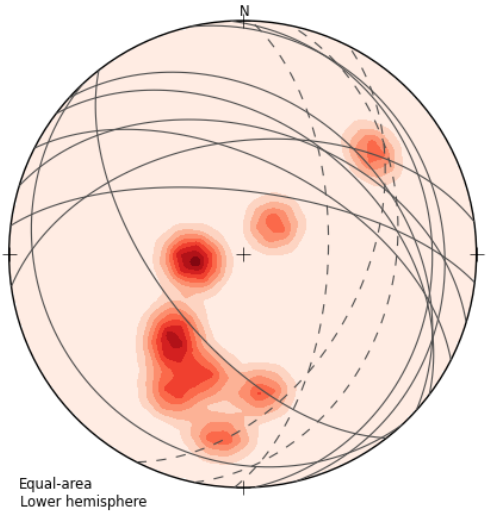

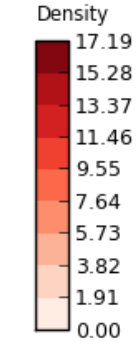

Maximum density: 17.2 %
at 260.0/73.7 (pole)
80.0/16.3 (plane)

Counting method:
Fisher Distribution

10 S_0/S_1 measurements and 3 fault planes (dashed lines) from the gully shown Figure 5-10 (p. 83)

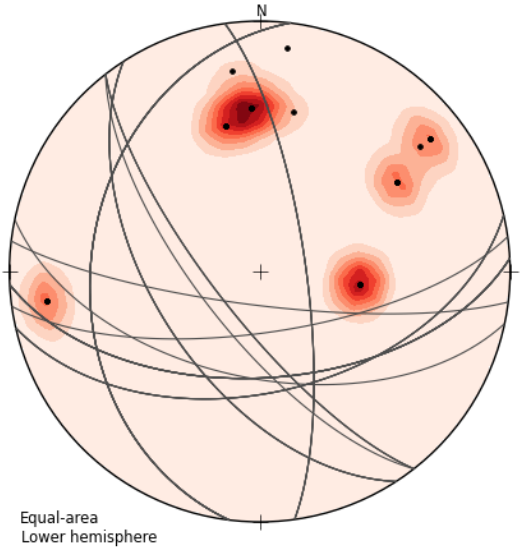

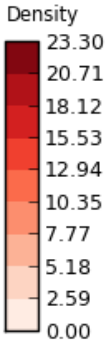

Maximum density: 23.3 %
at 354.0/33.7 (pole)
174.0/56.3 (plane)

Counting method:
Fisher Distribution

34 joints measured in the gully shown in Figure 5-10 (p. 83)

Figure 5-11 S_0/S_1 and fault direction (upper graph) and joints (lower graph) measured in the gully shown in Figure 5-10.

The most frequent joint directions were 155/55, similar to the major joint direction at the large Outcrop Y.

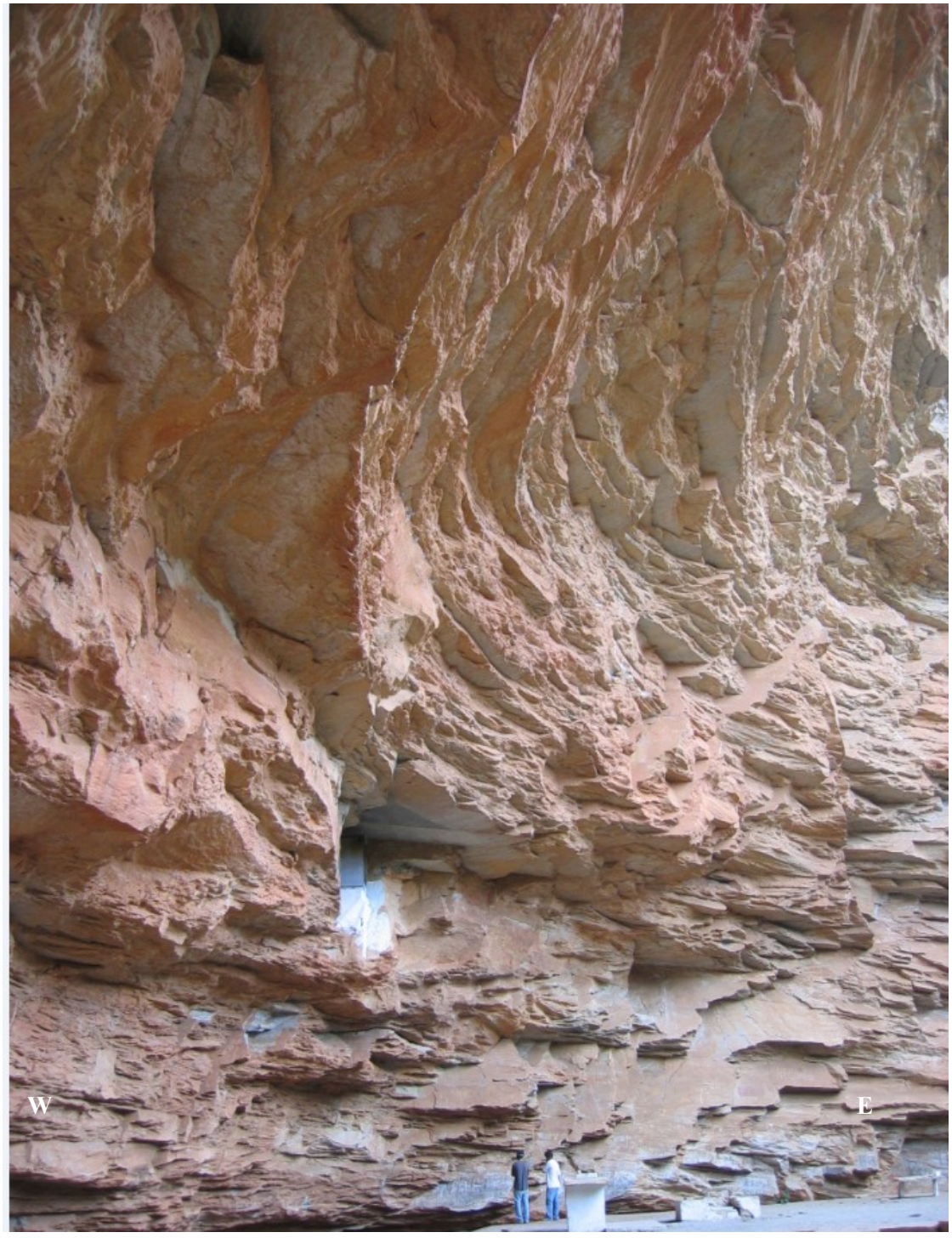

Outcrop Y: Large outcrop of a light colored limestone. Most of the joints dip 75°-85°south. Location: -19.706475/ -43.871304.

Same outcrop seen from a different perspective, highlighting the joints mentioned in the first photo from Outcrop Y (p. 86).

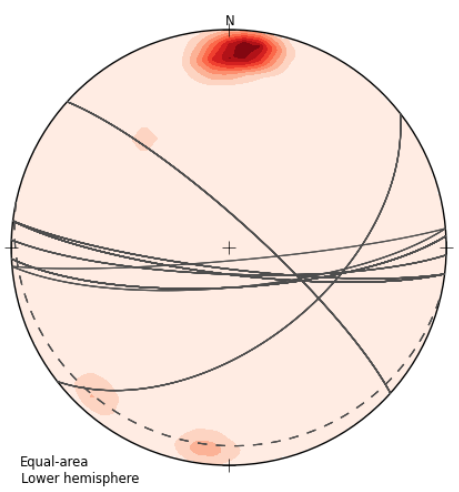

Figure 5-12 Stereonet plot of 81 joint measurements from Outcrop Y.

Since many joints were parallel, only eight different directions were measured. The dashed line indicates the thrust fault from Outcrop Z which is very close to Outcrop Y.

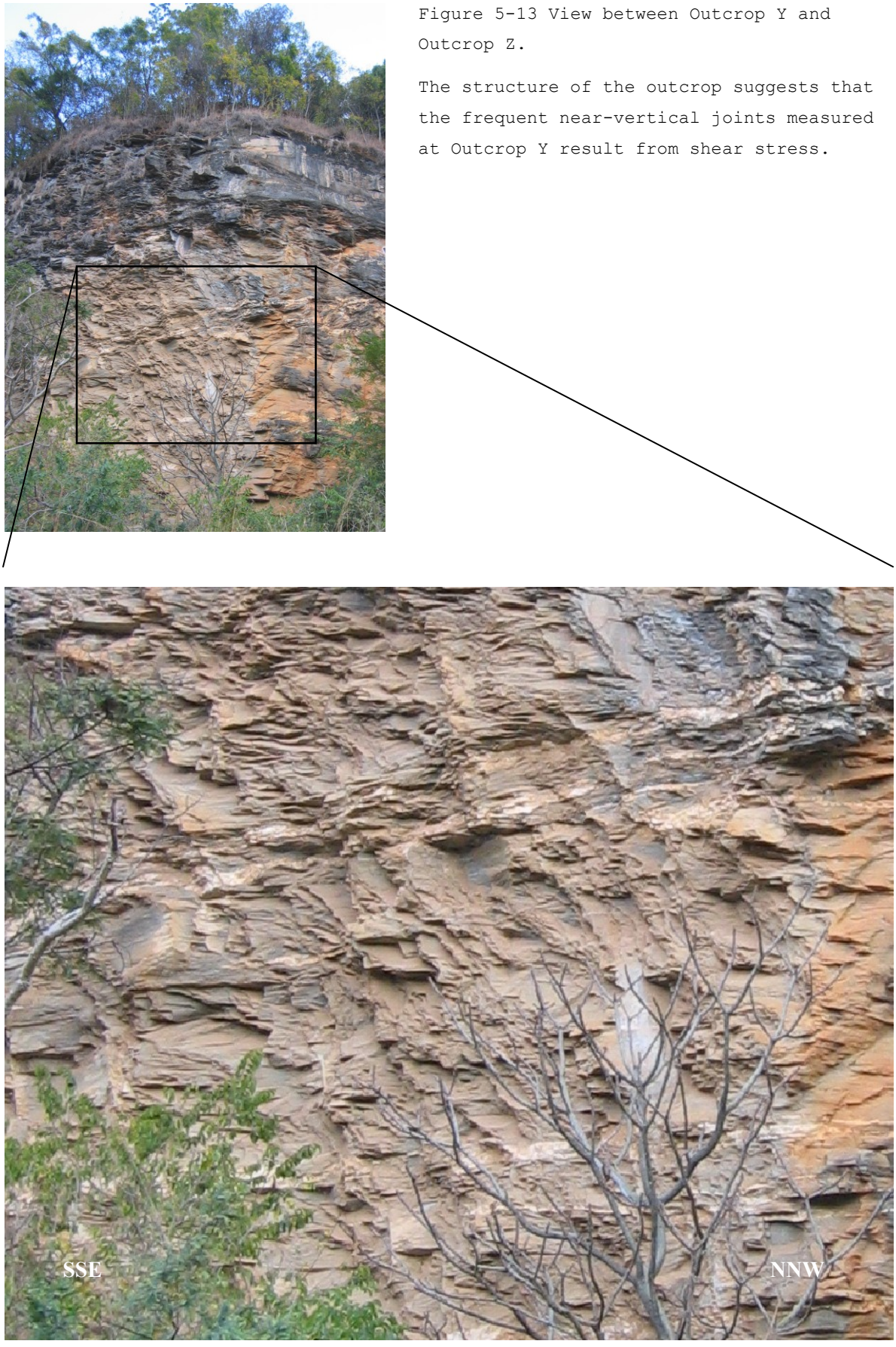

Figure 5-13 View between Outcrop Y and Outcrop Z.

The structure of the outcrop suggests that the frequent near-vertical joints measured at Outcrop Y result from shear stress.

Outcrop Z: more weathered part of the large Outcrop Y

Four parallel features can be interpreted as thrust faults dipping SSE (170 / 10). The fault planes are filled with calcite crystals up to 2 cm size. The bedding is subhorizontal and the shear planes from Outcrop Y are not visible. The width of the photo is approximately 50 cm. Location: -19.704726 / -43.872634.

5.6 Summary of joint measurements

Except at local faults or folds, both S_0 and S_1 are nearly horizontal, dipping slightly to the east as the stereonet diagram of 84 field measurements shows (Figure 5-14). Additionally 225 measurements of joints were made at 59 locations, resulting in a maximum density dipping steeply in SSE direction (157 / 76, Figure 5-15 A). Since many parallel joints were measured in some large outcrops (especially Outcrop Y), a second diagram (Figure 5-15 B) shows the same information leaving out all parallel joints to avoid the domination of these few large outcrops. In this second diagram, additional preferential joint directions stand out: near vertical joints striking NW-SE and N-S, joints dipping around 65° SW and around 70° NW.

Comparing these measurements with joint measurements and direction and length observations of caves from Horta et al. (1998) (Figure 4-6), a similarity can be found in the prevailing east-west direction. However, the frequent north-south directions documented for caves are not present in the joint measurements for this study. An explanation might be that most caves are located in the north-western part or outside the study area in the APA Carste de Lagoa Santa region, which might have other prevailing directions than the south-eastern part of the current study area where the measurements were taken (Figure 5-16).

Figure 5-16 shows that the joint directions vary considerably with their location.

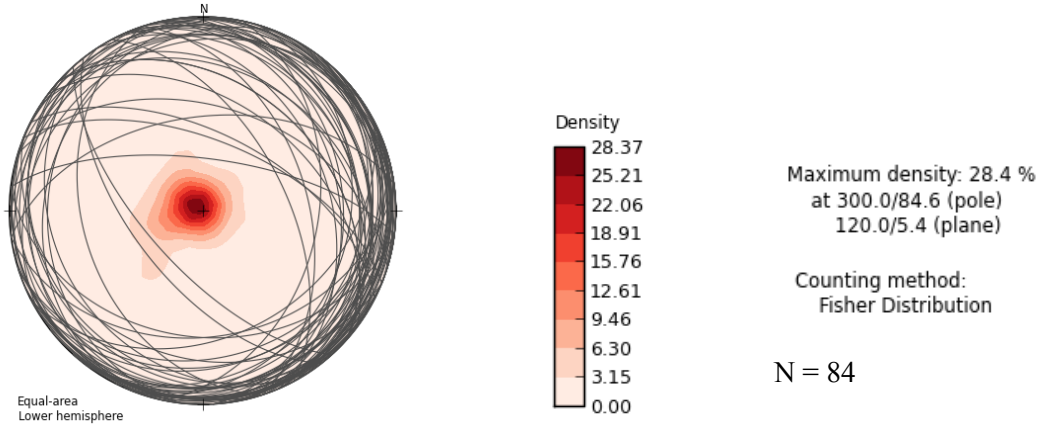

Figure 5-14 84 measurements of S_0 and S_1 (which are generally parallel in the region) show that the geological architecture is nearly always sub-horizontal with a prevalence of dips towards east.

The diagram shows densities of dip direction (poles to planes) and great circles drawn on the lower hemisphere.

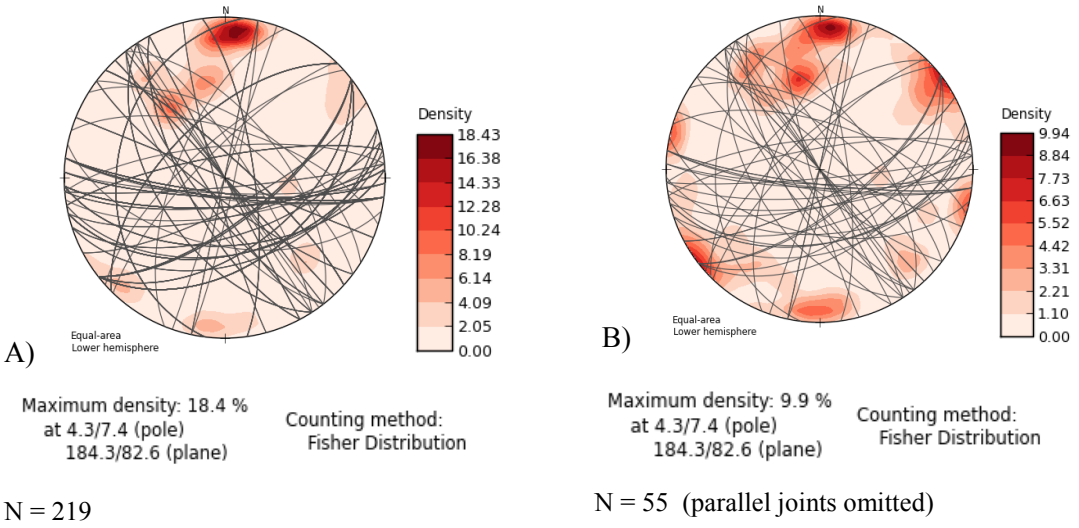

Figure 5-15 Equal area lower hemisphere stereonet diagrams show the dip directions (poles to planes and great circles) of joint measurements in the Bambuí meta-sediments of the study area.

Diagram A is based on all 219 measurements. Since many parallel joints were measured at only few large outcrops, all parallel joints were omitted for diagram B, resulting in a database of only 81 non-parallel joints that was constructed to avoid the dominance of few large outcrops.

5.7 Lineament analysis

Own lineament analysis of relief data using the hillshade - display of the digital elevation model that was generated from 10 m equidistant contour lines in ArcGIS resulted in the Map 33 shown in the annex. These relief structures are most often interpreted as directions of weakness (fracture zones or faults).

Based on the general tectonic setting, north-south striking topographic structures are interpreted as thrust faults (if this interpretation is in concordance with the spatial distribution of the geological units). East-west, southeast – northwest or southwest-northeast striking structures are on the other hand interpreted as fracture, normal fault or strike slip zones. These directions are often associated with valleys or local depressions that can be explained by normal faults or by collapse of overlying pelite layers into caves along weakness zones of the lower carbonaceous strata. Map 34 in the annex shows the structural interpretation of the lineaments from Map 33 on p. 370.

Comparing the joint measurements of Figure 5-16 with lineaments from relief, it can be noted that the prevailing joint directions are not always visible in the current relief. Especially the prominent east-west direction measured in the large Outcrop Y is not a very common feature of the topography.

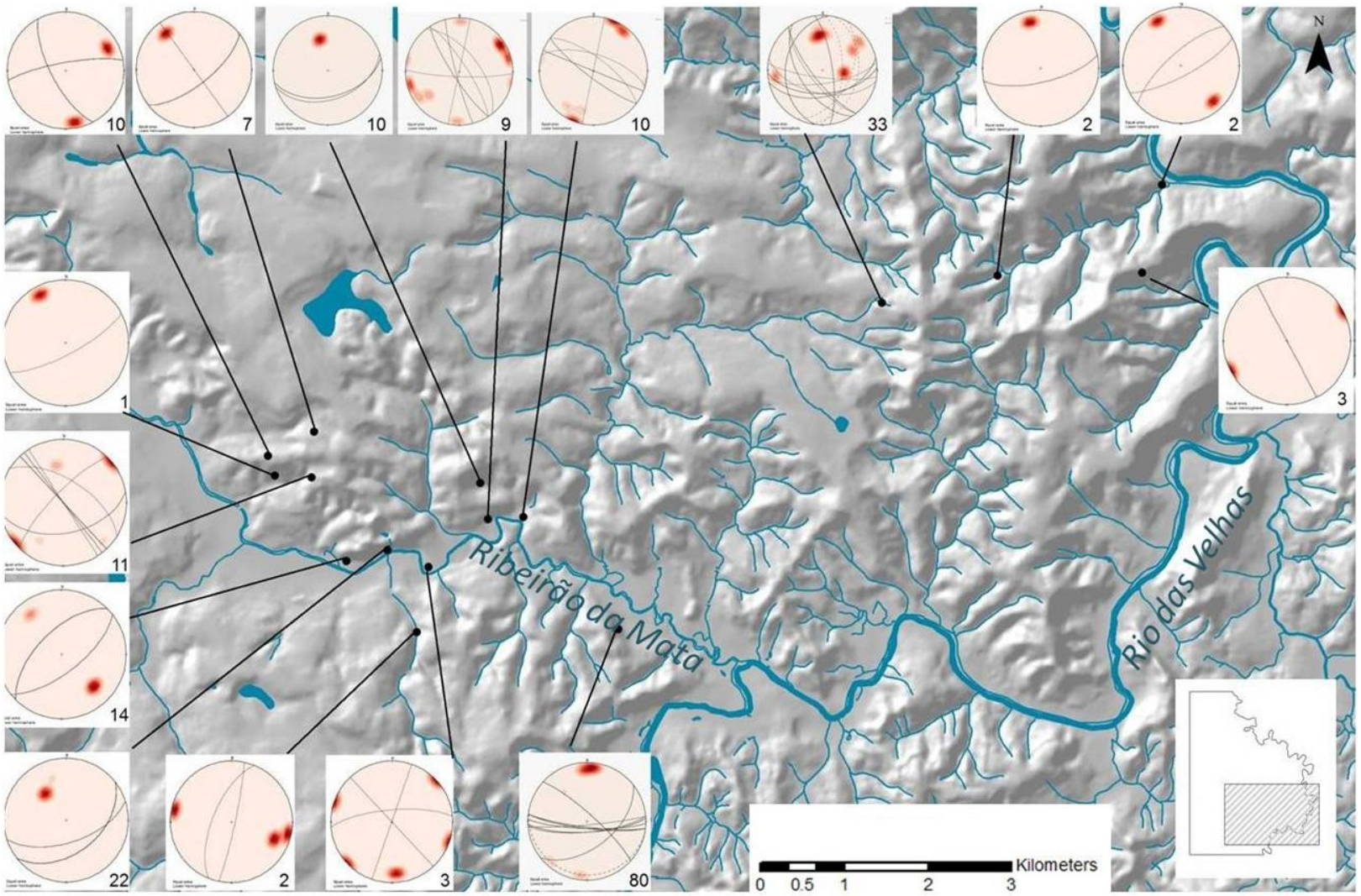

Figure 5-16 Location of joint measurements. Few large outcrops with parallel joints dominate the statistic.

Location of joint measurements. Few large outcrops with many parallel joints dominate the statistic.

5.8 Sedimentological study of the sedimentary system of the Riberão da Mata alluvium

(This section has been published in Hofmann et al. (2009), the sedimentological interpretation was done with the help from J. Hornung)

The sedimentary architecture of the central part of the alluvial plain of the Riberão da Mata was analyzed in an open sand pit in October 2006. The sand pit is located downstream of the confluence with the Riberão das Areias and upstream of the contact between the Archean basement and the carbonaceous sediments of the Late Proterozoic Bambuí Group (Figure 5-17).

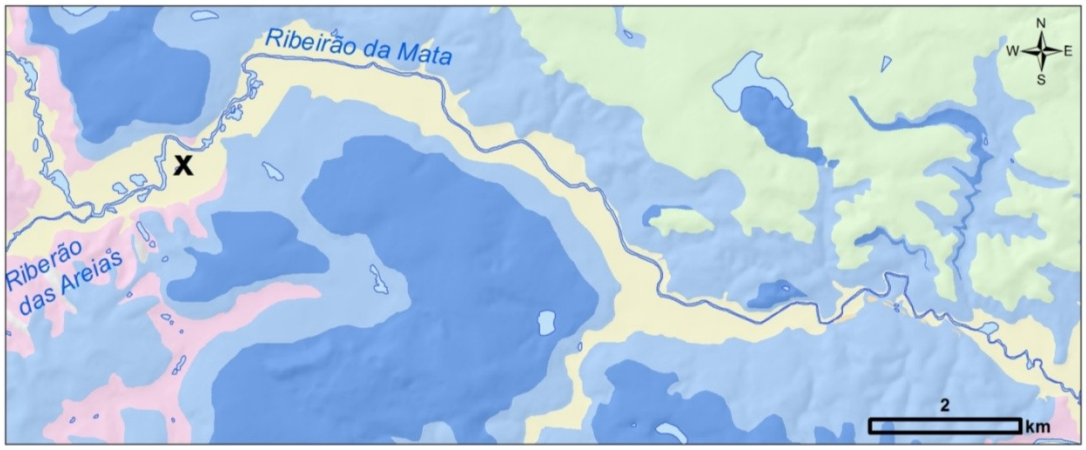

Figure 5-17 Location of the sand pit in the alluvium of the Riberão da Mata.

In this pit, ten sedimentary profiles exposed at the walls of the pit were logged and three radiocarbon age datings of clay horizons rich in organic material were performed to understand the depositional system of the fluvial sediments. The ten logged profiles together with their interpretation are shown in Figure 5-19 and Figure 5-20.

5.8.1 Fluvial styles and estimation of sand content

The succession reveals a clear overall fining-upward trend, which is represented in both lithofacies types and architectural element distribution. The exposed section starts with coarse-grained sand showing large scale trough cross-bedding (Figure 5-18 a) that frequently bears large trunks and other wood fragments (unit 1: Figure 5-18 b).
Towards the top of this first unit, small-scale channels occur in increasing numbers (Figure 5-18 c). They show an internal large scale channel trough master bedding comprising frequent intercalations of thick mud drapes and fine to very coarse sandy units. One of these mud drapes was dated to 4956 ± 53 B.P. by radiocarbon method. The coarse-grained sand layers within the master bedding display massive appearance, the finer ones ripple through cross-lamination.

Additionally, the uppermost part shows wavy channel-bulge stratification with an overall master bedding dipping to the right (north) with around 10° in Figure 5-18d. The small-scale channels are also governed by this overall master bedding.
Unit 1 (Figure 5-19, Figure 5-19) is topped by laminated sheet-like clay layers in which crude topsoils developed showing rooting, clay mineral dislocation, bleaching and chemoclines of iron hydroxides (unit 2a). Partly sandy layers are incorporated. Two other radiocarbon datings were carried out in almost pure clayey topsoil deposits 200 m to the NE from this location and revealed ages of 7258 ± 72 yr (lower one) and 5529 ± 72 yr (upper one) (unit 2b).
The top-unit (which is traceable over the entire area) consists of horizontally bedded clayey medium sand, intercalated with some ripple cross-laminated sand layers (unit 3). The stacking pattern of the fluvial architectural elements shows an overall multi-lateral and also multi-storey architecture.

The fluvial style of unit 1 can be interpreted as a low sinuous meandering system with a large and prominent main channel showing mid channel bars (Figure 5-18 b and lower part of Figure 5-18 a) and strongly fluctuating water levels.
This is supported by unit 1 indicating a high stream power which creates large trough cross-beds and a large transport capacity for the trunks and coarsest sand grain sizes. There is evidence only for slight formation of point bars due to channel migration cycles (Figure 5-18 d). Furthermore, the discharge pattern shows strongly fluctuating water levels with intense flood stages (due to wet seasons?) which are indicated by extended floodplain successions in profiles 4, 5, 7, 8 and intense formation of chute channels containing thick mud drapes between the point bar bulges (Figure 5-18 b and c). The overall thickness of that depositional system that filled the valley entirely comprises at least 8 m (base not exposed). A net-to-cross sand estimation of that kind of fluvial system reveals around 40 - 60% sand, depending on amalgamation rate, rate of channel switching and subsidence.
Unit 2a is genetically related to unit 1 as it represents the floodplains of the fluvial system that quickly covers the abandoned parts of the channel belt with prominent mud and silt deposits in times of flooding. Podsolization occurs in these layers. This unit (2a) is not linked to the floodplain deposits of unit 2b where the two other datings were accomplished.
Finally, unit 3 (thickness approximately 3 m) is interpreted as a near channel floodplain with topsoils and crevasse splays, which are considered to relate to the modern fluvial system as it covers all units sheetlike and is traceable in the entire area.

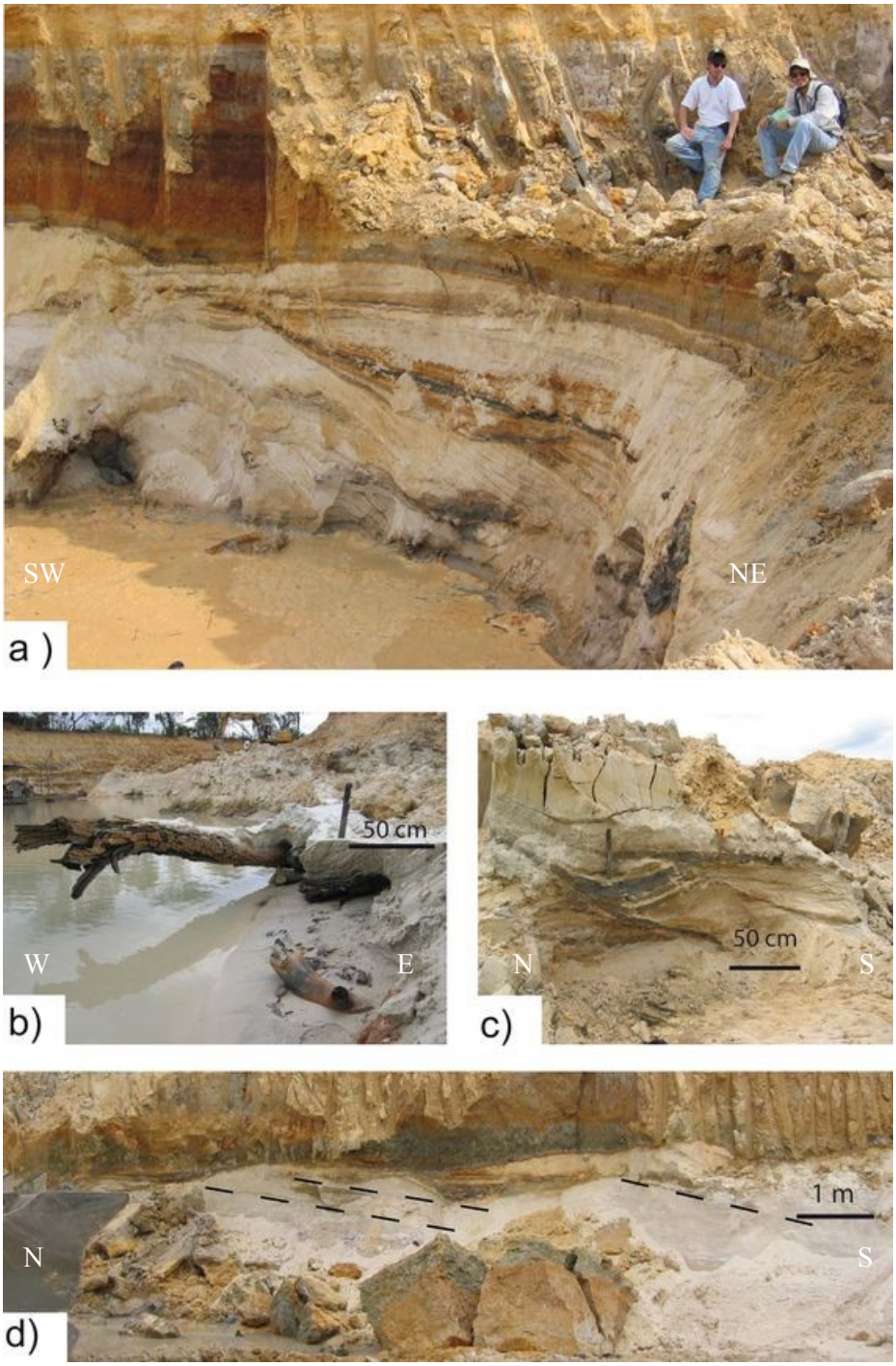

Figure 5-18 a) and c) Chute channels containing thick mud drapes between the point bar bulges at the top of unit 1. Age was determined from the mud drape in a similar unit revealing 4956 yr. b) Lower part of unit 1 in the investigated sand pit.

Large and frequent trunks, large-scale trough cross-beds, very coarse sand grain sizes and mud drapes indicate high stream-power with mid-channel bars and fluctuating water levels. d) Point bar stratification containing mud drapes between the bulges at top of unit 1. Some weak master-bedding dipping with 10° to the right is visible (dashed lines). The chute channels of picture a) are located to the right at the same level. Source: Hofmann et al. (2009).

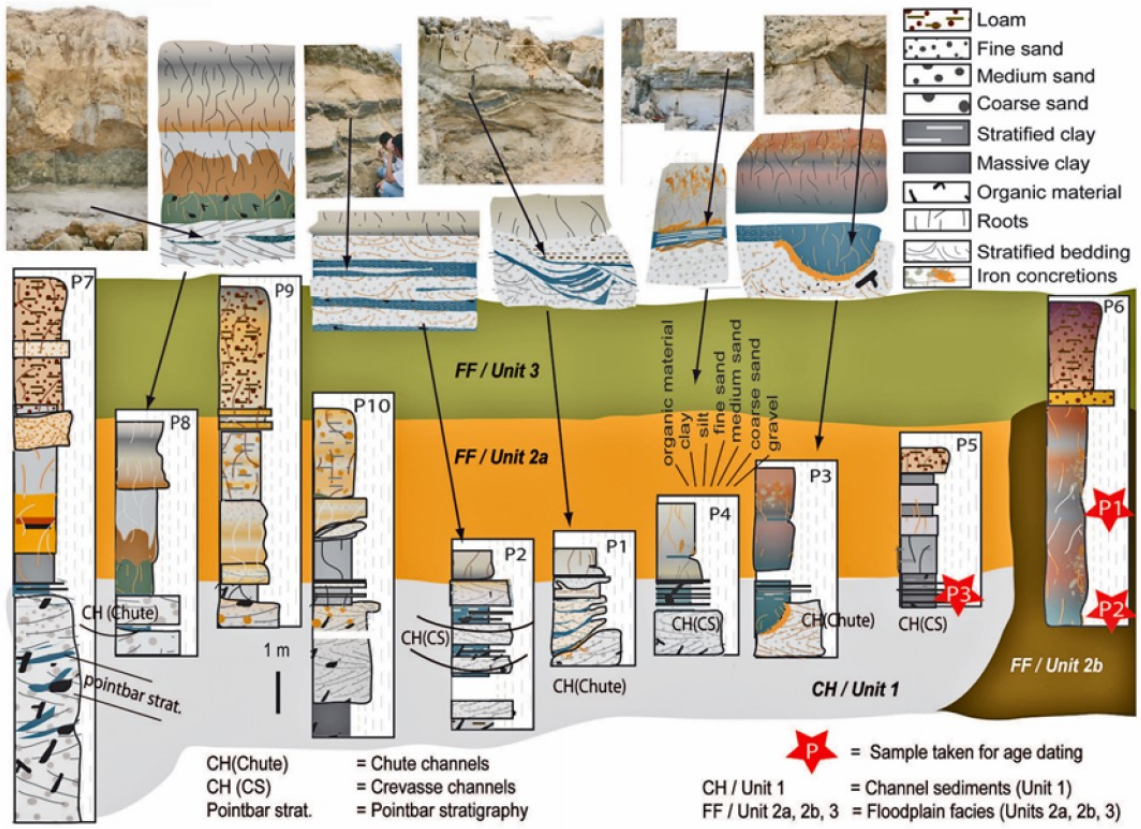

Figure 5-19 Sedimentary structure of ten profiles in a sand pit of the alluvium of Riberão da Mata.

For a detailed explanation of the model and correlation scheme see text. For location of the profiles see Figure 5-20 a), for location of the sand pit see Figure 5-17. Source: Hofmann et al. (2009).

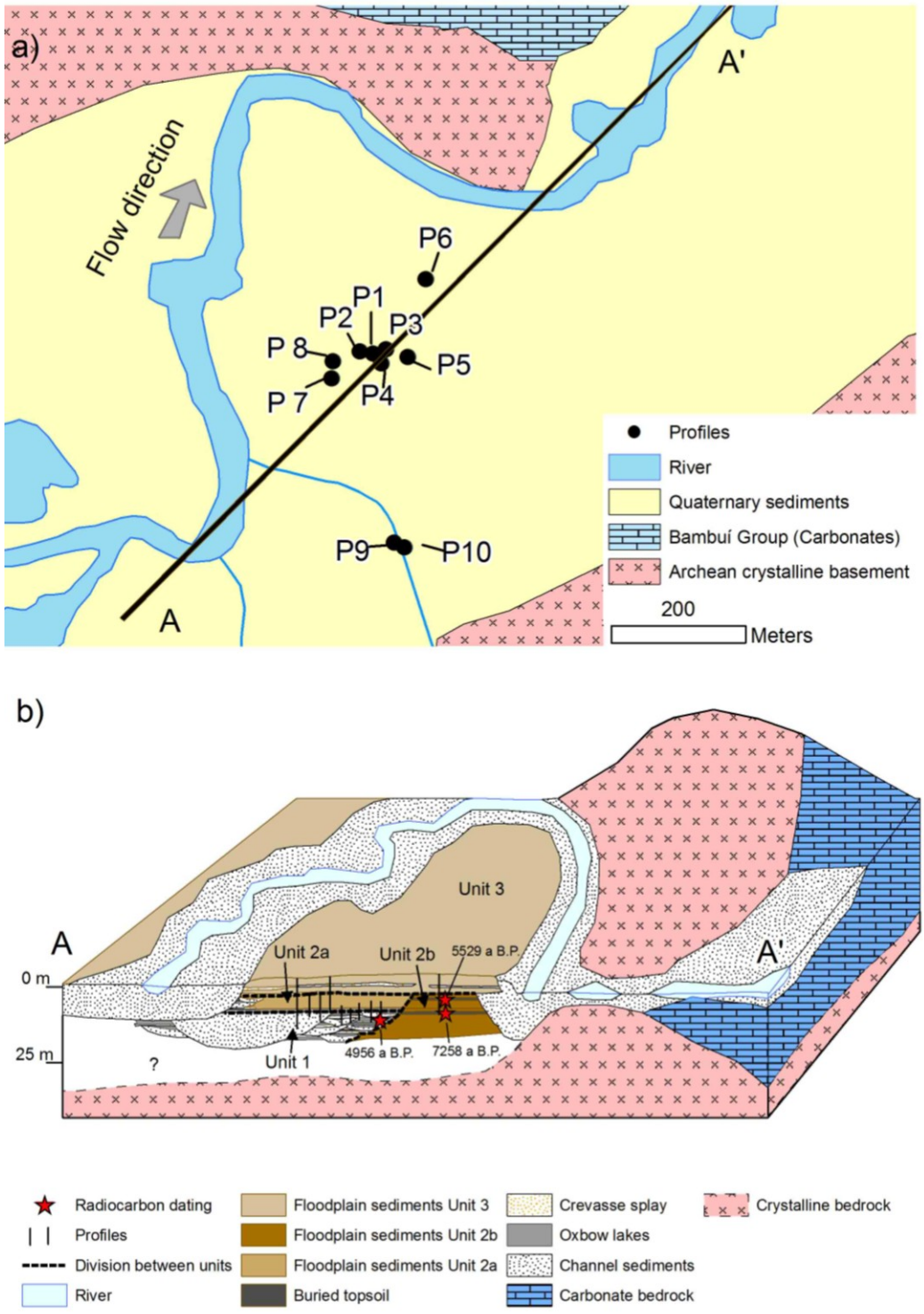

Figure 5-20 a) Locations of the profiles and b) model of the sedimentary architecture around the sand pit in the alluvium of Riberão da Mata based on the profiles shown in Figure 5-19.

Three radiocarbon datings are indicated by the red stars in the profiles 5 and 6 (P5, P6 in Figure 5-19). For explanation see text. Source: Hofmann et al. (2009)

5.8.2 Depositional model

The two uppermost radiocarbon datings were taken from buried topsoil horizons in unit 2b and show ages of about 7258 ± 72 yr (lower horizon) and 5529 ± 72 yr (upper horizon), which represent typical values for floodplain growth and crude topsoil development in such alluvial systems. A younger age (4956 ± 53 yr) was found in chute channel sediments of unit 1. All datings were done from disseminated organic carbon in dark coloured layers. However, the succession shows a partly inverse order of stratigraphic ages.

Based on this information a simplified depositional model of the sedimentary architecture in the location around the pit was constructed (Figure 5-20 b).

In general, the model is based on a continuous filling of the valley until 5500 BP (age of upper floodplain, unit 2b) and a very quick downcutting until 5000 BP (age of chute channel) leaving fluvial terraces. Wolfe et al. (2001) provide climate data from an isotope record of a Bolivian lake, which shows an increased humidity (related to present) around 5500 BP. However this could be a regional climate constraint, which could have caused this spontaneous downcutting due to increased discharge. After 5000 BP the valley was refilled with unit 1, 2a and 3. Additionally to climatic conditions, tectonic movement could have been responsible for the large sediment accumulation in the alluvial plain of the Riberão da Mata (oral communication from H.C.Kohler, see also section 6.2).

Recently, again an erosional downcutting is recorded in the modern river bed. The modern channel belt on the right probably did not move that much as it forms a cut bank that erodes further into the hill on the right, which may be the reason why the older floodplain sediments are preserved in this area.

Upstream of the pit at the contact to the Bambuí sediments, the Quaternary basis seemed very shallow as there is a small step in the riverbed where carbonate rocks are visible in the water. Also ten drill-holes that were obtained from the owner of a sand pit in the alluvial plain of Riberão das Neves, an affluent from the west to the Riberão da Mata, showed a fining-upward trend with sand layers up to ten meters below an overburden of finer sediments with a thickness of ten to fifteen meters or more. The results from these drill-holes are thus in concordance with the sedimentological model constructed from the information in the sand pit.

5.9 Results

5.9.1 Updated geological map

The resulting updated geological map is shown in Map 36 (p.373) in the annex. Eight cross-sections were drawn to illustrate the geological architecture of the study area (pp 374 - 375 in the annex).

As shown in the cross-sections, underground dissolution processes are responsible for many features of today's relief – even in areas where the soluble limestone is covered by meta-pelites (intrastratal karstification). Drill-hole data from Pessoa (2005) document large caves beneath the meta-pelites and support this assumption. Especially the depression of the Lake Lagoa Santa and the zone south-east of the lake Lagoa Santa, which are illustrated by the cross-sections 3, 7 and 8, are probably caused by intrastratal karstification. In the cross-sections, the thin-skinned tectonic concept of Ribeiro et al. (2003) and Pessoa (2005) was incorporated as well as facies interdigitation in the Sete Lagoas carbonates as described by Vieira et al. (2007a).

5.9.2 Facies distribution of the Sete Lagoas Formation

The estimated spatial distribution of the two facies of the Sete Lagoas Formation is illustrated in Map 37 in the annex. It is based on the map and field descriptions from Ribeiro et al. (2003), on drill-hole data from Pessoa (2005) and on own observations. In this map, the character of the top layer of the Sete Lagoas Formation is drawn, irrespective of its thickness. Thus, especially in the complex eastern part of the study area, this map simplifies the lithological architecture and layers of pure carbonates can exist below layers of impure carbonates (compare also the cross-sections 3,4,6,7 and 8 on page 374 and 375 in the annex and the cross-sections from Pessoa (2005) in Figure 4-8).

5.9.3 Idealized local stratigraphic column

The idealized stratigraphic column in Figure 5-21 summarizes the geological units and their lithology in the study area. It is a modification of the local stratigraphy published by Pessoa (2005) which itself is based on previous works of Ribeiro et al. (2003) and Schöll (1972). The difference to Pessoa (2005) is based on the descriptions of lateral interdigitation of the Facies Lagoa Santa and Facies Pedro Leopoldo as described in Vieira et al. (2007a) (compare also Figure 4-10 on p. 65).

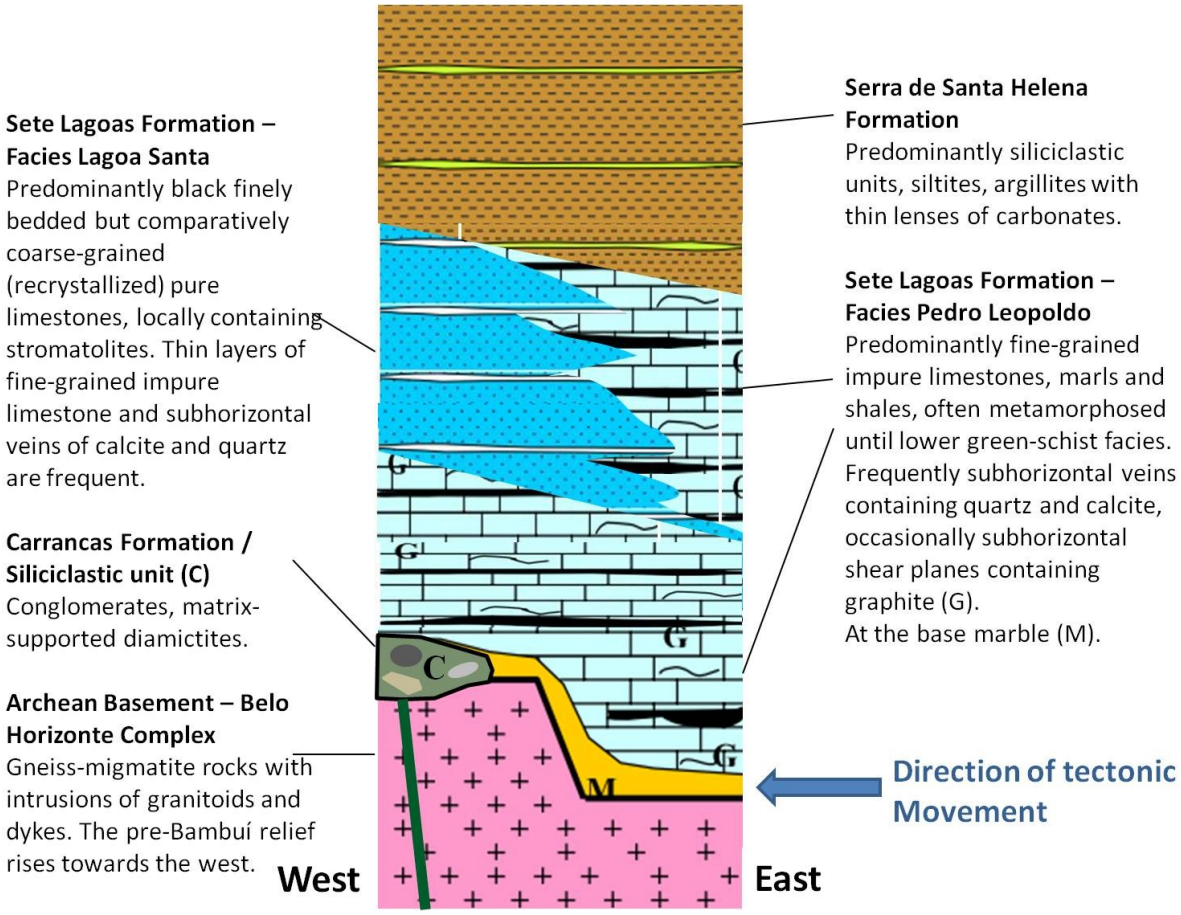

Figure 5-21 Idealized stratigraphic column of the study area.

Modified after Pessoa (2005).

5.9.4 Pre-Bambuí relief

From the 59 drillings of Pessoa (2005) that reached the basement, a surface of the top-basement was interpolated (Figure 5-22) using an algorithm optimized for interpolation of a surface relief shaped by water erosion (Hutchinson 1989) which is plausible for the pre-Bambuí relief. Pessoa (2005) interpreted three different ramps (Figure 5-22 lower part) that could have initialized thrust faults in the overlying strata during the Brasiliano Orogeny.

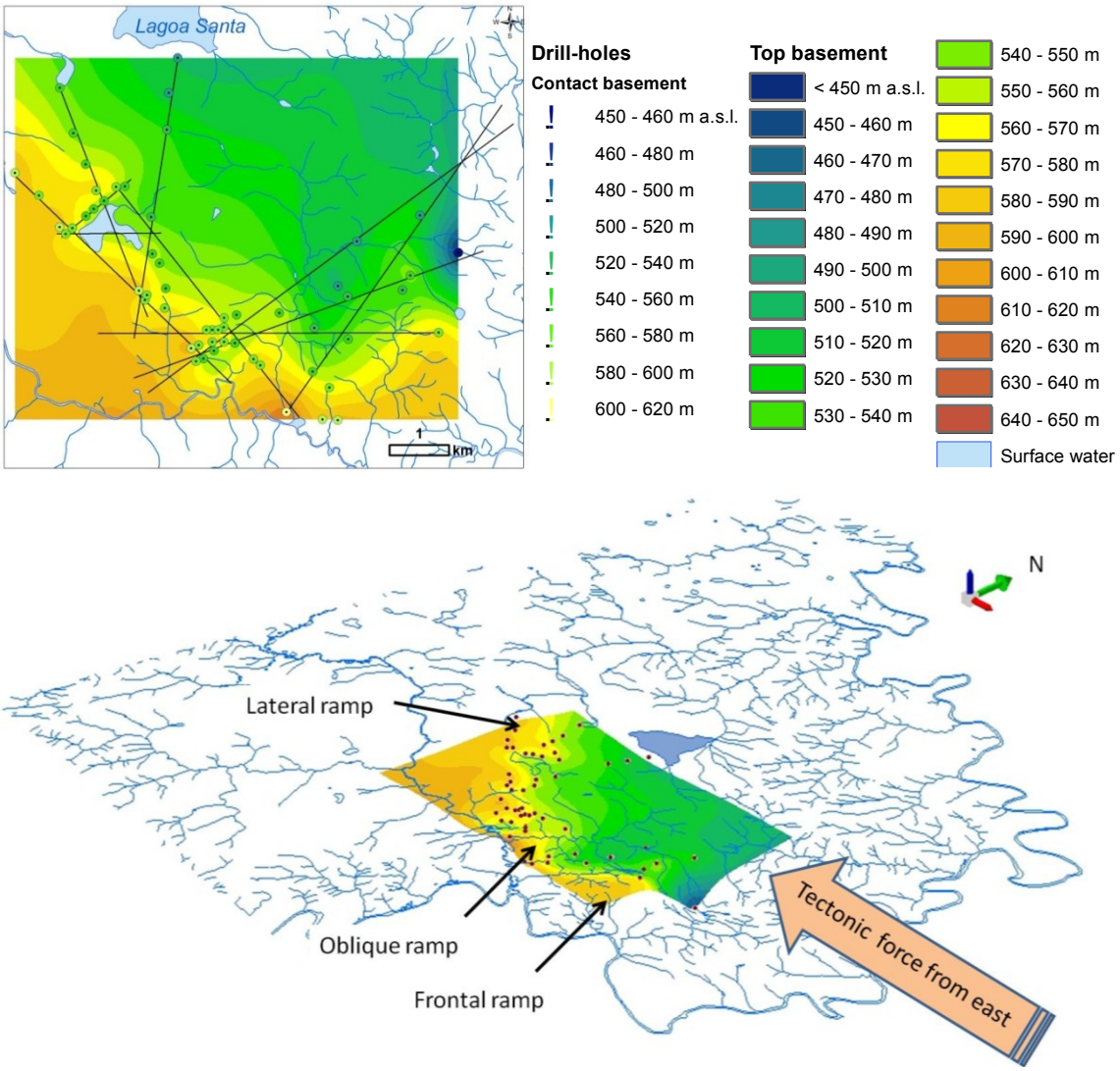

Figure 5-22 Upper part: Basement paleo-relief interpolated from drill-hole data Lower part: The uneven basement relief rising towards the south-west may have acted as ramp for thrust faults in a thin-skinned tectonic movement during the Brasiliano Orogeny (Pessoa 2005).

Compare also cross-section 7 on page 375 in the annex.

Using the information from Figure 5-22 and the surface contact line between crystalline basement and Bambuí sediments, plausible contour lines of the top surface of the crystalline basement were drawn (Figure 5-23). From these data, a surface of the top of the crystalline basement was interpolated for the south-western part of the study area. The result is also shown in Figure 5-23 and in Map 38 in the annex.

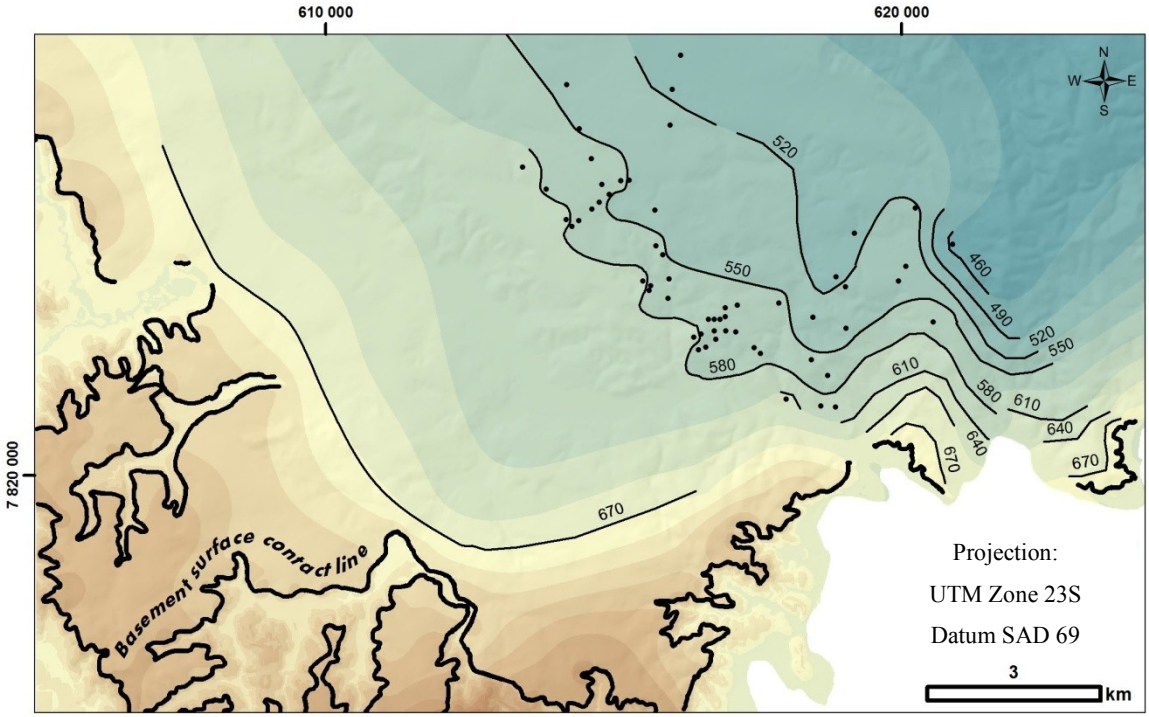

Figure 5-23 Interpolated surface of the top of the crystalline basement.

The equidistance of the contour lines and the color code is 30 m. Black points indicate locations of the drill-holes reaching basement from Pessoa (2005). For orientation: the SE-border is delineated by the Rio das Velhas.

6 Geomorphology and neotectonic movement

6.1 Overview and previous studies

The study area is located on hilly terrain between 600 and 900 m a.s.l. in a bend of the Rio das Velhas (see Figure 2-2 and Figure 6-3). In the south, the Serra do Curral marks the northern border of the Quadrilátero Ferrífero and in the east, the southern part of the Serra do Espinhaço marks the border of São Francisco Craton. The relief of the study area is dominated by flat hills reaching elevations between 800 m and 900 m.a.s.l; the maximum elevation is declining from south-west to north east (Map 3 in the annex). These plateau surfaces are dissected by north-east draining rivers with the exception of the broad alluvial plain of the Riberão da Mata, which drains to the south-east. Around the triangular lake in the central part of the study area, the city of Lagoa Santa was founded in the 18th century. North-west of Lagoas Santa, karstified limestone crops out. In this region, many dolines, limestone walls or towers, caves and sinking streams can be found. Near Lagoa Santa, south-east of the karst area, the limestone is covered by pelitic meta-sediments of the Serra de Santa Helena Formation and intrastratal karstification resulted in plugged depressions. Thus, this area is referred to as "covered karst" area. The hills east of Lagoa Santa are higher and steeper (outlined by the yellow line in Map 3 in the annex). Here, pelitic meta-sediments dominate the hilltops but the streams are often incised until the underlying limestone.

6.1.1 Karst studies

This karst region north-west of Lagoa Santa is famous for its speleological and archeological discoveries, which started in the 19th century with Peter Lund (1835) who described fossils of prehistoric fauna and early human settlers such as the 12 000 year old "Lagoa Santa Man" (Berbert-Born 2002). Kohler (1989) gave a detailed description and a map of the karst features that was the basis for later geomorphological maps of the region (CPRM 1994a, Kohler et al. 1998). In 1998, the area of the Lagoa Santa karst was declared an environmental protection zone called APA Carste de Lagoa Santa (APA = Area de Protecão Ambiental = Environmental Protection Area) and a large volume on the biological and physical environment, archeological and speleological heritage as well as of the socio-economic situation of the area was published (CPRM and IBAMA 1998). In 2000, the Lagoa Santa karst area was incorporated into the collection of Geological and Paleontological Sites of Brazil (Berbert-Born 2002). Planation surfaces in eastern Brazil.

6.1.2 Erosion cycles

The region around the study area has been a stable surface inside the São Francisco Craton since the Late Neoproterozoic. After the opening of the Southern Atlantic in the Lower Cretaceous, regional uplift of the region resulted in several erosion cycles that shaped today's relief. In 1956, King correlated the peneplanation surfaces of eastern Brazil with the peneplanation surfaces he was familiar with in Africa and his work (King 1956) is still the basis of many geomorphological studies in the region. He defined the following succession of peneplanation surfaces for eastern Brazil: the uppermost peneplain is the Gondwana Surface (Lower Cretaceous) followed by the Post-Gondwana Surface (Upper Cretaceous). The next surfaces are the Sul-Americana Surface (Lower Tertiary) and the Velhas Surface (Upper Tertiary). From all surfaces, the Sul-Americana Surface has the greatest extension and the most perfect peneplanation and was thus used as reference for the older and younger surfaces (King (1956) p.5). According to the same author (p.41), the Gondwana and Sul Americana Surfaces are often characterized by accumulation of hardened iron crusts (petroplinthite). Plinthite is a mixture of iron and aluminum oxides that accumulates in zones of seasonal groundwater level change. Recurrent oxidation of the iron transported in the groundwater leads to a local accumulation of iron oxides. After exposure, the plinthite hardens irreversibly and the iron crust, referred to as petroplinthite (or "Canga" in Brazil), protects the underlying rocks from erosion (Figure 6-1).

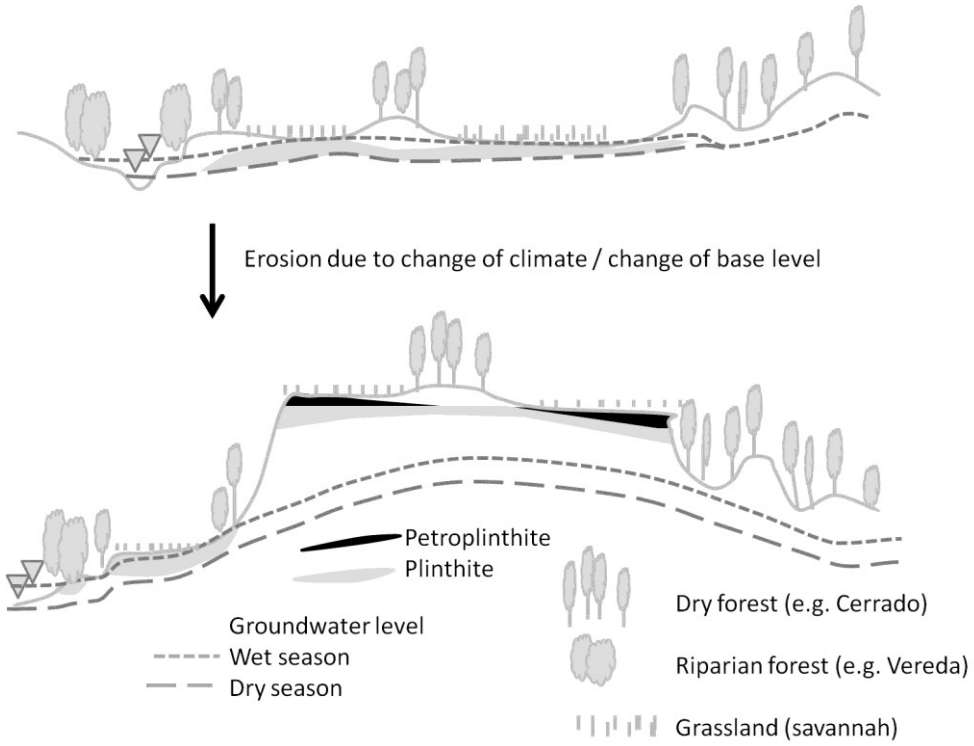

Figure 6-1 Relief inversion due to hardening of exposed plinthite in an eroding landscape.

(Hofmann et al. (2013), based on Driessen et al. (2000))

In the region of the study area, a medium elevation of the Sul-Americana Surface of 815 m a.s.l. was described by King (1956) for Belo Horizonte, declining towards the north and reaching 780 m a.s.l. near the city of Sete Lagoas north of the study area. Especially around the city Pedro Leopoldo in the west of the study area, King (1956) (p. 47) also described the Post-Gondwana Surface as major planation surface, lying above the Sul-Americana surface and declining towards the north until it is merged with the later near Curvelo, where both surfaces together form a major planation surface at 680 m a.s.l.. Nevertheless, these values need to be interpreted with care as there are even discrepancies about 50 m – 100 m regarding the elevation of the planation surfaces near the study area within the work of (King 1956), if the statements in the text are compared with the summarized values given in a table in another chapter (p. 56).
Based on King (1956), Kohler (1989), Kohler et al. (1998) interpreted all elevations above 810 m a.s.l. in the Lagoa Santa karst area as belonging to King's Sul-Americana peneplanation surface. This interpretation is sensible since this is the most common elevation for the high plateau areas in the study area (Map 3 in the annex). These plateau areas are typically covered with thick red Ferralsols and occasional occurrences of iron crusts (petroplinthite) support the correlation with King's Sul Americana Surface. Nevertheless, there are regions with higher elevations, reaching 860 m a.s.l. where the International Airport Tancredo Neves was built in the early 1980s and more than 900 m a.s.l. on the steep hills east of Lagoa Santa. This would support the original hypothesis of (King 1956) who described two high planation surfaces for the region: the Sul-Americana surface and above it the Post-Gondwana surface, although it is important to note that King assumed lower altitudes for these surfaces.
While the upper hillcrests are thus attributed to the Sul-Americana or the Post-Gondwana Surface, the lower hills around 750 m a.s.l. and the rest of the study area are attributed to the Velhas Surface (King 1956, Kohler 1989). Also the caves in the karst area north west of the city Lagoa Santa were drained during the Velhas erosion cycle, which occurred during the Plio-Pleistocene as fossil encounters in the caves suggest (King 1956, Berbert-Born 2002). During the more humid Holocene, erosion features of the Velhas cycle were again filled with sediments. The current erosion cycle that incises into the Holocene colluvial and alluvial sediments began probably at the end of the 17th century following intense land use change by human action (Coelho Netto (1999) see also section 14.1).

6.2 Geomorphological hints for neotectonic movement

For most studies in the region, neotectonic movement has been defined in a wider sense, not restricted to the Quaternary but also including the Tertiary since the opening of the South Atlantic. According to the INQUA Neotectonics Commission (Mörner 1978), neotectonics has no real boundary back in time but includes any active earth movement. Since for the current project

no direct age dating was possible but movement was only inferred from geomorphology, the broad definition of Mescherikov (1968) was applied, which was also used for previous neotectonic studies in the region (Penha et al. 2005). This definition stresses the importance of interrelation of the current topography with neotectonic movements. Inverting this argument, any contemporary geomorphological structure deviating from the regional context that is not explained by lithological differences can be interpreted as hint of neotectonic movement.
Some topographic anomalies in and around the study area suggest that there has been tectonic movement in the region that was recent enough to influence today's relief (compare section 6.2). The relief of the study area shows several remarkable features that could indicate neotectonic movement:

6.2.1 The alluvial plain of the Riberão da Mata

The wide valley of the Riberão da Mata does not match the erosion power of its small stream. It is even wider than the valley of its base level, the Rio das Velhas, whose flow rate is about ten times larger (compare also Figure 2-6 on p. 13) but flows through a very narrow valley. Also the direction of the Riberão da Mata is very unusual and opposite to the prevailing SE-NW direction of the other streams in the region (Figure 6-3). This anomaly together with the intense karstification NW of Lagoa Santa lead to the hypothesis that the wide alluvial plain of the Riberão da Mata was eroded by the Rio das Velhas, which was then flowing opposite to the current direction of the Riberão da Mata and continued as endokarstic river in towards the north (Kohler and Karfunkel 2002).
The accumulation of large amounts of alluvial sediments has led to frequent mining of sand and clay (chapter 2.3). A sedimentological study of a sand pit in the central part of the alluvium of the Riberão da Mata suggests a refilling of the valley during the last 5000 years (section 5.8). In a small region, shortly before it reaches the Rio das Velhas, the alluvial plain of the Riberão da Mata narrows considerably and limestone crops out at a river bend in the middle of the valley (Photo in Figure 5-8, location D in Map 35 in the annex).

6.2.2 Steep hills east of Lagoa Santa

While the general relief of the study area is characterized by a softly dissected planation surface at circa 800 m a.s.l., the eastern hills of Lagoa Santa (east of the yellow line in Map 3 in the annex) show a different morphology: they are steeper and the hilltops reach 850 m a.s.l. and sometimes 900 m a.s.l.. This is even more remarkable since this area is closer to the local baselevel Rio das Velhas and there is no strong difference in lithology.

6.2.3 The valley of the Riberão Antonio Ferreira

The valley of the Riberão Antonio Ferreira dissects the eastern hills from south-west to north east. It is unusually wide in its headwaters and narrows close to its confluence with the Rio das Velhas (Map 3 in the annex).

6.2.4 The bend of the Rio das Velhas

Not only the course of the Riberão da Mata deviates from the regional trend but also the Rio das Velhas abandons its regional course towards NNW and bends towards the east around the study area (Figure 6-3). Near the northern boundary of the study area, close to the Lagoa do Sumidouro, it again assumes its original direction.

To detect if this deviation from the regional course direction is also visible in the longitudinal profile, SRTM elevation data (90 m cell size from http://srtm.usgs.gov/index.php, downloaded 17.10.2010) were plotted along the course of the Rio das Velhas from the Represa Rio das Pedras in the Quadrilátero Ferrífero until the city of Presidente Juscelino in the north (Figure 6-3, Figure 6-2).

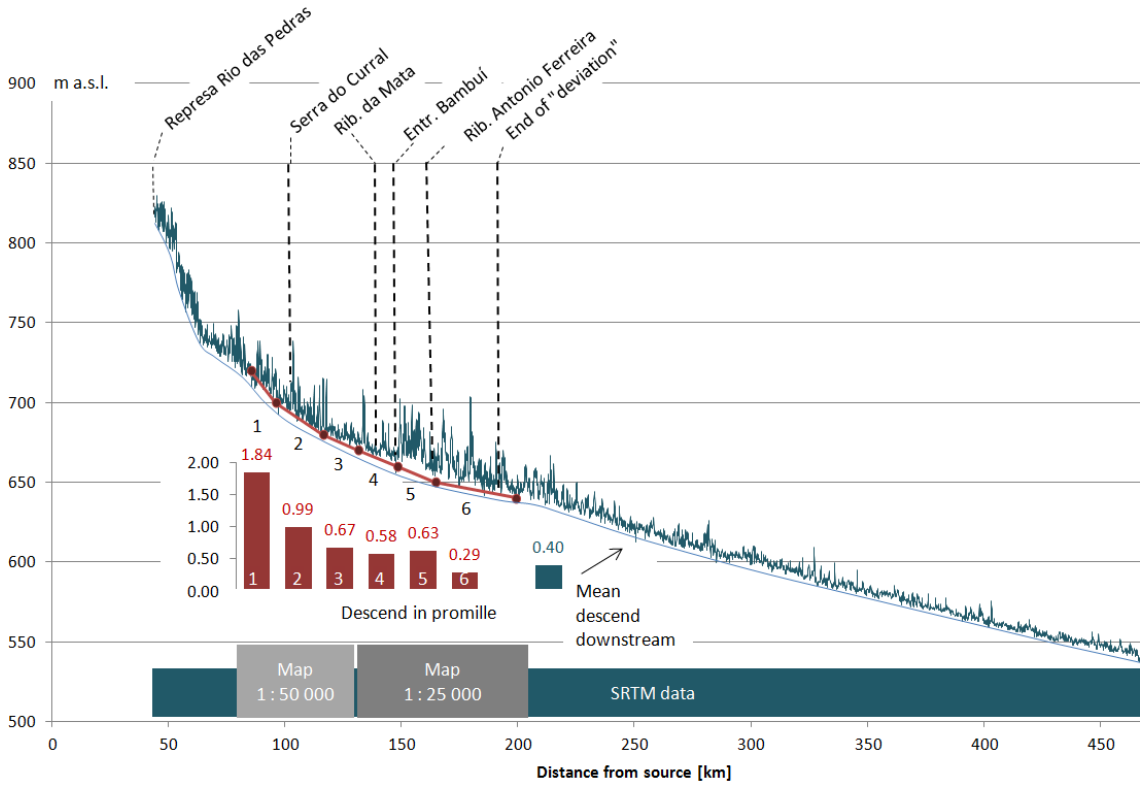

Figure 6-2 Vertically exaggerated longitudinal profile of the Rio das Velhas until the city of Presidente Juscelino.

Blue line: River profile derived from SRTM elevation data. Red line: Profile based on contour lines from topographic maps 1 : 50 000 and 1 : 25 000.

The scatter of the SRTM elevation data is due to the rugged topography hindering the radar signal to reach the lowest point in the valley. Scatter is stronger for regions where the river is deeply incised. Thus, the real elevation of the river is a continuously declining curve connecting the lowest points of the scattered data (blue line in Figure 6-2). Near the study area, the SRTM data were supplemented by contour lines from the topographical maps 1 : 50 000 and 1 : 25 000 (red points in Figure 6-2).

The sections between the contour lines are indicated in black and white in Figure 6-3 and numbered as follows:

Section 1: from 720 m a.s.l. - to 700 m a.s.l. = 10.9 km Descend: 1.84 ‰
Section 2: from 700 m a.s.l. - to 680 m a.s.l. = 20.1 km Descend: 0.99 ‰
Section 3: from 680 m a.s.l. - to 670 m a.s.l. = 14.9 km Descend: 0.67 ‰
Section 4: from 670 m a.s.l. - to 660 m a.s.l. = 17.1 km Descend: 0.58 ‰
Section 5: from 660 m a.s.l. - to 650 m a.s.l. = 16.0 km Descend: 0.63 ‰
Section 6: from 650 m a.s.l. - to 640 m a.s.l. = 34.8 km Descend: 0.29 ‰

Besides several knick-points in the area of the Quadrilátero Ferrífero, a knick-point can be detected at the end of the “deviation” at the northern boundary of the study area. The descend of section 6 is with 0.29 ‰ flatter than the mean descend downstream, which is approximately 0.4 ‰. Additionally, it can be noted that the descent of section 5 is steeper than the descent of section 4. While the river is flowing along the lithological contact in section 4, changing its original south-north-direction towards the east, it finally enters the Bambuí carbonates in section 5, reassuming its original direction. This knick-point could be caused by different lithologies, since the beginning of the “deviation” coincides with the entrance of the Rio das Velhas into the Bambuí sedimentary cover, locally represented by the carbonaceous Sete Lagoas Formation, and ends with its entrance into the meta-pelitic Serra de Santa Helena Formation. Another – nonexclusive – explanation for the knickpoints would be a local uplift in the region around Lagoa Santa. Also the NW-SE course of the Riberão da Mata could be explained by lithological differences, since the change of direction coincides with the lithological contact between carbonaceous sediments and crystalline basement. The river follows this contact for several kilometers from north-east to south-west (Figure 6-3). Nevertheless, based on the available data it is not possible to decide if only the lithological discontinuities are responsible for the observed knickpoints and river course anomalies or if a local uplift around Lagoa Santa also plays a role.

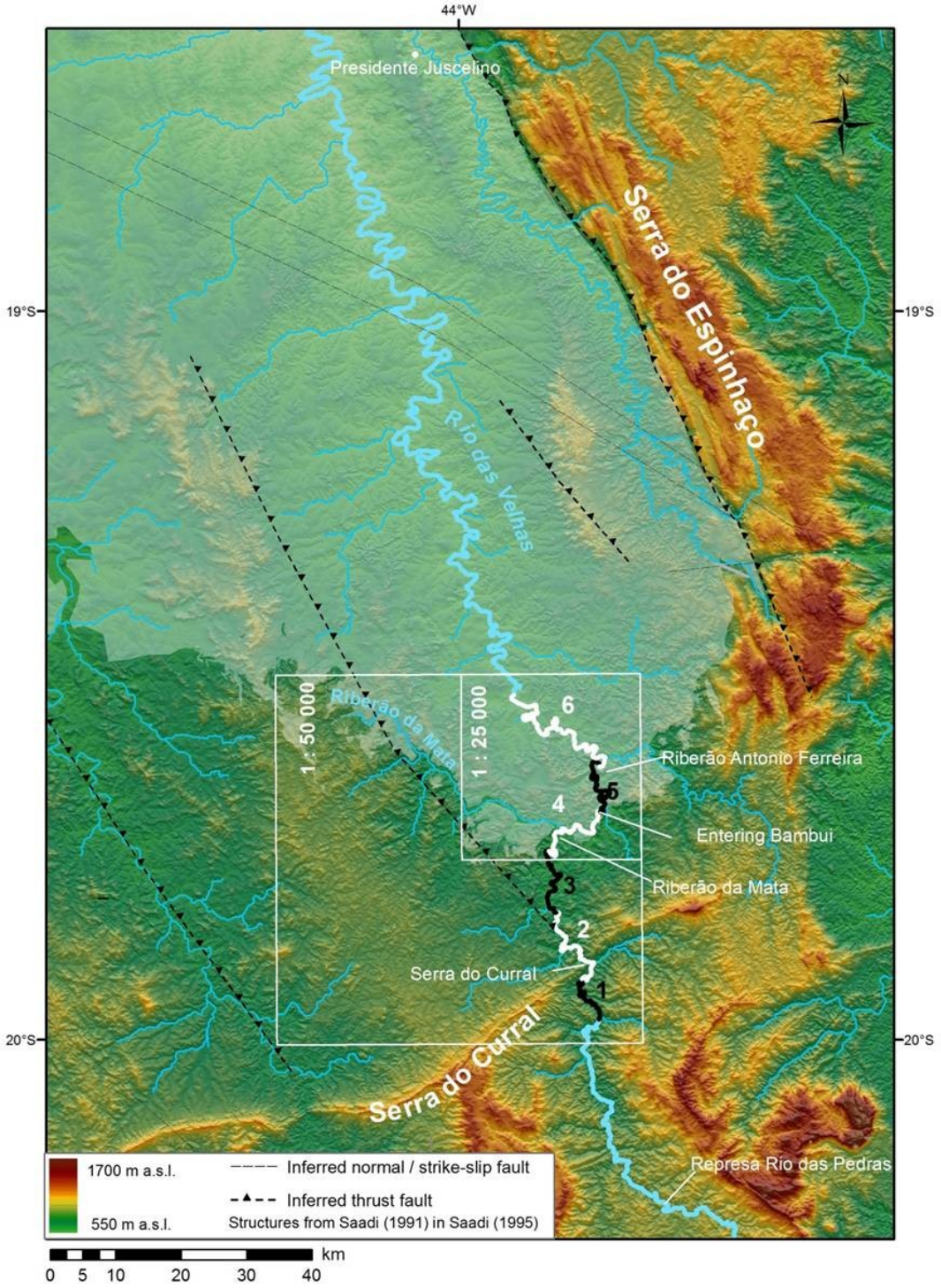

Figure 6-3 Regional topography derived from SRTM data together with inferred neotectonic faults from Saadi (1991) in Saadi (1995).

The region of the Bambuí sediments is indicated by a transparent pale overlay in the central and north-western part of the map. The rectangles delineate the area where digital data from topographic maps scale 1 : 50 000 and 1 : 25 000 were used for the longitudinal profile of the Rio das Velhas. The numbers and descriptions refer also to longitudinal profile of Figure 6-2.

6.3 Hypotheses for neotectonic movement

6.3.1 The Graben Vespasiano - Pedro Leopoldo

The unusual width and direction of the Riberão da Mata gave rise to investigations regarding neotectonic movements in the region: Karfunkel et al. (2006) and Pagung et al. (2007) propose a neotectonic graben structure (Vespasiano-Pedro Leopoldo graben, Figure 6-4 A, Karfunkel et al. (2006)) and describe discontinuities recorded in stonelines and the lateritic cover parallel to the wide, NW-SE orientated part of the alluvial plain of the Riberão da Mata. Also ground penetrating radar cross-sections in the alluvial plane and near high plateau areas support this hypothesis (Pagung et al. 2007). Although a neotectonic graben structure explains well the current relief anomalies of the Riberão da Mata, it does not explain the relief anomalies east of Lagoa Santa.

6.3.2 Reactivation of Neoproterozoic thrust faults

An alternative hypothesis to the above mentioned graben structure is the reactivation of Neoproterozoic thrust faults, which matches the context of regional neotectonic studies.
A lithological barrier or a local uplift in the region where the alluvial plain of the Riberão da Mata narrows would induce a sediment accumulation upstream and thus explain the width of the alluvial plain. Supporting this hypothesis is also the fact that not only the alluvial plain of the Riberão da Mata is unusually wide but also the valleys of its affluents. A system of transpressional faults as shown in Figure 6-4 B could lead to a barrier as described above.
Reactivation of Neoproterozoic thrust faults could also explain the elevation difference of 50 – 100 m between the hilltops east of Lagoa Santa and the plateau areas in the west. A reactivation of the graben structure at the side of the Riberão Antonio Ferreira orthogonal to the reactivated thrust faults would be compatible with the wide headwater region of this river.
While the knickpoints found in the longitudinal profile of the Rio das Velhas (Figure 6-3, Figure 6-2) can be explained by lithological differences, a local uplift of the region east of Lagoa Santa would also be compatible with the observed relief structures. Nevertheless, besides being coherent with the observed relief, no direct hints from field observation could be found to support the hypothesis of neotectonic transpressional structures and so the question of neotectonic movement is still unsolved for the region.

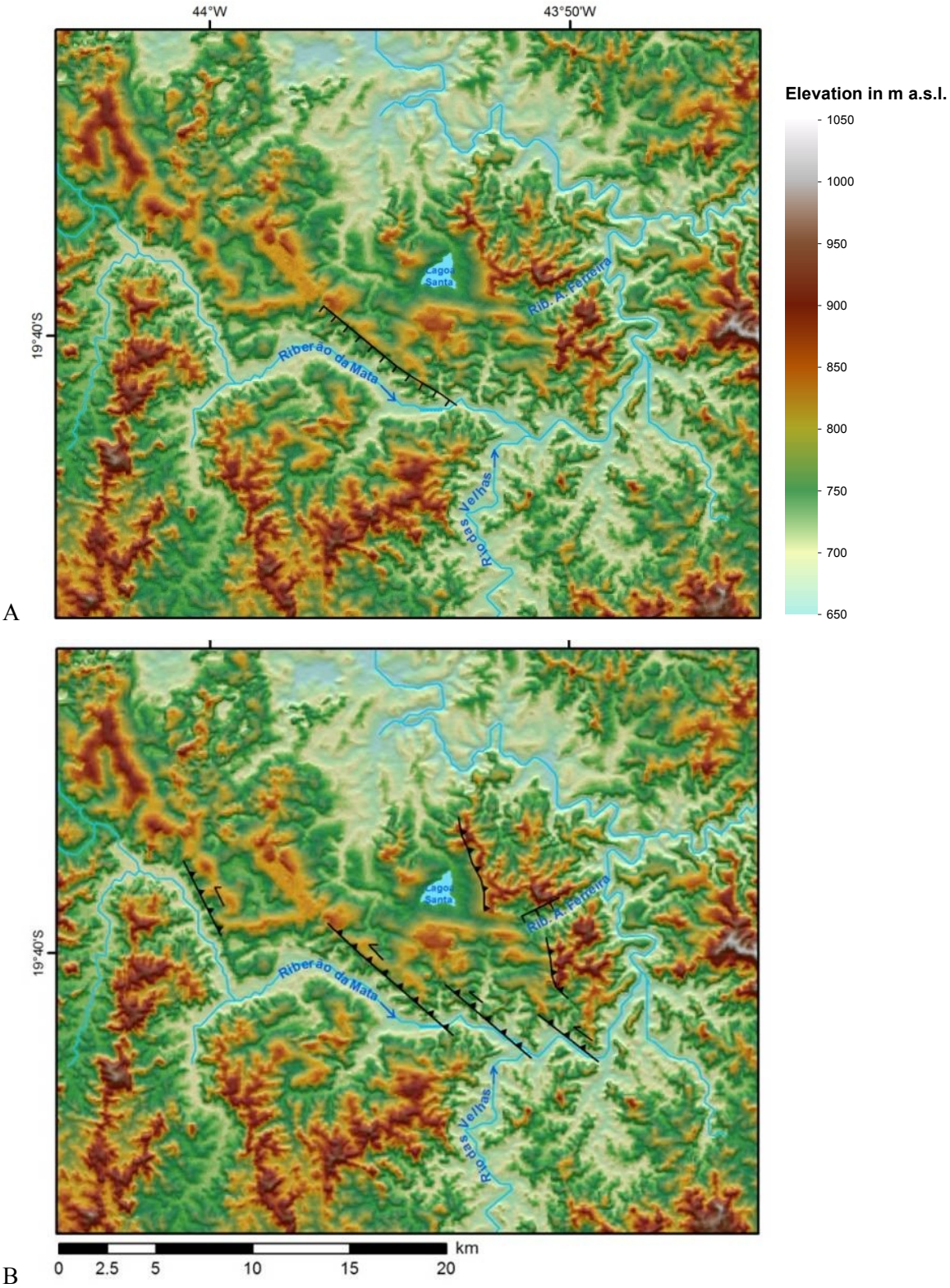

Figure 6-4 Illustration of different hypotheses of neotectonic movement in the study area.

A: Graben Vespasiano-Pedro Leopoldo (Karfunkel et al. 2006), B: Reactivation of Neoproterozoic thrust faults with transpressional movement.

6.4 Geomorphological evolution

A schematic drawing in Figure 6-5 summarizes the geomorphological evolution in the study area including different erosion cycles, karst development and neotectonic movement. The final drawing shows six geomorphological compartments for which idealized catenas of hydrological soil types are created in section 9.
The cross-section in Figure 6-5 is hypothetical and with strong vertical exaggeration for better visualization. Realistic cross-sections can be found in the annex on page 374 and 375.

The schematic drawing of Figure 6-5 shows the following time intervals:

A) Upper Cretaceous
Peneplanation of the area during the Upper Cretaceous (Post-Gondwana surface), the altitudes refer to the elevation where this surface is found today.

B) Lower Tertiary
Erosion and installation of a new, lower peneplain during the Lower Tertiary (Sul-Americana Surface) due to regional uplift and base level change in the course of the opening of the Atlantic. East of the current Lake Lagoa Santa, tectonic movements lift the Post-Gondwana surface to an elevation of today 900 m a.s.l. Some caves in the limestone beneath the Serra de Santa Helena Formation start to develop.

C + D) Upper Tertiary
Uplift of the craton and lowering of the base level to about 750 m above current sea level in the Upper Tertiary. When the base level drops beneath the contact of the Serra de Santa Helena meta-pelites and the Sete Lagoas carbonates, some caves fall dry and collapse. In the western part of the study area, collapsed areas have mainly direct contact with the groundwater (open karst area) whereas in the region around Lake Lagoa Santa, the overlying Serra de Santa Helena meta-pelites plug the karst features generating lakes (covered karst area). The red Ferralitic soil is redistributed by erosion and gravitational movements and often accumulates in lower slope positions or even enters caves. A third planation surface appears around 750 m a.s.l, which is approximately the upper limit of the Sete Lagoas carbonates in the northern part of the study area.

E) Plio-Pleistocene
Lowering of the base level below 700 m a.s.l drains most caves, fossil evidences of Plio-Pleistocene mammal fauna were found in some of the caves (Berbert-Born 2002). The roman numbers refer to geomorphological compartments as described above.

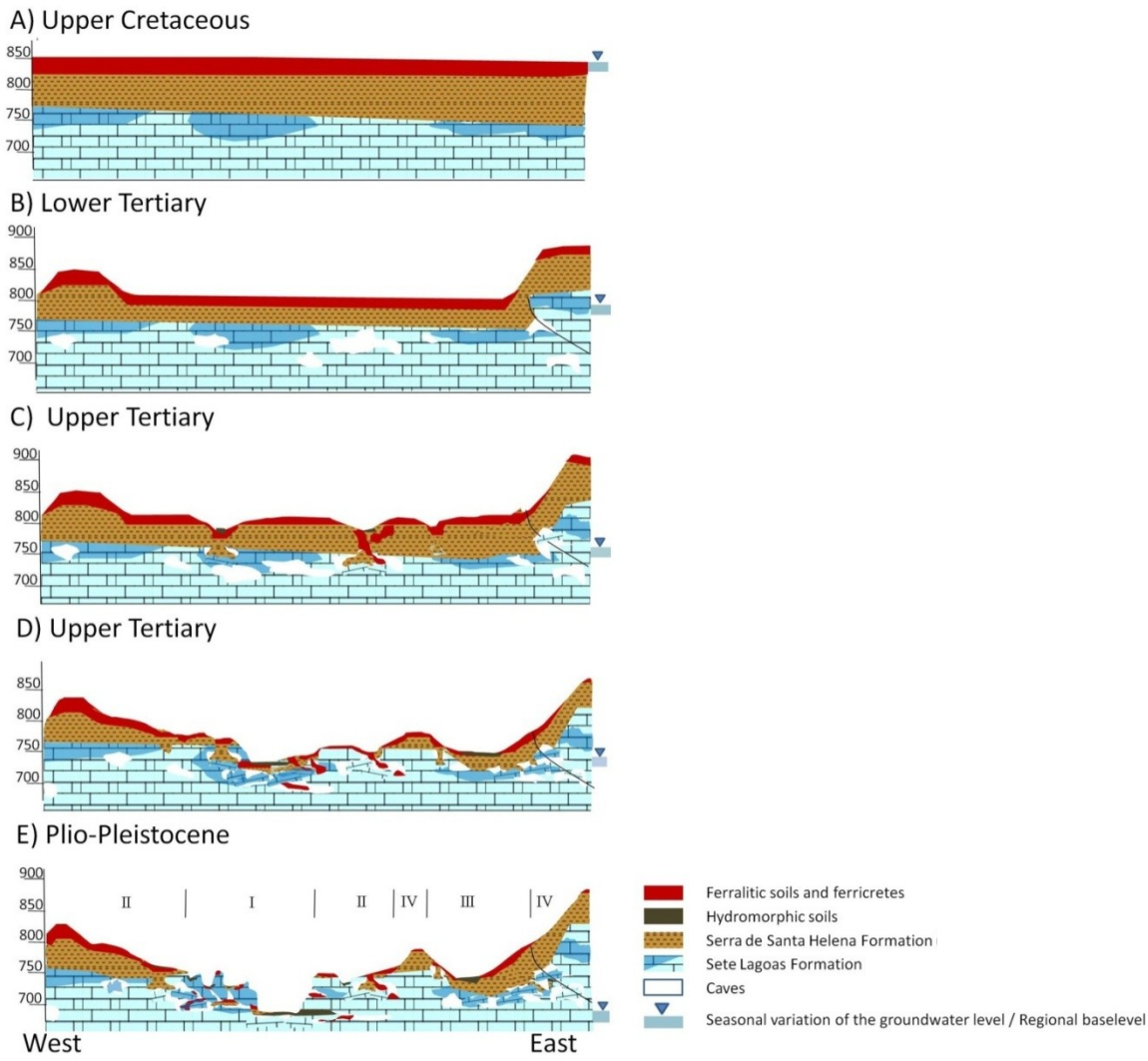

Figure 6-5 Schematic drawing of the relief evolution from Upper Cretaceous for the study area.

The roman numbers refer to geomorphologic compartments described in section 6.5. The drawing is schematic and not to scale, for details see text.

6.5 Geomorphological compartments

The landscape of the study area was classified into six characteristic geomorphologic compartments, taking into account erosion cycles and possible neotectonic movement. The descriptions are listed below and a typical soil catena for each compartment is shown in section 9. The compartments are indicated in Map 6 in the annex.

6.5.1 Compartment I)

In the north-western part of the study area, pure limestone (Lagoa Santa facies of the Sete Lagoas Formation) crop out that developed a very distinct karst relief. The meta-pelites of the Serra de Santa Helena Formation are nearly completely eroded. Remnants occur only in depressions protected from erosion or in plateau areas above 790 m a.s.l. where they are covered by thick Ferralsols. The landscape is characterized by an open karst plateau above 700 m a.s.l. with many dolines (Planalto de Dolinas, Kohler (1989)), which interchanges with deep uvalas and valleys below 700 m a.s.l. that are in contact with the karst groundwater.

6.5.2 Compartment II)

The NW-SE striking ridge with elevations above 790 m a.s.l., covered by thick red Ferralsols and occasionally petroplinthite (canga), is interpreted as remnant of the Post-Gondwana-/ Sul-Americana surface. Downslope follow softly shaped hills, whose plateau-tops around 750 m a.s.l. often bear rests of the Serra de Santa Helena meta-pelites and medium thick Ferralsols (Rio das Velhas surface). Due to the dominance of impure carbonates (Pedro Leopoldo Facies of the Sete Lagoas Formation) below the meta-pelites, the karstification is less intense compared to compartment I.

6.5.3 Compartment III)

Around and south-east of the lake Lagoa Santa, intrastratal karstification dominates. Collapsing cavities are plugged by the overlying Serra de Santa Helena meta-pelites which can be found even in the lower parts of the valleys. Characteristic are softly inclined plateaus and long slopes which are often incised by steep gullies. On altitudes above 790 m a.s.l., remnants of the Sul-Americana / Post-Gondwana surface can be identified. Especially around the military airport (see also Figure 9-9 on page 164) south of Lake Lagoa Santa, thick Ferralitic soils dominate.

6.5.4 Compartment IV)

The hills east of Lake Lagoa Santa reach elevations above 900 m a.s.l. - although they are closer to the regional baselevel river Rio das Velhas than the hills in the east. In this region, neotectonic uplift is assumed. The steep sides of these hills are often eroded until the saprolite, often showing a stony surface layer due to preferential erosion of fine material. Only shallow Ferralsols can be found at the top of these hills but thicker Ferralsols of accumulated material from upslope are located in protected downslope positions. The western flank of this compartment is characterized by the soft slopes of compartment I. Along the rivers, mainly impure limestone of the Sete Lagoas Formation crop out. The hills north-west of Lake Lagoa Santa and north of Lake Sumidouro show similar geomorphologic and pedologic features, although their elevation reaches only 800 m a.s.l. and no neotectonic movement is assumed.

6.5.5 Compartment V)

This zone is similar to zone II but the Bambuí cover rises and becomes shallower towards the south-west where finally the Archean basement crops out. Also the old planation surfaces rise gradually towards the south, finally reaching elevations above 900 m a.s.l.at the southern border of the study area. Although pure carbonates of the Lagoa Santa Facies crop out directly at the surface for a part of the area, karstification is not so intense compared to compartment I.

6.5.6 Compartment VI)

Compartment VI is similar to compartment II and V but the hillsides are incised more steeply and the valleys are narrower, indicating a higher hydraulic gradient. The Bambuí cover becomes thinner towards the south and basement rocks crop out at the foothills.

7 Typical soils in the study area – literature data

7.1 Overview

Soils in the region of the São Francisco Craton are generally old and deeply weathered.
The chemical properties are characterized by low activity clay minerals, low base saturation and low pH, often associated with aluminum saturation at a level that is toxic for plants. Some exceptions with more fertile soils exist in karst depressions and in the fluvial plains of rivers.

On higher plateau areas, deep red soils (Ferralsols resp. Latossolos) probably developed already during the Tertiary (King 1956). These very clayey red soils have a strong waterstable aggregation also known as "pseudo-sand" or "pseudo-silt" structure (Driessen et al. 2000) that controls their physical properties.
The soils on gentle slopes are composed of a mixture of eroded material from old plateau surfaces and weathered fragments of local parent material.
A yellowish subsurface horizon is typical for slopes in the limestone area. This horizon is generally less permeable than the upper red horizon and often enriched in clay (Lixisols or Acrisols resp. Solos Podzolicos).
On steep slopes on pelitic sediments or basement, a yellowish subsoil horizon is often missing and a shallow red horizon overlies directly the saprolite (Cambisols resp. Cambissolos).
The shallow soils on the Serra de Santa Helena meta-pelites in the eastern part of the study area are sometimes covered by a layer of angular to rounded stones stemming from quartz veins that cut through the pelitic meta-sediments.
Hydromorphic soils are characteristic soils for karst depressions and along rivers draining limestone areas (Gleysols resp. Gleyssolos). In the plains of the Riberão da Mata and the Rio das Velhas, alluvial soils (Fluvisols, fluvic Gleysols) developed on very heterogeneous Quaternary sediments.

7.2 Soil classification systems used in the study area

In previous local studies (CPRM 1994b, Shinzato and Lumbreras 1998), the soil profiles were classified according to the old Brazilian soil classification system (Camargo et al. 1987). This system was restructured in 1999 (Embrapa 1999).
For the current study, soil class names according to the World Reference Base of soil resources (WRB, IUSS Working Group (2007)) are used, supplemented by the original class names from the local maps.

An accurate re-classification of the profiles according to the WRB was not always possible. The classification rules differ between the systems and are based on analytical soil data that were not always available. Especially the differentiation between Nitisols, Ferralsols, Acrisols and Cambisols according to the WRB was difficult based on the given analytical data.

Soil classification in common classification systems is structured hierarchically. Prominent characteristics are excluded consecutively according to their importance on soil type definition. Thus, from the soils in the study area, very shallow soils (Leptosol resp. Solos Litólicos), soils on fluvic material (Fluvisols resp. Solos Aluviais) and soils with strong groundwater influence (Gleysols resp. Gleysolos) are sorted out first.
The next soil group are Nitisols, but since important diagnostic criteria (amount of active and free iron) were not available in the data base, no differentiation could be made between Nitisols and Ferralsols, which are the next lower reference soil group in the WRB key.
The definition of Ferralsols includes a Ferralic horizon (Table 7-1) starting within 150 cm from the surface, but also the absence of an Argic horizon containing more than 10% water dispersible clay is necessary. The main difference in the definition of a Ferralic horizon in the WRB to a Horizonte B Latossolico from the old Brazilian classification system is the low amount of water dispersible clay that is required in the WRB instead of a low silt / clay ratio (Table 7-1). Since the other parameters (low cation exchange capacity and low amount of weatherable minerals) are very similar, this difference is responsible for most deviating classification results in both systems.
Soils with an argic horizon are characterized by clay illuviation from above with a significant clay increase as diagnostic criteria. This is similar for the Brazilian Horizonte B Textural. In both systems, evidence of clay illuviation is diagnostic for this horizon, even if the clay increase is not strong enough. Depending on the base saturation, soils with an Argic horizon or a horizonte B Textural are classified as Lixisols / Acrisols in the WRB or as Podzólicos eutrophicos / distrophicos in the old Brazilian soil classification system.
Soils that do not meet the criteria of any of the above mentioned definitions are classified as Cambisols (WRB, IUSS Working Group (2007)) resp. Cambissolos (Camargo et al. 1987).

Horizonte B latossólico Shinzato and Lumbreras (1998) based on Camargo et al. (1987)	**Ferralic horizon** WRB (IUSS Working Group 2007)
Silt / clay ratio < 0.6 for clayey soils, < 0.7 for medium textured soils	Less than 10% water-dispersible clay, unless the eCEC < 1.5 cmolc / kg clay or pH (KCl) – pH (H_2O) > +0.1
eCEC < 13 cmolc/kg clay (without CEC of organic material)	eCEC < 12 cmolc/kg clay (without CEC of organic material)
SiO_2/Al_2O_3 < 2.2 in the clay fraction *(Data not available)*	Less than 10% weatherable minerals in the 50 -200 µm fraction *(Data not available)*
Thickness > 50cm	Thickness > 30cm

Horiozonte B Textural (Podzólicos) Shinzato and Lumbreras (1998) based on Camargo et al. (1987)	**Argic horizon (Lixisols, Acrisols)** WRB (IUSS Working Group 2007)
Relation of the B horizon clay content compared to the A horizon clay content > 1.5 OR Evidence of clay illuviation	Clay increase of less than 8% within 30 cm (if the soil contains more than 40% clay) AND Evidence of clay illuviation OR Clay increase of more than 8% within 30 cm (if the soil contains more than 40% clay) AND Upper 30 cm or the clay-increase horizon has more than 10% water dispersible clay and more than 1.5 cmolc/kg clay and pH(KCl) – pH(H_2O) < +0.1

Table 7-1 Diagnostic criteria for the characteristic horizons.

Latossolos (Camargo et al. 1987)compared to Ferralsols (WRB) and the characteristic horizons of Podzólicos (Camargo et al. 1987) compared to Lixisols / Acrisols (WRB). Only those criteria are listed that are relevant for the soils in the study area.

7.3 Description of typical soil classes

7.3.1 Ferralsols

Ferralsols are soils with a Ferralic horizon starting within 150cm from the surface. This horizon is similar to a Horizonte B Latossolico (Table 7-1) that is characteristic for Latossolos according to the old Brazilian classification system. Ferralsols are characterized by intense and deep weathering and depletion of primary silicates (desilification) with a relative accumulation of iron and aluminum oxides and a domination of low activity clays. They are deep, often more than two meters and well drained. While their macro-structure is usually weak and friable, Ferralsols typically have a strong micro-aggregation (pseudo-silt or pseudo-sand structure, Driessen et al. (2000), Zech and Hintermaier-Erhard (2002)) resulting from strong iron-aluminum-clay complexes. This micro-aggregation is responsible for the stable physical properties of Ferralsols, which are similar to sandy or silty soils in temperate regions even though the clay content of the Ferralsols in the study area is nearly always above 60%. Intense termite activity adds to the high permeability of these soils.

Figure 7-1 shows the texture and pore size distribution of a typical Ferralsol profile in the study area. The texture is very clayey with a clay content above 70 % throughout the profile. Water dispersible clay is much less, declining to nearly zero within the first two meters. The pore size distribution is dominated by macropores with instant drainage and micropores that store hygroscopic water. The mesopores storing the plant available water are few, thus water stress can arise during dry periods on these soils. Some of the soil profiles originally classified as Latossolos were interpreted as Acrisols according to the WRB (IUSS Working Group 2007) if a sufficient clay increase was documented within the first meters (e.g. Figure 7-5).
The chemical properties of Ferralsols are characterized by a strong deficiency of plant nutrients - especially phosphorous and calcium - and a low capacity to store nutrients from fertilizers due to their low cation exchange capacity. Base saturation and pH are low, often limiting the agricultural use due to aluminum toxicity and phosphorus fixation (IUSS Working Group 2007).
The typical position of Ferralsols in the region are plateau-areas around 800 m a.s.l. that are interpreted as remnants of a Tertiary peneplain (King 1956, Kohler 1989). At some locations, accumulation of iron can be strong enough to form hard petroplinthite also locally known as canga. The high plateau-areas are typically framed by steep convex slopes that are very susceptible to erosion because of the soft but low permeable saprolite underneath the Ferralsols, especially on Bambuí meta-pelites and granite / gneiss basement. During erosion, the red ferralitic material is redistributed and deposited in concave or flat downslope positions. Ferralsols in downslope positions can be very deep (Figure 7-2) and are often more fertile than autochthonous Ferralsols on the old plateau areas due to accumulation of topsoil material from above.

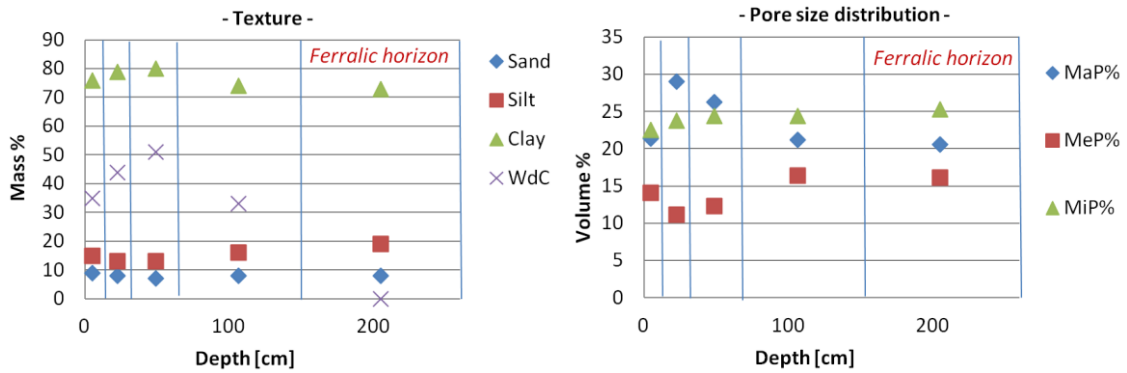

Figure 7-1 Latossolo Vermelho Escuro (Ferralsol), plateau surface at 850 m a.s.l. on Bambuí meta-pelites, 2% slope.

Profile 4 from (CPRM 1994a). Location: 19°39'5.257"S 43°56'41.704"W

MaP = Macropores, MeP = Mesopores MiP = Micropores (see also section 8.1).

WdC = water dispersible clay.

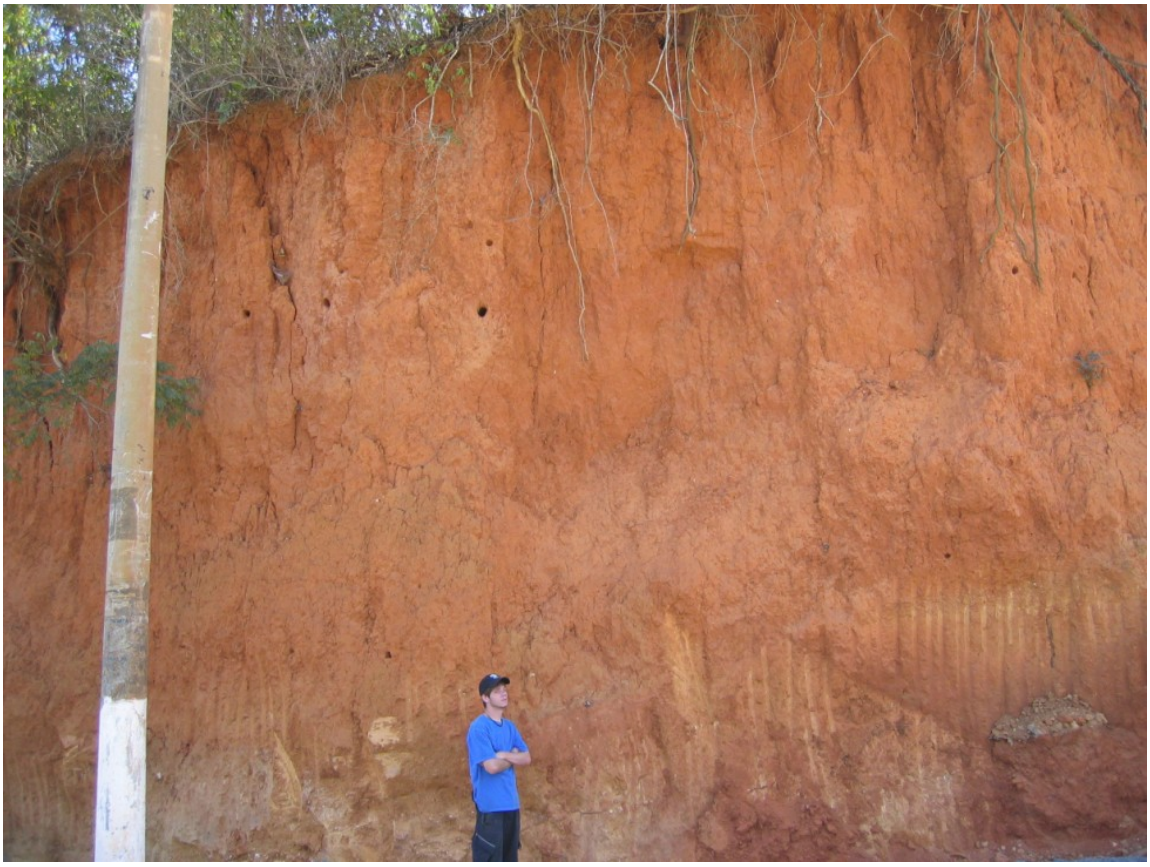

Figure 7-2 Deep Ferralsol at footslope position.

Holes from burrowing animals are common and add to the already very high permeability. Location: -19.691160/ -43.909275

7.3.2 Lixisols, Acrisols

Lixisols and Acrisols are characterized by pedogenetic clay accumulation in a diagnostic subsoil horizon (Argic horizon in the WRB, Horizonte B textural in the Brazilian system (Table 7-1). This textural differentiation is typically caused by an illuvial accumulation of clay in the subsoil but also other pedogenetic processes such as preferential erosion of clay in the topsoil or biological activity are accepted (IUSS Working Group 2007). Texture changes due to changes in parent material (e.g. in alluvial plains) are not accepted as diagnostic properties for these soils.

Depending on base saturation, Podzólicos are differentiated into Podzólicos eutrophicos or Podzólicos distrophicos, which correlate mainly to Lixisols resp. Acrisols in the WRB. The high base saturation (>50%) of Podzólicos eutrophicos (Lixisols) makes them some of the most fertile soils in the study area while Podzólicos distrophicos (Acrisols) have a similar low fertility as Ferralsols due to low base saturation and potential aluminum toxicity.
Both soil types appear on relatively steep slopes, especially on Bambuí carbonates. Podzólicos eutrophicos (Lixisols) are typical for the strongly karstified area in the north. Soil profiles classified as Podzólicos in the database from Projeto VIDA (CPRM 1994b) that do not show a sufficient clay increase (less than 8% increase within 30 cm if the amount of total clay is > 40%) are assumed to have been classified by field observation of clay illuviation. Thus, this classification was transferred directly. Soils with a sufficient clay increase for an argic horizon and more than 10% water dispersible clay that were nevertheless classified as Latossolos or Cambissolos were interpreted as Acrisols or Lixisols depending on their base saturation.

Figure 7-3 , Figure 7-4 and Figure 7-5 show the physical properties of three Acrisol / Lixisol profiles on different slope positions and lithologies near the study area. The texture shows a dominance of clay, but generally less than for Ferralsols. Characteristic is the increase in clay content within the first meter. Water dispersible clay decreases with depth for Acrisols but remains high for Lixisols. The pore size distribution is dominated by macropores with fast drainage. Second are micropores storing plant unavailable water and fewest are mesopores that are responsible for the effective field capacity.

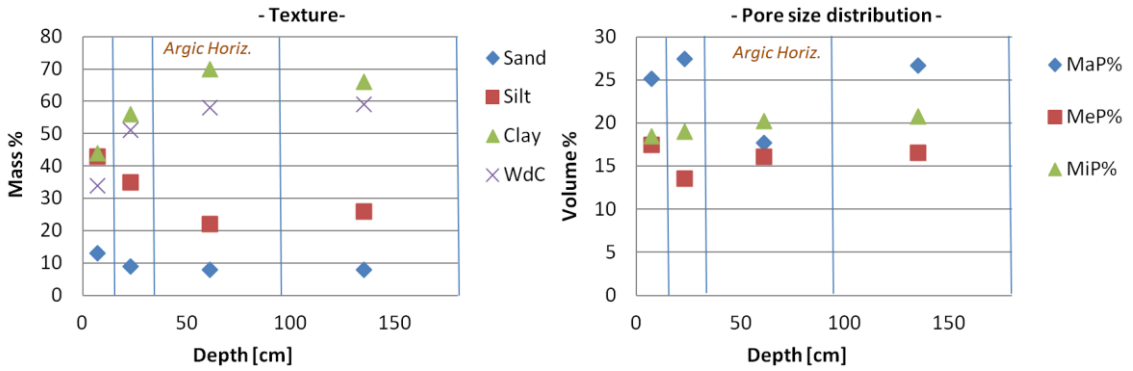

Figure 7-3 Podzólico vermelho escuro eutrófico (Lixisol)

Position: 760 m a.s.l. at 25% footslope on colluvial/alluvial sediments of Bambuí carbonates. Profile 10 from CPRM (1994a). Location: 19°31'17.533"S 44°4'36.498"W.

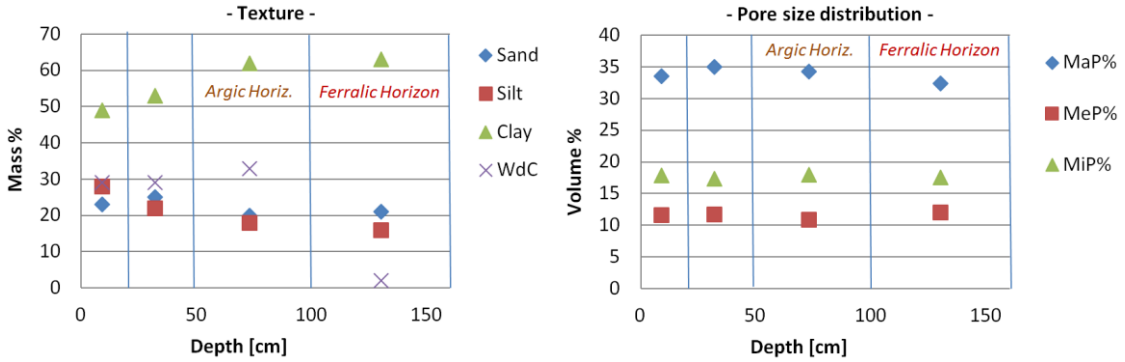

Figure 7-4 Podzólico vermelho amarelo distrófico (Acrisol), 12% midslope at 760 m a.s.l. on Bambuí carbonates close to crystialline basement.

Profile 3 from CPRM (1994a). Location: 19°43'31.643"S 43°55'38.773"W .

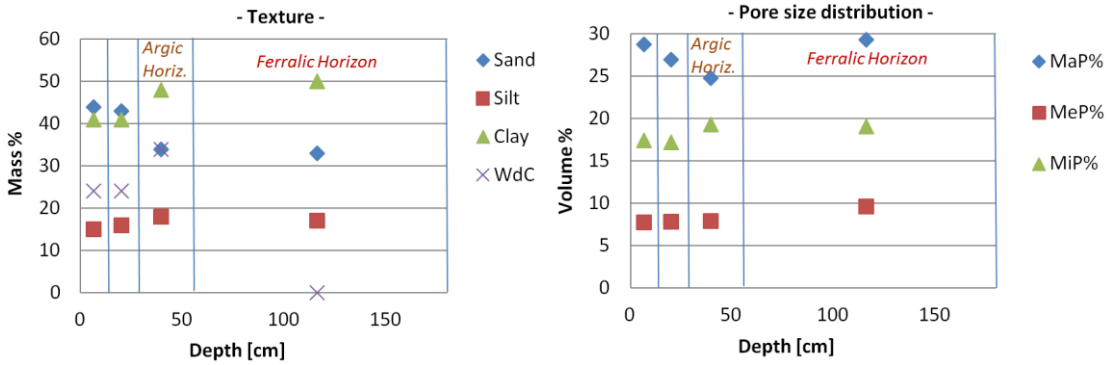

Figure 7-5 Latossolo vermelho amarelho distrofico (Acrisol), 10% midslope at 870 m a.s.l. on granite / gneiss basement.

Profile 15 from CPRM (1994a). Location: 19°33'46.767"S 44°11'32.857"W .

MaP = Macropores, MeP = Mesopores MiP = Micropores (see also section 8.1).

WdC = water dispersible clay.

7.3.3 Hydromorphic soils

In these soils, groundwater influences the subsoil creating a characteristic gleyic color pattern due to reducing conditions that prevail at least during some part of the year. For Gleysols according to the WRB, this reducing horizon needs to start within 50 cm from the surface, if it starts beween 50 cm and 1m, soils are classified as gleyic Cambisols or gleyic Fluvisols. Depending on lithology in the drainage area and landscape position, the texture can vary from silty-clayey in karst depressions or along karst rivers (Figure 7-9 , Figure 7-7 ,) until very variable on fluvial sediments of the alluvial plain of the Riberão da Mata (Figure 7-8). Gleysols and gleyic Fluvisols or gleyic Cambisols are the most fertile soils in the study area, especially those on Bambuí carbonates. Their agricultural use is only restricted by seasonal oxygen deficiency in the subsoil. Soils in karst depressions are often the most intensively used soils in the landscape (Figure 7-6).

Figure 7-6 Soils on doline floors have the highest natural fertility in the region.

A fact that is also reflected in the land use pattern.

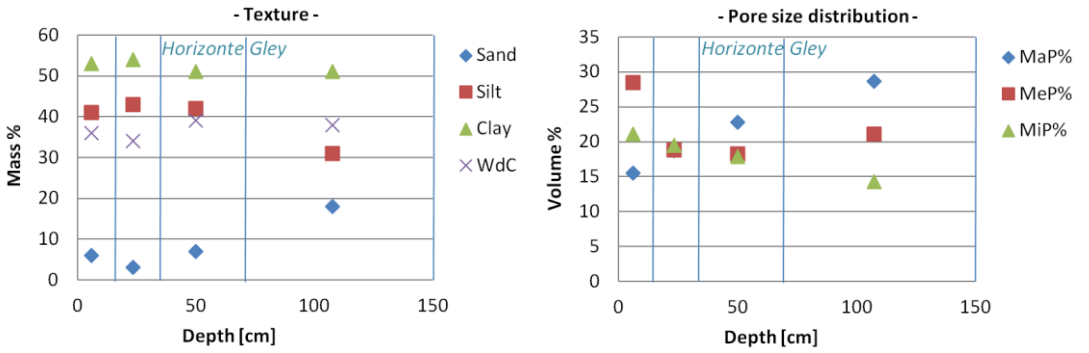

Figure 7-7 Gley pouco húmico eutrófico (Gleysol), alluvial sediments draining Bambuí carbonates.

Profile 8 from CPRM (1994a). Location: 19°30'24.896"S 44°0'56.289"W.

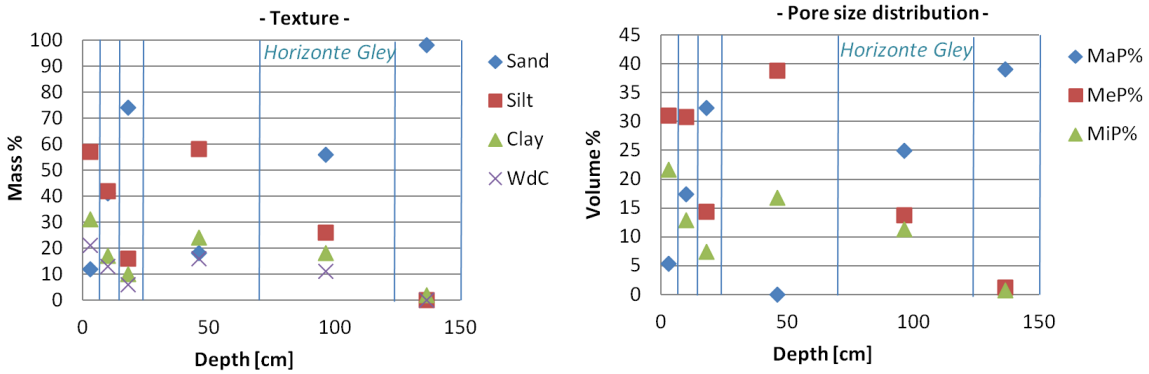

Figure 7-8 Gley pouco húmico eutrófico (gleyic Fluvisol), alluvial sediments of the Riberão da Mata.

Profile 11 from CPRM (1994a). Location: 19°38'9.553"S 44°1'4.68"W

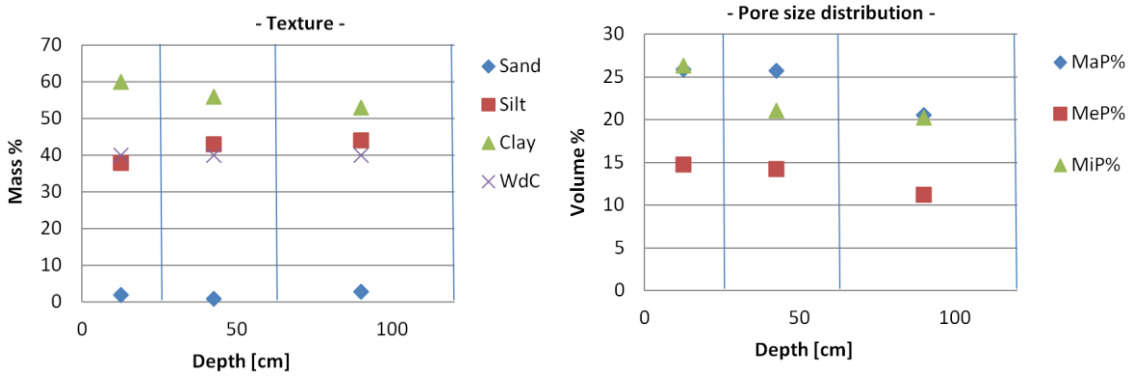

Figure 7-9 Cambissolo eutrófico gleico (gleyic cambisol), flat doline floor on Bambuí carbonates.

Profile 21 from CPRM (1994a). Location not specified.

MaP = Macropores, MeP = Mesopores MiP = Micropores (see also section 8.1).

WdC = water dispersible clay.

7.3.4 Cambisols, Leptosols

Cambisols (Cambissolos) are soils with incipient pedogenesis and transformation of the parent material. In tropical areas, they are nevertheless often difficult to distinguish from Ferralsols since they also show little differentiation of the horizons. Following hierarchical soil classification systems, Cambisols or their equivalents are soils that do not meet the diagnostic criteria of any other soil group. In the study area, the diagnostic horizon for Cambisols (Cambic horizon) is a horizon that does neither meet the criteria for a Ferralic horizon nor for an Argic horizon and also does not show any signs of water influence.
Since no data for the diagnostic mineralogical criteria that distinguishes Cambisols from Ferralsols were available, notation of primary rock structure visible in the subsoil was used to differentiate between Cambisols and Ferralsols.
The properties of Cambisols can be very variable, depending strongly on the parent material. Due to a less strong microstructure and a higher content of weatherable minerals compared to Ferralsols, they often have a lower permeability and sometimes better chemical properties.

Nevertheless, analytical data of profiles classified as Cambissolos on Bambuí meta-pelites show the lowest pH, lowerst base saturation and the highest aluminum saturation within the study area (CPRM 1994b, Shinzato and Lumbreras 1998). The scarce vegetation on steep Bambuí meta-pelites (Figure 7-10) is thus probably caused rather by aluminum toxicity that impedes root growth than by real water scarcity in the deeply weathered soil. The dominance of silt with a high amount of mesopores can even lead to water stagnation in the saprolite during wet periods (Figure 7-11).
Cambissolos on crystalline basement typically have a coarser texture and thus a higher amount of macropores (Figure 7-12). Thus, water stagnation is probably less frequent. Also the saprolites of the crystalline basement (with exception of basic dykes) often have low pH values and high aluminum saturation.
Cambissolos on carbonates have finer texture and would probably be classified as Ferralsols according to the WRB (e.g. Figure 8-1 p. 131). Cambisols in the Karst region, especially in doline floors, are the most fertile soils with highest pH and highest base saturation in the study area.

On very steep slopes or on exposed ridges, less than 25 cm topsoil covers the saprolite. These soils are classified as Solos Litólicos according to the Brazilian system or as Leptosols according to the WRB.

Figure 7-10 Scarce vegetation on shallow Cambisols / Leptosols on meta-pelites of the Serra de Santa Helena Formation.

Location: 19°39'28.22"S 43°52'3.802"W.

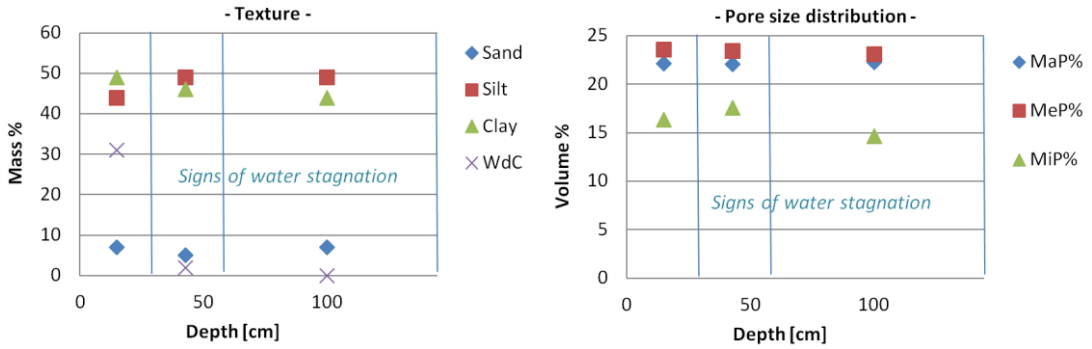

Figure 7-11 Cambissolo álico epidistrófico (Cambisol), 25% upper slope on Bambuí meta-pelites.

Profile 2 from CPRM (1994a). Location: 19°38'18.812"S 43°50'15.684"W

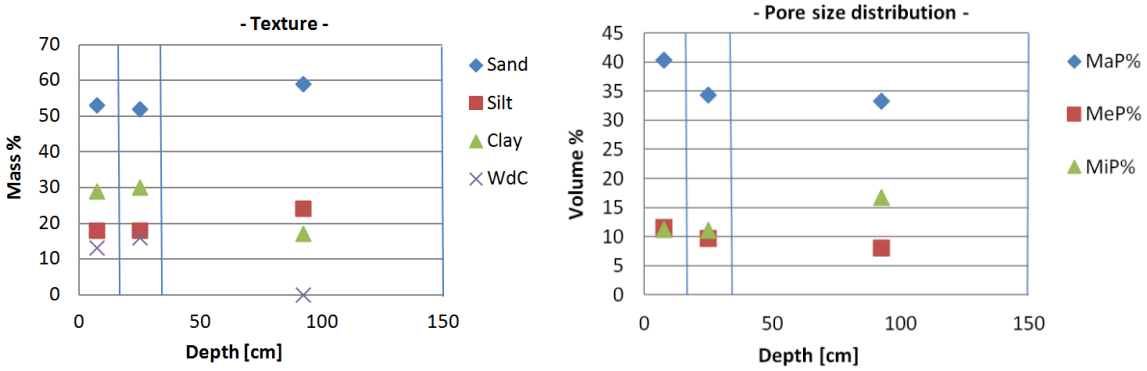

Figure 7-12 Cambissolo álico epidistrófico (Cambisol), 22% midslope crystalline basement.

Profile 27 from CPRM (1994b). Location not specified.

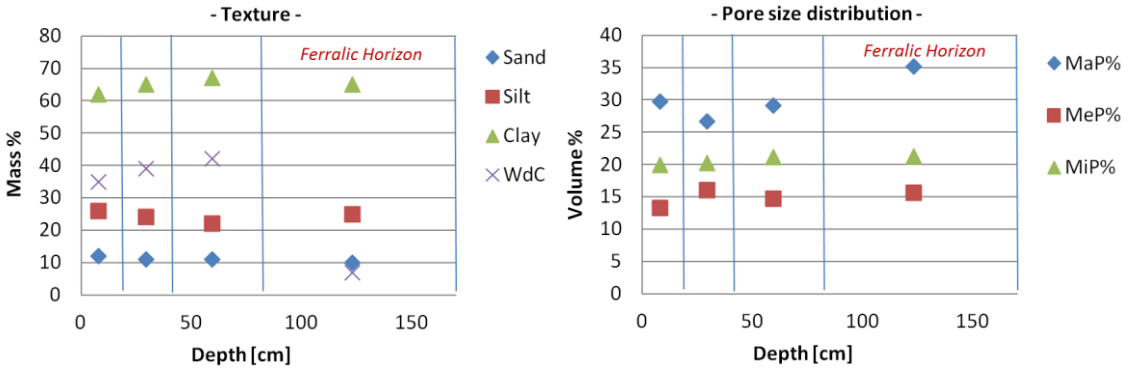

Figure 7-13 Cambissolo álico epidistrófico (Ferralsol), carste depression 5% footslope, Bambuí carbonates.

Profile 5 from CPRM (1994b). Location: 19°31'56.407"S 43°56'53.432"W

MaP = Macropores, MeP = Mesopores MiP = Micropores (see also section8.1).

WdC = water dispersible clay.

8 Hydrological soil classification

8.1 Typical water retention curves

Figure 8-1 shows a characteristic difference of the hydrological properties of tropical soils compared to equally textured soils from temperate regions: Very clayey deep red Ferralsols (Latossolo Vermelho Escuro) are hydrologically similar to sandy soils of temperate regions with the exception of the higher water content at pF[1] 4.2 (wilting point). Despite their high amount of clay, they drain fast and have a low storage capacity for plant available water.

The texture of these soils cannot be determined easily in the field since the high amount of sesquioxides (iron and aluminum oxides) creates water-stable aggregates of sand or silt size. Since the hydrological soil properties are thus less related to soil texture rather than to soil structure, the amount of large, medium and fine pores was used as an estimate of hydrological soil properties instead of soil texture (see also the analytical data of soil profiles in section 7.3). Due to the dominance of 1:1 layer-lattice clay minerals and the pseudo-sand structure, clayey soils in the study area also do not show characteristic cracks during the dry season.

For 27 profiles from CPRM (1994b),the amount of micro- meso- and macro-pores was calculated from total porosity and water content at pF 2 and pF 4.2 using the following scheme:

- Macropores (MaP) = Total porosity - water content at pF 2[2]. These pores drain quickly after each rain and are responsible for the main permeability of the soil.
- Mesopores (MeP) = water content at pF 2 - water content at pF 4.2. These pores store the plant available water and are equivalent to the effective field capacity.
- Micropores (MiP) = water content at pF 4.2, which is the soil water potential at the permanent wilting point. These pores store water that cannot be reached by plant roots (hygroscopic water).

Soils with a clay illuviation horizon from the carbonate region have similar properties to Ferralsols with a slightly lower amount of fine pores. The pore size distribution of Cambisols (Cambissolos) depends on the parent material: those on meta-pelites have the highest amount of medium size pores and thus the highest amount of plant available water (effective field capacity). Cambisols on granite/gneiss basement have coarser texture and thus fewer micropores.

The amount of meso- and macropores is similar to that of Ferralsols. Soils in the alluvial plains are so heterogeneously textured that the interpretation of a mean value is not sensible. Their pore size distribution is very variable.

[1] The pF-value is the logarithm of the soil water potential measured in hPa.

[2] In Germany, a value of pF 1.8 (equivalent pore size diamenter = 10 nm) is used instead of pF 2.0 to define the field capacity (AG Boden 2005). Internationally, also values between 1.5 and 2.0 are common . Since the available data base contained only measurements at pF 2 (10 kPa), this value was used for the definition of the limit between meso- and macropores.

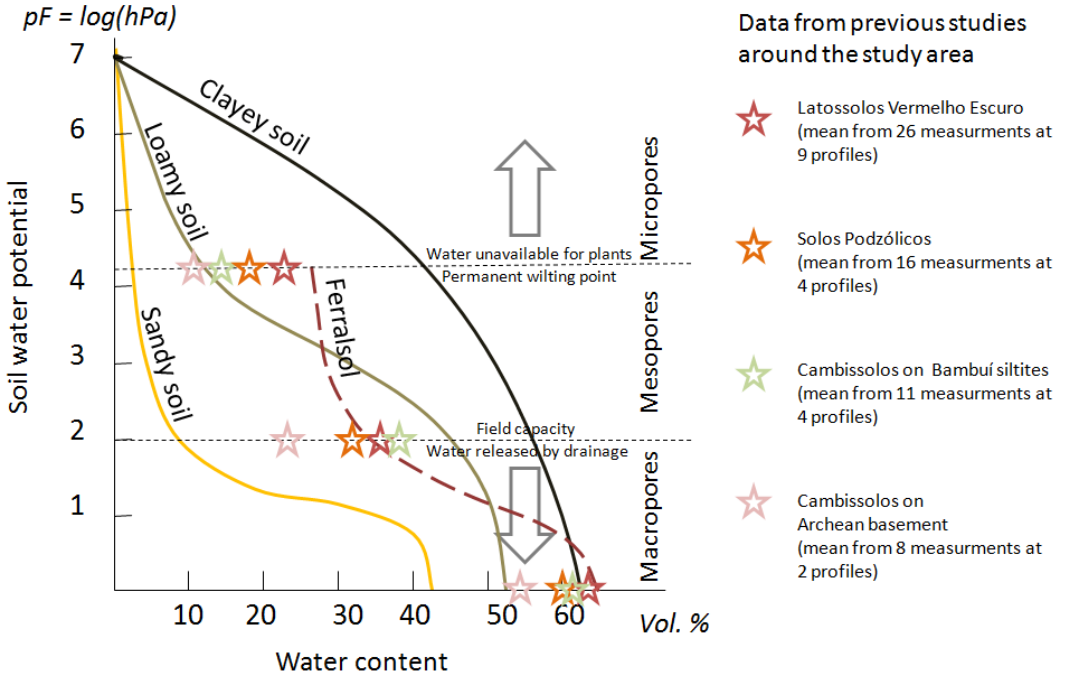

Figure 8-1 Typical water retention curves of clayey, loamy or sandy soils from temperate regions compared to data from a Ferralsol in the Brazilian Cerrado.

The Ferralsol has a clay content of 78% but shape of its water retention curve is parallel to that of a sandy soil with the exception of the higher amount of micropores. (Data from Hintermaier-Erhard and Zech (1997) and Gontijo et al. (2008)). The stars indicate data from soil profiles in or near the study area from Projeto VIDA (CPRM 1994b).

8.2 Own hydrological classification of soil material

Besides using the systematic soil classification rules described in section 7.2, (p. 118 ff)., a more practicable estimation of soil hydrological properties from field observation was used to define hydrological soil classes for the study area.

Hydrological properties of soils and soil horizons were estimated based on criteria such as visible soil macro- and micro-structure, existence of large macropores, root density, traces of soil fauna and hydromorphic colors.

The following hydrological soil materials were distinguished:

- Saprolite of crystalline basement
- Saprolite of Bambuí impure carbonates
- Saprolite of Bambuí meta-pelites
- Yellowish subsoil (most prominent on Bambuí carbonates)
- Red ferralitic topsoil
- Hydromorphic soil material from karst depressions and along rivers

- Fluvic soil material in alluvial plains.

A topsoil horizon with accumulation of organic material (A-Horizon) was not considered separately as hydrological unit since it is – with the exception of soils from karst depressions and alluvial plains - very thin compared to the thickness of other soil materials. The following sections describe the different hydrological soil materials on different geological units as documented by field observation.

Stonelines or stone layers of mostly angular to slightly rounded quartz stones can be found throughout the soils in the Bambuí region, often at the contact between red topsoil and saprolite (Figure 8-3, B or Figure 8-7). A plausible explanation is that they mark a paleo-surface (similar to the current surface in Figure 8-3, A) that was later covered by red topsoil material during a wetter period in the Holocene. Documented colluvial fills of paleo-gullies in neighboring areas (Bacellar et al. 2005) and general observations of recent geomorphologic cycles (Coelho Netto 1999) support this theory. The frequent quartz veins of the Serra de Santa Helena Formation that probably previously covered the carbonates of the Sete Lagoas in the whole study area are a very plausible source for the stones. Also other authors studying soils and colluvial sediments in the region interpret the frequent stonelines as limit between colluvial and eluvial horizons (Lacerda 2007, Muggler and Buurman 2000, Piló 1998) - although other hypotheses including bioturbation exist (Johnson et al. 2005).

8.2.1 Region of Bambuí meta-pelites (Serra de Santa Helena Formation)

In the Bambuí meta-pelites of the Serra de Santa Helena Formation, highly permeable red ferralitic topsoil with strong micro-structure and weak macro-structure (Figure 8-2, B and C) overlies a dense saprolite that sometimes shows signs of temporary water stagnation (bleached roots in Figure 8-2, D). This field observation of high difference in permeability of the red topsoil and the saprolite is supported also by the results of infiltration experiments (section 8.2.5, p. 142). The permeability difference covers probably about two to three orders of magnitude. The texture of the Serra de Santa Helena saprolite is rich in silt (Figure 7-11 , Figure 8-5, p. 135), which makes it very vulnerable to erosion as shown in the graph in Figure 8-4 (p. 135).

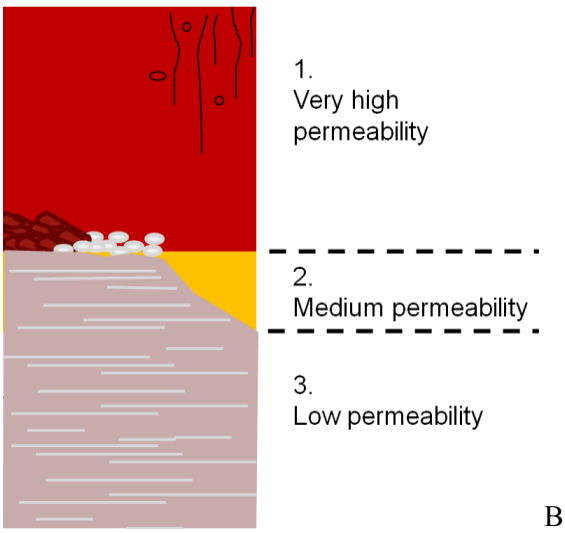

B

C

D

E

Figure 8-2 Field aspects of hydraulic soil properties (part 1).

A: Schematic soil profile for Bambuí meta-pelites.

B and C: Macro- and microstructure of the red topsoil. Location: -19.666104 / -43.895741.

D: bleached zones along fine roots in the subsoil (width of the photograph is approximately 5 cm). Location: -19.699300 / -43.825497.

E: A yellowish subsoil horizon with medium permeability can exist (foreground) but is often absent (background). Location: -19.663250 / -43.860774, view to SW.

A yellowish intermediate horizon between red topsoil and saprolite can exist but can also be absent (Figure 8-2, E). On exposed ridges east of Lagoa Santa, the topsoil is often completely eroded and the saprolite is covered only by a centimeter to decimeter thick layer of quartz stones (Figure 8-3, A). This stone layer probably developed by preferential erosion of the pelite saprolite, which is - especially east of the Lake Lagoa Santa - strongly dissected by quartz veins. Locally, hardened iron crusts (petroplinthite) can be found between topsoil and saprolite at high plateau-surface locations (Figure 8-3, C and D). A schematic soil profile for the meta-pelites of the Santa Helena Formation is shown in Figure 8-2, A.

A 

B 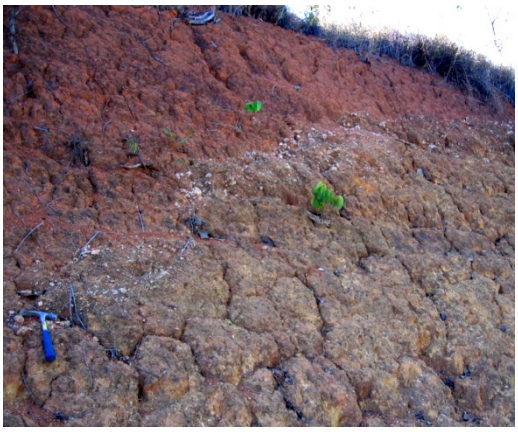

C 

D 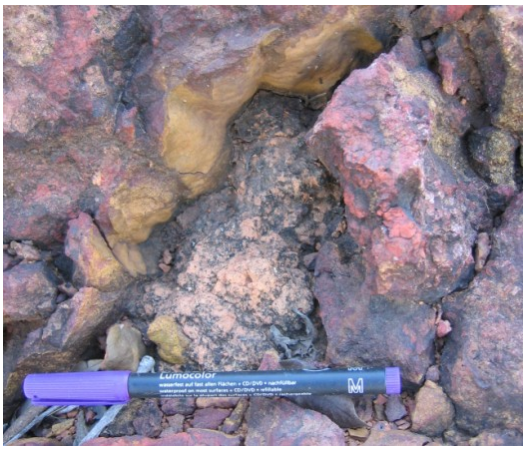

Figure 8-3 Field aspects of hydraulic soil properties (part 2).

A: Partially rounded quartz stones are accumulated on top of the saprolite of the Serra de Santa Helena Formation. Thickness of the surface stone layer is approximately 20 cm. Location: -19.640162 / - 43.844107 (see also Outcrop O on page 71).

B: Stoneline at the contact between red topsoil and saprolite.
Location: -19.668988 / -43.906656, view towards NW.

C: Lense of hardened petroplinthite at a road cut.

Location: -19.667424 / - 43.904203, view towards NW.

D: Detail of location C.

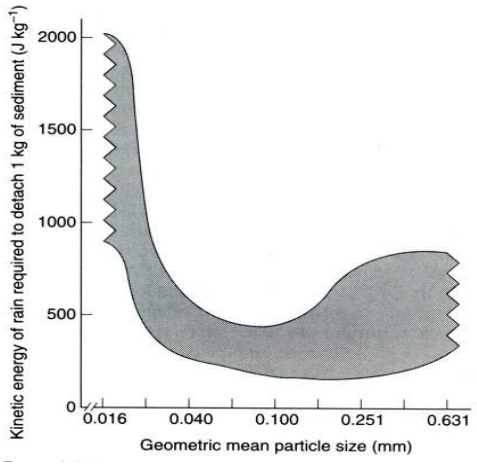

Figure 8-4 Silt (0.002 – 0.063 mm) and fine sand (0.063 – 0.2 mm) are most easy detached by rainfall and thus have the highest erodibility.

Morgan (2009).

The following specification of the saprolite material is taken from de Lima Cabral (1998):
The saprolite of the Serra de Santa Helena Formation is usually very thick, reaching more than 80 m (Figure 8-5). The texture is clayey and silty, lacking completely sandy or coarser material (with the exception of remnant of quartz veins, which are common). The permeability is low (10^{-4} – 10^{-6} mm/s) and the susceptibility to erosion is rated high to very high. Cation exchange capacity is moderate with 5 - 8 cmolc/kg.

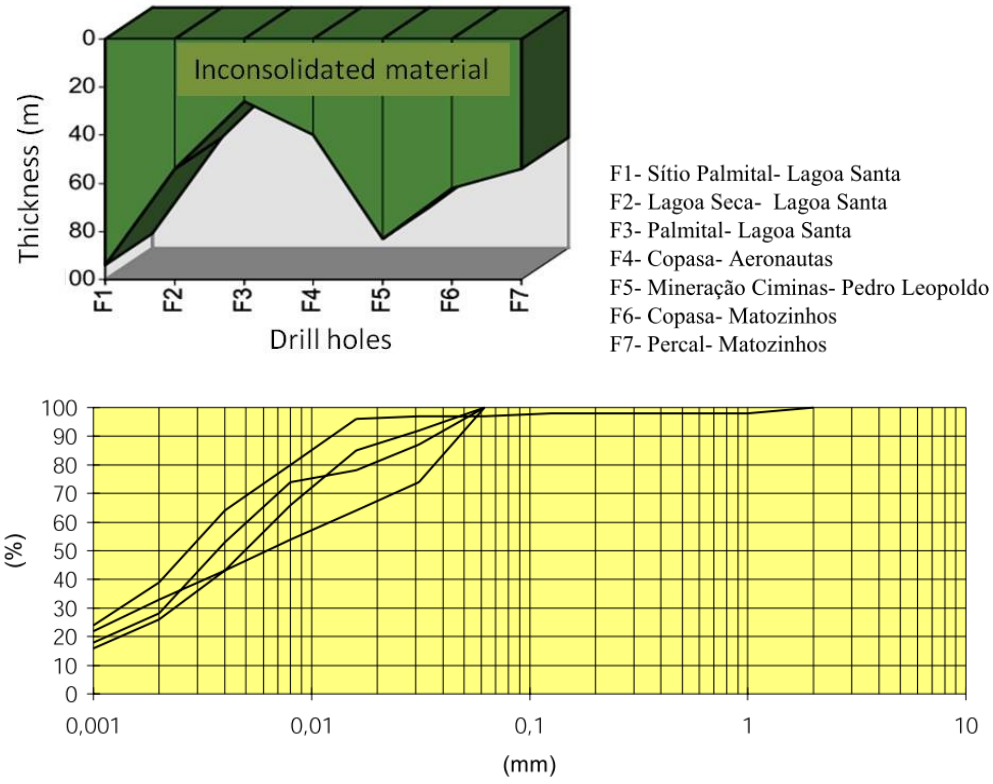

Figure 8-5 Upper part: Thickness of unconsolidated material on meta-siltites of the Serra de Santa Helena Formation. Lower part: typical granulometric curves for the saprolites of the meta-pelites.

Source: de Lima Cabral (1998).

8.2.2 Region of Bambuí carbonates (Sete Lagoas Formation)

In the region of Bambuí carbonates, two major hydrological soil layers are obvious in the field: highly permeable red topsoil and less permeable yellowish subsoil.

These two layers can be identified through their color and their macro-structure which is much more friable and crumbly in the red topsoil but compact and dense in the subsoil (Figure 8-6). In the topsoil, high faunal activity (especially termites) increases the already high permeability. This observation of two different soil materials is confirmed by literature data from a study on soil and karst development localized around the Baú-Massive in the study area (Piló 1998). Piló observed a strong difference in soil hydraulic properties of the red and yellow horizons due to their macro- and microstructure, although both had similar texture. He also noted that the epikarst development was more intense for rocks surrounded by red soil than for rocks surrounded by yellow soil. In the soil maps available for the region, soils on limestone are either classified as Podzólicos (Shinzato and Lumbreras 1998) or as Cambissolos (CPRM 1994b).

Total soil hydraulic properties were inferred by estimating the spatial distribution of the thicknesses of the red and yellow horizons. Especially at footslope locations, where eroded red topsoil was deposited on a paleo-relief, distinct stonelines separate the two characteristic horizons (left photograph of Figure 8-7).

In areas where impure limestones dominate, the rocks weather to a soft yellowish to red saprolite still showing the initial layer structure of the primary rock (right photograph of Figure 8-7). During field observation, its macrostructure appears denser and more compact with a horizontal structure following the original geological layers. Thus, its permeability is estimated lower than the yellowish subsoil but higher than the saprolite of Bambuí meta-pelites.

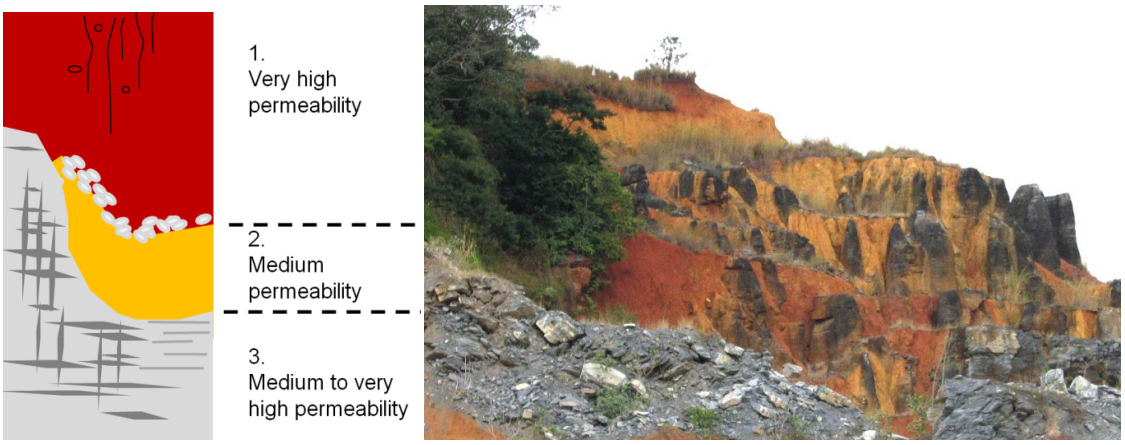

Figure 8-6 Schematic profile of the different soil materials on Bambuí carbonates.

Well structured and highly permeable red topsoil overlies yellow subsoil with medium permeability. The limestone itself has very high permeability due to karst features. The photo was taken at the cement mine in São José da Lapa (Location: -19.708704 / - 43.949219 view towards NE).

Figure 8-7 Left: stone layer separating red topsoil and yellow subsoil in a footslope location. Right: saprolite of impure Bambuí carbonates (Facies Pedro Leopoldo).

Location: left: -19.677166 / -43.946878, right: -19.65201312 / -43.84696855.

The following specification of the saprolite material is taken from de Lima Cabral (1998):
The thickness of residual soils on the impure carbonates (Facies Pedro Leopoldo) is very irregular, usually between 5 and 15 meters. In the highly karstified pure carbonates (Facies Lagoa Santa), thickness of residual soils is even more irregular and often shallow to very shallow on karst outcrops. Sample values from eleven drill holes in the carbonate region show higher values reaching more than 50 m (Figure 8-8).

Residual soil of the carbonates of the Sete Lagoas Formation has silty to clayey texture; part of it may also consist of remnants of the eroded silty meta-pelites of the Serra de Santa Helena Formation.
While the pure carbonates have very little residual components, the impure carbonates often weather to comparatively deep saprolites with intact primary structure (e.g. Outcrop S on page 81).
The permeability of the saprolite of impure carbonates is with 10^{-3} – 10^{-4} mm/s generally higher than in the saprolite of granite-gneiss basement.
The residual soil in the area of pure carbonates has a permeability of more than 10^{-3} mm/s.
In steep areas, the susceptibility to erosion is high, in the rest of the area low.
The cation exchange capacity is higher than in the basement, generally between 5 and 8 cmolc/kg for the Facies Pedro Leopoldo and 4 - 12 cmolc/kg for the Facies Lagoa Santa.

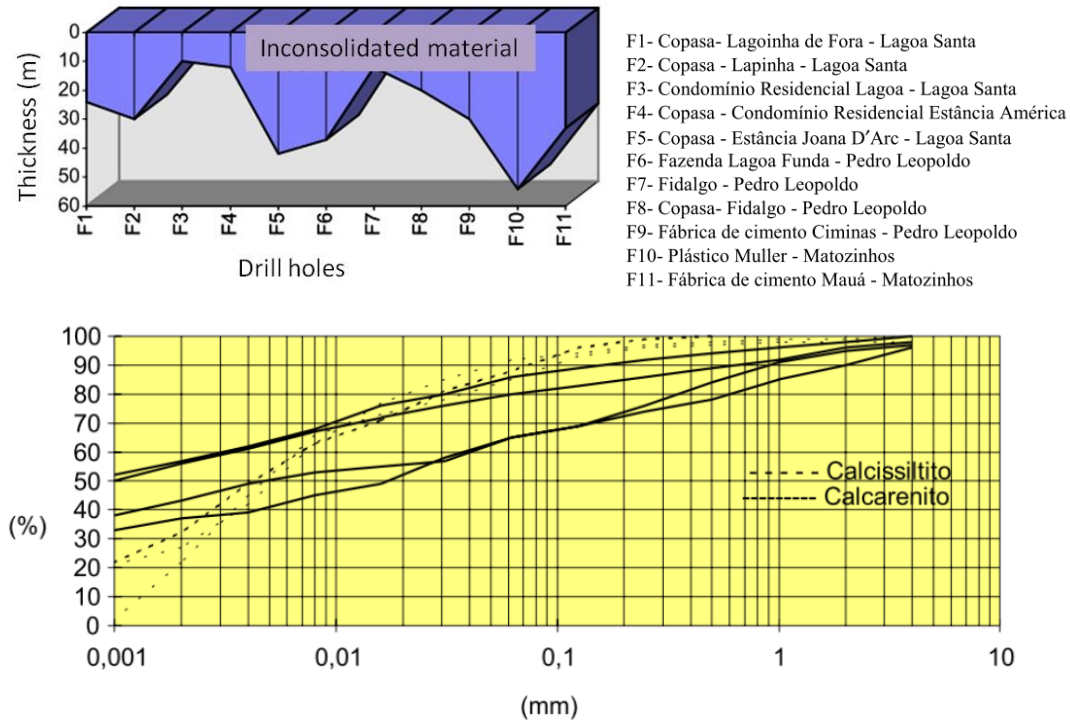

Figure 8-8 Upper part: Thickness of unconsolidated material on carbonates of the Sete Lagoas Formation. Lower part: typical granulometric curves for the residual soils of the carbonates. Calcisiltito = Facies Pedro Leopoldo, Calcarenito = Facies Lagoa Santa.

Source: de Lima Cabral (1998).

8.2.3 Basement region

In the basement region, well-structured permeable red topsoil overlies a dense granite-gneiss saprolite (Figure 8-9 A). Red topsoil thickness is difficult to predict since very thick accumulations of red topsoil in only slightly concave positions can appear, probably due to filling paleogullies (Coelho Netto 1999, Bacellar et al. 2005). On basic dykes, soil cover is often deeper and redder due to a higher content in iron and basic minerals in the parent material (Figure 8-9 C). On more acidic parent material, topsoil is shallower and sometimes nearly absent (Figure 8-9 B). The deep crystalline basement saprolite is eroded easily, with large gullies being no rare geomorphic features. In an infiltration experiment, compacted basement saprolite showed a very low permeability.

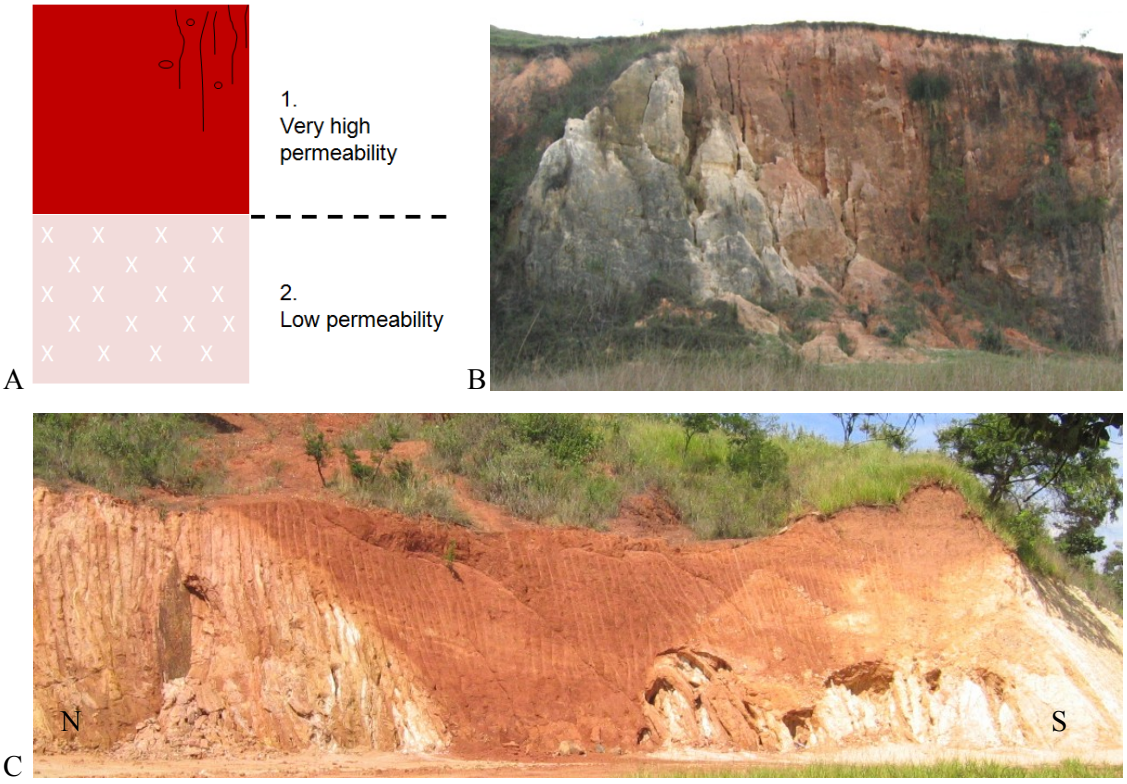

Figure 8-9 Field aspects of hydraulic soil properties (part 3).

A: Schematic profile of the permeability of soil material on crystalline basement. B: Basement saprolite with nearly no topsoil cover near Vera Cruz de Minas. C: Red topsoil of variable thickness covers granite-gneiss basement close to a basic intrusion. Height of the road cut approximately six meters. Location: -19.765035 /-43.947517.

The following specification of the saprolite material is taken from de Lima Cabral (1998):
The mean saprolite thickness is less than 10 meters in the crystalline basement. Sample values from six drill holes show also higher values around 15 m (Figure 8-10). Despite its medium texture, the permeability is medium to low (10^{-3} – 10^{-6} mm/s), depending on the weathering state.

The susceptibility to erosion is rated high to very high. Cation exchange capacity is generally lower than 5 cmolc/kg (with the exception of basic dykes). The color of the basement saprolite is a light rosé which makes it possible to distinguish from the saprolite of Bambuí sediments which are in a yellow tone (see also Outcrop A on page 68).

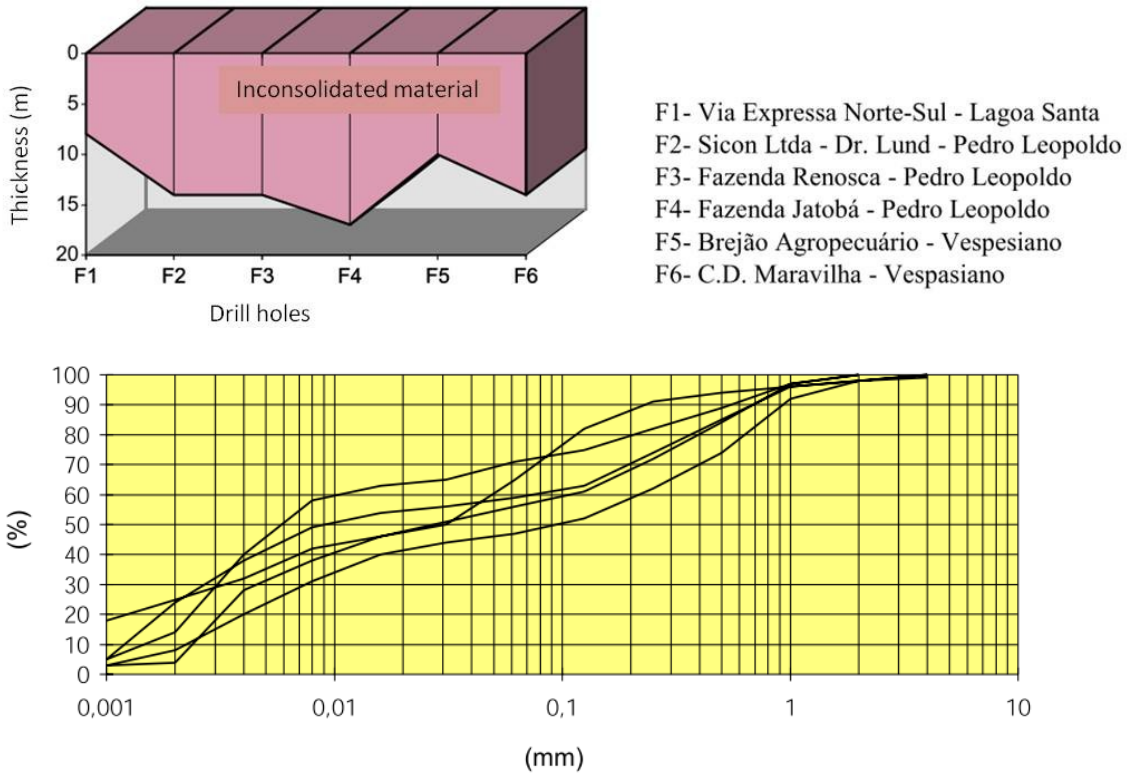

Figure 8-10 Upper part: Thickness of unconsolidated material on crystalline basement. Lower part: typical granulometric curves for saprolite of crystalline basement.

Source: de Lima Cabral (1998).

8.2.4 Alluvial plains

The alluvial plains of the the Rio das Velhas and the Riberão da Mata drain the basement area; the texture of the sediments range from pure sand to pure clay (see also the texture of the profile in Figure 7-8), which are both mined in open pit mines (Figure 8-11 A, B). Since the spatial distribution of the soil texture is largely unknown, a medium average permeability is assumed for the soils on these alluvial plains. The texture in the alluvial plains draining only Bambuí sediments is finer, consisting mainly of clay and silt (Figure 7-7). On higher terraces of the Rio das Velhas that are probably of Tertiary age (Heineck 1999) thick red soil covers gravel of pure quartz that are mined for metallurgical purposes (oral communication from C. A. Heineck). Since the quartz pebbles are cemented by iron oxides, the permeability of this subsoil is also quite low (Figure 8-11 C)

A  B 

C 

Figure 8-11 A) Open sand pit and B) clay pit showing the high spatial heterogeneity of the alluvial sediments in the fluvial system of the Riberão da Mata. C: Higher terraces of the Rio das Velhas consist of layers of pure quartz stones that are cemented by iron oxides.

(Location: A: -43.975274 / -19.682678, B: -43.994866 / -19.692176)

8.2.5 Exemplary infiltration experiments

The field observations of hydraulic soil properties were exemplarily tested by double – ring infiltration experiments on four different soil materials: saprolite of crystalline basement, saprolite of Bambuí meta-pelites, yellow subsoil on Bambuí carbonates and deep red topsoil on an old plateau surface at 800 m a.s.l..
The experiment setting was the following: two iron rings (diameter 30 cm and 60 cm) were buried 5 cm into the soil and a constant head was applied to the inner ring using a Mariott's bottle constructed out of common drinking water bottles, Figure 8-12. The amount of water infiltrated into the inner ring was logged in time. After some time, a constant infiltration rate was reached in the inner ring and converted into an estimation of saturated hydraulic conductivity using Equation 8-1 from Wu et al. (1997).

$$i_c = f * K_s$$

Equation 8-1 Saturated hydraulic conductivity in a ring infiltration experiment

With

i_c = characteristic infiltration rate of the ring infiltration experiment,
K_s = saturated hydraulic conductivity and
f = correction factor

Wu et al. (1997) list a correction factor of 1.2 to convert the observed infiltration rate from a double – ring infiltration experiment with an outer ring radius of 60cm to the saturated hydraulic conductivity of a soil. This correction factor has been calibrated for experiments with a constant head of 5 cm. A reduction of the head to 1 cm resulted in a reduction of the infiltration of ca. 15% for fine sandy or light clayey soils (Wu et al. 1997). Since it was not possible to keep a constant head of 5 cm for the highly permeable Ferralsol and for the yellow subsoil on carbonates, the calculated saturated hydraulic conductivity was raised for these soils by 15% respective 7.5% (Table 8-1).

Due to logistic restrictions, the experiment could be conducted only once for each soil material. This of course reduces the informative value of the experiment, since natural heterogeneity (e.g. roots, burrowing animals, local compaction and weathering status of the saprolite) can change the result of the experiment by more than 100%. Nevertheless, these experiments can give a hint on the scale range of permeability values: an about 10-fold permeability difference between saprolite of meta-pelite or crystalline basement and yellow subsoil on carbonates and a more than 10-fold permeability difference between this yellow subsoil and the red topsoil was observed.

Figure 8-12 Improvised setup of the constant head double ring infiltration experiment using common drinking water bottles.

	i_c [cm/min]	i_c [m/s]	f	Head	Correction for head ≠ 5 cm	K_s [mm/h]
Saprolite of basement	0.01	1.67E-06	1.2	5 cm	-	1.39E-06
Saprolite of meta-pelites	0.02	2.83E-06	1.2	5 cm	-	2.36E-06
Yellow subsoil carbonates	0.10	1.67E-05	1.2	3 cm	7.5%	1.49E-05
Ferralsol on high plateau surface	2.37	3.95E-04	1.2	1 cm	15%	3.79E-04

Table 8-1 Calculation of saturated hydraulic conductivity from four double ring infiltration experiments.

i_c = characteristic infiltration rate of the ring infiltration experiment, K_s = saturated hydraulic conductivity, f = correction factor after Equation 8-1.

8.3 Summary of soil properties for each geological unit

Next to a short description and a summary of available literature data, “optimality” values are assigned to the geological units regarding properties that are needed for the regionalization of geo-resource and geo-hazard parameters.

8.3.1 Lithology and weathering state

Only two horizons were differentiated for non-hydromorphic soils for the purpose of regionalizing hydrological soil properties: a generally red topsoil material with strong micro-aggregation (pseudo-sand structure) and a more compact subsoil material that is often lighter in color. For the purpose of regionalizing hydrological soil properties, saprolite (i.e. in situ weathered rock) is included into the definition of subsoil. Table 8-2 summarizes the lithology and weathering state of the geological units in the study area.

Geological unit	Lithology and weathering state
Quaternary fluvial sediments	Very heterogeneous unconsolidated sediments, mainly clay and sand, depending on the geological origin of the depositing streams. Depth is varying and can reach more than 30 meters as some drill-holes show (Pessoa 2005).
Lower fluvial terraces	Lower terraces of fluvial sediments that are probably slightly coarser textured than the recent alluvial plains.
Higher fluvial terraces	Old, probably Tertiary (Heineck 1999) terraces dominated by gravel which is sometimes cemented by iron oxide. Weathering depth, including the saprolite of the rocks below, is assumed middle to high with a rather high permeability.
Serra de Santa Helena Formation (Bambuí Group)	Predominantly fine siliciclastic sediments, meta-pelites with lenses of carbonates. They are weathered to considerable depth; in the study area, no fresh rocks could be found even in very deep gullies. The permeability of the saprolite is very low due to the fine-grained sediment structure, signs of temporal water stagnation can be observed in the field.

- First part of Table 8-2 -

Lagoa Santa Facies (Sete Lagoas Formation, Bambuí Group)	Predominantly black finely laminated pure limestones. While dissolution processes lead to extensive karstification, in flat areas a yellow subsoil that has a medium to low permeability covers the epikarst. In areas with strong relief, subsoil thickness is very variable, ranging from 0 at rock outcrops to 30-100 m above filled caves according to data from drill-holes.
Pedro Leopoldo Facies (Sete Lagoas Form., Bambuí Group)	Predominantly fine-grained impure limestone, marls and shales. Karstification is less intense than in the unit above and the yellowish subsoil generally thicker. Where the silicate content is higher, also saprolites of considerable depth can occur.
Carrancas Formation (Bambuí group)	Conglomerates, matrix supported diamictites. Since the matrix is carbonaceous, the same permeability and subsoil/saprolite depth as in the Pedro Leopoldo Facies are used.
Basic dykes	Basic dykes are typically weathered more deeply than the surrounding gneiss-migmatites. Their composition leads also to a higher clay content and thus a lower permeability than gneiss-migmatitic rocks.
Archean Gneiss-Migmatite basement (Belo Horizonte Complex)	Gneiss-migmatite rocks are often weathered to considerable depth; fresh outcrops are very rare in the study area. Nevertheless, this depth is difficult to estimate and is laterally heterogeneous, following preferential infiltration zones. With alteration and weathering grade, also the permeability and thus the mean retention time is spatially heterogeneous and generally increases with depth. Due to the higher quartz content, the saprolite is coarser textured than the pelitic unit of the Bambuí sediments and thus a slightly higher permeability is assumed.

Table 8-2 Hydrological properties of subsoil material on different geological units.

8.3.2 Subsoil properties

Table 8-3 shows examples of analytical data about soil texture, pore size distribution, available water capacity and field measured saturated hydraulic conductivity for the regionalization of hydrological subsoil properties.

In Table 8-4 maximum weathering depth as well as optimality values for karstification and basic subsoil permeability were estimated from the information in Table 8-3 and from the general description in Table 8-2

This information was used for creating maps of geo-potentials in chapter 10 - 12.

Parent material	**Subsoil texture (typical profile)**	**Pore size distribution (subsoil of a typical profile)**	**Saturated hydraulic conductivity (Ksat) [m/s] (section 8.2.5)**
Crystalline basement	Sand: 59% Silt: 24% Clay: 17% WdC: 0%	Micropores: 17 % Mesopores: 8% Macropores: 33 %	~1 E^{-06} measured at a site with mechanically exposed very dense saprolite, thus, saprolite closer to the surface might have higher permeability
	(Profile 27 from CPRM (1994b))		
Bambuí carbonates	Sand: 5% Silt: 15% Clay: 80% WcC: 1%	Micropores: 22 % Mesopores: 18% Macropores: 23 %	~ 2 E^{-05} measured on yellowish exposed subsoil at an excavation site close to carbonate rocks
	(Profile 7 from CPRM (1994b))		
Bambuí meta-pelites	Sand: 7% Silt: 49% Clay: 44% WdC: 0%	Micropores: 15 % Mesopores: 23% Macropores: 22 %	~ 2 E^{-06} measured on naturally exposed saprolite at a high plateau area
	(Profile 2 from CPRM (1994b))		
Alluvial S.	Very heterogeneous, ranging from pure sand to pure clay. No typical values		

Table 8-3 Exemplary analytical data on hydrological subsoil properties on different parent materials.

Geological unit	Maximum weathering depth	μ high subsoil permeability – basic (geo)	μ karst develop-ement (geo)	Typical subsoil eFC [mm/m]	Optimality value for high subsoil erodibility (compared to mean topsoil erodibility)
Quat. alluvial plains	35	0.5	0	Very heterogeneous, mean around 150 mm/m	0.75
Lower fluvial terraces	30	0.6	0	Coarser texture than QHA 120 mm/m	0.75
Higher fluvial terraces	30	0.6	0	Coarser texture than QPa1, cemented by iron oxides. 80 mm/m	0.75
Serra de Santa Helena Fm.	30m (OR total thickness)	0.1	0	220 - 230 mm/m	1
Facies Lagoa Santa	15	0.6	1	150 mm/m	0.5
Facies Pedro Leopoldo	20	0.5	0.8	150 mm/m	0.75
Carrancas Fm.	20	0.5	0.8	150 mm/m	0.75
Basic intrusions	20	0.2	0	100 mm/m	1
Crystalline basement	20	0.2	0	80 mm/m	1

Table 8-4 Estimated optimality values for subsoil properties (see also Table 8-2).

8.3.3 Topsoil physical properties

Table 8-5 and Table 8-6 summarize physical soil properties of topsoil material on different lithologies and slope positions.

Since structure is more important for hydraulic soil properties than texture due to water stable micro-aggregation (pseudo-sand structure), properties were not derived directly from texture values but from literature values of macro- and mesopores . The saturated hydraulic conductivity was estimated from the typical amount of macropores draining at 100 hPa. Table 8-5 shows the typical range of topsoil macropores percentage.

Effective field capacity is related to the amount of mesopores draining between 100 and 15000 hPa (see also Figure 8-1). Table 8-6 shows the estimated effective field capacity for typical topsoil material in the study area.

Topsoil location:	**Macropores %** **(range of typical profiles)**	**K_{sat} relative estimation for regionalization**
Basement region plateau surfaces and slopes	Around 25% - 35%	High
Basement region, aluvial plains (RdM):	Very heterogeneous, ranging between 5% and 30%	Low
Bambuí region, plateau surfaces and slopes	On plateau surfaces 30% - 40% In midslope and footslope position 25% - 35%	High
Bambuí region, dolines and alluvial plaines	In dolines: 25% In karst alluvial plains: 20%	Low

Table 8-5 Typical range of macropores % for topsoils on different geomorphological locations.

Data from CPRM (1994b).

Topsoil location:	Mesopores % typical range for toposoil material	Estimated eFC range [mm/m]
Basement region plateau surfaces and slopes	8 - 12 % lowest value at a flat hilltop location.	80 - 120 mm/m
Basement region, aluvial plains (RdM):	Very heterogeneous, ranging from 1% until 30%, mean around 15%	10 - 300 mm/m. Assumed mean: 150 mm/m
Bambuí region, plateau surfaces and slopes	On plateau surfaces 10 %, in midslope and footslope position 15 %	100 – 150 mm/m
Bambuí region, dolines and alluvial plaines	13 – 16 % in dolines, 20 % in karst alluvial plaines	130 – 200 mm/m

Table 8-6 Typical range of mesopores % and effective field capacity for topsoils on different geomorphological locations.

8.3.4 Topsoil chemical properties

Base saturation is the most important parameter in the region indicating elevated fertility. High base saturation does not only imply that a certain amount of macro-nutrients is available such as potassium, calcium and magnesium but also the absence of the risk of aluminum toxicity, which plays an important role at lower pH values. Base saturation is primarily related to the parent material and to the degree of weathering, i.e. deeply leached saprolites of acidic basement or meta-pelites generally have the lowest base saturation while soils in the karst area have more favorable conditions. Due to the accumulation of more fertile topsoil material, soils in downslope positions or in karst depressions are of the highest fertiligy.A descriptive overview of the distribution of base saturation in the study area is given in Table 8-7.

Location:	**Base saturation (relative values with respect to the study area)**
Granite / gneiss basement	In the topsoil low, in the subsoil very low with high Al saturation
Basic intrusions	Medium to high
Pure carbonates (Lagoa Santa Facies)	Variable, increasing with increasing slope or with lower topographic position
Impure carbonates (Pedro Leopolod Facies)	Lower than for pure carbonates
Meta-pelites (Serra de Santa Helena Formation)	In the topsoil low, in the subsoil very low with high Al saturation
Alluvial plains with mixed catchment, terraces	Medium to high
Alluvial plains in the karst area	Very high

Table 8-7 Typical base saturation for topsoils on different geological units.

9 Catenas for hydrological soil types

In this section, idealized hydrological soil catenas are presented for each geomorphologic compartment defined in section 6.5. The catenas are constructed to illustrate the geology-soil-landscape concept gained through field work and analysis of literature data but not based on real measurements or soil profiles. Only for the geomorphological compartment I, also data from soil trans-sections at the Baú karst massive (Piló 1998) could be used.
In the description, a focus is set on the estimated probability of surface flow, quick interflow and fast or slow infiltration. Additionally to the hydrological characteristics, an estimation of the potential erosion hazard (i.e. the erosion hazard independent from land use) is given. The zones defined in these idealized catenas are compared with real locations on satellite images and also with different topographic position indices. The calculation of topographic position indices (TPI, Weiss (2001)) is described in more detail in section 10.3.3. A TPI above average indicates a location that is higher than the surrounding neighborhood (e.g. a summit or high plateau) and a TPI below average indicates a location that is lower than the surrounding neighborhood (e.g. a valley or doline bottom). To capture topographic features at different scales, two differently sized neighborhoods (circle of 200 m and 3000 m radius) were chosen for the display in this chapter. Map 6 in the annex indicates the locations used to illustrate the soil catenas in this section:

9.1 Catena for compartment I

Figure 9-1 shows an idealized catena of typical soil zones for the geomorphologic compartment I.

Zone 1 **Autochthonous Ferralsols on old peneplanation surfaces above 790 m a.s.l.**
The highly permeable red topsoil is deep and often comprises several meters. Direct infiltration into the karst aquifer is hindered by dense subsoil of low permeability, sometimes consisting of remnants of the pelitic Serra de Santa Helena Formation containing quartz nodules.
Hydrological characteristics: Infiltration and deep interflow dominate, leading to a temporary aquifer during the rainy season. At its contact with the terrain surface at the plateau border, accumulation of iron oxide (petroplinthite) can occur.
Erosion hazard: Low erosion risk exists at the plateau center. At its border, medium risk of propagation of linear incision exists due to piping (where the shallow temporary aquifer is close to the surface). The incision is limited by the only shallow depth of erodible saprolite above hard limestone.

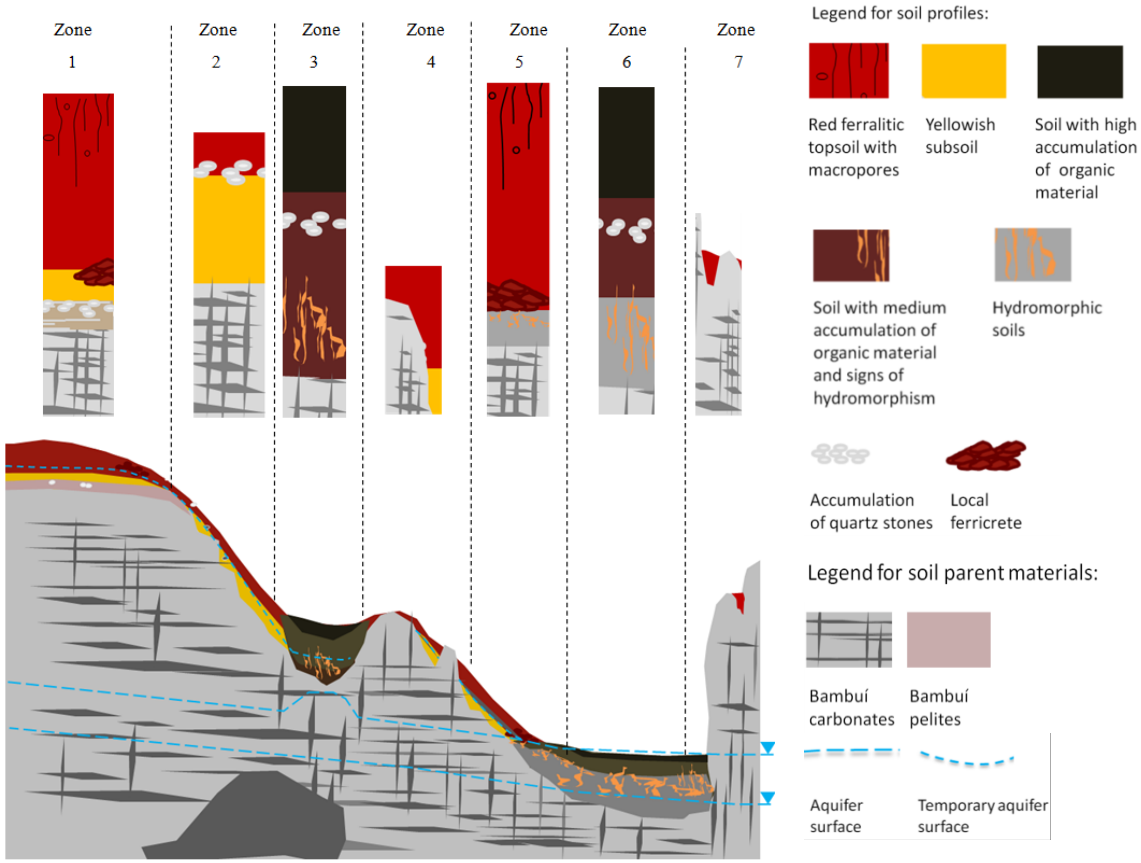

Figure 9-1 Idealized catena covering the most typical features of the geomorphologic compartment I.

For explanation of the profiles see text below.

<u>Zone 2</u> Acrisols / Lixisols of steep slopes

These soils are characterized by an illuvial clay accumulation horizon in the subsoil. They are younger and contain more weatherable minerals (especially Lixisols) than the autochthonous Ferralsols on the plateau surfaces. Stonelines of angular to rounded quartz pebbles often occur between topsoil and subsoil.

Hydrological characteristics: During heavy rains, shallow subsurface flow dominates. At locations with very thin soil above the epikarst, quick infiltration into the karst aquifer cannot be excluded.

Erosion hazard: Medium risk of shallow erosion exists due to steep slopes. The risk of gully propagation is low due to shallow depth of the soil mantle above hard rock.

<u>Zone 3</u> Eutrophic cambisols of doline floors

Eroded topsoil material from upslope accumulates in karst depressions. Due to seasonal water stagnation, organic material decomposes slowly and gives the soil a dark brown color. In the lower part of the profile, reducing colors and mottling due to temporal water logging can occur.

Hydrological characteristics: Zones of infiltration into the karst aquifer. The velocity of the infiltration depends strongly on soil depth and sealing of the doline floor.
Erosion hazard: Zone 3 is a zone of soil accumulation.

Zone 4 Cambisols / Lixisols / Leptosols of very steep hummocky slopes and rock outcrops
Soils from zone 4 are similar to soils from zone 2 but of very irregular depth. Direct contact between the epikarst and highly permeable topsoil can exist.
Hydrological characteristics: Infiltration and shallow subsurface flow occur. Occasionally, direct shortcuts into the karst aquifer exist.
Erosion hazard: High risk of shallow surface erosion due to steep slopes, deep incision is limited due to very shallow and irregular depth of the soil mantle above hard rock.

Zone 5 Allochthonous Ferralsols at footslope location
These soils consist of redistributed material from upslope: a mixture from material of old autochthonous Ferralsols and topsoil material from slopes. Very high permeability in the red horizons often even until considerable depth. Where the (temporary) aquifer crops out, accumulation of petroplinthite can occur.
Hydrological characteristics: Infiltration clearly dominates, sometimes also deep subsurface flow can occur.
Erosion hazard: Generally low erosion risk due to high infiltration capacity and strong soil structure. If incision takes place due to local unfavorable hydrological conditions, they can propagate to considerable depth in the soft material.

Zone 6 Eutrophic gleysols and cambisols of doline floors close to the groundwater level
Eroded topsoil material from upslope accumulates in karst depressions. Due to seasonal rising of the groundwater level above surface, organic material accumulates and gives the soil a dark brown color. In the lower part of the profile, mottling and bleached zones occur.
Hydrological characteristics: Doline floors are zones of direct infiltration into the karst aquifer, often through a swallow hole at the foot of a neighboring rock outcrop.
Erosion hazard: Erosion hazard is very low, soil accumulation dominates
.

9.2 Landscape examples for zones 1 - 4 (Comp. I)

Typical locations of the soil zones 1 - 4 in the geomorphological compartment I are indicated in Figure 9-2, which shows a typical karst plateau landscape in the north eastern part of the study area (rectangle Ia in Map 6 in the annex).

Additionally, the typical terrain positions of the soil zones using the topographic position index (TPI) are shown in Figure 9-3 A (regional TPI) and Figure 9-3 B (local TPI). The lighter the color, the higher is the relative position in the landscape compared to a neighborhood of 3000 m (regional TPI) and 200 m (local TPI). The typical terrain positions of the soil zones are the following:

Zone 1 is typical for very high regional TPI, medium to high local TPI and comparatively flat slopes.

Zone 2 is typical for high regional TPI, average local TPI and steep slopes.

Zone 3 is typical for average regional TPI, very low local TPI and completely flat slopes.

Zone 4 is typical for average regional and local TPI and very steep hummocky slopes.

Figure 9-2 Typical landscape of the karst plateau.

Image from Google Earth from 22nd August 2009 (rectangle Ia in Map 6 in the annex).

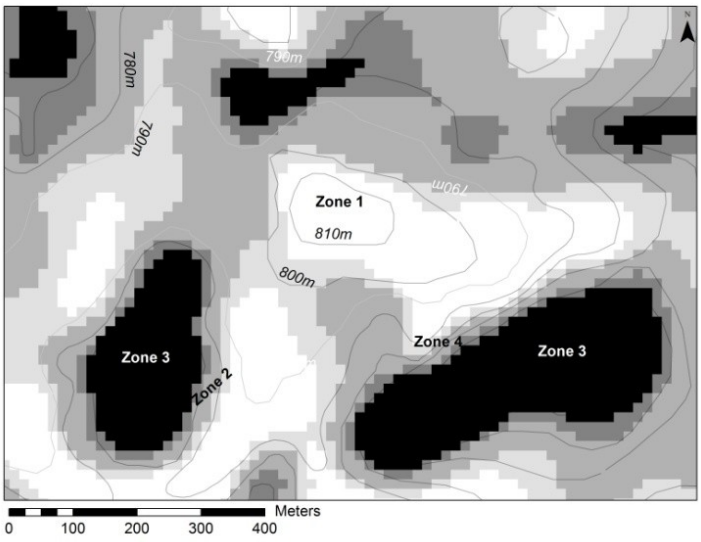

A

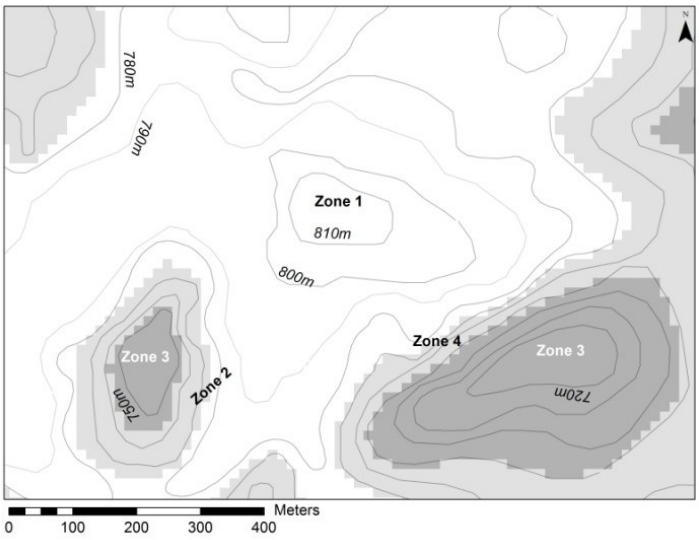

B

Figure 9-3 A) Regional TPI and B) local TPI of the area shown in Figure 9-2.

Dark colors indicate areas that are lower than surrounding average elevation, light colors indicate areas that are higher than the surrounding average elevation. For the regional TPI, the relevant neighborhood comprises a circle of 3000 m diameter, for the local TPI, a circle of 200 m diameter. More details about TPI calculation can be found in section 10.3.3.

9.3 Landscape examples for zones 5 – 7 (Comp. I)

Typical locations of the soil zones 5 – 7 from the catena above are indicated in Figure 9-4 which shows a low lying uvala (Lagoa do Sumidouro) in the north eastern part of the study area.

Figure 9-5 shows the typical relative terrain positions of the soil zones using the relative topographic position index (TPI).

Zone 5 is typical for low regional TPI, average local TPI and relatively flat slopes.

Zone 6 is typical for very low regional TPI, average local TPI and very flat slopes.

Zone 7 is typical for average regional TPI, high local TPI and very steep slopes.

Figure 9-4 Landscape of an uvala draining into a karst ponor during the rainy season A) and dry season B).

Images from Google Earth, from 26th Feb 2003 (A) and 20th July 2006 (B).
Location: Lagoa do Sumidouro, rectangle Ib in Map 6 in the annex.

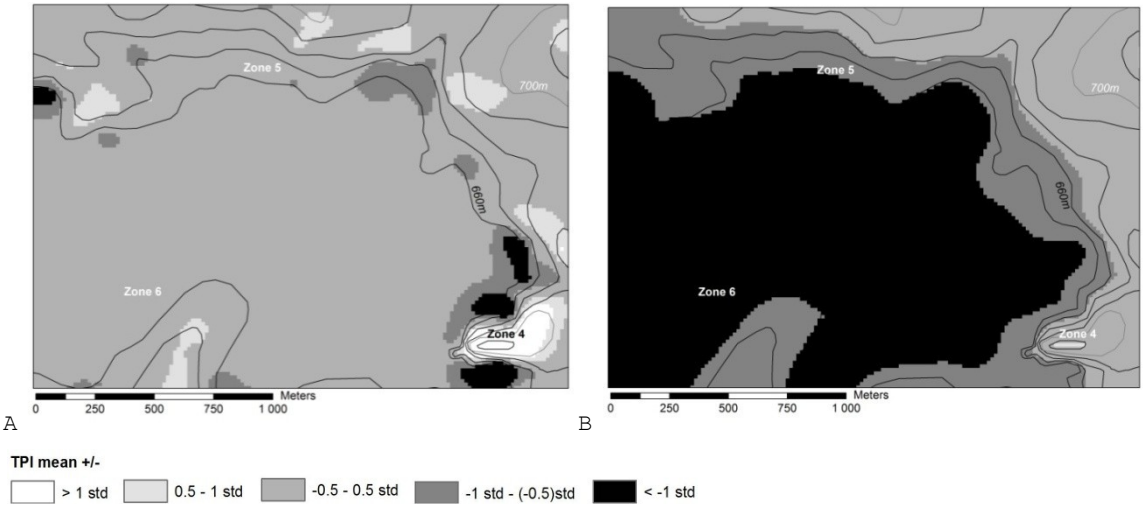

Figure 9-5 A) regional TPI and B) local TPI of the area shown in Figure 9-4.

Dark colors indicate areas that are lower than surrounding average elevation, light colors indicate areas that are higher than the surrounding average elevation. For the regional TPI, the relevant neighborhood comprises a circle of 3000 m diameter, for the local TPI, a circle of 200 m diameter. More details about TPI calculation can be found in section 10.3.3.

9.4 Catena for compartment II

Figure 9-6 shows an idealized catena of typical soil zones from the geomorphologic compartment II. The explanation of the physical properties of the soil zones (hydrological properties and erosion hazard) follows in the text below the catena.

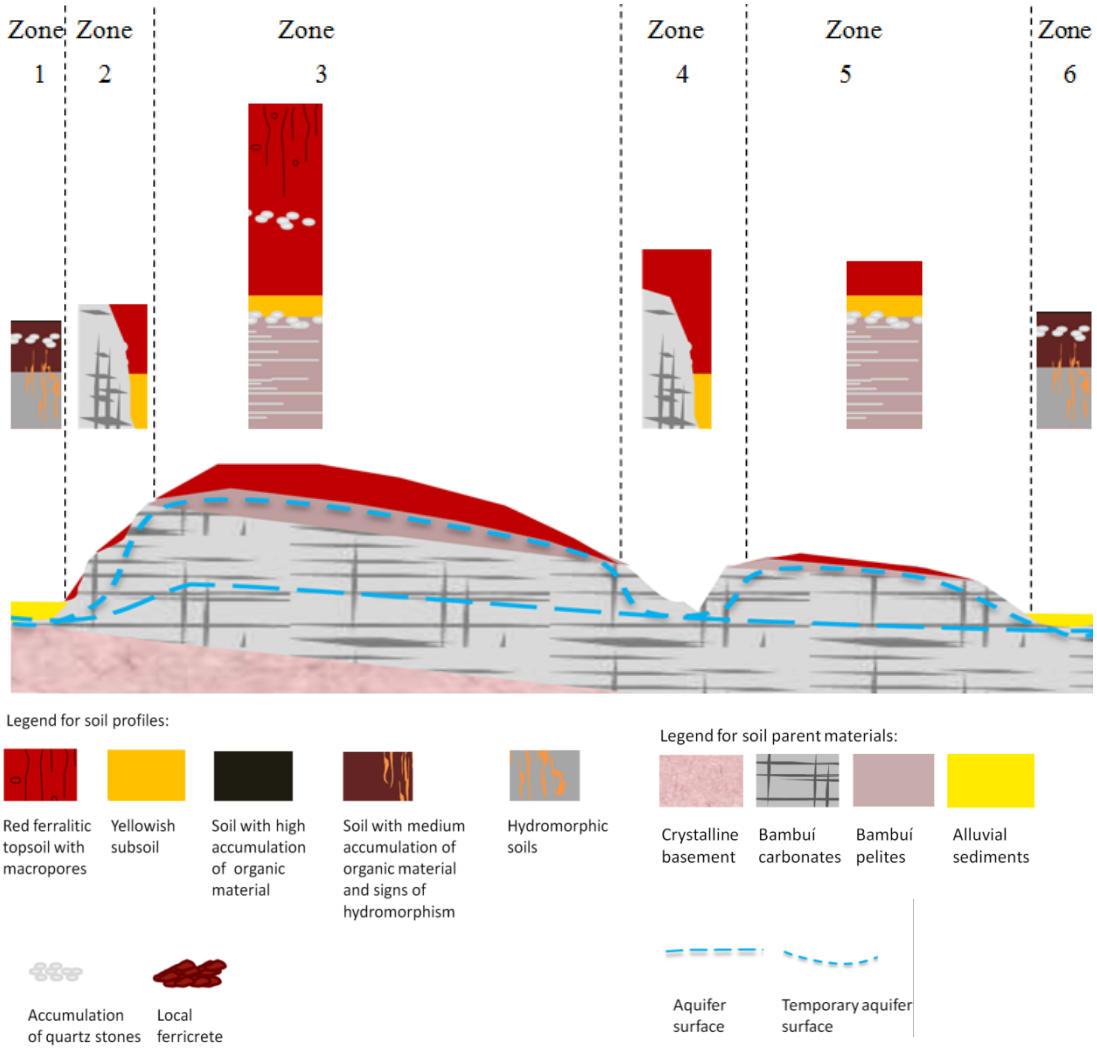

Figure 9-6 Idealized catena covering the most typical features of the geomorphologic compartment II.

For explanation of the profiles see text below.

Zone 1 Gleysols and Fluvisols of alluvial plains draining crystalline basement

Eroded topsoil material from upslope accumulates in the alluvial plains, but also very sandy material from the granite-gneiss region. In the lower part of the profile, mottling and bleached zones occur.

Hydrological characteristics: Infiltration and saturation excess surface runoff dominate. The permeability can be very heterogeneous even within one profile due to different layers of fluvial sediments.

Erosion hazard: The erosion hazard is generally very low, alluvial plains are zones of soil accumulation.

Zone 2 Cambisols / Lixisols / Leptosols of hummocky very steep slopes

Soils with highly permeable red topsoil above less permeable yellowish subsoil or saprolite of impure limestone. The subsoil / saprolite is of very variable depth and direct contact between the epikarst and highly permeable topsoil is possible.

Hydrological characteristics: Infiltration and shallow subsurface flow occur. Direct shortcuts into the karst aquifer are possible.

Erosion hazard: High risk of shallow surface erosion exists due to steep slopes, but deep incision is limited by to shallow and irregular depth of the soil mantle above hard rock.

Zone 3 Autochthonous Ferralsols on remnants of old peneplanation surfaces

Soils with very thick highly permeable red topsoil are typical. Occasionally, lenses of petroplinthite (canga) can occur. The karst aquifer is protected by saprolite of the pelitic Serra de Santa Helena Formation beneath the ferralic horizon. The contact between red topsoil and saprolite is sometimes gradually with an intermediate yellowish horizon or abrupt, in this case often indicated by a stoneline.

Hydrological characteristics: Infiltration and deep interflow dominate, leading to a temporary aquifer during the rainy season.

Erosion hazard: Low erosion risk at the plateau center. At its border, very high risk of propagation of linear incision due to piping (surface contact of the temporary aquifer), medium to thick saprolite of the Serra de Santa Helena Formation allows incision of deep gullies.

Zone 4 Cambisols / Lixisols / Leptosols of steep hummocky slopes

Typical for zone 4 are soils with highly permeable red topsoil above less permeable yellow subsoil of very variable depth. The Bambuí carbonates of the geomorphologic compartment II are generally less pure than in compartment I and thus karstification is less prominent and often plugged by saprolite of impure limestone. Nevertheless, direct contact between the epikarst and highly permeable topsoil is possible.

Hydrological characteristics: Infiltration and shallow subsurface flow occur. Direct shortcuts into the karst aquifer are rare but possible.
Erosion hazard: High risk of shallow surface erosion due to steep slopes, but low risk of deep incision due to shallow and irregular depth of the soil and saprolite mantle above hard rock.

Zone 5 Plateau surfaces on limestone covered by thin pelite saprolite
Less permeable yellowish subsoil is covered by well-structured permeable red topsoil. The epikarst is still protected by a shallow pelitic saprolite of the Serra de Santa Helena Formation.
Hydrological characteristics: Infiltration and shallow subsurface flow occur.
Erosion hazard: Generally, low erosion risk exists due to high infiltration capacity and strong soil structure combined with low slopes. At the borders, risk of shallow to medium deep linear erosion features, depending on the thickness of the saprolite above fresh rock.

Zone 6 Eutrophic Gleysols, gleyic Cambisols and Fluvisols of alluvial plains draining only Bambuí sediments
Eroded topsoil material from upslope accumulates in alluvial plains. Due to seasonal rising of the groundwater level above the surface, organic material accumulates and gives the soil a dark brown color. In the lower part of the profile, mottling and bleached zones occur. The texture of the soil is dominated by clay and silt.
Hydrological characteristics: The hydrology of zone 6 is dominated by infiltration and saturation excess surface runoff. The permeability of the soil is relatively low due to a very fine clayey texture and the absence of pseudo-sand structure.
Erosion hazard: Erosion hazard is very low, zone 6 is dominated by soil accumulation.

9.5 Landscape examples for compartment II

Typical locations of the soil zones 1 - 6 from geomorphologic compartment II are indicated in Figure 9-7, which shows a satellite image of the central study area (rectangle II in Map 6 in the annex). The terrain positions of the soil zones are indicated using the regional (Figure 9-7 B) and local (Figure 9-7 C) topographic position index.

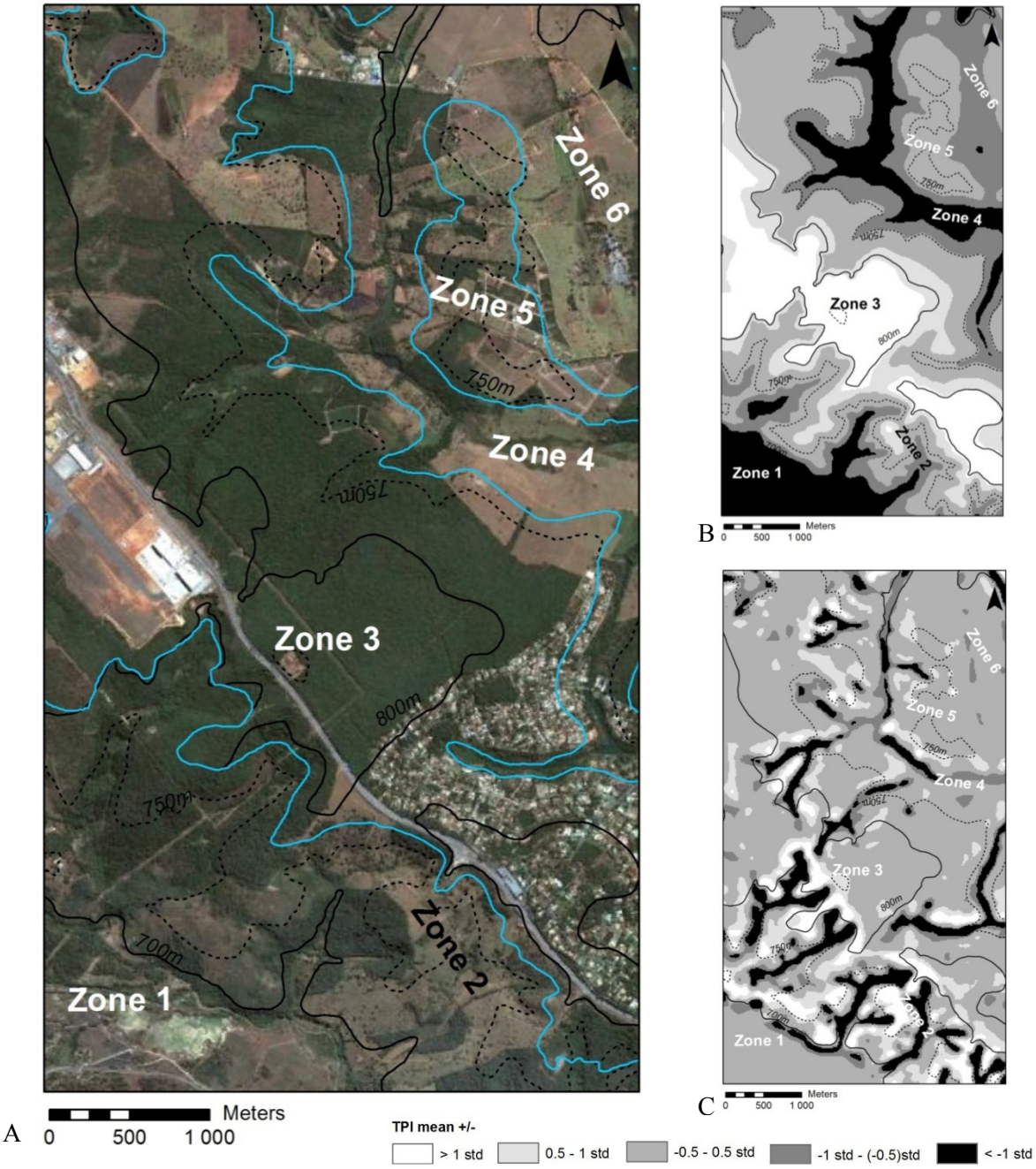

Figure 9-7 A) Landscape of geomorphologic compartment II west of Lagoa Santa. B) Regional TPI and C) local TPI of the area shown in (A).

Image (A) taken from Google Earth from 20th July 2010 (rectangle II in Map 6 in the annex). The green dashed line indicates the contact between meta-pelites (zones 3 and 5) and the carbonates.

In B) and C), dark colors indicate areas that are lower than surrounding average elevation, light colors indicate areas that are higher than the surrounding average elevation. For the regional TPI, the relevant neighborhood comprises a circle of 3000 m diameter, for the local TPI, a circle of 200 m diameter. More details about TPI calculation can be found in section 10.3.3.

9.6 Catena for compartment III

Figure 9-8 shows an idealized catena of typical soil zones for the geomorphologic compartment III. The explanation of the physical properties of the soil zones (hydrological properties and erosion hazard) follows in the text below the catena.

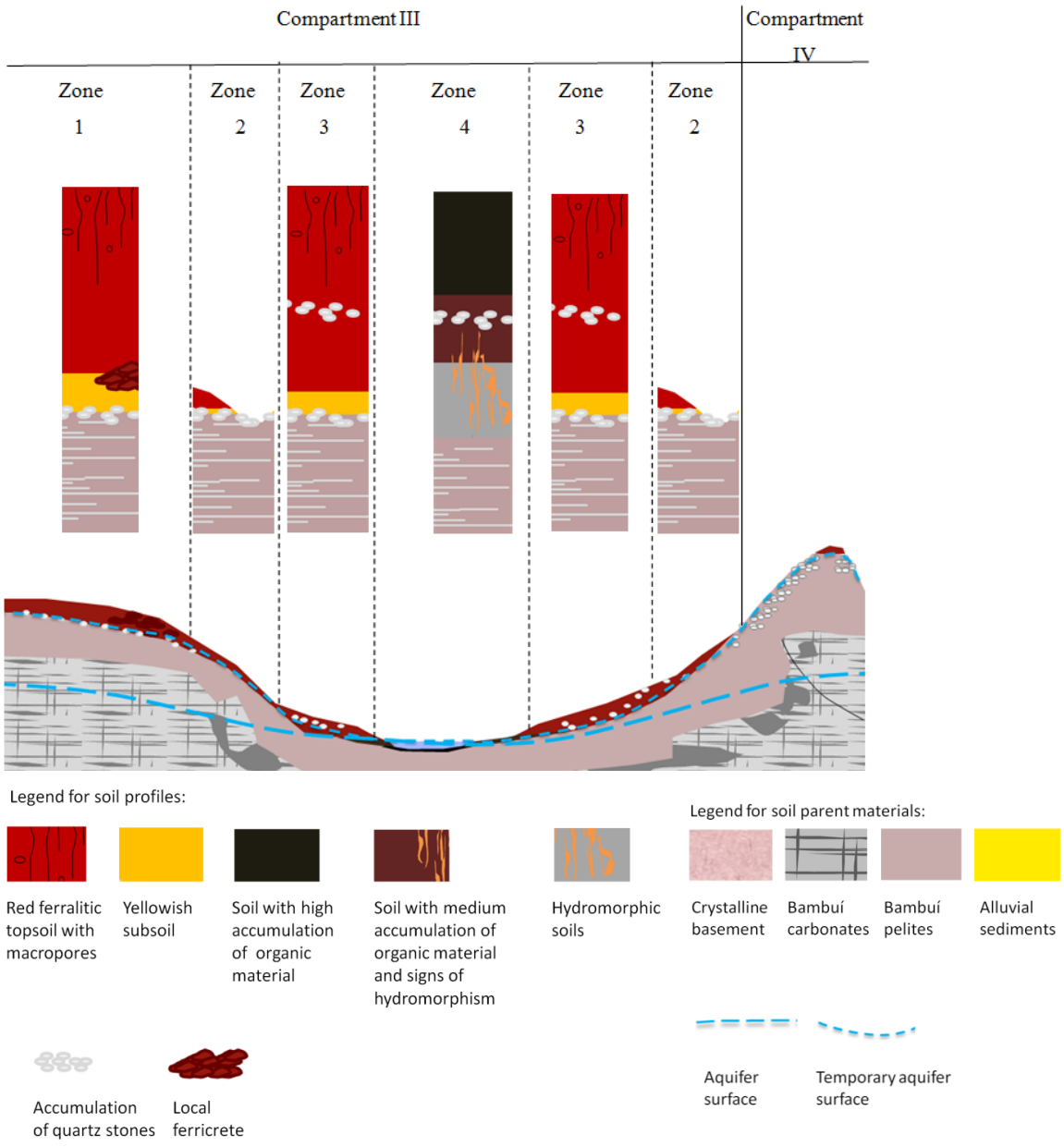

Figure 9-8 Idealized catena covering the most typical features of the geomorphologic compartment III.

For explanation of the profiles see text below.

Zone 1 Old autochthonous Ferralsols on remnants of old peneplanation surfaces

Soils with very thick and highly permeable red topsoil are typical. Occasionally, lenses of petroplinthite can occur at plateau-borders. The karst aquifer is protected by saprolite of the meta-pelites of the Serra de Santa Helena Formation in the subsoil, the contact is either gradually with an intermediate yellowish horizon or abrupt, in the second case often indicated by a stoneline.

Hydrological characteristics: Infiltration and deep interflow dominate, leading to a temporary aquifer during the rainy season.

Erosion hazard: Low erosion risk at the plateau center. At its border, very high risk of propagation of linear incision due to piping (surface contact of the temporary aquifer), thick meta-pelite saprolite allows deep incision of gullies.

Zone 2 Soils of steep slopes.

Due to erosion processes, the highly permeable red topsoil is relatively thin above the meta-pelite saprolite. Stonelines of angular to rounded quartz pebbles often occur between topsoil and saprolite.

Hydrological characteristics: Infiltration and shallow subsurface flow dominate.

Erosion hazard: Medium to high risk of shallow erosion features due to steep slopes, high risk of propagation of larger gullies due to surface and subsurface flow accumulation and deep soft saprolite.

Zone 3 Allochthonous Ferralsols at footslope locations.

Well-structured and permeable red topsoil material from upslope accumulates at footslope positions, often separated from the saprolite by a stoneline.

Hydrological characteristics:

Deep interflow and infiltration dominate.

Erosion hazard:

Low risk of shallow erosion features due to quick infiltration into thick topsoil material. Propagation of gullies is possible in areas of flow concentration.

Zone 4 Hydromorphic soils in local depressions.

Eroded topsoil material from upslope accumulates in local depressions. Organic material decomposes more slowly due to temporal water logging and gives the soil a dark brown color. In the lower part of the profile, mottling and bleached zones occur.

Hydrological characteristics: Zones of exfiltration of water from interflow from the neighboring slopes, surface runoff when the soil is completely saturated (lakes, rivers, swamps). Karst features are completely plugged.

Erosion hazard: none, zone of soil accumulation.

9.7 Landscape examples for Compartment III

Typical locations of the soil zones 1 - 4 of the geomorphologic compartment III are indicated in Figure 9-9, which shows a satellite image of the central study area (rectangle III in Map 6 in the annex). Figure 9-10 shows the terrain positions of the soil zones using the regional (A) and local (B) topographic position index.

Figure 9-9 Landscape of the geomorphologic compartment III.

Satellite image from Google Earth from 20th July 2010, location see rectangle III in Map 6.

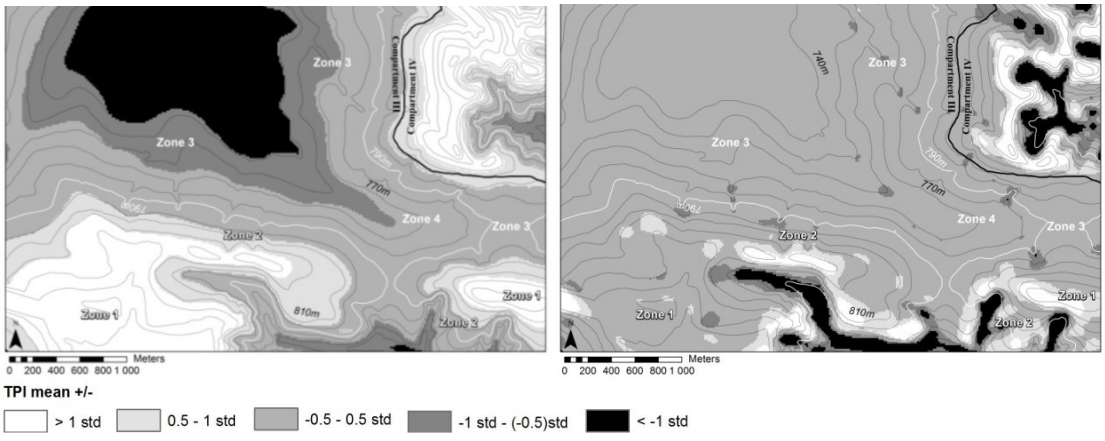

Figure 9-10 A) regional TPI and B) local TPI of the area shown in Figure 9-9.

Dark colors indicate areas that are lower than surrounding average elevation, light colors indicate areas that are higher than the surrounding average elevation. For the regional TPI, the relevant neighborhood comprises a circle of 3000 m diameter, for the local TPI, a circle of 200 m diameter. More details about TPI calculation can be found in section 10.3.3.

9.8 Catena for compartment IV

Figure 9-11 shows an idealized catena of typical soil zones for the geomorphologic compartment IV. The explanation of the physical properties of the soil zones (hydrological properties and erosion hazard) follows in the text below the catena.

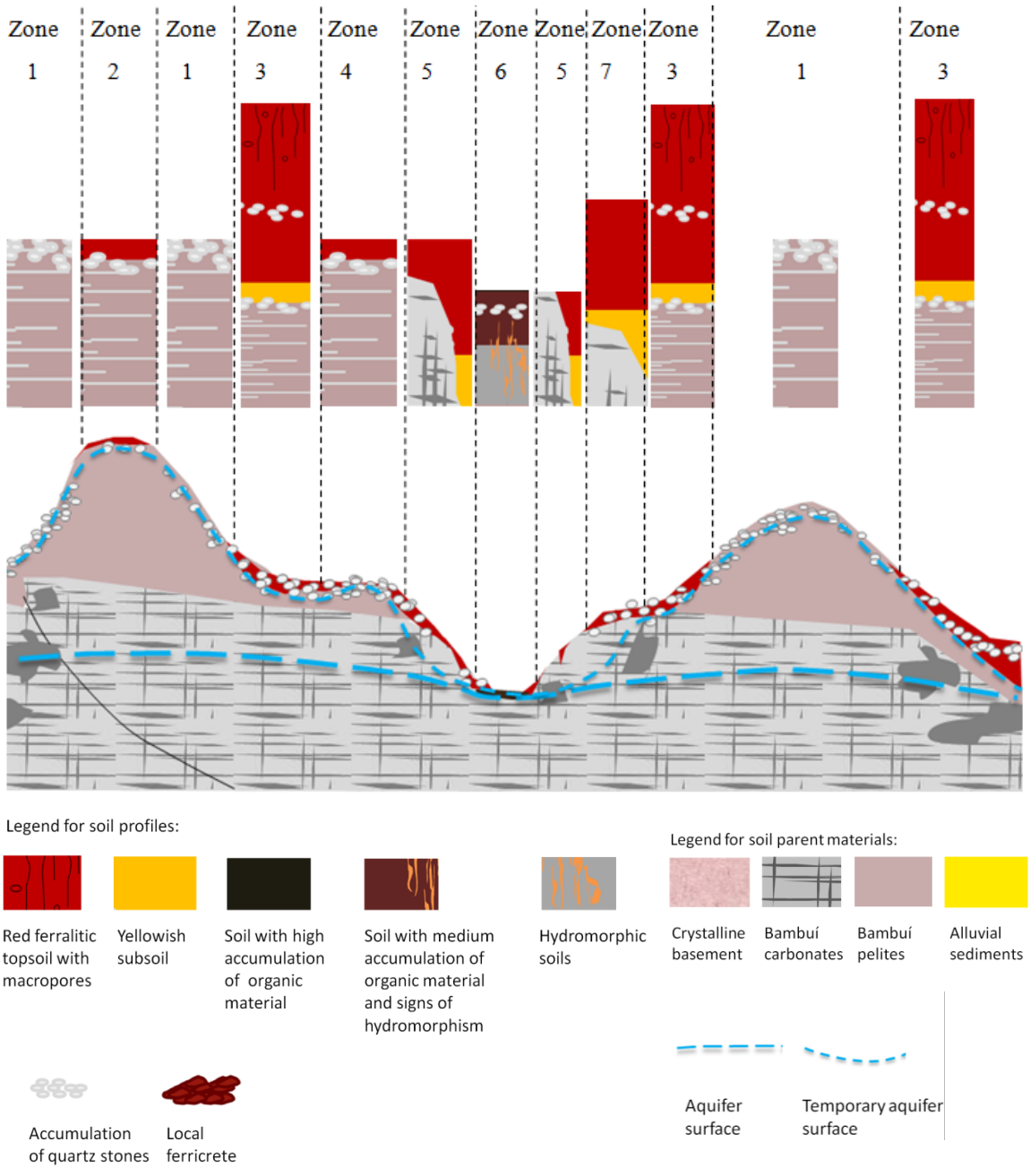

Figure 9-11 Idealized catena covering the most typical features of the geomorphologic compartment IV.

For explanation of the profiles see text below.

Zone 1 **Eroded soils on steep slopes of the Serra de Santa Helena meta-pelites**

The silt-dominated saprolite is only occasionally covered by thin highly permeable red topsoil, otherwise only a thin dense yellowish horizon can be found on top of the saprolite, often covered by a layer of quartz stones.

Hydrological characteristics: Hortonian surface runoff is frequent during medium to heavy rainfall events.

Erosion hazard: High risk of shallow erosion features if thick protecting stone layers (Figure 8-3 A) are absent. Medium risk of propagation of deep erosion features (gullies) since most of the softest saprolite material has already been eroded and subsurface flow concentration is absent or very slow in the dense saprolite. At very steep slopes, risk of landslides exists as documented by scars in the landscape.

Zone 2 **Eroded Ferralsols at narrow high summits of the Serra de Santa Helena meta-pelites**

Remnants of old Ferralsols exist at the summits of the meta-pelite hills east of Lagoa Santa. Nevertheless, the permeable red topsoil is shallow, its thickness is generally less than 0.5 m.

Hydrological characteristics: Infiltration and shallow subsurface flow dominate.

Erosion hazard: Medium risk of shallow erosion at the summit borders, low risk of deeper incision due to lack of flow concentration.

Zone 3 **Allochthonous Ferralsols at footslope locations.**

Similar to Zone 3 of compartment III but with less extensive topsoil accumulation.

Zone 4 **Eroded Ferralsols at lower summits of the Serra de Santa Helena meta-pelites**

Similar to zone 2, topsoil depth depends on the width of the summit.

Zone 5 **Cambisols / Lixisols / Leptosols of steep hummocky slopes**

Similar to zone 4 in compartment II.

Zone 6 **Eutrophic Gleysols, gleyic Cambisols and Fluvisols of alluvial plains draining only Bambuí sediments**

Similar to zone 6 in compartment II, although the valleys are narrower and the alluvial area smaller, riverside erosion is possible.

Zone 7 **Plateau surfaces on limestone**

Less permeable yellowish subsoil is covered by well-structured highly permeable red topsoil. The depth of epikarst is very variable with the possibility of direct infiltration from the red topsoil into the karst aquifer.

Hydrological characteristics: Infiltration and shallow subsurface flow occur. Direct shortcuts into the karst aquifer are possible.

Erosion hazard: Generally low erosion risk due to high infiltration capacity and strong soil structure combined with low slopes. At the borders risk of shallow erosion features.

9.9 Landscape examples for Compartment IV

Typical locations of the soil zones 1 - 7 from geomorphologic compartment IV are indicated in Figure 9-12 which shows a satellite image of the central study area (rectangle IV in Map 6 in the annex). The maps below show the terrain positions of the soil zones using the regional (Figure 9-13 A) and local (Figure 9-13 B) topographic position index.

Figure 9-12 Landscape of geomorphologic compartment IV east of Lagoa Santa.

Image taken from Google Earth from 20th July 2010 (rectangle IV in Map 6). The green dashed line indicates the contact between Serra de Santa Helena meta-pelites (zones 1 - 4) and the carbonates of the Sete Lagoas Formation (zones 5 and 7).

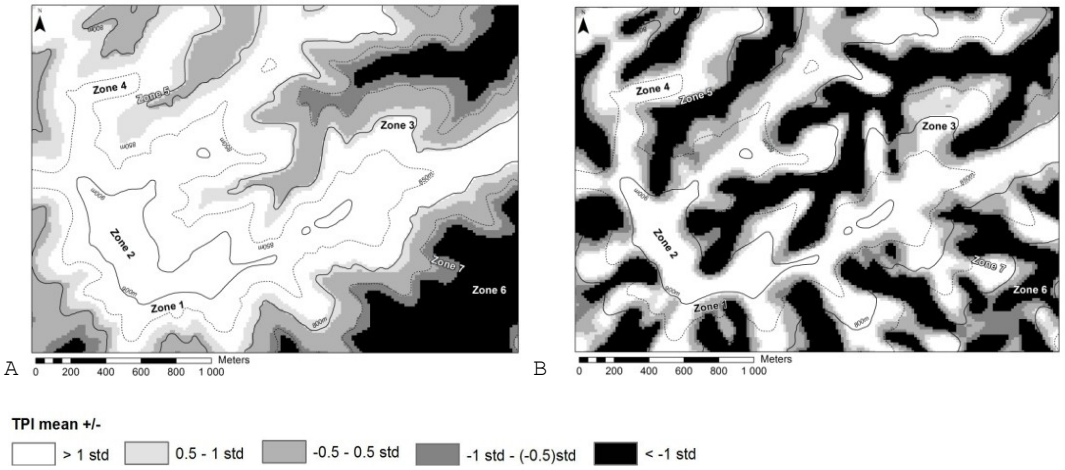

Figure 9-13 A) Regional TPI and B) local TPI of the area shown in Figure 9-12 .

Dark colors indicate areas that are lower than surrounding average elevation, light colors indicate areas that are higher than the surrounding average elevation. For the regional TPI, the relevant neighborhood comprises a circle of 3000 m diameter, for the local TPI, a circle of 200 m diameter. More details about TPI calculation can be found in section 10.3.3.

9.10 Catena for compartment V

Figure 9-14 shows an idealized catena of typical soil profiles for the geomorphologic compartment V.

Zone 1 Gleysols and Fluvisols of alluvial plains draining basement area

Similar to zone 1 in compartment II.

Zone 2 Cambisols / Ferralsols of hummocky very steep slopes on basement.

Typical soils have shallow highly permeable red topsoil above less permeable basement saprolite. The depth of the red topsoil can vary considerably (see Figure 8-9, C on page 139).

Hydrological characteristics: Infiltration and shallow subsurface flow occur. If the red topsoil is absent, Hortonian overland flow can occur even during medium rainfall events.

Erosion hazard: High risk of shallow surface erosion due to steep slopes, deep gully incision is possible depending on flow concentration and weathering state of the saprolite.

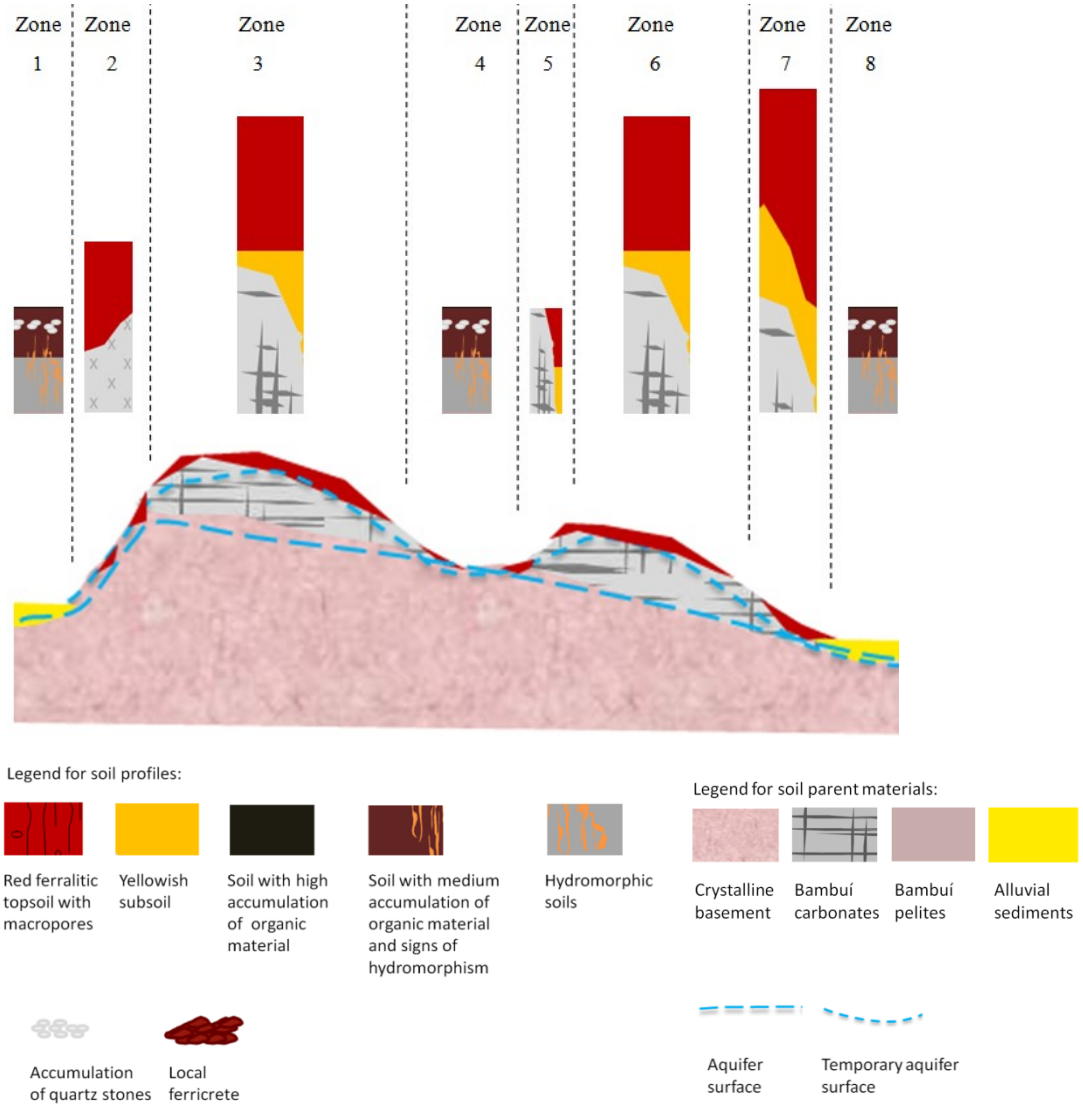

Figure 9-14 Idealized catena covering the most typical features of the geomorphologic compartment V.

For detailed explanation of the profiles see text below. Blue dashed lines indicate karst groundwater level (lower line) and a shallow perched aquifer during the rainy season (upper line).

Zone 3 Old autochthonous Ferralsols on remnants of old peneplanation surfaces

Very high permeability is characteristic for the red topsoil, which can be several meters thick. Below, a less permeable yellowish subsurface horizon overlies the karst aquifer but saprolite of the pelitic Serra de Santa Helena Formation is absent.

Hydrological characteristics: Infiltration and deep interflow dominate, leading probably also to a temporary shallow aquifer during the rainy season, but less pronounced than in areas with Bambuí meta-pelites. Plugging of karst features is also not as effective as in areas with Bambuí meta-pelites.

Erosion hazard: Low erosion risk at the plateau center. At its border, medium risk of propagation of linear incision due to piping (outcrop of the shallow temporary aquifer), the depth of incision is limited by the thickness of subsoil above hard limestone rock.

Zone 4 Gleysols of small alluvial plains and karst depressions above basement

Eroded topsoil material from upslope accumulates in the alluvial plains, clayey material dominates. Due to seasonal rising of the groundwater level above the surface, organic material accumulates and gives the soil a dark brown color. In the lower part of the profile, mottling and bleached zones occur.

Hydrological characteristics: Zone of exfiltration of the local karst aquifer and infiltration into the less permeable, mainly fissural or granular basement saprolite aquifer. Saturation excess surface runoff occurs frequently during the rainy season.

Erosion hazard: Generally low since it is a zone of soil accumulation but riverside erosion can occur, especially if the basement is reached.

Zone 5 Cambisols / Lixisols / Leptosols of steep hummocky slopes on Bambuí carbonates

Similar to zone 4 in compartment I – although karstification is less intense.

Zone 6 Old autochthonous Ferralsols on remnants of old peneplanation surfaces

Similar to zone 3 in the same compartment.

Zone 7 Allochthonous Ferralsols at footslope positions

These soils consist of redistributed material from upslope which is a mixture of old autochthonous Ferralsols and topsoil material from steep slopes. The red accumulation horizon is very permeable and can be very deep. The contact between topsoil and subsoil is often irregular, following a pre-relief and is often marked by stonelines (Figure 8-7).

Hydrological characteristics: Infiltration clearly dominates, sometimes also deep subsurface flow occurs.

Erosion hazard: Generally low erosion risk due to high infiltration capacity and strong soil structure. If incision takes place due to local unfavorable hydrological conditions, it can propagate to considerable depth in the soft material.

Zone 8 Eutrophic Gleysols, gleyic Cambisols and Fluvisols of alluvial plains draining only Bambuí sediments

Similar to zone 6 in compartment II but with smaller rivers.

9.11 Landscape examples for Compartment V

Typical locations of the soil zones 1 - 4 from the geomorphologic compartment V are indicated in Figure 9-15 (A), which shows a satellite image of the central study area (rectangle Va in Map 6 in the annex). The maps at the side show the terrain positions of the soil zones using the regional (B) and local (C) topographic position index. Figure 9-16 shows the same for the soil zones 5 – 8 of the catena for the geomorphological compartment V (rectangle Vb in Map 6).

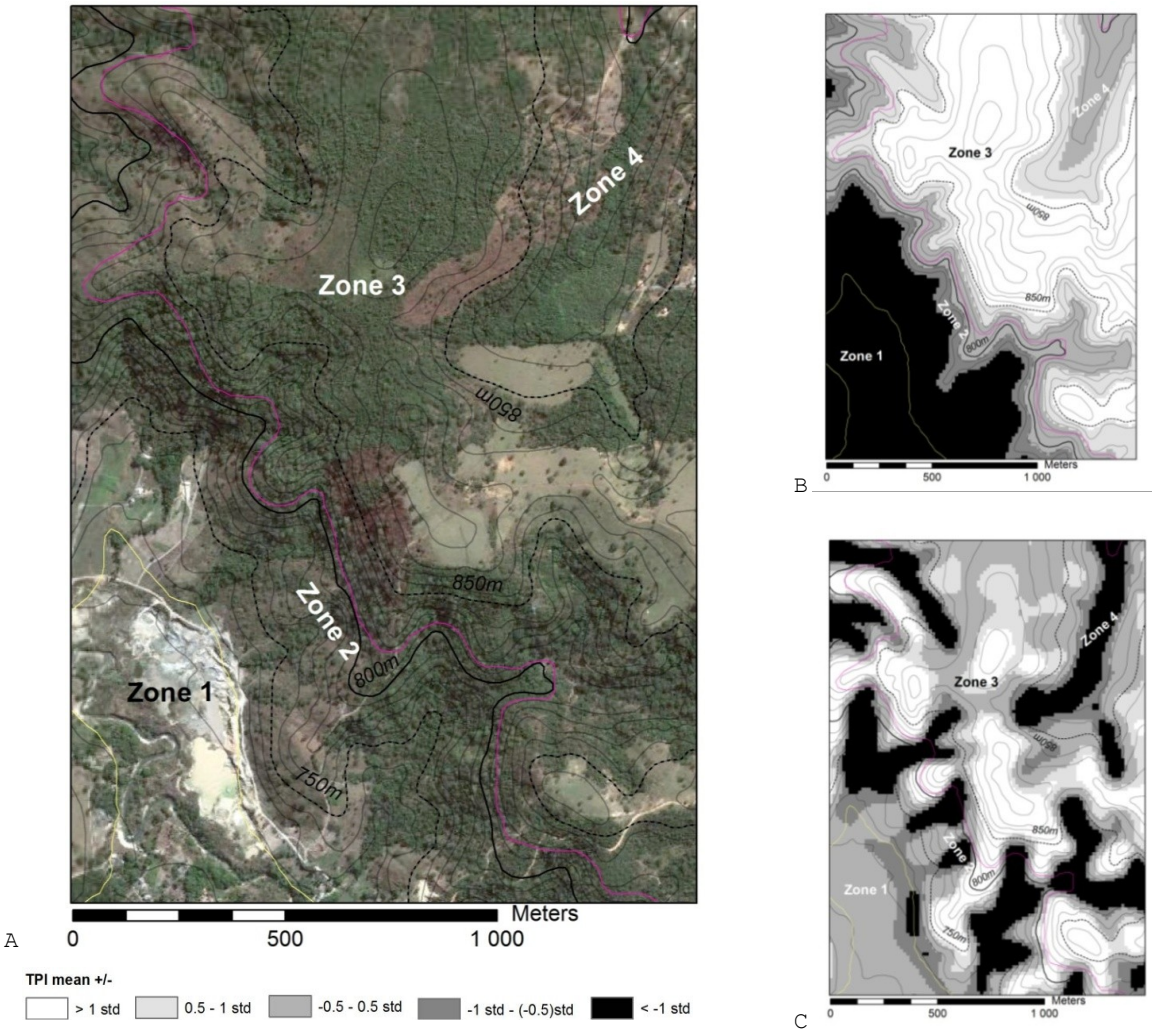

Figure 9-15 A) Landscape of the geomorphologic compartment V (rectangle Va in Map 6). B) Regional TPI and C) Local TPI of the area shown in A).

Image from Google Earth from 20th July 2010. The pink line indicates the contact between basement and Bambuí. Dark colors in B) and C) indicate areas that are lower than surrounding average elevation, light colors indicate areas that are higher. For the regional TPI, the neighborhood comprises a circle of 3000 m diameter, for the local TPI, 200 m. More details about TPI calculation can be found in section 10.3.3.

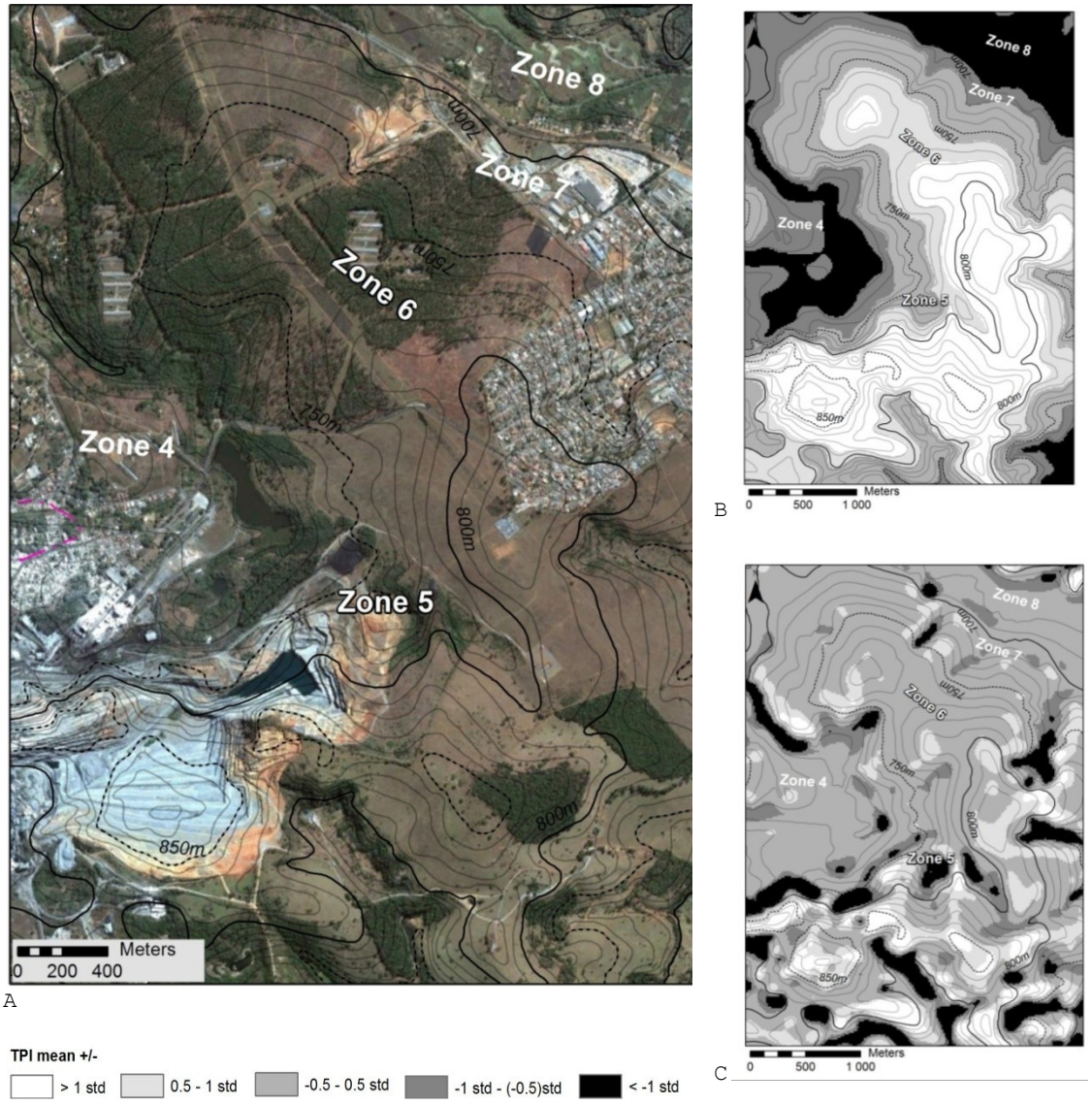

Figure 9-16 A) Landscape of the geomorphologic compartment V (rectangle Vb in Map 6). B) Regional TPI and C) Local TPI of the area shown in A).

Image from Google Earth from 20th July 2010. The pink dashed line indicates the contact between basement and Bambuí. Note: the contour lines represent the relief before the mining pit was excavated.

Dark colors in B) and C)indicate areas that are lower than surrounding average elevation, light colors indicate areas that are higher than the surrounding average elevation. For the regional TPI, the relevant neighborhood comprises a circle of 3000 m diameter, for the local TPI, a circle of 200 m diameter. More details about TPI calculation can be found in section 10.3.3.

9.12 Catena for compartment VI

Figure 9-17 shows an idealized catena of typical soil zones for the geomorphologic compartment VI. The explanation of the physical properties of the soil zones (hydrological properties and erosion hazard) follows in the text below the catena.

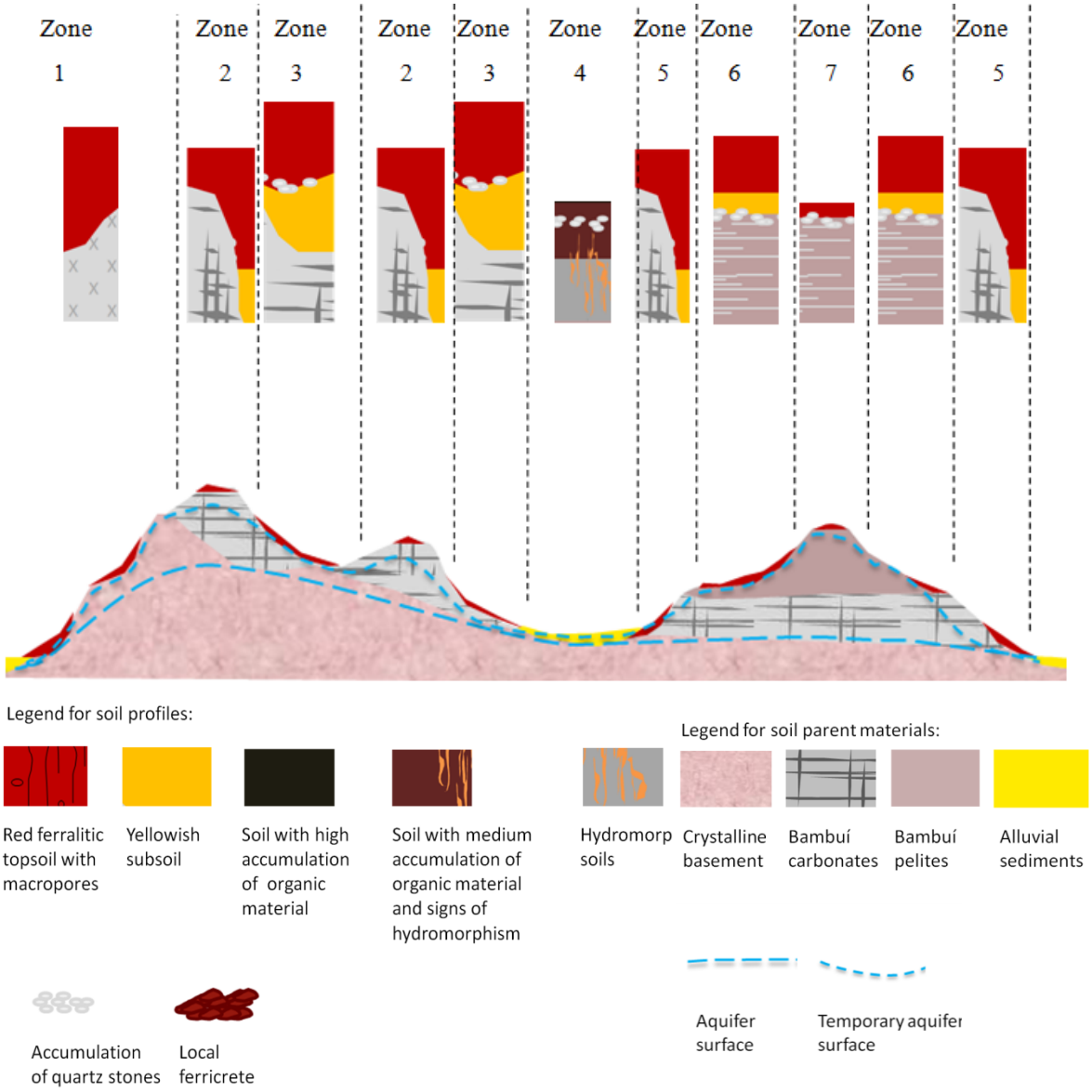

Figure 9-17 Idealized catena covering the most typical features of the geomorphologic compartment VI.

For explanation of the profiles see text below.

<u>Zone 1</u> Cambisols / Ferralsols of hummocky steep slopes on basement.

Similar to zone 2 in compartment V, generally steeper.

<u>Zone 2</u> Cambisols / Lixisols of summits and steep slopes on carbonates.

Similar to zone 4 in compartment II but often steeper.

<u>Zone 3</u> Allochthonous Ferralsols at concave locations.

Depending on slope, well-structured and permeable red topsoil material of variable thickness accumulates at footslope or concave positions, often separated from the subsoil by a stoneline.

Hydrological characteristics:

Shallow to deep interflow and infiltration dominate, depending on local slope and depth to epikarst.

Erosion hazard:

Medium to high risk of shallow erosion exists at headwater locations. Propagation of gullies is possible but limited by the comparatively shallow depth of the subsoil.

<u>Zone 4</u> Gleysols and Fluvisols of alluvial plains draining basement area

Similar to zone 1 in compartment II and V.

Zone 5) Cambisols / Lixisols of steep hummocky footslopes on carbonates.

Similar to zone 4 in compartment II.

<u>Zone 6</u> Allochthonous Ferralsols at locally concave locations on siltite.

Similar to Zone 3 of compartment III but with less extensive topsoil accumulation.

<u>Zone 7</u> Eroded Ferralsols at lower summits of the Serra de Santa Helena meta-pelites

Similar to zone 2 in compartment IV

9.13 Landscape examples for Compartment VI

Typical locations of the soil zones 1 - 7 from the geomorphologic compartment VI are indicated in Figure 9-18, which shows a satellite image of the central study area (rectangle VI in Map 6 in the annex). The maps below show the terrain positions of the soil zones using the regional (Figure 9-19 A) and local (Figure 9-19 B) topographic position index.

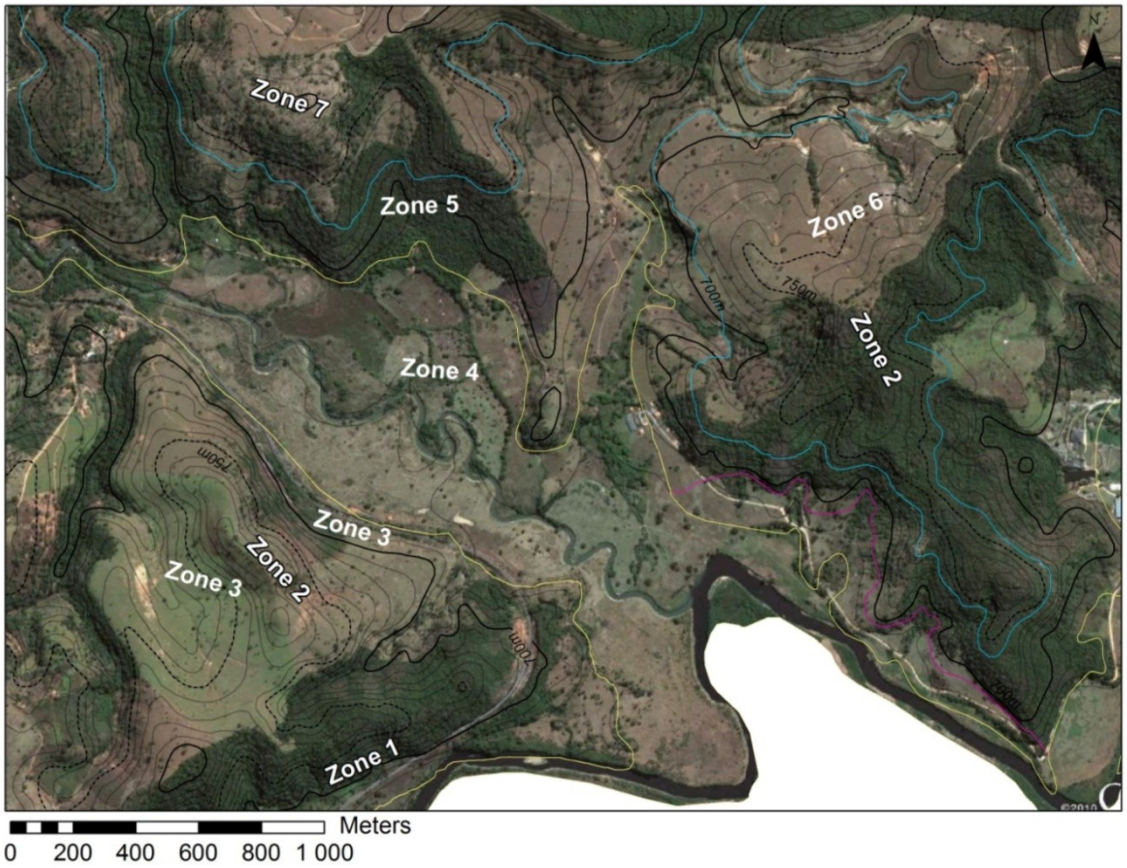

Figure 9-18 Landscape of geomorphologic compartment VI south-east of Lagoa Santa.

Image taken from Google Earth from 20th July 2010 (rectangle VI in Map 6). The blue line indicates the contact between Serra de Santa Helena meta-pelites (zones 6 - 7) and the carbonates of the Sete Lagoas Formation (zones 2,3 and 5). The pink line indicates the contact between basement (zones 1) and Bambuí sediments.

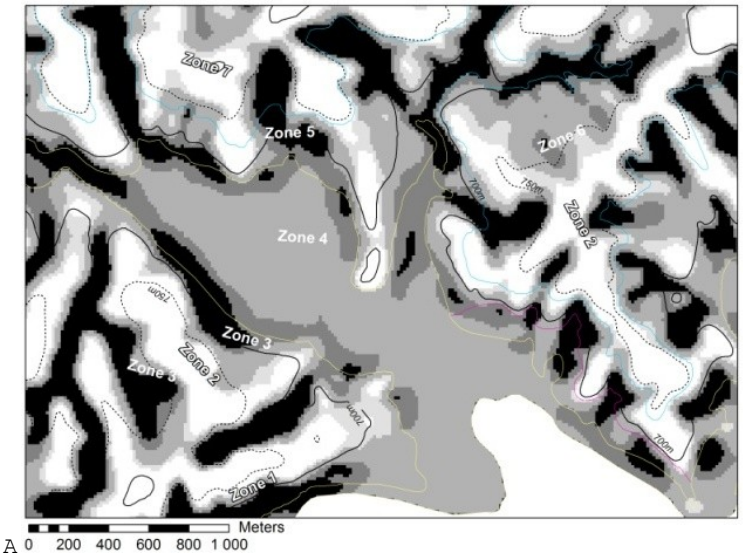

A

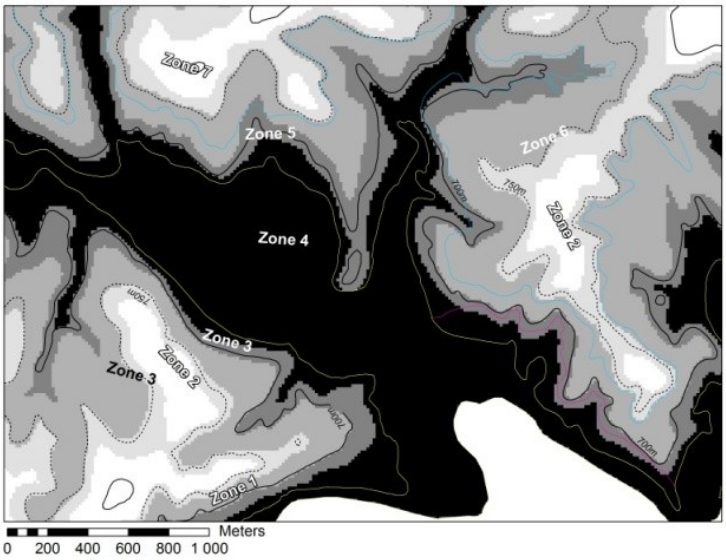

B

Figure 9-19 (A) regional TPI and (B) local TPI of the area shown in Figure 9-18.

Dark colors indicate areas that are lower than surrounding average, light colors indicate areas that are higher than the surrounding average. For the regional TPI, the zone of comparison comprises a circle of 3000 m diameter, for the local TPI, the zone of comparison a circle of 200 m diameter. More details about TPI calculation can be found in section 10.3.3.

10 Regionalization of hydrological soil properties

10.1 Literature review

10.1.1 Digital soil mapping

Extracting hydrological soil properties for modeling at catchment scale from traditional soil maps is often difficult. These maps combine several properties into one mapping unit: chemical-, physical-, soil genesis-, and sometimes also geomorphological- and biogeographical parameters or features. Traditional soil mapping units are crisp in attribute space as well in as in their geographic space: the attributes of soil classes are sharply defined by soil classification systems and the spatial distribution of soil units is delimited by discrete polygons. In nature, soils and soil properties vary continuously in both aspects, even though some boundaries can be sharp, e.g. when following geological units (Burrough et al. 1997). In attribute space, characteristic soil properties such as texture, horizon thickness or chemical properties vary continuously between soil classes. In geographic space, there is a continuous gradient of soil types along a catena, e.g. between ridgetop and footslope of a hill. Thus, hydrological properties may vary considerably within one traditional soil unit while being similar between two different units.
Since many spatial parameters are nowadays available continuously at catchment scale, many successful methods have been published that automatically derive continuous soil properties or soil classes from readily available spatial parameters (McBratney et al. 1992, Moore et al. 1993, Burrough et al. 1997, McBratney et al. 2000, Shi et al. 2004, Henderson et al. 2005, Qi et al. 2006, Shi et al. 2009, Behrens et al. 2010).

The major difficulty for most projects of digital soil mapping has been knowledge acquisition from field experienced soil surveyors (Weibel et al. 1995, Shi et al. 2004, Qi et al. 2006, Shi et al. 2009). Hudson (1992) states that *"trained soil scientists can delineate bodies of soil accurately on the landscape by directly examining less than one thousandth of the soil below the surface. They can do this because of the validity of the soil-landscape model."* Thus, soil maps and their legends can be seen as representations of structured knowledge of soil-landscape interrelation (Bui 2004) which is nevertheless difficult to extract and write down explicitly. This large amount of tacit knowledge in soil survey, which is also discussed in Hudson (1992) often results in discrepancies in legends (attribute space) as well as in the spatial outlines of soil units (geographical space) between adjacent soil maps generated by different soil surveys. Based on the concept of treating soil maps as knowledge system, Bui (2004) formulates the workflow in Figure 10-1 to show how human knowledge can be transformed into a database that can drive an inference engine for extracting specific, case relevant knowledge.

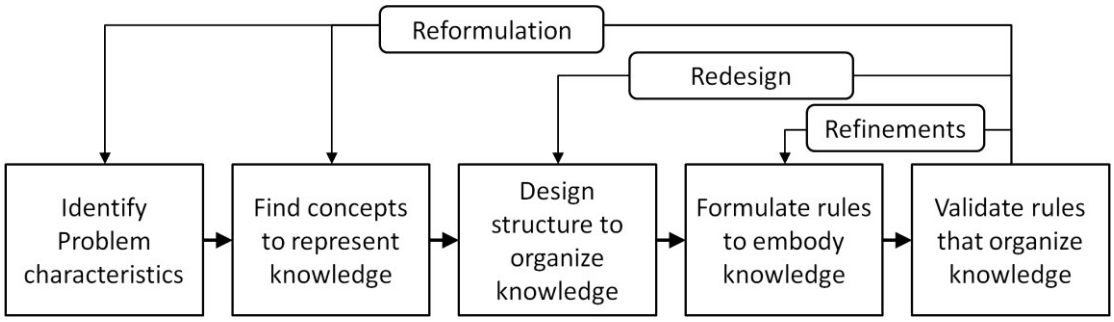

Figure 10-1 Schematic of knowledge system development.

Published in Hofmann et al. (2013) and based on Bui (2004).

10.1.2 Knowledge acquisition

To overcome the difficulty in soil knowledge acquisition and to better extract the tacit information of the soil-landscape model of experienced soil surveyors, Qi et al. (2006) suggest a procedure based on the prototype theory developed in the area of cognitive psychology (Rosch 1973, 1978). This theory provides a concept about how the human mind deals with categories: while categorizing an object, attribute or an action, we internally compare it with a prototype example that we see as most characteristically. Thus, instead of defining a tree as an object with leaves and a wooden stem, we unconsciously compare it with a typical tree (e.g. a beech or a spruce tree) and then decide how "treeish" the object at hand might be. This leads not only to a fairly consistent (but culturally dependent) category structure but also to a grade notion about the typicality of a given instance.

Opposed to categorization in everyday life, in science categories are often defined exactly by their boundary conditions to reach a well defined standard for communication and analysis. Thus, soil classes or soil categories are well defined through specific taxonomic limits (e.g. minimum horizon thickness, maximum cation exchange capacity). Nevertheless, during field survey, soil scientists often do not use these exact rules (which often need also verification by laboratory analysis) but compare a local soil profile with a prototype soil profile in mind and then decide how mu it deviates from this prototype. The more experienced a soil surveyor, the more instances of a soil prototype he or she can use for comparison. Field experienced soil scientists usually do not only have a notion about how typical a soil profile is but also how typical the landscape position is at which it occurs and how far a continuous soil unit stretches in space. Using these ideas from Rosch's prototype theory, Qi et al. (2006) asked soil scientists to define typical soils for a study area and describe typical environmental factors associated with them (e.g. flat slope, convex topography) as well as how changing factors would influence the optimality of a location.

10.1.3 The semantic import model (SIM) approach

From this descriptive information, optimality curves can be created using the Semantic Import Model (SIM) approach (Burrough 1989, Burrough et al. 1997, McBratney and Odeh 1997). In the SIM approach, fuzzy membership functions ("optimality curves", Zhu A-X (1999)) are defined without direct reference to data but constructed from "soft" knowledge described in normal language. In the study of Qi et al. (2006), the prototype base1567890ßd Semantic Import Model performed better at least for the main soil types of the test region than a similar approach where the fuzzy membership functions were derived directly from a given data base. The later method on the other hand performed better for local exceptions that were not represented in the overall soil-landscape model the experts had in mind. Nevertheless, the data based generation of membership functions has the disadvantage that a large database is needed for the construction of the model. When extracting continuous soil properties such as topsoil texture, both approaches performed significantly better than soil properties extracted from classical double - crisp maps.

10.2 Regionalization method chosen for the study area

Taking into account the experiences from Qi et al. (2006), the workflow for regionalizing hydrological soil properties in the study area north of Belo Horizonte was designed as following: The basis is a sound understanding of geology-soil-landscape interrelation as described in the previous chapters, especially the idealized catenas for the six geomorphological compartments (chapter 9). For each prototype location along a catena, typical soil properties as well as typical environmental parameters are listed. These statements are then used for GIS-based regionalization of physical soil properties. The created maps are validated using experience from field observation, plausibility analysis and comparison with visual information from satellite data. Afterwards, the input functions and their combinations are modified if necessary.
This plausibility check means also that the tacit part of the internal soil-landscape model that cannot be represented through catenas or regionalization rules is nevertheless used as validation instrument. Thus, in a recursive process, the input regionalization rules are modified until the spatial result is in concordance with the internal geology-soil-landscape model (Figure 10-2).

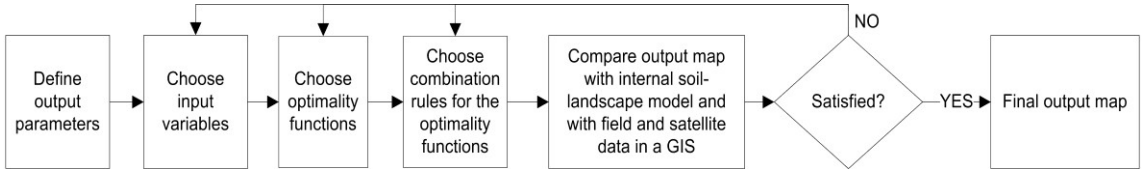

Figure 10-2 General workflow for regionalizing hydrological soil properties using the semantic import approach.

This workflow describes step 3 in Figure 3-1 (Hofmann et al. 2013).

The workflow is stored transparently in tools inside the GIS environment and is thus open to updates if new information on soil-landscape interrelation is available.
Although continuous soil maps are used for mapping specific parameters, classified soil maps with sharply outlined units are still the most common because they can combine many different parameters into one map layout most easily. Even when working with continuous soil maps, it is often necessary to create maps of sharp soil classes out of several continuous maps for final presentations. This process if often referred to as defuzzification (Janikow 1998, McBratney and Odeh 1997). Also in the current study, classified maps of hydrological soil types and dominant flow regimes area created out of several continuous maps.

10.2.1 Optimality functions

While optimality values based on geology were estimated directly for each geological unit (section 8.3), the optimality values based on topographical values were calculated using continuous functions.
In a first step, all topographical parameters were standardized to a range of [0,1] by subtracting the minimum value and then dividing the result by the value range. This was done for a better comparison of the optimality functions used, especially since some work only for positive input values.
In a second step, the following optimality functions $\mu(v)$ were applied:
Fuzzy small, as implemented in the software ArcGIS 10 (Tsoukalas and Uhrig 1996):

$$\mu_{small}(v_{x,y}) = \frac{1}{1+\left(\frac{v_{x,y}}{s}\right)^{c}}$$

Equation 10-1 "Small"

Fuzzy large, as implemented in the software ArcGIS 10 (Tsoukalas and Uhrig 1996):

$$\mu_{large}(v_{x,y}) = \frac{1}{1+\left(\frac{v_{x,y}}{s}\right)^{-c}}$$

Equation 10-2 "Large"

with

$v_{x,y}$ = input variable value at point x, y

$\mu(v_{x,y})$ = output optimality value in a range from [0,1]

c = crossover of the curve with $\mu(c) = 0.5$

s = spread of the curve, a parameter modifying the steepness of the curve

Equation 10-1 and

Equation 10-2 are interrelated as follows:

$$\mu_{large}(v_{x,y}) = 1 - \mu_{small}(v_{x,y})$$

Equation 10-3 Interrelation between "Small" and "Large"

$\mu_{small}(v_{x,y})$ is not symmetric to the crossoverpoint *c*, i.e. $\mu_{small}(c + x) \neq \mu_{small}(c - x)$
Thus, $\mu_{small}(v_{x,y})$ should be denoted more correctly $\mu_{Notsmall}(v_{x,y})$ instead of $\mu_{large}(v_{x,y})$.

The steepness of $\mu_{small}(v_{x,y})$ depends not only on the spread *s* but also on the crossoverpoint *c* and on the scale range of the input data (Figure 10-3). Thus, for a better comparison, all input data were standardized to a range between 0 and 1.
To translate the meaning of "very", the square of an optimality function can be calculated, and to translate the meaning of "somewhat" its square-root. This is commonly known as "hedge" (McBratney and Odeh 1997). Also for the function with hedges, the counterpart is defined by subtracting it from 1.

$$\mu_{very\ small}(v_{x,y}) = \mu^2_{small}(v_{x,y})$$

Equation 10-4 "Very small"

$$\mu_{somewhat\ small}(v_{x,y}) = \mu^{0.5}_{small}(v_{x,y})$$

Equation 10-5 "Somewhat small"

$$\mu_{not\ very\ small}(v_{x,y}) = 1 - \mu_{very\ small}(v_{x,y})$$

Equation 10-6 "Not very small"

$$\mu_{not\ somwhat\ small}(v_{x,y}) = 1 - \mu_{somewhat\ small}(v_{x,y})$$

Equation 10-7 "Not somewhat small"

For optimality functions that are symmetrically high around a given optimal value ("Near"), Equation 10-8 (Zhu A et al. 2010), a variation of a gaussian curve, was used. Other than the Gaussian "NEAR" function implemented in ArcGIS, this function allows to directly define the crossover point c.

$$\mu(v_{x,y}) = e^{-\left(\frac{(v_{x,y}-m)\cdot 0.8362}{c}\right)^2}$$

Equation 10-8 "Near"

with

$v_{x,y}$ = input variable value at point x,y

$\mu(v_{x,y})$ = output optimality value in a range from [0,1]at point x,y

m = midpoint of the curve with $\mu(m) = th\ e\ int\ ith\ E(m)$
$= 1\ and\ the\ crossoverpoint\ c\ with\ E(m +/- a\ given\ value,$

c = crossover point of the curve with $\mu(m \pm c) = 0.5$

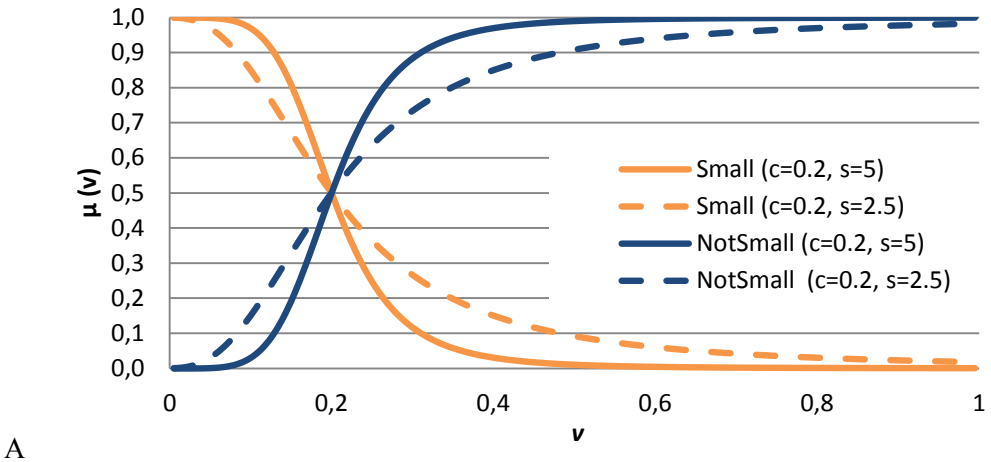

A

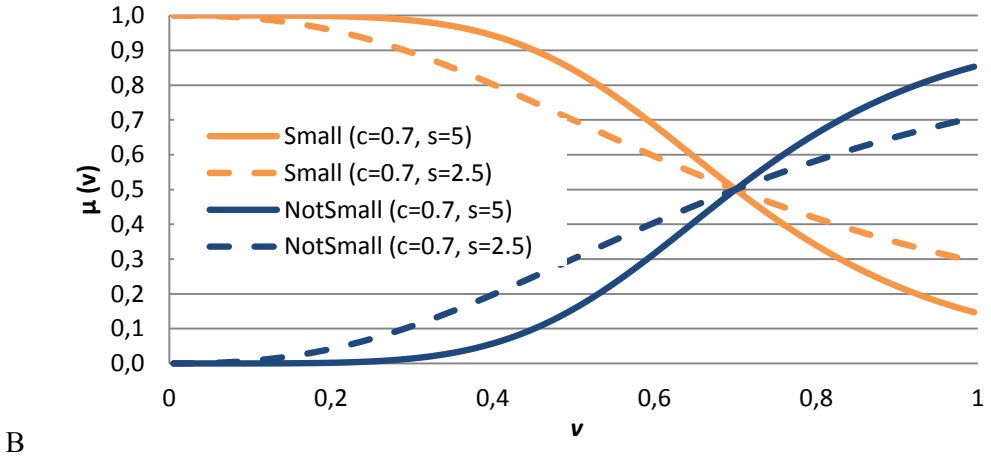

B

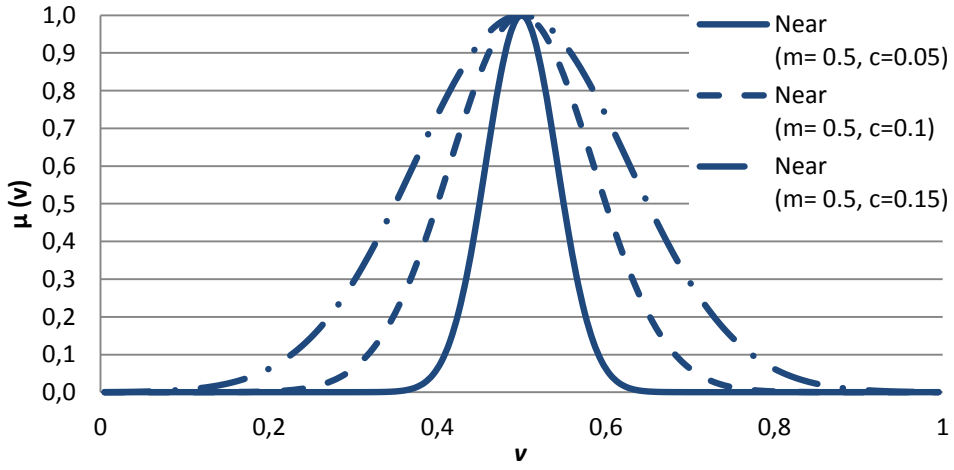

C

Figure 10-3 (A, B) Examples of optimality curves for "small" and "not small" (C) Examples of optimality curves for "near the optimal value 0.5"

M = midpoint, c = crossover point, s = spread. Input values are standardized to the range between 0 and 1.

10.2.2 Overlay functions

To combine the optimality values $\mu_i(v_{i,x,y})$ of *n* different variables, the following overlay functions $P_{i=1}^{n}\left[\mu_i\left(v_{i,x,y}\right)\right]$ were used:

$$Fuzzy\ AND = min_{i=1}^{m}\ \mu_i(v_{i,x,y})$$

Equation 10-9 Fuzzy "AND"

$$Fuzzy\ OR = max_{i=1}^{n}\ \mu_i(v_{i,x,y})$$

Equation 10-10 Fuzzy "OR"

$$Multiplication = \prod_{i=1}^{n} \mu_i(v_{i,x,y})$$

Equation 10-11 Multiplication

$$Weighted\ Sum = \sum_{i=1}^{n} a_i\mu_i(v_{i,x,y})$$

Equation 10-12 Weighted sum

with a_i = weight of variable v_i so that $\sum_{i=1}^{n} a_i = 1$

Figure 10-4 shows the effect of different overlay functions $P_{i=1}^{n}\left[\mu_i\left(v_{i,x,y}\right)\right]$ combining two exemplary optimality curves. All functions are have their output range again between [0,1]. Fuzzy AND simply outputs the minimum value of the input optimality curves and Fuzzy OR outputs the maximum of the input optimality curves. The weighted sum (in this special case of $a_1 = a_2 = 0.5$ equal to the weighted average) results in a value between all input functions. It is always equal or lower than the highest input value and equal or higher than the lowest. The multiplication operator on the other hand results in a value that is always equal or lower than the lowest input value $\mu(v)$ since $\mu(v) \leq 1$. Thus, Fuzzy OR and weighted average are best used for combinations of variables whose influences on the output variable are cumulative and independent whereas fuzzy OR or multiplication are optimal for combinations of interrelated restrictive variables.

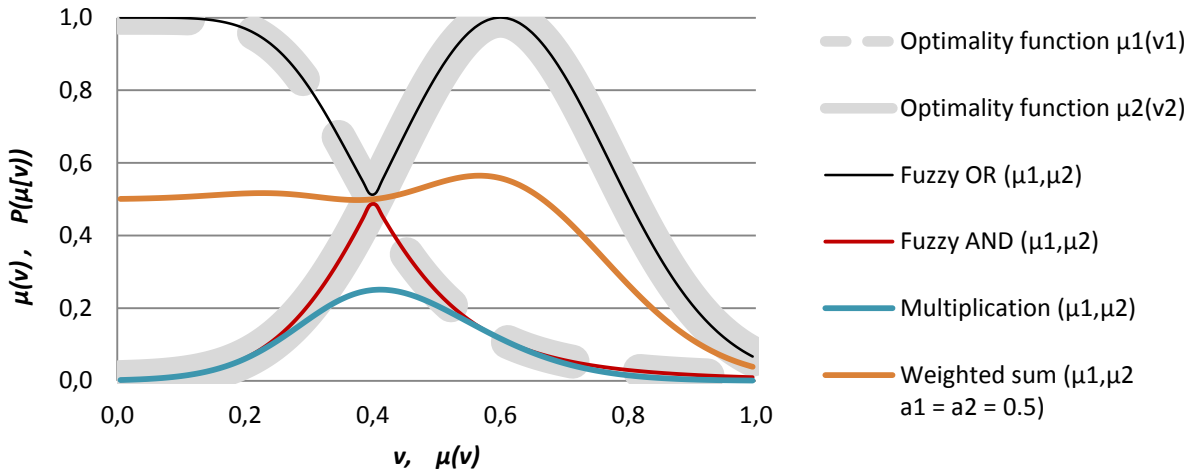

Figure 10-4 Output of different overlay functions $P_{i=1}^{n}[\mu_i(v_i)]$ in a combination of two exemplary optimality functions $\mu_1(v_1)$ and $\mu_2(v_2)$.

10.2.3 Location of two exemplary areas

For the illustration of the regionalization process, the spatial parameter characteristics are shown in higher resolution map extracts in two exemplary characteristic areas: one in the intensely karstified area in the north-west (A) and the other in the covered karst and pelite area near the lake Lagoa Santa (B) (Figure 10-5).

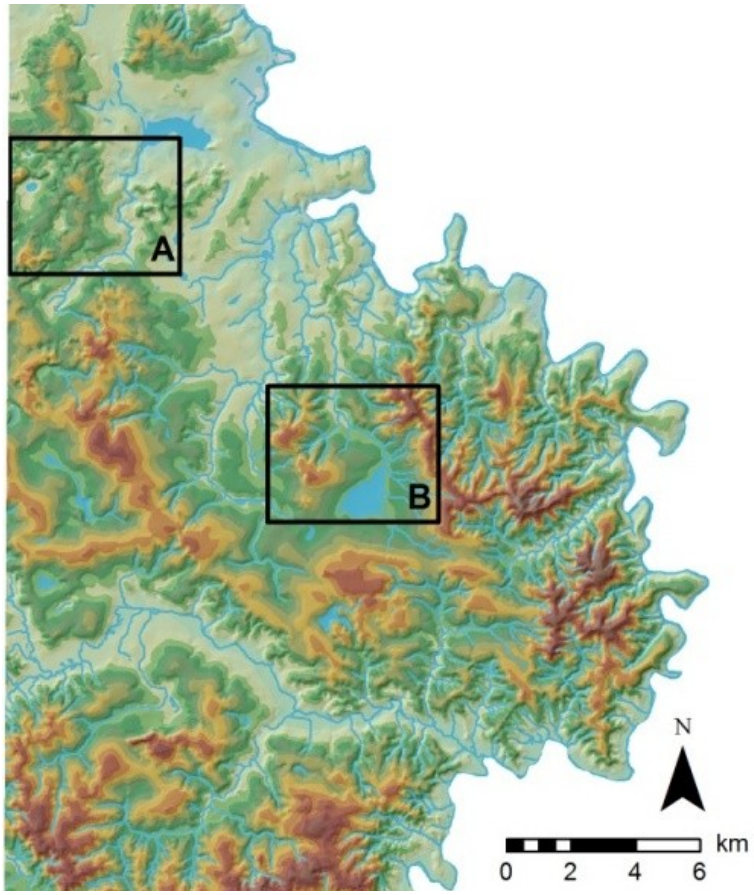

Figure 10-5 Topographic overview of the study area.

Two exemplary areas are used to demonstrate the typical characteristics of the regionalized parameters in the karst region (rectangle A) and in the covered karst region (rectangle B) the following chapters.

10.3 Input basic relief variables

10.3.1 Digital elevation model

The base digital elevation model (DEM) used for all further calculations was interpolated from 10 m equidistant contour lines of a digital topographic map (scale 1 : 25 000) using the Topo to Raster algorithm implemented in ArcGIS (Hutchinson 1989). The river network could not be used as input since the algorithm requires all rivers line features to point downstream, which was not the case. Although some local stair-like artifacts appear due to the too high resolution in areas with less dense contour lines, a resolution of the DEM of 15 x 15 m was necessary to maintain the full information from the topographical map in areas with very dense contour lines, e.g. around limestone outcrops.

10.3.2 Slope

Slope was calculated using the D-infinity algorithm from Tarboton (1997). It is important to note that vertical rock outcrops are difficult to identify via contour lines since the resolution is not high enough and rock outcrops were not identified in the topographic map. Comparing the calculated slope and the geomorphological map 1 : 50 000 fromKohler et al. (1998), nearly all areas in Figure 10-6 A with orange to red colors (i.e. steeper than a calculated slope of 20°) and often also areas with a calculated slope of 15° (yellow areas) are documented rock outcrops. On Bambuí meta-pelites (Figure 10-6 B), no outcrops of hard rocks are documented even at very steep locations.

When calculating the optimality values for "flat" slope using to the equation for fuzzy "small" (Equation 10-1, page 180), the following criteria were applied:

The crossover point *c* (where the optimaltiy value is 0.5 by definition), was set to the mean slope of the whole study area (9°) to define "flat" slopes The stretch *s* defining the steepness of the function was chosen based on the histogram of the slope values in the study area (Figure 10-7) and the visual plausibility of the output maps (Figure 10-8) compared with field experience. The functions are listed below:

$$\mu_{flat\ slope} = \mu_{small}(standardized\ slope) \text{ with } c = 0.18\ (=\ 9°\ slope) \text{ and } s = 2.5$$

Equation 10-13 "Flat slope"

$$\mu_{not\ flat\ slope} = 1 - \mu_{flat\ slope}$$

Equation 10-14 "Not flat slope"

With μ_{small} defined by Equation 10-1 from page 180.

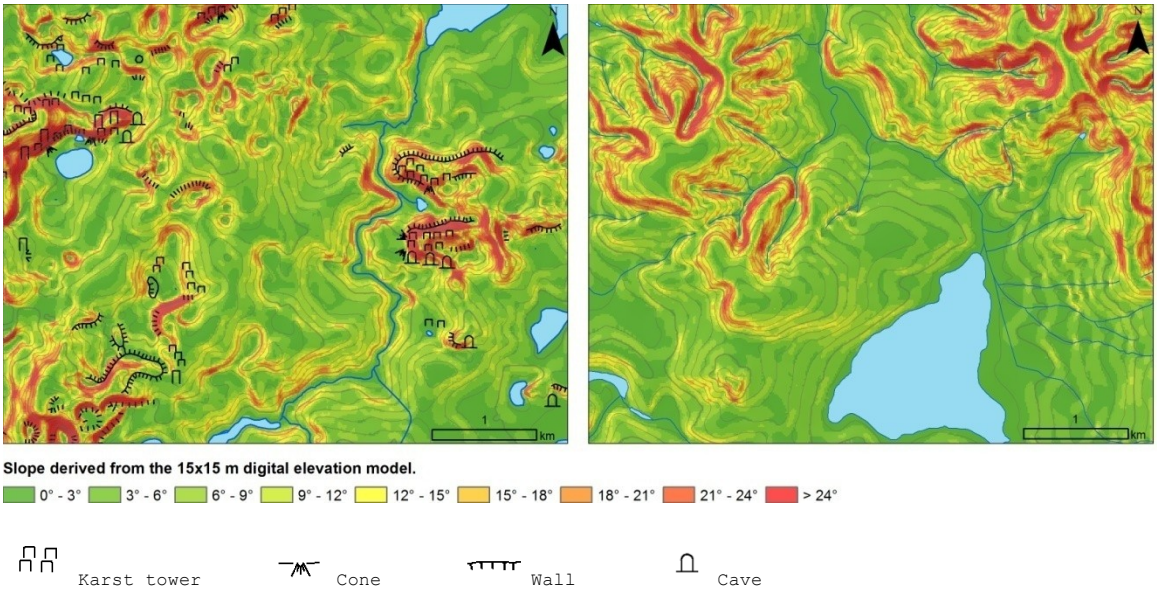

Figure 10-6 Slope values in degree.

The values were derived from the 15 x 15 m DEM, which itself was interpolated from 10 m equidistant contour lines using the algorithm from Hutchinson (1989). The location of the exemplary areas is indicated in Figure 10-5 (karstified terrain A on the left, covered karst area B on the right). Orange to red colors on the left map are correlated with documented limestone outcrops from Kohler et al. (1998). See also Map 8 in the annex.

Additionally, the square function of "flat slope" was calculated that decreases the "flat slope" optimality values and can be interpreted as "very flat slope" (compare Equation 10-4). This procedure of translating the meaning of "very" using the square of an optimality function is also known as "hedge" (McBratney and Odeh 1997). If this function is subtracted from 1, it can be interpreted as "not very flat slope". The shape of the optimality curves are shown in Figure 10-7. To to identify areas of potential karst outcrops on very steep slopes, a similar function but with crossover at 15° and stretch of 5 was useful (Figure 10-7, compare also Figure 10-6). Completely flat areas on the other hand were identified using an optimality function with crossover point at 3° and a stretch of 2. The equations for "very steep" and "completely flat" slope are listed below and the spatial characteristics of the distribution of optimality values is shown in Figure 10-8.

$$\mu_{very\ steep\ slope} = \mu_{not\ small}\,(standardized\ slope) \text{ with } c = 0.297\ (= 15°\ slope) \text{ and } s = 5$$

Equation 10-15 "Very steep slope"

$$\mu_{not\ very\ steep\ slope} = 1 - \mu_{very\ steep\ slope}$$

Equation 10-16 "Not very steep slope"

$$\mu_{Completely\ flat\ slope} = \mu_{small}(standardized\ slope) \text{ with } c = 0.0594\ (= 3°\ slope) \text{ and } s = 2$$

Equation 10-17 "Completely flat slope"

$$\mu_{Not\ completely\ flat\ slope} = 1 - \mu_{completely\ flat\ slope}$$

Equation 10-18 "Not completely flat slope"

With μ_{small} defined by Equation 10-1 from page 180.

To avoid stair-like artifacts that are typical results of the DEM interpolation algorithm if the cell size is much smaller than the distance between the contour lines (which is the case for flat slopes, as can be seen in Figure 10-8), the optimality value for "flat slop" was averaged within a circular surrounding of 120 m diameter and that of "completely flat slope" within a surrounding of 240 m.

Figure 10-8 shows examples of the spatial output of the optimality functions at two exemplary locations. While for "flat" or "not flat" optimality functions the slope classes are equally distributed in both locations, "very flat" slopes reach high optimality values only for hilltops, alluvial plains or doline floors. The "very steep" function singles out known karst outcrops from location A but also reaches high optimality values for steep slopes on meta-pelites where no rock outcrops are documented.

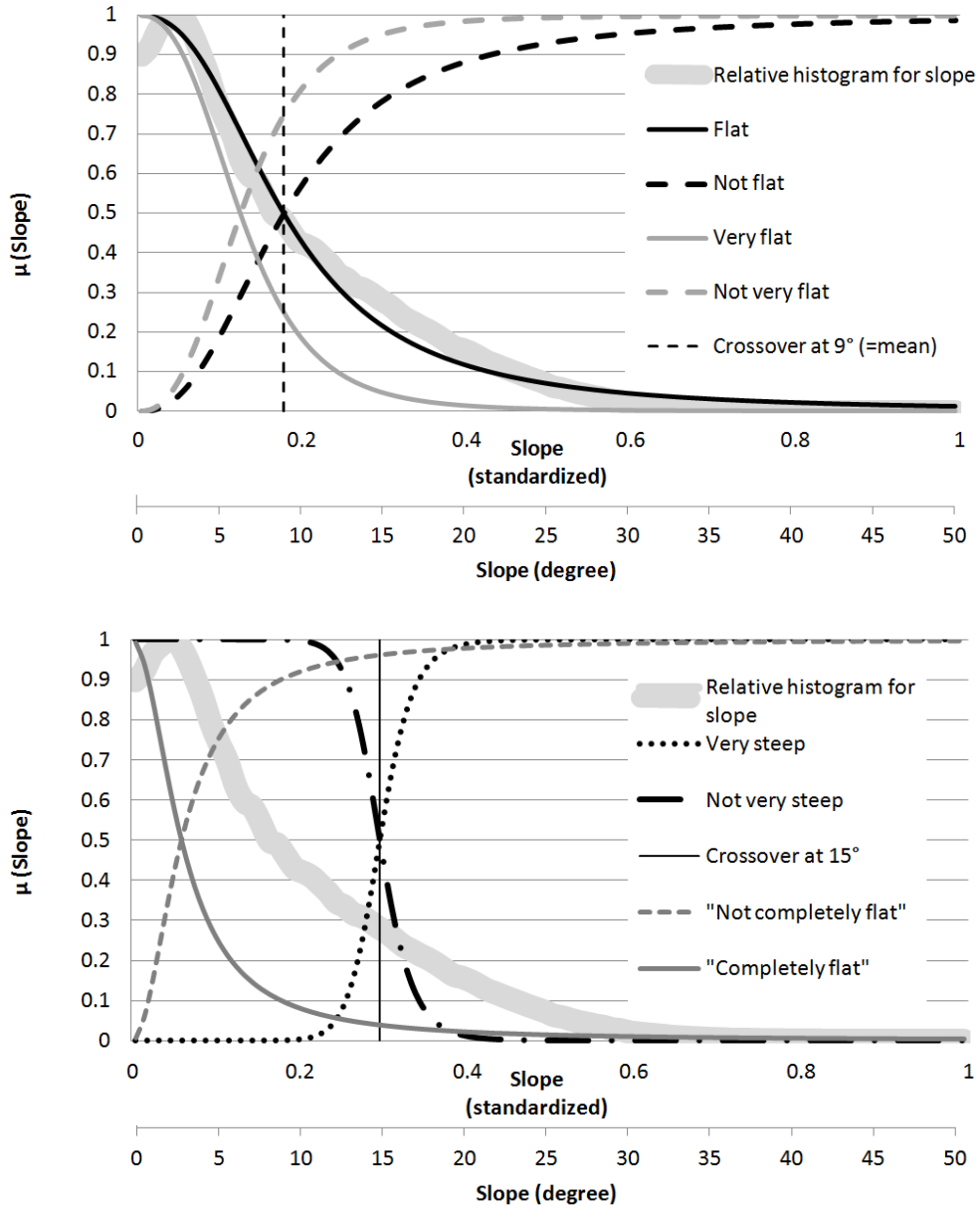

Figure 10-7 Optimality functions for different semantic statements regarding slope.

The relative histogram shows the frequency of slope values in the study area for comparison.

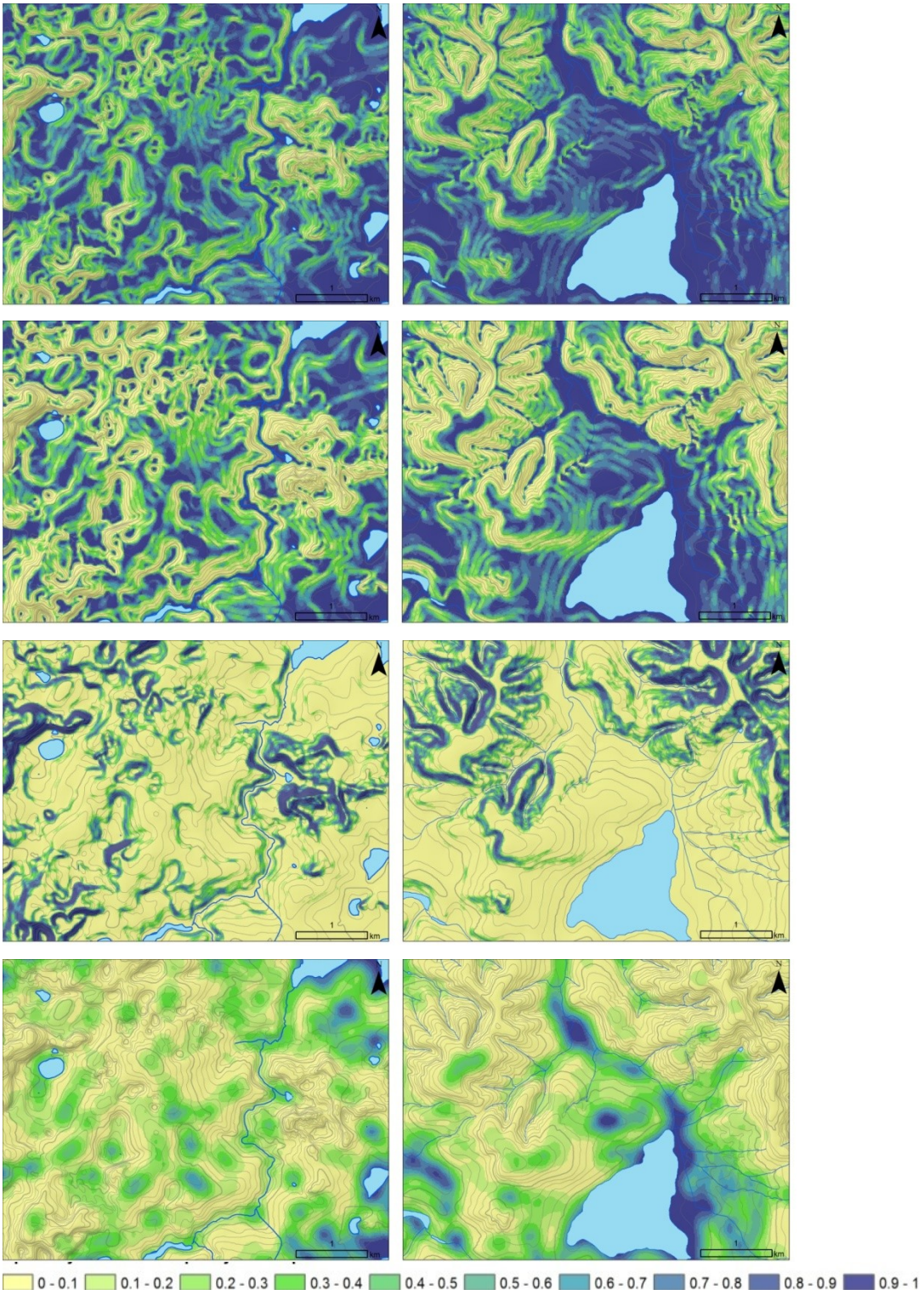

Figure 10-8 Spatial characteristics of the optimality maps (from top to bottom): "flat", "very flat", "very steep" and "completely flat" slope in the areas shown in Figure 10-5.

To avoid stair-like artifacts, the values for "flat" and "very flat" were averaged within 120m and those for "completely flat" within a neighborhood of 240m. The opposite functions (e.g. "not flat") can be visualized by inverting the legend.

10.3.3 Topographic Position Index (TPI):

Since landscape position is an essential part for the description of a prototype location, different parameters were used to describe it most adequately. Weiss (2001) describes a simple but elegant method for the derivation of a topographic position index by subtracting the average elevation of a neighborhood region from the elevation of the central raster cell (Figure 10-9).
The thus derived topographic position index (TPI) is positive for ridges and hilltops and negative for valleys and depressions. Since the TPI is zero for midslope positions as well as for flat areas, it is important to include slope for the final determination of the landscape position.
The size of the neighborhood decides whether small topographic features are identified by the TPI-calculation or not (Figure 10-9). According to Weiss (2001), a circular neighborhood of 300 m diameter can identify many individual ridge lines and valleys including small lateral drainages while wide valleys cannot be distinguished from flat areas. A larger neighborhood of 2000 m diameter identifies the highest mountains and major ridge lines as well as large valleys but neglects smaller lateral features. Since the absolute difference of elevation of the cell compared to the average of its surroundings varies depending on the neighborhood size, a good measure is to classify the TPI in intervals equal to the standard deviation of all values within the study area (Figure 10-10).
For the project, three different topographic indices were chosen that together describe well the morphology of the terrain: a local topographic index (LPTI) with a circular neighborhood size of 200 m diameter, a medium topographic index (MTPI) with a circular neighborhood size of 1000 m diameter and a regional topographic index (RTPI) with a circular neighborhood size of 3000 m diameter.
The output of the LTPI looks similar to the that of the curvature algorithm implemented in ArcGIS that was used in other studies (Moore et al. 1993, Zevenbergen and Thorne 2006), but with less interpolation artifacts (Figure 10-10 upper pictures) because of the larger neighborhood compared to the 3x3 calculation window of the standard curvature algorithm. The MTPI indicates footslopes and hilltops along small to medium sized rivers (Figure 10-10 central pictures) and the RTPI indicates large depressions such as uvalas or alluvial plains of larger rivers and high ridges of regional importance such as the old plateau surfaces (Figure 10-10 bottom pictures).

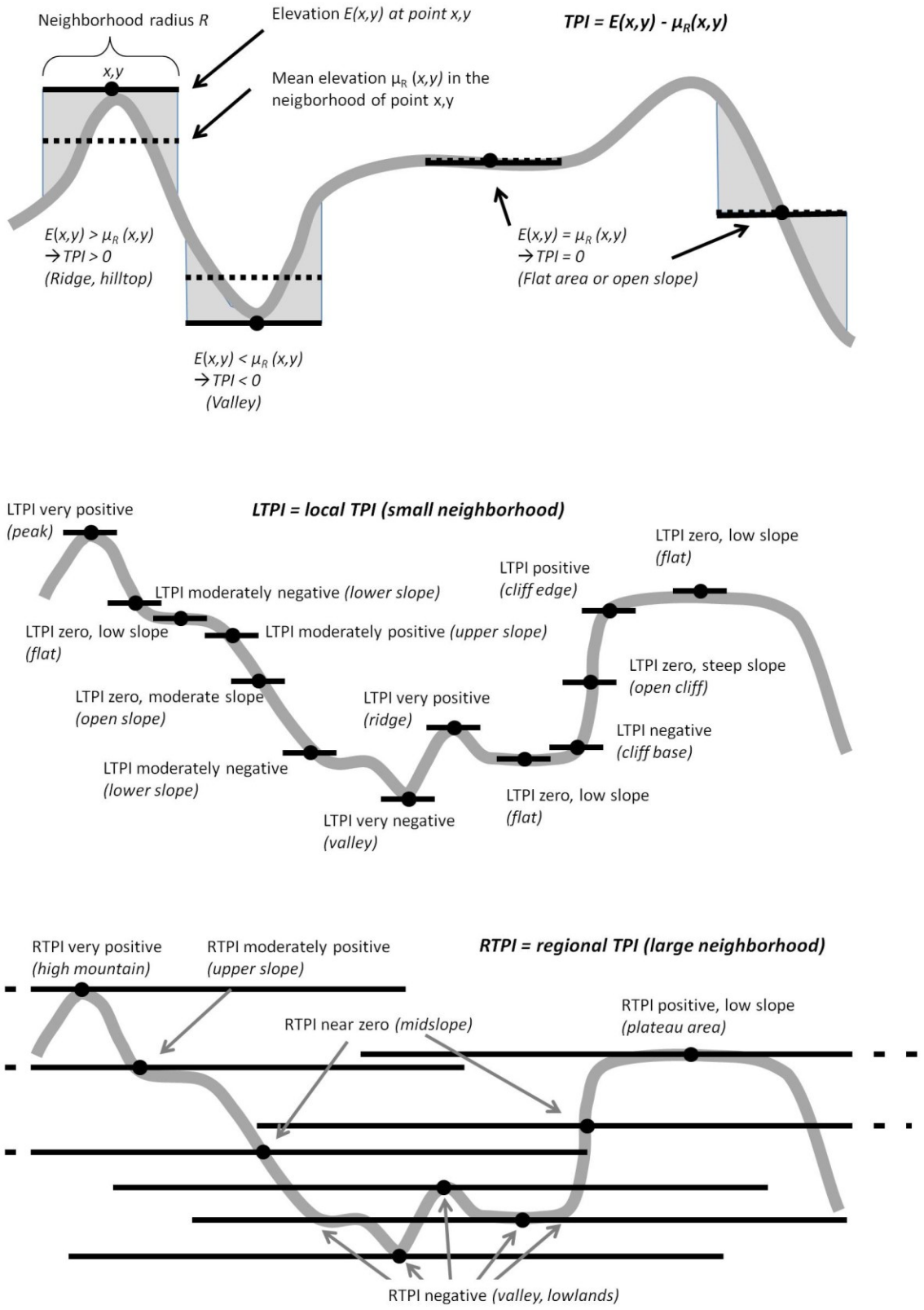

Figure 10-9 Illustration of the calculation of regional or local topographic position index.

Graphic from Hofmann et al. (2013) modified after Weiss (2001).

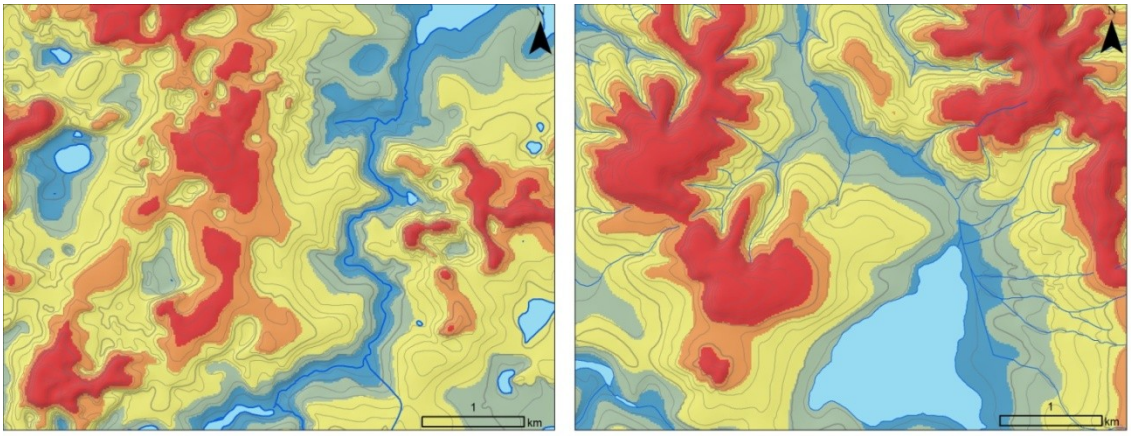

Regional topographic position index (RTPI) calculated using a circular neigborhood of 3000 m diameter.

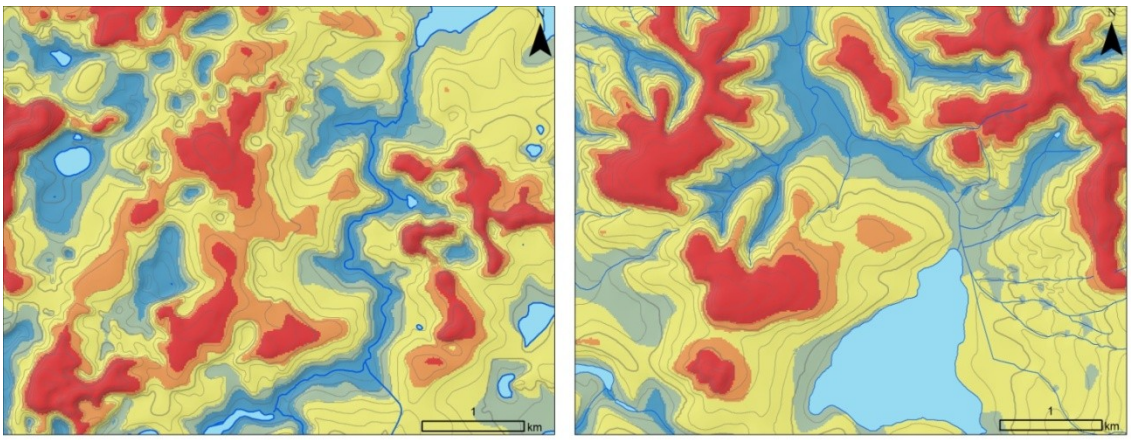

Medium topographic position index (MTPI) calculated using a circular neigborhood of 1000 m diameter.

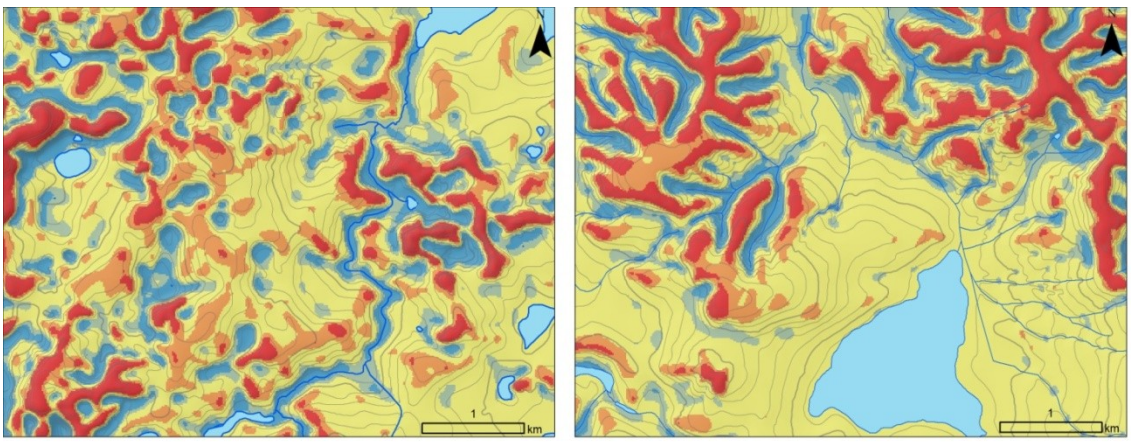

Local topographic position index (LTPI) calculated using a circular neigborhood of 200 m diameter.

< Mean - 1.0 Stdv | (Mean - 1.0 Stdv) until (Mean - 0.5 Stdv) | Mean +/-0.5 Stdv | (Mean + 0.5 Stdv) until (Mean + 1.0 Stdv) | > Mean + 1.0 Stdv

Figure 10-10 Local, medium and regional TPI visualized for the exemplary areas indicated in Figure 10-5.

Karstified terrain A on the left, covered karst area B on the right. See also Map 13 - Map 20 in the annex.

Local TPI (LTPI)

The local topographic index (LTPI) was transferred into one general optimality function "low" LTPI and its counterpart "not low" LTPI using the following parameters:

$$\mu_{low\ LTPI} = \mu_{small}\ (standardized\ LTPI) \text{ with } c = 0.51\ (= 0\ \text{m LTPI}) \text{ and } s = 11$$

Equation 10-19 "Low LTPI"

$$\mu_{not\ low\ LTPI} = 1 - \mu_{low\ LTPI}$$

Equation 10-20 "Not low LTPI"

With μ_{small} = defined by Equation 10-1 from page 180.

The function is nearly symmetrical (Figure 10-11) with the crossover point set to the zeropoint of the original data, i.e. where the elevation of the local cell is equal to the average of its neighborhood. The stretch was chosen according to the histogram of the input data and the plausibility of the spatial distribution of the optimality values.
The spatial output of this optimality function for "low" local TPI can be seen in Figure 10-12 for the two exemplary areas A and B outlined in Figure 10-5. In both areas, high optimality values of "low" local TPI indicate narrow, deeply incised water courses. In the karst area (location A), also dolines and footslopes of rock outcrops receive high optimality values and in the Bambuí meta-pelite area (location B), typical headwater locations are also highlighted. Low optimality values define sharp ridges and in the karst area also limestone rock outcrops.
For some destination variables (deep topsoil, no direct contact with epikarst), it was important to exclude locally convex areas. For this purpose, a combination of a Gaussian function and a manual threshold was used to construct the optimality curve (Figure 10-11 B). The equation for this membership function of "not convex" LTPI areas is:

$$\mu_{not\ convex\ LTPI}(v) = \begin{cases} 1 & if\ \ local\ TPI \leq 0 \\ e^{-\left(\frac{(v-m)\cdot 0.8362}{c}\right)^2} & if\ local\ TPI > 0 \end{cases}$$

Equation 10-21 "Not convex LTPI"

With

μ = optimality value, v = standardized LTPI

m = 0.5149 = standardized zero-point of the local TPI = midpoint of the Gaussian curve, c = 0.2 = crossover point = distance from the midpoint with

$\mu_{not\ convex\ LTPI}\ (m + c) = 0.5$

The value for the crossover-point was chosen by visual analysis of the resulting maps.
The opposite function of "not convex", "convex" is calculated by subtracting the function from 1:

$$\mu_{convex\ L\,TPI}(v) = 1 - \mu_{not\ convex\ L\,TPI}(v)$$

Equation 10-22 "Convex LTPI"

Similarly, a fuzzy membership map was created to exclude concave areas:

$$\mu_{not\ concave\ LTPI}(v) = \begin{cases} e^{-\left(\frac{(v-m)\cdot 0.8362}{c}\right)^2} & if\ local\ TPI < 0 \\ 1 & if\ local\ TPI \geq 0 \end{cases}$$

Equation 10-23 "Not concave LTPI"

With

μ = optimality value, v = standardized LTPI value

m = 0.5149 = standardized zero-point of the LTPI = midpoint of the Gaussian curve, c = 0.2 = crossover point = distance from the midpoint with

$\mu_{not\ concave\ LTPI}(m-c) = 0.5$

The opposite function of "not concave", i.e. "concave", is calculated by subtracting the function from 1:

$$\mu_{concave\ L\,TPI}(v) = 1 - \mu_{not\ concave\ L\,TPI}(v)$$

Equation 10-24 "Concave LTPI"

The spatial result of the parameters is shown in Figure 10-12.

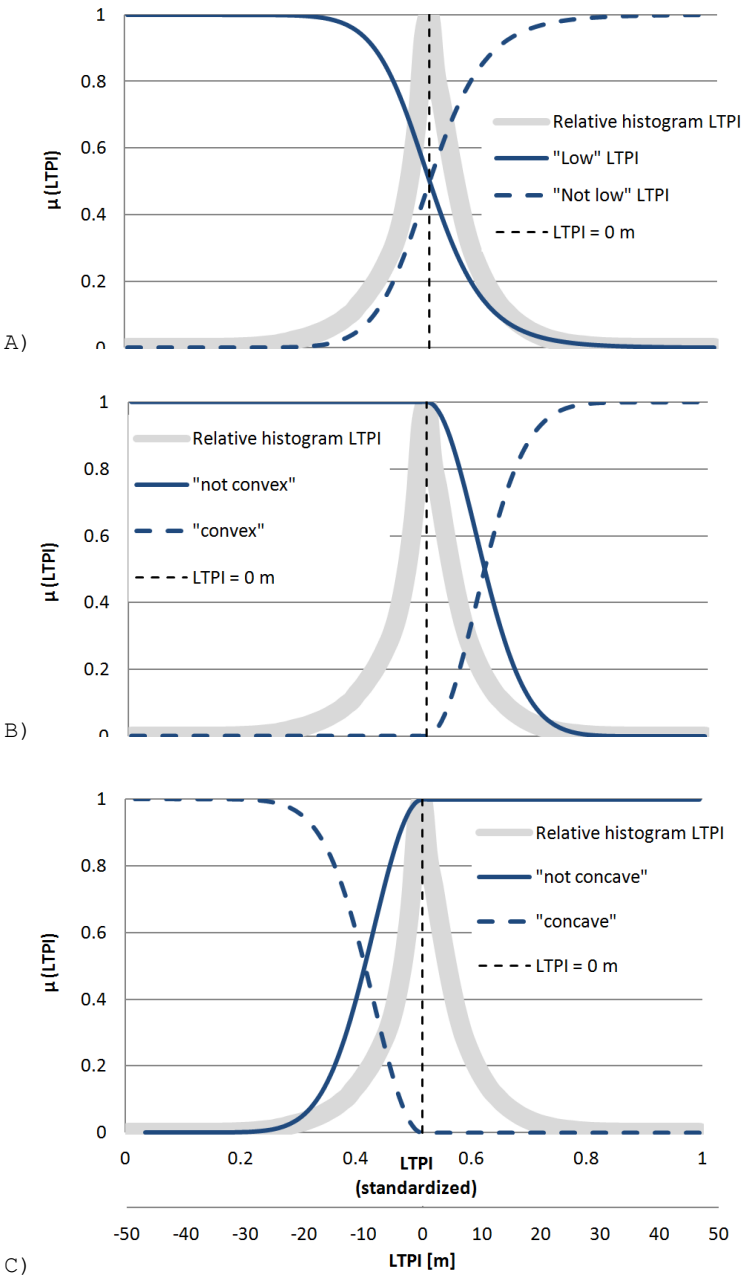

Figure 10-11 Optimality functions defining A) "low" and "not low" LTPI, B) "convex" and "not convex" LTPI and C) "concave" and "not concave" LTPI.

The curves are based on Equation 10-19 until Equation 10-23. For comparison, the relative histograms show the frequency distribution of LTPI values in the study area.

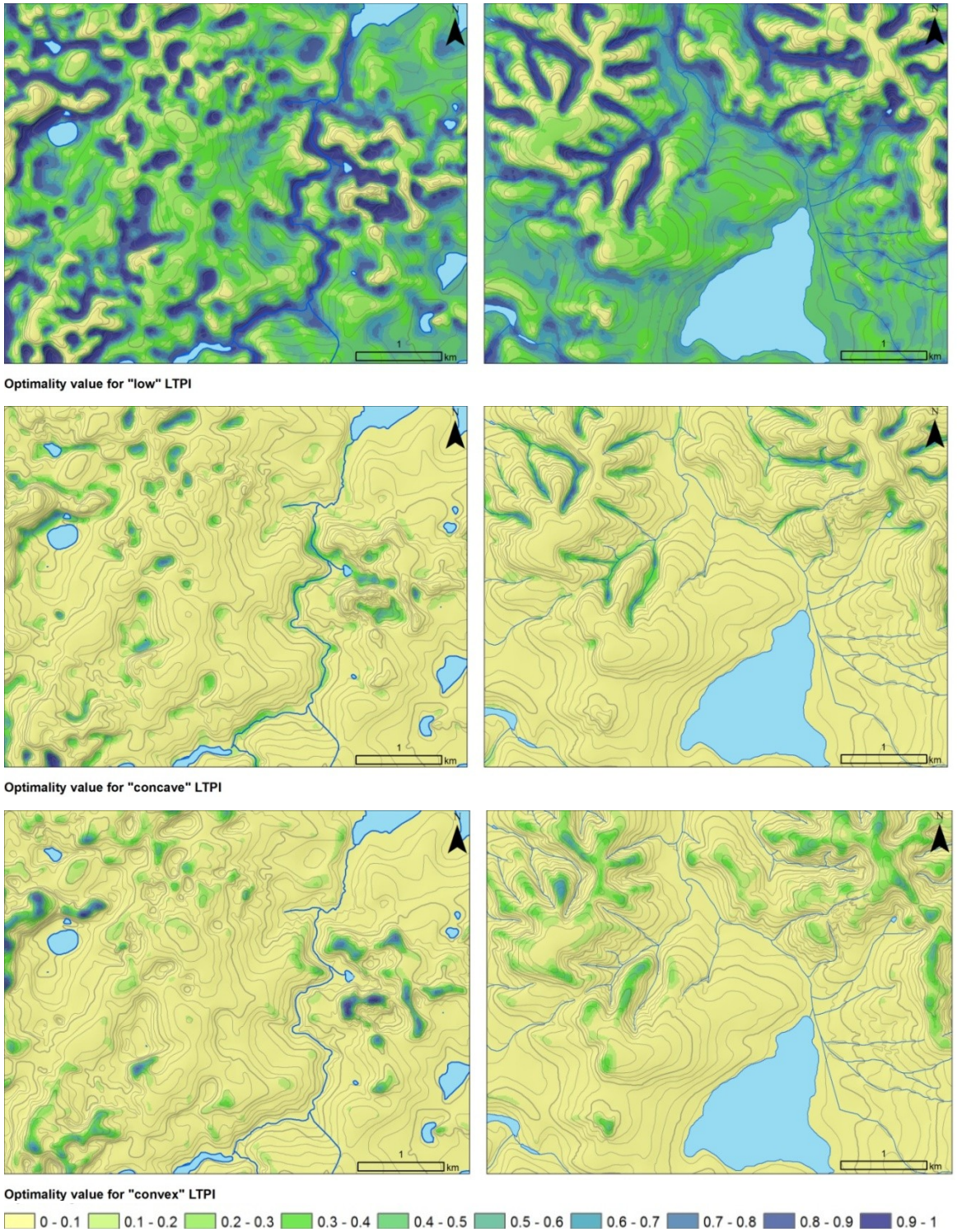

Figure 10-12 Spatial characteristics of the optimality function "low" (upper pictures), "convex" (middle) and "concave" (bottom pictures) LTPI.

The location of the exemplary areas is indicated in Figure 10-5 (karstified terrain A on the left, covered karst area B on the right). Very convex locations often indicate rock outcrops in the karst area but not in the meta-pelite hills. The opposite functions (e.g. "not concave" LTPI) can be visualized by inverting the legend.

Medium TPI (MTPI)

For the medium topographic position index (MTPI), the following optimality function and its opposite were used:

$$\mu_{Low\ MTPI} = \mu_{small}\ (Standardized\ MTPI) \text{ with } c = 0.40\ (= 0\ \text{m MTPI}) \text{ and } s = 5$$

Equation 10-25 "Low MTPI"

$$\mu_{Not\ low\ MTPI} = 1 - \mu_{Low\ MTPI}$$

Equation 10-26 "Not low MTPI"

The optimality function for "very low" MTPI is defined as the square of the "low" MTPI function:

$$\mu_{Very\ low\ MTPI} = \mu^2_{Low\ MTPI}$$

Equation 10-27 "Very low MTPI"

Also for medium TPI, a combination of a Gaussian function and a manual threshold was used to exclude concave or convex areas.

The equation for this membership function of "not convex" MTPI areas is:

$$\mu_{Not\ convex\ M\ TPI}(v) = \begin{cases} 1 & if\ \ MTPI \leq 0 \\ e^{-\left(\frac{(v-m)\cdot 0.8362}{c}\right)^2} & if\ MTPI > 0 \end{cases}$$

Equation 10-28 "Not convex MTPI"

With

μ = optimality value, v = standardized medium TPI value

m = 0.4 = standardized zero-point of the medium TPI (m = midpoint of the Gaussian curve), c = 0.2 = crossover point = distance from the midpoint with $\mu_{Not\ convex\ MTPI}(m + c) = 0.5$

The value for the crossover point was chosen by visual analysis of the resulting maps.
The opposite function of "not convex", i.e. "convex" is calculated by subtracting the function from 1:

$$\mu_{Convex\ M\ TPI}(v) = 1 - \mu_{Not\ convex\ M\ TPI}(v)$$

Equation 10-29 "Convex MTPI"

Similarly, a fuzzy membership map was created to exclude concave areas:

$$\mu_{Not\ concave\ MTPI}(v) = \begin{cases} e^{-\left(\frac{(v-m)\cdot 0.8362}{c}\right)^2} & if\ M\ TPI < 0 \\ 1 & if\ MTPI \geq 0 \end{cases}$$

Equation 10-30 "Not concave MTPI"

With

μ = optimality value

v = standardized medium TPI value

m = 0.4 = standardized zero-point of the medium TPI = midpoint of the Gaussian curve

c = 0.2 = crossover point = distance from the midpoint with

$\mu_{not\ concave\ MTPI}(m - c) = 0.5$

The opposite function of "not concave", i.e. "concave" is calculated by subtracting the function from 1:

$$\mu_{Concave\ MTPI}(v) = 1 - \mu_{Not\ concave\ M\ TPI}(v)$$

Equation 10-31 "Concave MTPI"

The curve for the function "low", "concave" and "convex" MTPI in comparison with the relative histogram of MTPI values for the study area is shown in Figure 10-13. Examples of the spatial output of the optimality functions for the MTPI can be found in Figure 10-14.

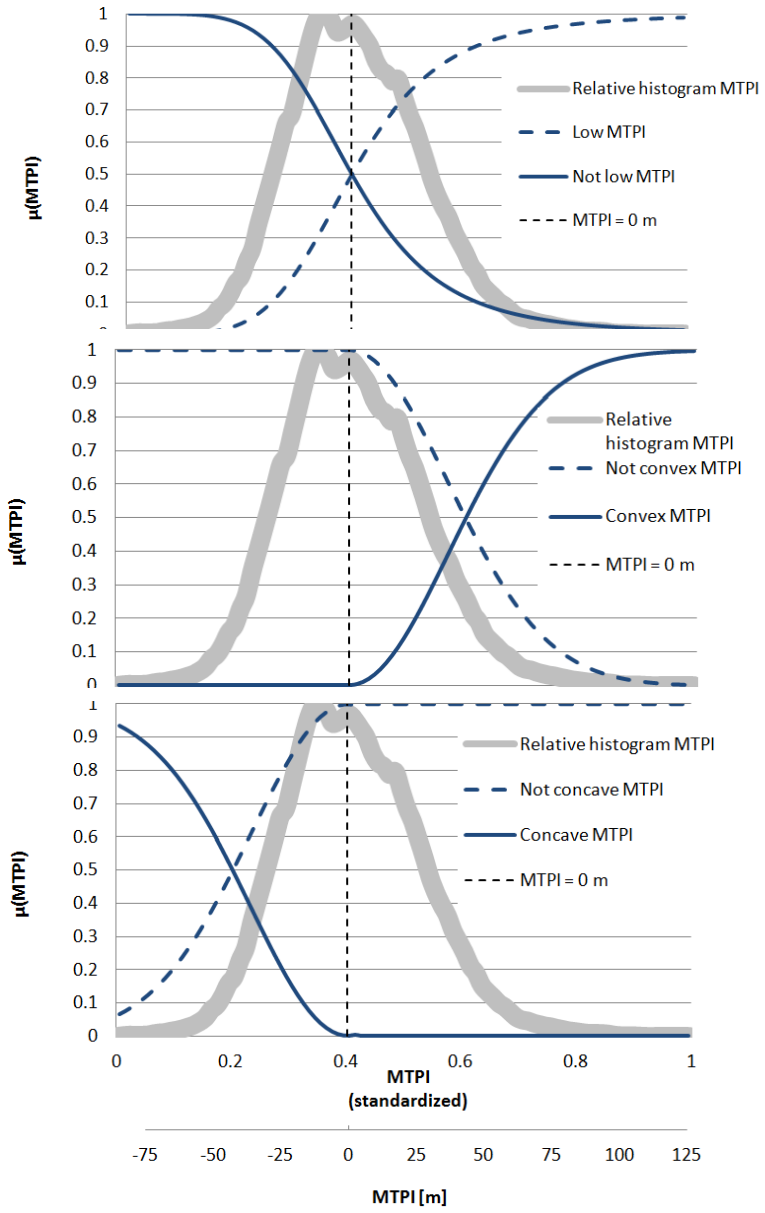

Figure 10-13 Optimality functions defining A) "low" MTPI and "not low" MTPI, B) "convex" and "not convex" LTPI and C) "concave" and "not concave" LTPI.

The curves are based on Equation 10-25 until Equation 10-29. For comparison, the relative histograms show the frequency distribution of LTPI values in the study area.

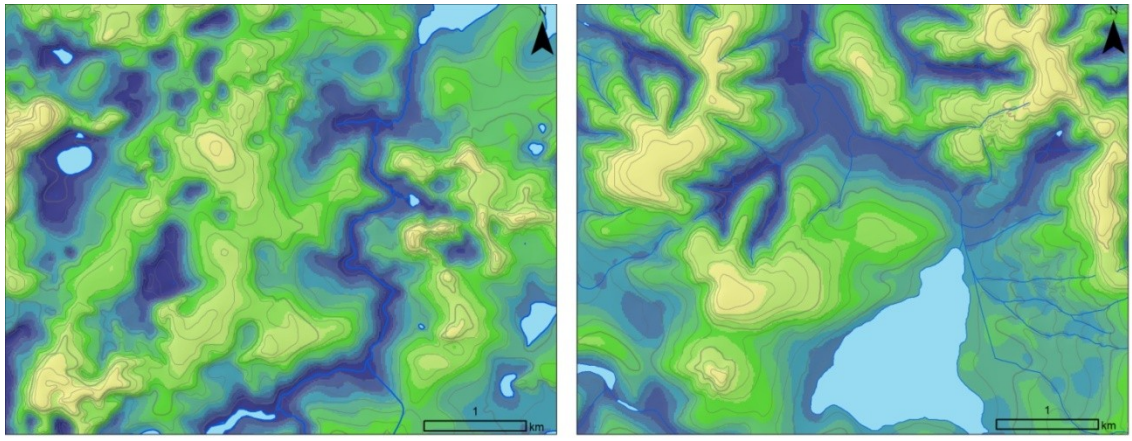

Figure 10-14 Spatial characteristics of the optimality function “low”, “convex” and “concave” MTPI.

The location of the exemplary areas is indicated in Figure 10-5 (karstified terrain A on the left, covered karst area B on the right). The opposite functions can be visualized by inverting the legend.

Regional TPI (RTPI)

For the regional topographic position index (RTPI), the following optimality function was used:

$$\mu_{low}(RTPI) = \mu_{small}\,(Standardized\ RTPI) \text{ with } c = 0.38\ (= 0\ \text{m RTPI}) \text{ and } s = 4$$

Equation 10-32 "Low RTPI"

$$\mu_{high}\,(RTPI) = \mu_{not\ low}\,(RTPI) = 1 - \mu_{low}(RTPI)$$

Equation 10-33 "High RTPI"

The graph of the "low" RTPI optimality function and its spatial result is shown in Figure 10-15.

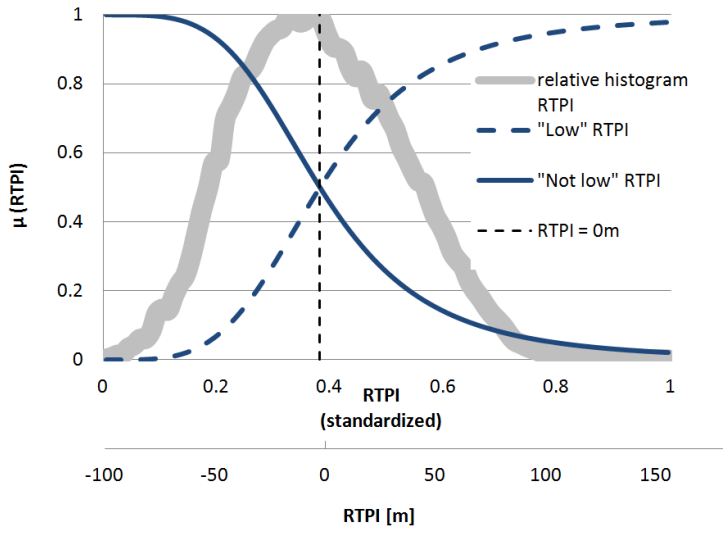

A)

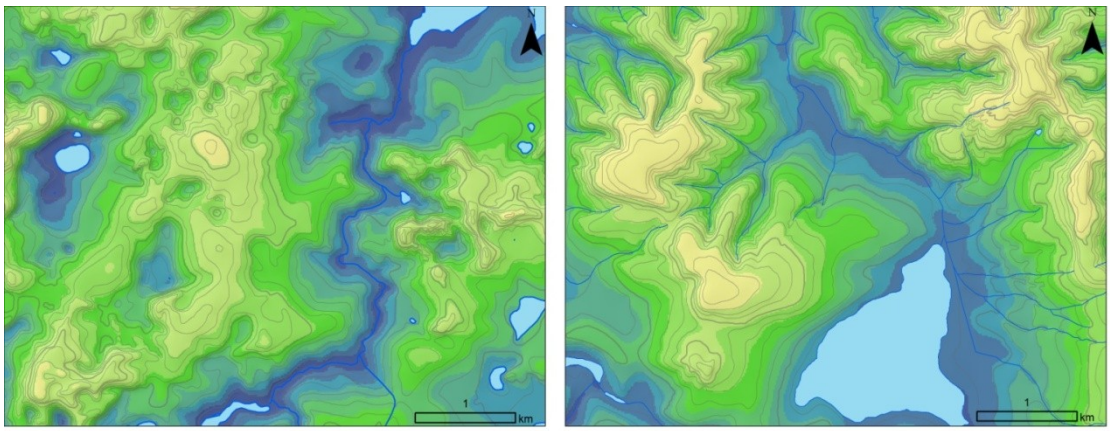

B)

Figure 10-15 A) Optimality curves for "low" RTPI and "not low" RTPI compared to the statistical distribution of RTPI values in the study area. B) Spatial characteristics of the optimality function "low" RTPI.

The location of the exemplary areas is indicated in Figure 10-5 (karstified terrain A on the left, covered karst area B on the right). The opposite function "not low" regional TPI can be visualized by inverting the legend.

10.4 Input hydrological terrain properties

10.4.1 Preparation of the digital elevation model

From the digital elevation model (DEM), hydrological terrain properties can be derived using various algorithms implemented in ArcGIS. All algorithms calculate the water routing and the drainage network from the elevation data of each pixel. Nevertheless, before starting, the digital elevation model has to be modified to take account of artifacts created by the algorithm and to incorporate additional information from existing drainage network and geomorphological data. The preparation of the raw DEM for derivation of hydrological terrain properties was done using the following workflow:

- From the 10 m-equidistant contour lines of the topographic map 1 : 25 000, a digital elevation model was created using the "Topo To Raster" algorithm implemented in ArcGIS (Hutchinson 1989).
- To guarantee that the automatically generated drainage network follows the known hydrology of the topographic map, the elevation of raster cells along digitized rivers and lakes was lowered through a division by ten (a modification of a well-known procedure called “stream-burning” (Saunders 2000).
- Depressions (dolines, uvalas, lakes) indicated in the geomorphological map 1 : 25 000 (Kohler et al. 1998) and lakes from the topographical map 1 : 25 000 were set three meters deeper to modify the flow routing even if the depression was not indicated by contour lines.
- Steepest downhill flow direction (D8-algorithm implemented in ArcGIS) was calculated to identify potential sink locations and their drainage basins.
- Basins and sinks were manually checked if a swallow hole was plausible or if the calculated sink was an interpolation artifact.
- All plausible sinks were selected and converted to a raster file.
- The plausible sinks were reclassified into NoData-values while the rest of the area received the value 1.
- The original DEM was multiplied by the reclassified sink raster so that NoData-values appeared at each verified sink location
- Afterwards, artificial sinks and dead ends due to discontinuous river features created during the stream burning procedure were raised to the elevation of their surrounding cells using a fill algorithm.
- From the filled DEM, watersheds of all plausible sinks and all rivers draining out of the study area were derived.

The watersheds were merged manually to represent the following zonation used for the assessment of karst groundwater vulnerability (see also section 13.5):

- Surface catchment of the Riberão da Mata
- Surface catchment of the Rio das Velhas
- Internal karst drainage towards the Riberão da Mata
- High internal karst drainage towards the Rio das Velhas
- Low internal karst drainage towards the Rio das Velhas

Map 22 in the annex gives an overview of the surface and subsurface drainage situation in the study area. The subsurface hydrology is discussed in section 11.1 and section 13.5.

10.4.2 Elevation above surface water (rivers, lakes or swallow holes)

The elevation above surface water or doline floor can indicate zones of seasonal surface water influence.
Swallow holes were identified using contour lines, hydrological and geomorphological maps, field observation or satellite data. Since the exact location of a swallow hole inside a doline is in most cases unknown, the calculated sink location from the D8-flow routing algorithm was chosen. Lakes were taken from topographic and geomorphologic maps, verified (if possible) by field observation or satellite data. Rivers were taken from the topographic map 1 : 25 000 and adapted to match a continuous flow routing.

The calculation of elevation above local surface water or swallow hole is not easily derived from the DEM since the elevation of the surface water changes. It has to be decided which point along a river should be used as reference for which location around it. Finally, the following method proved to give satisfying results:

For the watershed function implemented in ArcGIS, all cells at river, lake or swallow hole locations were set as pour points with their elevation above sea level (in integer values) as identification number. Thus, for each section along a river having the same elevation in integer-meters, a corresponding sub-watershed was calculated that received this elevation as identification number.
The output raster layer consists of an integer raster of all sub-watersheds with each watershed receiving the elevation value of the surface water or swallow hole it is draining into. Subtracting

this value from the cell elevation according to the digital elevation model, elevation above the nearest river, lake or swallow hole was calculated.

Based on the assumption that a location 10 m higher than the next surface water or swallow hole is not anymore influenced by it, a linear stretch was applied to the absolute values with 0 m receiving the maximum optimality value for “low above next river, lake or swallow hole” and 10 m and higher receiving an optimality value of zero (Figure 10-16).

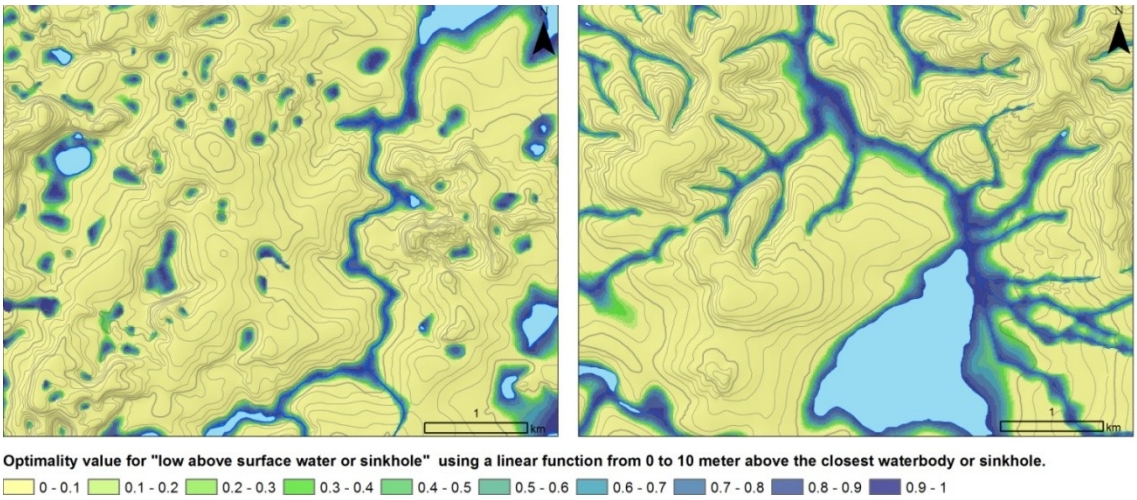

Figure 10-16 Optimality values for “low above next river, lake or swallow hole”.

A linear stretch was used with 0 m receiving the optimality value 1 and 10m and higher receiving the optimality value 0. The location of the exemplary areas is indicated in Figure 10-5 (karstified terrain A on the left, covered karst area B on the right). See also Map 23 in the annex.

10.4.3 Distance to surface water (rivers, lakes or swallow holes)

The distance to surface water or doline floors is related to the risk of surface water contamination via surface runoff.
Swallow holes were also included since the subsurface water velocity in karst areas is similar to surface streams and connected to them via karst springs. As before, swallow holes were based on plausible sinks identified during the preparation of the digital elevation model.
The distance to rivers, lakes or swallow holes was calculated using the "flow length" algorithm from ArcGIS, which calculates the length of the steepest path downhill.

For most purposes, a distance of 500 m is already far from surface water. Thus, 500 m and more received an optimality value of zero for the map showing areas "close to rivers, lakes or sinks". Again, a linear function was applied for shorter distances until a distance of 0 m, which received the optimality value 1 (Figure 10-17).

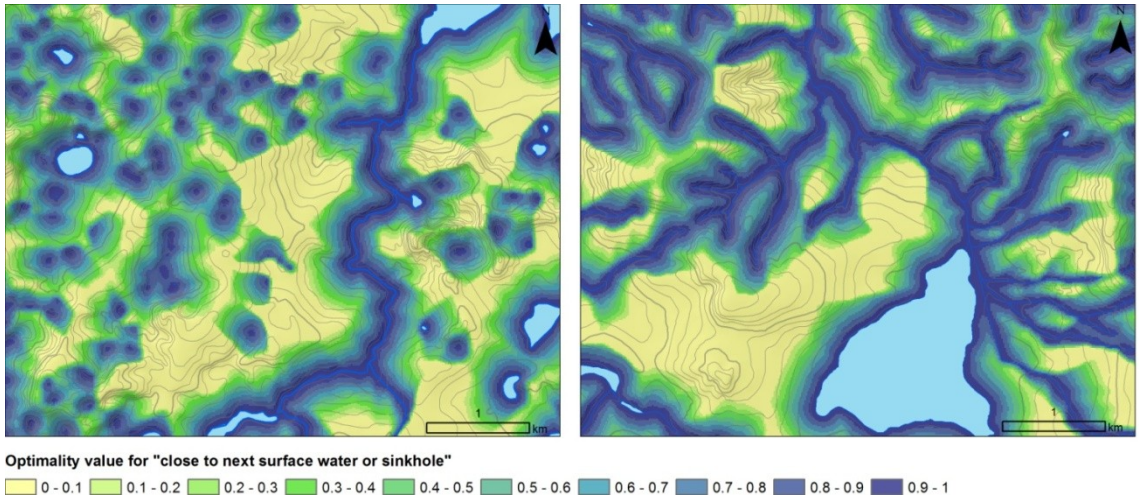

Figure 10-17 Optimality values for "close to the next river, lake or swallow hole".

A linear stretch was used with 0 m receiving the optimality value 1 and 500 m (and further) receiving the optimality value 0. The location of the exemplary areas is indicated in Figure 10-5 (karstified terrain A on the left, covered karst area B on the right). See also Map 24 in the annex.

10.4.4 Contributing area per unit contour length

The contributing area per unit contour length (=specific catchment area) was calculated using the D-Infinitiy-algorithm from Tarboton (1997) since the single flow D8 algorithm implemented in ArcGIS often produces unrealistic results in headwater areas. The optimality values for high flow

accumulation were derived using a linear stretch on the logarithm of the specific catchment area (Figure 10-18). The optimization of the function was done regarding slopes that are not yet incised by defined drainage lines and thus water bodies already documented in the topographic map nearly always receive an optimality value of 1.

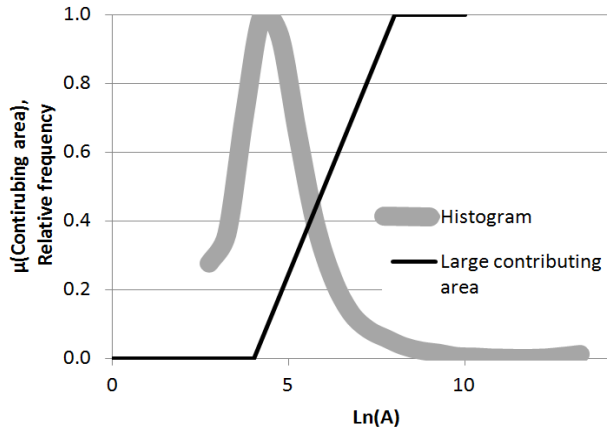

Figure 10-18 Relative frequency (histogram) of values for the natural logarithm of the specific contribution area (A) compared to the optimality function chosen for the semantic statement "large contributing area".

This statement is optimized for previously unchanneled slopes as can be seen in its spatial distribution in Figure 10-19.

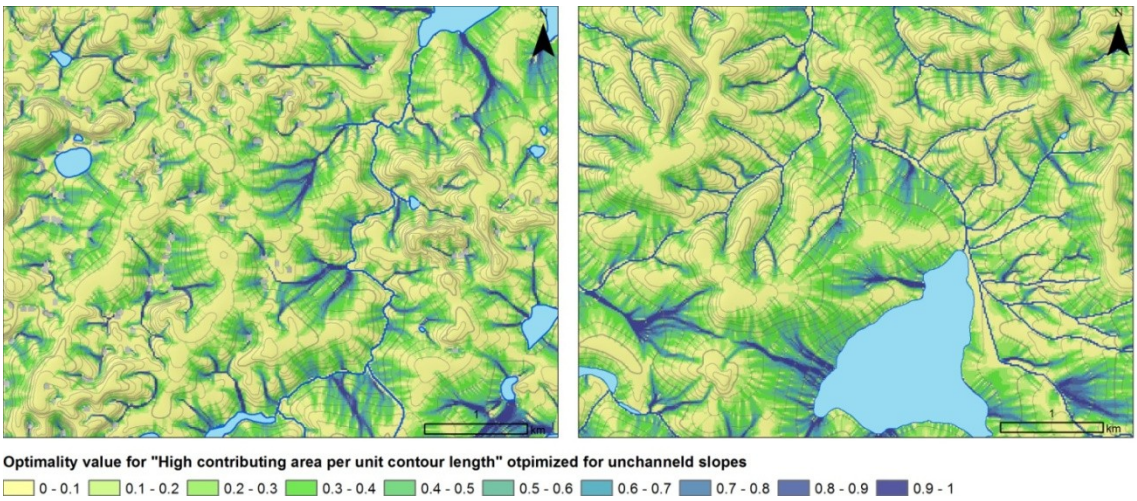

Figure 10-19 Optimality values for "Large contributing area" using the D-infinity flow accumulation algorithm from Tarboton (1997).

The location of the exemplary areas is indicated in Figure 10-5 (karstified terrain A on the left, covered karst area B on the right). See also Map 25 in the annex.

10.4.5 Wetness index

The wetness index, originally developed by Beven and Kirkby (1979) to outline areas in a catchment with frequent saturation excess surface flow, is a common hydrological index. The combination of low slope angle and high drainage area identifies areas prone to water saturation or with close groundwater level and thus high risk of saturation excess surface flow.
It is calculated as the natural logarithm of the specific catchment area divided by the tangent of the slope angle:

$$\text{Wetness index} = \ln\left(A/\tan(S)\right)$$

Equation 10-34 Wetness index

With [A] = specific catchment area, [S] = Slope in degree

To derive the optimality value that describes best the zones of recurrent water saturation, a linear optimality function was used that clips off all values for which water saturation was rated improbable (wetness index = 8) and reaches a value of 1 at a wetness index of 12, cutting off the long tail of extreme values in the histogram.
Also a medium to high wetness index optimality value was derived using a similar linear function but starting from wetness index 6 and clipping off all values beyond 10, thus including also areas that are not necessarily frequently saturated but nevertheless have a high water accumulation together with comparatively flat slope (Figure 10-20).
The wetness index is not calculated for water bodies already documented in the topographic map (Figure 10-21), which always receive a value of 1.
To avoid local artifacts, the wetness index is averaged in a circular neighborhood with a diameter of 90 m.

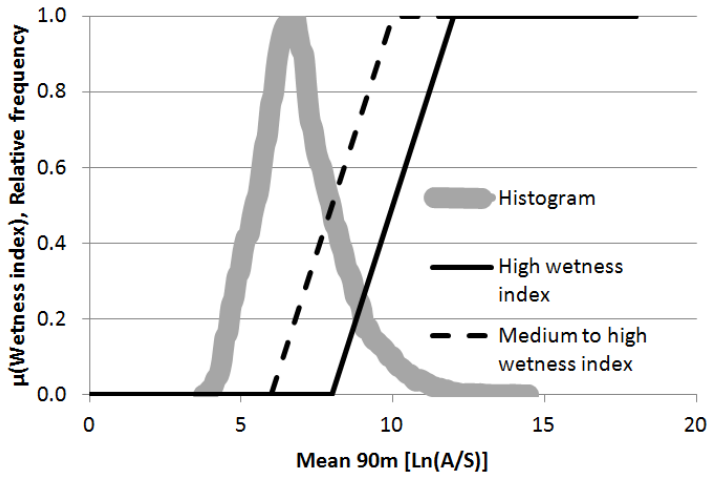

Figure 10-20 Relative frequency (histogram) of the wetness index Ln(A/S) compared to the linear optimality function chosen for the statement "high" and "medium to high" wetness index.

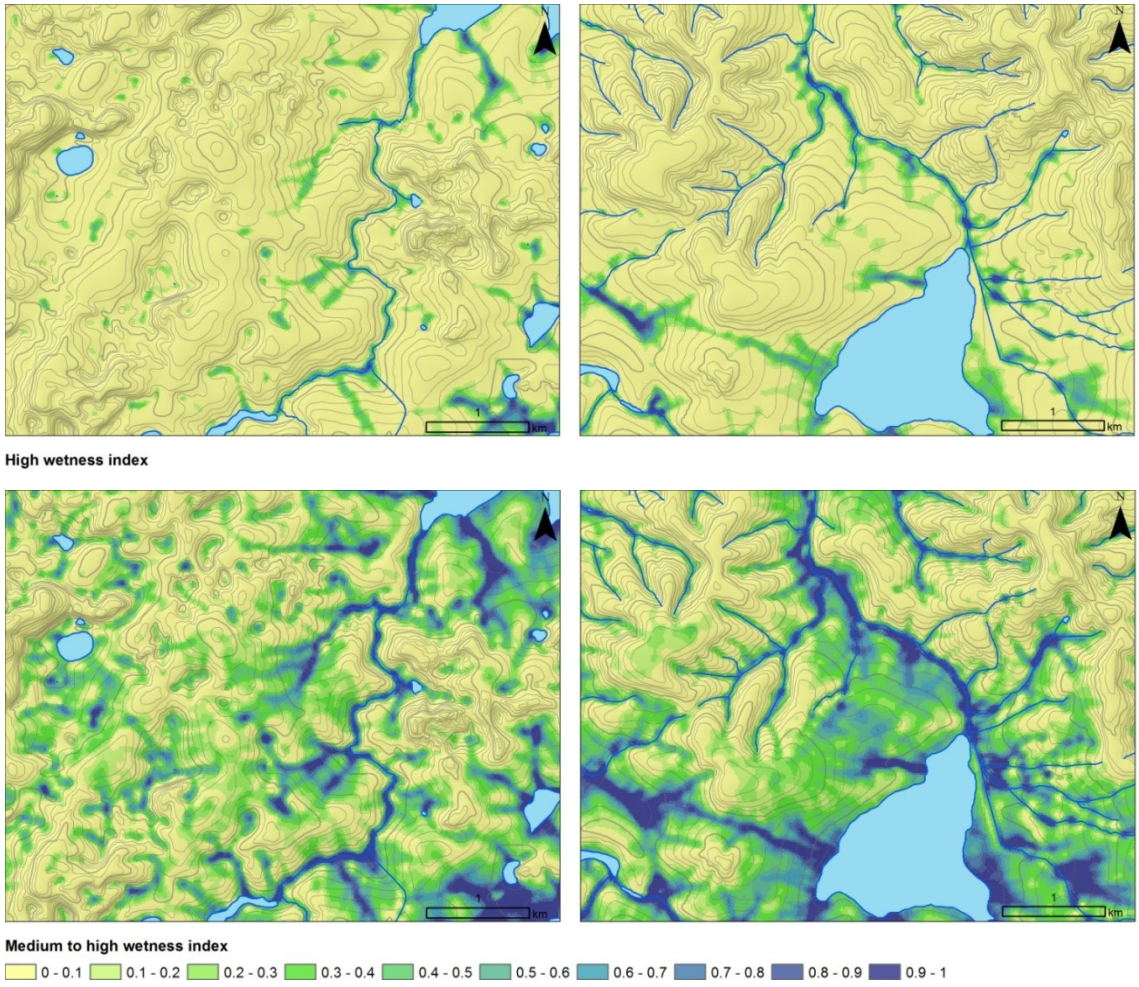

Figure 10-21 Spatial distribution of optimality values for "high" and "medium to high" wetness index.

The location of the exemplary areas is indicated in Figure 10-5 (karstified terrain A on the left, covered karst area B on the right). See also Map 26 in the annex.

10.4.6 Stream power

Stream power is – similar to the wetness index – a function of slope and specific catchment area. For the current study, it is based on the ideas from Bagnold (1966), who defined it as available power supply or time rate of energy supply to unit length of a stream. Bagnold (1966) calculated the kinetic energy available for bed erosion as equal to the release of potential energy of the liquid. The part of the kinetic energy that is not accelerating the water is dissipated against the stream bed leading to erosion.

$$\Omega = \rho \, g \, Q \, S$$

Equation 10-35 Stream power

With [Ω] = available stream power, [ρ] = density of water, [g] = acceleration due to gravity [Q] = total discharge, [S] = slope

Substituting the discharge with the specific catchment area, Equation 10-35 can be re-written as follows:

$$\Omega \sim A\ S$$

Equation 10-36 Relation between stream power, specific catchment area and slope

With

A = specific catchment area (section 10.4.4), S = slope in m/m

For better visualization, the natural logarithm of the stream power was used as basis for the optimality functions (Figure 10-22). Starting approximately from a value of 5, higher values of Ln (AS) are typically located in existing streams. Thus, two different optimality values were calculated for stream power:

- "high" stream power – no rivers, with a linear stretch from 2 to 6 and
- "high" stream power – rivers, with a linear stretch from 5 to 9.

For better visualization, the maximum of a 3x3 cell neighborhood was used for the stream power index along existent rivers (see also Figure 10-23)

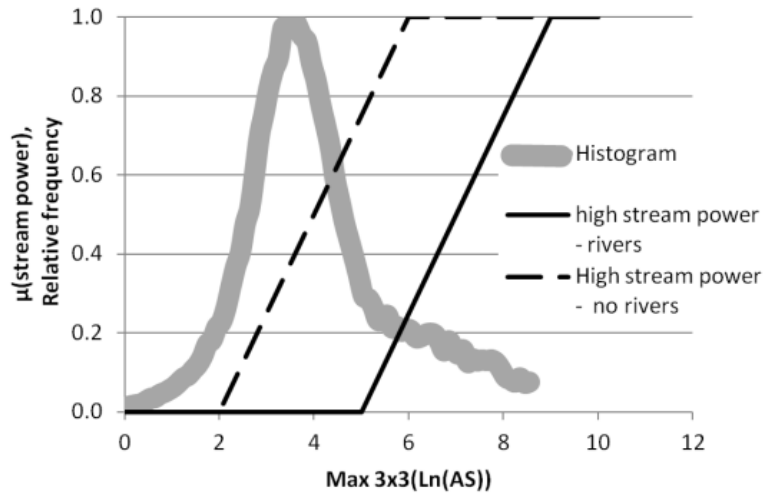

Figure 10-22 Relative frequency (histogram) of values for Ln(AS)= stream power compared to two linear optimality function chosen for the semantic statement "high" stream power.

The dashed function is optimized for unchanneled areas and the solid function is optimized for the existing drainage network.

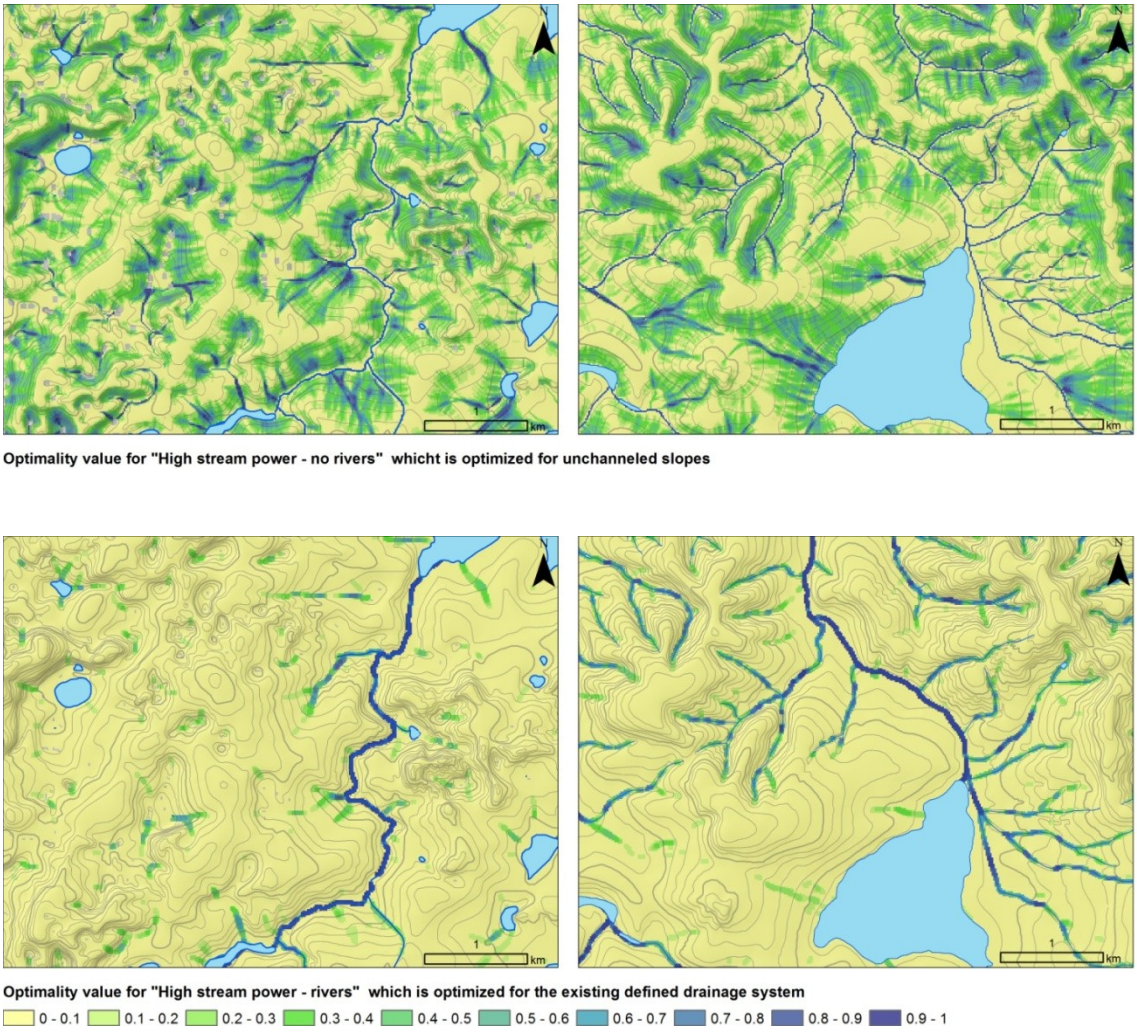

Figure 10-23 Spatial distribution of the optimality values of "high" stream power, optimized for unchanneled slopes (upper maps) and for the existing drainage network (lower maps).

See also Map 29 in the annex.

10.5 Output: Near surface epikarst

Occurrence of exokarst or near surface epikarst is very important for catchment hydrology and groundwater vulnerability. It is related to the risk of direct infiltration into the karst aquifer through limestone outcrops or through contact between the highly permeably red topsoil and covered karst features. Nevertheless, it is difficult to map. Rock outcrops are not included as signatures in 1 : 25 000 topographic map, thus only the slope calculated from contour lines could be used as indication for rock outcrops. Karst features documented in the geomorphological map 1 : 50 000 (Kohler et al. 1998) were also used as indicators for near surface epikarst occurrence. Since they did not match exactly the more detailed topography of the 1 : 25 000 map, a buffer zone of 50 m around karst features received an optimality value of 0.5 for the risk of near surface epikarst occurrence, declining with further distance from the mapped feature. Besides the direct integration in the workflow, the information from the geomorphological map and from the soil map were used for validation of the created optimality maps. For example, a slope of 15° (Figure 10-6) indicated areas in the karst region where near surface epikarst seemed probable according to satellite data and the geomorphological map while a slope value of more than 20° was typical for documented large rock outcrops. The optimality rule for very steep slopes (Figure 10-7) was adapted to this observation. Also summits are typical areas of rock outcrops if they are very narrow i.e. very locally convex. The optimality curve for "convex" local TPI (Figure 10-11) was created to include these special cases. Additionally, riverbeds with high stream power were included as risk areas since here erosion is strongest. Naturally, this observation has to be restricted to the geological underground most prone to karstification. Thus, for each geological unit an optimality value $\mu_{karstification}(\mathrm{GEO})$ was defined based on lithology (Table 8-4) and the following rule was created to regionalize the risk of near surface epikarst:

$$\mu_{\ Near\ surface\ epikarst} = \begin{bmatrix} \mu_{\ very\ steep\ slope}\ OR \\ \mu_{\ Very\ convex\ LTPI}\ \ OR \\ \mu_{near\ mapped\ karst\ features}\mathrm{OR} \\ \mu_{high\ stream\ power-\ river} \end{bmatrix} TIMES\ \ \mu_{Karstification}(\mathrm{GEO})$$

Equation 10-37 "Near surface epikarst"

$$\mu_{No\ near\ surface\ epikarst} = 1 - \mu_{\ Near\ surface\ epikarst}$$

Equation 10-38 "No near surface epikarst"

The first part of the equation considers the morphology that is typical for karst outcrops and the second term excludes all non-carbonate areas from the calculation.

10.5.1 Remarks for the interpretation of the map

The rule for "steep" slope was optimized to minimize the error of real exokarst features being attributed a low value of $\mu_{Near\ surface\ epikarst}$. This leads to a certain toleration of attributing areas visibly covered by soil with a high optimality value of $\mu_{Near\ surface\ epikarst}$. This was done because near surface epikarst can be hidden below a shallow topsoil without being visible at surface and nevertheless posing a high risk for a hydrological shortcut into the karst aquifer. Since the importance of groundwater protection was ranked higher than possible land use restrictions based on the risk map, the error of attributing a high optimality value of $\mu_{Near\ surface\ epikarst}$ to areas with thick soil cover is rated less grave than the opposite error. Thus, it has to be remembered when interpreting the map that due to the irregular surface of the epikarst, deep soils exist frequently in filled karst pockets even at locations with very high optimality values of $\mu_{near\ surface\ epikarst}$.

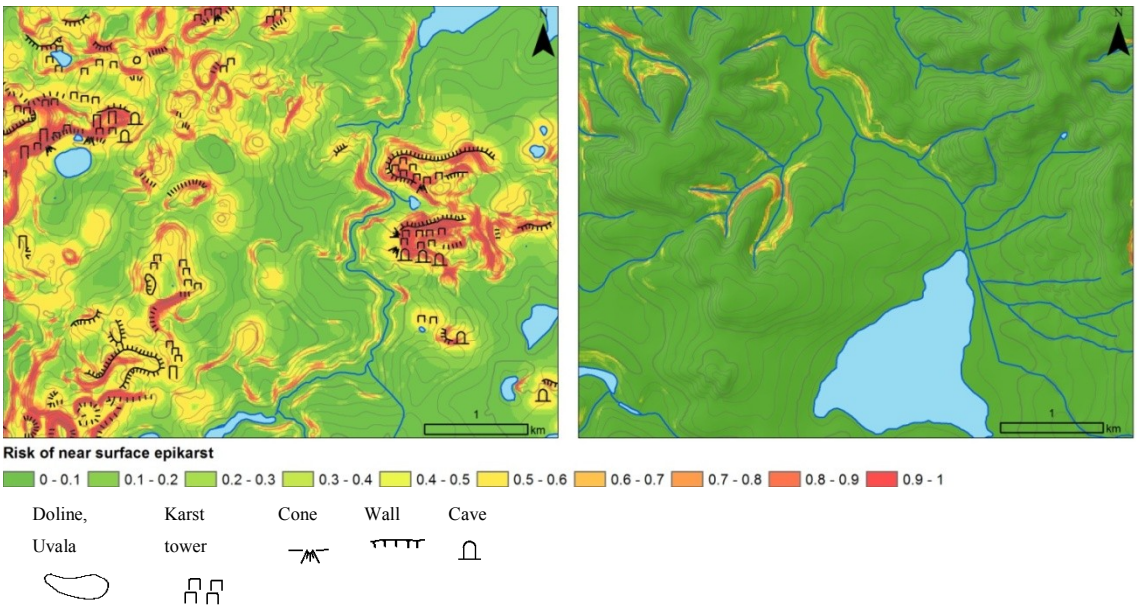

Figure 10-24 Map example showing the risk of near surface epikarst occurrence.

The optimality value $\mu_{near\ surface\ epikarst}$ is high for very steep or convex areas on pure limestone. In the karst area on the left, this variable has a high coincidence with mapped karst features fom Kohler et al. (1998). In the covered karst area on the right, the value is zero on meta-pelites and reaches 0.8 on steep impure carbonates cropping out at footslope locations. For locations of the maps see Figure 10-5. Map 41 in the annex shows an overview map of the risk of near surface epikarst for the total study area.

10.6 Output: Topsoil types and depth

10.6.1 Fluvisols

Topsoils with fluvic material are simply linked to the geological unit of Quaternary alluvial plains:

$$\mu_{Fluvisols} = \begin{cases} 1 \; for \; Quaternary \; alluvial \; plains \\ 0 \; otherwise \end{cases}$$

Equation 10-39 "Fluvisols"

10.6.2 Gleysols

The optimality value map for soils with hydromorphic conditions (Gleysols) is modeled using the following overlay:

$$\mu_{Gleysols} = \begin{bmatrix} \mu_{low \; above \; mapped \; rivers \; or \; lakes} \; \text{OR} \\ \mu_{\text{High wetness index}} \; \text{OR} \\ (\; \mu_{Fluvisols} \; \text{TIMES } 0.5 \;) \end{bmatrix}$$

Equation 10-40 "Gleysols"

The optimality value for $\mu_{deep \; Gleysols}$ is derived by an additional focus of completely flat slopes:

$$\mu_{Deep \; Gleysols} = \mu_{Gleysols} \; \text{AND} \; \mu_{Comletely \; flat \; sslope}$$

Equation 10-41 "Deep Gleysols"

10.6.3 Red topsoil depth optimality values

For the purpose of modeling hydrological soil properties, the red topsoil material of Ferralsols, Acrisols and Lixisols is combined into an upper hydrological layer called "red topsoil". This red topsoil material is characterized by a strong microstructure and a high permeability (see also chapter 8). It is especially deep on the high Tertiary plateau-regions described in the chapter on geomorphology (chapter 6, p. 104), but also accumulates after erosion in footslope positions or local depressions. Here it can reach several meters thickness (Figure 10-25). In steep or locally convex areas, red topsoil material is often completely eroded or very thin.
Autochthonous red topsoil in plateau areas and allochthonous red topsoil in concave downslope positions were modeled separately:

Deep autochthonous red topsoil

High plateau surfaces are typically covered by old and deep Ferralsols and are interpreted as remnants of a Tertiary peneplain (King 1956, Kohler et al. 1998). This peneplain is largely independent from lithology but on limestone, the deep red Ferralsols are more prominent even at slightly steeper slopes. The reason for this could be the slower physical erosion of limestone compared to meta-pelites or crystalline basement rocks. The weathering products of limestone dissolve in water and only the siliciclastic impurities remain and thus the Tertiary Ferralsols remain unchanged for a long period of time. Especially in the steep meta-pelite hills east of Lagoa Santa (geomorphological compartment IV, see Map 6 in the annex) weathering products of meta-pelites mix with Ferralsol material even on slight slopes and the hilltops and upper slopes bear usually only shallow red topsoil material.

Thus, for the regionalization of plateau surfaces in the study area, regionally very high but not locally convex landscape positions were chosen in combination with flat slopes. In geomorphological compartment IV, also convex upper slopes were excluded using a "somewhat low" MTPI rule. In this compartment, also "very flat" slope was required instead of "flat" slopes. Also areas with a high risk of near surface epikarst and very gleyic soils were excluded for the total area.

The complete regionalization rule is written as follows:

For geomorphological compartment IV:

$$\mu_{Deep\ autochthonous\ red\ topsoil} = \begin{bmatrix} [\mu_{flat}(Slope)]^2\ AND \\ [\mu_{Low}(MTPI)]^{0.5} AND \\ [\mu_{high}(RTPI)]^2 AND \\ [\mu_{Not\ convex}(LTPI)]^2\ AND \\ \mu_{No\ near\ surface\ epikarst}\ AND \\ 1 - [\mu_{Gleysols}]^2 \end{bmatrix}$$

Equation 10-42 "Deep autochthonous red topsoil in compartment IV"

For the rest of the study area:

$$\mu_{Deep\ autochthonous\ red\ topsoil} = \begin{bmatrix} \mu_{flat}(Slope)\ AND \\ [\mu_{high}(RTPI)]^2 AND \\ [\mu_{Not\ convex}(LTPI)]^2\ AND \\ \mu_{No\ near\ surface\ epikarst}\ AND \\ 1 - [\mu_{Gleysols}]^2 \end{bmatrix}$$

Equation 10-43 "Deep autochthonous red topsoil in the rest of the area"

In both equations, the square of an optimality value is interpreted as “very” and the square root as “somewhat”. This is known as hedges, compare section 10.2.1.
An example of the spatial distribution of deep autochthonous red topsoil in the karst and covered karst area is shown in the upper images of Figure 10-26.

Deep allochthonous red topsoil

Locations of deep allochthonous red topsoil material were predicted as follows:

$$\mu_{Deep\ allochtonous\ red\ topsoil} = \begin{bmatrix} \mu_{Flat}\,(Slope)\ AND \\ [\,\mu_{Low}\,(MTPI)]^{0.5} AND \\ \mu_{Notconvex}\,(MTPI)\ AND \\ \mu_{Notconvex}\,(LTPI)\ \ AND \\ \mu_{No\ near\ surface\ epikarst}\ AND \\ 1-[\mu_{Gleysols}]^2 \end{bmatrix}$$

Equation 10-44 “Deep allochthonous red topsoil”

The reasoning behind this equation is the following: flat slope and low medium topographic index indicate flat footslope locations where accumulation of eroded topsoil material is probable. Areas with a high risk of near surface epikarst or very gleyic soils are excluded.
Taking into account the long geomorphologic history and the documented small scale depth variation of accumulated red topsoil material due to unknown paleo-relief (e.g. Figure 10-25), this parameter is one of the most difficult to predict for the area. A general equation like the one used for this study must neglect many local conditions that cannot be predicted by a function that is valid for the whole study area.
An example of the spatial distribution of deep allochthonous red topsoil in the karst and covered karst area is shown in the middle images of Figure 10-26.

Figure 10-25 Accumulation of very thick red topsoil material in a morphological concave area, probably a filled paleogully.

The locations of these thick accumulations are very difficult to predict on a regional scale.

Deep red topsoil

Both autochtonous and allochtonous red topsoil optimality values are combined to a red topsoil optimality value using a maximum overlay function.

$$\mu_{Deep\ red\ topsoil} = \mu_{Deep\ allochtonous\ red\ topsoil} \text{ OR } \mu_{Deep\ autochtonous\ red\ topsoil}$$

Equation 10-45 "Deep red topsoil"

An example of the spatial distribution of deep autochthonous red topsoil in the karst and covered karst area is shown in the upper images of Figure 10-26.

The maximum depth for red topsoil material was estimated approximately four meters. Although locations with deeper allochthonous red topsoil material exist (see Figure 10-25), they are usually very local and very difficult to predict. Thus, a higher maximum value than four meters may lead to unrealistic results in most other areas.

$$\text{Red topsoil depth} = \mu_{Deep\ red\ topsoil} * 4\ \text{meter}$$

Equation 10-46 Red topsoil depth

Deep all topsoil

A combination map of red topsoil and hydromorphic topsoil was created using the sum of $\mu_{\text{deep red topsoil}}$ and $\mu_{\text{deep Gleysols}}$. If the sum reached values > 1 it was set to the value 1. Again, an optimality value of 1 was attributed a topsoil depth of 4 meters. An example of the spatial distribution of deep autochthonous red topsoil in the karst and covered karst area together with the spatial distribution of hydromorphic soils is shown in Figure 10-26.

$$\mu_{Deep\ topsoil} = \text{Minumum}[\mu_{Deep\ red\ topsoil} + \mu_{hydromorphic\ soil}), 1]$$

Equation 10-47 "Deep topsoil"

$$\text{General topsoil depth} = \mu_{Deep\ all\ topsoil} * 4\ \text{meter}$$

Equation 10-48 General topsoil depth

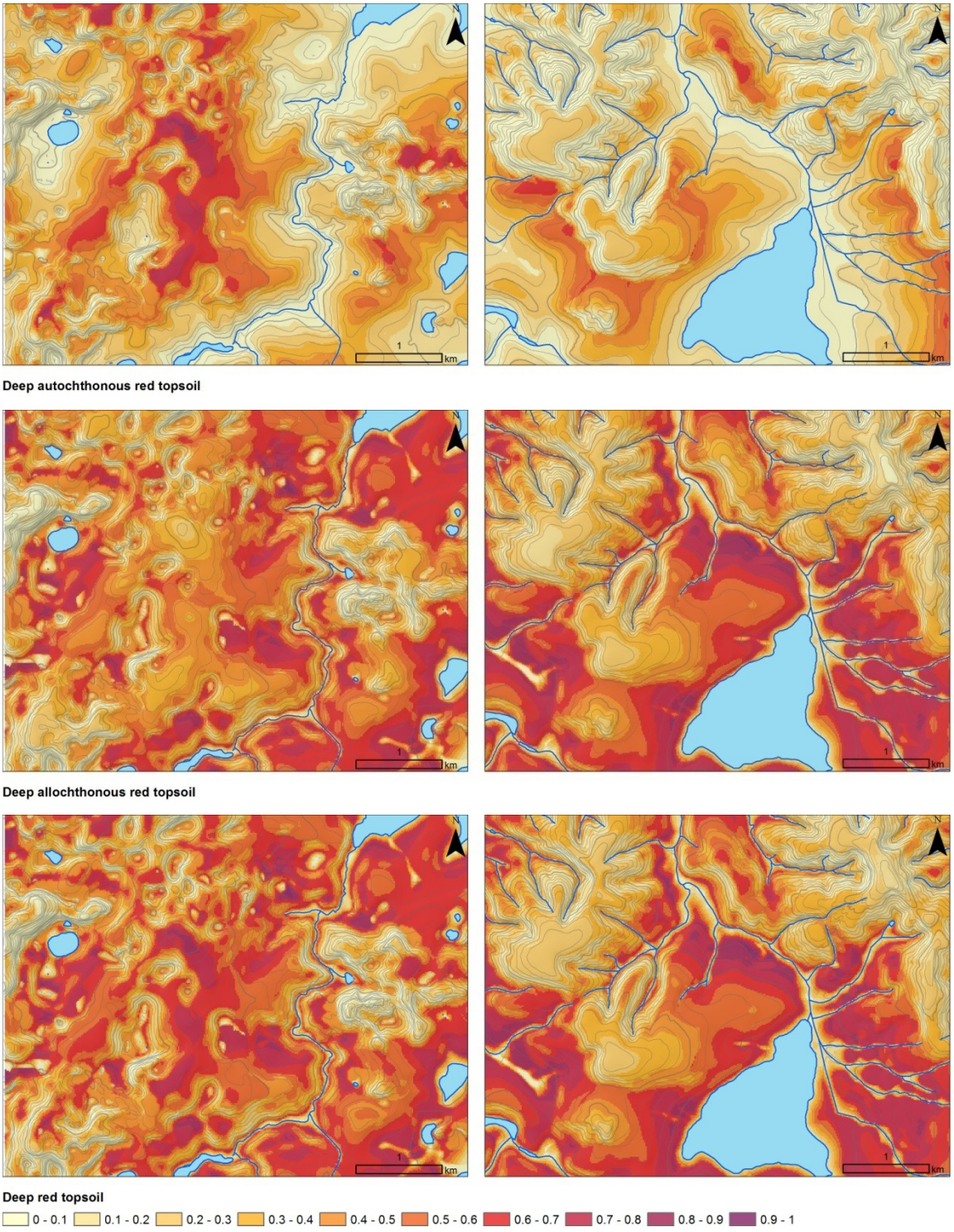

Figure 10-26 Optimality values for deep autochthonous red topsoil, deep allochthonous red topsoil and an overlay of both indicating deep red topsoil.

The optimality values are visualized for the exemplary areas indicated in Figure 10-5 (karstified terrain A on the left, covered karst area B on the right). An optimality value of 1 is related to an absolute depth value of approximately 4 meters. See also Map 55, Map 56 and Map 57 in the annex.

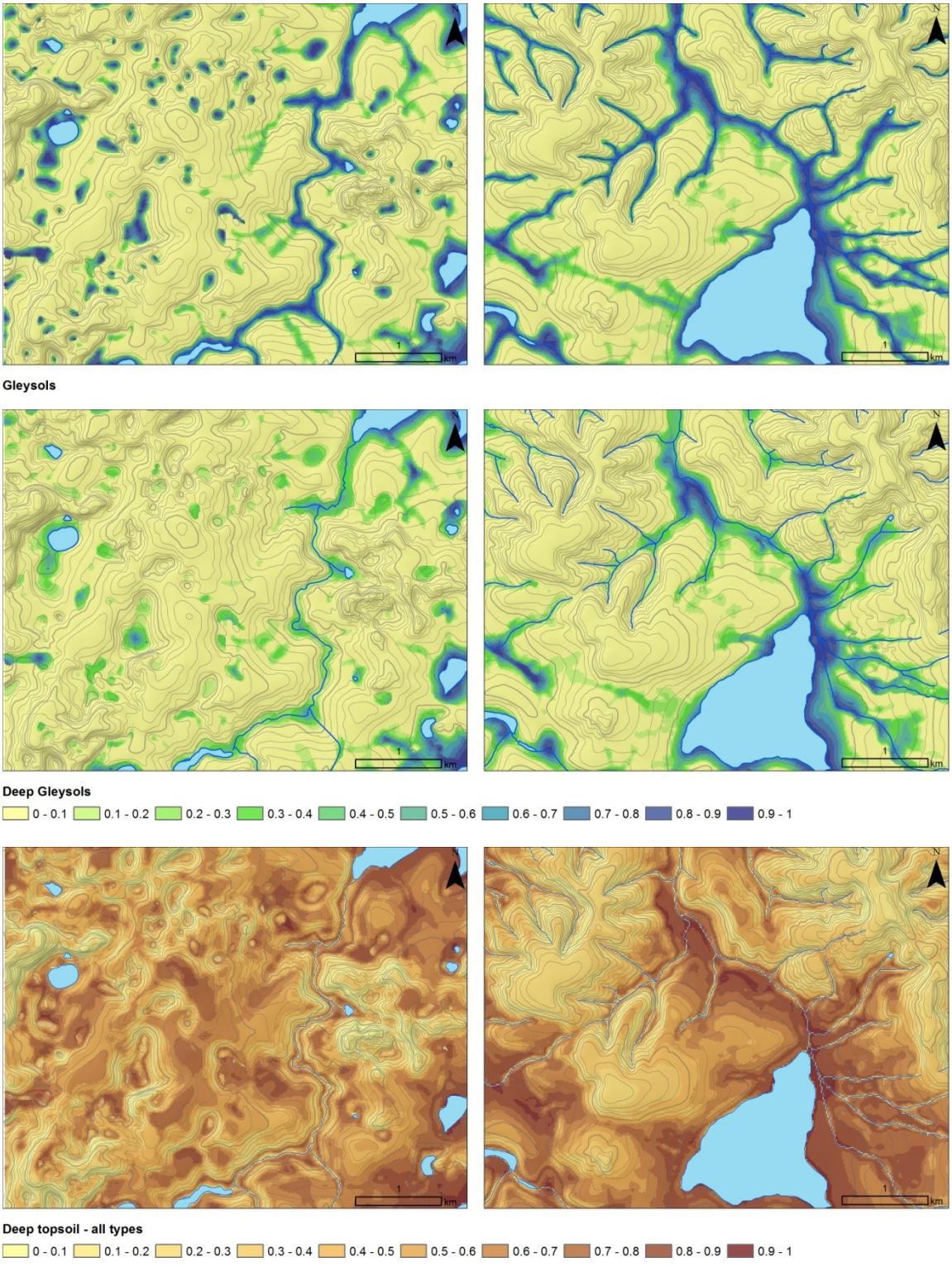

Figure 10-27 Optimality values for deep hydromorphic topsoil and general deep topsoil (deep all topsoil) visualized for the exemplary areas indicated in Figure 10-5.

Karstified terrain A on the left, covered karst area B on the right. An optimality value of 1 is related to an absolute depth value of approximately 4 meters. See also Map 53, Map 54 and Map 58 in the annex.

10.7 Output: Dominant hydrological topsoil type

Using the definitions of topsoil material described in the previous sections, a map of dominant hydrological topsoil types was created by the following workflow:

If $\mu_{Fluvisols} = 1$

Dominant topsoil type = Fluvisol

Else if $\mu_{Gleysols} > 0.5$

Dominant topsoil type = Gleysol

Else if $\mu_{Deep\ autochtonous\ red\ topsoil} > 0.75$

Dominant topsoil type = Deep autochthonous red topsoil

Else if $\mu_{Deep\ allochtonous\ red\ topsoil} > 0.75$

Dominant topsoil type = Deep allochthonous red topsoil

Else if $\mu_{Deep\ red\ topsoil} < 0.25$

Dominant topsoil type = Shallow red topsoil

Else if $\mu_{Deep\ red\ topsoil} < 0.5$

Dominant topsoil type = Medium shallow red topsoil

Else

Dominant topsoil type = Medium deep red topsoil

This workflow creates sharp soil classes out of four continuous soil attribute maps. This has the disadvantages that continuous information is lost and artificial details are created (class borders). Nevertheless, the resulting combination map is easier to understand and interpret than four continuous maps next to each other.

The title “dominant topsoil type” should remind the reader that within each map unit, different topsoil types occur and the one indicated in the map is only the most typical.
The spatial distribution of the dominant topsoil type is shown in Figure 10-28 for the two exemplary areas indicated in Figure 10-5.

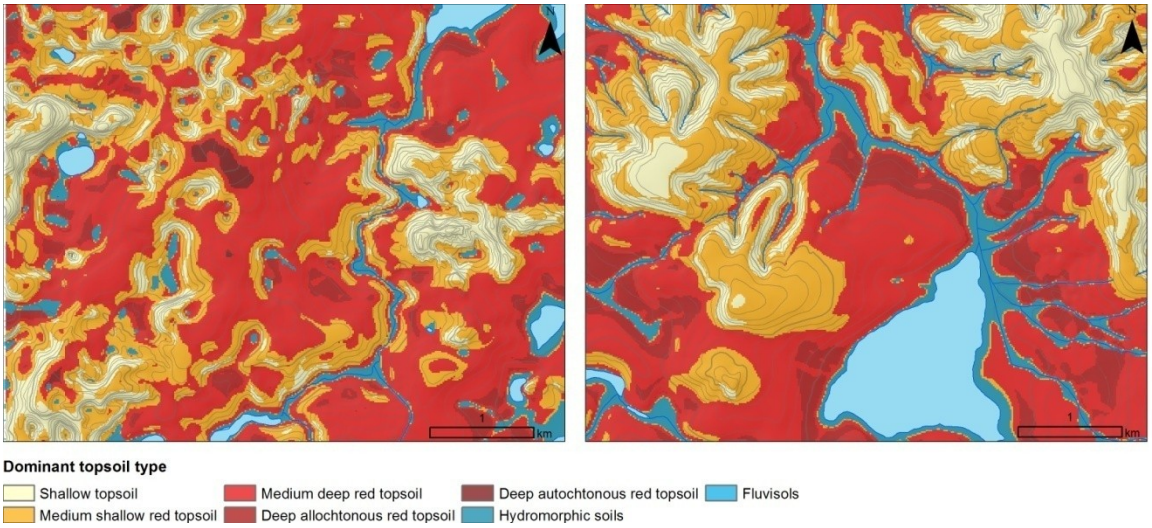

Figure 10-28 Spatial distribution of dominant hydrological topsoil type visualized for the exemplary areas indicated in Figure 10-5.

Karstified terrain A on the left, covered karst area B on the right. Fluvisols are not displayed in the map since they are assigned only to the large alluvial plains of the Rio das Velhas and the Riberão da Mata. See also Map 59 in the annex.

10.8 Output: Effective field capacity

10.8.1 Topsoil effective field capacity (eFC)

The effective field capacity (eFC), also known as available water capacity (USDA 2010) is the soil water content between field capacity and permanent wilting point (see also Figure 8-1). The eFC within the first meter is a useful parameter for the estimation of plant available water for agricultural purposes but is also used for the estimation of groundwater vulnerability. When regionalizing the eFC, its application is nevertheless important: while for agricultural purposes a mean eFC is the desired parameter, the regionalization of its groundwater protective function requires the estimation of the local minimum eFC, especially at sites with very variable soil thickness near karst outcrops. In this study, the regionalization of effective field capacity (eFC) within 1 meter was optimized for its interpretation as protecting layer for groundwater vulnerability. Thus, its applicability for the estimation of plant available water for agricultural purposes is not optimal for the intensely karstified areas.

10.8.2 Topographic optimality value for topsoil eFC

The following general assumption was used for regionalizing the eFC:

Since the eFC is directly related to the amount of mesopores in the soil, it should be lower for plateau areas and hilltops with strong pseudo-sand structure and higher for footslopes and depressions because of accumulation of finer particles and organic material downslope due to preferential erosion.

Thus, the following topographic optimality value for "high topsoil eFC" was created:

$$\mu_{High\ Topsoil\ eFC}\ (Relief)\ = MEAN \begin{bmatrix} \mu_{Low\ LTPI} \\ \mu_{Low\ \ MTPI} \\ \mu_{Low\ RTPI} \end{bmatrix}$$

Equation 10-49 "High topsoil eFC (Relief)"

This parameter describes only the relative influence of the relief and has to be scaled to the typical minimum and maximum eFC values of each geological unit.

10.8.3 Absolute eFC of the topsoil

The minimum and maximum topsoil effective field capacity values (resp. available water capacity values) are taken from Table 8-6 on page 149. For the Bambuí region, a maximum value of 200 mm/m (in alluvial plains) and a minimum value of 100 mm/m (upper slopes) were set. For basement and mixed alluvial plain region, the maximum value was 150 mm/m (mean value in alluvial plains) and the minimum value 80 mm/m (at high hilltops).

The following equations scale the relative $\mu_{High\ Topsoil\ eFC}\ (Relief)$ optimality value to a range of 100 and 200 respective 80 and 150 mm/m using a linear function:

$$eFC_{Topsoil\ \ Bambuí}\ = 100\ mm/m * \mu_{High\ Topsoil\ eFC}\ (Relief) + \ 100\ mm/m$$

Equation 10-50 eFC of the topsoil (Bambuí)

$$eFC_{Topsoil\ \ basement}\ = 70\ mm/m\ * \mu_{High\ Topsoil\ eFC}\ (Relief) + 80\ mm/m$$

Equation 10-51 eFC of the topsoil (Basement)

10.8.4 Subsoil eFC

The subsoil eFC was estimated as described in Table 8-3 on page 146 using estimated values for each geological unit.

10.8.5 Effective field capacity within 1 m

Since the effectiv field capacity (eFC) within the first meter is the destination variable for assessment of groundwater vulnerability (see chapter 13), subsoil eFC values have to be included for soils with a topsoil of less than one meter depth.
The topsoil depth was estimated as described in section 10.6.3, setting an optimality value of 0.25 equal to a topsoil depth of 1 meter.

The depth of subsoil within the first meter was estimated as follows:

If *Topsoil depth > 1 m*

Subsoil depth within 1 m = 0

Else if *Weathering depth > 1m*

Subsoil depth within 1 m = (1m – Topsoil depth)

Else

Subsoil depth within 1 m = Weathering depth – Topsoil depth

The total eFC within one meter from the surface is then calculated as:

If

Topsoil depth ≥ 1 m

$$eFC_{1\,meter} = eFC_{Topsoil} * 1m$$

Else

$$eFC_{1\,meter} = eFC_{Topsoil} * Topsoil\ depth + eFC_{Subsoil} * Subsoil\ depth\ within\ 1\ m$$

Since the $\mu_{\text{near surface epikarst}}$ membership indicates only the possibility of near surface epikarst, the thus calculated subsoil depth is a minimum estimation and should be used only for risk estimation of direct infiltration of water into the karst aquifer. The average effective field capacity which is useful for the calculation of plant available water is probably higher.
Using the procedure described above, a spatially continous estimation of the effective field capacity within the first meter was realized for the whole area, with the connotation that this estimation is only minimum estimation for areas of near surface epikarst.

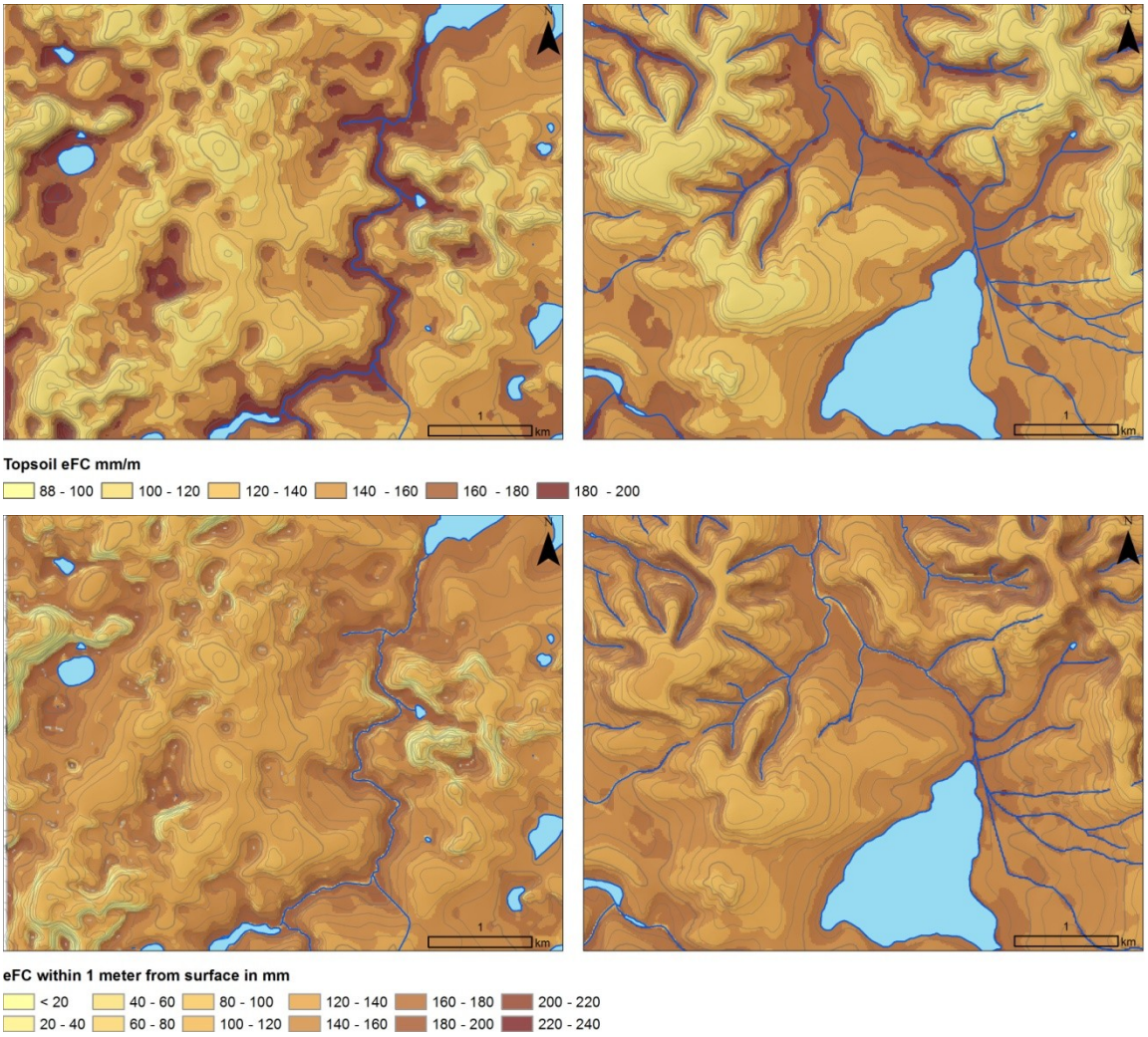

Figure 10-29 Effective field capacity of the topsoil in mm/m (upper image) and the eFC within the first meter from surface.

For the location of the exemplary areas see Figure 10-5 (karstified terrain A on the left, covered karst area B on the right). See also Map 60 and Map 61 in the annex.

10.9 Output: Soil permeability

10.9.1 Topsoil permeability

The permeability of the upper red topsoil layer defined in chapter 8 is mainly controlled by the amount of macropores in the soil. The lateral variability of the amount of macropores is strongly controlled by soil structure which is more related to the age and temperature/wetness regime during soil formation than to parent material. Parent material has an effect on the overall texture of the soil, but very clayey Ferralsols on carbonates or meta-pelites have similar amount of macropores than lighter textured Ferralsols on gneiss-migmatite basement due to a strong and water resistant pseudo-sand structure. On the other hand, topsoil of autochthonous Ferralsols of old plateau regions has a much higher permeability than the topsoil of hydromorphic soils in karst depressions or along rivers. Generally, lower or concave areas are less permeable due to preferential erosion of finer material upslope and its accumulation downslope. Thus, position in the landscape is more important than lithology. Exemplary soil data from and around the study area are consistent with this reasoning (Table 8-5 on page 148). Following this reasoning, an equally weighted sum of $\mu_{low\ LTPI}$, $\mu_{low\ MTPI}$ and $\mu_{low\ RTPI}$, i.e. the average of low topographic positions at three regional scales was used to create an optimality function for low topsoil permeability:

$$\mu_{Low\ topsoil\ permeability} = MEAN \begin{bmatrix} \mu_{Low\ LTPI} \\ \mu_{Low\ MTPI} \\ \mu_{Low\ RTPI} \end{bmatrix}$$

Equation 10-52 "Low topsoil permeability"

$$\mu_{High\ topsoil\ permeability} = 1 - \mu_{Low\ topsoils\ permeability}$$

Equation 10-53 "High topsoil permeability"

10.9.2 Subsoil permeability

For subsoil permeability, the optimality values from Table 8-4 were taken and supplemented with the optimality values for risk of near surface epikarst to take into account the possible local absence of the subsoil layer at these locations. The complete reasoning can be written as follows:

If $\mu_{Near\ surface\ epikarst} \geq 0.75$, then $\mu_{Subsoil\ permeability} = 1$

If $\mu_{Near\ surface\ epikarst}$ is between 0.5 and 0.75, then $\mu_{Subsoil\ permeability} = 0.9$

If $\mu_{Near\ surface\ epikarst} \leq 0.5$, then

$\mu_{Subsoil\ permeability} = \mu_{Basic\ Subsoil\ permeability}$ (Geology)

The spatial distribution of topsoil and subsoil permeability optimality values are shown in Figure 10-30 and in Figure 10-31.

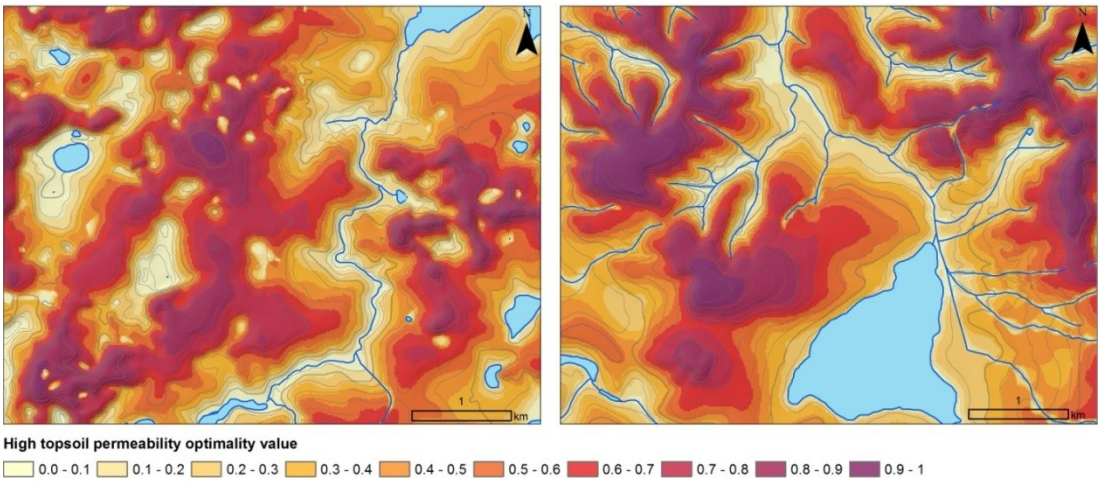

Figure 10-30 Map indicating a "high topsoil permeability" optimality value.

For the location see Figure 10-5 (karstified terrain A on the left, covered karst area B on the right). See also Map 62 in the annex.

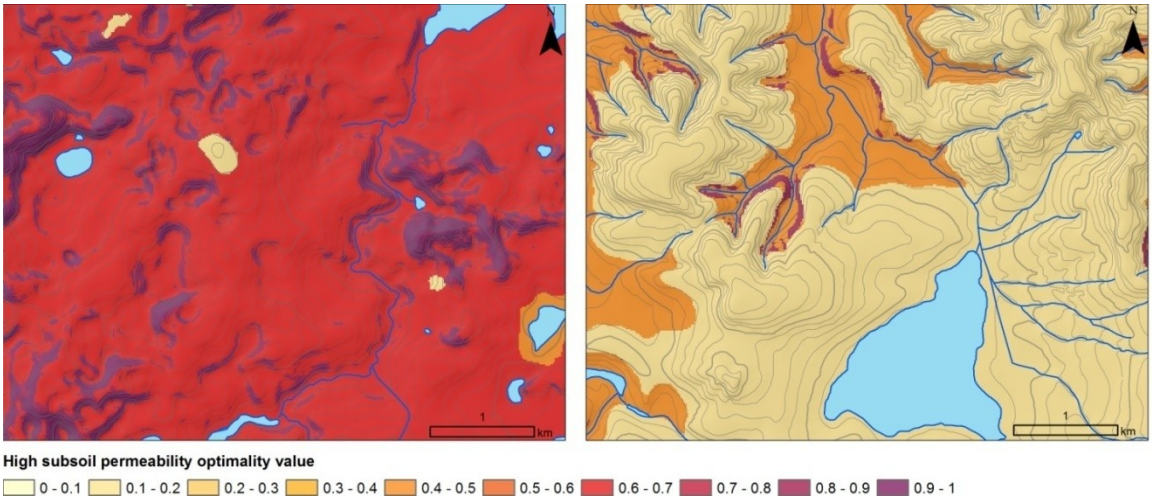

Figure 10-31 Map indicating a "high subsoil permeability" optimality value.

For the location see Figure 10-5 (karstified terrain A on the left, covered karst area B on the right). See also Map 63 in the annex.

10.10 Output: Dominant flow processes

In the USA, the Curve Number Method (USDA 2004) is a common tool for catchment hydrological modeling. In this method, hydrological soil units are combined with land use types

to a “curve number” that is used to estimate the average percentage of fast response flow after rainfall events at catchment scale. The hydrological soil units in the curve number method are based on mean saturated hydraulic conductivity of the soil horizons and the depth to low permeable layers.
A similar classification of hydrological soil units (respective dominant flow processes) can be found in the PI-method (Goldscheider 2002, Goldscheider et al. 2000) used for the estimation of groundwater vulnerability. This method extends traditional groundwater vulnerability estimation to karst areas by explicitly taking into account the hazard posed by surface or near surface lateral flow into karst swallow holes (see chapter 13).

The classification of dominant flow processes in this study is similar to that proposed by Goldscheider (2002) but modified to the local conditions and data availability.
As is done in curve number method and PI- method, the dominant flow process classes (resp. hydrological soil units) are determined only from soil parameters without taking into account slope or relief position.

For the current study, the map of the dominant flow processes is based on the map of dominant topsoil type (Figure 10-28) and on the map of subsoil permeability (Figure 10-31). Since lateral flow is more prominent if the depth to the lower permeable layer is shallower, a higher value of subsoil permeability was accepted for the definition of “shallow subsurface flow” compared to “deep subsurface flow”. The parameter combinations used for the definition of dominant flow process classes are summarized in Table 10-1.

Dominant flow process	Parameter combination
Hortonian surface flow / very shallow subs. flow	Dominant topsoil = “Shallow topsoil” AND $\mu_{Subsoil\ permeability} < 0.75$
Shallow subsurface flow	Dominant topsoil = “Medium shallow red topsoil” AND $\mu_{Subsoil\ permeability} < 0.5$
Deep subsurface flow	Dominant topsoil = “Medium deep red topsoil” AND $\mu_{Subsoil\ permeability} < 0.25$
Infiltration	Dominant topsoil = “Deep red topsoil” OR $\mu_{Subsoil\ permeability} \geq 0.75$ OR (Dominant topsoil = “Medium shallow red topsoil” AND $\mu_{Subsoil\ permeability} \geq 0.5$) OR (Dominant topsoil = “Medium deep red topsoil” AND $\mu_{Subsoil\ permeability} \geq 0.25$) OR Dominant topsoil = Fluvisol
Infiltration / saturation excess surface flow	Dominant topsoil = “Hydromorphic soils” AND $\mu_{Subsoil\ permeability} < 0.75$

Table 10-1 Rules for deriving a classified map of dominant flow processes based on soil paramters.

Examles of the resulting map are shown in Figure 10-32 .

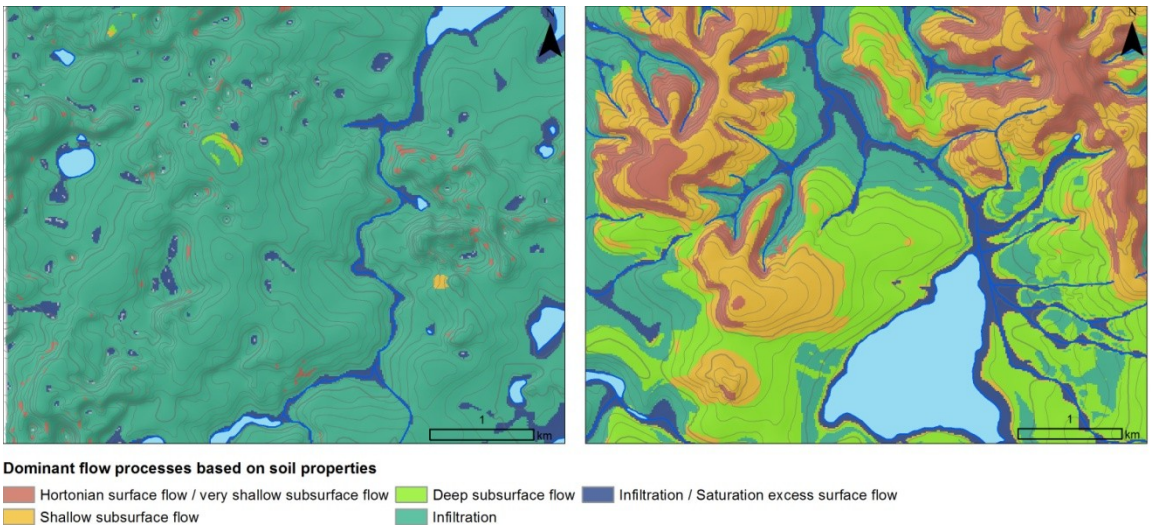

Figure 10-32 Map showing the dominant flow process classes defined in Table 10-1.

For the location see Figure 10-5 (karstified terrain A on the left, covered karst area B on the right. Compare also Map 64 in the annex.

10.11 Output: Soil erodibility

Erodibility of the soil was regionalized using the following considerations:
Since the erodibility of the topsoil is nearly always considerably lower than the erodibility of the underlying saprolite due to higher permeability and stable macro-structure, the thickness of the topsoil material is the most important parameter. It is combined with the relative erodibility of the subsoil / saprolite for each geological unit (Table 8-4 on page 147) and the absence of limestone rock outcrops.
Thus, erodibility for non-hydromorphic soils is calculated as:

$$\mu_{High\ soil\ erodibility} = \begin{bmatrix} \mu_{not\ deep\ topsoil}\ \text{TIMES} \\ \mu_{high\ subsoil\ erodibility}\ \text{TIMES} \\ \mu_{no\ risk\ of\ near\ surface\ epikarst} \end{bmatrix}$$

Equation 10-54 "High soil erodibility"

Examples of the spatial distribution of "high soil erodibility" optimality values are shown in Figure 10-33.

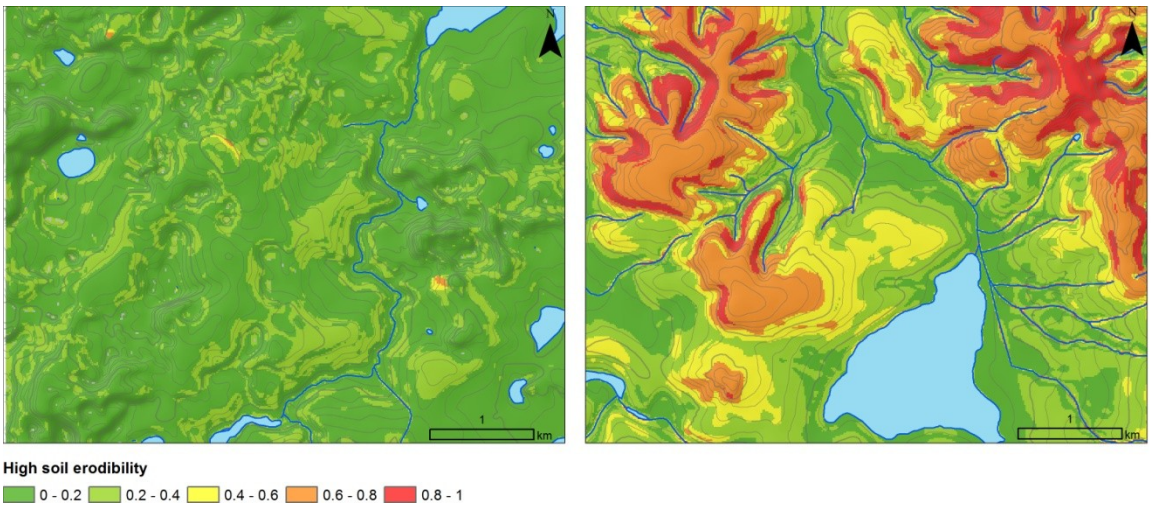

Figure 10-33 Spatial distribution of "high soil erodibility" optimality values.

The location of both exemplary areas is indicated in Figure 10-5 (karstified terrain A on the left, covered karst area B on the right). See also Map 68 in the annex.

11 Bedrock architecture above groundwater level

11.1 Elevation above groundwater

In the study are, no groundwater model exists. In the north-western part of the area, isolines of the groundwater level with 20 m equidistance could be taken from a general vulnerability map for the protection area APA Carste de Lagoa Santa (Pessoa 1998, Pessoa and Mourão 1998). Nevertheless, the information how these isolines were generated was not available and also no information whether they indicated the groundwater level during dry or rainy season - which could be a difference of several meters, as the changing water level in karst lakes document (Figure 9-4).

In the central area around the Lapa Vermelha mining area, piezomentric data from Pessoa (2005) were available for one day in the rainy season and one day in the dry season. From these data, 20 m groundwater isolines were inferred, taking also into account underground routing documented by tracer tests (Auler 1994, 1998, Pessoa 2005). To model the vulnerability during the season with highest probability of groundwater contamination, the higher groundwater level of the rainy season was used for interpolation.

For the rest of the area, no information on groundwater level was available. Here, 20 m isolines were estimated using only relief and surface hydrology.

After the 20 m isolines were thus assigned, the groundwater level was interpolated using the "Topo to Raster" algorithm implemented in ArcGIS (Hutchinson 1989). For a plausibility check, the groundwater surface was subtracted from the digital elevation model, which had been derived using the same interpolation algorithm from 10 m equidistant contour lines of a topographical map. The difference of these two models can be interpreted as surface elevation above groundwater and compared with known areas of seasonal groundwater outcrops. Using this information, the groundwater isolines were locally adapted until the seasonally flooded areas matched the calculated groundwater outcrops. For the alluvial plain of the Riberão da Mata and the Rio das Velhas - both as determined in the geological map - an exception had to be made because of artifacts of the DEM. In valleys flanked by steep hills the “Topo to Raster” algorithm typically produces a wavy structure of sinks and hills. Thus, an estimated uniform elevation above groundwater level of five meters was assumed for the larger alluvial plains – a value which seemed plausible from field experience of the rugged terrain left by small scale open pit sand mining. Figure 11-1 shows the elevation above groundwater for the two exemplary areas. The resulting maps of mean groundwater level and mean elevation above groundwater for the total study area are shown in Map 43 and Map 44 in the annex.

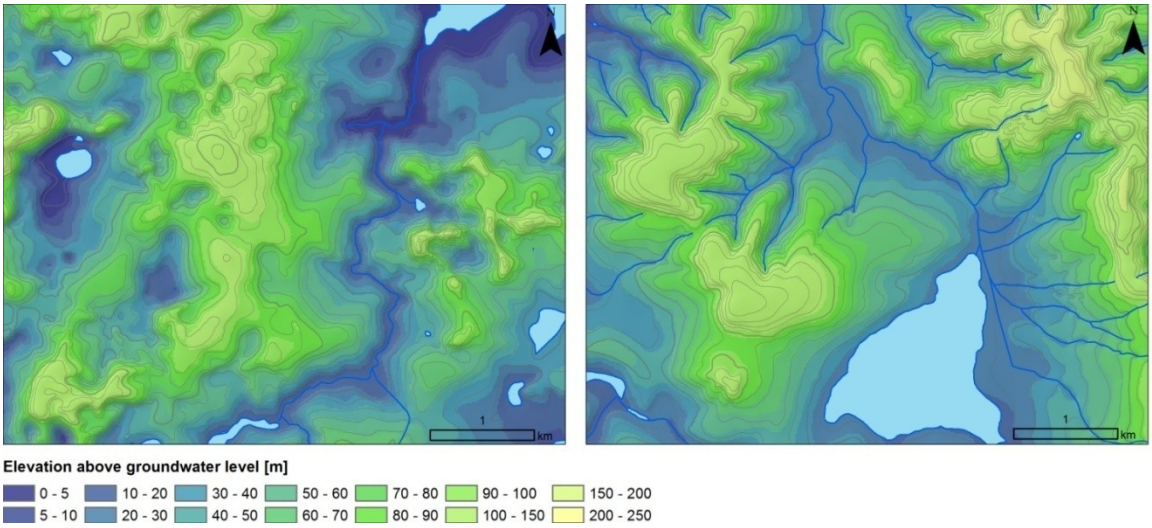

Figure 11-1 Elevation above groundwater.

The location of both exemplary areas is indicated in Figure 10-5 (karstified terrain A on the left, covered karst area B on the right). See also Map 44 in the annex.

11.2 Weathering and subsoil depth

Weathering depth is the depth until which the parent material has been chemically modified until the strong mineral compound of the initial rock is weakened. This results in a soft material that can store water in the inter-granular pore space and is easily eroded when cropping out at the surface.
For limestone areas, the regionalized weathering depth is defined until the highest epikarst feature, i.e. not including material in karst pockets (Figure 11-3, p. 235).

While the upper part of the weathered layer is mixed by biological processes, the lower part often conserves the initial rock structure and is also termed saprolite. In the study area, highly permeable topsoil overlies denser subsoil / saprolite, leading to temporary lateral subsurface flow at their interface during and shortly after rainfall events and thus redistributing water in the catchment. Thus, especially the lower part of the weathering mantle is an effective protection layer against fast infiltration into the limestone aquifer. Its thickness also indicates the amount of erodible soil above hard rock and thus influences the risk of deep gully incision.
For the current study, the subsoil and saprolite is combined in one layer “subsoil”, which summarizes the total weathering depth below the topsoil.
For each geological unit in the study area, a maximum weathering depth has been defined in Table 8-4 according to best knowledge. For limestone areas, this maximum value is the estimated maximum depth until the highest local epikarst feature (Figure 11-3).

Since slope is an indicator of how much of the weathered subsoil material has already been eroded, the geological maximum value is multiplied by an optimality value based on relief:

$$\mu_{High\ weathering\ depth}(Relief) = \mu_{flat\ slope}\ \text{AND}\ \mu_{No\ Near\ Surface\ Epikarst}$$

Equation 11-1 "High weathering depth (Relief)"

$$\text{Weathering depth [m]} = \begin{bmatrix} [\mu_{Weathering\ depth}(Relief)\ TIMES \\ \text{Max. weathering depth } (Geology) \end{bmatrix} OR\ \text{Topsoil depth}$$

Equation 11-2 Weathering depth

To take account of the intrastratal karstification in geomorphologic compartment III, the maximum weathering depth of each geological unit has been multiplied by 1.5 for this compartment:

$$\text{Weathering depth [m]} = \begin{bmatrix} [\mu_{Weathering\ depth}(Relief)\ TIMES \\ 1.5\ \text{Max. weathering depth } (Geology) \end{bmatrix} OR\ \text{Topsoil depth}$$

Equation 11-3 Weathering depth for geomorphologic compartment III

Afterwards, subsoil depth is calculated by subtracting the topsoil depth from the weathering depth:

Subsoil depth [m] = Weathering depth – Topsoil depth

Equation 11-4 Subsoil depth [m]

11.3 Thickness of the Serra de Santa Helena Formation

In the center of the study area, the carbonate sediments are overlain by pelitic meta-sediments of the Serra de Santa Helena Formation. These meta-pelites are so deeply weathered that it was impossible to find a fresh outcrop in the study area; even at the bottom of deep gullies the material is soft. Since also boreholes document a depth of weathered material of up to more than 100 m, their complete thickness was classified as subsoil material according to the practical purpose defined above.

The base surface of the Serra de Santa Helena meta-pelites was interpolated from the mapped outline of the geological unit and data from drill-holes from Pessoa (2005). Since the base surface is influenced by intrastratal karstification, simple interpolation of the outline does not take account of these features and errors occur especially in depressions such as the Lake Lagoa Santa. When the Serra de Santa Helena base surface is subtracted from the DEM, negative values

indicate sunken regions. For the estimation of the real thickness of the Serra de Santa Helena Formation, the following strategy was used:

The thickness of the sunken meta-pelites is probably highest at the deepest point of the depression (Figure 11-2). Thus, the absolute value of the calculated difference between the topographic surface and the interpolated base of the meta-pelites can be used as a first estimate of its thickness.

The raw thickness of the Serra de Santa Helena Formation interpolated according to Figure 11-2 is shown in Map 40 in the annex. The base surface of this formation is derived by subtracting the topographic surface from the calculated thickness (Map 39 in the annex).

For the estimation of subsoil depth, an error occurs of course where the calculated thickness crosses 0 at the borders of the depressions. Also near the outline of the geological unit, where the meta-pelitic cover is very thin, this does not imply that the subsoil material is also thin, since soft subsoil material from carbonates is probably below the covering meta-pelites.

Thus, the weathering depth is calculated as the maximum value of the interpolated thickness of the Serra de Santa Helena Formation as shown in Figure 11-2 and the weathering depth according to Equation 11-3. In Figure 11-4, the results are shown for two exemplary areas. See also Map 42 and Map 45 in the annex for an overview of the total study area.

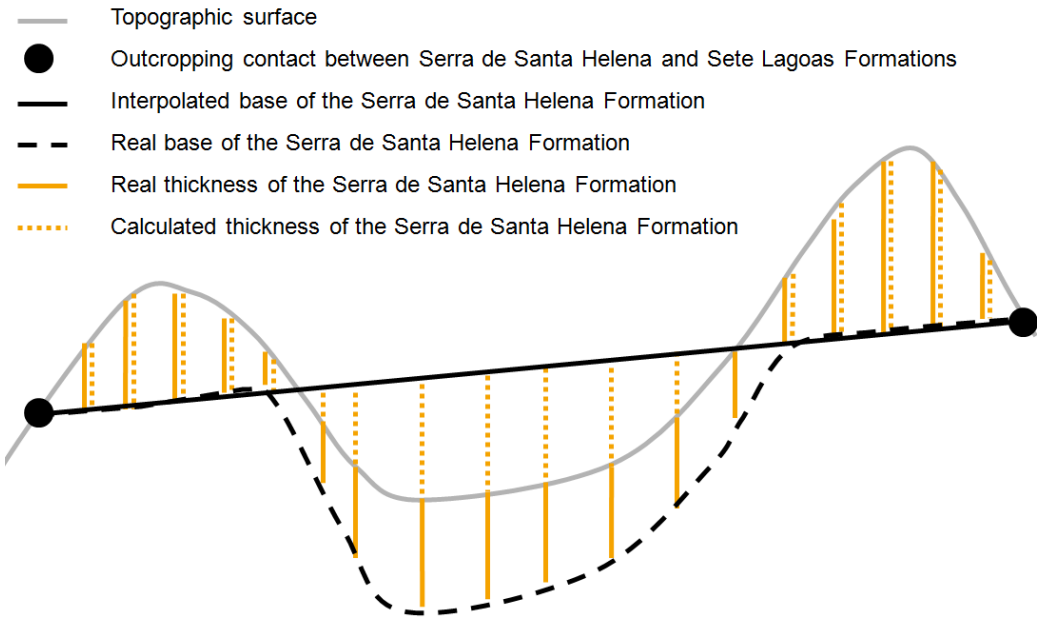

Figure 11-2 Thickness estimation for the Serra de Santa Helena Formation.

In depressions caused by intrastratal karstification such as the lake Lagoa Santa, the interpolation of the outcrop line of the Serra de Santa Helena Formation leads to errors. As a first estimate, the absolute value of the calculated thickness of the strata was used.

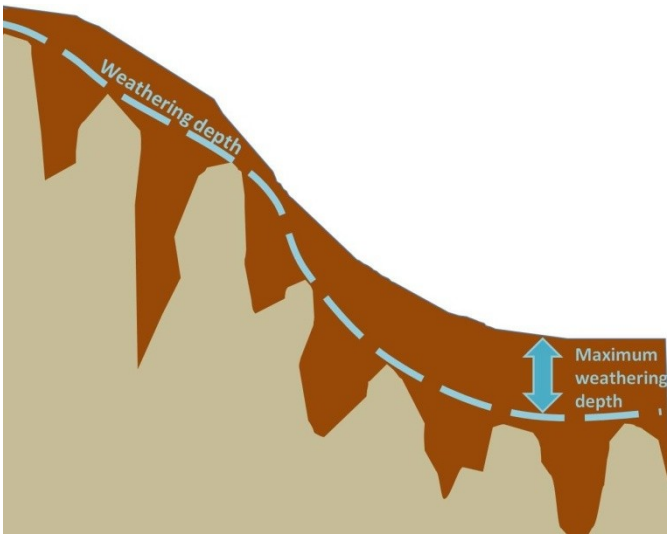

Figure 11-3 Weathering depth concept used for regionalization.

The parameter considers the thickness of soft material (topsoil + subsoil) above the highest epikarst feature in the karst environment. In karst pockets, weathering depth can be very much deeper.

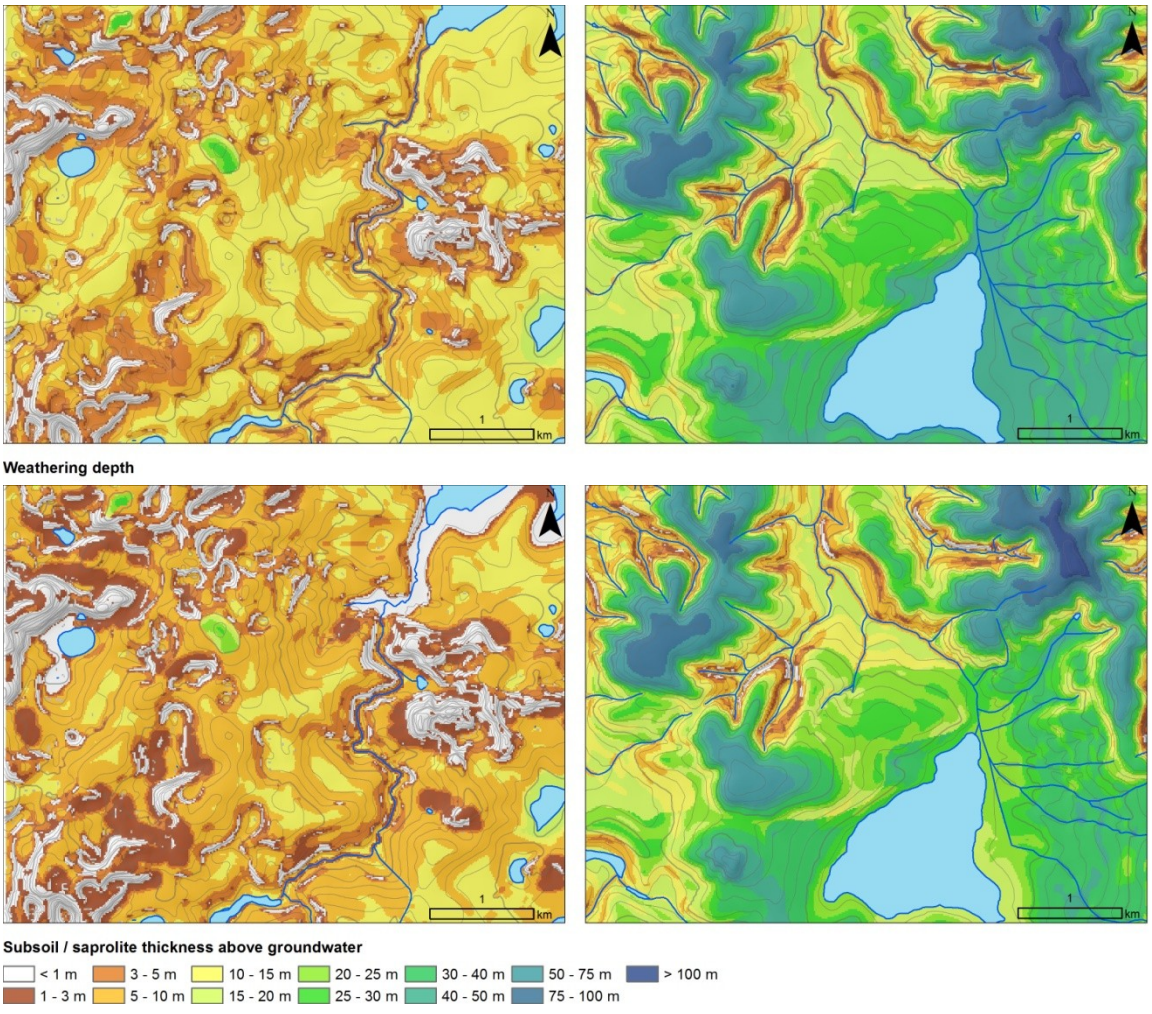

Figure 11-4 Weathering depth (= topsoil + subsoil) and subsoil depth above groundwater.

The location of both exemplary areas is indicated in Figure 10-5 (karstified terrain A on the left, covered karst area B on the right). See also Map 42 in the Annex.

11.4 Thickness of hard bedrock above groundwater

Subtracting the weathering depth from the elevation above groundwater level, the thickness of hard bedrock above groundwater level can be calculated. This comprises the unweathered part of the carbonates of the Sete Lagoas Formation and of the crystalline basement. An example of this result is given in Figure 11-5 and an overview of for the whole study area in Map 46.

The comparison of the interpolated top basement surface (section 5.9.4) with local groundwater level results in a map showing the thickness of crystalline bedrock above groundwater level (Map 48 in the annex). If this thickness is subtracted from the thickness of hard bedrock above groundwater level, the thickness of unweathered carbonates of the Sete Lagoas Formation above groundwater level can be derived (Map 47 in the annex).

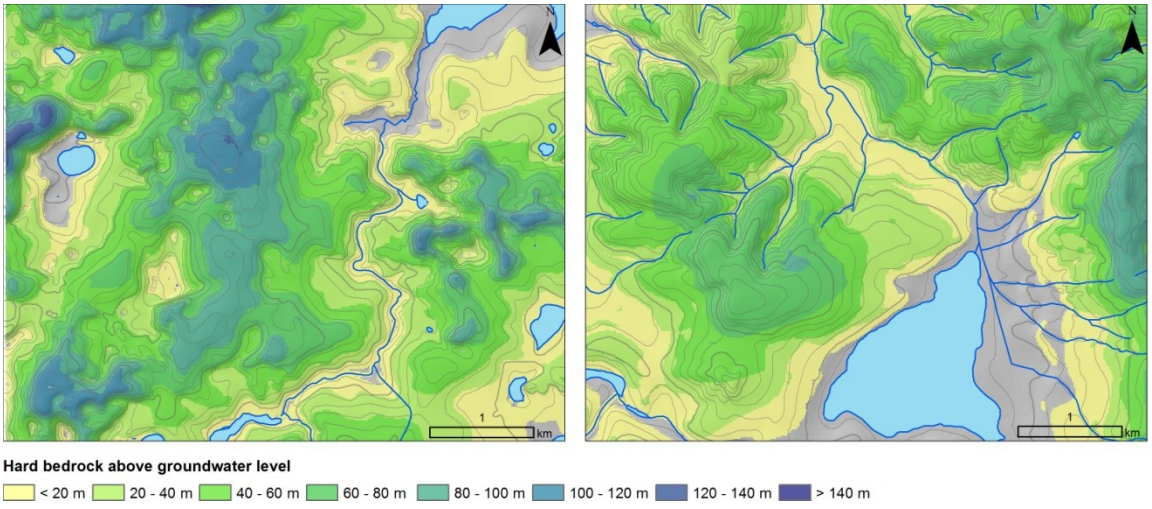

Figure 11-5 Thickness of hard bedrock above groundwater level (Sete Lagoas Formation).

The location of both exemplary areas is indicated in Figure 10-5 (karstified terrain A on the left, covered karst area B on the right). See also Map 46 in the annex.

12 Resources

This chapter gives an overview of the availability of mass resources in the study area, namely carbonate rocks used for cement and crushed stone production and sand from alluvial plains that is mainly used for concrete. While the later is discussed in an article published in "Neues Jahrbuch für Geologie und Paläontologie" (see page 237), an optimality value for limestone mining is derived from lithology and weathering depth following the workflow described in chapter 5. Additionally, the resource value of soils for agricultural production is considered.

12.1 Limestone

To estimate the resource availability of limestone, two essential parameters were used: resource thickness and thickness of overburden. Environmental parameters are not yet considered but need to be added in a separate layer. Both have been calculated in chapter 5 and 6, where thickness of hard rock and thickness of soft material above groundwater level were used to estimate the protection of the aquifer by overlying layers.
For resource estimation, an optimality value was assigned that increases linearly with increasing resource thickness until a thickness of 100 m (Map 49 in the annex). Resource thickness values larger than 100 m were assigned an optimality value of 1. Also for thickness of overburden a linear optimality function was used that assigned an optimality value of 1 to a overburden thickness of 0 meters and an optimality value of 0 for an overburden thickness of 15 meters or more (Map 50 in the annex).
Since both parameters are equally important and both needed, the product of both optimality values was used to derive the optimality value of limestone resource availability (Map 51 in the annex).
Map 37 in the annex shows the facies distribution of the Sete Lagoas Formation and thus gives additional information on carbonate content of the limestone strata, which can be used to assign optimality values for specific purposes.

12.2 Sand

Sand is a resource that is sometimes neglected, as it is not a precious mineral appropriate to be exported but is consumed near its extraction location. Despite the low value of the basic products, natural aggregates are a major contributor to and an indicator of the economic wellbeing of a nation (Terpodei 1999). With aggregate consumption at 2.1 tons per capita - 1.5 t of it sand (DNPM 2006, IBGE 2006) - compared to 8.7 t per capita aggregate consumption in the United

States (Terpodei 1999), Brazil shows a latent demand for aggregates, which represents a need for housing and infrastructure (Coelho 2001).
For economic reasons, aggregates for construction purposes need to be extracted close to the site of their application because they are needed in large amounts but relatively low-priced (Poulin et al. 1994, Valverde 2001). Depending on the distance, the transport costs make up for 1/3 to 2/3 of the total costs for aggregates in Brazil (Valverde 2005). A negative example regarding sand transportation is the metropolitan region of São Paulo: here, half of the sand is transported from areas more than 150 km away due to sealing and to restrictions of locally abundant as well as potentially available sand resources (Coelho 2001). This circumstance is estimated to generate traffic of 20.000 trucks permanently involved in the transportation of sand (Rangel 1997), provoking high costs, elevated CO_2 emission, damage to roads, congestion and increased accident risk. In the region of Belo Horizonte, sand is usually not transported further than 50 km (oral communication from the owner of a sand pit).

12.2.1 Method

There exist only very few drilling results that are available from public organizations such as the geological survey (CPRM) or the COPASA (water supply company). Thus, to calculate the sand resources for the whole fluvial system of the Riberão da Mata, the study had to rely on regional topographical and geological data and additional information gained from the sedimentary structure of an active sand pit in October 2006 (Figure 5-19). The depositional architecture and sedimentary structures visible in this sand pit were used to estimate composition and sedimentary structure of the deposits, e. g. net-to-cross sand distribution. The resources of the sand pit itself have been estimated to 330,000 m³ sand according to a regional map listing the geological resources of the area (Heineck 1999).
For a good estimate of the total volume of Quaternary sediments relevant for economically viable sand extraction in the Riberão da Mata system, it is essential to have an orthogonal profile with respect to the Riberão da Mata showing the thickness of the alluvium i.e. the border of the Basement / Bambuí to the overlying Quaternary. This presupposes costly sophisticated methods and / or systematic boreholes. This is out of the scope of the present work due to a limited financial budget. For these reasons, the following GIS-based method is suggested:
As the sand resources are restricted to the alluvial plains draining sand-yielding lithologies, the maximum possible amount of these sediments was estimated by means of topographical analysis. From topographical data (20 m interval contour lines from the topographical map 1:50 000) a digital elevation model was generated. In general, the accumulation of exploitable sand requires a minimum source area and a maximum slope. Slope and drainage area were calculated using the flow direction algorithm from Garbrecht and Martz (1997) that is implemented in the software

TAUDEM (Tarboton 2005). A slope angle of less than 3° and a contribution area of more than 0,5 km² yielded reasonable results for identifying floodplain areas that would also have been interpreted as such by visual analysis of the relief.

The analysis was restricted to the central parts of the alluvium where the sediment accumulation is considered to be larger. To do so, a buffer of 50 m from the outlines of the flat areas was subtracted and then added again. By this procedure, flat parts that are narrower than 100 m (e. g. small side valleys) were clipped off. After that, all areas smaller than 0,5 km² were deleted to take into account only the deposits large enough for economic extraction.

After defining the area of the alluvial plains, the Quaternary basis had to be estimated to calculate the volumes of sand. For rivers running through the Archean gneiss and migmatite basement, a shallow rounded profile of the contact to the Quaternary basis was assumed. For limestone areas that have a different weathering regime, a profile was assumed that is steeper at the borders but does not reach the same depth as the basement profile in the middle (Figure 12-1). The values for these geometries were adapted from the very few available drill holes in the area and general erosion and sedimentologic processes observed in the region.

Areas already urbanized are no longer available for resource extraction. Thus, the urbanized area in the region was delineated using a Landsat 7 ETM+ image from 2002 and a maximum likelihood classification algorithm implemented in the software ERDAS Imagine 9.0. The classification was validated by visual comparison with higher resolution data (e.g. from Google Earth).

The depth of the Quaternary sediments outside urbanized areas is shown in Map 52 in the annex.

To compare the width of the alluvial plains with the longitudinal profiles of the rivers, longitudinal profiles of the Riberão da Mata and its affluents were generated using the topographical map with 20 m equidistant contour lines that was also the basis for the digital elevation model (Figure 12-2). In the lower parts of Riberão da Mata and Rio das Velhas, this information could be supplemented by 10 m equidistant contour lines from the topographical map 1:25 000. The discontinuities of the longitudinal river profiles from Figure 12-2 are shown as white lines across the alluvium. It can be seen that the discontinuities of the length profile coincide with broader alluvial plains and confluence zones upstream. Thus they support the rough GIS-model used for estimating the volume of the Quaternary sediments. For some knick points, comparison with a geological map reveals a close relationship to lithological contrast related to dykes and a change of crystalline to limestone bedrock. Other knick points seem to be related to base level changes of the receiving stream Rio das Velhas. Base level changes of the receiving stream result in knick points moving upstream with distinct velocities proportional to the discharge area of the contributing rivers.

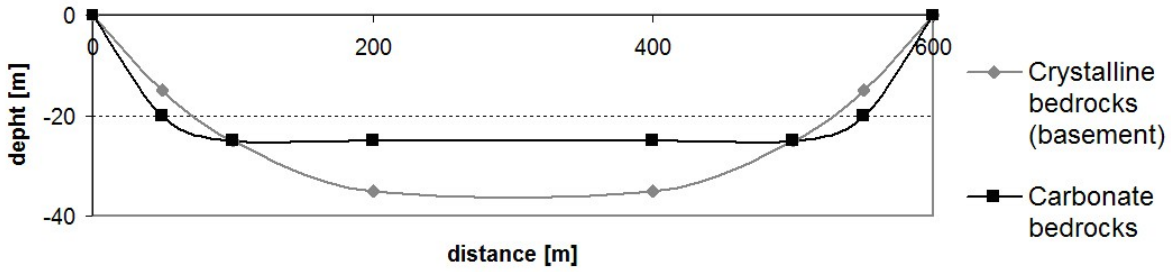

Figure 12-1 Idealized profiles of the Quaternary basis that were used to estimate the volume of the Quaternary sediments along the Riberão da Mata.

For crystalline basement and carbonate sediments two different profiles were assumed.

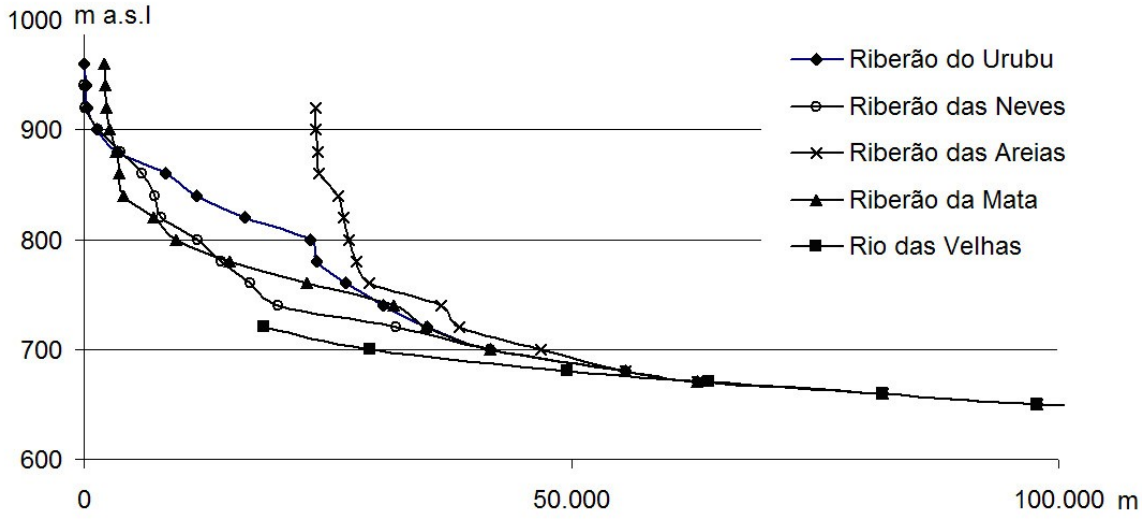

Figure 12-2 Longitudinal profiles of Riberão da Mata and its affluents.

The profiles show several steps (knickpoints) that coincide with broader alluvial plains upstream (compare Map 52 in the annex). Clearly visible are the overall shapes of graded river profiles (EINSELE 2000) exponentially related to the discharge rate and distance from the source area.

Taking the sedimentological observations of the sand pit as a case study (compare section 5.8), it was attempted to regionalize these findings for the sedimentological architecture of the Riberão da Mata system. This regionalization is based on the similar bedrock of the studied sand pit and most of the drainage area, which is crystalline basement. The different inclination of the rivers as they are indicated by the knick points in the length profiles may restrict the transfer of the findings of one sand pit to the rest of the river system. Nevertheless, the drill holes in the Riberão das Neves alluvial plain are located upstream of a (shallow) knick point and show also a fining-upward pattern similar to the one observed in the sand pit. Thus – having no other data - the

observations of the sand pit were used for a general estimation of the sand content in the studied alluvial plains.
Based on this local case study, it is assumed that the sand content is around one third of the Quaternary sediments and often buried below a thick overburden, which may hinder an economically viable exploitation of the sand resources (Lorenz and Gwosdz 2002). Due to geometrical reasons and the large overburden, probably only about 1/3 of the existing sand resources is economically exploitable.

12.2.2 Result

Based on the assumptions made in section 12.2.1 , the total volume of extractable sand in the Riberão da Mata fluvial system can be estimated to about 230 Million m³.
The analysis of the Landsat 7 ETM+ image from 2002 shows that about 20% of the alluvial plains selected in the GIS calculations above are already sealed and thus no longer available for mass resource extraction. Given the federal legislation of Brazil that defines a protected buffer zone of 30 to 50 meters along rivers similar to Riberão da Mata and its affluents, it may be estimated that again 10 to 20% of the remaining resources cannot be extracted due to environmental legislation. Taking all these considerations into account, roughly about 100 Million m³ extractable sand resources might be found in the alluvial plains of the Riberão da Mata.
To compare the available sand resource with the transport costs, a cost-distance value is calculated for the area around the center of urban growth near the city of Lagoa Santa and the International Airport Tancredo Neves. This cost-distance value incorporates the distance weighted by the inclination of the terrain that has to be crossed. This is a much more realistic index for transport distance than the direct distance, as roads are usually built along valleys to avoid steep legs. The grey background shades on Map 52 in the annex show five equidistant classes of cost-distance values for the region. In the closest zone, around 33 Million m³ of extractable sand are estimated, in the next zone around 40 Million m³ and in the two outermost zones around 13 Million m³ extractable sand each. Although these values are based on very rough estimates, they might give a hint about the dimension of the resources lying in the alluvium of this river system.

12.3 Agricultural value of the soils

12.3.1 Favorable chemical properties

Strong relief and unfavorable chemical properties are the main limiting factors for agricultural use of the soils in the study area. Chemical properties are generally better on footslope positions than on hilltops. Eroded topsoil material with more favorable conditions accumulates in downslope positions and the soils on high planation surfaces are the oldest soils in the landscape and are depleted of most nutrients. The cation exchange capacity is generally low (< 12 cmolc/kg) due to the domination of two-layer clay minerals (kaolinite). Higher values occur only on steep slopes on carbonates or in locations where organic material accumulates due to hydromorphic conditions. The spatial distribution of base saturation is similar: the base saturation is generally low in the study area (< 50%), only in alluvial plains, doline bottoms or on steep slopes on carbonates higher values are common. Especially on steep slopes on Bambuí meta-pelites or crystalline basement, very low base saturation is accompanied by high saturation of aluminum, often reaching levels that are impeding plant growth. Thus, the optimality value for "favorable chemical properties" is calculated using the following parameters:

Favorable topographic position:

- An overlay of "low" MTPI *OR* "low" RTPI yields high optimality values for footslopes and low optimality values for hilltops and plateau areas.

Hydromorphic conditions / Gleysols:

- Hydromorphic conditions are usually associated with the accumulation of organic material, high base saturation and higher effective cation exchange capacity. Thus, the optimality values for Gleysols (section 10.6.2) is interpreted as favorable chemical soil properties.

Favorable lithology:

- This optimality value was set to 1 for pure limestone, 0.8 for impure limestone and 0.1 otherwise.

Favorable slope:

- For limestone areas, slope has a positive effect on chemical properties, since the weathering products are rich in basic cations. For basement and pelite areas, slope has a negative effect on chemical properties, since the base saturation and effective cation exchange capacity of the saprolite are even lower than for the lateritic topsoil. Thus, the optimality value for slope was set equal to "not flat slope" (compare section 10.3.2) for limestone areas and equal to "flat slope" for the rest of the study area.

The resulting optimality value for "favorable chemical properties" was then calculated using a weighted overlay of the four parameters, with "favorable topographic position" and "favorable

lithology" receiving the double weight compared to "hydromorphic conditions" and "favorable slope".

Two extracts of the resulting map is shown in Figure 12-3.

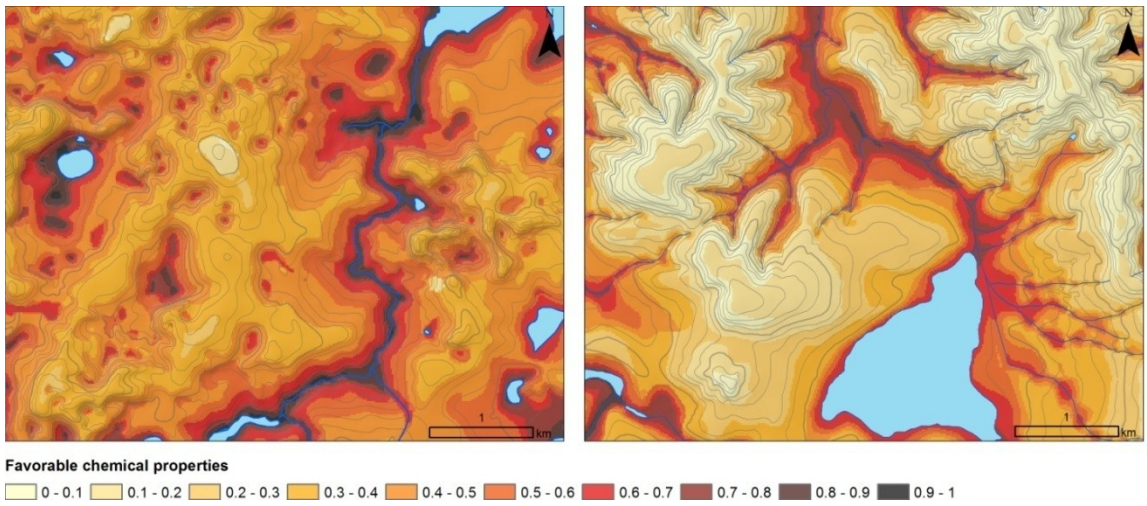

Figure 12-3 Spatial distribution of the optimality value for "favorable chemical properties".

The location of the exemplary areas is indicated in Figure 10-5 (karstified terrain A on the left, covered karst area B on the right). See also Map 65 in the Annex.

12.3.2 High agricultural value

For the estimation of the agricultural value of the soil, also other properties are important: waterlogging impedes mechanical preparation of the soil during at least part of the year and also limits the use to plants that are able to cope with temporary oxygen deficiency. Low eFC, which is common in deep and highly permeable Ferralsols, can limit the agricultural value due to water deficiency during the dry season. Thus, the variables "no hydromorphic conditions", "high eFC within 1 meter" (compare section 10.8.5), and "favorable chemical properties" were combined in a weighted overlay. For this overlay, chemical properties were rated 2.5 as important as the absence of hydromorphic conditions which certain crops can tolerate.

From the resulting map, steep areas were excluded by a minimum overlay with the spatial properties "flat slope". The workflow can be noted as:

$$\mu_{high\ agricultural\ value} = \frac{\mu_{favorable\ chemical\ properties} * 2.5 + \mu_{no\ hydromorphic\ conditions}}{3.5}\ AND\ \mu_{flat}\ (Slope)$$

Equation 12-1 "High agricultural value"

A detail of the result is shown in Figure 12-4, an overview for the total study area is given in the annex (Map 65).

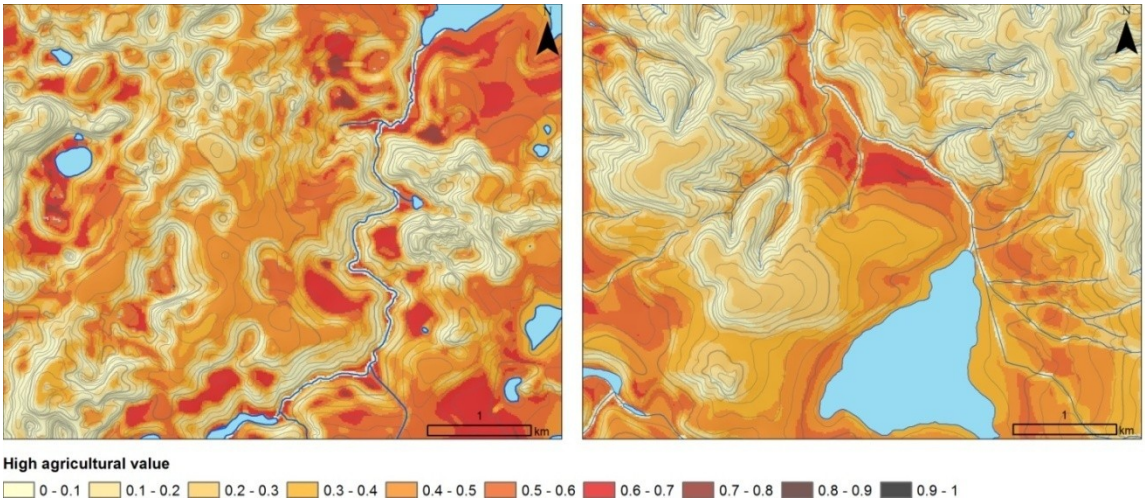

Figure 12-4 Spatial distribution of the optimality value for "favorable chemical properties" and "high agricultural value".

The location of the exemplary areas is indicated in Figure 10-5 (karstified terrain A on the left, covered karst area B on the right).

13 Groundwater vulnerability

The natural vulnerability of aquifers to contamination is a qualitative, relative, non-measurable and dimensionless property (Vrba and Zaporozec (1994) in Goldscheider (2005)), indicating the amount of natural protection against contamination of the groundwater. In the last decades, many methods have been developed to map this property and to provide decision aids for land use management. An overview can be found in Magiera (2000). Some of the most known methods are parametric system models that define a rating system or point count for each parameter that is relevant for groundwater protection (e.g. Aller et al. (1987), Hölting et al. (1995)). Since karst aquifers are generally highly vulnerable but at the same time important and large sources for drinking water, specialized methods have been developed for karst regions (e.g. Doerfliger et al. (1999)). For the Pan-European Approach to vulnerability mapping in karst aquifers proposed by COST Action 620 (Zwahlen 2004), a new method was developed that is known as the PI-method (Goldscheider et al. 2000, Goldscheider 2002). The PI-method itself uses concepts from the German GLA-method (Hölting et al. 1995), the EPIK method for karst aquifers (Doerfliger et al. 1999) and the Irish method (GSI 1999). The PI-method classifies groundwater vulnerability according to estimated travel time through overlying layers with additional considerations of possible bypassing into karst sink holes. It is a method designed for mapping intrinsic groundwater vulnerability, i.e. groundwater vulnerability that is independent of the nature of the contaminant. The target is the surface of the first relevant aquifer (resource vulnerability mapping) and does not consider the direction of saturated flow in the aquifer. Since the PI-method combines the general, well established ground water vulnerability assessment from Hölting et al. (1995) with specific characteristics for karst areas it was chosen with minor adaptations for the partly karstified study area.

13.1 Overview of the PI-Method

The basic idea of the PI-method for assessing groundwater vulnerability is the dependence of a possible contamination of the aquifer on the cumulated travel time through all protecting layers. This protective function of the overlying layers is called the P-factor and includes the protection by the topsoil (1), the subsoil or unconsolidated sediments (2) and the karstic or non-karstic bedrock above the water table (3,4) (Figure 13-1). So far, the approach is very similar to the method proposed by Hölting et al. (1995). Additionally, the risk of direct infiltration into the karst aquifer by surface and shallow subsurface flow into sinking streams is accounted for by a separate parameter, the I-factor. This factor is 1 for areas where infiltration through all protecting layers dominates (eg. flat, permeable areas), and ranges between 0 and 1 for areas where lateral surface and subsurface flow can bypass the protecting layers and infiltrate into a swallow hole The I-

factor depends on infiltration conditions and the hydraulic closeness (catchments of sinking streams) to swallow holes. By multiplying the P and I factor, the resulting total vulnerability is calculated. A simplified flow chart of the PI-method is shown in Figure 13-1.

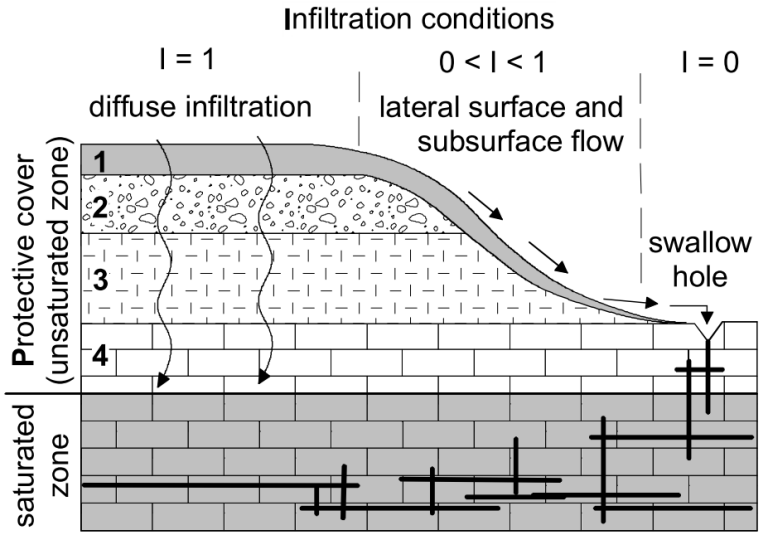

Illustration of the PI method: The P factor takes into account the effectiveness of the protective cover (1. topsoil, 2. subsoil, 3. non-karstic bedrock, 4. unsaturated karstic bedrock). The I factor expresses the degree to which the protective cover is bypassed by lateral surface and subsurface flow, especially within the catchments of sinking streams.

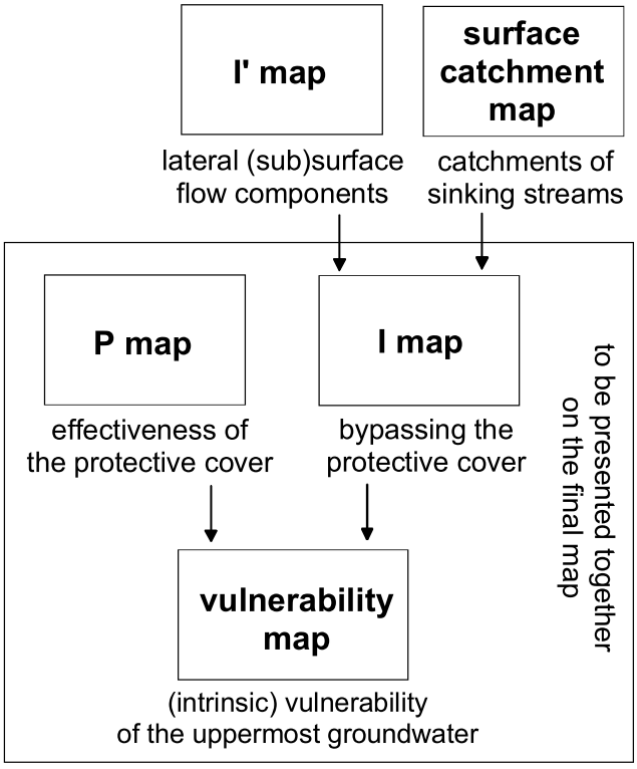

Figure 13-1 General concept and flow chart of the PI method (Goldscheider 2002).

13.1.1 The P-Factor

The calculation of the P-Factor is similar to the protective function after Hölting et al. (1995). A point system assigns protection scores for topsoil, subsoil and bedrock (Figure 13-2). For the first meter, the effective field capacity (eFC) of the topsoil is used as an estimate for the protective function. The eFC is equivalent to the storage capacity of plant available water and thus controls the residence time of possibly contaminated water. The T-value score varies from 0 for soils with less than 50 mm eFC up to 750 for soils with more than 250 mm eFC. The topsoil value is calculated uniformly for the first meter, independent of real soil thickness or rooting depth. If the topsoil is shallower and overlies unconsolidated sediments (e.g. alluvial sand), these sediments are included up to 1 meter depth into the calculation of the topsoil protection value. The relatively low score for very clayey soils is justified by shrinking cracks during dry periods that lead to preferential flow.

The subsoil protection S-value score is derived from grain size distribution, the score values are originally based on the typical cation exchange capacity of each texture class (Hölting et al. 1995). The list ranges from 500 for clay until 5 for gravel. The subsoil score is used not only for subsoil in a pedological sense but also to unconsolidated sediments where intergranular pores have a large influence on water storage capacity.

The bedrock protection value (B) applies only to hard rocks where water transport is dominated by fissures and cracks. It is calculated using a score for lithology (L-value) multiplied by a score for fracturing (F-value) that includes also the intensity of karstification. The subsoil and bedrock values are multiplied by the thickness of each layer and then added to the topsoil score value. The total sum is them multiplied with the recharge factor R, which is 1 for an annual recharge of 200-300 mm, higher for less recharge and lower for higher recharge.

Topsoil - T

eFC [mm] up to 1 m depth	T
> 250	750
> 200-250	500
> 140-200	250
> 90-140	125
> 50-90	50
< 50	0

Recharge - R

Recharge [mm/y]	R
0-100	1.75
>100-200	1.50
>200-300	1.25
>300-400	1.00
>400	0.75

Subsoil - S

Type of subsoil (grain size distribution)	S	Type of subsoil (grain size distribution)	S
clay	500	very clayey sand, clayey sand, loamy silty sand	140
loamy clay, slightly silty clay	400	sandy silt, very loamy sand	120
slightly sandy clay	350	loamy sand, very silty sand	90
silty clay, clayey silty loam	320	slightly clayey sand, silty sand, sandy clayey gravel	75
clayey loam	300	slightly loamy sand, sandy silty gravel	60
very silty clay, sandy clay	270	slightly silty sand, slightly silty sand with gravel	50
very loamy silt	250	sand	25
slightly clayey loam, clayey silty loam	240	sand with gravel, sandy gravel	10
very clayey silt, silty loam	220	gravel, gravel with breccia	5
very sandy clay, sandy silty loam, slightly sandy loam, loamy silt, clayey silt	200	non-lithified volcanic material (pyroklastica)	200
sandy loam, slightly loamy silt	180	peat	400
slightly clayey silt, sandy loamy silt, silt, very sandy loam	160	sapropel	300

Lithology - L

Lithology	L
claystone, slate, marl, siltstone	20
sandstone, quarzite, volcanic rock plutonite, metamorphite	15
porous sandstone, porous volcanic rock (e.g. tuff)	10
conglomerate, breccia, limestone, dolomitic rock, gypsum rock	5

Fracturing - F

Fracturing	F
non-jointed	25.0
slightly jointed	4.0
moderately jointed, slightly karstified or karst features completely sealed	1.0
moderately karstic or karst features mostly sealed	0.5
strongly fractured or strongly karstified and not sealed	0.3
Epikarst strongly developed, not sealed	0.0
not known	1.0

Thickness of each stratum in [m] - M

Bedrock - B
$B = L \cdot F$

Artesian pressure A
1500 points

Total protective function P_{TS}

$$P_{TS} = \left[T + \left(\sum_{i=1}^{m} S_i \cdot M_i + \sum_{j=1}^{n} B_j \cdot M_j \right) \right] \cdot R + A$$

score P_{TS}	effectiveness of protective cover	P-factor	example
0-10	very low	**1**	0-2 m gravel
>10-100	low	**2**	1-10 m sand with gravel
>100-1000	medium	**3**	2-20 m slightly silty sand
>1000-10000	high	**4**	2-20 m clay
>10000	very high	**5**	> 20 m clay

P-map

Figure 13-2 Calculation of the P-factor (Goldscheider (2002) after Hölting et al. (1995)).

13.1.2 The I-factor

The I-factor quantifies the degree of bypassing the protecting layers used for the estimation of the P-factor. Surface flow that reaches a sinking stream will infiltrate through the swallow hole directly without traveling through all layers vertically below its origin. Thus, the dominant flow process is the primary variable used in determining the I-factor. The method distinguishes between dominant infiltration and subsequent percolation for highly permeable soils (A), fast or very fast subsurface stormflow (B and C) and rare or frequent Hortonian surface flow for low permeable soils (E,F). If an impermeable layer exists within 100 cm from the surface, saturated surface flow is assumed (D). The different categories are summarized in Figure 13-3 .
In a second step, the domains of dominant flow processes receive an I'-factor score depending on slope and land use (Figure 13-4). In a third step, this I'-factor is rated according to its hydrological closeness to a swallow hole, with the swallow hole, its sinking stream and 100 m buffer being the highest risk unit, the catchment of the sinking stream the second unit and the total karst area the third unit. If an area is draining outwards of the karst area, a uniform I-factor of 1.0 is used (Figure 13-4).

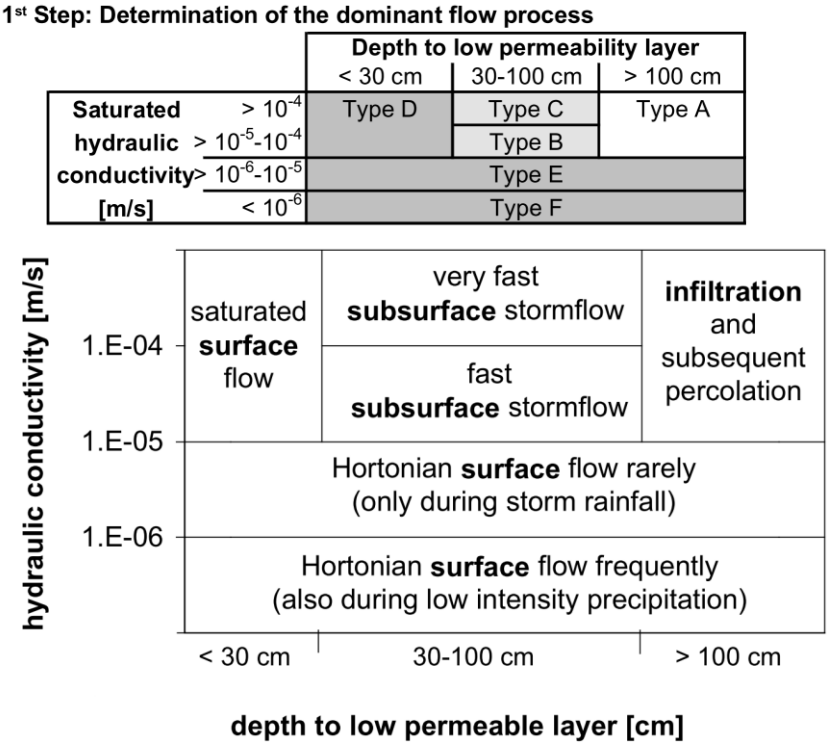

Figure 13-3 1st step of the determination of the I-factor: Dominant flow processes for different soil types (Goldscheider 2002).

2nd Step: Determination of the I'-factor

Forest				
dominant flow process		Slope < 3.5 %	Slope 3.5 - 27 %	Slope > 27 %
infiltration	Type A	**1.0**	**1.0**	**1.0**
subsurface flow	Type B	1.0	0.8	0.6
	Type C	**1.0**	**0.6**	**0.6**
surface flow	Type D	0.8	0.6	0.4
	Type E	1.0	0.6	0.4
	Type F	**0.8**	**0.4**	**0.2**

Field/Meadow/Pature				
dominant flow process		Slope < 3.5 %	Slope 3.5 - 27 %	Slope > 27 %
infiltration	Type A	**1.0**	**1.0**	**0.8**
subsurface flow	Type B	1.0	0.6	0.4
	Type C	**1.0**	**0.4**	**0.2**
surface flow	Type D	0.6	0.4	0.2
	Type E	0.8	0.4	0.2
	Type F	**0.6**	**0.2**	**0.0**

3d Step: Determination of the I-factor

Surface Catchment Map		I' factor					
		0.0	**0.2**	**0.4**	**0.6**	**0.8**	**1.0**
a	swallow hole, sinking stream and 10 m buffer	0.0	0.0	0.0	0.0	0.0	0.0
b	100 m buffer on both sides of sinking stream	0.0	0.2	0.4	0.6	0.8	1.0
c	catchment of sinking stream	0.2	0.4	0.6	0.8	1.0	1.0
d	area discharging inside karst area	0.4	0.6	0.8	1.0	1.0	1.0
e	area discharging out of the karst area	1.0	1.0	1.0	1.0	1.0	1.0

I-map

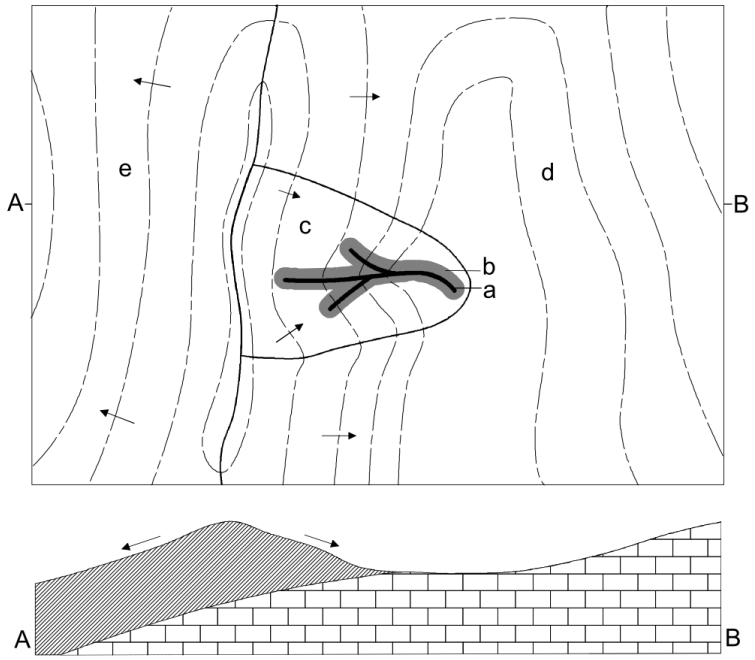

Figure 13-4 2nd and 3rd step for the determination of the I-Factor: Categories for slope, land use and surface catchment (Goldscheider 2002).

13.1.3 The final vulnerability map

The final vulnerability map, also called the PI-map or π-map, is calculated by multiplying the P - factor with the I - factor. A ranking is applied for P, I and π-map that classifies the area in five units (Figure 13-5):

	vulnerability map vulnerability of groundwater		**P-map** protective function of overlying layers		**I-map** degree of bypassing	
	description	π-factor	description	P-factor	description	I-factor
red	extreme	0-1	very low	1	very high	0.0-0.2
orange	high	>1-2	low	2	high	0.4
yellow	moderate	>2-3	moderate	3	moderate	0.6
green	low	>3-4	high	4	low	0.8
blue	very low	>4-5	very high	5	very low	1.0

Figure 13-5 Final groundwater vulnerability based on the P-map and I-map. The π-factor is defined as the product of P-factor and I-factor (Goldscheider 2002).

All three maps together supply relevant information about the total intrinsic groundwater vulnerability and also whether the highest risk of groundwater contamination is trough direct local infiltration or through lateral surface or subsurface flow processes into sinking streams.

13.2 Adaptation of the PI-method to the study area

To assess the groundwater vulnerability for the study area, the PI method (Goldscheider et al. 2000) was adapted to the specific conditions of the tropical environment of the study area.

Most applications of the PI-method in Europe were based on detailed soil, geology and groundwater data (Andreo et al. 2006, Goldscheider 2002, 2005, Schmidt F 2003). The spatial scale was detailed and covered usually less than 100 km². When the method was transferred to a remote tropical area with scarce database, it had to be simplified but still yielded good results (Nguyet and Goldscheider 2006).

For the current study, geological, geomorphological and pedological information was available at a scale of 1:50 000, only the topographic map was available at a scale of 1: 25 000. The geological map was revised during the study as described in chapter 5 and the bedrock architecture above groundwater level is regionalized as described in chapter 11. A similar approach using a detailed three-dimensional analysis of the protecting layers above groundwater

to enhance a given groundwater protection method has been successfully applied by other members of the working group (Lamelas et al. 2007, Lerch and Hoppe 2007).
Additionally, hydrological soil properties were regionalized using a SIM approach that is described in chapter 10.

13.2.1 P-Factor

For the P-factor, all protecting layers above the groundwater level are assigned a protection value which is multiplied by the thickness of each strata (Equation 13-1) .

$$P_{TS} = \left[T + \left(\sum_{i=1}^{m} S_i \cdot M_i + \sum_{j=1}^{n} B_j \cdot M_j \right) \right] \cdot R + A$$

Equation 13-1 Total protective function P_{TS} from Goldscheider (2002)

T = Topsoil protection score for the first meter

S = Subsoil protection value

B = Bedrock protection value

M = thickness of each strata

R = Recharge factor

A = Addtiive component for artesian pressure

According to Goldscheider (2002) the uppermost aquifer should be always the target of vulnerability mapping. In the study area, a temporary perched aquifer can appear in the higher plateau regions due to deep interflow at the border between highly permeable ferralitic soil and pelite saprolite (see also catenas in section 9). Nevertheless, because of the temporary character of this aquifer, it was not taken into account for this study.

In the following sections, the calculation of these protection values is described for each layer.

13.2.2 Topsoil protection score T

This score is usually taken from a discrete table (Figure 13-2 on p. 248, upper part), relating ranges of effective field capacity within the first meter to a topsoil protection score T. Effective field capacity is a good indicator for traveling time for the water through soil since it defines the amount of water that can be stored in the soil. Opposed to a classification by texture, the eFC values take into account that very fine soils (e.g. pure clay soils) tend to have low protection due

to shrinking cracks. Although these are not common in the study area due to the domination of non-expansive clay minerals and strong water-stable aggregation, the eFC is also here a better measure for the hydraulic properties of the soil than soil texture.

Effective field capacity within the first meter was regionalized as a spatial continuous variable in section 10.8.5. A classification according to Figure 13-2 would result in a loss of spatial information. Thus, a trend function was fitted to the topsoil scores T and their related mean effective field capacity from the upper part of Figure 13-2. A second order polynomial was chosen as best trend function:

$$T(eFC) = 0.0107\ (eFC)^2 - 0.2092\ eFC$$

Equation 13-2 Topsoil protection score (eFC)

This equation was then used to create a spatially continuous distribution of the topsoil protection score T (Figure 13-7).

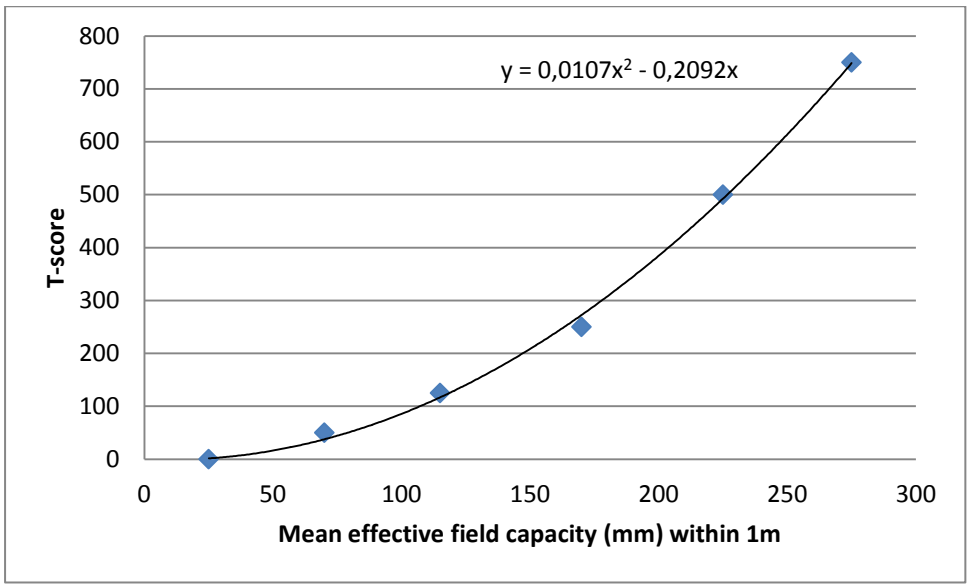

Figure 13-6 Trend function relating continous T-values to effective field capacity of the topsoil.

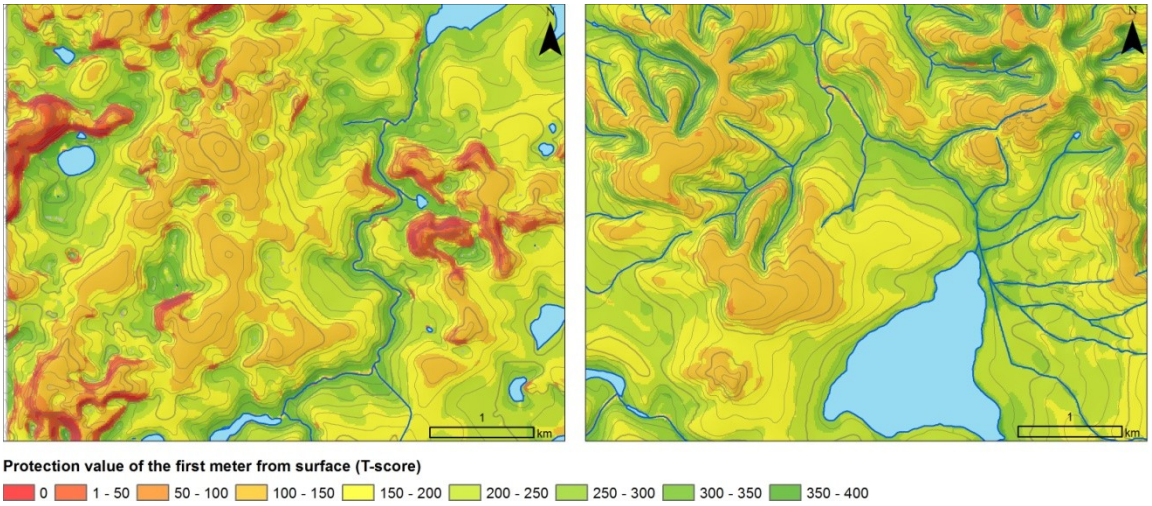

Figure 13-7 Topsoil protection score derived from the eFC of the first meter using the polynomial trend function of Figure 13-6 .

The location of the exemplary areas is indicated in Figure 10-5 (karstified terrain A on the left, covered karst area B on the right).

13.2.3 Subsoil protection score S

The table from the PI-method to derive the subsoil protection value (Figure 13-2 middle part) is based on Hölting et al. (1995), who relate protection value for subsoil or unconsolidated sediments to their effective cation exchange capacity. Since in temperate regions, effective cation exchange capacity is directly related to soil texture, these values were transferred into soil texture classes for the PI-method.

In the tropical study area around Lagoa Santa, the dominance of low activity clays and the strong water resistant micro structure of the soil limits the direct application of this table. Thus, instead of using subsoil texture only, other parameters were incorporated to estimate the mean travel time through the subsoil: the percentage of large pores as determined by the total porosity minus the water drained at 0.1 atm (data from CPRM (1994b), see also section 7.3) and infiltration measurements using a double ring infiltrometer (section 8.2.5).

Nevertheless, these data are not statistically significant due to the small number of soils profiles for which hydrological data were available and the only exemplary nature of the infiltration experiments. Thus, they were used as a first estimation that would need deeper research in future projects.

The chosen protective values together with the base data are summarized in Table 13-1 .

Bedrock	Estimated S-Value
Alluvial plains and terraces	Quaternary sediments are very variable, thus an estimated mean value of 200 is used. Higher terraces receive lower values (150 resp. 100) due to dominance of sand and gravel.
Bambuí meta-pelites	260 Equal to clayey silt - silty clay
Bambuí Carbonates (Carrancas unit, Sete Lagoas Formation)	160: impure carbonates with moderate karst development 100: pure carbonates with strong karst development. The value of 160 is equivalent to pure silt, since clay is mainly aggregated to grains of silt-size in the study area. The lower values for karstified terrain account for the possible existence of epikarst features in the subsoil that reduce the protective value.
Crystalline basement (granite / gneiss and basic dykes)	200 This is an estimate between highly permeable upper part of the topsoil (~loamy sand) and very dense lower part of the saprolite as documented in the infiltration experiment..

Table 13-1 Estimated subsoil protection values for geological units of the study area.

See also Table 8-2 and Figure 13-8.

Weathering depth above ground water level has been estimated in section 11.2.
From this value, one meter was subtracted that was already taken into account for the topsoil value T.
Since topsoil and subsoil definitions are based on hydrological properties in the current study (see chapter 8), also topsoil material below one meter from the surface is possible.
In this case, the T-value was calculated for the topsoil material as described in Figure 13-6 and its thickness was subtracted from the thickness of subsoil material.

Thus, the subsoil protective value was calculated as follows:

$$Total\ subsoil\ protection\ score = \left[\left(\begin{matrix} Weathering\ depth\ AND \\ depth\ to\ groundwater\ level \end{matrix}\right) - 1\ meter - topsoil\ depth\ below\ 1\ meter\right] * S + topsoil\ depth\ below\ 1\ meter * T$$

Equation 13-3 Total subsoil protection score

With

T = topsoil protection value derived from the eFC of the topsoil material using the equation in Figure 13-6

S = subsoil protection value according to Table 13-1.

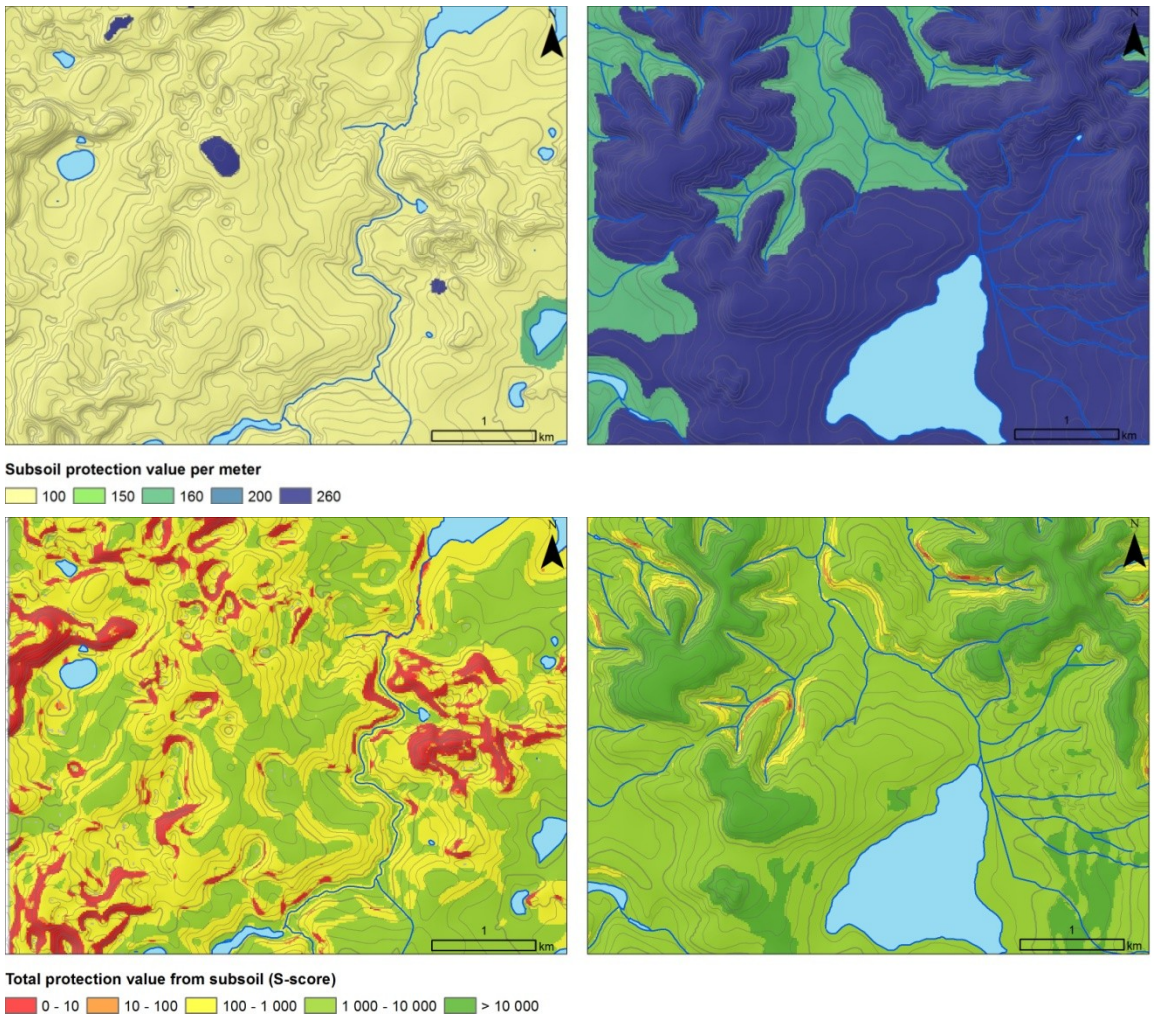

Figure 13-8 Details of the subsoil protection value and the total subsoil protection score.

The location of the exemplary areas is indicated in Figure 10-5 (karstified terrain A on the left, covered karst area B on the right).

13.2.4 Bedrock protective value B

For the bedrock protective value, only hard rocks are considered where water circulates along joints or karst features. Unconsolidated or weathered material is included in the subsoil protection value since its inter-granular water storage capacity adds a high protection value. Thus, the deeply weathered meta-pelites of the Serra de Santa Helena Formation and the Quaternary alluvial sediments and terraces are completely incorporated into the subsoil protection value. Only the carbonates of the Sete Lagoas Formation and the crystalline basement rocks are included in the bedrock protection value.

According to Figure 13-2, the bedrock value B of the PI-method consists of two separate values that are multiplied:

the L-value, which considers lithology and the F-value, which considers fracturing of the rocks.

The L and F values for hard bedrock in the study area is summarized in Table 13-2. The higher the L-factor, the higher its protection function for the groundwater.

The Sete Lagoas Formation was ranked according to the purity of its carbonates, with the pure carbonates of the Lagoa Santa Facies being assigned the L-value of 5 for carbonates according to the table in Figure 13-2 and the impure limestone of the Pedro Leopoldo facies a slightly higher value of 7.

The F-factor indicating the amount of fracturing or karstification was chosen based on the geomorphological compartment and whether the carbonates are covered by meta-pelites or alluvial sediments or not.

For the basement, a uniform L-factor of 15 and a medium fracturing value of 1 was chosen. The bedrock protection factor (B-factor) is then calculated by multiplying the L- and F-factor (Table 13-2).

	L-factor	F-factor	B-Factor = L·F
No hard rock above GW	0	0.0	0.0
Karst outcrops	5	0.0	0.0
Pure limestone, karst strongly developed	5	0.3	1.5
Pure limestone	5	0.4	2.0
Impure limestone	7	0.5	3.5
Covered impure limestone	7	1.0	7.0
Crystalline basement	15	1.0	15.0

Table 13-2 Lithology and fracturing factors for the study area.

Values are based on the table in Figure 13-2 from Goldscheider (2002).

The total bedrock protection score is calculated by multiplying the B-factor with the thickness of each layer above groundwater level as calculated in chapter 11.
Map 71 and Map 72 in the annex show the spatial distribution of the L- and F-factor in the study area. The estimated thickness of hard bedrock of the Sete Lagoas carbonates and the crystalline basement is shown in Map 47 and Map 48 in the annex.

The total bedrock protection score was calculated by:

$$L_{SL} \cdot F_{SL} \cdot M_{SL} + L_B \cdot F_B \cdot M_B$$

Equation 13-4 Total bedrock protection score

With

L_{SL} = L-factor of the Sete Lagoas Formation

F_{SL} = F-factor of the Sete Lagoas Formation

M_{SL} = Thickness of the Sete Lagoas Formation above groundwater

L_B = L-factor of the basement (= 15)

F_B = F-factor of the basement (= 1)

M_B = Thickness of the basement above groundwater

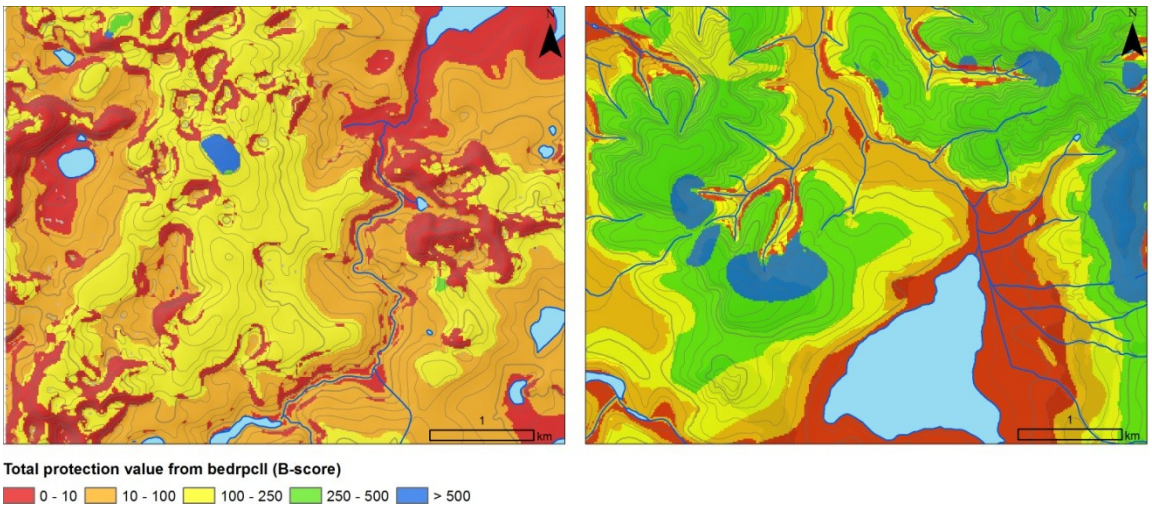

Figure 13-9 Spatial distribution of the total bedrock protection score.

The location of the exemplary areas is indicated in Figure 10-5 (karstified terrain A on the left, covered karst area B on the right).

13.3 The final P-Map

The map of the protective function (P- map) is created by summing up the total topsoil, subsoil and bedrock protection factors which is then multiplied by the recharge factor:

P_{ts} = (topsoil score + subsoil score + bedrock score) TIMES Recharge factor

Equation 13-5 Total protective function P_{ts}

See also Figure 13-2.

Since the annual water balance yields a recharge of 274,5 mm (Pessoa and Mourão (1998), p. 189), the recharge factor is 1.25 according to the table from Goldscheider (2002) in Figure 13-2. The classification scheme defined in the lower part of Figure 13-2 then associates five P-factor categories to the total protective function $P_{Totoal\ Score}$:

P = 1 : very low effectiveness of protective cover ($P_{Totoal\ Score}$ < 10)
P = 2: low effectiveness of protective cover ($P_{Totoal\ Score}$ 10 - 100)
P = 3: medium effectiveness of protective cover ($P_{Totoal\ Score}$ 100 - 1 000)
P = 4 : high effectiveness of protective cover ($P_{Totoal\ Score}$ 1 000 - 10 000)
P = 5: very high effectiveness of protective cover ($P_{Totoal\ Score}$ > 10 000)

An example of the spatial distribution of the P-values is given in Figure 13-10.

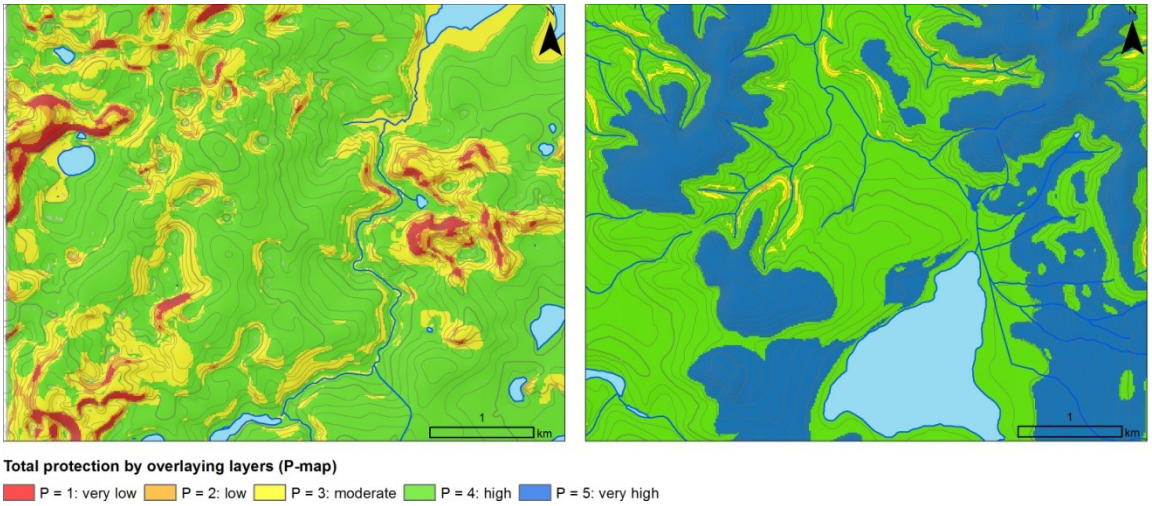

Figure 13-10 Spatial distribution of the total protective function of all layers above groundwater level.

The location of the exemplary areas is indicated in Figure 10-5 (karstified terrain A on the left, covered karst area B on the right).

13.4 Degree of lateral flow: I'-Map

The I'-Map indicates the intensity of lateral flow independent of its location within the catchment. In a first step (Figure 13-3), the dominant flow process has to be determined. For the current study area, five dominant flow process classes were distinguished as described in section 10.10 and assigned to the categories defined for the PI-Method in Figure 13-3:

- Hortonian surface flow: Type E
- Shallow subsurface flow: Type C
- Deep subsurface flow: Type B
- Infiltration: Type A
- Infiltration / saturation excess surface flow: Type D

The classification of dominant flow processes for the study area was mainly based on field observation of hydrological soil properties (mainly on soil macro- and microstructure) rather than direct measurements. The thresholds of saturated hydraulic conductivity from Figure 13-3 were not followed closely since the intense tropical rainfall in the study area produces surface runoff or fast subsurface flow even for higher permeable soil layers than it does in temperate regions.
In the second step (Figure 13-4), the map of dominant flow process is combined with slope and land use to create a map showing the intensity of lateral flow. A matrix table assigns an I'-value for each combination of dominant flow process, slope category and land use.
In this original table from Goldscheider (2002), only two land use categories are listed: forest and field/meadow/pasture. For the current study, sealed areas (urban areas, roads) and water bodies were added as land use category. For water bodies (mainly lakes), an I'-factor of 0.2 was chosen since lateral flow is direct but nevertheless slow in lakes. Sealed areas were treated similar to soils with dominant flow category F (frequent Hortonian surface flow) on fields, pastures or meadows.
Slope was derived from the digital elevation model and land use data from a Landsat 7 ETM+ image from 03.08.2002. The Landsat image was classified using an unsupervised maximum likelyhood classifyier implemented in ArcGIS. First, a higher number of land use classes was generated automatically that were later combined by visual analysis into the four categories forest, open area, sealed areas and water bodies. Afterwards, a majority filter was applied to remove scatter. Although higher resolution data are available through internet services (Google maps, Bing maps), they are difficult to classify automatically due to their heterogeneous mosaic and were thus used for visual comparison only. Nevertheless, the inclusion of high resolution land use data would stronlgly improve the predicitve accuracy of the lateral flow map and is suggested for further studies.
Figure 13-11 shows the spatial distribution of slope and land use categories and the resulting map of the intensity of lateral flow. A version for the total study area can be found in the annex (Map 2, Map 75 and Map 76).

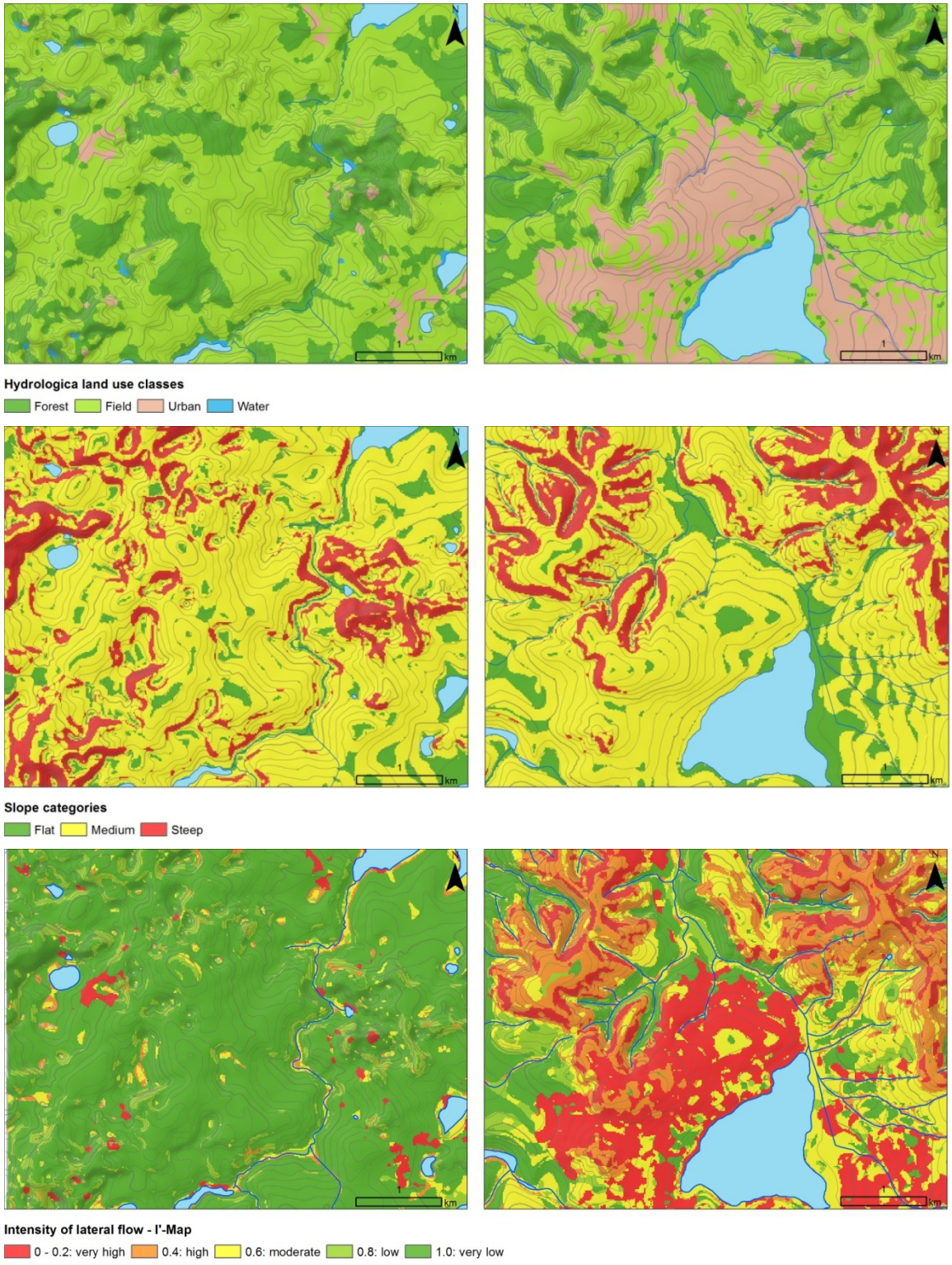

Figure 13-11 Spatial distribution of hydrological slope and land use categories (see Figure 13-4) and the resulting map of intensity of lateral flow (see also Map 76 in the annex).

The very high values are due to sealed urban areas. The location of the map extracts is indicated in Figure 10-5 (karstified terrain A on the left, covered karst area B on the right).

13.5 Karst surface catchment zonation: I-Map

For the assessment of the degree of bypassing protective layers (I-Map), the intensity of lateral flow is weighted according to its location in the watershed. Thus, a map indicating the risk of bypassing the protecting layers of the P-Map is created. This is usually done using the matrix table of Figure 13-4.

The PI-method divides the area into five categories:

Zone a) Swallow hole, sinking stream and 10 m buffer
Zone b) 100 m buffer on both sides of the sinking stream
Zone c) Catchment of the sinking stream
Zone d) Area discharging inside the karst area
Zone e) Area discharging out of the karst area

The rating of the surface catchment can be interpreted differently:
Large parts of the karst plateau drain into more or less well identified local sinks without being channeled into a sinking stream before. If this area is classified into surface catchment *Zone d)* (area discharging inside the karst area) it would receive a lower risk factor than the drainage area of a sinking stream. In the study area, this would not reflect the actual vulnerability correctly: The largest sinking stream (Córrego Samambaia) enters the aquifer very close to the base level river Rio das Velhas (Figure 13-12) and thus poses a comparatively low risk to contaminate the total aquifer. Thus, the catchment of the Lagoa do Sumidouro with the Córrego Samambaia and a small sinking stream entering a similarly low ponor close to the Lagoa do Sumidouro were classified as zones of internal karst drainage with low entrance point into the aquifer (Map 77 in the annex). To stress the contamination risk of the high karst plateau aquifer, which is the largest groundwater resource in the area, a zonation according to entering point into the aquifer was used.

Also the case of streams traversing karst area but not directly infiltrating into a swallow hole is not covered in the original surface catchment classification of the PI-method (Figure 13-4). This is the case for most areas of the covered karst area. Since also some riverbeds may represent zones of infiltration into the karst aquifer, an intermediate classification was used that represented less risk than areas with low entrance point but more than areas draining completely out of the catchment.
The modified zonation rule is shown in Map 77 in the annex and described below in section 13.5.1 .

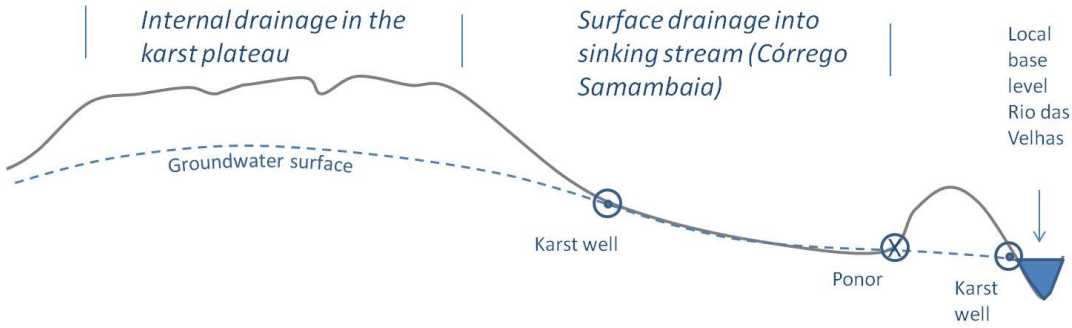

Figure 13-12 Schematic cross-section from the karst plateau to the Rio das Velhas.

The sinking stream Córrego Samambaia poses a comparatively low risk to the karst aquifer since it enters it close to the base level Rio das Velhas.

13.5.1 Modification of the zonation rules for the study area

The following zones were defined for the study area:

High karst area

Zone (a)

Swallow hole, sinking stream and 10 m buffer.

The karst sinks determined by the work flow on described in section 10.4.1 were not used as zone (a) because their location is not certain enough to justify a 10 m buffer.

Zone (b1)

100 m buffer around zone (a) and around plausible sink locations that were determined as described in section 10.4.1 .

Zone (c1)

Catchment of zone (a), i.e. the whole high karst area lacking defined surface drainage.

Low karst area

Zone (b2)

Swallow hole, sinking stream and 10 m buffer.

Zone (c2)

100 m buffer around zone (b2).

Zone d)

Catchment of zone (b2), i.e. the whole catchment of the low karst area.

Other

Zone e1)

Area discharging out of the karst area including catchments traversing karst area but not discharging into a swallow hole.

Zone e2)

Area discharging out of the karst area without traversing karst area.

Interpretation:

- Zone (b1) and (b2) were treated equally to zone (b) in the matrix table of Figure 13-4
- Zone (c1) and (c2) were treated equally to zone (c) in Figure 13-4 .
- For zone (e1), a new classification was created that yielded lower vulnerability values than zone (b) but more than in zone (e) of Figure 13-4.

The resulting I-values for the study area are listed in Table 13-3 and the resulting maps are shown in Figure 13-13 and in Map 78 in the annex.

Zone	I' = 0.0	I' = 0.2	I' = 0.4	I' = 0.6	I' = 0.8	I' = 1.0
a)	0.0	0.0	0.0	0.0	0.0	0.0
b1), b2)	0.0	0.2	0.4	0.6	0.8	1.0
c1), c2)	0.2	0.4	0.6	0.8	1.0	1.0
d)	0.4	0.6	0.8	1.0	1.0	1.0
e1)	0.6	0.8	1.0	1.0	1.0	1.0
e2)	1.0	1.0	1.0	1.0	1.0	1.0

Table 13-3 Determination of the I-factor from the I'factor map and the surface catchment zone.

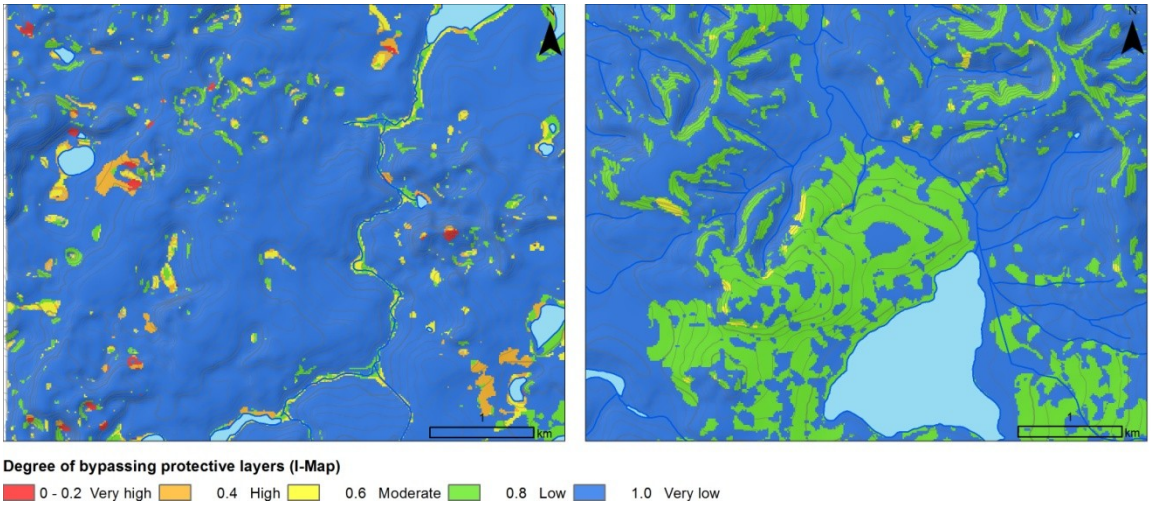

Figure 13-13 Spatial distribution of the risk of bypassing protective layers (I-map).

The location of the exemplary areas is indicated in Figure 10-5 (karstified terrain A on the left, covered karst area B on the right).

13.6 The final PI-groundwater vulnerability map

The final PI-groundwater vulnerability is derived by multiplying the I-map and the P-map. While the map for the whole study area can be found in the annex (Map 79), the two details from the karst and covered karst region are shown in Figure 13-14.

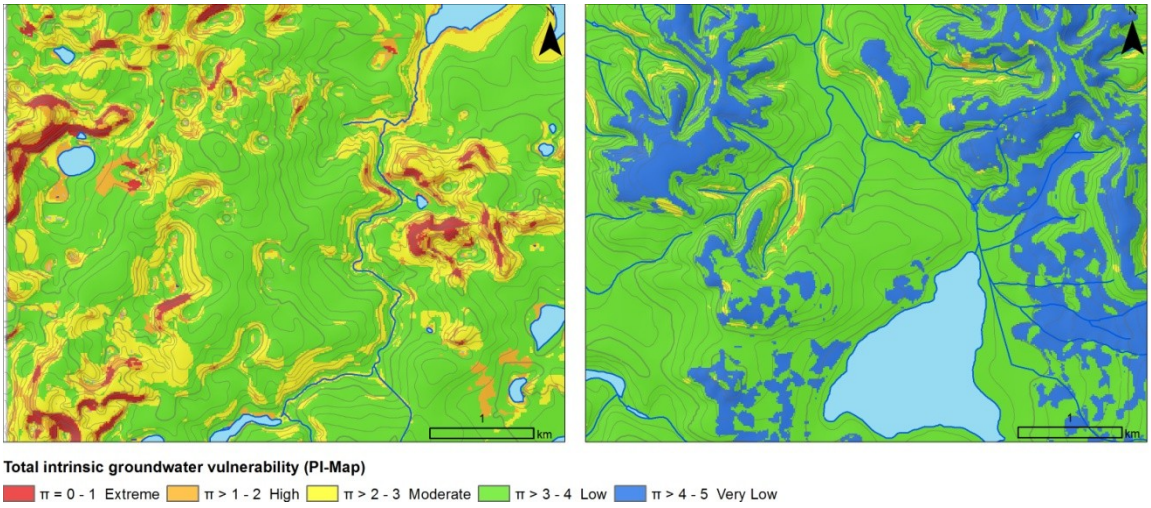

Figure 13-14 Spatial distribution of the total intrinsic groundwater vulnerability (PI-Map).

The location of the exemplary areas is indicated in Figure 10-5 (karstified terrain A on the left, covered karst area B on the right). The total vulnerability is calculated by multiplying the P-Map and the I-Maps shown above for comparison. See also Map 79 in the annex.

14 Gully erosion hazard

14.1 Gully erosion: Situation in eastern Brazil

In South-Eastern Brazil, gullying is often associated with certain geomorphological features, especially so-called headwater hollows or amphitheaters (Coelho Netto 1999, Bacellar et al. 2005). On basement rocks in the Quadrilátero Ferrífero about 70 km south-east of Lagoa Santa, Bacellar et al. (2005) describe typical locations of gullies as follows: *"gullies tend to be concentrated […] at the fringes of broad and flat interfluves. At the detailed scale (1 : 10 000), gullies are more common in amphitheatre-like headwater hollows that frequently represent upper Quaternary gullies (paleogullies) […]. So, gullies occur in areas of thicker saprolites […] in places with a natural concentration of surface and underground water (hollows)."*
These headwater hollows are colluvial filled hollows above the current drainage incision. According to Coelho Netto (1999), they often represent paleogullies from the Pleistocene that were filled again during the Holocene with alluvial and colluvial sediments. Current erosion began probably as a consequence of intense land use change with the arrival of European settlers at the end of the 17th century (Coelho Netto (1999), Figure 14-1). Especially digging of boundary ditches ('valos') are seen as triggers for gully erosion (Bacellar et al. 2005, Augustin and Aranha 2006).

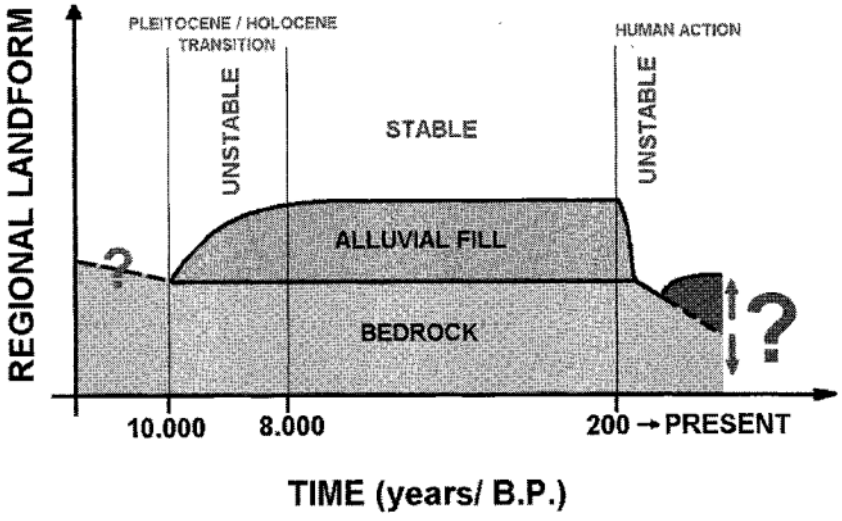

Figure 14-1 Regional landscape evolution in South-Eastern Brazil since the Pleistocene (Coelho Netto 1999).

According to Bacellar et al. (2005), these paleogully hollows are – if not cut by a recent gully - often pressurized due to a thick seal of colluvial clay layer and thus represent zones of instability with a high risk of gullying once the protecting soil cover is eroded or cut (Figure 14-2). Also Coelho Netto (1999) describes hanging hollows, (i.e. hollows above the channel head) as main areas for gully incision: even without assuming a pressurized aquifer, surface erosion can lead to

the exposition of temporary subsurface flow in the highly permeably colluvium. This interflow can lead to gully head progressioin, particularly at locations of interflow confluence. Coelho Netto (1999) describes the gullying process common in South-Eastern Brazil as follows:

"Initially, river incision exposes a seepage face at the base of the thick, loose and highly permeable Quaternary alluvium-colluvium; exfiltration of temporary subsurface flows may attain critical discharge particularly at the confluence with tributary topographic hollow axis, involving seepage erosion and tunneling; as tunnel excavation progresses headwards, the roof tends to collapse; the mechanism will repeat itself since the collapsed materials are removed from the seepage face, especially by washing processes and bank scouring. Once the Quaternary fills are removed, channel incision may progress into the saprolite and reach the regional aquifer; lateral and backward retreat rates tend to accelerate; when it gets closer to lateral slopes, it may trigger landslides."

Thus, availability of deep erodible material together with deep interflow and the location inside a colluvial filled headwater hollow are factors favoring gully development. Actual gully incision is then triggered by surface incision that cuts into the topsoil until it reaches the level of temporal subsurface flow.

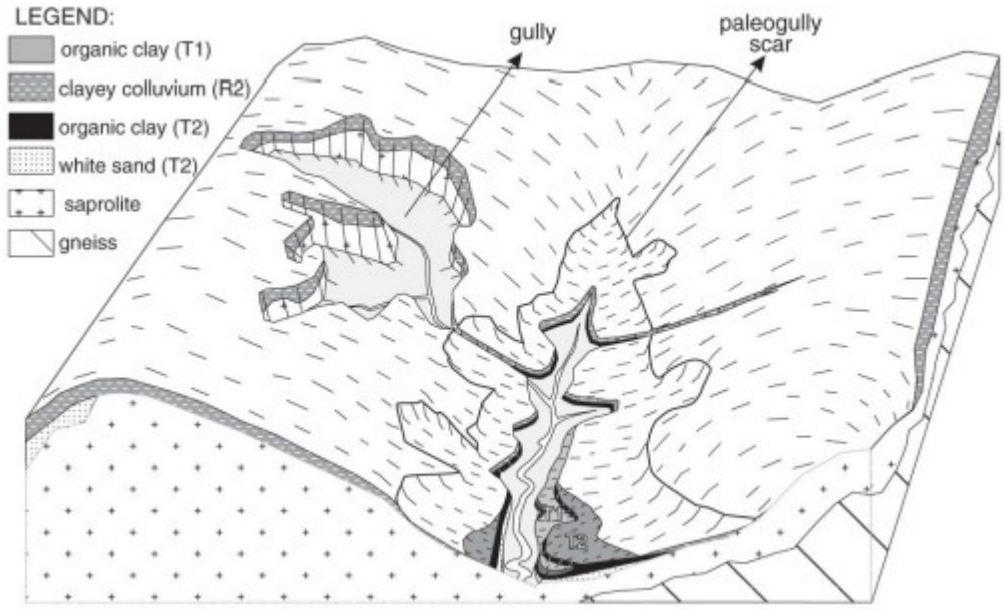

Figure 14-2 Schematic diagram of typical headwater hollow, which represents a paleogully, filled by upper Quaternary sediments (T2/R2 and T1).

The channel incision cuts the less erodible sediments (organic clays and colluvial soils) and reaches the more erodible gneiss saprolite. The further natural convergence of underground and surface water towards the hollows leads to the development of a new gully. Where the saprolite is thinner (right), deep gullies do not develop (Bacellar et al. 2005).

Especially at steep borders of plateau areas covered by thick Ferralsols, gully propagation is controlled by interflow. Mendonça et al. (1994) describe in a case study from the plateau-regions around the capital Brasília, that interflow at the contact between saprolite and Ferralsol following the quick incision of a large gully has led to piping effects that were strong enough to create pseudo-sinkholes in the plateau surface, destroying over 50 houses.

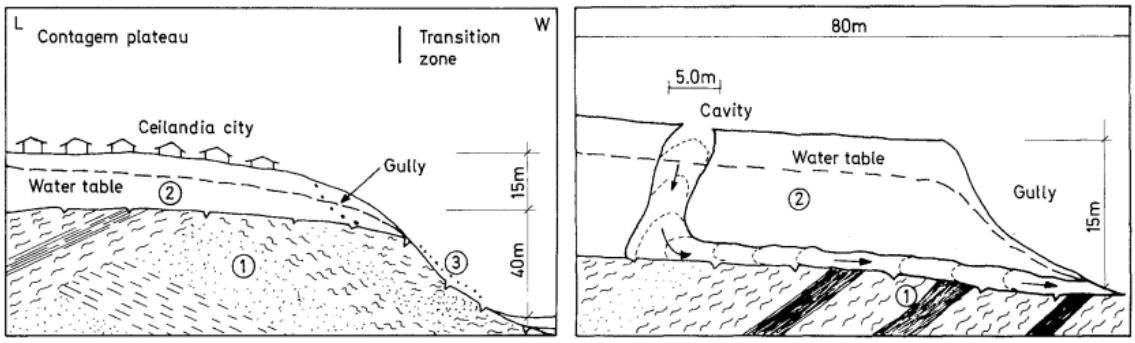

Figure 14-3 Pseudo-sinkhole occurrences by piping erosion near Brasília following the incision of a large gully.

1): Precambrian rocks 2): Ferralsol, 3):rocky soil (Mendonça et al. 1994).

14.2 The concept of topographic threshold

Valentin et al. (2005) and Poesen et al. (2003) give good overviews of the processes involved in gully erosion and the current modeling approaches regarding gully erosion hazard. One of the most commonly used methods is the assessment of a local or regional topographic threshold, which combines slope and drainage area to indicate potentially unstable areas. Upslope drainage area is - for a given climate – connected to peak water discharge and slope indicates the amount of potential energy that is liberated while the water is flowing downstream. These topographic threshold based methods for estimating risk of channel or gully initiation have been used since a long time: Patton and Schumm (1975) found a negative trend for slope / drainage area for data collected at gully heads in the USA. Afterwards, Begin and Schumm (1979) suggested a critical slope / drainage area relationship which they determined by fitting a line through the lowermost data points plotted on a log-log paper. Below this line, no incision occurs and not incised valley floors above the line are defined as unstable. Since then, the method has been applied to incision processes from rill development until deep gullying in various regions. Vandaele et al. (1996) gives an overview of 10 different datasets on channel initiation from Europe and USA (Figure 14-4). This threshold line on a log-log-paper can also be represented by the power function

$$S_{cr} = a\ A^{-b}$$

Equation 14-1 Critical slope

with [A] = unit drainage area, [S_{cr}] = critical slope, [a] a coefficient and [b] an exponent (Vandaele et al. 1996).

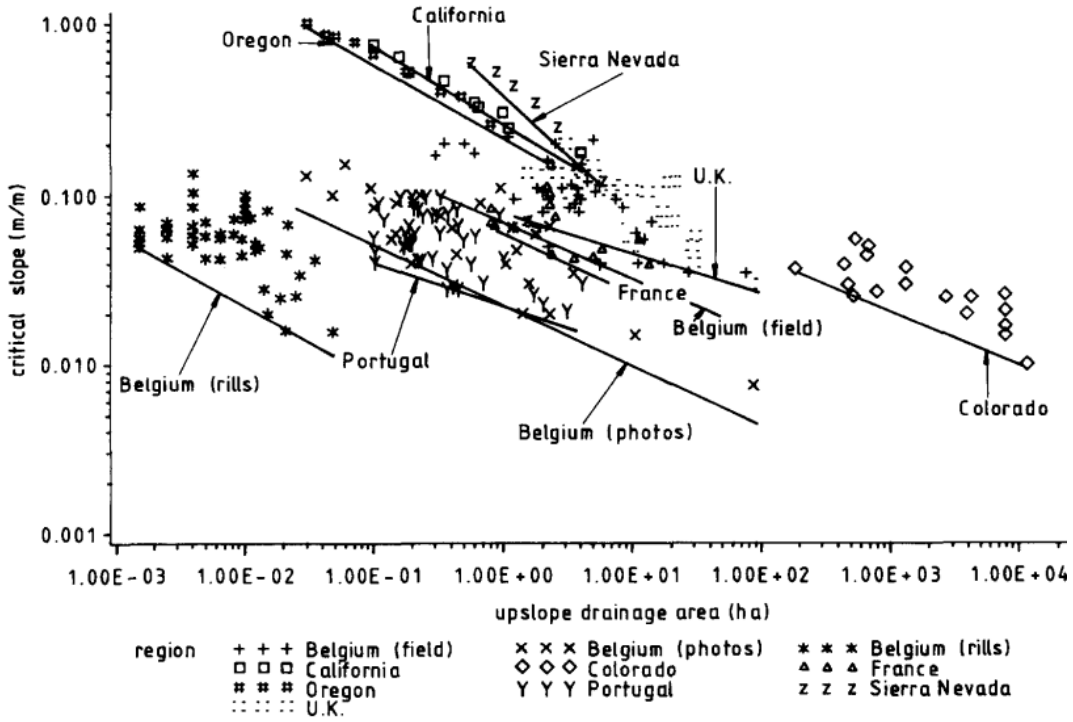

Figure 14-4 Critical slope gradient versus upslope drainage area for various study sites collected by Vandaele et al. (1996).

The data points mark initiation points of rills or gullies.

Since the drainage area is a substitute for the amount of water available for erosion, it depends also on the amount of rainfall that is not infiltrating in the upstream catchment. This interpretation can be denoted as:

$$S_{cr} = a_m [A(R-I)]^{-b}$$

Equation 14-2 Critical slope including infiltration capacity

With a_m = modified coefficient, R = rainfall intensity, I = infiltration capacity of the soil in the catchment.

14.2.1 Physical interpretation of the topographic threshold

Begin and Schumm (1979) related the equation to the concept of critical shear stress, which is often used to assess the potential for rill and gully erosion (e.g. Léonard and Richard (2004). Also Montgomery and Dietrich (1988) compared their data with an equation based on critical shear stress for channel initiation in steep terrain. Later they extended their model to different processes leading to channel initiation such as small scale landsliding, Hortonian overland flow, saturation

excess overland flow and to areas influenced by roads (Montgomery 1994, Montgomery and Dietrich 1994).

14.2.2 Hortonian surface flow

For areas where channel initiation is controlled by Hortonian overland flow, i.e. overland flow due to a rainfall intensity exceeding the infiltration capacity of the soil (Horton 1933), Montgomery and Dietrich (1994) provide two analytical equations, one for incision due to laminar surface flow (Equation 14-3) and one for incision due to turbulent (Equation 14-4) surface flow. For the first, flow velocity is calculated according to Poiseuille's law, for the second according to Manning's equation. Both equations are limited by the steady state assumption and the assumption of spatially uniform soil properties. Using a similar mathematical development than Montgomery and Dietrich (1994), Torri and Borselli (2003) formulated a threshold based on the unit stream power (Equation 14-5). The concept of stream power (see also section 10.4.6) is often used in models about drainage evolution and stream incision. Originally introduced by Bagnold (1966), it relates the liberation of the waters potential energy to its dissipation against the stream bed, which leads to erosion.

$$A = \frac{2\tau_{cr}^{\ 3}}{(R-I)k\nu\rho_w^{\ 3}g^2S_{cr}^{\ 2}}$$

Equation 14-3 Threshold for laminar Hortonian overland flow

$$A = \frac{\tau_{cr}^{\ 5/3}}{(R-I)n(\rho_w g)^{5/3}S_{cr}^{\ 7/6}}$$

Equation 14-4 Threshold for turbulent Hortonian overland flow

$$A = \frac{P_{cr}}{(R-I)\rho_w g S_{cr}}$$

Equation 14-5 Threshold based on the stream power concept

With

A= drainage area per unit contour length, S_{cr} = Slope in m/m or sin(α)

τ_{cr}= critical shear stress necessary to erode the soil, ρ_w = density of water

R = rainfall intensity, I = infiltration rate

k = hydraulic roughness coefficient, ν = kinematic viscosity of water

g = gravitational constant, n = Manning's coefficient

P_{cr} = critical stream power

All three equations can be rearranged to the form of Equation 14-2, summarizing most physical parameters of the catchment into the coefficient a_m.

$$S_{cr} = a_1 \cdot [A(R-I)]^{-0.5}$$

Equation 14-6 Equation 14-3 rearranged according to Equation 14-2

$$S_{cr} = a_2 \cdot [A(R-I)]^{-6/7}$$

Equation 14-7 Equation 14-4 rearranged according to Equation 14-2

$$S_{cr} = a_3 \cdot [A(R-I)]^{-1}$$

Equation 14-8 Equation 14-5 rearranged according to Equation 14-2

a_m, m = 1…3: coefficient related to the physical soil properties in the area.

Thus, the exponent b in Equation 14-2 varies according to the erosion mechanism. For graphic display, Equation 14-2 can be log-transformed into Equation 14-9 and the effects of the different exponents are visualized in Figure 14-5:

$$\log(S_{cr}) = \log a_i - b \cdot \log[A(R-I)]$$

Equation 14-9 log-transformation of Equation 14-2

With

a_m, m = 1…3: threshold coefficient

b = exponent related to the flow regime (compare Equation 14-6 - Equation 14-8):

b = 0.5 for laminar Hortonian surface flow

b = 6/7 for turbulent Hortonian surface flow

b = 1 for unit stream power

The linear threshold for Hortonian overland flow drawn on a log slope / log drainage area graph is steeper for turbulent flow than for laminar flow (Figure 14-5). This shows that for turbulent flow, drainage area is more important than for laminar flow.

Increasing critical shear stress (i.e. higher restistance agains erosion) raises the threshold line in a parallel way.

Torri and Borselli (2003) noted the discrepancy between these theoretically derived values for the exponent [b] and the experimentally found exponents between 0.133 and 0.414 in Mediterranean Europe (Vandekerckhove et al. 2000).

Vandaele et al. (1996) compared ten studies from Europe and USA and found that despite the large differences of the study areas, most values for [b] were around 0.4 with only two exceptions where [b] was around 0.25 and only one case from the Sierra Nevada with [b] = 0.6.

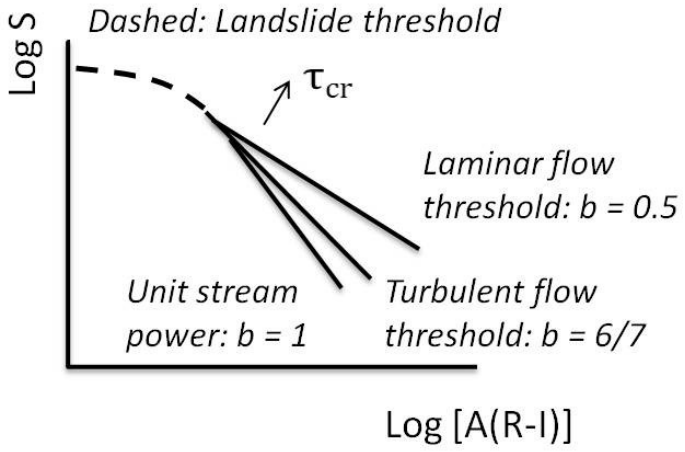

Figure 14-5 Schematic graph showing the theoretically derived threshold lines for Hortonian overland flow and land sliding.

The flow regime defines the steepness of the threshold while higher critical shear stress moves the threshold line in a parallel way. Modified after Montgomery and Dietrich (1994).

14.2.3 Saturation excess surface flow

Based on an overlay of erosion by laminar surface flow and the concept of wetness index of Beven and Kirkby (1979), Montgomery and Dietrich (1994) developed a non-linear equation indicating erosion by saturation overland flow:

$$A = \frac{2\tau_{cr}^{\ 3}}{R\nu\rho_w^{\ 3} g^2 S_{cr}^{\ 2}} + \frac{TS_{cr}}{R}$$

Equation 14-10 Threshold for saturation excess surface flow

(for explanation of the parameters see page 271)

The wetness index, calculated as Ln (A/S), was originally used to estimate the distribution of saturated areas in a catchment (see also section 10.4.5). Thus, for steep slopes, erosion by

saturation excess surface flow increases with decreasing slope because the saturated area increases that contributes to the surface flow. On the other hand, for a given saturated area, erosion increases with increasing slope since a higher potential energy is liberated during the downstream flow.

14.2.4 Interflow or piping

If saturated conditions are not reached, lateral subsurface flow can also contribute to erosion, often known as piping. This is usually not modeled by a classical threshold model but also related to areas of water convergence in highly permeable soils above low permeable saprolite.

14.2.5 Landslide erosion

Erosion by landslide is mainly controlled by slope and dominates as soon as the slope becomes steeper than half of the angle of internal friction for non-cohesive soils (Montgomery and Dietrich 1994).

14.2.6 Combination of erosion processes

The combination of erosion by Hortonian overland flow and other erosion processes may be responsible for a comparatively low observed exponent [b] compared to the theoretical considerations. A summary of the different erosion processes depending on slope and upslope drainage area is given in Figure 14-6 .

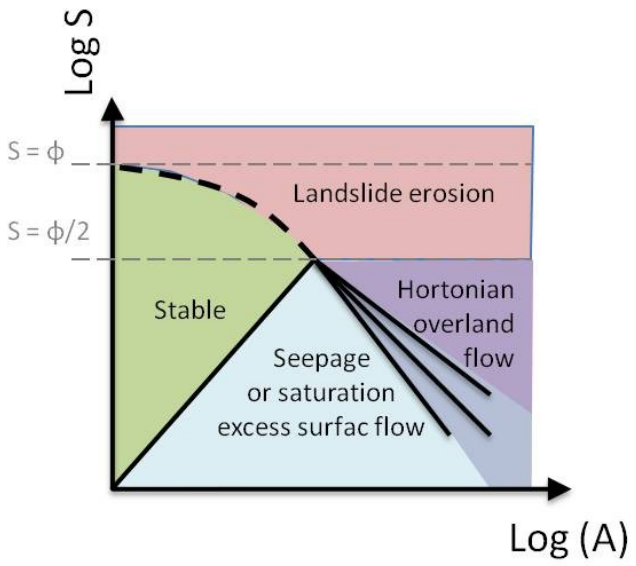

Figure 14-6 Erosion processes and topographical thresholds.

Φ = Angle of internal friction. Modified after Montgomery and Dietrich (1994).

Using the topographic threshold function in Equation 14-1, Desmet et al. (1999) also found a strong discrepancy between a rather high exponent [b] (0.7 to 1.5) necessary to predict the complete trajectory of an ephemeral gully and a low exponent [b] around 0.2 for the identification of the gully starting points.
Following their arguments, this might reflect the different processes associated with gullying: for a given geological underground and climate, a gully might be initiated by a small landslide or a scar by laminar erosion – a process controlled mainly by slope, i.e. with a low exponent [b] – but for erosion and maintenance of a channel a certain amount of flow concentration is needed in a topographic hollow, which results in a higher exponent [b].

14.3 Workflow for erosion hazard assessment

For modeling gully erosion hazard in the study area, the workflow shown in Figure 14-7 was used. It is based on the considerations described in section 14.1 and 14.2 and a combination of topographic thresholds with vulnerable landscape positions and soil erodibility.
The risk of gully erosion is split into two sub-processes: the risk of gully initiation and the risk of gully propagation. While the first is related to the primary incision of the topsoil by Hortonian surface flow or small landslides, gully propagation is favored by deep interflow or saturation excess surface when the temporary or regional aquifer is reached (see section 14.1).

For the risk of gully initiation, the mean value of a high topographic threshold and high soil erodibility is used to estimate the general risk of primary linear incision by Hortonian surface flow. The mean value was chosen since the process is additive: a very high topographic threshold may incise even in soils of low erodibility (with the exception of karst outcrops) and soils with

very high erodibility (e.g. bare saprolite) can show rill erosion even in nearly flat areas under the intense rainfall that is common in the study area. If both values are high, the risk of gully initiation is highest. Additionally, the risk of gully initiation by landslide is considered using a maximum overlay (OR).

The gully propagation hazard, on the other hand, is estimated by a multiplication of areas vulnerable to gully propagation with a high topographic threshold. Multiplication was chosen since the definition of the areas vulnerable to gully propagation was set in a restrictive way, limiting the propagation of gullies even for areas with very high topographic threshold. Also gullies will not propagate if the topographic threshold is too low, even if a high vulnerability to gully propagation exists.

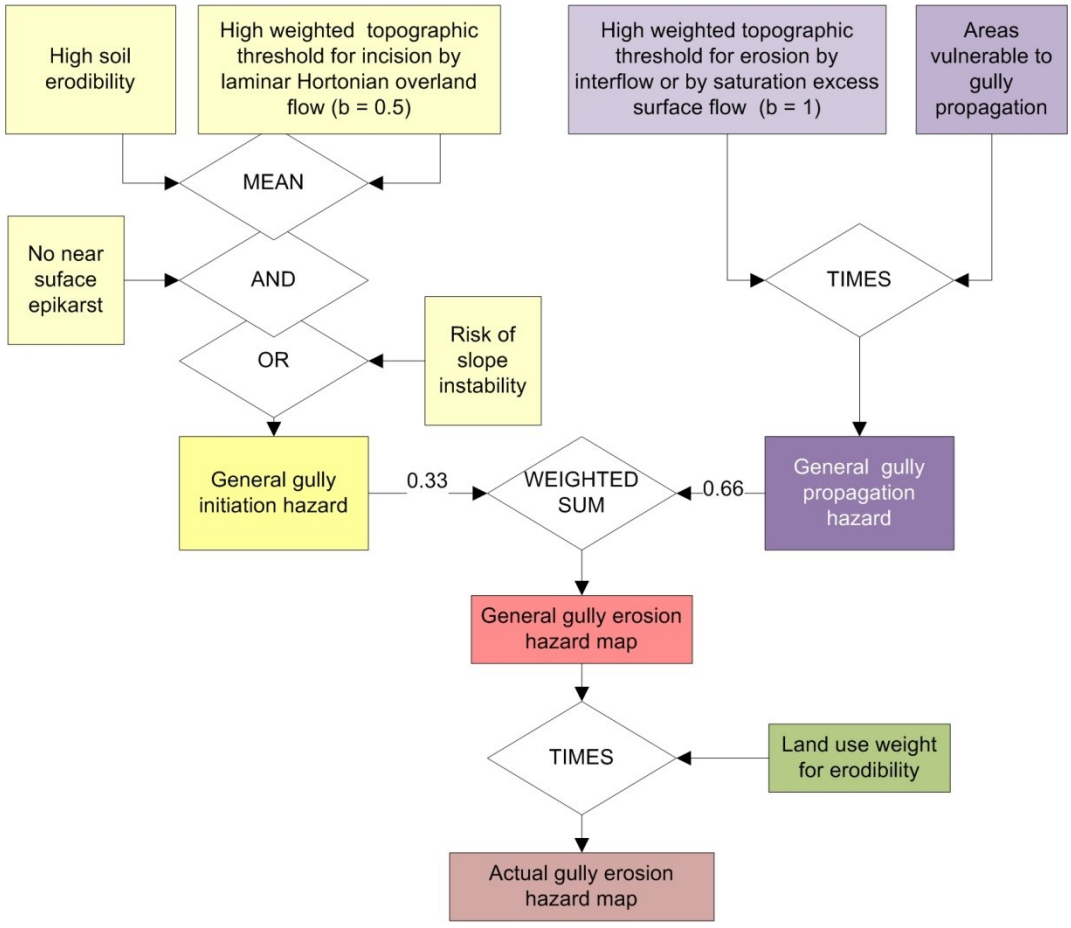

Figure 14-7 Overview of the workflow for gully erosion hazard assessment.

Both risks of gully initiation and gully propagation are combined in a weighted sum overlay to estimate the general gully erosion hazard. For this overlay, the hazard of gully propagation was estimated twice as important as the hazard of gully initiation since the last parameter decides

whether the gully will grow and deepen to reach a stage that is problematic for infrastructure, slope stability and local water balance.

Finally, the result is weighted by a land use parameter that defines the protection of the landscape by vegetation or urban features to derive the actual gully erosion hazard.

14.4 Gully initiation hazard

14.4.1 Topographic threshold for hortonian surface flow

According to the considerations above (section 14.2.2), the topographic threshold for infiltration excess (Hortonian) surface flow is calculated using a comparatively low exponent [b] = 0.5 (Equation 14-3).

Since only the part of the rainfall that does not directly infiltrate contributes to the eroding quantity of water (Equation 14-2), the calculation of the upstream catchment area as described in section 10.4.4 was modified so that each contributing pixel was weighted by the optimality value for intensity of lateral flow. This optimality value is based on the I'-factor (Figure 13-11). This factor was previously calculated to estimate the risk of bypassing protective layers for karst groundwater vulnerability (section 13.4), the lower the I'-value, the higher the risk of lateral near surface flow. If subtracted from 1 it can be used as weight for the calculation of infiltration excess surface flow accumulation. Nevertheless, to avoid unrealistic results of large areas having no contribution to surface flow at all, zero values are substituted by a value of 0.1 (Figure 14-8).

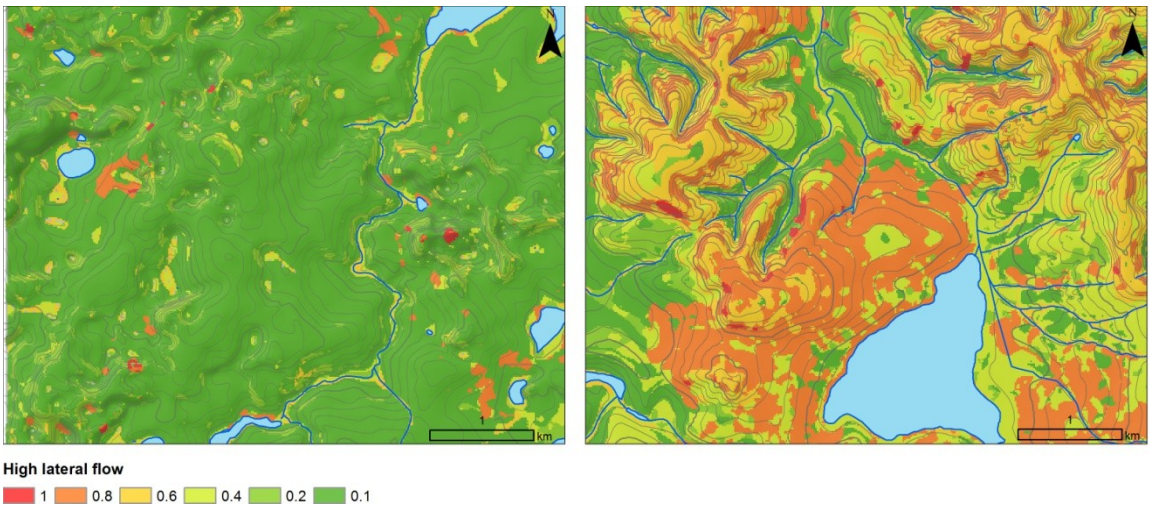

Figure 14-8 Optimality values for "high lateral flow" derived from the I´-Factor (Figure 13-11).

The optimality value is used as weight for the calculation of the weighted drainage area A_{wi} for the topographic threshold considering Hortonian surface flow. Location of both exemplary areas is indicated in Figure 10-5 (karstified terrain A on the left, covered karst area B on the right).

For the GIS-based calculation of the topographic threshold for gully initiation by Hortonian surface flow, the logarithm of the threshold coefficient [a_1] was mapped using Equation 14-11.

$$\log(a_1) = \log(S) + 0.5 \cdot \log(A_{Wi})$$

Equation 14-11 Topographic threshold for gully initiation

with

a_1 = topographic threshold coefficient indicating the risk of incision by Hortonian surface flow

S = slope in percent

A_w = weighted unit drainage area

Due to the weighted calculation of the drainage are, the resulting topographic threshold $\log(a_1)$ from Equation 14-11 cannot be directly compared with literature values. Instead, for local interpretation, $\log(a_1)$ was converted into a scale from 0 – 1 using a two standard deviation linear stretch that cuts off very high and very low values. The resulting relative map for "high weighted topographic threshold for Hortonian surface flow" is shown in Figure 14-9.

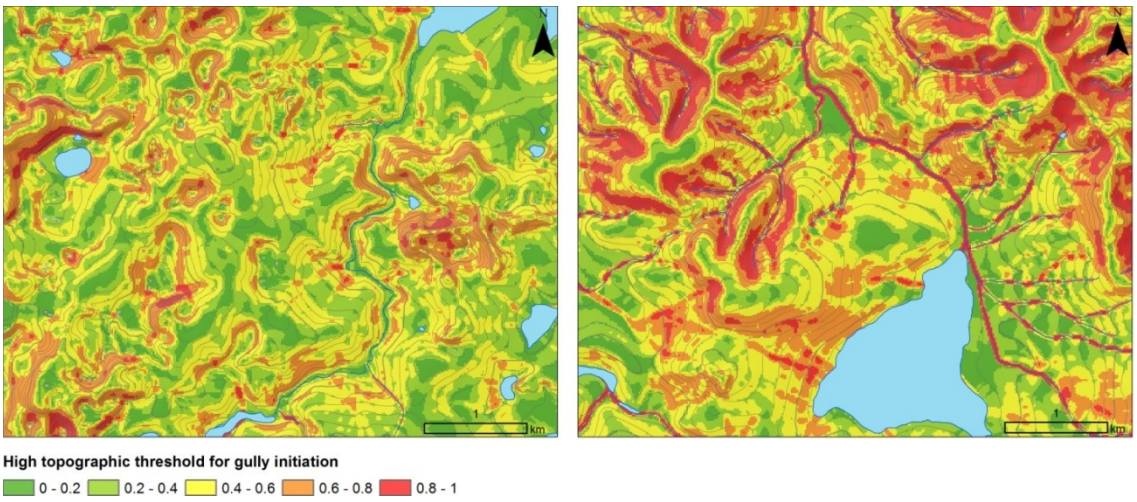

Figure 14-9 Optimality values for "high topographic threshold for Hortonian surface flow".

This map was created using a linear two standard deviation stretch of the original values resulting from Equation 14-11. The drainage area is calculated using the weights for "high lateral flow" from the map in Figure 14-8.

14.4.2 Slope instability

In steep areas, gullies are often initiated by small landslides and thus a measure for slope instability is included into the risk of gully initiation. The parameter slope stability can also be used separately, e.g. for purposes such as road building or restrictions for settlement.

Slope stability is calculated by a minimum overlay of "very steep slope" and "No Risk of near surface epikarst". Thus, it is only a function of slope since no data of internal cohesion of the subsoil / saprolite material were available. The difference in subsoil material is only addressed by the restriction "No Risk of near surface epikarst", which automatically results in a low risk of slope instability in the carbonate region.

The choice of the slope function is the same criteria used for the estimation of "Risk of near surface epikarst" in 10.5. A detailed analysis of the critical slope angle for each subsoil material could improve the risk map for slope instability considerably.

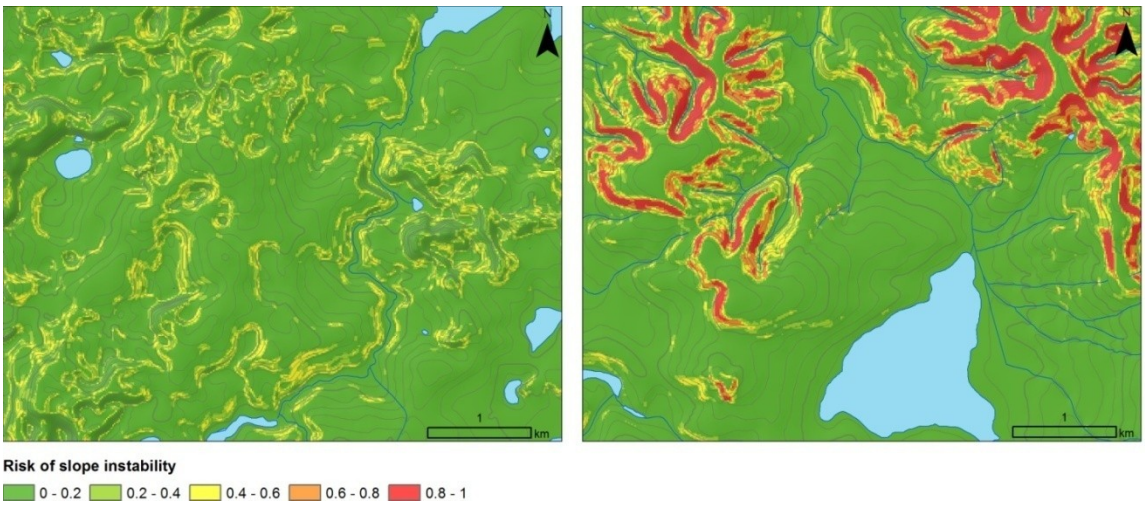

Figure 14-10 Risk of slope instability derived from topography and lithology.

The location of the areas is indicated in Figure 10-5 (karstified terrain A on the left, covered karst area B on the right).

14.4.3 Map for gully initiation hazard

Gully initiation hazard is calculated by an equally weighted sum (= mean value) of topographic threshold for Hortonian surface flow and soil erodibility as shown in the workflow of Figure 14-7. Examples of its spatial distribution are shown in Figure 14-11.

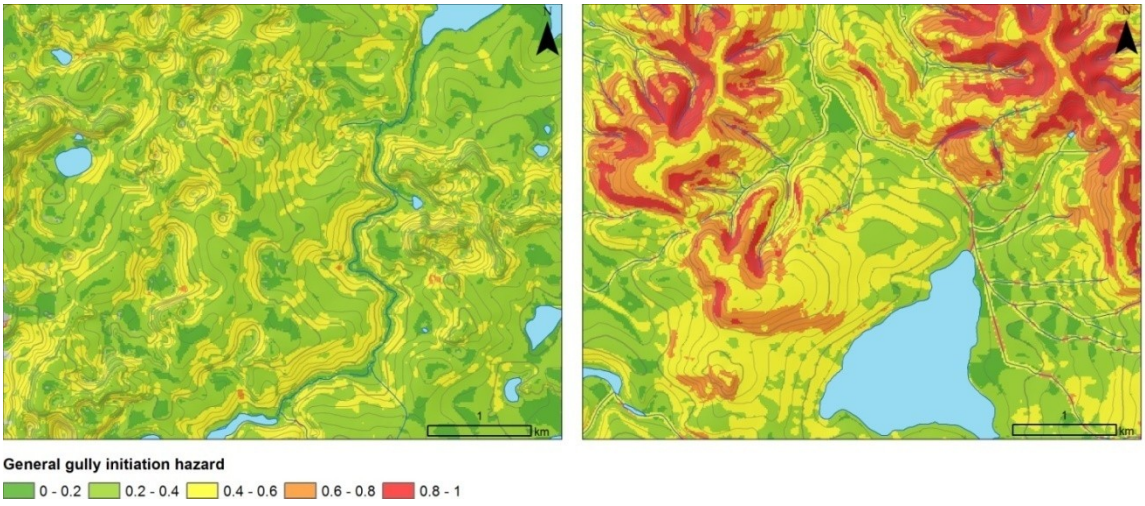

Figure 14-11 General risk of linear erosion due to Hortonian surface flow (= gully inititation hazard).

The location of both exemplary areas is indicated in Figure 10-5 (karstified terrain A on the left, covered karst area B on the right).

The risk of gully initiation is highest for steep areas with very thin topsoil on highly erodible saprolite of the Serra de Santa Helena formation, diminishing to low or very low values in flat downslope areas that are covered by thick red topsoil material. In the karst area, gully initiation hazard is generally low to very low, reaching medium values only in steep areas. Here, high gully initiation hazard is restricted to very few pixels in steep concave areas.

14.5 Risk of Gully propagation

While gully initiation is related to the first incision of the topsoil, propagation of this initial erosion scar to larger gullies is enhanced when the erosion reaches the zone of interflow between topsoil and subsoil or a regional aquifer (compare section 14.1). Thus, a topographic threshold adapted for interflow or saturation excess surface flow is combined with areas that are known to have a high vulnerability to gully propagation (Figure 14-7). This vulnerability to gully propagation (14.5.3) is calculated by a maximum overlay (Fuzzy OR) of the vulnerability to erosion by interflow (14.5.1) and the vulnerability to erosion by saturation excess surface flow (14.5.2). The total workflow for deriving the vulnerability to gully propagation is visualized in Figure 14-12.

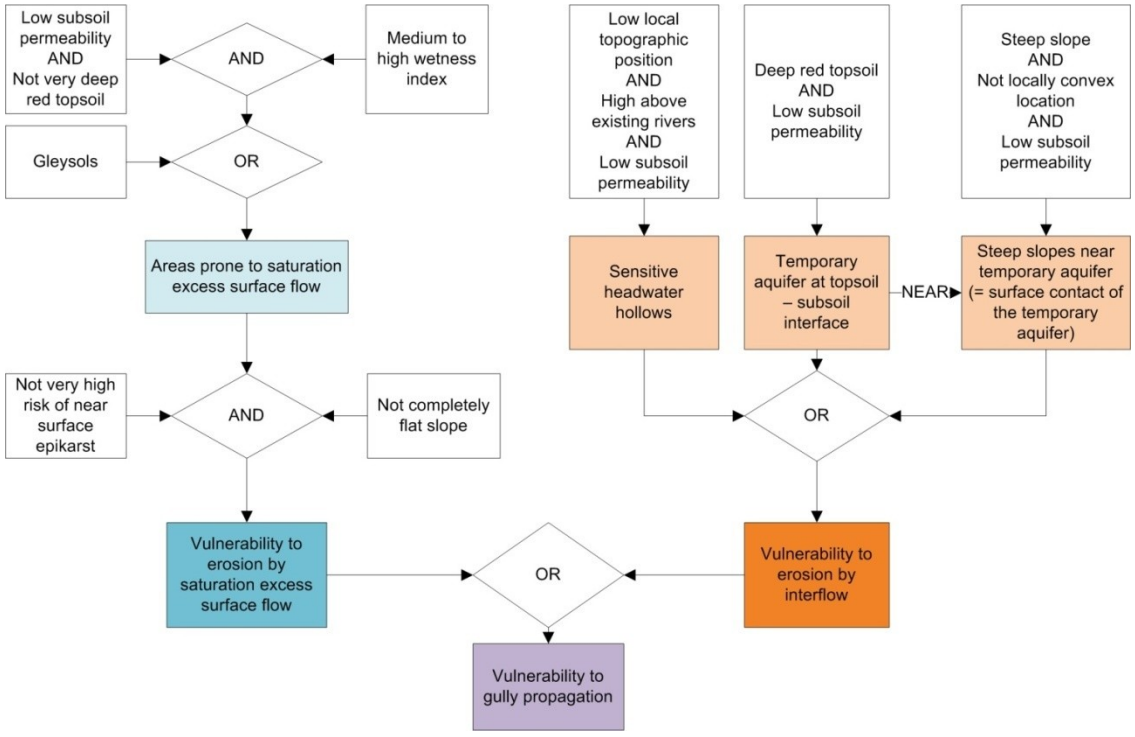

Figure 14-12 Flow diagram showing the modeling concept for vulnerability to gully propagation in the study area.

14.5.1 Vulnerability to subsurface erosion or piping

The risk of erosion by strong subsurface flow or piping is related to the existence of a temporary aquifer at the contact between soil and saprolite, which depends on topsoil thickness and the difference of permeability of both layers (see below). Also steep areas close to a temporary aquifer are considered areas of high gully propagation hazard, since they are potential locations where the temporary aquifer reaches the surface.
As mentioned by Bacellar et al. (2005) and Coelho Netto (1999), headwater hollows above the current drainage line (i.e. potentially unstable valley floors) are also as potential risk areas for gully propagation by interflow.
These three areas of high vulnerability to erosion by subsurface flow are combined in a maximum overlay (Fuzzy OR) to generate a map showing areas favoring subsurface flow. Afterwards, the vulnerability of erosion by subsurface flow is calculated by restricting these areas to locations of absence of near surface epikarst and high subsoil erodibility. The total workflow is shown in Figure 14-12.

Existence of a temporary perched aquifer

As described in section 9, a perched aquifer can exist during the rainy season in the plateau areas at the contact between highly permeable topsoil and less permeable subsoil / saprolite. This parameter is important for the estimation of gully erosion hazard since linear erosion features that reach the temporary aquifer propagate more quickly and are more difficult to control (CPRM 1994b). The following criteria were used to regionalize the probable existance of such a temporary perched aquifer: The combination of deep red topsoil (i.e. highly permeable deep topsoil) and low permeable subsoil are the main factors defining a high probability of a temporary aquifer:

$$\mu_{Temp.\ Aquifer} = \mu_{Deep\ red\ topsoil}\ \text{AND}\ \mu_{Low\ subsoil\ permeability}$$

Equation 14-12 "Existence of a temporary aquifer"

With

$\mu_{Deep\ red\ topsoil}$ as calculated in section 10.6.30 and $\mu_{Subsoil\ permeability}$ as defined on page 225.

Since gully erosion hazard is especially high at the outcrop of this temporary aquifer at the borders of the high plateau areas, steep areas close to the temporary aquifer are also included as highly vulnerable areas for erosion by interflow. Examples of the spatial distribution of the result is shown in Figure 14-13.

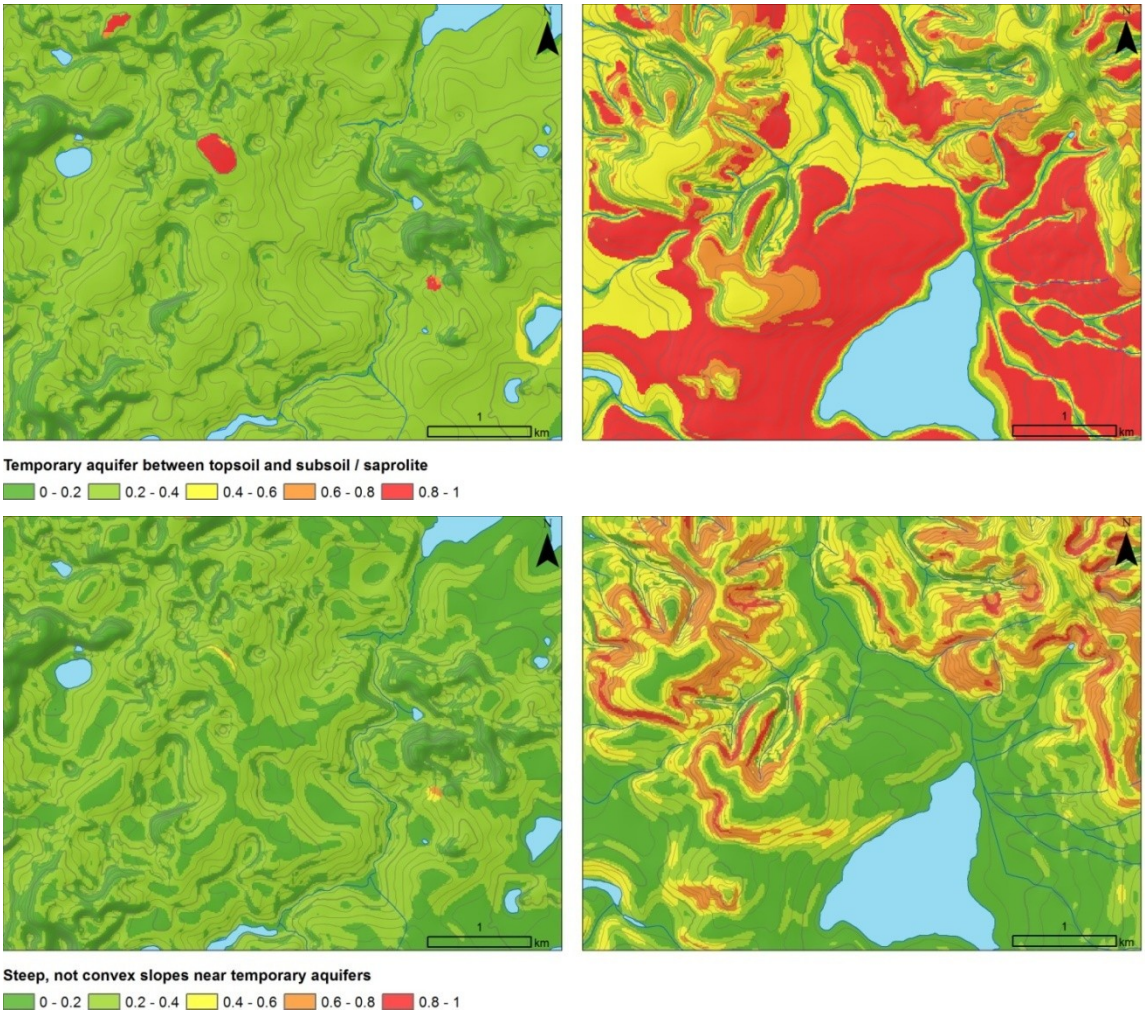

Figure 14-13 Upper maps: Spatial distribution for the optimality values "Existence of a temporary aquifer" which represent areas vulnerable to gully propagation by interflow. Lower maps: also steep and not convex areas close to a temporary aquifer are considered areas of high risk for erosion by interflow.

The location of the exemplary areas is indicated in Figure 10-5 (karstified terrain A on the left, covered karst area B on the right).

Potentially unstable headwater hollows

Headwater hollows are concave regions that lie upstream of permanent waterways. Thus, they are modeled using the restriction:

$$\mu_{Headwater\ hollows} = \mu_{Low}(LTPI)\ AND\ \mu_{High\ above\ surface\ water\ or\ sinkhole}$$

Equation 14-13 "Location inside a headwater hollow"

With $\mu_{Low}(LTPI)$ as described in section 10.3.3 and

$\mu_{High\ above\ surface\ water\ or\ sinkhole} = 1 - \mu_{Low\ above\ surface\ water\ or\ sinkhole}$ as described in section 10.4.2 on p.204.

In the non-karstified area, headwater hollows are locations of potential retreating gully head cuts while in karst areas this function indicates the walls of small dolines in high areas.
To generate a map of potentially unstable headwater hollows with respect to interflow favoring gully erosion, the result of Equation 14-13 is restricted to areas with low subsoil permeability and no risk of near surface epikarst.
Examples of the spatial distribution of the result is shown in Figure 4-6.

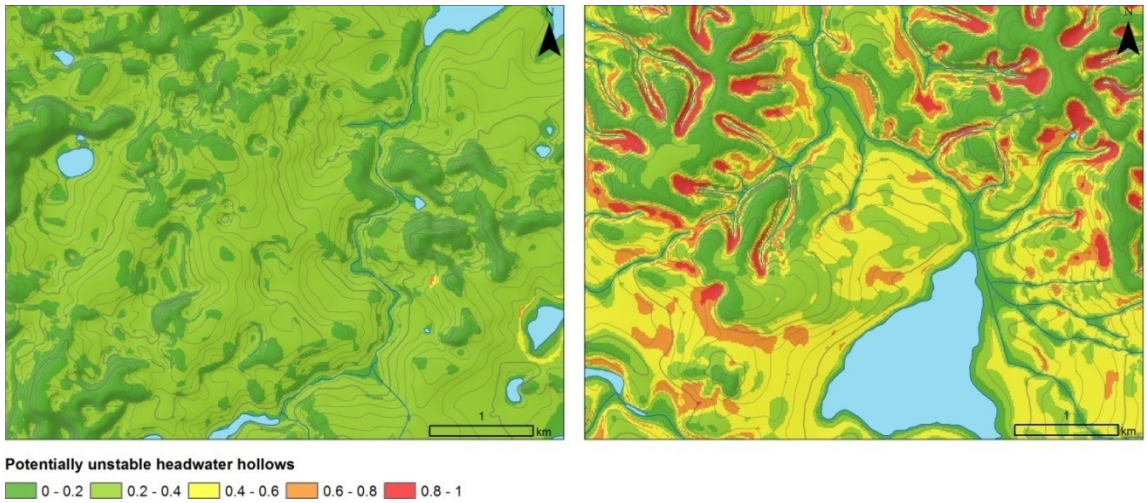

Figure 14-14 Spatial distribution of the optimality values "Potentially unstable headwater hollows", which represent areas vulnerable to gully propagation by interflow.

The location of the exemplary areas is indicated in Figure 10-5 (karstified terrain A on the left, covered karst area B on the right).

Result: Areas vulnerable to erosion by subsurface flow

The map: "Areas vulnerable to erosion by subsurface flow" combining the different parameters described above:

$$\mu_{High\ vulnerability\ to\ erosion\ by\ subsurface\ flow} = \begin{bmatrix} \mu_{Temporary\ aquifer}\ OR \\ \mu_{Steep\ slopes\ near\ temporary\ aquifer}\ OR \\ \mu_{Potentially\ unstable\ headwater\ hollows} \end{bmatrix}$$

Equation 14-14 "High vulnerability to erosion by subsurface flow"

The result is shown in Figure 14-15 and in the Map 86 (annex).

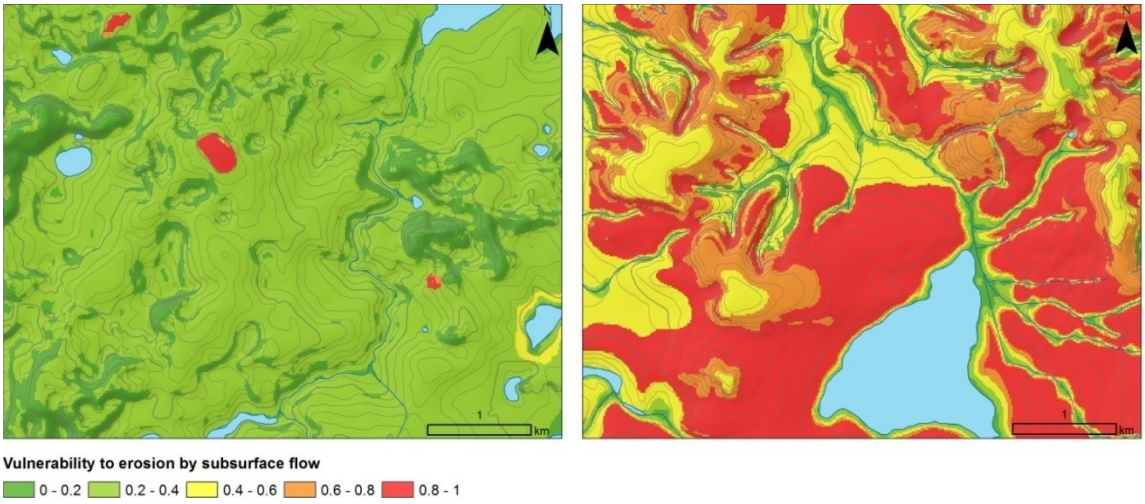

Figure 14-15 Optimality values for "High vulnerability to erosion by subsurface flow".

The location of the exemplary areas is indicated in Figure 10-5 (karstified terrain A on the left, covered karst area B on the right).

14.5.2 Vulnerability to erosion by saturation excess surface flow

Surface flow leading to erosion can also occur when the soil is completely saturated and cannot absorb additional water. This situation is typical for Gleysols along rivers or in areas with medium to high topographic wetness index (section 10.4.5) i.e. in zones of water confluence that are comparatively flat. Additionally to the topographic condition of high wetness index, a low permeability of the subsoil is necessary for the situation of saturation excess surface flow. After thus defining areas of possible saturation excess surface flow in section 0, these areas are combined with restricting conditions such as high soil erodibility and not completely flat slopes to generate a map of areas vulnerable to erosion by saturation excess surface flow.

Areas prone to saturation excess surface flow

To define areas prone to saturation excess surface flow, hydromorphic soils (Gleysols and Fluvisols as derived in section 10.6.2) are interpreted as risk areas. Additionally, after long, intense rainfall also areas having only a medium to high wetness index (section 10.4.5) in combination with low subsoil permeability and not very deep red topsoil may show saturation excess surface flow. These areas can also be interpreted as zones of exfiltration from the temporary aquifer. Thus, the complete statement can be written as:

$$\mu_{High\ risk\ of\ saturation\ excess\ surface\ flow} = \begin{bmatrix} \mu_{Hydromorphic\ soils}\ OR \\ \mu_{Buffer\ around\ riverbed}\ OR \\ \begin{bmatrix} \mu_{Medium\ to\ high\ wetness\ index}\ AND \\ \mu_{Low\ topsoil\ permeability}\ AND \\ \mu_{Not\ very\ deep\ red\ topsoil} \end{bmatrix} \end{bmatrix}$$

Equation 14-15 "High risk of saturation excess surface flow"

(Compare Figure 14-12)

Examples of the resulting map are shown in Figure 14-16.

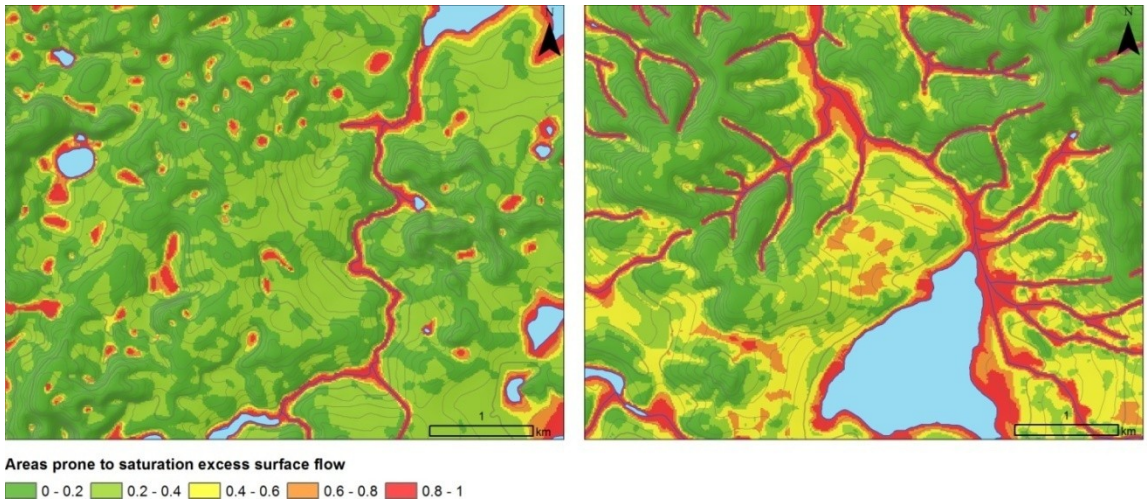

Figure 14-16 Spatial distribution for the optimality values for "Areas prone to saturation excess surface flow".

The location of the exemplary areas is indicated in Figure 10-5 (karstified terrain A on the left, covered karst area B on the right).

Vulnerability to erosion by saturation excess surface flow

To estimate the vulnerability to erosion by saturation excess surface flow, the map in Figure 14-16 is restricted by the conditions "Not completely flat slope" and "High soil erodibility". The result is shown in Figure 14-17.

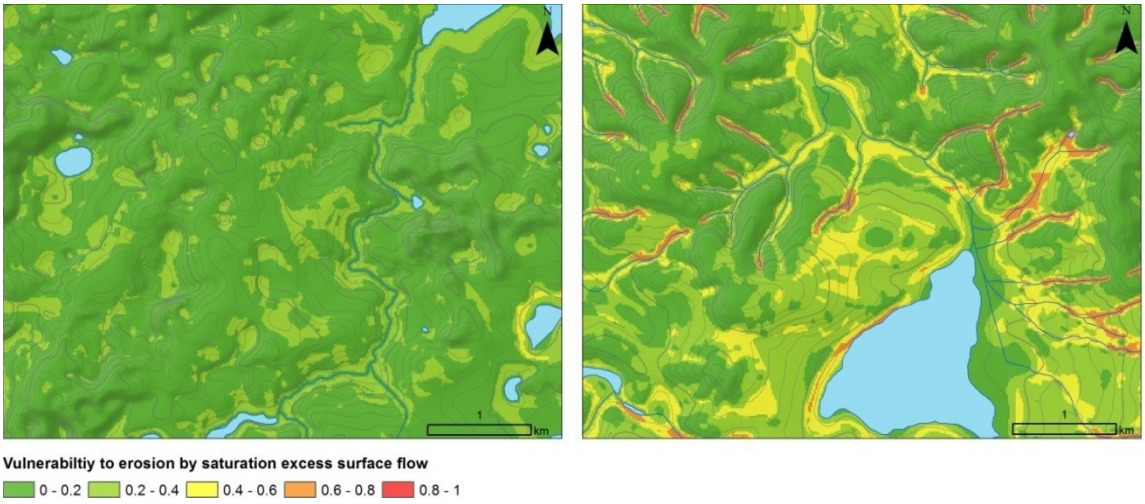

Figure 14-17 Spatial distribution "High vulnerability to erosion by saturation excess surface flow".

Location of the exemplary areas is indicated in Figure 10-5 (karstified terrain A on the left, covered karst area B on the right).

14.5.3 Vulnerability to gully propagation

The final map showing the vulnerability to gully propagation is created using a maximum overlay (fuzzy OR) of the vulnerability to erosion by subsurface flow and the vulnerability to erosion by saturation excess surface flow (Figure 14-18).

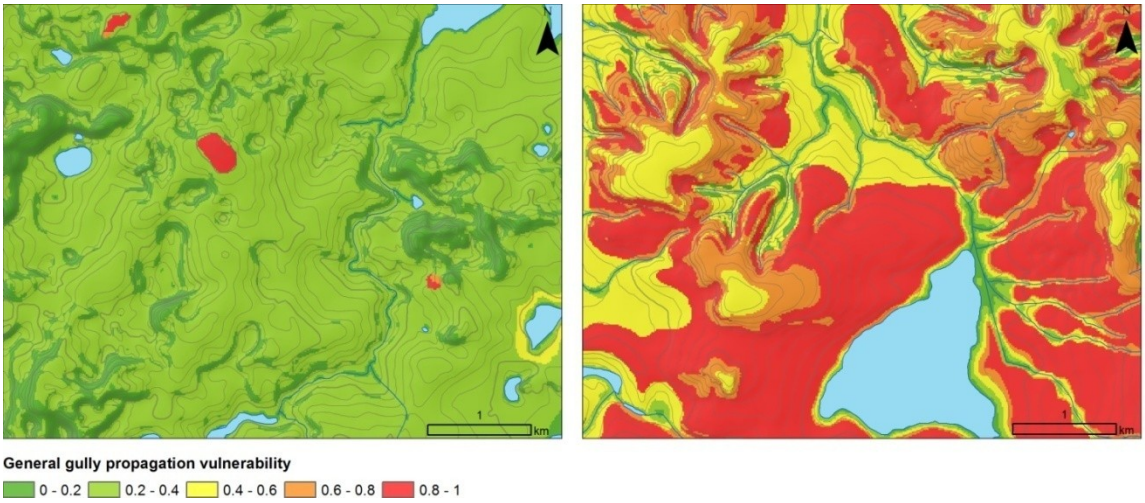

Figure 14-18 Examples of the map showing general vulnerability to gully propagation. High values in this map show conditions that do not restrict gully growth.

The location of both exemplary areas is indicated in Figure 10-5 (karstified terrain A on the left, covered karst area B on the right).

14.5.4 Topographic threshold for gully propagation

The threshold for gully propagation is calculated using an exponent [b] = 1 as suggested by Desmet et al. (1999) for complete gully trajectories (compare section 14.2).
Since gully propagation is related to subsurface flow or saturation excess surface flow, the upstream catchment area is weighted according to conditions of deep interflow. Optimality values for "High recharge for deep interflow" are calculated as follows:

$$\mu_{High\ recharge\ for\ deep\ interflow} = \left(1 - \mu_{\text{high lateral flow}}\right) \cdot \mu_{Low\ subsoil\ permeability}$$

Equation 14-16 "High recharge for deep interflow"

With $\mu_{High\ lateral\ flow}$ as defined on p. 278.

The result is shown in Figure 14-19.

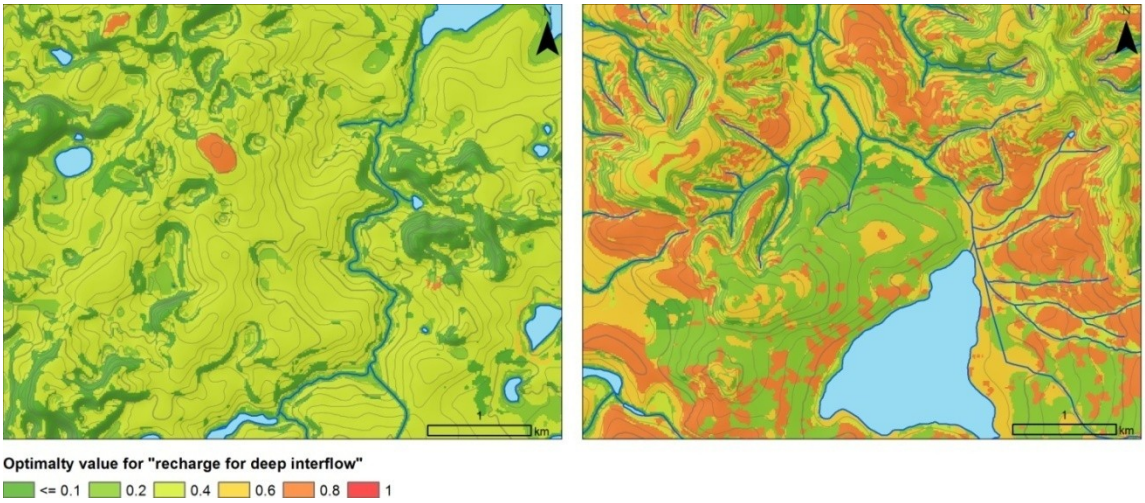

Figure 14-19 Weights for "recharge for deep interflow" used to calculated the specific drainage area A_{wp} for gully propagation.

The location of both exemplary areas is indicated in Figure 10-5 (karstified terrain A on the left, covered karst area B on the right).

For the GIS-based calculation of the topographic threshold for gully propagation, the logarithm of the threshold coefficient [a_3] was mapped using Equation 14-17.

$$\log(a_3) = \log(S) + \log(A_{wp})$$

Equation 14-17 Topographic threshold for gully propagation

with

a_1 = topographic threshold coefficient indicating the risk of incision by Hortonian surface flow

S = slope in percent

A_{wp} = weighted unit drainage area with regard to recharge of deep interflow

Again, due to the weighted calculation of the drainage are, the resulting topographic threshold log (a_3) from Equation 14-17 cannot be directly compared with literature values. Similar to the weighted topographic threshold for gully initiation mentioned above, log(a_3) was converted into a scale from 0 – 1 using a two standard deviation linear stretch which cuts off very high and very low values. The resulting relative map for "high weighted topographic threshold for gully propagation by interflow or saturation excess surface flow" is shown in Figure 14-20 .

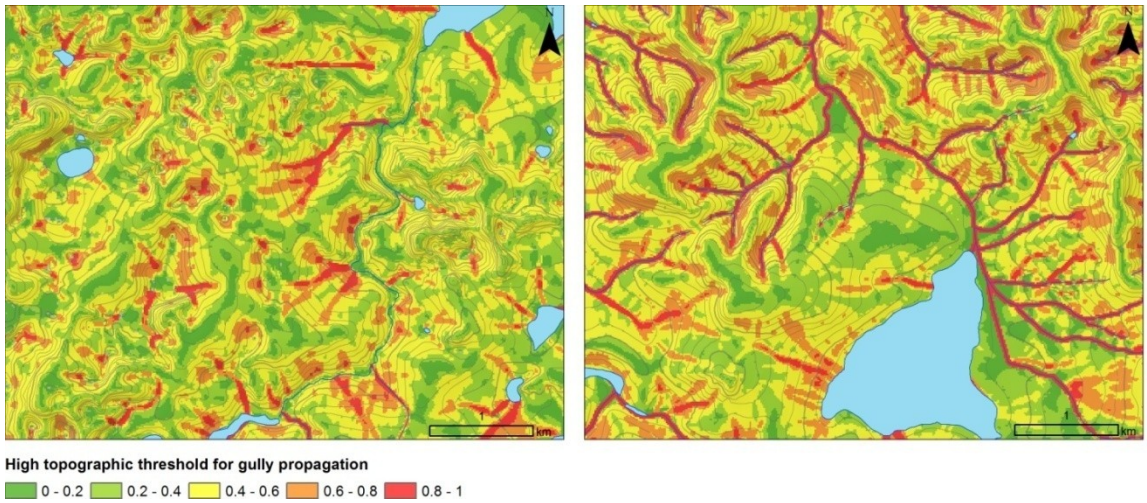

Figure 14-20 Optimality values for "high topographic threshold for gully propagation by interflow or saturation excess surface flow".

This relative map was created using a linear two standard deviation stretch of the original values resulting from Equation 14-17. The drainage area is calculated using the weights from the map in Figure 14-19.

14.5.5 Map for gully propagation hazard

Gully propagation hazard is calculated by multiplying the topographic threshold for gully propagation (Figure 14-21) with the general vulnerability to gully propagation (Figure 14-18). The high values along rivers flowing over meta-pelites can be interpreted as risk for bank erosion and deep incision of these existing rivers.
Examples of the spatial distribution of the result are shown in Figure 14-21.

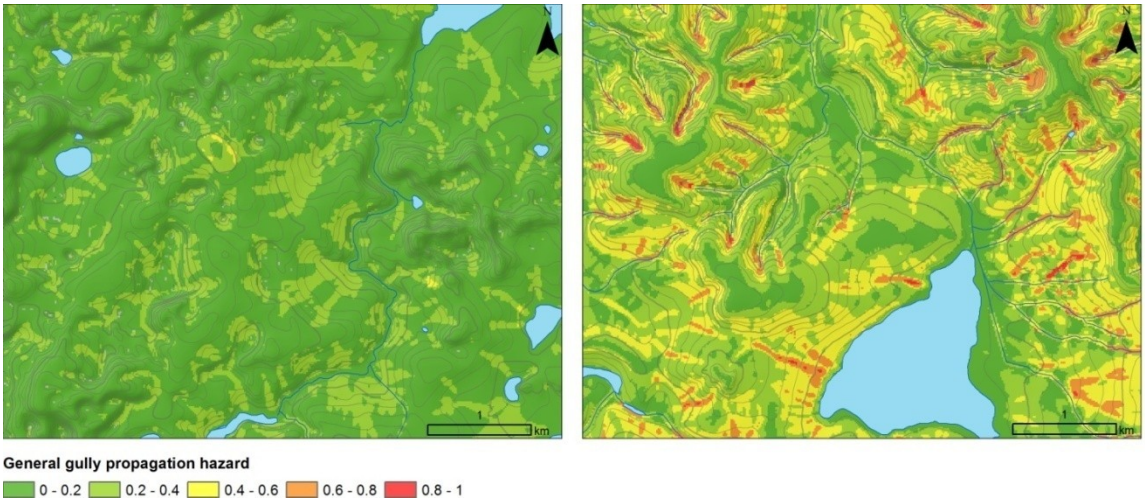

Figure 14-21 General gully propagation hazard generated by multiplying the upper map with the topographic threshold from Figure 14-20.

The location of the two exemplary areas is indicated in Figure 10-5 (karstified terrain A on the left, covered karst area B on the right).

14.6 Final gully erosion hazard maps

The final general gully erosion hazard map is created by a weighted sum overlay of the gully initiation hazard (Figure 14-11) and gully propagation hazard (Figure 14-21).
Since the risk of gully propagation was rated more important for the estimation of the total gully erosion hazard, it received the double weight compared to the risk of gully initiation in the weighted overlay calculation (compare also the workflow shown in Figure 14-7).

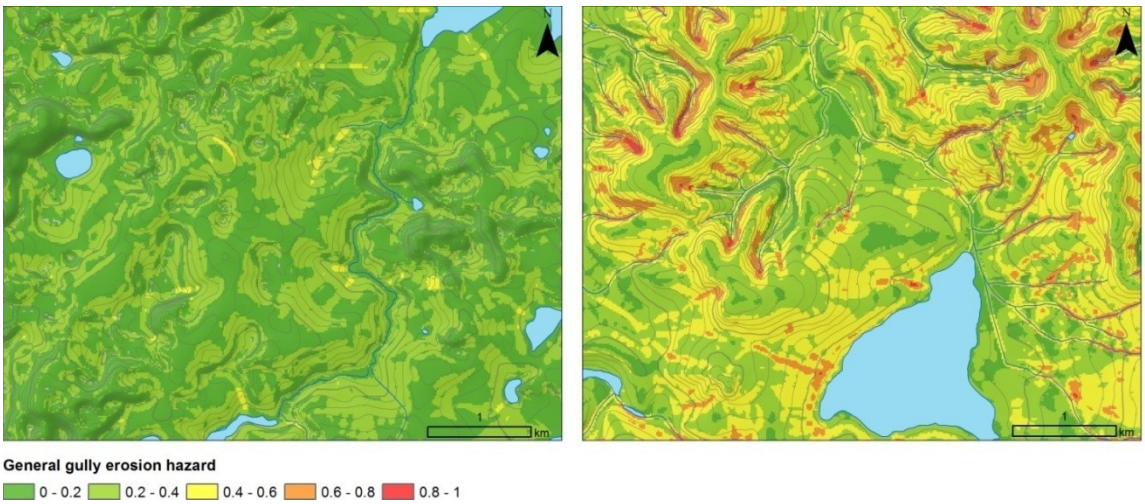

Figure 14-22 General gully erosion hazard generated by a weighted overlay of gully initiation and gully propagation hazard.

For the location see Figure 10-5 (karstified terrain A on the left, covered karst area B on the right).

14.6.1 Protection by land use

To estimate the actual gully erosion hazard, the resulting map was multiplied by the land use weights from Table 14-1.

The land use parameter is derived from the classified Landsat 7 image also used in previous calculations (see also Figure 13-11). Since the resolution of the image and the classification is very coarse and land use changes very quickly in the area, protection against erosion by land use was incorporated into the workflow only at the latest stage to allow for easy modifications if better or more recent land use data are available. Due to the coarse classification, the land use categories summarized in Table 14-1 cover several – often heterogeneous – land use types.

Category	Land use vulnerability to erosion	Weight
Fields, pastures, general open area	Agricultural fields are rare, most open areas are pastures in different conditions. Open area is seen as the typical standard condition for erosion assessment and thus receives a weight of 1.0	1.0
Natural forest (Cerrado, Vereda), Eucalyptus plantations	Natural forests reduces the risk of erosion considerably, especially dense Vereda vegetation near water courses. Nevertheless, less dense Cerrado vegetation is also included into the category and also eucalyptus plantations, which are known to even favor erosion due to absence of undergrowth and high kinetic energy of large raindrops falling from the canopy (Valentin et al. 2005). Thus, the value of 0.7 can be interpreted as a compromise between these different vegetation types.	0.7
Urban areas, sealed areas, roads	Gully vulnerability in urban areas is very heterogeneous. Gully erosion hazard is highest in unsealed mudroads and excavations that expose the subsoil. Nevertheless, as soon as the soil is sealed by asphalt or stone cover and the water courses are channeled as is common in well-planned housing areas, erosion hazard declines to zero. As a compromise considering a relatively high percentage of protected surface in the urban area, a weight of 0.3 was chosen for sealed areas.	0.3
Water	Areas identified as water bodies receive a weight of zero.	0.0

Table 14-1 Weight of land use classes for vulnerability to gully erosion.

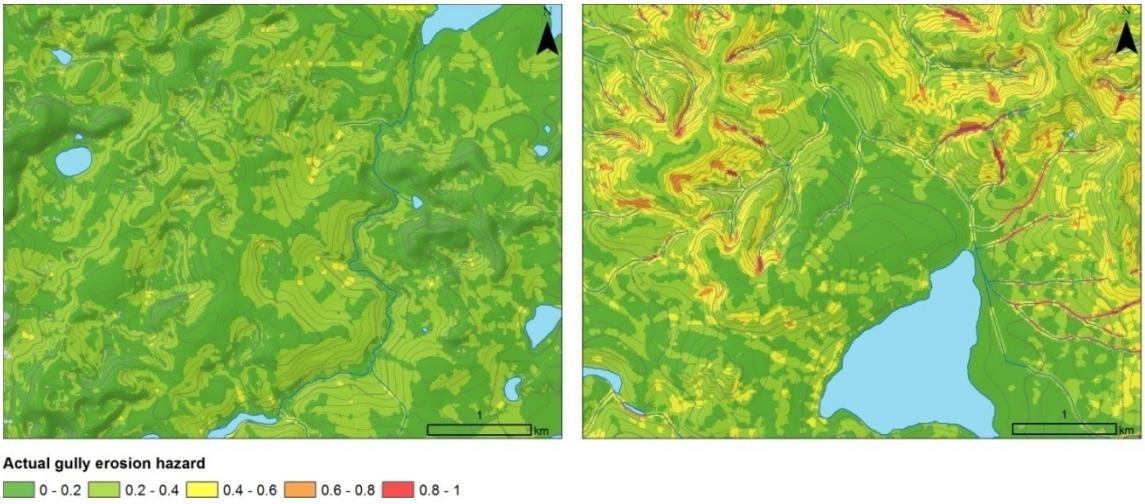

Figure 14-23 Actual gully erosion hazard generated by multiplying the general gully erosion hazard with the land use weights from Table 14-1.

The location of the exemplary areas is indicated in Figure 10-5 (karstified terrain A on the left, covered karst area B on the right).

14.7 Risk of contamination of surface water

The following parameters

- $\mu_{\text{areas of possible saturation excess surface flow}}$ (Figure 14-17),
- $\mu_{\text{close to mapped rivers, lakes or swallow holes}}$ (Figure 10-17),
- $\mu_{\text{high topographic threshold for Hortonian surface flow}}$ (Figure 14-9), and
- $\mu_{\text{high lateral flow}}$ (Figure 14-8)

are combined in a weighted sum overlay to create hazard maps regarding the risk of contamination of surface water. The first two parameters, which stand for hydraulic closeness to surface water or sinkholes, are rated more important and thus weighted double. The other two parameters indicate the amount of lateral flow generated at each pixel and its erosive power while heading downstream. These parameters receive only a single weight. The result is shown in Figure 14-24.

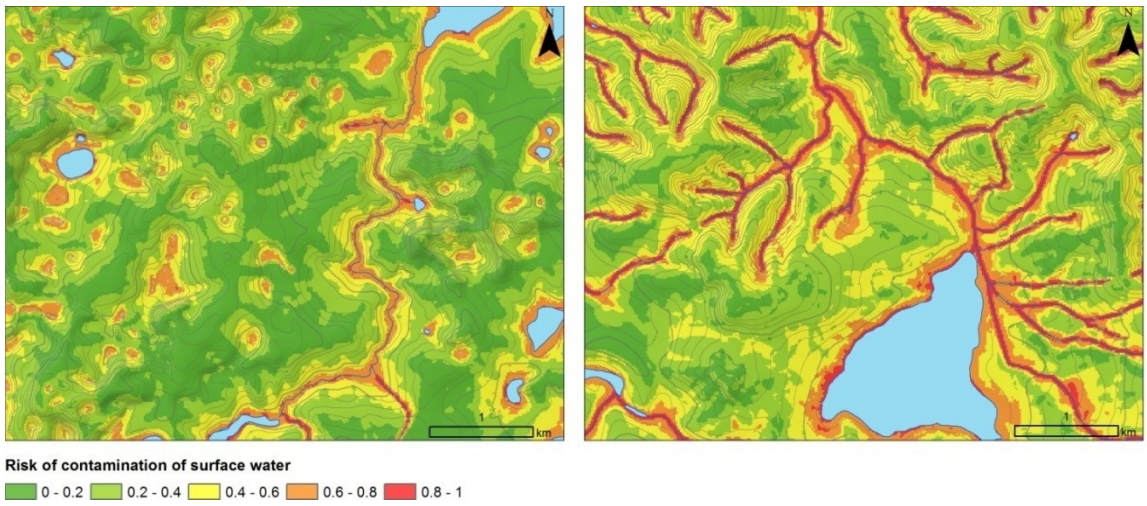

Figure 14-24 Hazard map regarding the risk of contamination of surface water or sinkholes.

The upper map is based on topography and soil properties only while the lower map also includes the current land use. The location of the areas is indicated in Figure 10-5 (karstified terrain A on the left, covered karst area B on the right).

15 Summary of the results

Summarizing the study, the following gain of information results from this project (for a list, see also Annex pp. 329-332.

15.1 Gain of base information (Step 1 + 2 in Figure 3-1)

- The existing geological map in the region has been updated using available literature, new field data and relief analysis in a GIS.
- An idea of the three-dimensional structure of the geological underground is described and illustrated in eight cross-sections.
- A map of the facies distribution of the Sete Lagoas Formation has been created
- Contact surfaces between Basement / Sete Lagoas Formation and Sete Lagoas Formation / Serra de Santa Helena Formation have been interpolated.
- The sedimentary structure seen in a sand pit in the alluvial plain of the Riberão da Mata is visualized and interpreted including three radiocarbon datings.
- Changes in land use pattern following sand mining in the alluvial plains have been analyzed covering the time range of 40 years.
- The sediment volume eroded by the gullies on the southern and eastern hills of the city of Lagoa Santa has been estimated from contour lines and compared with pre-historic sedimentation rate derived from drill holes in the lake Lagoa Santa.
- River profiles have been analyzed and interpreted for the for the Rio das Velhas and the Riberão da Mata and its affluents
- An overview of the relief evolution is given and illustrated in a schematic drawing incorporating possible neotectonic movements.
- A general model of the distribution of hydraulically relevant soil horizons is described and illustrated in eight idealized catenas representing six geomorphological compartments.
- Land use has been roughly classified into four categories from a Landsat 7 image from 2002.
- A hydrologically correct elevation model has been developed from contour lines including possible sink locations and surface drainage basins.
- Important hydrological and relief parameters have been derived from the digital elevation model such as slope, specific catchment area, topographic position, elevation above river, lake or sinkhole and distance to river, lake or sinkhole (altogether 16 topographic parameters).

Base information that have been derived or modified during the first part of the project is indicated light green in the parameter list in .

Gain of secondary information (Step 3 in Figure 3-1)

- 6 absolute and 9 relative parameters have been associated with geological units.
- 19 relative topographic parameters have been derived.
- 6 absolute and 13 relative soil parameters have been regionalized for the study area.
- 13 absolute parameters regarding the architecture of the geological strata above groundwater have been derived and regionalized for the study area.
- 3 parameters regarding resource quality have been regionalized for the study area
- 10 relative parameters used for gully erosion hazard have been regionalized.

15.2 Gain of tertiary information (Step 4 in Figure 3-1)

15.2.1 Resources

- Evaluation of limestone resource accessability
- Estimation of sand resources in transport distance to Lagoa Santa
- Agricultural value

15.2.2 Groundwater vulnerability

- Protection of the groundwater by overlying strata
- Degree of bypassing protective layers
- Intrinsic groundwater vulnerability

15.2.3 Risk of erosion and contamination of surface water

- Risk of slope instability
- Risk of gully initiation
- Risk of gully propagation
- Areas vulnerable to gully propagation
- General risk of gully erosion (without considering land use)
- Actual risk of gully erosion (considering also land use)
- Risk of contamination of surface water

15.3 Complementary information for land use decision

These data have not been modified but only added for comparison:

- Infrastructure

- Speleological protection zones
- Biotic protection zones

16 Error analysis

16.1 Error sources during the regionalization process

From the beginning to the end of the regionalization workflow shown in Figure 3-1, different types of possible errors can be distinguished, summarized in the following questions:

1. Geology-soil-landscape model:
    - Is the influence of lithology for soil development appropriately described?
    - How did the erosion cycles redistribute the material along a catena?
    - What happened during climate and land use change?
    - Is the simplification into very few hydrological soil units acceptable?
2. Selection of the input parameters:
    - Could an unknown parameter be critical for soil development at a certain location?
3. The input parameter itself (see also section 16.2):
    - Are there errors in the digital elevation model?
    - Are there errors in the derivation of hydrological parameters (e.g. elevation above a river, location of a swallow-hole)?
    - Are there errors and insecurities in the geological map?
4. Choice of the input parameter optimality curve:
    - Which shape of the optimality curve represents the influence of the parameter best?
    - Is the steepness / cross-over point realistic?
    - Is the function itself suitable for the task?
    - Is the cutoff (e.g. 10 meters above a water course indicating no water influence on soils) realistic?
5. Combination rules of different optimality values:
    - Which overlay function is best?
    - Weighted overlay, minimum, maximum or multiplication of the different input optimality values?
    - What are the best weights?
6. Physical interpretation of the output optimality value:
    - How deep is “deep” topsoil? 2 meter or 4 meter?
    - How high is a high effective field capacity in mm/m?
    - How should local extreme values be handled (e.g. very deep topsoil in karst pockets or in paleo-relief structures)?

7. Thresholds for creating classified maps out of continuous parameters:
    - E.g. which optimality value for “deep” topsoil separates “shallow” from “medium deep” hydrological topsoil classes?

In the following section, the influence and measurability of each error type is shortly discussed:

- The quality of the geology-soil-landscape model (1) is central to the method but very difficult to assess. It also needs the highest effort and time to reduce to a well defined level since it depends on intensive field and literature studies. This error is also present in traditional soil survey and decreases only with experience of the surveyor. The benefit of the method presented here is that the geology-soil-landscape model is explicitly described and can thus be passed on and updated if new base information is gained.
- The correct selection of input parameters (2) is equally important and also difficult to assess. Nevertheless, since the workflow is transparent and adjustable, new relevant information can be added without major problems.
- The insecurity of the input parameters themselves (3) is maybe the easiest to assess and considerable effort has been taken to reduce its error to an acceptable level: The geological map has been updated using topographic, remote sensing and field observation data. Considerable effort was put into correct interpolation of the digital elevation model, derivation of flow routing and identification of possible sink locations. Physical data on soil properties were collected from literature but did not always match the desired parameters to be regionalized. Here, more analytical soil data would improve the result considerably. For a more detailed analysis see section 16.2.
- The suitability of the input parameter curve (4) is difficult to assess since its shape was adjusted by recurrent comparison with the expected spatial distribution of the parameters according to the internal geology-soil-landscape model. Thus, it is related to the first type of error.
- The combination rules of the different optimality values (5) are adjusted in a similar way using the tacit part of the internal geology-soil-landscape model, which makes the assessment of the associated error again very difficult.
- The physical interpretation of the optimality values (6) is essential for the final output maps but also during intermediate steps, e.g. when the regionalized topsoil depth in centimeter is needed for the assessment of the dominant flow process. Nevertheless, errors of this type are easy to adapt to new information since they are at the end of the workflow and usually do not change the spatial pattern of the modeled parameter but only its absolute values.

- The choice of thresholds (7) is only relevant if several continuous maps are combined into one classified map. If the classification process is well documented, this error can also be well controlled and the thresholds adapted if necessary.

Altogether, the errors of the first, fourth and fifth type are the most difficult to assess and to minimize while having nevertheless a large influence in the output. The other errors are also important but can be controlled and reduced more easily through new data.

Generally, the workflow diagram in the Annex p. 327 and the list of the variable dependencies in on pp. 329 - 332 can help to estimate the error sensitivity of a parameter. The parameter "risk of near surface epikarst" is for example highly sensitive for the prediction of topsoil thickness and weathering depth and thus influences nearly all modeled output parameters.

16.2 Input data quality and its relevance for the output

16.2.1 Geological architecture

Geological mapping is difficult in an area where firm rock is covered by deep saprolites for large parts of the area. Thus, next to rare rock outcrops (which are mainly limestone), highly weathered saprolite material or even indirect hints such as vegetation, soil color change or morphology had to be used in large parts of the area for mapping. Own field data were mainly gained in the eastern part of the study area, in the western and northern part the updated map is based mainly on literature data, relief analysis or remote sensing. In Map 32 in the annex, an overview of the field and drill-hole database is given to show transparently the spatial quality of the modified geological map.

The three dimensional geological architecture is based on a structural model (flat lying sediments modified by a thin skinned tectonic movement) and only locally supported by drill-hole data. Intrastratal karstification complicates the estimation of strata thickness, especially the rough assumptions used to interpolate the recent base of the Serra de Santa Helena Formation (Figure 11-2) is only a temporary working base that should be revised as soon as more drill-hole data are available.

It has also to be remembered that in the drill-hole data the saprolite material was not differentiated but altogether associated to the pelitic Serra de Santa Helena Formation. Based on the information from field outcrops, this might not always be correct since also impure carbonates of the Pedro Leopoldo Facies can weather to thick saprolites.

The interpolated top surface of the basement has its data base only in the south-eastern part of the study area. Thus, the interpolation result in the north-western part of Map 38 in the annex is highly doubtful.

16.2.2 Geomorphologic evolution and neotectonics

The concept of the geomorphologic evolution in the area (Figure 6-5) is mainly based on literature, especially the ideas from King (1956), Kohler (1989) and Parizzi et al. (1998), supplemented with own analysis of relief structures and ideas of neotectonic movement. Although relief and analyzed river profiles support the hypothesis of neotectonic movement, the concept explained in section 6.3 is still at the stage of a hypothesis that needs to be proven by field data.
The geomorphological zonation (section 6.5) was chosen to represent homogenous units that can be described by idealized catenas (section 9) rather than to standard geomorphological zonation rules and should also be interpreted in this way.

16.2.3 Geomorphologic features

The geomorphological features mapped by Kohler (1989) are used for the estimation of the very important parameter “Risk of near surface epikarst”. Here, an updated higher resolution map of geomorphological features would improve the estimation of many important parameters related to the existence of near surface epikarst.
Erosion features have not been mapped during this study – although a more or less theoretically based risk map regarding gully erosion hazard has been created. Mapping of existing erosion features together with higher resolution land use data would improve the erosion hazard maps considerably and a serve as quality assessment of the created risk map.

16.2.4 Soil landscape model

The soil landscape model described in section 9 summarizes literature data (mainly from CPRM (1994b) and Shinzato and Lumbreras (1998)) and own soil-landscape knowledge gained during field work. It is a necessarily generalized model that tries to cover the typical distribution of hydrological soil parameters but does not cover special local situations which can be very variable due to the long history of the landscape. The catenas are not based solely on real field data but are illustrating a general concept. More studies, especially more local soil catenas with deep soil profile descriptions would be desirable to validate this model.

16.2.5 Hydrological interpretation of the different soil materials

The hydrological interpretation of the different soil materials is based mainly on soil macro-structure visible in the field and few analytical data from literature, supplemented by a exemplary field tests using a double ring infiltrometer. Nevertheless, the interpretation was not always clear

and the input data for subsoil permeability and effective field capacity were not satisfying and sometimes contradicting. For example, it seems strange that meta-pelite subsoil should have at the same time a very high effective field capacity and a very low permeability, since the first is based on the existence of a high amount of medium sized pores that should allow at least a moderate permeability. Similarly, a high sand content and high amount of large pores should lead to a high permeability of the basement rock subsoil - but instead a very low permeability was measured during a double ring infiltration experiment. Field observation from surface erosion marks for meta-pelite and basement saprolite support the assumption of low permeability - at least low enough to result in concentrated surface flow. Here, more field data on water retention curves and permeability of the soils and saprolites of the region could enhance the quality of the output thematic maps.

16.2.6 Topography and hydrology

The digital elevation model is based on contour lines from a topographic map 1 : 25 000. The elevation values of many contour lines had to be corrected manually and it is possible that some minor errors due to false identification of a contour line persist. The interpolation algorithm used to create the DEM is optimized for reliefs shaped by water ((Hutchinson 1989). Nevertheless it produces artifacts in flat alluvial plains (wavy pattern of hills and sinks pattern) and on flat slopes (stair – like pattern). These errors have been considered during further derivation of topographic parameters, i.e. by calculating a spatial mean of the slope for the assessment of very flat slope values and by substituting the calculated elevation above groundwater in alluvial plains by a mean value related to the geological unit. Also vertical walls (e.g. at karst outcrops) are not correctly represented in the DEM, which has lead to a comparatively low slope threshold for the identification of karst outcrops. A directly measured elevation model with higher resolution, e.g. from TerraSar-X, would clearly enhance correctness of relief data thus also for the regionalized parameters.

The interpolated elevation model was modified to guarantee correct hydrological routing. This included also the identification of potential sink locations in the karst environment. Many of these sink locations are not supported by field or literature data but only by a plausibility analysis of the relief. Their exact location is nearly always unknown. Here, a field check would improve the data quality considerably, since many parameters such as elevation above or distance to sinkholes or the drainage area of sinkholes depend on this information. Other regionalized parameters - especially those regarding soil thickness or thickness of layers above groundwater - rely on assumptions and estimations whose insecurity is much higher than those of relief parameters. These parameters would not profit very much from a higher accuracy of the DEM.

16.2.7 Groundwater

Groundwater isolines are of mixed data quality. While in the central part of the area, isolines could be interpolated from drill-holes, the study had to rely on literature data in the north-western part of the area. In the southern and eastern part of the area, no groundwater data could be retrieved. Here, the insecurity is very high and could easily be reduced by adding new data to the project. Since the influence of this parameter is very high for output maps regarding groundwater vulnerability, an enhancement of the accuracy of groundwater isolines would improve the results very much.

16.2.8 Landuse

The land use classification of the Landsat 7 ETM+ image from 2002 is very coarse, much coarser than the detailed relief data. Since the availability of recent high resolution remote sensing data is high and increases rapidly, this information could be used and added to the project. High information gain is expected if high resolution land use information is included into the estimation of intensity of lateral flow, risk of gully initiation and propagation and risk of bypassing protective layers above the groundwater.

16.2.9 Summary

The following table summarizes the possibilities to improve the input data quality, also estimating the necessary effort and the expected gain in information for geo-potentials in the study area.

Base parameter (Quality)	Could be improved by:	Effort necessary	Would improve especially the following output parameter:	Gain of information	Gain / effort
Geological architecture *(Medium quality)*	Drill holes distinguishing also different types of soft material	High to very high	- Weathering depth - Protective function of overlying layers above groundwater - Limestone resource accessibility - Sand resources	Medium to high	**Medium to low**
Geomorphology *(Medium quality)*	Mapping karst features more precisely, mapping erosion features	Medium	- Risk of near surface epikarst - Groundwater vulnerability - Limestone resource accessibility - Risk of gully initiation and propagation	High	**High**
Neotectonics *(Low quality)*	Field data proving neotectonic movement	High	- Thickness of alluvial / colluvial sediments - Sand content in the alluvial plains	Low	**Low to very low**
Soil-landscape model *(Medium to low quality)*	Creation of real soil catenas for each geomorphological unit	Medium - high	- Dominant topsoil type - Intensity of lateral flow - Risk of gully erosion - Agricultural value	High	**Medium to high**
Hydrological soil properties	Permeability and erodibility measurements	Medium	-Intensity of lateral flow - Groundwater vulnerability - Risk of gully initiation and propagation	High	**High**
Topography and hydrology *(High quality)*	High resolution remote sensing DEM	Medium to high	- Risk of near surface epikarst - Dominant topsoil types - Degree of bypassing protective layers - Risk of contamination of surface water - Risk of gully erosion - Agricultural value	Medium	**Medium**
Groundwater isolines *(Medium to low quality)*	Complementation of groundwater isolines in the south and east of the area	High (Low, if existing data can be retrieved)	- Groundwater vulnerability - Limestone resource accessibility	High	**Medium (High, if existing data can be used)**
Land use *(Very low quality)*	Classification of a recent high resolution satellite image	Medium	- Intensity of lateral flow - Risk of gully erosion - Actual risk of gully erosion - Degree of bypassing protective layers - Risk of contamination of surface water	Very high	**High – very high**

Table 16-1 Methods to improve the input data quality and the expected effect on information gain for geo-potentials in the study area.

17 Interpretation and quality of the results

17.1 Soil maps – continuous and classified maps

Most maps of soil parameters created in this study are continuous to make full use of the available continuous based data derived from relief structure. For a better overview, they are usually classified into five categories in the small scale maps in the annex which cover the whole study area. Nevertheless, the continuous data are still available in the GIS database and stored in the .img – format that can be read by most GIS software. Thus, higher resolution thematic maps than the maps found in the annex can be created easily and the continuous parameters can be used as input for other modeling purposes without losing information due to the definition of sharp class borders.

An exception to this are the two soil maps showing hydrological topsoil types and dominant flow processes in Map 59 and Map 64, which show sharply outlined soil units similar to traditional soil maps. They have been created by aggregation of several continuous soil property maps. The loss of continuous information is counterbalanced by higher information density of the combination map compared to the base maps. For the interpretation of these aggregated maps, the continuous base maps are still available in the data base. Thus, core areas of unambiguous soil classification can be separated from areas of transition between soil units. By identifying problematic areas and their representation in the primary continuous maps, the mapping rules can be adapted until the result is satisfying.

17.2 Comparison with traditional soil maps

As can be seen comparing the soil maps from CPRM (1994b) and Shinzato and Lumbreras (1998) (Figure 17-1), not only the spatial distribution of the soil units is different but also the mapped soil categories. This is characteristic for traditional soil maps that are usually very individual, depending on the experience and local knowledge of the mapping person. The soil units are aggregations of different parameters including soil genesis, soil texture, chemical properties, nutrient status and relief. Thus, it is difficult to extract hydrological properties from these units since some are similar in their physical properties but are differentiated based on their chemical properties or relief. Other soil units have very varying physical properties but are combined into one unit. In these traditional maps, it is also not possible to identify areas of insecurity from core areas where typical soils can be found for each unit and thus quality assessment is difficult. Comparing both traditional soil maps in Figure 17-1, it is difficult to say which represents the continuous reality better than the other since the mapping process and the internal soil-landscape model of the soil scientist is not explicitly documented. For the same reason, it is not possible to

extent one of the existing soil maps to previously not mapped regions (e.g. the region east of Lagoa Santa for the map from Shinzato and Lumbreras (1998) without losing overall consistency of the map. While data-mining methods can be used to collect the intrinsic soil-landscape model hidden in a traditional soil map (e.g. Moran and Bui 2002, Schmidt et al. 2008, Behrens et al. 2010), the generated regionalization models are usually difficult to convert into a descriptive soil-landscape model. Thus, a plausibility check using local expert knowledge is not possible.
In the study area, the existing soil maps are of the scale 1 : 50 000 and thus often do not match exactly the topographic information which is available at a scale of 1 : 25 000. The maps created by the Semantic Import Model workflow on the other hand can make use of every spatial detail shown in the topographic map. Thus, although many rough assumptions had to be made during the workflow, the resulting maps are of a very high spatial detail. In this sense, the automatic soil mapping method can be used to add spatial detail to existing soil information based on the highest resolution of a given input map. Nevertheless, when interpreting the high spatial details of the automatically generated classified maps, information from continuous maps at intermediate workflow steps should be used for quality assessment. The main disadvantage of the automatically generated soil maps is that local special conditions visible in the field are difficult to integrate in a general regionalization rule that is applicable for the total area. Thus, these special conditions have to be added later manually or the study area has to be split into smaller units and a regionalization rule established for each homogeneous area separately. This has also been done in the current study using the geomorphological compartments defined in section 6.5.

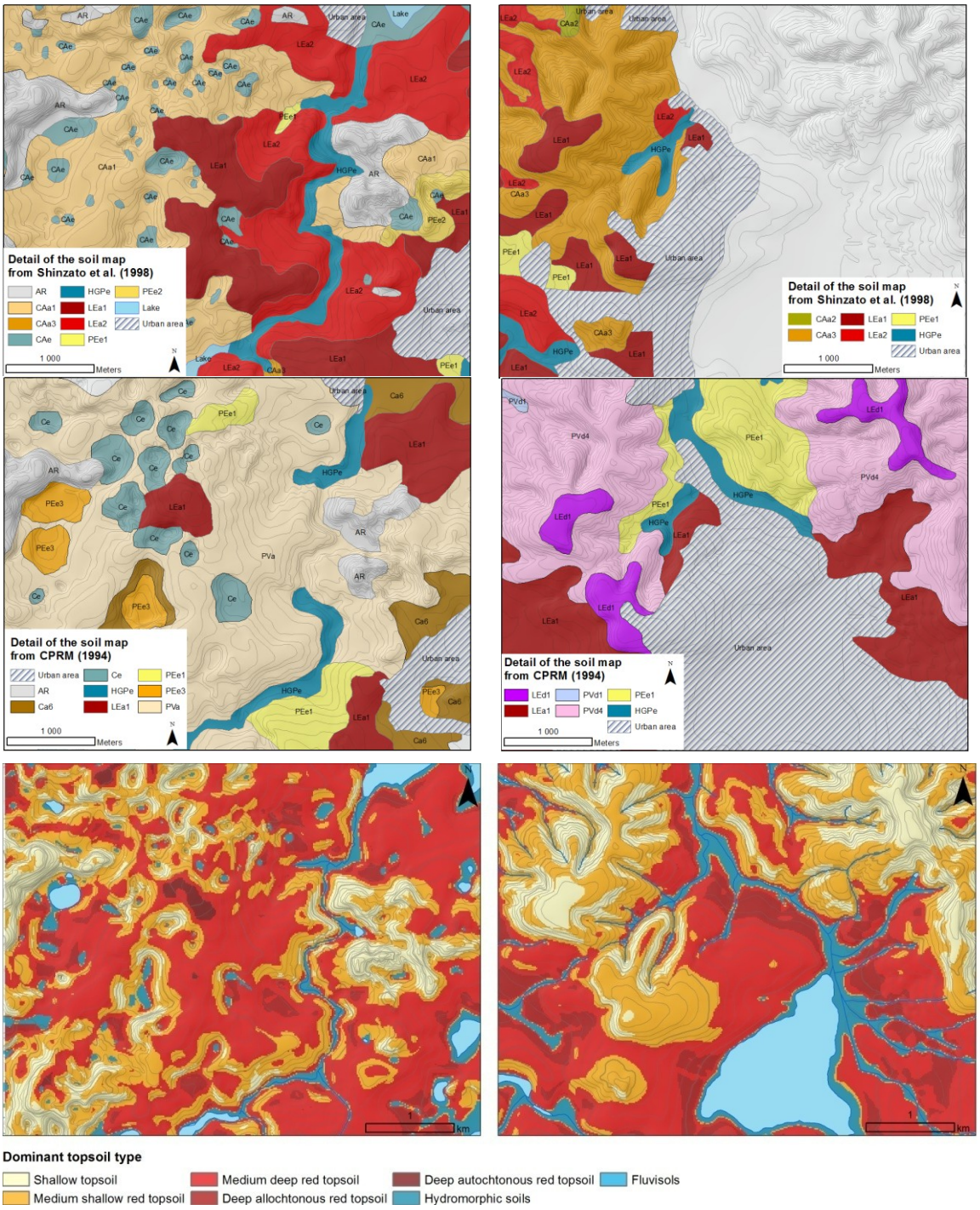

Figure 17-1 Detail of the traditional soil map created for the Projeto VIDA in 1994 (CPRM 1994b), for the environmental protection area APA Carste de Lagoa Santa (Shinzato and Lumbreras 1998) and of the map of dominant topsoil types (Figure 10-28) from the current project.

17.3 Resources

The estimation of mass resources is based on several interpolated parameters: Groundwater level, thickness of geological strata and weathering depth. Also the central parameter "Risk of near surface epikarst" has a high influence on the result. Since all these input parameters are associated with high insecurity, also the resulting optimality values "thickness of overburden", "resource thickness" and "accessibility of limestone resources" have to be interpreted with care. Nevertheless, it is difficult to achieve a higher data quality since the necessary effort for a considerable improvement is very high and requires many drill-holes well distributed in the study area. Although private data of mining companies exist that are of a higher quality, no spatially continuous data are publicly available on limestone resource availability. The results shown in this study can give at least a general overview for decision makers involved in sustainable land use planning.

17.3.1 Sand

Although the resources available in the Riberão da Mata fluvial system are very roughly estimated and based on many assumptions, they can give an idea about the amount of extractable sand resources in this area. It should also be noted that the large overburden some distance away from the recent river often hinders an economical exploitation. Nevertheless - as can be seen in the open sand pit that was studied - if the location is close enough to the region of demand, even sand resources with larger overburden can be exploited. To identify locations where this extraction is possible and economically viable and which thus should be excluded from urbanization, more detailed sedimentological studies need to be conducted in the Riberão da Mata system.
The total population in the four municipalities Lagoa Santa, Confins, São José da Lapa and Vespasiano increased from 26.000 in 1970 to 45.000 in 1980, then to 85.000 (1990), 134.000 (2000) and 165.000 in 2005 (Data from IBGE). Based on the average consumption of 1,5 t sand per capita and year (DNPM 2006, IBGE 2006), the population of these municipalities may have needed up to 4.2 million tons of sand for the development of their city between 1964 and 2004. Considering an estimated 7.7 million m³ of extracted material (see page 28) with a possible sand content of 50% in areas with low overburden and an average weight per m³ of 2 tons, 7.7 million tons of sand may have been extracted alone in the area of the multi-temporal study. This value shows the importance of this small area for the development of the entire region.
If the plans for the development of the northern periphery of Belo Horizonte proceed, 3.2 million tons (or 1.6 million m³) of sand might be necessary to satisfy the demand of the four adjacent municipalities for the next ten years (estimation based on a population of 165.000 in 2005, recent growth rate of 3.4% (IBGE 2006) and a per capita consumption of sand 1.5 tons of sand per year). Still, this might be a conservative estimate, as it is based on the past growth rate without

considering the enhancement by the new motorway and the new legislation. Additionally, with increasing industrialization, the per capita consumption of sand rises. If 1.5 tons of sand per year are the mean consumption of Brazilian people, the consumption in and around urban areas is probably much higher and may reach the consumption rate of industrialized countries such as the United States with around 8.7 tons per capita (Terpodei 1999). Taking this into consideration, the real demand for sand in the region might be six to ten times higher.

17.3.2 Agricultural value

The agricultural value is estimated using the most important restricting factors for the soils in the region, which are chemical poverty / acidity on the one hand and relief position (steep slopes or water logging) on the other hand. Soil texture or effective field capacity, which play a major role in assessment of soil quality in temperate regions, are less important for the soils in the study area. The soil and relief properties were regionalized using the soil-landscape model described in section 7 - 9, which is based on literature data and exemplary field excursions. No existing fertility evaluation system was used but instead a relative method that is adapted to the knowledge base available for the area. Taking this into account, the map can help decide where in the area the soils with highest natural fertility and highest agricultural value can be found. Since the different input parameters were weighted subjectively, the transparently stored workflow should be adapted and the weights modified depending on the specific land use problem to be solved.

17.4 Groundwater vulnerability

17.4.1 Protective function of the overlying layers (P-Map)

The map of protective function (P-Map) is very similar to the map of the subsoil protection value (S-score). This shows that subsoil and saprolite are the most important protective layers above groundwater in this area. The highest values area reached on the deeply weathered Serra de Santa Helena meta-pelites. The bedrock score adds important protection in other areas that area high above groundwater level or in the basement area. The score of the protection by the first meter from the surface is highest for areas where saprolite and dense subsoil material are close to the surface such as in the steep eastern hills. Also hydromorphic soils along small rivers give a high protection since their effective field capacity is higher than that of the red soils on plateau areas. The topsoil value adds important protection in areas with shallow weathering depth or in areas close to the groundwater level. The P-Map is generally plausible; its highest insecurities are the very roughly estimated groundwater level and weathering depth, especially the determination of potential occurrence of near surface epikarst.

The assessment quality of groundwater protection by overlaying layers (P-map) depends largely on the correctness of the geological architecture system, which has been interpolated using a very heterogeneous database. From all parameters, the elevation above groundwater and the optimality value “Risk of near surface epikarst” are maybe the most sensitive parameter in this estimation. Nevertheless, also the thickness of subsoil / saprolite is a very important parameter due to its high protective potential. Compared to the insecurity in estimating these three important parameters, the other variables such as the effective field capacity of the topsoil or the correct choice of the L- F- and S- values have lower influence on the output map.

Degree of bypassing protective layers (I-Map)

The degree of bypassing protective layers (I-map), is based on the intensity of lateral flow (I’-Map) and the definition of drainage basins.

The I’ map shows highest intensity of lateral flow on the steep hills east of Lagoa Santa and on sealed areas that are not completely flat. Since the red upper soil layer in the karst area is highly permeable, infiltration is the most common flow process in the karst area with the exception of sealed areas.
Thus, land use – especially the definition of urban features - is the most important parameter for the estimation of lateral flow into karst sinks. Since land use classification is of a very low data quality, it has to be considered that each sealed area in the karst region should be automatically assigned a very high groundwater vulnerability – even if a low vulnerability is indicated in the map due to incorrect land use classification. Here, enhanced land use input data would result in a strong accuracy increase.
The I’-map can also be used separately for other tasks that need the amount of lateral flow or fast response flow as input (e.g. catchment hydrology of erosion hazard).

Although the PI-method was originally designed for general resource protection, i.e. the surface of the aquifer is the target of protection independent of the direction of subsurface flow, the location of the entrance point was included into the catchment classification for the study area. Depending on the task for which the vulnerability map is used, a different surface catchment classification should be considered.

17.4.2 Total vulnerability map (PI-Map)

The final groundwater vulnerability map (Map 79 in the annex) seems generally plausible. It shows highest vulnerability around karst outcrops and for sealed areas in the catchment of sinking

streams. The largest part of the area has low vulnerability and high plateau areas on meta-pelites have very low vulnerability.
It is remarkable that also most neighboring areas of exokarst features are classified as medium to low vulnerable due to the relatively thick soil cover and permeable topsoil hindering quick surface runoff. Although the area shows many karst features, shallow soils such as rendzic Leptosols that are common in European karst areas are not widespread in the area. Instead, deep Lixisols, ferralic Cambisols or Ferralsols occur even close to karst outcrops.
Nevertheless, it has to be taken into account during urban planning that each new settlement or sealed area in the karst plateau results immediately in high or very high vulnerability of the aquifer due to increased surface runoff and risk of bypassing protective layers. Thus, good hydrological engineering is essential for urban planning in the karst area (black outline in the PI-map in the annex) even in areas with currently low mapped natural vulnerability.
An update of the I-Map using recent high resolution land use data will certainly identify more high risk areas in the karst area than the map created during this study.

17.5 Erosion hazard

The estimation of erosion hazard is only a transfer of general observation from literature regarding factors that increase the vulnerability of an area to gully erosion combined with a modification of the topographic threshold method. Thus, it is only based on theoretical considerations but not validated by observed erosion features in the landscape.
Although some erosion features were mapped using the satellite images provided by Google Earth (Map 7 in the annex), the mapping is not comprehensive. A well structured comprehensive mapping together with field validation would be necessary to validate the erosion hazard map. Until then, it can solely be stated that the output of the gully erosion hazard maps is plausible from a geo-scientific point of view and also matches most of the larger erosion features identified in the landscape. An exception are the gullies directly east of the lake Lagoa Santa. Here, the dented contour lines result in a wrong slope calculation, which is inherent to the interpolation algorithm (and would be worse using other interpolation algorithm such as nearest neighbor interpolation). A higher resolution elevation data would be needed for a sound estimation of gully erosion hazard in this area. Nevertheless, since it is already clear that these gullies exist, the solution to this problem has not a very high priority regarding assessment of gully erosion hazard for the total study area.
There is a general problem with topographic threshold method for downstream river areas: given a large enough catchment area, the threshold value will always be very high, even with very low slope values. Thus, the main predictive power of the topographic threshold method lies in previously not incised slopes. In areas with already defined drainage system, it can nevertheless

indicate areas of active riverbed erosion – although the results need to be interpreted with care due to interpolation artifacts of the DEM which are especially noticeable in low slope areas and along incised drainage ways.

Maybe the weakest point in erosion assessment is the inclusion of land use data, which are of a very low resolution and not up to date. Their strongest effect is clearly when the "general gully erosion hazard" (Map 91) is multiplied by a land use protection index to derive the map of "actual gully erosion hazard" (Map 92). But since the input value "intensity of lateral flow" is used as weight for the calculation of the drainage area for both topographic thresholds (Map 81 and Map 83), this vague land use parameter is already included to a less noticeable degree in the calculation of the risk of gully initiation, propagation and general risk of gully erosion (Map 82, Map 90 and Map 91).

18 Conclusion

For the current project that aims at supplying the region around Lagoa Santa with an easily interpretable set of geo-scientific variables, out of a very heterogeneous database a structured workflow has been created which resulted in over 90 consistent thematic maps.
These maps can be interpreted as a digital atlas of geo-potentials for the region around Lagoa Santa. They are visualizations of complex topics that are understandable as single maps but yield more comprehensive information as a set. The relatively high number is due to the fact that also most intermediate results of long workflows are displayed as maps. This offers the possibility for a visual check of the integrity and plausibility of the regionalization method following the parameter interrelation displayed on a flow-chart scheme.
One of the major problems in the project was the scarce database that often required rough assumptions for the regionalization of parameters. While it is easy to criticize the inaccuracy and sometimes also the seeming arbitrariness of the chosen regionalization rules, the reader should take in mind that the maps display a visual translation of a geology-soil-landscape model that would have otherwise been available only in the form of text descriptions and would need a lot of expertise to understand and transfer to specific land use projects.
While accepting these uncertainties, the gain of information availability and its spatial display in the form of maps make this knowledge accessible to a larger group of stakeholders and thus favor its active incorporation in land use planning. From this viewpoint, one of the largest benefits of the project lies in the graphic display of geo-scientific arguments as maps that would need a long explanation in the form of text or in tables.
Using this atlas, also new combinations of geo-scientific parameters can be created for specific land use projects. This overlay is done most easily in a GIS environment and most effectively using Spatial Decision Support Systems methods but it is also possible using the analogous print version of the maps, for example for a first overview or in discussion groups. Additionally, further projects that are important for the sustainable development of the region can use the regionalized parameters as input. Gully erosion and floods seem to be the most strongly perceived geo-hazards in the region. For a sound assessment of the associated risks, a dynamic model of the catchment hydrology is essential. Such a model needs high resolution data on hydrological soil parameters as input, which can be drawn from the created database.
The weakest point of the input data is land use. Due to the low data quality, land use was incorporated at the latest possible stage in the workflow, especially during assessment of groundwater vulnerability and erosion hazard. In most other thematic maps, such as agricultural value or availability of limestone resources, land use is not included at all. However, the methods developed and described here allow an adaptation to fast developing changes of land use. Next to a field validation that checks the regionalization rules by systematic analysis, a classification of

recent high resolution land use data would be an ideal supplement to the current work and enhance its accuracy and applicability considerably.

19 Literature

Alkmim FF, Marshak S (1998) Transamazonian Orogeny in the Southern São Francisco Craton Region, Minas Gerais, Brazil: evidence for Paleoproterozoic collision and collapse in the Quadrilátero Ferrífero. Precambrian Research 90 (1–2): 29-58.

Alkmim FF, Martins-Neto MA (2001) A bacia intracratônica do São Francisco: Arcabouço estrutural e cenários evolutivos. In: Martins-Neto MA, Pinto CP (eds) A Bacia do São Francisco – Geologia e Recursos Naturais. SBG/MG, Belo Horizonte, pp 9-30.

Aller L, Bennett T, Lehr JH, Petty R, G H (1987) DRASTIC–a standardized system to evaluate groundwater pollution potential using hydrogeologic settings. US Environmental Protection Agency EPA/600/2–87/036, 622 p.

Almeida FFM (1977) O Cráton do São Francisco. Revista Brasileira de Geociências 7: 285-295.

Andreo B, Goldscheider N, Vadillo I, Vías JM, Neukum C, Sinreich M, Jiménez P, Brechenmacher J, Carrasco F, Hötzl H (2006) Karst groundwater protection: First application of a Pan-European Approach to vulnerability, hazard and risk mapping in the Sierra de Líbar (Southern Spain). Science of the Total Environment 357 (1): 54-73.

Arndt D, Bär K, Fritsche J-G, Sass I, Hoppe A (2011) 3D structural model of the Federal State of Hesse (Germany) for geopotential evaluation. Zeitschrift der Deutschen Gesellschaft für Geowissenschaften (ZDGG) 162 (4): 353-369.

Augustin CHRR, Aranha PRA (2006) A Ocorrência de Voçorocas em Gouveia, MG: características e processos associados. Geonomos 14 (1-2): 75-86.

Auler A (1994) Hydrogeological and Hydrochemical Characterization of the Matozinhos-Pedro Leopoldo Karst, Brazil. Master thesis. Western Kentucky University, 110 p.

Auler A (1998) Base-Level Changes Inferred from Cave Paleoflow Analysis in the Lagoa Santa Karst, Brazil. Journal of Cave and Karst Studies 60 (1): 58-62.

Bacellar LdAP, Coelho Netto AL, Lacerda WA (2005) Controlling factors of gullying in the Maracujá Catchment, southeastern Brazil. Earth Surface Processes and Landforms 30 (11): 1369-1385.

Bagnold RA (1966) An approach to the sediment transport problem from general physics Professional Paper, vol. 422 -1, 42 p. United States Geological Survey

Baltazar OF, Zucchetti M (2007) Lithofacies associations and structural evolution of the Archean Rio das Velhas greenstone belt, Quadrilátero Ferrífero, Brazil: A review of the setting of gold deposits. Ore Geology Reviews 32 (3–4): 471-499.

Bär K, Arndt D, Fritsche J-G, Götz AE, Kracht M, Hoppe A, Sass I (2011) 3D-Modellierung der tiefengeothermischen Potenziale von Hessen - Eingangsdaten und Potenzialausweisung. Zeitschrift der Deutschen Gesellschaft für Geowissenschaften (ZDGG) 162 (4): 371-388.

Barbosa O (1965) Série Bambuí. Simpósio das Formações Eo-Paleozóicas do Brasil. SBG, Congresso Brasileiro de Geologia, XIX Rio de Janeiro, Publicação avulsa, pp 1-15.

Begin Z, Schumm S (1979) Instability of alluvial valley floors: a method for its assessment. Transactions of the American Society of Agricultural Engineers 22 (2): 0347-0350.

Behrens T, Zhu A, Schmidt K, Scholten T (2010) Multi-scale digital terrain analysis and feature selection for digital soil mapping. Geoderma 155 (3): 175-185.

Behzadian M, Kazemzadeh RB, Albadvi A, Aghdasi M (2010) PROMETHEE: A comprehensive literature review on methodologies and applications. European Journal of Operational Research 200 (1): 198-215.

Berbert-Born MLC (2002) Carste de Lagoa Santa, MG - Berço da paleontologia e da espeleologia brasileira. In: Schobbenhaus C, Campos DA, Queiroz ET, Winge M, Berbert-Born MLC (eds) Sítios Geológicos e Paleontológicos do Brasil. , vol 1. DNPM/CPRM/SIGEP, Brasilia, pp 415-430.

Berking H, Löw M (2008) Die Eigenlogik der Städt. Neue Wege in der Stadtforschung. Interdisziplinäre Stadtforschung 1. Campus Verlag, Frankfurt am Main, 335 p.

Beven K, Kirkby M (1979) A physically based, variable contributing area model of basin hydrology/Un modèle à base physique de zone d'appel variable de l'hydrologie du bassin versant. Hydrological Sciences Journal 24 (1): 43-69.

Branco JJR, Costa MT (1961) Roteiro para a excursão Belo Horizonte-Brasilia. Instituto de Pesquisas Radioativas da Universidade Federal de Minas Gerais, Congresso Brasileiro de Geologia, XIV, Belo Horizonte, 15, pp 1-19.
Brandalise LA, Heineck CA (1999) Folha SE.23-Z-C-VI. Estado de Minas Gerais. Escala 1:100.000 Programa levantamentos geológicos básicos do Brasil. CPRM, Belo Horizonte
Brandt Meio Ambiente (2002) Plano de diretrizes de ação para a Bacia do Riberão da Mata. Belgo Mineira Bekaert / Copasa / Soeicom, Belo Horizonte, 82 p. unpublished report
Brans J-P, Vincke P, Mareschal B (1986) How to select and how to rank projects: The PROMETHEE method. European journal of operational research 24 (2): 228-238.
Braun OPG (1968) Contribuição à estratigrafia do Grupo Bambuí. SBG, Congresso Brasileiro de Geologia, XXII, Belo Horizonte, Anais, pp 166-166.
Büchi A, Pagung R (2008) Mapeamento geológico (1:25.000), neotectônica e georecursos da região de Vespasiano e São José da Lapa (MG). Belo Horizonte Minas Gerais. Graduation thesis. Instituto de Geociências Departamento de Geologia, Universidade Federal de Minas Gerais, 74 p.
Bückner C, Hoppe A (2012) Kartierte Städte - Main und Wiesbaden im Spannungsfeld von Naturraum und Vergesellschaftung. Interdisziplinäre Stadtforschung 13. Campus Verlag, Frankfurt am Main, 229 p.
Bui EN (2004) Soil survey as a knowledge system. Geoderma 120 (1–2): 17-26.
Burrough PA (1989) Fuzzy mathematical methods for soil survey and land evaluation. Journal of Soil Science 40 (3): 477-492.
Burrough PA, van Gaans PFM, Hootsmans R (1997) Continuous classification in soil survey: spatial correlation, confusion and boundaries. Geoderma 77 (2–4): 115-135.
Camargo MN, Klamte E, Kauffman JH (1987) Classificação de solos usada em levantamentos pedológicos no Brasil. Boletim informativo da Sociedade Brasileira de Ciência do Solo 12 (1): 11-13.
Campos JEG, Dardenne MA (1997) Origem e evolução tectônica da bacia sanfranciscana. Revista Brasileira de Geociências 27 (3): 283-294.
Chaves AdO (1996) Enxames de diques máficos Proterozóicos da porção meridional do cráton do São Francisco (MG, Brasil). Master thesis. Universidade Federal de Minas Gerais, Belo Horizonte, 99 p.
Coelho JM (2001) The mining of aggregates in the metropolitan region of São Paulo. International Institute for Environment and Development, IIEE, England, 11 p.
Coelho Netto AL (1999) Catastrophic landscape evolution in a humid region (SE Brazil): inheritances from tectonic, climatic and land use induced changes. Geogr. Fis. Dinam. Quat: 21-48.
Copasa (2009) Noticias: Obras trarão melhorias para o abastecimento de água http://www.copasa.com.br/cgi/cgilua.exe/sys/start.htm?infoid=1452&sid=129 (16.10.2012)
CPRM (1994a) Caracterização geomorfológica da região cárstica de Sete Lagoas-Lagoa Santa (MG). Série Projeto VIDA, Viabilidade Industrial e Defesa Ambiental. CPRM/CETEC, Belo Horizonte, 37 p.
CPRM (1994b) Caracterizacão pedológica. Informacoes Básicas para a Gestão Territorial: Região de Sete Lagoas – Lagoa Santa. Série Projeto VIDA, Viabilidade Industrial e Defesa Ambiental. CPRM/CETEC, Belo Horizonte, 37 p.
CPRM, CETEC (1994) Projeto VIDA. Viabilidade Industrial e Defesa Ambiental.
CPRM, IBAMA (1998) Apa Carste de Lagoa Santa Série Apa Carste de Lagoa Santa (CD)
Cúpula dos povos (2012) Final declaration of the people's summit "at Rio+20" for social and environmental justice in defence of the commons, against the commodification of life Rio de Janeiro, 20 p.
D'Arrigo HBP (1995) O Descolamento basal do Grupo Bambuí e o Alto de Sete Lagoas. Master thesis. Departamento de Geologiea, Escola de Minas, Universidade Federal de Ouro Preto, Ouro Preto, 89 p.
Dardenne MA (1978) Síntese sobre a estratigrafia do Grupo Bambuí no Brasil central. SBG, Congresso Brasileiro de Geologia, XXX, vol. 2, Recife, Anais, pp 597-610.

de Lima Cabral JA (1998) Zoneamento geotécnico e aptidão dos terrenos. Série APA Carste de Lagoa Santa - Meio físico., vol. I. CPRM/IBAMA, Belo Horizonte, 41 p.
de Lima Cabral JA, de Souza HA, Chapadeiro E (1998) Zoneamento ambiental da APA Carste de Lagoa Santa. Série APA Carste de Lagoa Santa, vol. I. CPRM/IBAMA, Belo Horizonte, 61 p.
de Souza HA, de Lima Cabral JA, Berbert-Born MLC, de Senna Horta LC, Dutra GM (1998) Mapa de Zoneamento Espeleológico da APA Carste de Lagoa Santa Série APA Carste de Lagoa Santa - Meio físico., vol. I. CPRM/IBAMA, Belo Horizonte, 21 p.
Derby OA (1880) Reconhecimento geológico do Vale do São Francisco. . In: Roberts WM (ed) Relatórion sóbre o exame do Rio São Francisco. Tipographia Nacional, Rio do Janeiro, pp 1-24.
Desmet PJJ, Poesen J, Govers G, Vandaele K (1999) Importance of slope gradient and contributing area for optimal prediction of the initiation and trajectory of ephemeral gullies. CATENA 37 (3–4): 377-392.
DNPM (2006) Anuário Mineral Brasileiro 2006 http://www.dnpm.gov.br/conteudo.asp?IDSecao=68&IDPagina=789 (04.04.2013)
Doerfliger N, Jeannin P-Y, Zwahlen F (1999) Water vulnerability assessment in karst environments: a new method of defining protection areas using a multi-attribute approach and GIS tools (EPIK method). Environmental Geology 39 (2): 165-176.
Dorr JVN (1969) Physiographic stratigraphic and structural development of the Quadrilátero Ferrífero, Minas Gerais, Brazil. DNPM/USGS, Washington Prof. Paper 641-A, 109 p.
Driessen P, Deckers J, Spaargaren O, Nachtergaele F (2000) Lecture notes on the major soils of the world. Food and Agriculture Organization (FAO) 94, 307 p.
DVGW (2006) Richtlinien für Trinkwasserschutzgebiete, I. Teil: Schutzgebiete für Grundwasser. In: Deutscher Verein des Gas und Wasserfaches e.V. (ed) Technische Regel, Arbeitsblatt W101, Bonn, 23 p.
Einsele G (2000) Sedimentary basins: evolution, facies, and sediment budget. Springerp.
Embrapa (1999) Sistema Brasileiro de classificação de solos. Empresa Brasileira de Pesquisa Agropecuária, Centro Nacional de Pesquisa de Solos, Brasília, 412 p.
Farida F (2010) Quantification of sediment volume from gully erosion into Lake Lagoa Santa, Brazil. Scientific training report. Institut für Angewandte Geowissenschaften, TU-Darmstadt, 23 p.
Fatheuer T (2011) Buen Vivir: A brief introduction to Latin America's new concepts for the good life and the rights of nature. Publication series on ecology 17. Heinrich-Böll-Stiftung, 36 p.
Garbrecht J, Martz LW (1997) The assignment of drainage direction over flat surfaces in raster digital elevation models. Journal of Hydrology 193: 204-213.
Goldscheider N (2002) Hydrogeology and vulnerability of karst systems – examples from the Northern Alps and Swabian Alb. PhD thesis. Fakultät für Bio- und Geowissenschaften, Universität Karlsruhe KIT, Karlsruhe, 236 p.
Goldscheider N (2005) Karst groundwater vulnerability mapping: application of a new method in the Swabian Alb, Germany. Hydrogeology Journal 13 (4): 555-564.
Goldscheider N, Klute M, Sturm S, Hötzl H (2000) The PI method–a GIS-based approach to mapping groundwater vulnerability with special consideration of karst aquifers. Zeitschrift für angewandte Geologie 46 (3): 157-166.
Gontijo I, Dias Junior MdS, Guimarães PTG, Araujo-Junior CF (2008) Atributos físico-hídricos de um latossolo de cerrado em diferentes posições de amostragem na lavoura cafeeira. Revista Brasileira de Ciência do Solo 32: 2227-2234.
Grohmann CH, Campanha GAC (2010) OpenStereo: open source, cross-platform software for structural geology analysis. Presented at the AGU 2010 Fall Meeting, San Francisco, CA.
GSI (1999) Groundwater Protection Schemes. Department of the Environmental and Local Government, Environmental Protection Agency and Geological Survey of Ireland, Dublin, 24 p.

Heineck CA (1999) Capitulo 4: Metalogenia / Geologia Econômica. . In: Brandalise LA, Heineck CA (eds) Programa levantamentos geológicos básicos do Brasil. Folha SE.23-Z-C-VI. Estado de Minas Gerais. Escala 1:100.000. CPRM, Brasília, 24 p.
Heineck CA, Silva Leite CA, da Silva MA, Vieira VS (2003) Mapa Geológico do Estado de Minas Gerais, 1 : 1 000 000. CPRM, Belo Horizonte
Henderson B, Bui E, Moran C, Simon D (2005) Australia-wide predictions of soil properties using decision trees. Geoderma 124 (3): 383-398.
Hermann G, Kohler HC, Duarte JC (1998) Estudo do meio biótico. Série APA Carste de Lagoa Santa, vol. I. CPRM/IBAMA, Belo Horizonte, 92 p.
Hintermaier-Erhard G, Zech W (1997) Wörterbuch der Bodenkunde. Ferdinand Enke Verlag Stuttgart, 338 p.
Hofmann M, Büchi A, Hoppe A, Hornung J, Karfunkel J, Pagung R (2009) Resources for a growing city sand extraction north of Belo Horizonte (Brazil). Neues Jahrbuch für Geologie und Paläontologie-Abhandlungen 253 (1): 61-78.
Hofmann M, Hoppe A, Karfunkel J, Büchi A (2013) Regionalizing hydrological soil properties in the Brazilian Cerrad region usins a Semantic Import Model Approach. Catchments: classification, modelling and environmental assessment. Nova Publisers, New York
Hölting B, Haertle T, Hohberger KH, Eckl H, Hahn J, Koldehoff C (1995) Konzept zur Ermittlung der Schutzfunktion der Grundwasserüberdeckung. Geologisches Jahrbuch Reihe C, vol C63. Schweizerbart'sche Verlagsbuchhandlung, Stuttgart, p 65.
Hoppe A (2011) Geowissenschaften und die Eigenlogik der Städt. In: Hoppe A (ed) Raum und Zeit der Städte, Städtische Eigenlogik und jüdische Kultur seit der Antike, vol 12. Campus Verlag, Frankfurt am Main, pp 25-46.
Hoppe A, Janicka J, Lerch C, Brübach J (2008) Geothermal resources in the shallow, unsaturated zone of the Wiesbaden spa district, Germany. Geothermics 37 (2): 173-188.
Hoppe A, Karfunkel J, Noce CM (2002) Sitio Inhaúma, MG - Camadas aragoniticas pré-cambrianas. . In: Schobbenhaus C, Campos DA, Queiroz ET, Winge M, Berbert-Born MLC (eds) Sítios Geológicos e Paleontológicos do Brasil. , vol 1. DNPM/CPRM/SIGEP, Brasilia, pp 175-180.
Hoppe A, Lang S, Lerch C, Marinoni O (2006) Geology and a spatial decision support system for the surroundings of urban areas: An example from southern Hesse (Germany). Zeitschrift der Deutschen Gesellschaft für Geowissenschaften 157 (1): 135-145.
Hoppe A, Mittelbach G (eds) (1999) Geowissenschaftlicher Atlas von Hessen. Mit Beiträgen von H. Abel, G. Aderhold, W. Barth, R. Blum, K. Friedrich, H. Heggemann, M. Hemfler, M. Hoffmann, T. Kirnbauer, W. Liedmann, U. Mattig, M. Peter, W. Pöschl, F. Rosenberg, K.-A. Sabel, A.-K. Theuerjahr, T. Vorderbrügge. Hessisches Landesamt für Bodenforschung, Wiesbaden, 61 p.
Hoppe A, Schobbenhaus C, Walde DHG (1987) Precambrian iron formations in Brazil. In: Appel P, La Berge G (eds) The Precambrian iron formations. Teophrastus, Athens, pp 347-390.
Horta LCdS, Berbert-Born MLC, Dutra GM (1998) Patrimônio espeleológico historic e cultural. Série APA Carste de Lagoa Santa,, vol. III. CRPM / IBAMA, 198 p.
Horton RE (1933) The role of infiltration in the hydrologic cycle. Transactions, American Geophysical Union 14: 446-460.
Hudson BD (1992) The soil survey as paradigm-based science. Soil Science Society of America Journal 56 (3): 836-841.
Hundecha Y, Bárdossy A (2004) Modeling of the effect of land use changes on the runoff generation of a river basin through parameter regionalization of a watershed model. Journal of Hydrology 292 (1): 281-295.
Hutchinson MF (1989) A new procedure for gridding elevation and stream line data with automatic removal of spurious pits. Journal of Hydrology 106 (3–4): 211-232.
IBGE (2006) Estimativas de População: Estimativas para 1º de Julho de 2006. Instituto Brasileiro de Geografia e Estatística http://www.ibge.gov.br/home/estatistica/populacao/estimativa2006/estimativa.shtm (15.08.2007)

IBGE (2010) Censo Populacional 2010. Instituto Brasileiro de Geografia e Estatística http://www.ibge.gov.br/home/estatistica/populacao/censo2010/ (11.10.2012)
IGA (1982) Folha Lagoa Santa. Mapeamento Geológico da Região Metropolitana de Belo Horizonte. Instituto de Geociências Aplicadas, Belo Horizonte, MG p.
IUSS Working Group (2007) World Reference Base for Soil Resources 2006, first update 2007. World Soil Resources Reports No. 103. FAO, Rome, 128 p.
Janikow CZ (1998) Fuzzy decision trees: issues and methods. Systems, Man, and Cybernetics, Part B: Cybernetics, IEEE Transactions on 28 (1): 1-14.
Johnson DL, Domier JEJ, Johnson DN (2005) Animating the biodynamics of soil thickness using process vector analysis: a dynamic denudation approach to soil formation. Geomorphology 67 (1–2): 23-46.
Karfunkel J (2013) Geologische Kartierung in Gebieten mit tropischem Klima: Fallstudie Kimberlite aus W Minas Gerais, Brasilien. . Der Aufschluß 64 (1): 1-9.
Karfunkel J, Aranha PRA, Büchi A, Pimenta F, Pagung R, Silva Pinto JA, Hofmann M, Hoppe A (2006) Registros neotectônicos entre Vespasiano e Pedro Leopoldo ão norte de Belo Horizonte, Minas Gerais. SBG, Congresso Brasileiro de Geologia, XLII Aracaju, Anais, p 292.
Karfunkel J, Hoppe A (1988) Late Proterozoic glaciation in central-eastern Brazil: Synthesis and model. Palaeogeography, Palaeoclimatology, Palaeoecology 65 (1–2): 1-21.
Karfunkel J, Noce CM, Hoppe A (2002) Serra da Água Fria e Vizinhanças, MG – Vestígios de glaciação neoproterozóica. In: Schobbenhaus C, Campos DA, Queiroz ET, Winge M, Berbert-Born MLC (eds) Sítios Geológicos e Paleontológicos do Brasil. , vol 1. DNPM/CPRM/SIGEP, Brasilia, pp 415-430.
King LC (1956) A geomorfologia do Brasil Oriental. Revista Brasileira de Geografia 18: 186-263.
Kohler HC (1989) Geomorfologia Cárstica na região de Lagoa Santa, MG PhD thesis. Universidade de São Paulo, São Paulo, 113 p.
Kohler HC, Karfunkel J (2002) The quartenary morphogenesis of the Lagoa Santa tropical karst, Minas Gerais State, SE Brazil. Theoretical and Applied Karstology 15: 93-99.
Kohler HC, Parizzi MG, de Souza HA, Carvalho de Castro VH (1998) Mapa Geomorfológico Série APA Carste de Lagoa Santa - Meio físico., vol. I. CPRM/IBAMA, Belo Horizonte, 21 p.
Lacerda WA (2007) Landslide initiation in saprolite and colluvium in southern Brazil: Field and laboratory observations. Geomorphology 87 (3): 104-119.
Lagoa Santa - revista virtual da cidade (2006) Solução para o Problema de Água de Lagoa Santa. http://www.lagoasanta.com.br/prestadoras_servicos/solucao_para_o_problema_de_agua_.htm (16.10.2012)
Lamelas MT, Hoppe A, de la Riva J, Marinoni O (2009) Modelling environmental variables for geohazards and georesources assessment to support sustainable land-use decisions in Zaragoza (Spain). Geomorphology 111 (1–2): 88-103.
Lamelas MT, Marinoni O, Hoppe A, Riva J (2007) Groundwater vulnerability map for the Ebro alluvial aquifer between Jalón and Ginel tributaries (Spain). Environmental Geology 53 (4): 861-878.
Lamelas MT, Marinoni O, Hoppe A, Riva J (2008a) Doline probability map using logistic regression and GIS technology in the central Ebro Basin (Spain). Environmental Geology 54 (5): 963-977.
Lamelas MT, Marinoni O, Hoppe A, Riva J (2008b) Suitability analysis for sand and gravel extraction site location in the context of a sustainable development in the surroundings of Zaragoza (Spain). Environmental Geology 55 (8): 1673-1686.
Lamelas MT, Marinoni O, Hoppe A, Riva J (2010) Sustainable decision making in a complex 3D environment of an urban area: design of an auditable decision process based multi-criteria analysis. In: H. SM, Clark PD (eds) Geomorphology: Processes, Taxonomy and Applications. Nova Science Publisher, New York, pp 1-44.

Lamelas MT, Marinoni O, Hoppe A, Riva J (2012) Comparison of Multicriteria Analysis Techniques for Environmental Decision Making on Industrial Location. In: Jao EC (ed) Decision Support Systems. InTech Publisher, Rijeka, Croatia, pp 197-222.
Léonard J, Richard G (2004) Estimation of runoff critical shear stress for soil erosion from soil shear strength. CATENA 57 (3): 233-249.
Lerch C (2005) Methoden zur GIS-gestützten Erzeugung von Geo-Ressourcen und Geo-Risikokarten für eine nachhaltige Landnutzungsplanung am Beispiel der Hanau-Seligenstädter Senke, südliches Rhein-Main Gebiet PhD thesis. Fachbereich Material- und Geowissenschaften, Technische Universität Darmstadt, Darmstadt, 146 p.
Lerch C, Hoppe A (2007) Erstellung eines geologischen 3D-Modells zur verbesserten Berechnung der Schutzfunktion der Grundwasserüberdeckung. Grundwasser 12: 144-153.
Lesquer A, De Almeida FFM, Davino A, Lachaud JC, Maillard P (1981) Signification structurale des anomalies gravimetriques de la partie sud du craton de Sao Francisco (Bresil). Tectonophysics 76 (3–4): 273-293.
Lorenz W, Gwosdz W (2002) Bewertungskriterien für Industrieminerale, Steine und Erden. Teil 5: Gesteinskörnungen Kies, Sand und gebrochener Naturstein. Geologisches Jahrbuch Reihe H. Schweizerbart'sche, Hannover, 247 p.
Lund PW (1835) Memórias científicas, Transl. Damásio L, Biblioteca Mineira de Cultura, Belo Horizonte.

Magiera P (2000) Methoden zur Abschätzung der Verschmutzungsempfindlichkeit des Grundwassers. Grundwasser 5 (3): 103-114.
Malczewski J (1999) Spatial multicriteria decision analysis. In: Thill JC (ed) Spatial Multicriteria Decision Making and Analysisi - A Geographic Information Sciences Approach. Ashgate, New York, pp 11-48.
Marinoni O (2004) Implementation of the analytical hierarchy process with VBA in ArcGIS. Computers & Geosciences 30 (6): 637-646.
Marinoni O (2005) A stochastic spatial decision support system based on PROMETHEE. International Journal of Geographical Information Science 19 (1): 51-68.
Marinoni O, Hoppe A (2006) Using the analytical hierarchy process to support sustainable use of geo-resources in metropolitan areas. Journal of Systems Science and Systems Engineering 15 (2): 154-164.
Martins-Neto MA (2007) Proterozoic first-order sedimentary successions of the Sao Francisco Basin in eastern Brazil. Zeitschrift der Deutschen Gesellschaft für Geowissenschaften 158 (1): 31-43.
Martins-Neto MA, Alkmim FF (2001) Estratigrafia e evolução tectônica das bacias Neoproterozóicas do paleocontinente São Francisco e suas margens: Registro da quebra de Rodínia e colagem de Gondwana. In: Martins-Neto MA, Pinto CP (eds) A Bacia do São Francisco – Geologia e Recursos Naturais. SBG/MG, Belo Horizonte, pp 31-54.
Martins-Neto MA, Pedrosa-Soares AC, Lima SAA (2001) Tectono-sedimentary evolution of sedimentary basins from Late Paleoproterozoic to Late Neoproterozoic in the São Francisco craton and Araçuaí fold belt, eastern Brazil. Sedimentary Geology 141: 343-370.
Mathias Kondolf G (1994) Geomorphic and environmental effects of instream gravel mining. Landscape and Urban Planning 28 (2): 225-243.
McBratney AB, De Gruijter JJ, Brus DJ (1992) Spacial prediction and mapping of continuous soil classes. Geoderma 54 (1): 39-64.
McBratney AB, Odeh IOA (1997) Application of fuzzy sets in soil science: fuzzy logic, fuzzy measurements and fuzzy decisions. Geoderma 77 (2): 85-113.
McBratney AB, Odeh IOA, Bishop TFA, Dunbar MS, Shatar TM (2000) An overview of pedometric techniques for use in soil survey. Geoderma 97 (3–4): 293-327.
Mendonça AF, Pires ACB, Barros JGC (1994) Pseudosinkhole occurrences in Brasilia, Brazil. Environmental Geology 23 (1): 36-40.

Mescherikov Y (1968) Neotectonics. In: Fairbridge R (ed) Encyclopedia of earth sciences series, 111, Encyclopedia of geomorphology. Reinhold, New York, Amsterdam, London pp 768-773.
Montgomery DR (1994) Road surface drainage, channel initiation, and slope instability. Water Resources Research 30 (6): 1925-1932.
Montgomery DR, Dietrich WE (1988) Where do channels begin? Nature 336 (6196): 232-234.
Montgomery DR, Dietrich WE (1994) Landscape dissection and drainage area-slope thresholds. In: Kirkby M (ed) Process Models and Theoretical Geomorphology. John Wiley & Sons, Chichester, pp 221-246.
Moore I, Gessler P, Nielsen GAe, Peterson G (1993) Soil attribute prediction using terrain analysis. Soil Science Society of America Journal 57 (2): 443-452.
Morgan RPC (2009) Soil erosion and conservation, 3rd Edition. Wiley-Blackwell, 316 p.
Mörner NA (1978) The INQUA Neotectonics Commission. . Geologiska Föreningen i Stockholm Förhandlingar 100 (3): 286.
Muggler CC, Buurman P (2000) Erosion, sedimentation and pedogenesis in a polygenetic oxisol sequence in Minas Gerais, Brazil. CATENA 41 (1–3): 3-17.
Nguyet VTM, Goldscheider N (2006) A simplified methodology for mapping groundwater vulnerability and contamination risk, and its first application in a tropical karst area, Vietnam. Hydrogeology Journal 14 (8): 1666-1675.
Ortu JC (1990) Modelagem tectono-geofísica da porção sul de Minas Gerais. Master thesis. Departamento de Geologia, Escola de Minas, Universidade Federal de Ouro Preto, Ouro Preto, 194 p.
Padmalal D, Maya K, Sreebha S, Sreeja R (2008) Environmental effects of river sand mining: a case from the river catchments of Vembanad lake, Southwest coast of India. Environmental Geology 54 (4): 879-889.
Pagung R, Pimenta F, Karfunkel J, Aranha PRA, Büchi A, Hofmann M, Hoppe A (2007) Investigação de feições neotectônicas em Vespasiano – MG utilizando o georadar (GPR). SBG/MG, Simpósio de geologia do Sudeste, X, Diamantina, p 105.
Parizzi MG, Salgado-Labouriau ML, Kohler HC (1998) Genesis and environmental history of Lagoa Santa, southeastern Brazil. The Holocene 8 (3): 311-321.
Patrus MLRA (1998) Estudos Hidrológicos e Qualidade das Águas de Superfície. Série APA Carste de Lagoa Santa - Meio físico., vol. I. CPRM/IBAMA, Belo Horizonte, 21 p.
Patton PC, Schumm SA (1975) Gully Erosion, Northwestern Colorado: A Threshold Phenomenon. Geology 3 (2): 88-90.
Peel MC, Finlayson BL, McMahon TA (2007) Updated world map of the Köppen-Geiger climate classification. Hydrology and Earth System Sciences Discussions 4 (2): 439-473.
Penha UC, Karfunkel J, Angeli N (2005) Diamondiferous deposits in the Jequitai area (Minas Gerais, Brazil): a consequence of neotectonic processes. N. Jb. Geol. Palaont. Abh. 236 (112): 207-224.
Peryt TM, Hoppe A, Bechstädt T, Köster J, Pierre C, Richter DK (1990) Late Proterozoic aragonitic cement crusts, Bambuí Group, Minas Gerais, Brazil. Sedimentology 37 (2): 279-286.
Pessoa PFP (1998) Mapa de vulnerabilidade natural dos aquíferos da APA Carste de Lagoa Santa – MG. Série APA Carste de Lagoa Santa - Meio físico. CPRM/IBAMA, Belo Horizonte.
Pessoa PFP (2005) Hidrogeologia dos aqüíferos cársticos cobertos de Lagoa Santa, MG PhD thesis. Escolha de Engenharia, UFMG, Belo Horizonte, 575 p.
Pessoa PFP, Mourão MAA (1998) Levantamento hidrogeológico. Série APA Carste de Lagoa Santa - Meio físico, vol. I. CPRM/IBAMA, Belo Horizonte., 58 p.
Piló LB (1998) Morfologia cárstica e materiais constituintes: Dinâmica e evolução da Depressão Poligonal Macacos-Baú - Carste de Lagoa Santa, Minas Gerais. PhD thesis. Departamento de Geografia da Faculdade de Filosofia, Letras e Ciências Humanas, Universidade de São Paulo, São Paulo, 269 p.
Poesen J, Nachtergaele J, Verstraeten G, Valentin C (2003) Gully erosion and environmental change: importance and research needs. CATENA 50 (2–4): 91-133.

Poulin R, Pakalnis R, Sinding K (1994) Aggregate resources: Production and environmental constraints. Environmental Geology 23 (3): 221-227.
Qi F, Zhu A, Harrower M, Burt JE (2006) Fuzzy soil mapping based on prototype category theory. Geoderma 136 (3): 774-787.
Rangel AdS (1997) A exploracao de areia na RMSP. In: Garcia F, Farina EMMQ, Alves MC (eds) Padrão de concorrência e competitividade da indústria de materiais de construção, São Paulo pp 89-102 p.
Ribeiro JH, Tuller MP, Filho AD, Padilha AV, Córdoba CV (2003) Projeto VIDA: mapeamento geológico, região de Sete Lagoas, Pedro Lepoldo, Matozinhos, Lagoa Santa, Vespasiano, Capim Branco, Prudente de Morais, Confins e Funilândia, Minas Gerais - relatório final, mapas e anexos, escala 1:50.000. Série Programa Informações Básicas para Gestão Territorial – GATE, versão digital e convenção. CPRM, Belo Horioznte, 54 p.
Rimann E (1917) A Kimberlita no Brasil. Anais de Escola de Minas, Ouro Preto 15: 27-32.
Rinaldi M, Wyżga B, Surian N (2005) Sediment mining in alluvial channels: physical effects and management perspectives. River Research and Applications 21 (7): 805-828.
Rosch EH (1973) Natural categories. Cognitive psychology 4 (3): 328-350.
Rosch EH (1978) Principles of categorization. In: Rosch E, Lloyd BB (eds) Cognition and categorization. Hillsdale, New Jersey
Saaty TL (1977) A scaling method for priorities in hierarchical structures. Journal of Mathematical Psychology 15 (3): 234-281.
Saaty TL (2003) Decision-making with the AHP: Why is the principal eigenvector necessary. European journal of operational research 145 (1): 85-91.
Salgado-Labouriau ML, Barberi M, Ferraz-Vicentini KR, Parizzi MG (1998) A dry climatic event during the late Quaternary of tropical Brazil. Review of Palaeobotany and Palynology 99 (2): 115-129.
Santos Viana H, Kohler HC, Pinho Tavaresi V (1998) Síntese da geologica, recursos minerais e gemorfologia Série APA Carste de Lagoa Santa - Meio físico., vol. I. CPRM/IBAMA, Belo Horizonte, 21 p.
Saunders W (2000) Preparation of DEMs for use in environmental modeling analysis. Hydrologic and hydraulic modeling support with geographic information systems. ESRI Press, New York: 29-52.
Schmidt F (2003) Vulnerabilitätskartierung für den Trinkwasserschutz im Karst—Anwendungsbeispiel Veldensteiner Mulde. Grundwasser 8 (2): 103-112.
Schmidt HL (1972) Fazieswechsel in der Sao Francisco-Serie (Bambuí) bei Bocaiuva, Espinhaco-Zone, Minas Gerais, Brasilien. Zur Geologie von Nordost-Brasilien und Minas Gerais, Geologisches Jahrbuch. Beihefte : 121: 59-94.
Schöll WU (1972) Der südwestliche Randbereich der Espinhaço-Zone, Minas Gerais, Brasilien. Geologische Rundschau 61 (1): 201-216.
Schöll WU (1973) Sedimentologie der Bambuí-Gruppe im SE-Teil des São Francisco Beckens (Minas Gerais, Brasilien). Münster. Forsch. Geol. Paläont. 31/32: 71-91.
Shi X, Long R, Dekett R, Philippe J (2009) Integrating different types of knowledge for digital soil mapping. Soil Science Society of America Journal 73 (5): 1682-1692.
Shi X, Zhu A, Burt JE, Qi F, Simonson D (2004) A case-based reasoning approach to fuzzy soil mapping. Soil Science Society of America Journal 68 (3): 885-894.
Shinzato E, Lumbreras F (1998) Caracterização pedológica e mapa semidetalhado de solos da APA Carste de Lagoa Santa – MG Série APA Carste de Lagoa Santa - Meio físico. CPRM/IBAMA, Belo Horizonte.
Tarboton DG (1997) A new method for the determination of flow directions and upslope areas in grid digital elevation models. Water resources research 33 (2): 309-319.
Tarboton DG (2005) Terrain analysis using digital elevation models (TauDEM). Utah Water:
Teixeira W, Sabaté P, Barbosa J, Noce CM, Carneiro MA (2000) Archean and Paleoproterozoic tectonic evolution of the São Francisco Craton. In: Cordani UG, Milani EJ, Thomaz FA, Campos DA (eds) Tectonic evolution of South America, Rio de Janeiro, pp 101-137.
Terpodei VV (1999) Natural Aggregates - Foundation of America's Future. USGS Fact Sheet FS 144-97: 4.

Thapa P, Hoppe A (2010) Landslide hazard prediction modelling in the central Nepal Himalaya GeoDarmstadt2010, vol. 68. Schriftenr. Dt. Ges. Geowiss, pp 550-552.
Thornthwaite CW, Mather JR (1955) The water balance. Publications in Climatology 8. Drexel Institute of Technology Centerton, NJ, USA, 104 p.
Torri D, Borselli L (2003) Equation for high-rate gully erosion. Catena 50 (2): 449-467.
Tsoukalas LH, Uhrig RE (1996) Fuzzy and neural approaches in engineering. John Wiley & Sons, Inc., New York, 587 p.
Tuller MP, Ribeiro JH, Danderfer Filho A (1991) Geologia da região cárstica de Sete Lagoas-Lagoa Santa (MG) Projeto Vida - Programa Gestão e Administração Territorial. CRPM, Belo Horizonte p.
Uhlein GJ, de Carvalho JFMG, Uhlein A, Caxito FdA, Halverson GP, Sial AN (2012) Estratigrafia e sedimentologia da Formação Carrancas, Grupo Bambuí, nas regiões de Belo Horizonte e Pitangui, MG. Geonomos 20 (2): 79 - 97.
United Nations (1987) Our common future: Report of the World Commission on Environment and Development, 247 p. Nations U
United Nations (2002) World Urbanizations Prospects. The 2011 Revision, Data Tables and Highlights. UN, New York, 50 p.
United Nations (2011) Urban population, development and the Environment 2011 - Wall paper. Department of Economic and Social Affairs, New York, 2 p.
USDA (2004) Chapter 6. Hydrologic soil–cover complexes. National Engineering Handbook, Part 630 Hydrology, 20 p.
USDA (2010) Soil properties and qualities. National Soil Survey Handbook, Part 618, 140 p.
v. Eschwege WL (1832) Beiträge zur Gebirgskunde Brasiliens. . Reimer, Berlin, 488 p.
v. Freiberg B (1932) Ergebnisse geologischer Forschungen in Minas Geraes (Brasilien). N. Jb. Min. Geol. Paläont., Sonderb. 2, 401 p.
Valentin C, Poesen J, Li Y (2005) Gully erosion: Impacts, factors and control. Catena 63 (2–3): 132-153.
Valverde FM (2001) Agregados para construção civil. Balanço Mineral Brasileiro 2001. DNPM, Brasília, 15 p.
Valverde FM (2005) Agregados para construção civil. Sumário Mineral Brasileiro 2005. DNPM, Brasília, pp 25-25 p.
Vandaele K, Poesen J, Govers G, Wesemael Bv (1996) Geomorphic threshold conditions for ephemeral gully incision. Geomorphology 16 (2): 161-173.
Vandekerckhove L, Poesen J, Oostwoud Wijdenes D, Nachtergaele J, Kosmas C, Roxo MJ, de Figueiredo T (2000) Thresholds for gully initiation and sedimentation in Mediterranean Europe. Earth Surface Processes and Landforms 25 (11): 1201-1220.
Vieira LC (2007) A Formação Sete Lagoas (Grupo Bambuí) e as variações paleoambientais no final do Proterozóico. PhD thesis. Instituto de Astronomia, Geofísica e Ciências Atmosféricas, Universidade de São Paulo, São Paulo, 198 p.
Vieira LC, Almeida RP, Trindade RIF, Nogueira ACR, Janikian L (2007a) A Formação Sete Lagoas em sua área-tipo: fácies, estratigrafia e sistemas deposicionais. Revista Brasileira de Geociências 37 (4 - supplemento): 1-14.
Vieira LC, Trindade RIF, Nogueira ACR, Ader M (2007b) Identification of a Sturtian cap carbonate in the Neoproterozoic Sete Lagoas carbonate platform, Bambuí Group, Brazil. Comptes Rendus Geoscience 339 (3–4): 240-258.
Vrba J, Zaporozec A (eds) (1994) Guidebook on mapping groundwater vulnerability. International Contributions to Hydrogeology, Hannover, 131 p.
Weibel R, Keller S, Reichenbacher T (1995) Overcoming the knowledge acquisition bottleneck in map generalization: the role of interactive systems and computational intelligence. In: Frank A, Kuhn W (eds) Spatial Information Theory: A Theoretical Basis for GIS. Springer, London, pp 139-156.
Weiss A (2001) Topographic Position and Landforms Analysis, Poster presentation ESRI User Conference, San Diego, CA.
Wellmer FW, Becker-Platen JD (1999) Mit der Erde leben: Beiträge geologischer Dienste zur Daseinsvorsorge und nachhaltigen Entwicklung. Springer-Verlag, 273 p.

Wolfe BB, Aravena R, Abbott MB, Seltzer GO, Gibson JJ (2001) Reconstruction of paleohydrology and paleohumidity from oxygen isotope records in the Bolivian Andes. Palaeogeography, Palaeoclimatology, Palaeoecology 176 (1): 177-192.
Wu L, Pan L, Roberson M, Shouse P (1997) Numerical evaluation of ring-infiltrometers under various soil conditions. Soil science 162 (11): 771-777.
Zech W, Hintermaier-Erhard G (2002) Böden der Welt - ein Bildatlas. Spektrum Akademischer Verlag, Heidelberg, Berlin, 120 p.
Zevenbergen LW, Thorne CR (2006) Quantitative analysis of land surface topography. Earth surface processes and landforms 12 (1): 47-56.
Zhu A-X (1999) A personal construct-based knowledge acquisition process for natural resource mapping. International Journal of Geographical Information Science 13 (2): 119-141.
Zhu A, Yang L, Li B, Qin C, Pei T, Liu B (2010) Construction of membership functions for predictive soil mapping under fuzzy logic. Geoderma 155 (3): 164-174.
Zwahlen F (ed) (2004) Vulnerability and risk mapping for the protection of carbonate (karst) aquifers, Final report COST Action 620, EUR 20912. 7 European Commission, Directorate-General XII Science, Research and Development, Brussels, 297 p.

Curriculum Vitae

Persönliche Daten:

Name:	Monika Hofmann
Geboren:	01.11.1977 in Aschaffenburg

Schulische und universitäre Ausbildung:

1988 – 1997:	Spessart-Gymnasium Alzenau
1997 – 1998:	Studium der Physik an der Universität Leipzig (ohne Abschluss)
1998 - 2004:	Studium der Geoökologie an der Universität Bayreuth, Abschluss mit Diplom
2004 – 2013:	(mit zweimaliger Unterbrechung durch Elternzeit): Wissenschaftliche Mitarbeiterin und Doktorandin am Institut für Angewandte Geowissenschaften der TU-Darmstadt

Erklärung

Hiermit versichere ich an Eides statt, dass ich die vorliegende Arbeit selbstständig und ohne Benutzung anderer als der angegebenen Hilfsmittel angefertigt habe.
Stellen, die wörtlich oder sinngemäß aus anderen Schriften entnommen sind, sind als solche kenntlich gemacht. Die Arbeit ist in gleicher oder ähnlicher Form noch nicht als Prüfungsarbeit eingereicht worden.

Darmstadt, den _____

Annex I: List of all variables and their dependency

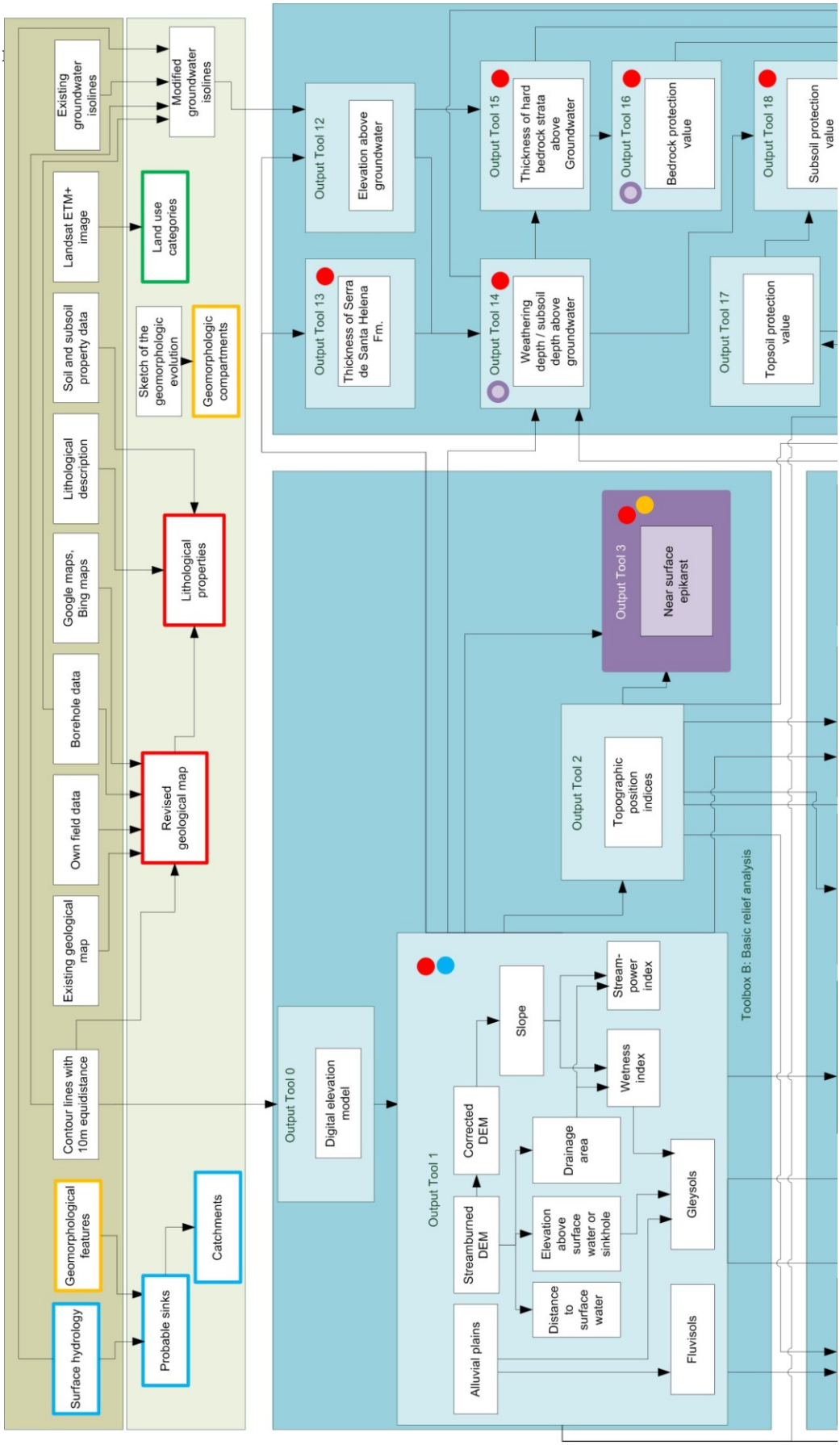

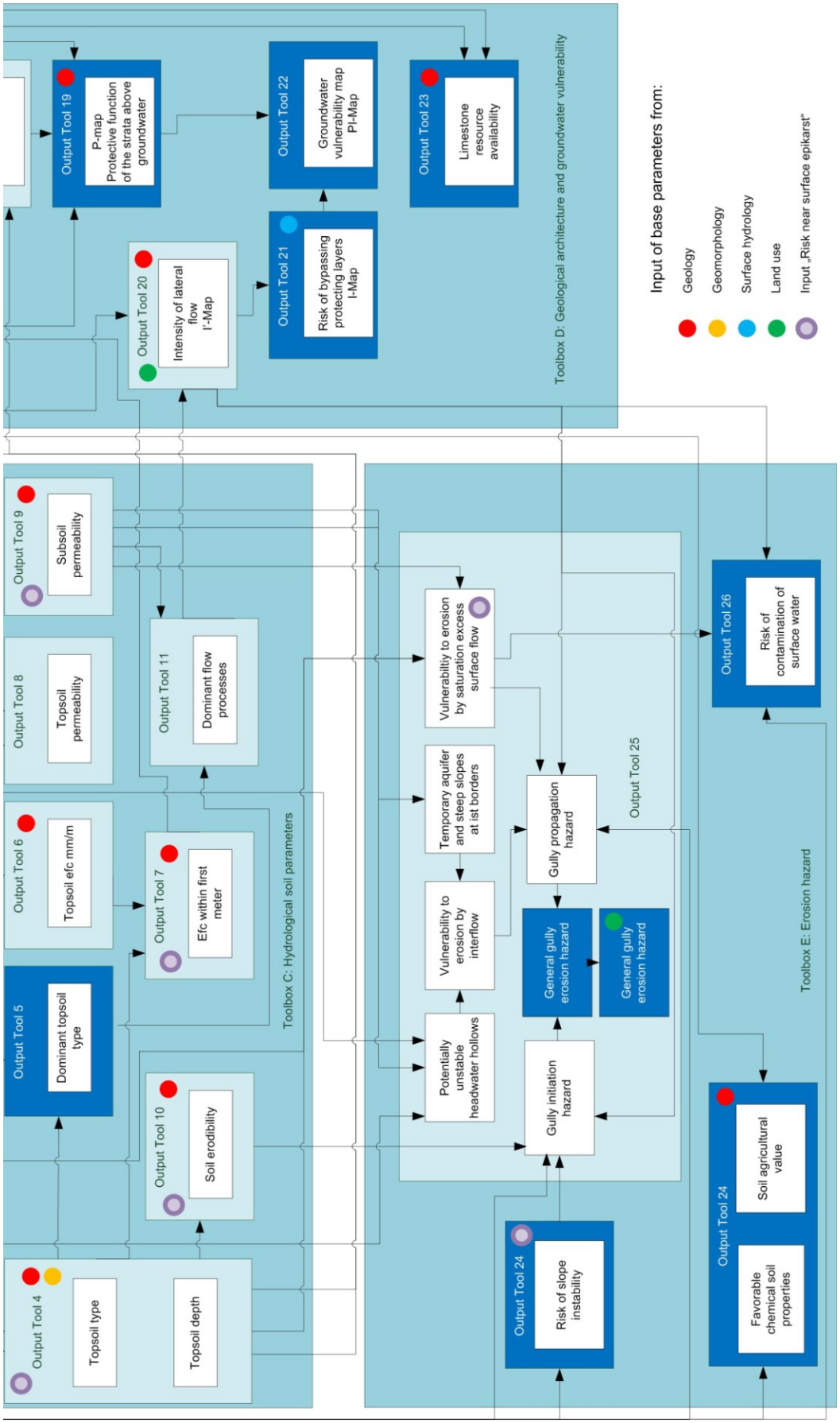
Toolbox D: Geological architecture and groundwater vulnerability
Output Tool 19
P-map
Protective function of the strata above groundwater
Output Tool 20
Intensity of lateral flow
I'-Map
Output Tool 21
Risk of bypassing protecting layers
I-Map
Output Tool 22
Groundwater vulnerability map
PI-Map
Output Tool 23
Limestone resource availability
Input of base parameters from:
Geology
Geomorphology
Surface hydrology
Land use
Input „Risk near surface epikarst"
Toolbox C: Hydrological soil parameters
Output Tool 4
Topsoil type
Topsoil depth
Output Tool 5
Dominant topsoil type
Output Tool 6
Topsoil efc mm/m
Output Tool 7
Efc within first meter
Output Tool 8
Topsoil permeability
Output Tool 9
Subsoil permeability
Output Tool 10
Soil erodibility
Output Tool 11
Dominant flow processes
Toolbox E: Erosion hazard
Output Tool 24
Risk of slope instability
Potentially unstable headwater hollows
Vulnerability to erosion by interflow
Temporary aquifer and steep slopes at ist borders
Vulnerabilitiy to erosion by saturation excess surface flow
Gully initiation hazard
Gully propagation hazard
General gully erosion hazard
General gully erosion hazard
Output Tool 25
Output Tool 26
Risk of contamination of surface water
Output Tool 24
Favorable chemical soil properties
Soil agricultural value

Data type	Data name (Normal: absolute values, *italics: optimality values)*	INPUT for Tool 0	1	2	3	4	5	6	7	8	9	10	11	12	13	14	15	16	17	18	19	20	21	22	23	24	25	26	27	**frequency of use as direct input**
Vector	Mask	x												x																**2**
Vector	Contour lines: Elevation	x																												**1**
Vector	Rivers		x																											**1**
Vector	Water bodies		x																											**1**
Vector	Location of probable sinks		x																											**1**
Vector	Rivers buffer					x																								**1**
Vector	Surface catchment: draining into karst																						x							**1**
Vector	Karst features from Kohler (1998)				x																									**1**
Vector	Geomorphological compartments: ID = 4					x																								**1**
Vector	Groundwater isolines													x																**1**
Vector	Drill hole data from Pessoa (2005): Subsoil base elevation														x															**1**
Vector	Basement ramp: *contour*																x													**1**
Vector	Basement exclude from interpolation																x													**1**
Geology vector	*GW influence*					x																								**1**
	Karstification				x																								x	**2**
	efc topsoil class							x																						**1**
	efc subsoil								x																					**1**
	subsoil permeability										x																			**1**
	subsoil erodibility												x																	**1**
	Minimum subsoil depth														x															**1**
	Outline SSH														x															**1**
	Maxdepth															x														**1**
	Sigla																x													**1**
	ID_new																x													**1**
	Bedrock L value																	x												**1**
	Bedrock F value																	x												**1**
	Subsoil S value																			x										**1**
	Resource quality																								x					**1**
	Base saturation																												x	**1**
Table	Remap																					x								**1**
Raster base data	Landsat 7 2002 classified																					x					x			**2**
Parameter	*Gleysol optimality value for alluvial plains*		x																											**1**
Parameter	Estimated GW depth in alluvial plains													x																**1**
Parameter	R value (Rainfall for GW vulnerability estimation)																				x									**1**
Parameter	b (exponent for topographic threshold)																										x			**1**

Figure Annex I - 2 List of input- / output data of the tools stored in the ArcGIS toolbox. White: base data from other sources. Light green: newly generated base data. Light blue: inferred parameters for geological units (see also section 8.3).

Data type	Data name (Normal: absolute values, *italics: optimality values)*	INPUT for Tool 0	1	2	3	4	5	6	7	8	9	10	11	12	13	14	15	16	17	18	19	20	21	22	23	24	25	26	27	**frequency of use as direct input**
Output Tool 0	DEM raw		x																											**1**
Output Tool 1	DEM corrected		x	x										x	x	x	x													**6**
	Hillshade																													**0**
	Slope degree		x																											**1**
	Slope m/m		x																			x					x			**3**
	Very steep slope				x																					x				**2**
	Flat slope					x										x											x		x	**4**
	Very flat slope																												x	**1**
	Completely flat slope					x																					x			**2**
	Flow direction D8		x																											**1**
	Flow direction Dinf		x																								x			**2**
	Continous streams raster					x																								**1**
	Elevation above surface water or sinkhole		x																											**1**
	Distance to surface water or sinkhole		x			x																								**2**
	Contributing area per unit contour length		x																											**1**
	Wetness index		x																											**1**
	Stream power		x																											**1**
	Fluvisols		x			x	x																							**3**
	High flow accumulation																													**0**
	Medium to high wetness index																										x			**1**
	High wetness index		x																											**1**
	Low above rivers, lakes or sinkholes		x			x				x																	x			**4**
	Riverbed buffer zone				x																						x			**2**
	Close to rivers, lakes or sinkholes																											x		**1**
	High stream power along river		x		x																								x	**3**
	High stream power no river																													**0**
Output Tool 2	LTPI original			x																										**1**
	MTPI original			x																										**1**
	RTPI original			x																										**1**
	Low LTPI							x																			x			**2**
	Concave LTPI																													**0**
	Convex LTPI				x	x																					x			**3**
	Low MTPI					x		x		x																			x	**4**
	Concave MTPI																													**0**
	Convex MTPI					x																								**1**
	Low RTPI					x		x		x																			x	**4**

Figure Annex I - 3 List of input- / output data of the tools stored in the ArcGIS toolbox.

Light green: newly generated base data. Dark green: relative topographic values derived from topographic base data.

Data type	Data name (Normal: absolute values, *italics: optimality values*)	INPUT for Tool 0	1	2	3	4	5	6	7	8	9	10	11	12	13	14	15	16	17	18	19	20	21	22	23	24	25	26	27	frequency of use as direct input
Output Tool 3	*Near surface epikarst*					x			x		x		x			x		x								x	x			8
Output Tool 4	*Deep authochthonous red topsoil*					x	x																							2
	Deep allochthonous red topsoil					x	x																							2
	Deep red topsoil					x	x																				x			3
	Deep all topsoil					x							x																	2
	Gleysols					x	x						x														x		x	5
	Fluvisols						x							x													x			3
	Deep Gleysols					x																								1
	Red topsoil depth max. 4 meter								x							x														2
	All topsoil depth max. 4 meter																			x										1
Output Tool 5	Dominant topsoil type											x																		1
Output Tool 6	Topsoil efc mm/m								x																					1
Output Tool 7	efc first meter																		x										x	2
Output Tool 8	*High topsoil permeability*																													0
Output Tool 9	*High subsoil permeability*											x															x			2
Output Tool 10	Dominant flow processes																					x								1
Output Tool 11	*Subsoil erodibility*												x																	1
	Soil erodibility																										x			1
Output Tool 12	Groundwater surface													x			x													2
	Elevation above groundwater															x	x													2
Output Tool 13	Elevation of the basis of the Serra de Santa Helena Fm.														x															1
	Depth of Serra de Santa Helena Fm.															x														1
Output Tool 14	Weatheringdepth															x									x					2
	Softmaterial above groundwater															x	x			x										3
	Subsoil depth																													0
	Subsoil depth above groundwater																													0
	Top bedrock																x													1
Output Tool 15	Bedrock above groundwater																x													1
	Top bedrock basement																x													1
	Basement bedrock above groundwater																x	x												2
	Sete Lagoas Fm. bedrock above groundwater																	x							x					2

Figure Annex I - 4 List of input- / output data of the tools stored in the ArcGIS toolbox.

Light orange: soil parameters for geo-scientists. Medium and dark orange: aggregated information on soil properties.

Light + dark blue: geological architecture above groundwater

Data type	Data name (Normal: absolute values, *italics: optimality values*)	INPUT for Tool 0	1	2	3	4	5	6	7	8	9	10	11	12	13	14	15	16	17	18	19	20	21	22	23	24	25	26	27	**frequency of use as direct input**
Output Tool 16	Bedrock L value																	x												**1**
	Bedrock F value																	x												**1**
	Bedrock LF value																	x												**1**
	Total bedrock protection value																				x									**1**
Output Tool 17	T value (Topsoil protection value)																			x	x									**2**
Output Tool 18	S value (Subsoil protection value)																				x									**1**
Output Tool 19	P map (Protective function of overlying layers)																							x						**1**
Output Tool 20	Soil dominant flow proc. Categories																					x								**1**
	Hydrological land use classes																					x								**1**
	Slope categories																					x								**1**
	I strich map / I strich integer																						x							**1**
	High lateral flow																										x	x		**2**
Output Tool 21	I map																							x						**1**
Output Tool 22	P I map																													**0**
Output Tool 23	*Limestone thickness above GW optval.*																								x					**1**
	Optimality value overburden																								x					**1**
	Limestone resources accessibility																													**0**
Output Tool 24	*Risk of slope instability*																										x			**1**
Output Tool 25	*High topographic threshold Hortonian surf. flow b = 0.5*																										x	x		**2**
	High Topographic threshold interflow / sat. excess surf. Flow b=1																										x			**1**
	Infiltration deep lateral flow																										x			**1**
	Vulnerability to saturation excess surf. flow																										x			**1**
	Areas with possible saturation excess surf. flow																										x	x		**2**
	Vulnerabiltiy to subsurface erosion																										x			**1**
	Vulnerable headwater hollows																										x			**1**
	Steep not convex slopes near temp. aquifers																										x			**1**
	Temporary aquifer																										x			**1**
	General gully propagation vulnerability																										x			**1**
	Risk of gully initiation																										x			**1**
	Risk of gully propagation																										x			**1**
	General risk of gully erosion																										x			**1**
	Actual risk of gully erosion																										x			**1**
Output Tool 26	*Risk of contamination of surface water*																													**0**
Output Tool 27	*Favorable chemical properties*																												x	**1**
	Agricultural value																													**0**

Figure Annex I - 5 List of input- / output data of the tools stored in the ArcGIS toolbox.

Light blue: protection scores associated to the geological architecture above groundwater. Dark blue: maps for intrinsic groundwater vulnerability. Light + dark violet: simple and aggregated maps for geo-resources. Light + dark red: simple and aggregated maps for geo-hazards.

Content of the DVD

The DVD supplied with this manuscript contains:

- own input vector data listed in Annex I (file geodatabase and shapefile format)
- ArcGIS toolbox as shown in Figure 3-3.
- output parameters listed in Annex I as raster data in the format .img, which is readable by ArcGIS, Erdas Imagine and other GIS-programs
- ArcGIS map project for the most important maps in Annex II
- the manuscript of the thesis in .pdf/A format